

Immobilization of Homogeneous Oxidation Catalysts

DIRK E. DE VOS, BERT F. SELS, AND PIERRE A. JACOBS

*Centre for Surface Chemistry and Catalysis
Katholieke Universiteit Leuven
3001 Leuven, Belgium*

Homogeneous oxidation catalysts would find more widespread technological application if suitably anchored versions were available. This article discusses the anchoring strategies that have been used for 16 elements. Each element and each type of redox catalysis require a specific approach. Typical supports are oxides such as silica and alumina, zeolites, organic polymers, and activated carbon. The retention of the active metal compound within the catalyst may be based on physisorption, on the formation of covalent bonds between the metal ligand and the support, on ion exchange, or on physical entrapment. Particular attention is devoted to stability tests, which show whether catalytically active metal species are leached from the support. Many metals have the lowest affinity for a support when they are in their most oxidized or most peroxidized state. Therefore, leaching must always be investigated in the presence of the oxidant. It appears that simple adsorption of Mo, V, or W on silica or alumina, for example, does not result in heterogeneous catalysis, whereas ion exchange and covalent methods are often more reliable. In designing a catalyst immobilization method, it is preferable to know all states of the metal during the catalytic cycle; the support should have considerable affinity for all these states. The stability of a catalyst can be promoted by the presence of base, as in the case of metal ion exchanged zeolites, and by appropriate solvent choice. On the other hand, strong or chelating acids tend to cause leaching. Immobilization of a homogeneous oxidation catalyst often greatly enhances its lifetime because of the suppression of bimolecular deactivation. Moreover, unprecedented activities and selectivities may be observed, surpassing the performances of the corresponding homogeneous catalysts. © 2001 Academic Press.

Abbreviations: AD, asymmetric dihydroxylation; BPY, 2,2'-bipyridine; DMTACN, 1,4-dimethyl-1,4,7-triazacyclonane; EBHP, ethylbenzene hydroperoxide; ee, enantiomeric excess; HAP, hydroxyapatite; LDH, layered double hydroxide or hydrotalcite-type structure; mCPBA, *meta*-chloroperbenzoic acid; MTO, methyltrioxorhenium; NMO, *N*-methylmorpholine-*N*-oxide; OMS, octahedral molecular sieve; Pc, phthalocyanine; phen, 1,10-phenanthroline; PILC, pillared clay; PBI, polybenzimidazole; PI, polyimide; Por, porphyrin; PPNO, 4-phenylpyridine-*N*-oxide; PS, polystyrene; PVP, polyvinylpyridine; SLPC, supported liquid-phase catalysis; *t*-BuOOH, tertiary butylhydroperoxide; TEMPO, 2,2,6,6-tetramethyl-1-piperdinyloxy; TEOS, tetraethoxysilane; TS-1, titanium silicalite 1; XPS, X-ray photoelectron spectroscopy.

I. Introduction

Catalytic oxidation is in general less widely used in technology for the preparation of complex organic molecules than, for example, catalytic reduction. Nevertheless, technology for liquid-phase oxidation has undergone a remarkable evolution since its beginning. Early procedures involved stoichiometric organic or inorganic oxidants. The latter class of reagents, including OsO_4 and CrO_3 , has gradually become a class of true catalysts by the use of auxiliary oxidants such as peroxides, which bring the metal back to its highest oxidation state (1–3). Developments based on thorough investigations of free radical processes have enabled the conversion of these seemingly chaotic reactions into selective transformations that are the basis of numerous industrial oxidation processes (4–6). Particularly in the preceding two decades, investigations of homogeneous catalysis have revealed new mechanisms for unprecedented oxidative transformations. Examples include biomimetic porphyrin chemistry (7), enantioselective metal-catalyzed oxidations (8), organometallic oxidation by catalysts such as CH_3ReO_3 (9), and purely organic catalysis, as in the case of the dioxiranes (10).

A majority of oxidation catalysts are homogeneous, even though there is general agreement that there are many advantages offered by solid oxidation catalysts. Only in rare cases, such as epoxidation catalyzed by Ti/SiO_2 and Ti-silicalite-1 , has research produced solid oxidation catalysts for which no soluble precedent exists (11, 12). One of the fundamental reasons for the scarcity of solid inorganic oxidation catalysts is that catalytically active metals in the highest oxidation state tend to be less strongly associated with a support than in a more reduced state. Consequently, oxidizing conditions, such as caused by the presence of a peroxide, cause extraction of catalytic metal species from supports; for instance, supported Cr_2O_3 dissolves to form alkylchromate species.

Therefore, anchoring of a homogeneous oxidation catalyst ideally implies that all the different states of a metal complex during the whole catalytic cycle should be well-known and that the strategy for immobilizing the metal complex should be effective for all chemical states of the metal involved, particularly for the most highly oxidized (or peroxidized) form of the metal (e.g., octavalent Os or W or Mo with several peroxo ligands). All commonly known catalyst immobilization strategies may be employed for oxidation catalysts, including ion exchange, physisorption, covalent bonding of metal ligands, entrapment of complexes in porous matrices, and incorporation of metals into lattices. Which strategy is preferred depends on the nature of the metal catalyst and the reaction conditions. For example, Mo can occur as a neutral Mo(VI) peroxo complex in organic

solvents, but it forms anionic compounds under aqueous conditions. These two situations require different approaches. Efficient anchoring is difficult when several metal species with widely differing physical/chemical properties are simultaneously present under catalytic conditions. Particularly when these species equilibrate rapidly (e.g., between water-soluble and more organophilic compounds) it may be impossible to trap all these compounds in a single solid.

Because of the specificity of each metal as a catalyst, this chapter is organized in the simple order of Mendeleev's table. For each element, the catalysts are grouped according to the reactions they catalyze since this grouping roughly corresponds to catalytic cycles and catalytically active, oxygen-transferring species. A small section at the end is a discussion of the increasingly popular organic catalysts such as (fluoro)ketones. Catalysts are discussed only when they have a homogeneous counterpart. In the approach of this review, two questions are central:

1. Which concept is employed to immobilize the catalyst during all steps of the catalytic cycle?
2. Is there clear experimental evidence for complete immobilization, i.e., is the filtrate fully devoid of catalytic activity?

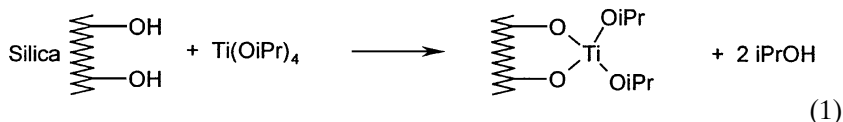
II. Titanium

Amorphous Ti/SiO₂ oxides and crystalline Ti zeolites are two classes of well-studied solid Ti catalysts (11–14). In both classes, a Lewis-acidic Ti atom is anchored to the surrounding siliceous matrix by Si–O–Ti bonds. The oxidant of choice for Ti zeolites such as titanium silicalite 1 (TS-1) and Ti-β is H₂O₂, whereas the amorphous, silica-based materials function optimally with organic peroxides such as *t*-butyl hydroperoxide (*t*-BuOOH) or ethyl benzene hydroperoxide. However, there are strictly no homogeneous analogues of these materials, and they therefore do not fit within the context of anchoring of homogeneous catalysts.

Whereas these solid catalysts tolerate water to some extent, or even use aqueous H₂O₂ as the oxidant, the use of homogeneous Ti catalysts in epoxidation reactions often demands strictly anhydrous conditions. The homogeneous catalysts are often titanium alkoxides, possibly in combination with chiral modifiers, as in the Sharpless asymmetric epoxidation of allylic alcohols (15). There has recently been an increase in interest in supporting this enantioselective Ti catalyst.

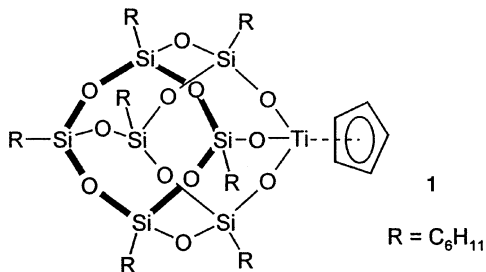
A. SOLID ACHIRAL EPOXIDATION CATALYSTS BASED
ON ORGANOMETALLIC Ti SOURCES

A classical method for preparation of a Ti/SiO₂ catalyst is to treat a silica surface with a Ti source, for example, TiCl₄ or a titanocene such as (η^5 -C₅H₅)₂TiCl₂ (16); alternatively, a mixture of Si and Ti alkoxides is hydrolyzed (17). In many cases, a subsequent calcination completely removes the organic ligands. However, it has become clear that active epoxidation catalysts are also obtained if the organic ligands around Ti are left intact or only partially removed. Ti sources that have been used include Ti(OiPr)₄, Ti[OSi(OtBu)₃]₄, the ansa-bridged titanocene [SiMe₂(η^5 -C₅H₄)₂]₂TiCl₂, and tetra-nepentyltitanium (18–26). When these precursors are used, one or more of the Ti ligands (e.g., Cl or an alkoxide) reacts with a surface silanol group, resulting in a surface-bound Ti compound with a Ti–O–Si link (19, 25):



Most of the resulting materials have been used in epoxidations with *t*-BuOOH or another organic peroxide as the oxidant. The precise pretreatment of the material critically influences its activity; for instance, Ti(OiPr)₄-treated SiO₂ has a maximum activity after activation at 413 K under vacuum (18). In a few cases, the organo-Ti-treated SiO₂ materials have also been shown to be active in combination with H₂O₂, as exemplified by materials treated with Ti(OiPr)₄ or tetra-nepentyltitanium (22, 25, 26).

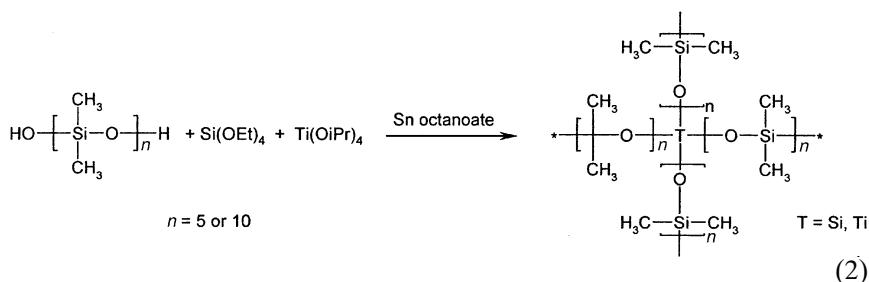
Two approaches deviate from this general scheme. First, catalysts were prepared by physisorption of the Ti silsesquioxane **1** [(c-C₆H₁₁)₇Si₇O₁₂]-Ti(η^5 -C₅H₅) in the mesopores of the MCM-41 structure (27, 28).



As a catalytic test reaction, the epoxidation of cyclooctene with *t*-BuOOH was studied. Although the complex leaches from an Al-containing MCM-41,

it seems that making the structure hydrophobic by silylation, or use of a purely siliceous MCM-41, results in retention of the complex catalyst within the mesoporous structure. All the physical/chemical evidence indicates that the structure of the Ti silsesquioxane is unaltered by the sorption; hence it seems that van der Waals interactions between the hydrophobic surface and the apolar cyclohexyl groups at the periphery of the complex keep it immobilized on the surface.

Ti has also been incorporated into elastomeric Si-containing networks. These are prepared by Sn-catalyzed polymerization of tetraethoxysilane (TEOS) and oligomeric dimethyl silanols, containing 5 or 10 Si atoms. Part of the TEOS can be replaced by Ti(OiPr)₄ or Ti tetrakis(2-ethylhexyloxyde):



The resulting gels are insoluble in toluene and contain covalently incorporated Ti; they are catalysts for epoxidation with *t*-BuOOH (29).

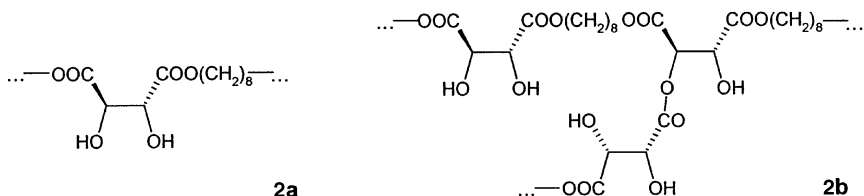
B. SUPPORTED VERSIONS OF SHARPLESS' Ti CATALYST FOR ASYMMETRIC EPOXIDATION OF ALLYLIC ALCOHOLS

The typical protocol of the catalytic Sharpless epoxidation requires 5–10 mol% of Ti(OiPr)₄, which is chelated *in situ* by an equimolar amount of enantiomerically pure dimethyl or diethyl tartrate (15). The reaction proceeds in anhydrous CH₂Cl₂, and a 4A zeolite is added to make the reaction catalytic. An early attempt by Farrall *et al.* (30) to anchor the catalyst was carried out with a tartrate monomer covalently attached to a cross-linked polystyrene resin. The enantiomeric excess (ee) values obtained (about 60%) were significantly lower than in the homogeneous reaction, for which values greater than 90% ee have been regularly achieved.

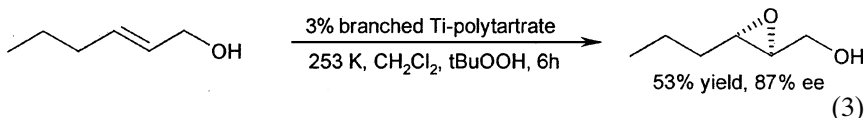
A tartrate-modified solid Ti catalyst has also been prepared starting from a montmorillonite clay (31). This clay can be pillared with Ti polycations prepared by acid hydrolysis of Ti(OiPr)₄. In the presence of tartrate ester, an allylic alcohol such as *trans*-2-buten-1-ol is epoxidized in 91% yield with 95% ee. These results are superior even to those for the homogeneous catalyst. Moreover, the reaction also proceeds in the absence of the molecular

sieve. Because the pillared clay (Ti-PILC) is dried just before the reaction, we infer that the clay may well function as a water scavenger. However, there is considerable doubt in the community as to whether the tartrate and the Ti are really firmly linked to the clay phase. The same Ti-PILC + tartrate catalyst has also been applied to enantioselective sulfoxidation (32).

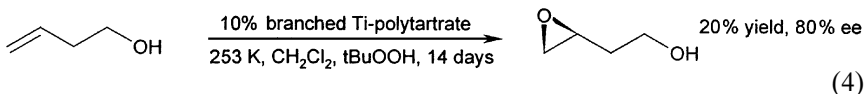
A more refined approach consists of the preparation of condensation polyesters of α,ω -diols and optically active tartaric acid as ligands for the $\text{Ti}(\text{OiPr})_4$ (33–37). A diol spacer between the tartrates that is too short decreases the ee of the epoxidation; with 1,8-octanediol, the individual binding sites are sufficiently independent for the ee to match that of the reaction with homogeneous tartrate esters. The initial, C_8 -spaced polymers were linear (**2a**) and completely soluble in CH_2Cl_2 . However, when the polyesterification is conducted at higher temperature and for longer periods, branched polyesters are obtained, in which the secondary alcohol groups of the tartrate residues function as branching points, as in **2b** (34).



After chelation of added $\text{Ti}(\text{OiPr})_4$, these branched polytartrates are largely insoluble in dichloromethane and may hence be used as solid catalysts. The ee values, for example, in the epoxidation of *trans*-2-hexen-1-ol, compare favorably with those of the homogeneous reaction:



Surprisingly, the branched Ti-polytartrates yield considerable ee values for *cis*-allylic and homoallylic alcohols, even though the reactions take several days or even weeks (36). Nevertheless, this is a remarkable result since Sharpless' homogeneous protocol is not very effective with *cis*-allylic or homoallylic alcohols:



Although the recovery of the polytartrate ligand by filtration amounts to about 90%, the Ti recovery levels are significantly lower (34). The fact that part of the Ti remains in the solution means that the binding of Ti to the anchored ligand is less efficient than it is to the ligand in solution. It seems unlikely that the polymeric nature of the ligand allows the formation of the same 2:2 Ti:tartrate complexes that are formed in solution. Moreover, no recycle experiments have provided evidence that the catalyst is reusable.

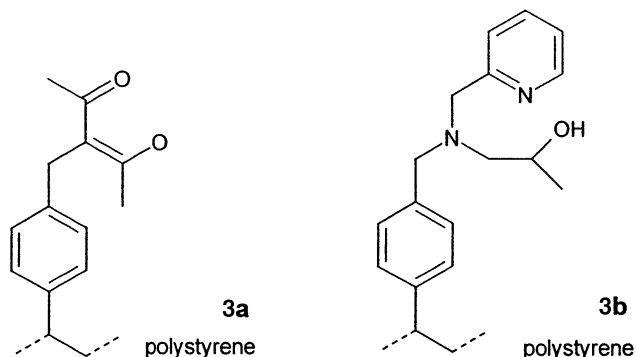
III. Vanadium

Vanadium catalysts, in combination with peroxides, are most useful for the epoxidation of allylic alcohols or simple olefins and, at slightly elevated temperature, for the hydroxylation of alkanes and aromatic compounds (333–373 K). Although the epoxidation is based on a purely Lewis acid mechanism, with V being present as V(V) throughout the catalytic cycle, V-catalyzed hydroxylation generally involves one-electron redox reactions, with the oxidation state of V alternating between 4 and 5 (3). The exact nature of the oxidizing species is often not clear. High valent V can occur in a cation (e.g., VO^{2+}), an anion (e.g., VO_4^{3-}), and a neutral compound, as in vanadyl acetylacetonate. Because such species are easily interconverted upon interaction with various oxidants ($t\text{-BuOOH}$ and H_2O_2) and under various conditions (dry or aqueous and various values of pH), one has to be extremely cautious in claiming that a V oxidation catalyst is stably anchored to a support. In early reports, the evaluation of whether the catalyst was actually fully anchored may have been less rigorous than is required.

A. V EPOXIDATION AND ALKANE HYDROXYLATION CATALYSTS

1. Functionalized Polymers as Supports

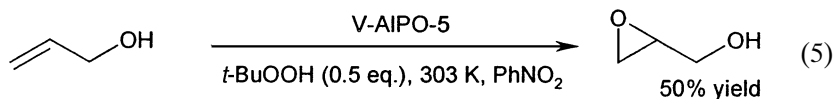
In early reports, VO^{2+} ions were anchored to functionalized polymers (38–40). For example, in the absence of a peroxide, the vanadyl ion (VO^{2+}) is easily retained on polyvinylpyridine or on polymers with ethylenediamine functions (38). Unfortunately, when reactions were performed with $t\text{-BuOOH}$, only part of the activity was associated with the solid, and gradual leaching of V occurred. Strong ligand fields, as in the immobilized ethylenediamine, were slightly more effective than other ligands in retaining the V. Vanadyl ions were also anchored to a cross-linked polystyrene, functionalized with acetylacetonate ligands (**3a**), or with a hydroxypropylated aminomethylpyridine (**3b**) (39, 40).



The materials catalyze the epoxidation of cyclohexene with *t*-BuOOH. Although the catalytic activity is more stable for polymer-supported V than for a homogeneous catalyst, the activity decreased as a result of loss of V from the support (39, 40).

2. Inorganic Supports

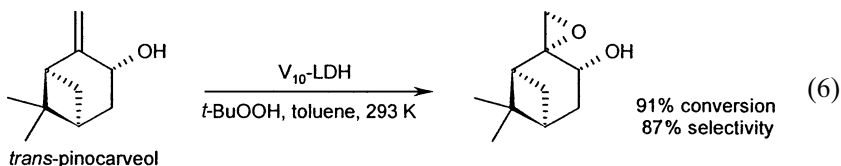
V has been incorporated in the framework of molecular sieves, for example, V-AIPO-5 and V-silicalites. With V-AIPO-5, epoxidation of allylic alcohols proceeds with excellent selectivity (41):



However, it has been shown clearly that V-AIPO-5 and related zeolite materials are prone to leaching, even if the extent of the leaching likely depends on the reaction conditions (42, 43). V has been entrapped as a complex in zeolites, usually starting from a VO^{2+} -exchanged zeolite NaY. Ligands that have been used are bipyridine (44), the Schiff bases salen and (2-hydroxyphenyl)salicylideneimine (45, 46), and 2-picolinate (47). Invariably, the use of these materials led to varying degrees of release of V during epoxidation or alkane hydroxylation, whatever the reaction conditions (46, 47).

In all previous cases, V was incorporated in a monomeric form. There are also methods to introduce oligomeric V into inorganic structures. Choudary *et al.* (48) advocated the use of a montmorillonite, pillared with V oligomers (V-PILC). V-PILC catalyzes the epoxidation of allylic alcohols with *t*-BuOOH. Oligomeric V is also used to pillar anionic clays such as layered double hydroxides (LDHs) with decavanadate anions ($\text{V}_{10}\text{O}_{28}^{6-}$) (49).

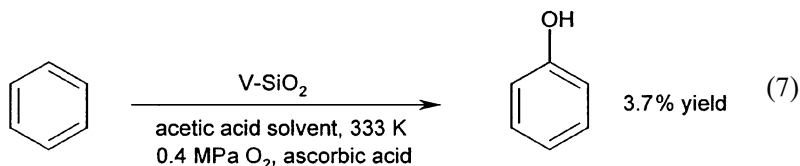
Decavanadate is easily prepared by adjusting the pH of a NaVO_3 solution to 4.5. The negatively charged pillars are retained essentially by electrostatic attraction to the positively charged brucite-type sheets of the LDH. Each V atom in a decavanadate pillar is linked by at least five V–O–V bonds to the rest of the pillar. Thus, as long as one works under anhydrous conditions, it is unlikely that any of the V is released from the decavanadate–LDH (V_{10} –LDH) structure. Even complicated allylic alcohols (e.g., those from the group of the terpenes) are epoxidized in high yield:



This material successfully withstands a series of tests for successful anchoring, for example, (i) no activity in the clear filtrate, (ii) no further conversion on addition of new oxidant and reactant, and (iii) full activity of V and no release of active V on preexposure of the catalyst to *t*-BuOOH. In contrast, in comparative tests, VO^{2+} on polyvinylpyridine, V–AlPO–5, and V on SiO_2 underwent varying degrees of leaching (49).

B. V-CATALYZED HYDROXYLATION OF AROMATIC COMPOUNDS

O_2 can be used as an oxidant for the benzene-to-phenol conversion, provided that a reductant such as ascorbic acid is used. Various supported V catalysts were used, for example, V/ SiO_2 and V/ TiO_2 :



In all cases, some of the V was released into solution; this amount can be decreased by cosupporting Cu on the catalyst (50). Kumar *et al.* (51) used a polymer-bound Schiff base to chelate VO^{2+} ; the resulting polymer was active for benzene hydroxylation with H_2O_2 :



However, no figures were given to assess the degree of leaching or the percentage of activity retained by the solid in consecutive runs. During reaction, the V was oxidized to EPR-silent V(V), but neither the precise nature of this species nor its interaction with the support was investigated.

C. V-CATALYZED ALCOHOL OXIDATION

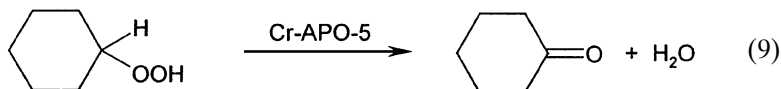
Rohan and Hodnett (52) showed that V supported on TiO₂ with H₂O₂ catalyzes the oxidation of 2-butanol to give methyl ethyl ketone, but the activity is largely attributed to dissolved V.

IV. Chromium

A. ALCOHOL OXIDATION: OXIDATION OF C–H BONDS, PARTICULARLY IN ALLYLIC AND BENZYLIC POSITIONS

Chromium is useful as an oxidation catalyst, especially with *t*-BuOOH or O₂ as the oxidant. When a Cr precursor [e.g., a Cr(VI) compound] is used, alcohols can be oxidized to ketones with *t*-BuOOH. Moreover, CH₂ groups with relatively weak C–H bonds, for instance, in allylic or benzylic positions, are easily converted to carbonyl groups in the presence of Cr and *t*-BuOOH or O₂. Often these reactions are free radical autoxidations, in which alkylhydroperoxide and alcohol products react further to form ketones (2, 4, 6). Relatively little is known about the active Cr species in these reactions, but it is plausible that high valent, neutral Cr compounds such as alkylchromates(VI) are involved.

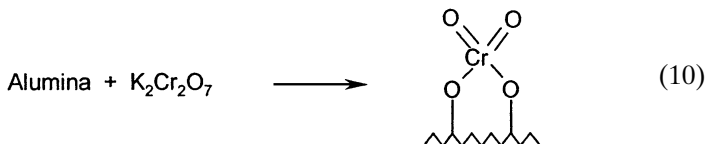
Generally, the issue of whether a truly solid Cr catalyst has been created for the aforementioned reactions is unresolved. This point is illustrated most clearly by all the work that has been devoted, in vain, to Cr molecular sieves (53–57). Particularly the silicates Cr-silicalite-1 and Cr-silicalite-2 and the aluminophosphate Cr-AIPO-5 have been investigated. These materials have been employed, among others, for alcohol oxidation with *t*-BuOOH, for allylic (aut)oxidation of olefins, for the autoxidation of ethylbenzene and cyclohexane, and even for the catalytic decomposition of cyclohexyl hydroperoxide to give mainly cyclohexanone:



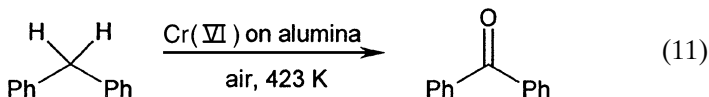
Although Cr³⁺ as such forms stable associations with the framework of the silicalite or aluminophosphate, the presence of organic peroxides, whether

added deliberately or formed during the reaction, causes leaching of Cr into solution. It has been clearly demonstrated that leaching of even as little as 0.3% of the Cr is sufficient to cause a completely homogeneous catalytic reaction (56). This result implies that multiple successful reuses of the solid material do not guarantee the truly heterogeneous nature of the catalysis (57). The use of Cr redox molecular sieves in liquid-phase reactions has been abandoned.

Alternative approaches have been proposed over the years. In none of these cases is there sufficient experimental evidence for truly heterogeneous catalysis. Fréchet *et al.* (58) used a polyvinylpyridinium (PVP) material for supporting chlorochromate $[\text{Cr(IV)O}_2\text{Cl}^-]$ or dichromate $[\text{Cr(VI)}_2\text{O}_7^{2-}]$. Cr^{3+} can be immobilized by simple ion exchange on polymers such as Nafion or on a Y zeolite (59, 60). However, it is doubtful whether these methods ensure complete Cr anchoring when the material is brought into contact with oxidants. Clark *et al.* (61) advocated the use of alumina-anchored dichromate. Particularly when a neutral alumina is used, surface-anchored species are formed:

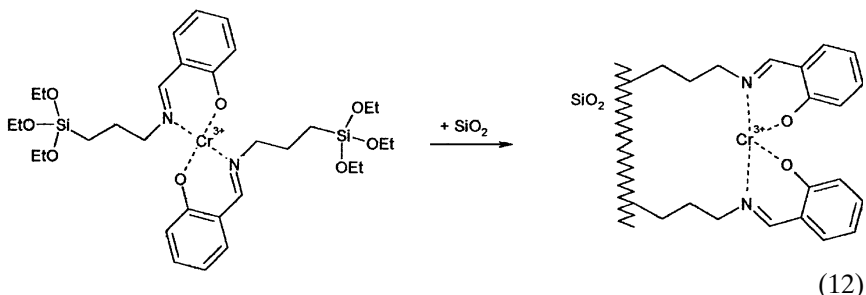


In the presence of air at 423 K, such materials catalyze the autoxidation of neat hydrocarbons, for example, diphenylmethane:



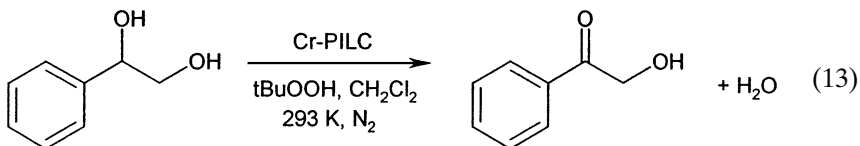
Alcohols may be oxidized in a similar way. However, these reactions strongly resemble those reported for Cr molecular sieves, and a small concentration of Cr in solution may well account for most of the observations of catalysis. Binary molybdenum-chromium oxides supported on alumina have been used in the autoxidation of cyclohexene with O_2 and *t*-BuOOH as an initiator (62). This is a complex reaction in which uncatalyzed and Cr-catalyzed oxidation combine to yield 2-cyclohexen-1-one, 2-cyclohexen-1-ol, and 2-cyclohexenyl hydroperoxide; the Mo compound can use the hydroperoxide formed *in situ* as an oxidant for the epoxidation of cyclohexene. Although much lower oxygen consumption was observed for the reaction filtrate than for the suspension, it is unclear how the Cr is held by the oxide.

In a later development, Cr^{3+} was chelated by Si-functionalized Schiff bases, and the whole complex was chemically bound to a silica surface (63):



The materials showed some activity in the autoxidation of alkylaromatics such as ethylbenzene at 403–418 K, even though at these temperatures there is a considerable blank background reaction. The stability of a salicylidene imine under the conditions of high-temperature autoxidation is questionable in any event.

Choudhary *et al.* (64–66) used a montmorillonite clay pillared with cationic polyoxochromium oligomers (Cr-PILC). The pillars were prepared by hydrolysis of chromium nitrate using Na_2CO_3 as the base. After mixing of the pillaring solution with the clay suspension, X-ray diffraction (XRD) gave evidence that the structure was expanded, with an interlayer spacing of 1.4 nm. Obviously, this material contains a large amount of Cr, up to 2.5 mmol g^{-1} . It is significant that the binding mode of Cr in such a material is clearly different from that of each of the preceding examples. One might anticipate that as long as one works under strictly anhydrous conditions, the pillars might well preserve their structural integrity and keep the Cr within the solid material. Reactions reported with Cr-PILC include the allylic oxidation of olefins, the ketonization of benzylic compounds, the oxidative deprotection of allyl and benzyl ethers to give ketones, and the oxidative deprotection of allyl amines leading to the amines. These reactions are usually performed with anhydrous *t*-BuOOH in CH_2Cl_2 at mild temperatures. In alcohol oxidation, secondary are preferred over primary alcohols (66):



However, in the latter reaction water is formed, and this may eventually lead to pillar desintegration and release of Cr.

Cr^{3+} can also be integrated into the structures of layered double hydroxides. A mixed oxide, prepared by calcination of ZnCr-LDH-CO_3 , was used in combination with *t*-BuOOH for the ketonization of alkyl and of benzyl pyridines and for the oxidation of benzyl amines to give Schiff bases (67, 68). In contrast to MgAl-LDHs , for example, these materials display hardly any basicity so that base-catalyzed side reactions such as aldol condensations are avoided.

In summary, there is a lack of a clear concept that would allow stable anchoring of the catalytically active forms of Cr for oxidation of alcohols or hydrocarbons with *t*-BuOOH or O_2 . Immobilization of Cr by structural incorporation or ion exchange before addition of the oxidant is obviously not a guarantee for obtaining a heterogeneous catalytic process.

B. Cr-CATALYZED EPOXIDATIONS

Cr^{3+} chelated in planar salen-type ligands is a catalyst for olefin epoxidation with single oxygen donors such as PhIO. A Cr(V)=O(salen)^+ compound transfers the active oxygen atom to the olefin (69). Cr remains firmly bound by the ligand throughout the catalytic cycle, and this may offer an opportunity to immobilize a Cr epoxidation catalyst. However, in a report on immobilization of such a Cr(salen)^+ complex in Al-containing MCM-41, it was stated that the complex is simply physisorbed on the support (70); it is doubtful whether this provides a stable link. Moreover, the relevance of Cr(III)(salen)^+ as an oxidation catalyst is limited since other metallosalen complexes are far more effective.

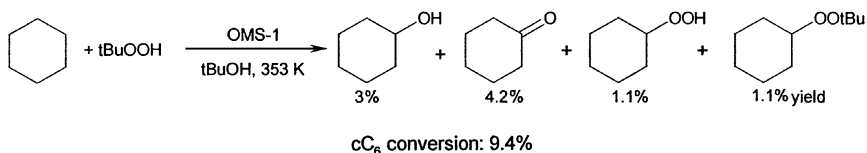
V. Manganese

Mn catalysts are useful in one- and two-electron redox processes. Reactions of immobilized Mn porphyrins and phthalocyanines are discussed later with the corresponding Fe complexes.

A. SOLID Mn CATALYSTS FOR ONE-ELECTRON REDOX REACTIONS

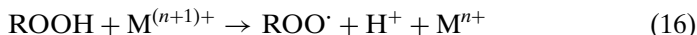
A new class of Mn redox solids are the octahedral molecular sieves (OMS). OMS-1, the synthetic analog of the mineral todorokite, consists of MnO_6 octahedra linked by corners and edges to form unidimensional channels with a diameter of 0.69 nm. These materials are prepared by controlled sympportionation of Mn^{2+} and MnO_4^- . As indicated by the formula of OMS-1, $\text{Mg}_{0.98-1.35}^{2+}\text{Mn}_{1.89-1.94}^{2+}\text{Mn}_{4.38-4.54}^{4+}\text{O}_{12} \cdot n\text{H}_2\text{O}$, the material contains lattice Mn in different oxidation states (71). Moreover, there is a considerable cation exchange capacity. OMS-1 has been employed in the oxidation of

liquid-phase cyclohexane with *t*-BuOOH as the oxidant (72). Although cyclohexyl hydroperoxide is an important product at 333 K, it is decomposed at higher temperatures to yield cyclohexanol and predominantly cyclohexanone and *t*-butyl cyclohexyl perether:



(14)

Obviously, this product distribution reflects a free radical reaction in which Mn intervenes as a Haber–Weiss catalyst for peroxide homolysis:



Leaching and reuse tests indicate that OMS-1 is fully insoluble. Because the Mn in the todorokite easily changes its valence, one can conceive that lattice Mn²⁺/Mn³⁺ or Mn³⁺/Mn⁴⁺ couples are involved. Because the Haber–Weiss reaction normally takes place in the primary coordination sphere of the metal, the peroxide must displace one of the framework O²⁻ ions in order to interact with lattice Mn. On the other hand, even if some of the Mn leaves its lattice positions, it may still remain within the todorokite structure as an exchanged cation. Such a double-immobilization mechanism seems to provide a safe means to keep the catalysis heterogeneous. The OMS-1 structure has been doped with several other transition metals (e.g., Fe, Co, Cr, and Cu); however, this doping leads only to marginal differences from the OMS-1 material itself. The oxidation of saturated alkanes with *t*-BuOOH is also possible in the presence of Mn²⁺-exchanged clays (73). An example of a suitable catalyst is a Mn²⁺-exchanged fluorotetrasilicic mica. Even Mn-montmorillonite is active, but only when zeolite 4A is added as a drying agent. This may mean that coordination of the peroxide on Mnⁿ⁺ is crucial in the catalysis. However, no data characterizing the heterogeneity of the catalysis were provided.

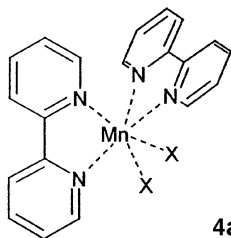
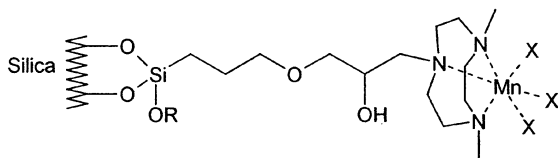
The combination of Mn and H₂O₂ is very effective for catalytic bleaching (74). As a laundry bleaching agent, H₂O₂ has numerous advantages over hypochlorite, but H₂O₂ requires high temperature to acquire bleaching activity, unless a bleach activator, typically a Haber–Weiss catalyst, is used. Dissolved Mn is environmentally harmless, but it may cause cloth staining upon oxidation to Mn³⁺ or Mn⁴⁺. Such problems are solved by immobilization of the Mnⁿ⁺ on zeolite A. (Zeolite A is added to laundry powders in any

event as a detergent builder). Whatever the Mn oxidation state, the selectivity of the exchange always favors the immobilization of the Mn. Moreover, laundry operations typically are carried out at a pH of about 10, which prevents loss of Mn from the zeolite through competitive proton exchange.

B. NON-HEME-TYPE Mn CATALYSTS IN TWO-ELECTRON, ACHIRAL REDOX PROCESSES

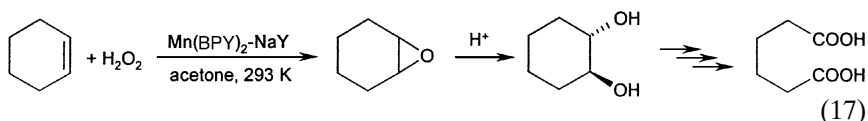
Apart from the catalytic properties of the Mn–porphyrin and Mn–phthalocyanine complexes, there is a rich catalytic chemistry of Mn with other ligands. This chemistry is largely bioinspired, and it involves mononuclear as well as bi- or oligonuclear complexes. For instance, in Photosystem II, a nonheme coordinated multinuclear Mn redox center oxidizes water; the active center of catalase is a dinuclear manganese complex (75, 76). Models for these biological redox centers include ligands such as 2,2'-bipyridine (BPY), triaza- and tetraazacycloalkanes, and Schiff bases. Many Mn complexes are capable of heterolytically activating peroxides, with oxidations such as Mn(II) \rightarrow Mn(IV) or Mn(III) \rightarrow Mn(V). This chemistry opens some perspectives for alkene epoxidation.

In solution, bis-bipyridine complexes of Mn (**4a**) easily form dinuclear complexes, in which the two Mn nuclei are linked through μ -oxo or μ -hydroxy ligands. These complexes are highly active catalysts for the decomposition of H₂O₂.

**4a**X = available, *cis*-positioned coordination sites**4b**

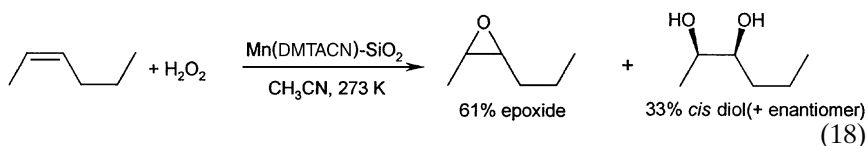
The formation of these dinuclear complexes can be impeded by entrapment of the Mn(BPY)₂²⁺ complexes in the structure of zeolite Y. Preferably, Mn(BPY)₂²⁺ is assembled via “ship-in-a-bottle” synthesis in zeolite Y, through BPY adsorption on a NaY zeolite partially exchanged with Mn²⁺. Because a single zeolite Y supercage can contain only one Mn(BPY)₂²⁺ complex, the formation of dinuclear complexes is impossible for steric reasons. The reaction of H₂O₂ with the zeolite-entrapped Mn(BPY)₂²⁺ complex does not lead to the same vigorous peroxide decomposition as occurs in solution. Instead, H₂O₂ is heterolytically activated on the Mn complex with *cis*-bipyridine ligands to form a Mn(IV)=O or Mn(V)=O species. The latter is a

particularly effective catalyst for epoxidation. Thus, the entrapment in zeolite cages changes the nuclearity of the complex from 2 to 1 and turns a peroxide decomposition catalyst into a useful epoxidation catalyst (77). Because the zeolite Y contains some residual acidity as a consequence of the Mn exchange, the epoxides are labile. Only with a $\text{Mn}(\text{BPY})_2^{2+}\text{-NaX}$ zeolite, with lower acid strength, can high epoxide selectivities be obtained. When some acidity is deliberately introduced into the zeolite, the epoxide is transformed into a *trans* diol, and further oxidation can ultimately lead to α, ω -diacids such as adipic acid:



Because mononuclear $\text{Mn}(\text{BPY})_2^{2+}$ complexes are positively charged, they may also be immobilized by ion exchange in the pores of an Al-containing MCM-41 (78).

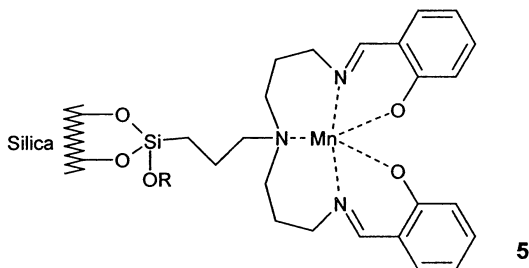
Competition between H_2O_2 disproportionation and selective olefin oxidation is also the major issue with the Mn complexes of 1,4,7-trimethyl-1,4,7-triazacyclononane (TMTACN). In solution, the epoxidation can be favored by addition of coligands such as oxalate or by working in acetone, which forms perhemiketals with H_2O_2 at subambient temperature (79, 80). An alternative method for suppressing the H_2O_2 decomposition is covalent anchoring of the dimethyltriazacyclononane (DMTACN) to SiO_2 by use of a glycidyloxypropyl linking group (**4b**) (81, 82). Curiously, such site isolation not only strongly improves yields based on peroxide but also opens a new mechanistic route, with direct formation of *cis* dihydroxylation products from olefins. For example, from *cis*-2-hexene, apart from the *cis* epoxide, a *cis* diol is formed with 33% selectivity:



As was demonstrated by addition of epoxide under reaction conditions, the epoxide is not the precursor of the *cis* diol. The *cis* dihydroxylation is probably a two-step reaction, first with addition of a H_2O_2 -derived oxygen atom to the double bond, followed by insertion of a Mn-coordinated oxygen atom (water or OH^-). It is clear that the availability of free coordination sites in *cis* positions on the Mn (**4b**) is important for understanding the formation of *cis* dihydroxylated products. This is the first example of a *cis* dihydroxylation that is catalytic and uses Mn; the route is therefore an alternative to stoichiometric permanganate reactions or to catalytic methods with more

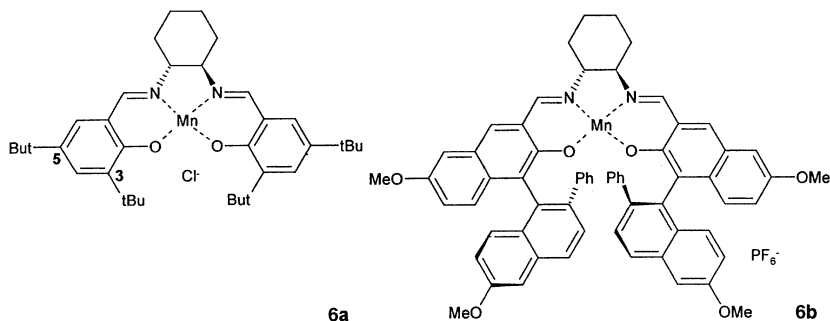
expensive or toxic metals, such as Ru and Os (81). An alternative method for immobilizing Mn–triazacyclononane complexes is by entrapment in a zeolite; the resulting material is a useful catalyst for epoxidation with H_2O_2 , provided that acetone is used as a solvent (83, 84).

A popular method for immobilizing Schiff base complexes involves covalent linking. Sutra and Brunel (85) constructed a pentadentate Schiff base in the pores of a mesoporous silicate, starting from grafted aminopropyl groups. After complexation with Mn, material **5** catalyzed the epoxidation of cyclohexene with PhIO in 58% selectivity.



C. Mn CATALYSTS FOR ENANTIOSELECTIVE EPOXIDATION

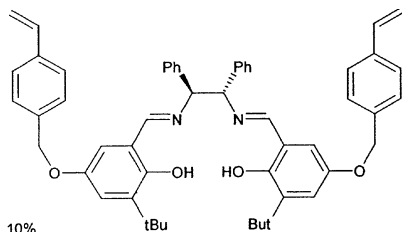
The Jacobsen–Katsuki Schiff base Mn complexes (**6a** and **6b**) are the most advanced catalysts for enantioselective epoxidation of double bonds. With the typical reactants, *cis* disubstituted and trisubstituted aromatic olefins, ee values up to 98% are achieved, even if the total number of turnovers is quite limited. In Jacobsen's complex **6a**, particularly the bulky *t*-butyl substituents at positions 3 and 5 of the aromatic ring are crucial in directing the reactant and obtaining high ee values (86).



Since the affinity of the Schiff base ligand for the Mn is extremely high, Mn immobilization is largely not an issue, provided that a reliable method is used to anchor the ligand irreversibly to a support. The real challenge is to create a catalyst with chemoselectivity and enantioselectivity that matches or even surpasses the results representing the homogeneous catalysts (87, 88).

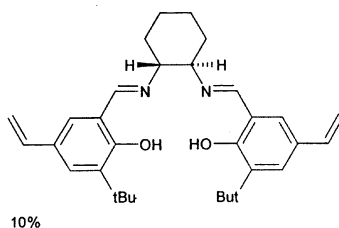
1. Covalent Linking of Chiral Schiff Bases to Polymeric Supports

Covalent linking remains the most popular approach. The important variables are the degree of cross-linking of the polymer, the chemical nature of the backbone, the location and number of attachment points on the complex (one or two), and the presence of a spacer between the support and the complex. Since reviews of this subject have appeared recently, only the most illustrative examples are discussed (87, 88).



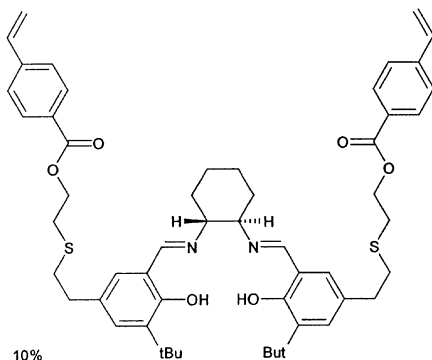
90% ethylene glycol dimethacrylate

7a



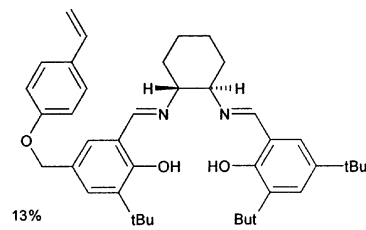
75% styrene
15% divinylbenzene

7b



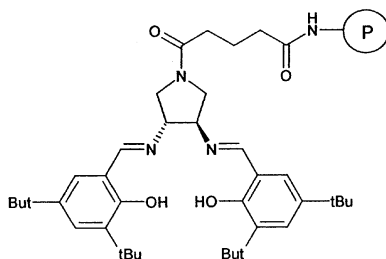
75% styrene
15% divinylbenzene

7c



19% methyl methacrylate
68% ethylene glycol dimethacrylate

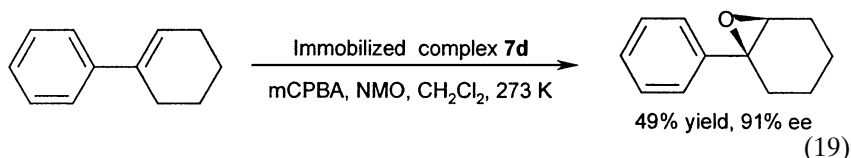
7d



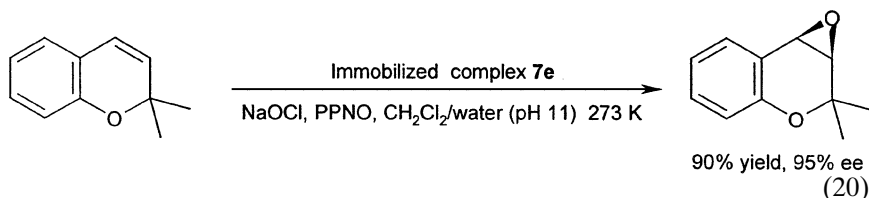
7e

In catalysts **7a–7c**, the complex is attached by its two aromatic rings to the polymer backbone. Catalyst **7a** has a degree of cross-linking of 90%, and the pronounced structural rigidity of the polymer results in disappointing ee values (89). Better results are obtained when the degree of cross-linking is decreased, as in **7b**, and when a spacer group is introduced between the complex and the polymer backbone (90, 91). With catalyst **7c**, *cis*- β -methylstyrene was epoxidized with 87% chemical yield and an ee of 62%.

A one-sided binding of the complex to the support resulted in further improvements (92). This requires synthesis of nonsymmetric salen-type ligands, which is complicated by the tendency of such ligands to equilibrate to give mixtures containing symmetric Schiff bases. Excellent results were obtained with monomer **7d**, diluted in a methacrylate polymer, by using a combination of meta-chloroperbenzoic acid (mCPBA) and *N*-methyl-morpholine-*N*-oxide (NMO) as the oxidants:



Instead of attachment of the complex by its aromatic rings, the asymmetric diamine moiety was used as an anchoring point (93). With the pyrrolidine–salen type complex **7e**, high yields and ee values were observed in the epoxidation of chromene derivatives:

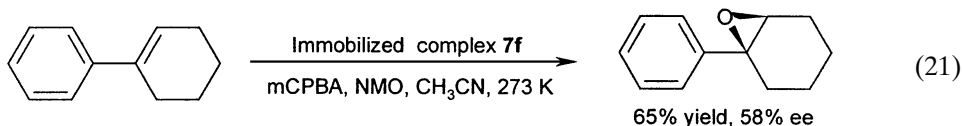


The oxidants were mCPBA and 4-phenylpyridine-*N*-oxide (PPNO). However, the catalyst was partially decomposed under reaction conditions, as was evidenced by the loss of the dark brown complex color.

2. Covalent Anchoring to Inorganic Supports

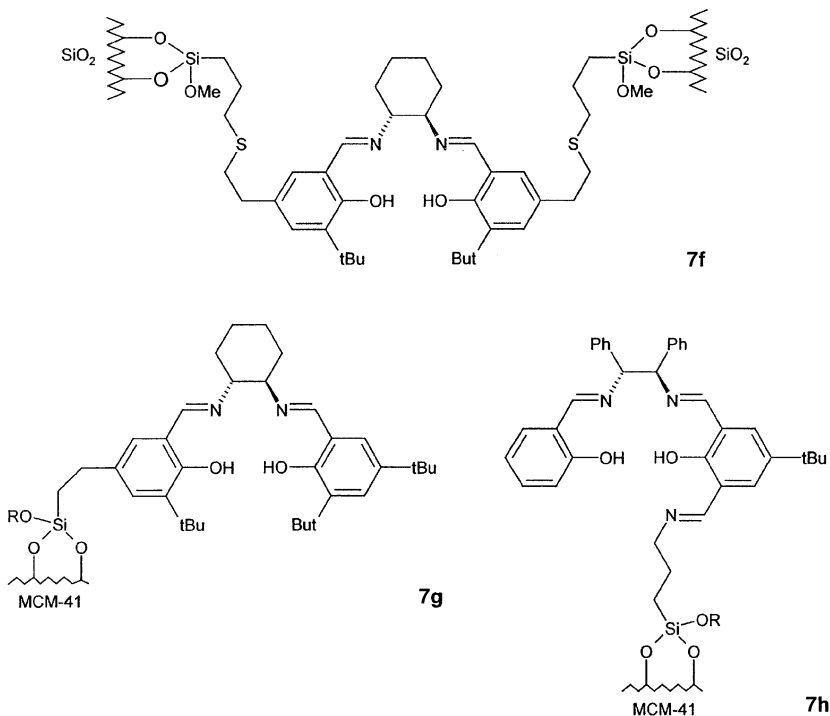
Inorganic supports have been used less, but they have undeniable advantages, such as the relatively high oxidative stability of the support. A first attempt was made with salen complexes that are vinyl functionalized at both aromatic rings. By coupling in a thioether, catalyst **7f** is obtained. For

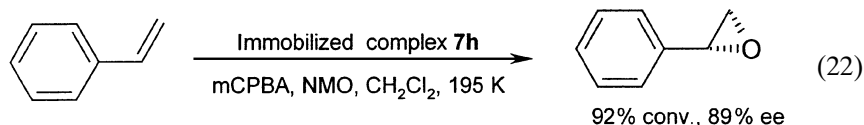
phenylcyclohexene, the ee is considerably lower than with the best polymer catalysts (94):



A one-sided attachment of a vinyl-functionalized salen monomer to an MCM-41 material was reported by Janssen (95). In the epoxidation of 1-phenylcyclohexene with PhIO in acetonitrile, the Mn-functionalized structure **7g** gave an ee of 75%, which is the same as for the soluble Jacobsen complex and considerably higher than that obtained with **7f**. Moreover, the chemoselectivity, the olefin conversion, and the enantioselectivity remained unchanged over four consecutive cycles.

A sequential synthesis, starting from aminopropyl-modified MCM-41 and 2,6-diformyl-4-*tert*-butylphenol, was used to obtain the catalyst precursor **7h**; with the Mn-containing material, an ee of 89% was observed at 92% conversion in the epoxidation of styrene with NMO at 195 K (96):





This is an unexpected result, since one of the phenyl groups in the immobilized complex is devoid of bulky substituents.

3. Methods for Noncovalent Immobilization

Salen-type complexes have been immobilized by coordinative bonding on polyvinylpyridine-type polymers (97). However, ee values did not exceed 46%. The retention of the complex on the polymer was reported to be excellent.

Zeolites have also been used to entrap chiral salen-type ligands by ship-in-a-bottle synthesis. Zeolite Y (FAU topology) and the hexagonal faujasite with EMT topology have been used (98, 99). The cages in EMT are more spacious than those in FAU. Nevertheless, in both cases, less bulky substituents were used to allow incorporation of the complex in the cage. For FAU, protons were used at positions 3 and 5, whereas for EMT only the 5-tBu group was replaced by a methyl group. The EMT approach is apparently more rewarding, with a surprising 88% ee in the epoxidation of *cis*- β -methylstyrene with NaOCl as the oxidant (99). However, the reuse possibilities offered by this material are limited, probably because of oxidative degradation of the complex. Similar problems were encountered with chiral Mn–salen complexes exchanged on laponite or on Al-MCM-41 (100, 101). In these cases, the small charge of the monocationic Mn(III)–salen complex seems sufficient to guarantee retention of the complex. Particularly with the clays, incorporation of the Schiff base complexes in the structure was evidenced by an increased basal spacing.

Hutchings *et al.* (102, 103) synthesized enantioselective Mn catalysts by adsorption of chiral salen ligands on Mn-exchanged Al-MCM-41 and used the materials in selective epoxidation of *cis*-stilbene with PhIO. Although the simplicity of this approach is appealing, reuse of the material in a second run led to a dramatic decline of the epoxide yield from 69 to 18%, and of the ee of the *trans* epoxide from 70 to 30%.

VI. Iron

A. Fe AND Mn PORPHYRIN AND PHTHALOCYANINE CATALYSIS

Mn porphyrins and Mn phthalocyanines are discussed together with their Fe counterparts because the catalytic chemistry and the immobilization

strategies are similar. There are many proven methods for immobilization of such porphyrins (Por) and phthalocyanines (Pc) on a variety of organic or inorganic supports (Table I):

- Since Lewis bases such as pyridine and imidazole have high affinities for the axial coordination site in Por and Pc chelates, the complexes are well retained on immobilized ligands, for example, imidazole covalently linked to SiO₂ (104–106). Moreover, this axial coordination often improves the catalytic activity and selectivity, as in the Mn porphyrin-catalyzed epoxidation with H₂O₂ (7, 107). However, immobilization by coordinative binding can be quite sensitive to solvent effects and competitive binding of ligands.

- Ion-exchange methods are simple and reliable; even the small negative charge of a silica surface is sufficient to retain a cationic porphyrin (104, 108–115).

- Attachment of a trialkoxy-Si group to the macrocycle leads to a precursor that can be mixed with TEOS in a sol-gel preparation; this leads to a matrix with superior oxidative stability (116).

- Covalent bonds are the most stable links to a surface, but they may necessitate substantial chemical modification of both the macrocycle and the support (117–120).

- Even simple adsorption can be sufficient to immobilize Fe macrocycles (121, 122). For instance, van der Waals interactions occur between the π system of a planar phthalocyanine and the aromatic zones in carbon black (121).

- Metal phthalocyanines are easily synthesized by vapor-phase condensation of four molecules of dicyanobenzene in the presence of molecular sieves such as faujasites or AlPO-5 (123–126). This results in direct entrapment of the macrocycle inside the molecular sieve's channels and cages. There are also reports of ship-in-a-bottle synthesis of porphyrins in zeolites, but since porphyrin synthesis requires a mixture of pyrrole and an aldehyde instead of a single compound, porphyrin synthesis is a much less clean process than phthalocyanine preparation (127). Alternatively, soluble porphyrins or phthalocyanines can be added to the synthesis gel of, for example, zeolite X. This also results in entrapped complexes (128).

All these approaches lead to materials in which the mobility of the complexes is very much reduced in comparison with solutions. Often, truly site-isolated metal centers are obtained. Moreover, many approaches allow careful control of the metal complex content of the support.

Simple Fe or Mn salts are active mainly for one-electron redox processes, such as the Fenton free radical decomposition of H₂O₂. In contrast, Fe and Mn porphyrins and phthalocyanines [M(Por) and M(Pc)] are able to

TABLE I
Strategies for Immobilization of Phthalocyanine and Porphyrin Complexes

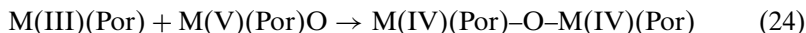
Strategy	Support	Modification to porphyrin, phthalocyanine	Reference
Coordination	Imidazole-modified cross-linked polystyrene; pyridine-modified silica	—	Cooke <i>et al.</i> (104), Gilmartin and Lindsay Smith (105), Miki and Sato (106)
Cation exchange	Montmorillonite, silica	4- <i>N</i> -methylpyridiniumyl-substituted porphyrin	Cooke <i>et al.</i> (104), Battioni <i>et al.</i> (108), Bartoy <i>et al.</i> (109)
	Zeolites	4- <i>N</i> -methylpyridiniumyl-substituted porphyrin	Chen (110)
	Polyacrylate, sulfonated polymers	4- <i>N</i> -methylpyridiniumyl-substituted porphyrin	Lindsay Smith and Lower (111)
Anion exchange	Amberlite IRA 900	Sulfonated porphyrins, phthalocyanines	Sorokin and Meunier (112), Mirkhani <i>et al.</i> (113)
	Polyvinylpyridinium polymer		Labat and Meunier (114)
	Layered double hydroxides		Chibwe and Pinnavaia (115)
	Siliceous framework	(EtO) ₃ Si-modified porphyrin	Battioni <i>et al.</i> (116)
Sol-gel preparation	Tyrosine-based isocyanide polymer	4-(3- <i>Br-<i>n</i></i> -propoxy)phenyl-substituted porphyrin	van der Made <i>et al.</i> (117)
Covalent bonding	Chloromethylated polystyrene	4-aminophenyl-substituted porphyrin	Tangestaninejad and Mirkhani (118)
	NH ₂ -propyl or Cl-propyl modified MCM-41	-SO ₂ Cl- or -NH ₂ -substituted phthalocyanine	Ledon and Brigandat (119), Sorokin and Tuel (120)
Adsorption	Carbon black	Planar phthalocyanines	Parton <i>et al.</i> (121)
	MCM-41	—	Ernst <i>et al.</i> (122)
Encapsulation	Zeolites, aluminophosphates, <i>in situ</i>	(Nitro)phthalocyanines	Meyer <i>et al.</i> (123), Parton <i>et al.</i> (124–126)
	Faujasite zeolites, template method	Perfluorophthalocyanines	Balkus <i>et al.</i> (128)

activate “single oxygen donors” (XO), such as H₂O₂, *t*-BuOOH, PhIO, or NaOCl in a two-electron redox reaction:



This reaction is quite sensitive to effects of ligands, solvents, etc; for example, H₂O₂ reacts with Mn(III)-tetrakis(2,6-dichlorophenyl)porphyrin to form only a Mn(V)=O species in the presence of an axial imidazole ligand (107). These Fe(V) and Mn(V) oxo species can then convert an olefin into an epoxide, an alkane into an alcohol, etc.

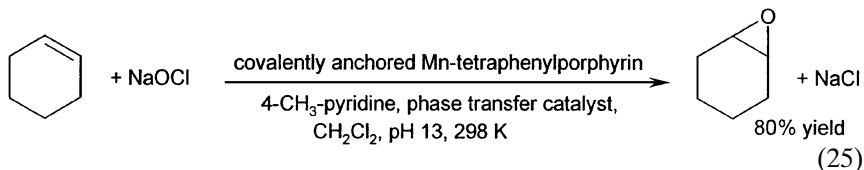
The catalytic chemistry of immobilized Mn and Fe phthalocyanines and porphyrins largely parallels that of the dissolved complexes. However, the homogeneous complexes tend to react with each other, leading to irreversible oxidative damage. Moreover, inactive μ -oxo dimers are formed in the following reaction:



Such deactivation reactions are almost impossible with a properly immobilized complex. As a result, the numbers of turnover for immobilized complexes are many times higher than for the analogous complex in solution (124). Furthermore, several groups have used porphyrins or phthalocyanines substituted with electron-withdrawing groups such as -NO₂, -F, or -Cl. These complexes have higher reactivities because of the electron-withdrawing effects; moreover, the oxidative stability is generally superior (116, 126, 129). Only in one case has a higher catalytic activity been observed for the dinuclear complexes, namely in the oxidation of 2-methylnaphthalene catalyzed by covalently immobilized iron phthalocyanines (120).

1. Catalytic Epoxidation

Under ideal conditions, epoxidations with homogeneous or anchored Mn and Fe porphyrin catalysts are characterized by high numbers of turnovers and high stereospecificities (104–106, 116, 117, 130, 131). For example, 93% *cis*-epoxide was obtained from *cis*-stilbene, with H₂O₂ and Fe-tetraphenylporphyrin on imidazole-modified SiO₂ (106). Various oxidants, including NaOCl, can be used (117):

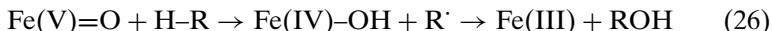


On the other hand, these reactions are also limited by the typical reactant preferences of porphyrin catalysts. For instance, *cis*-disubstituted olefins react much faster than *trans*-disubstituted olefins as a consequence of the

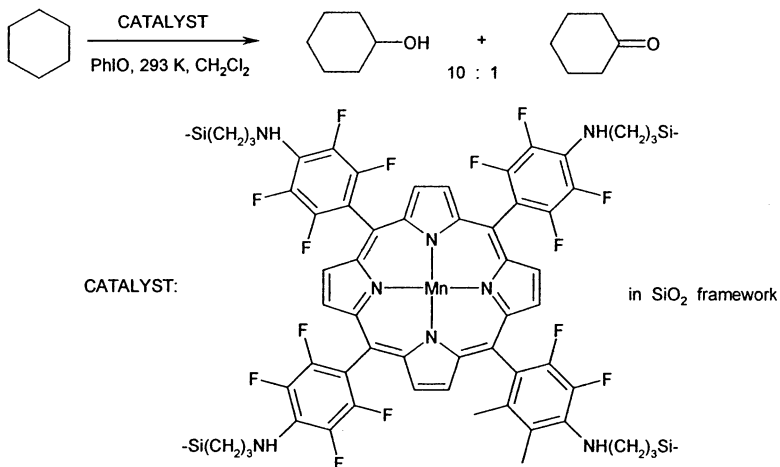
steric hindrance at the porphyrin metal center. A steric hindrance that is too pronounced, as in tetrasubstituted alkenes, may even impede the epoxidation (105). To our knowledge, there is no report of a successful use of phthalocyanine complexes for epoxidations.

2. Paraffin Hydroxylations

Just as cytochrome P450 is a catalyst for highly selective paraffin hydroxylations, proper combinations of a macrocyclic complex and an oxidant are capable of oxidizing paraffin to give an alcohol (108, 109, 116, 121, 122, 124–126, 132, 133). The reaction of an Fe(V)O or Mn(V)O species with a C–H bond occurs via H[•] abstraction; however, the metal-bound [•]OH and the C[•] radical immediately recombine to form an alcohol:

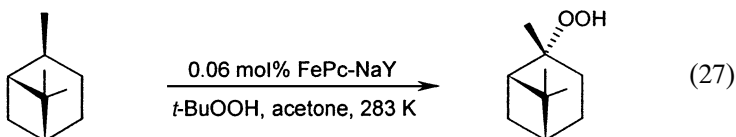


With this “oxygen-rebound” mechanism, the radicals remain with the metal complex, and no chain reaction is started in the solution. For several anchored complexes, strong evidence for the oxygen-rebound mechanism has been gathered, for example, large kinetic isotope effects in the cyclohexane oxidation or a high alcohol to ketone ratio in oxidation of CH₂ groups. The latter test is based on the fact that ketones and alcohols are the primary products of a free radical oxidation, whereas the oxygen-rebound mechanism initially yields only the alcohol. Mn-porphyrins, immobilized on silica or montmorillonite, use a pure oxygen-rebound mechanism for alkane hydroxylation with PhIO (116) (Scheme 1).



SCHEME 1

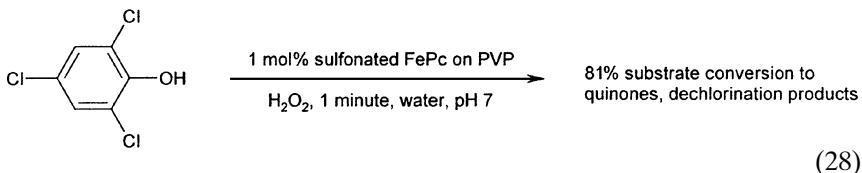
The same holds for *t*-BuOOH and Fe phthalocyanines encapsulated in zeolites or adsorbed on carbon black (121, 124). On the other hand, hydroperoxides have been detected as products in the oxidation of *cis*-pinane by *t*-BuOOH in the presence of zeolite Y-encapsulated FePc (133). This is irrefutable evidence of trapping of a radical by dissolved O₂. Superior hydroperoxide yields are obtained with FePc in zeolite NaY in comparison with the homogeneous reaction, particularly at subambient temperature:



The paraffin oxidation by immobilized Por and Pc complexes is strongly influenced by the polarity of the support. This has been studied in detail for the oxidation of cyclohexane with *t*-BuOOH by immobilized phthalocyanines. Thus, adsorption of the polar reaction products cyclohexanol and *t*-butyl alcohol competes with sorption of the cyclohexane reagent, particularly when a polar support such as a zeolite Y is used (124, 134). Consequently, the activity decreases rapidly, and it can be restored only by extensive solvent extraction. In contrast, FePc on the apolar support carbon black is much less sensitive to this type of deactivation (121).

3. Oxidation of Aromatic Compounds

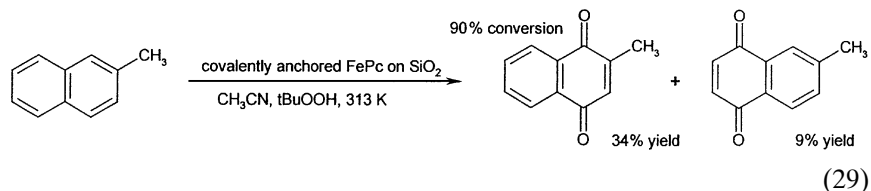
Sulfonated Fe and Mn phthalocyanines are catalysts for the oxidative degradation of chlorinated phenols such as 2,4,6-trichlorophenol, a contaminant from paper mills that use chlorine for bleaching. Fe-tetrasulfophthalocyanine supported on poly(vinyl-4-methylpyridinium) converts 2,4,6-trichlorophenol with the K⁺ salt of Caro's acid, KHSO₅, or H₂O₂ as the oxidant (112):



Even pentachlorophenol can be degraded with this catalytic system. Another reaction relevant to the paper industry is the degradation of 3,4-dimethoxybenzyl alcohol. This aromatic compound is a model for the lignin fraction, which must be removed to produce white paper. Supported

sulfonated FePc has been used in the oxidation of 3,4-dimethoxybenzyl alcohol with KHSO_5 or H_2O_2 . High conversions of the reactant were obtained, but blank tests indicated that KHSO_5 is a potent oxidant for this reaction even in the absence of a catalyst (135).

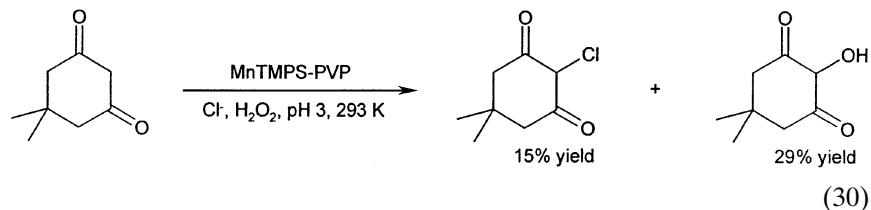
A reaction with relevance to fine chemicals production is the oxidation of 2-methylnaphthalene with *t*-BuOOH. With a silica-anchored Fe phthalocyanine, a mixture containing 6-methylnaphthoquinone and 2-methylnaphthoquinone (vitamin K_3) is obtained:



However, undesired oxidation of the methyl groups is also observed (120).

4. Oxidation of Inorganic Compounds

Halides can be oxidized by Mn(V)-oxo species. This reaction has been performed with Mn *meso*-tetrakis(4-sulfonatophenyl)porphyrin (MnTMPS) exchanged onto partially protonated PVP. The protonated pyridine groups provide anion exchange capacity, and the nonprotonated pyridine moieties function as axial ligands for the metallomacrocycles. Such catalysts mimic the function of haloperoxidase enzymes (114). Although V-containing haloperoxidases are excellent catalysts for bromide oxidation, heme-dependent haloperoxidases oxidize even chloride anions. In the presence of a suitable trapping agent such as dimedone, a chlorinated product is formed. However, a disadvantage of the porphyrin mimics is that part of the H_2O_2 is employed to hydroxylate the dimedone reagent:



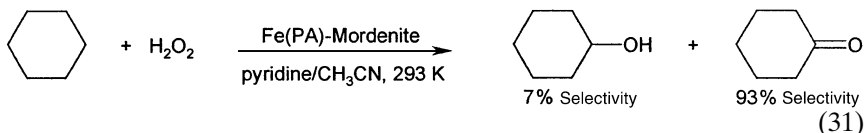
More selective haloperoxidase mimics, without interference of hydroxylation, can be designed containing W (Section XV).

Another inorganic reaction that can be catalyzed by supported porphyrins is the air oxidation of sulfite to sulfate. Sulfite is formed upon absorption of SO_2 from flue gases. For this reaction, a 2-*N*-methylpyridiniumyl-substituted

Fe porphyrin was exchanged onto the outer surface of zeolite 4A; pH and ionic strength of the solution strongly affect the rates, and a slightly alkaline solution seems to be optimal (110).

B. CATALYSIS WITH IMMOBILIZED NON-HEME-TYPE Fe COMPLEXES

Although most of the work has focused on immobilization of porphyrin and phthalocyanine complexes, other Fe complexes have also been immobilized in zeolites, mostly by the ship-in-a-bottle technique. For instance, the tetradentate ligand 5,7,12,14-tetramethyl-1,4,8,11-tetraazacyclotetradeca-4,6,11,13-tetraene was used to form chelates in the cavities of zeolite Y with exchanged Fe^{3+} . However, only modest results were obtained in the cyclohexene epoxidation with PhIO (136). Picolinic acid (PA) was also used as a chelating ligand for zeolite-exchanged Fe^{3+} (137). Under the so-called "Gif" oxidation conditions, i.e., in a pyridine–acetonitrile solvent mixture, cyclohexane is oxidized mainly to cyclohexanone with H_2O_2 as the oxidant. This observation might well mean that radicals are the actual oxidizing species:

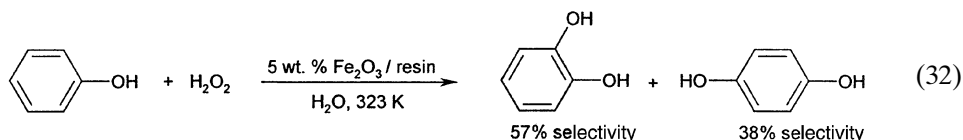


However, there are no clear data characterizing the catalyst reuse or the stability of anchoring of the catalyst.

C. FENTON AND RELATED REACTIONS WITH IMMOBILIZED Fe CATALYSTS

The Fenton reaction is carried out with H_2O_2 and a soluble Fe salt to dissociate hydrogen peroxide to, among others, HO^\cdot radicals. Ion exchange is the obvious way to anchor the catalytic Fe ions. Examples of catalytic materials are Fe-exchanged ZSM-5 zeolite, a supported γ -Fe-oxohydroxide, Fe bound to β -cyclodextrin-linked gallic acid, and Fe_2O_3 nanoparticles deposited in macroporous resins (138–142). There are two types of applications of such catalysts. First, they can be used for the hydroxylation of aromatic compounds, as in the classical Fenton reaction. For example, benzene was converted into catechol in 73% yield with the Fe complex of immobilized gallic acid (141). In the phenol hydroxylation, supported Fe nanoparticles were prepared by exchange of a sulfonate resin with Fe^{3+} and subsequent refluxing

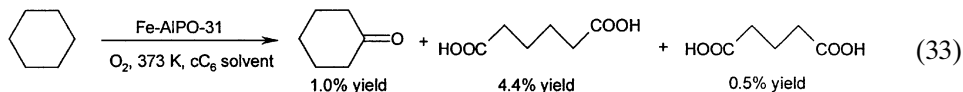
in H_2O_2 (142). Characterization data show that mainly β - FeOOH particles are formed. At a phenol conversion of 22%, catechol was the main product:



The yield, based on H_2O_2 consumed, was 60%.

A second application of anchored Fenton catalysts is depollution by wet oxidation with aqueous H_2O_2 at temperatures between 293 and 363 K. Typical pollutants are formic, acetic, propionic, and benzoic acids and phenol (138–140). The degree of immobilization of the catalytic Fe species is largely determined by the pH. For example, with Fe-ZSM-5 a pH that is too-low induces leaching, possibly by competitive exchange of protons. Thus, solutions of higher pH are preferred, even if the catalyst is slightly less active in those conditions.

One-electron Fe redox catalysts may also be immobilized by incorporation into aluminophosphate frameworks. Dugal *et al.* (143) reported the oxidation of cyclohexane to give adipic acid with air as the oxidant in the presence of Fe-AlPO-31. This molecular sieve has narrow pores, with a 0.54-nm diameter. Cyclohexane is easily adsorbed in the micropores, but desorption of initial products such as cyclohexyl hydroperoxide or cyclohexanone is slow. Consequently, subsequent radical reactions occur until the cyclohexyl ring is broken to form linear products that are sufficiently mobile to diffuse out of the molecular sieve:



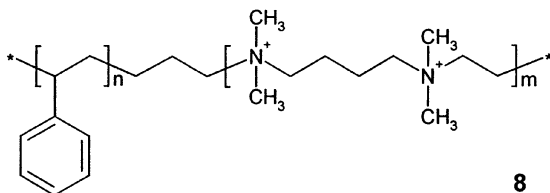
In contrast, with the larger-pore Fe-AlPO-5, cyclohexanol and cyclohexanone account for about 60% of the oxidation products (144). Thus, localization of a free radical reaction inside micropores seems to give rise to particular selectivities.

VII. Cobalt

Co catalysts are used to catalyze a series of oxidations that involve one-electron redox reactions, such as oxidation of phenolic compounds, thiol oxidation, and oxyfunctionalization of saturated hydrocarbon groups.

A. THIOL OXIDATION

Cobalt phthalocyanines, and to a lesser extent the oxidatively less stable Co porphyrins, are the established catalysts for the autoxidation of thiols to disulfides. This process is of industrial importance in the sweetening of crude oil fractions. Early attempts to support the catalysts were carried out with activated carbon, for example, as an adsorbent to facilitate recovery of the phthalocyanine catalysts (145, 146). However, any technique for immobilization of Fe and Mn porphyrins and phthalocyanines can easily be adapted to the corresponding Co chelates—for instance, covalent attachment to organic polymers (147) or SiO₂ (148, 149), entrapment in zeolites (150), or intercalation or exchange in cationic clays, polymers, or LDHs (150–154). Phthalocyanines can be exchanged onto LDHs, or they can be adsorbed on the mixed oxides that are formed by calcination of LDHs (155). An original approach is the preparation of an antimonyphosphate, pillared with Co-tetraphenylporphyrin (156). For the preparation of this catalyst, the Sb-phosphate is first ion exchanged with Co²⁺. Addition of equimolar amounts of benzaldehyde and pyrrole then results in *in situ* formation of tetraphenylporphyrin. Sophisticated cationic polymers have been developed by German *et al.* (157) for ion exchange of sulfophthalocyanines. For example, latices were prepared based on block copolymers of styrene and 2,4-ionenes (8). The polystyrene is located in the interior of the latex particles, whereas the flexible cationic ionene groups extend into solution and provide steric and electrostatic stabilization.



There is general agreement regarding the main steps of the mechanism of thiol oxidation. First, the thiol is deprotonated and coordinates to the Co macrocycle. Simultaneous coordination of the thiol and O₂ in the *trans* positions of the Co chelate is crucial. The Co then mediates transfer of an electron from RS⁻ to coordinated O₂:



Transfer of an electron of a second thiolate to O₂⁻ results eventually in O₂²⁻

and a second thiol radical. The two thiol radicals then recombine to form a disulfide:



The activity is strongly influenced by the state of aggregation of the phthalocyanines and porphyrins. The aggregation of phthalocyanines can conveniently be investigated with the help of visible electronic spectra. Not only monomeric species but also dimers seem to have a high activity (148, 157). Consequently, the immobilization method and the loading with complex strongly affect the rates.

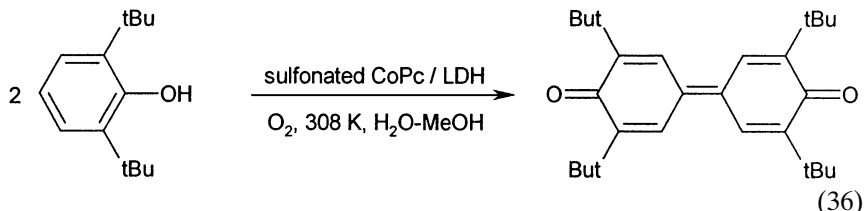
Catalytic experiments have focused on apolar thiols, such as 1-decanethiol, or on small, water-soluble reactants such as 2-mercaptoethanol. The use of alkaline water as a solvent is advantageous since the thiol autoxidation is accelerated by base. However, too high of a base concentration may degrade organic polymer supports, and therefore the use of inorganic supports (such as the antimony phosphate) may be preferable (156). Although aqueous base can be used to form thiolate anions, the support may have basic properties that facilitate the deprotonation; this is the case for LDHs with intercalated sulfonated phthalocyanines (150–153, 155). The basicity of these LDHs can be modulated, for example, by using a NiMgAl instead of a MgAl composition (155). Moreover, it may be necessary to remove naphthenic acids from kerosene feed streams by prior washing with alkali. Alternatively, quaternary ammonium groups on a polymer may attract thiolate anions and thus enrich the immediate environment of the catalytic sites with reactant (157), or base functions may even be incorporated into the porphyrin, for example, in porphyrins with pendant amine or carboxylate groups (147).

Apart from the charge density of the surface, its hydrophilicity or hydrophobicity may play a role. In this context, it has been claimed that hydrophobization of an LDH by partial exchange with dodecylsulfate increases the thiol oxidation activity because of better adsorption of long thiols (150). Similar effects have been obtained by exchanging the outer surface of a phthalocyanine-containing zeolite with tetrabutylammonium ions (150). The activity of carbon-supported Co phthalocyanines is also greatly affected by the pretreatment of the surface; thus, a more active catalyst for mercaptoethanol autoxidation is obtained with carbon black instead of a more polar oxygen-pretreated activated carbon (158).

B. OXIDATION OF PHENOLIC REACTANTS

Oxidative coupling of phenols to give diphenoquinones is a particularly well-studied reaction. Simple O_2 can be used as the oxidant, and the process is accelerated by Co porphyrins, phthalocyanines, and Schiff bases. The most frequently used immobilization technique is anion exchange, requiring

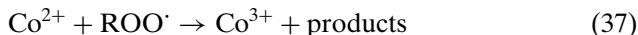
sulfonated forms of, for example, the Schiff bases (159) and anion exchangers such as resins or LDHs (115, 160). In the case of a sulfonated CoPc, the intercalation in the LDH stabilizes the catalyst against self-destruction. Whereas only 25 turnovers can be achieved in solution, the LDH-supported species remains stable after more than 3200 turnovers (115):



A similar reaction of a phenol to give a quinone and a diphenoquinone can be catalyzed by simple Co^{2+} ions exchanged onto zeolite X. In this case, $t\text{-BuOOH}$ is required as an oxidant (161).

C. OXIDATION OF ALIPHATIC C–H BONDS WITH O_2 OR WITH PEROXIDES

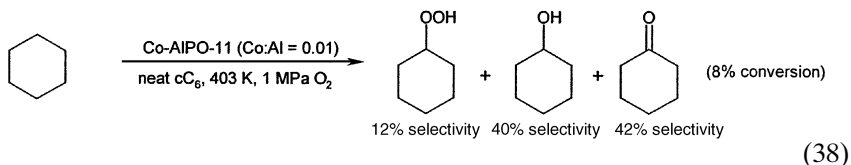
Soluble Co compounds are generally employed in the autoxidation of hydrocarbons, i.e., the oxidation with O_2 as the oxidant. In neat hydrocarbons, low concentrations of Co compounds accelerate the autoxidation since the $\text{Co}^{2+}/\text{Co}^{3+}$ couple is excellent for decomposing alkyl hydroperoxides and thus initiates free radical chain reactions. However, at high conversions, the Co may be deactivated by formation of insoluble clusters with side products of the hydrocarbon autoxidation. Moreover, high concentrations of a Co compound may actually inhibit the reaction because Co also terminates radical chains by reaction with ROO^\cdot radicals:



On the other hand, different mechanisms can operate when autoxidation is performed with Co in acetic acid as a solvent. Under these conditions, Co^{3+} is a very strong oxidant, capable of reacting directly with the hydrocarbon reactant instead of the hydroperoxide, resulting in unusual regioselectivities and other patterns that deviate from classical free radical chemistry (5). The previously stated considerations, and particularly the distinction between reactions in neat hydrocarbon and in acetic acid, have an important bearing on any strategy for immobilization of Co autoxidation catalysts.

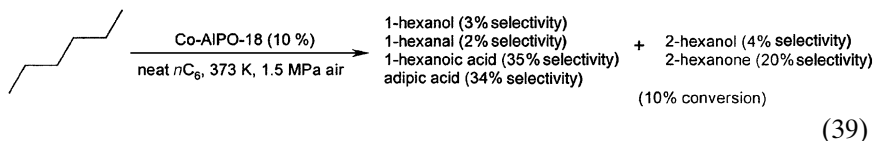
Much effort has been devoted to aluminophosphates with isomorphous Co^{2+} substitution (Co-AIPOs) (162). These structures are of interest for two reasons. First, Co is immobilized at lattice sites, and formation of clusters of Co is therefore impossible. Such clusters, which are catalytically less active, can in contrast be formed in materials with mobile Co, for example, Co-exchanged zeolite Y. Second, calcination of Co-AIPOs brings at least

part of the Co into the trivalent state. Thus, the redox couple $\text{Co}^{2+}/\text{Co}^{3+}$ becomes accessible for lattice Co. Co-AlPO-5 and Co-AlPO-11 with different Co contents have been employed in the autoxidation of neat cyclohexane (162). At 403 K in neat cyclohexane, cyclohexanol and cyclohexanone are formed in a ratio typical of free radical reactions:



Comparison with a similar overall concentration of a soluble Co-naphthenate catalyst shows that (i) the Co-naphthenate is subject to much faster deactivation because of Co precipitation and (ii) with Co-AlPO-5 and Co-AlPO-11, the combined selectivity for monooxygenated products (cyclohexyl hydroperoxide, cyclohexanol, and cyclohexanone) is considerably higher than with a homogeneous Co complex. A higher selectivity for monofunctionalized oxygenated products is economically interesting because the first step of cyclohexane autoxidation is carried out with the aim of maximizing the alcohol and ketone yield. Incorporation of high concentrations of Co in Co-AlPO-5, (e.g., 4% of the tetrahedral positions) leads to less activity than with a 1%-substituted Co-AlPO-5. At high Co contents, part of the Co is no longer located at lattice positions, but instead occupies cation-exchange positions in the Co-AlPO-5 lattice. The latter type of Co is mobile and may retard the reaction by chain termination on Co clusters. The Co in Co-AlPO-5 with low Co contents is perfectly anchored in the cyclohexane autoxidation at relatively low conversions, when the formation of acids is minimal. Too-high conversions and formation of acids cause framework dissolution, and release of Co may occur.

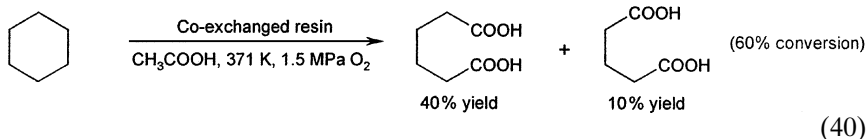
The theme of Co-AlPO catalysis has been taken up in subsequent work by Raja *et al.* (163). In their view, narrow dimensions of the pore containing the Co^{3+} site can direct the free radical oxidation to well-defined sites of a hydrocarbon such as *n*-hexane. Thus, with the Co-AlPO-18 structure, the selectivity for terminal oxidation is 74%, whereas 2-hexanol and 2-hexanone amount to only 24% of the products. Moreover, with an appropriate concentration of lattice Co ions, *n*C₆ is oxidized at both terminal sites:



This chemistry is in contrast with common free radical chemistry (3–6). First, primary CH_3 groups are almost never oxidized by a radical species since the

C–H bond energy is 22 kJ mol^{-1} higher than for a C–H bond in a CH_2 group. Second, even if products of subsequent oxidation are formed, the typical products of an *n*-hexane autoxidation, acetic and propionic acids, are apparently formed only in minimal amounts. This example illustrates how profoundly site immobilization may affect autoxidation chemistry. It is unclear whether the unusual selectivities are solely a consequence of framework effects or due to a direct reaction of the strongly oxidizing Co^{3+} with the hydrocarbon, as mentioned previously. Moreover, the effect of the formation of chelating acids, such as adipic, succinic, and glutaric acid, on the stability of the Co framework was not investigated (163). Particularly when Co-AIPO-5 is used in acetic acid as a solvent (164, 165), strong leaching is to be expected.

Polymers with chelated Co have also been used as catalysts for alkane autoxidation. Kulkarni *et al.* (166) employed a tyrosine-based polymer for autoxidation in pure cyclohexane, but very different conditions were used by Shen and Weng (167, 168) in the autoxidation of cyclohexane or cyclohexanone. The latter authors, used glacial acetic acid as a solvent and a Co-exchanged weak acid resin as the catalyst. At high conversions, adipic acid is formed:



However, there was clear evidence for elution of Co from the resin during reaction. Since leaching of Co was promoted by the water formed in the autoxidation, some acetic anhydride was added to trap the water. Even then, leaching remained substantial, and the anhydride caused some polymerization. Clearly, since acetic acid is a corrosive medium and dissolves Co compounds well, it is probably impossible to find a supported equivalent of Co catalysis in acetic acid. Similar problems of leaching by acid might arise in the autoxidation of propionaldehyde to give perpropionic acid with Co- or Mn-exchanged resins as catalysts (169).

A catalyst for cyclohexane oxidation with *t*-BuOOH has been designed by immobilization of a well-defined trinuclear Co cluster in a MCM-41 with covalently bound glycine ligands. Particularly high selectivities for cyclohexanone were obtained (170).

VIII. Copper

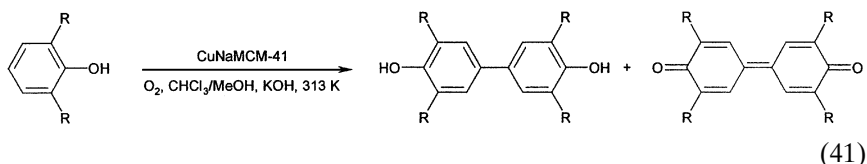
Cu compounds in solution are usually active catalysts for oxidation reactions because of the favorable redox potential of the Cu(II)/Cu(I) couple.

Two-electron redox phenomena are rare for Cu, and therefore Cu is not a suitable catalyst for epoxidations, for example. However, Cu is useful for free radical reactions such as deep oxidation of organic molecules in waste streams and ring or side chain oxidation of aromatic compounds.

A. SUPPORTED Cu CATALYSTS FOR OXIDATION OF AROMATIC COMPOUNDS

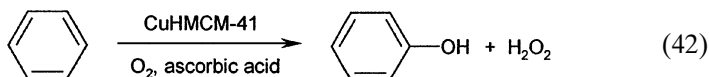
Several groups have used Cu-containing solid catalysts in oxidations with O_2 or H_2O_2 . Because unchelated Cu^{2+} ions display a considerable activity, ion exchange of Cu^{2+} ions is an obvious immobilization route.

Tsuruya *et al.* (171–174) employed a Cu-exchanged MCM-41 or Cu-containing PVP as a catalyst in the oxidation of 2,6-di-*tert*-butylphenol with O_2 . The MCM-41 has a limited cation exchange capacity because of the incorporation of a small amount of Al^{3+} in the structure (Si/Al = 60) (171). In the presence of base (e.g., as dissolved KOH), two C–C coupling products are formed:



The base promotes the formation of a phenolate ion, which undergoes a one-electron oxidation to form Cu(I) and a phenoxy radical. Two of these radicals combine to give the 4,4'-dihydroxybiphenyl compound, which can be further dehydrogenated to give the diphenoquinone. Within the detection limit of atomic absorption spectroscopy no Cu was observed in solution. Cu retention on the molecular sieve in this case is favored by the apolarity of the solvent, the absence of competing anions (e.g., acetate in solution), and the presence of base, with the latter promoting formation of copper hydroxides.

The same authors reported the liquid-phase oxidation of benzene to phenol, with O_2 as the oxidant and Cu-zeolite or Cu-MCM as the catalyst (175, 176). However, phenol yields were low, a large amount of supported Cu was required, and ascorbic acid was used as a stoichiometric coreductant. Phenol production was accompanied by the formation of H_2O_2 in solution:

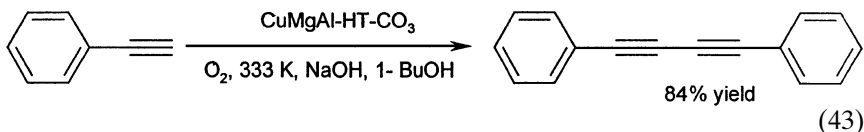


A layered double hydroxide with Cu as the main constituent of the octahedral layers was used for hydroxylation of phenol with H_2O_2 . Catechol and hydroquinone formed in a 3:2 ratio, with a yield of approximately 50%

based on peroxide. The mechanism of this reaction undoubtedly is based on a Cu-initiated decomposition of H_2O_2 with formation of OH^\cdot radicals. The structural integrity of the CuAl-LDH- CO_3 after the reaction is unclear (177). Raja and Ratnasamy (178) claimed that Cu dimers in zeolite Y and MCM-22 are supported catalysts for oxidation of, among others, phenol with O_2 ; zeolite-supported Cu phthalocyanines are active for the same reaction with H_2O_2 as the oxidant (179).

Cationic clays have also been used as supports for Cu. Cu-doped alumina-pillared montmorillonites have been employed in the oxidation of toluene and of xylenes with H_2O_2 . The pillaring and the Cu exchange are performed under acidic conditions at pH 2 and 3.5, respectively. It is unclear whether the Cu^{2+} remains fully associated with the clay in the presence of H_2O_2 , which is itself acidic. Moreover, the reactions are unselective; mixtures of ring-hydroxylated and side chain-oxidized products are obtained (180).

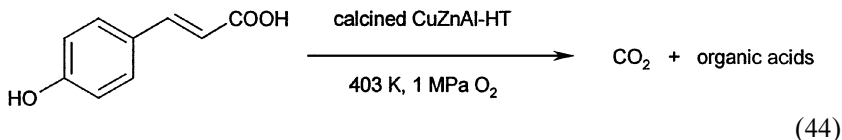
Oxidative coupling of phenylethyne is another Cu-catalyzed reaction that involves one-electron redox steps. Substituted, conjugated alkynes are valuable components for liquid crystal applications. Auer *et al.* (181) used a calcined CuMgAl-LDH- CO_3 to catalyze the air oxidation of phenylethyne to give 1,4-diphenylbuta-1,3-diyne:



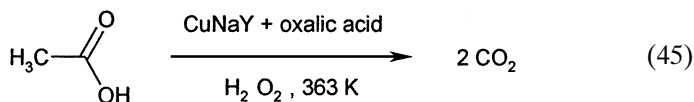
As in the oxidative coupling of 2,6-di-*tert*-butylphenol, a cooperation between base and Cu sites is required in the catalytic cycle. Even if MgAl-LDH is a strong basic support, extra NaOH is required to form the phenylethynilide anion. The latter reduces Cu(II) to Cu(I), and coupling of the resulting radicals gives the conjugated product. As in the oxidative phenol coupling, it seems that Cu is truly anchored. The nature of the solvent and the alkaline conditions are probably decisive in preventing dissolution of Cu.

B. DEEP OXIDATION WITH LIQUID-PHASE REACTANTS

Oxidation is frequently used as a method for removal of organic pollutants from aqueous streams. In this wet oxidation, the aim is to convert the organics into CO_2 at high temperatures using harmless oxidants such as H_2O_2 or O_2 . Typical reactants are acetic acid, polyethylene glycol, phenol, and phenolics such as para-coumaric acid (182–187). Para-coumaric acid is a typical component of olive processing and wine distillery wastewaters:



Cu catalysts are preferred, for example, copper oxide, Cu-exchanged zeolites, or LDH-based materials such as a calcined CuAl-LDH or CuZnAl-LDH. The reactions are generally performed in continuous reactors, and the catalytic activity often gradually decreases as a result of leaching of Cu. The leaching is influenced by the pH and the presence of chelating organic acids. However, in some cases, the presence of an acid actually improves the catalyst's characteristics (187). Thus, treatment of a Cu²⁺-exchanged zeolite NaY with oxalic acid resulted in a superior catalyst for the total oxidation of acetic acid with H₂O₂ as the oxidant:



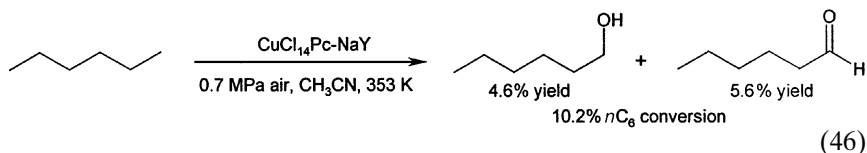
The oxalic acid also contributed to an improved retention of the Cu. The effect of oxalic acid was interpreted in terms of removal of Na⁺ or Al³⁺ from the structure, but a specific complex formation between Cu²⁺ and oxalate may also play a role.

C. Cu-CATALYZED SULFOXIDATIONS

Chiral Cu Schiff bases were entrapped in zeolites and used as catalysts for sulfoxidation with H₂O₂ or *t*-BuOOH, but no useful EE was observed (188).

D. SUPPORTED Cu PERHALOPHTHALOCYANINES AS CATALYSTS FOR PARAFFIN OXIDATION

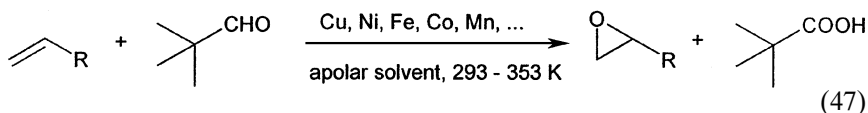
Mn and Fe chemistry has shown that zeolites are excellent supports for anchoring of metallophthalocyanines. There is a report of *n*-hexane oxidation with O₂ and zeolite-supported Cu-perchlorophthalocyanine catalyst (189):



Remarkably, oxidation was observed only at the primary CH_3 group. This unusual product distribution weighs strongly against a free radical mechanism, which would normally be expected for a Cu-catalyzed oxidation reaction (190). Selective oxidation at C1 is a peculiar observation that certainly needs confirmation.

IX. Metal-Assisted Oxidations with Sacrificial Use of an Aldehyde

Autoxidation of an aldehyde is a facile process, occurring at temperatures between 293 and 353 K. When this reaction is conducted in the presence of an olefin, the latter is easily epoxidized. This procedure was first worked out by Mukaiyama *et al.* (191, 192). According to a generally accepted mechanism, the aldehyde is autoxidized to give a peracid, which can epoxidize an olefin even in an uncatalyzed reaction. Alternatively, the epoxidizing agent might be an acylperoxy radical ($\text{RCO}_3\cdot$) formed as an intermediate in the aldehyde autoxidation. Although the retention of *cis* or *trans* configuration during epoxidation has been proposed as a criterion to distinguish between peracids and acylperoxy radicals, the distinction between the two mechanisms is actually more complex (193). In any event, the aldehyde is eventually converted to an acid so that at least 1 mol of acid is produced per mole of epoxide produced:



Under similar conditions, ketones in the reaction mixture are converted to esters via Baeyer–Villiger oxidation with *in situ* formed peracid, or thioethers can be converted to the sulfoxides or sulfones.

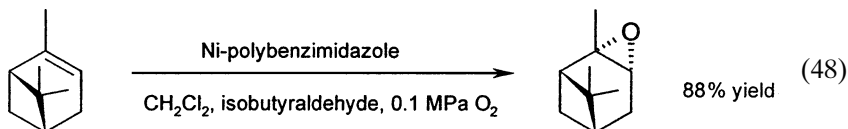
Metals can play a clear but small role in such epoxidations or esterifications with a sacrificial aldehyde. First, it has long been known that the free radical aldehyde autoxidation can be initiated and therefore accelerated by metal ions. For instance, high concentrations of peracid can be obtained with dissolved Fe catalysts (5). As a rule, the presence of a metal allows autoxidation at considerably lower temperature than for the noninitiated reaction. The exact nature of the metal is not critical. Second, epoxidations by a peracid may be metal centered; however, at the typical temperatures of the Mukuyiama epoxidation, the uncatalyzed reaction of peracid and olefin is usually fast enough to make the metal redundant for this second step.

A large number of anchored metals have been proposed as catalysts or, more correctly, initiators for the olefin epoxidation or other oxidations under

TABLE II
Supported Initiators of Oxidations with O_2 and a Sacrificial Aldehyde

Reaction	Metal	Catalyst	Reference
Epoxidation	Mn	Mn(III)-AIPO structures 5, 18, and 36	Raja <i>et al.</i> (194)
	Co	Co(III)-AIPO structures 5, 18, and 36	Raja <i>et al.</i> (194)
		Co^{2+} , chelated by SiO_2 -tethered propionic acid	Butterworth <i>et al.</i> (195)
	Ni	Ni(acac) ₂ impregnated on K_{10} -montmorillonite	Bouhleb <i>et al.</i> (196), Laszlo and Levart (197)
		Ni^{2+} , chelated by aromatic carboxylic acid tethered to SiO_2	Chisem <i>et al.</i> (198)
	Ni^{2+} on polybenzimidazole	Wentzel <i>et al.</i> (199)	
Baeyer–Villiger oxidation of ketones	V, Mo	$H_5PV_2Mo_{10}O_{40}$ on MCM-41	Khenkin <i>et al.</i> (200)
	Fe	FeMgAl-HT	Kaneda <i>et al.</i> (201)
		Fe_2O_3	Murahashi <i>et al.</i> (202)
	Ni	Ni^{2+} , chelated by aromatic carboxylic acid tethered to SiO_2	Chisem <i>et al.</i> (203)
	Cu	CuMgAl-HT	Kaneda <i>et al.</i> (201)
Oxidation of thioethers	Co	Co, chelated in polyacrylate-anchored acetylacetate	Dell'Anna <i>et al.</i> (204)

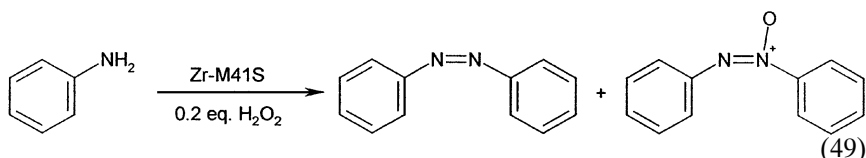
Mukaiyama conditions (194–204). Some of these reports are summarized in Table II. Excellent epoxide yields are obtained, even for olefins with very acid-sensitive epoxides such as α -pinene (199):



As mentioned previously, the role of the metal is not specific. Even transition metal free layered double hydroxides are suitable catalysts for the olefin epoxidation with O_2 and a sacrificial aldehyde (205). Leaching of the metal from the solid catalyst is a serious problem since organic acids that are potential metal ligands accumulate during the reaction. Leaching occurs, for example, with the polybenzimidazole-supported Ni^{2+} catalyst (199).

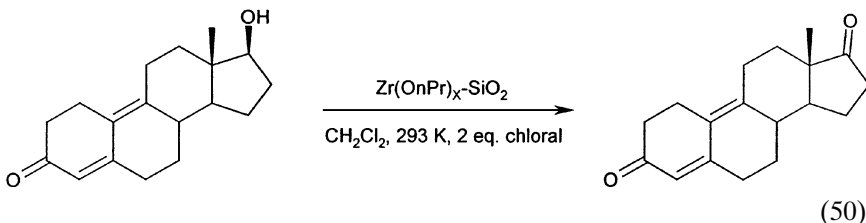
X. Zirconium

Zr-containing mesoporous silicas offer some potential for the oxidation of aniline with H_2O_2 as the oxidant. The Zr is introduced as $\text{Zr}(\text{OiPr})_4$ during the micelle-templated hydrothermal synthesis of the MCM-41-type structure (206). The materials are calcined prior to use in catalytic experiments. Azobenzene and azoxybenzene are formed:



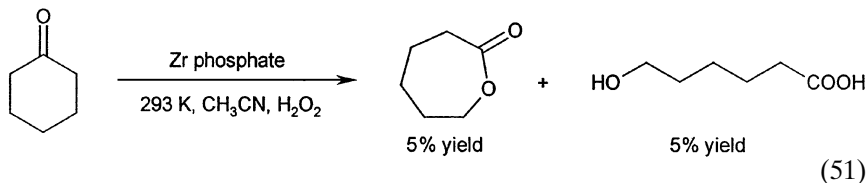
Silica-anchored Zr alkoxides can be used for olefin epoxidation with peroxides (207).

In the Oppenauer oxidation, an activated carbonyl compound acts as a hydride acceptor in the selective oxidation of an alcohol to give a ketone. Krohn *et al.* (208) used SiO_2 -anchored $\text{Zr}(\text{OnPr})_4$ in combination with chloral:



Typical for the Oppenauer reaction is high chemoselectivity, even in the presence of other oxidation-sensitive functional groups such as double bonds. Stable anchoring is not a problem with these SiO_2 -based Zr catalysts, which is evident since the surface chemistry of Zr is reminiscent of that of Ti.

The Lewis acidity of Zr in amorphous zirconium phosphate has been exploited for the Baeyer–Villiger oxidation of ketones with H_2O_2 as the oxidant (209). Excellent results are obtained for reaction in acetic acid. However, it is difficult to distinguish between the contributions of *in situ* formed peracetic acid and an inorganic Zr peracid. In the reaction in acetonitrile, the yields of oxidized products are modest:



XI. Molybdenum

A. SUPPORTED MO CATALYSTS WITH ALKYL HYDROPEROXIDES AS OXIDANTS

Molybdenum complexes are the most effective catalysts known for the selective epoxidation of olefins with alkyl hydroperoxides (210–212). Commonly known is the Arco or Halcon process for the large-scale manufacture of propylene oxide from propylene. This process uses *t*-BuOOH or ethyl benzene hydroperoxide (EBHP) as an oxidant and Mo(CO)₆, for example, as a source of Mo. The Mo(CO)₆ acts as a catalyst precursor, which is converted into a soluble active form by complexation with diols (3). Chemists have designed several supported versions of the catalysts for this epoxidation chemistry. A clear classification can be made on the basis of the nature of the support.

1. Impregnation and Deposition on Inorganic Materials

Molybdenum trioxide (MoO₃) deposited on silica was one of the first supported Mo catalysts to be prepared. In contrast to Ti/SiO₂, which is used industrially, Mo/SiO₃ did not break through commercially, mainly owing to substantial leakage of Mo under catalytic conditions. Trifiro *et al.* (213) showed that when MoO₃ on silica is used for the epoxidation of cyclohexene with *t*-BuOOH in benzene at 353 K, part of the activity originates from dissolved Mo. The main reason why Mo is not entirely retained on silicas and aluminas is thought to be the formation of soluble neutral Mo–diol complexes.

An identical observation was made when calcined zeolites impregnated with Mo(CO)₆ or MoCl₅ were used in the epoxidation of propylene. Notwithstanding the superior catalytic activity in comparison with the homogeneous catalyst, 10% of the Mo was found in solution and is responsible for a continuous homogeneous epoxidation activity. An additional disadvantage of zeolites in particular is the intrazeolitic polymerization of the propylene oxide catalyzed by acidic sites. However with zeolites, a clear contribution of the supported Mo to the reaction was observed in addition to the homogeneous catalysis. Although the exact nature of the immobilized Mo is not clear, poisoning experiments with various amines have demonstrated that the activity is mainly associated with Mo located in the pores rather than with Mo situated at the outer surface (214–217).

Recently, isolated dioxoMo entities were docked onto the surfaces of ordered mesoporous materials such as MCM-41 and MCM-48. Mo grafting was performed by impregnation of the calcined and dehydrated silica with MoO₂X(THF)₂ (with X = Br or Cl) in dry dichloromethane. The resulting supported Mo complexes catalyzed the epoxidation of cyclooctene

with *t*-BuOOH as the oxygen source at 328 K. The best results were obtained with MCM-41-MoO₂Cl(THF)₂, giving yields of 31% cyclooctene oxide after 2 h of reaction (218). However, the degree to which the catalyst was retained on the support was not evaluated. Bearing in mind the experience with Mo, we question whether the observed activity is indeed associated with the supported Mo.

2. Polymer-Supported Mo Complexes

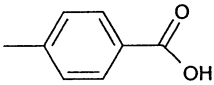
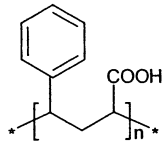
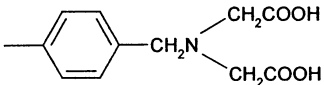
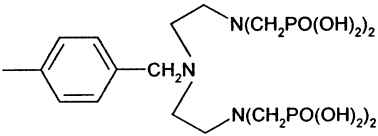
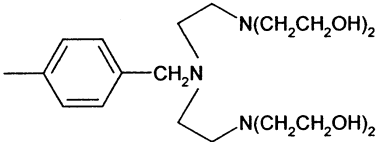
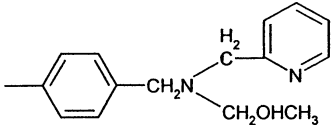
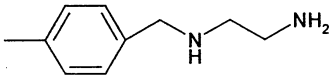
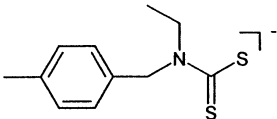
Experience in homogeneous catalysis with Mo complexes teaches that, besides 1,2-diols, other ligands such as carboxylic acids, nitroxides, phosphoramides, phosphonates, phosphates, and various (aromatic) amines have high affinities for Mo complexes, for example, by covalent, coordinative, or electrostatic interactions (219, 220). Inspired by this excellent binding between Mo and organic compounds, many attempts at anchoring Mo catalysts have focused on the immobilization of functional organic groups to which Mo can bind. The majority of early investigations were done with commercially available polystyrene-type polymers with various functional groups or specially tailored chelating ion-exchange functions. A summary of the docking points in polymers and the respective Mo sources is given in Table III (40, 221–233).

All the polymers of Table III have been applied for the epoxidation of olefins with alkyl hydroperoxides. For example, the polymers with iminodiacetic acid or diethylene triamine groups were used for the regioselective epoxidation of (E)-geraniol with *t*-BuOOH to the 2,3-epoxide (225), whereas the Mo anchored to the diphenylphosphinopolystyrene catalyst is used in the epoxidation of cyclohexene with *t*-BuOOH (228). The polymer-supported molybdenyl thioglycolate has also been used for the catalytic oxidation of thiols and phosphines with air or pyridine N-oxide as the oxidant (234).

As shown in Table III, supported Mo catalysts may be derived not only from the traditional MoO₂(acac)₂, Mo naphthenate, or Mo(CO)₆ precursors. A yellow Mo peroxide complex, synthesized from Mo metal and hydrogen peroxide, was immobilized on a cross-linked polystyrene functionalized with triethylenetetramine (229). This Mo-containing material was capable of catalyzing the epoxidation of various olefins with *t*-BuOOH as the oxidant in the temperature range of 298–333 K. For example, cyclohexene oxide was obtained in 90% yield after 5 h of reaction at 333 K in benzene.

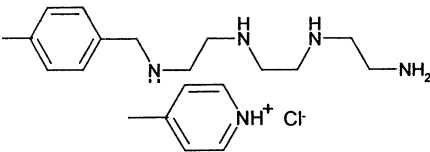
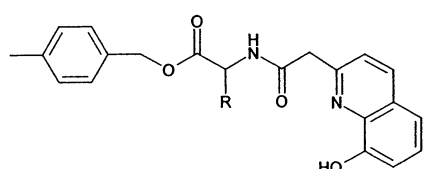
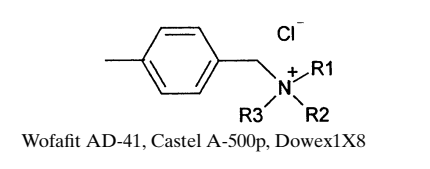
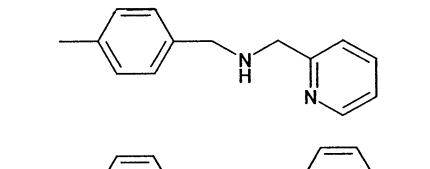
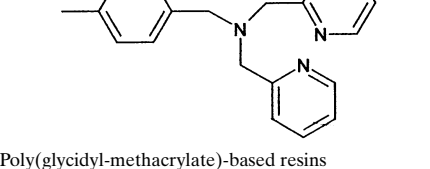
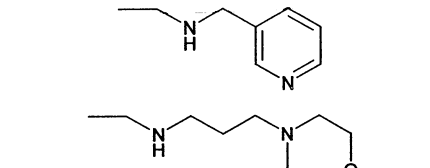
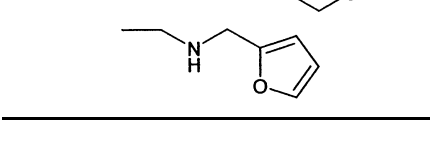

Supported Mo epoxidation catalysts were also obtained by supporting anionic Mo complexes on traditional cross-linked polystyrene anion-exchange resins. Examples of negatively charged Mo complexes are [Mo(V)₂O₄(ethyleneglycolate)₂(H₂O)₂]²⁻, [Mo(V)₂O₄(amygdalate)₄(H₂O)₂]²⁻ (232), and tetrabromo oxomolybdate Mo(V)OBr₄⁻ (230). The Mo(V)OBr₄⁻-exchanged cross-linked polystyrene catalyst has also been applied for

TABLE III
 MODIFIED ORGANIC POLYMERS AS SUPPORTS FOR MO OXIDATION CATALYSTS

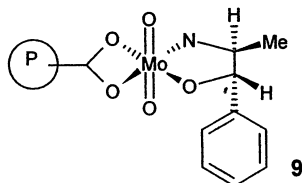
Docking entity in polymer	Mo catalyst precursor	Reference
Polystyrene-based resins		
	MoO_2^{2+}	Ivanov <i>et al.</i> (221)
	MoO_2^{2+}	Boeva <i>et al.</i> (222)
		Ivanov <i>et al.</i> (223)
		
Wofatit CA 20		
	MoO_2^{2+}	Kotov and Boneva (224)
	K_2MoO_4 at pH = 4	Yokoyama <i>et al.</i> (225)
	K_2MoO_4 at pH = 4	Yokoyama <i>et al.</i> (225)
	K_2MoO_4 at pH = 4	Yokoyama <i>et al.</i> (225)
	$\text{MoO}_2(\text{acac})_2$	Sherrington and Simpson (40)
	$\text{MoO}_2(\text{acac})_2$ + 2-mercaptoacetic acid	Gil <i>et al.</i> (226)
	$\text{Mo}_2\text{O}_3(\text{SCNEt}_2)_4$	Bhaduri and Khwaja (227)

(continued)

TABLE III (continued)

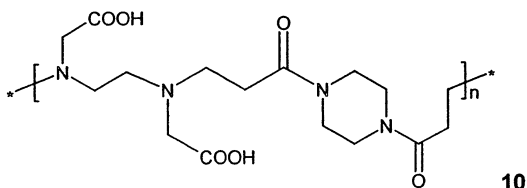
Docking entity in polymer	Mo catalyst precursor	Reference
Polystyrene-based resins (<i>continued</i>)		
Diphenylphosphino polystyrene	Mo(CO) ₆	Goto and Goto (228) Goto and Goto (228)
	Mo(CO) ₆ Oxoperoxomolybdate	Kurusu <i>et al.</i> (229)
	MoOBr ₄ ⁻	Kurusu and Masuyama (230)
	MoO ₂ (acac) ₂	Okamoto and Still (231)
	MoOBr ₄ ⁻	Kurusu and Masuyama (230)
Wofafit AD-41, Castel A-500p, Dowex1X8	[Mo ₂ O ₄ (OX) ₂ (H ₂ O) ₂] ²⁻	Sobczak and Ziolkowski (232)
	MoO ₂ (acac) ₂	Sherrington and Simpson (233)
	MoO ₂ (acac) ₂	Sherrington and Simpson (233)
Poly(glycidyl-methacrylate)-based resins		
	MoO ₂ (acac) ₂	Sherrington and Simpson (233)
	MoO ₂ (acac) ₂	Sherrington and Simpson (233)
	MoO ₂ (acac) ₂	Sherrington and Simpson (233)

alcohol oxidation. Polymer-supported Mo catalysts can also be prepared by simple exchange of cationic MoO_2^{2+} with weakly acidic cation-exchange resins (221–224).



Obviously, the way to heterogeneous enantioselective catalysis is open when chiral ligands are introduced into the polymers. This idea was first proposed by Okamoto and Still (231). However, the first catalytic results were published by Cazaux and Caze (235). These authors use the asymmetric Mo(VI) complex (**9**) covalently bound to a cross-linked polystyrene resin for the enantioselective epoxidation of geraniol. Unfortunately, the enantiomeric excess obtained was low—far below that obtained with the Tartarate catalyst (Section II,B). Moreover, the polymeric structure appeared to be unstable.

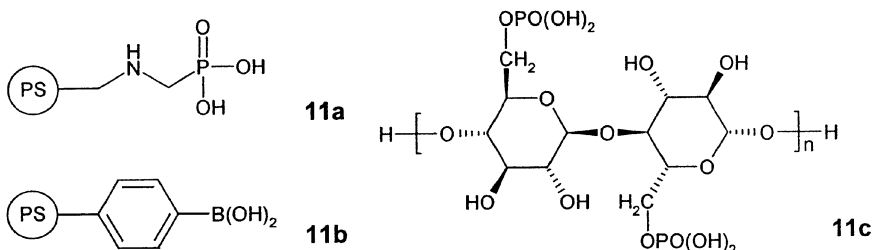
Generally, commercial resins often lack the flexibility to allow manipulation of the structure and properties of the eventual catalyst. To overcome this disadvantage, polymer synthesis specialists took on the design and synthesis of carefully tailored supports. One example of their work is the synthesis of Mo(VI)-grafted poly(amido amine) resins (236). The catalytic activity was found to depend strongly on the distance between the amine and carboxylic acid groups. The catalyst prepared with *N,N'*-ethylenediaminoacetic acid (**10**) in particular was successful for the epoxidation of cyclohexene. The reaction was performed with EBHP as the oxidant in ethylbenzene at 353 K. Unfortunately, the stability of the anchoring of the catalyst in epoxidation was not evaluated.



Other authors have used different polymers with backbones such as poly(ethylene-propylene) rubbers or poly(ethylene oxide) grafted or interpenetrated with poly(acrylic acid), poly(methacrylic acid), poly(*p*-vinyl pyridine), or poly(vinyl alcohol) (237). The immobilization protocol was not

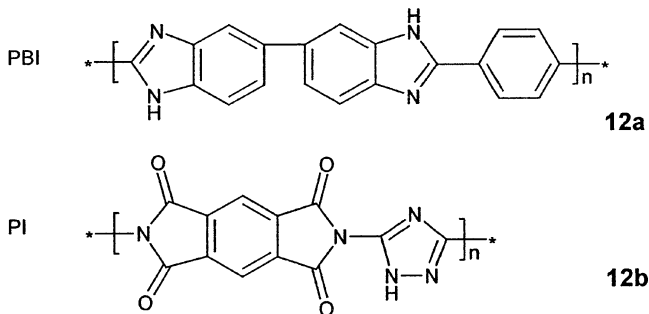
clear from this report, but the supported Mo catalysts were active for the epoxidation of styrene with EBHP as the oxidant.

Tempesti *et al.* (238) used organoboronic acids (**11b**) for the immobilization of Mo(VI). It is assumed that the interaction of Mo occurs through a condensation with the supported acid. Reactions reported with the bimetallic material showed an activity and selectivity comparable to those of homogeneous bimetallic analogs. In a comparable approach, Mo was anchored to immobilized phosphorus-containing acids, for example, of cellulose phosphate (**11c**) (239) or phosphonate resins (**11a**) (240).

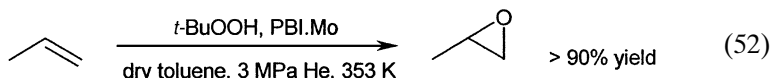


Notwithstanding all these results, one has to bear in mind that Mo polymers do have some disadvantages for use in oxidation chemistry. The degree of anchoring of the Mo in a full range of polymers was examined in detail for the epoxidation of propylene and the more reactive cyclohexene (37, 40, 241). Although most of the early reports mention only limited dissolution of anchored Mo, the authors found a continuous leaking of Mo from most of the resins, which is of course detrimental. A second weak point of the organic polymers is that they are generally associated with thermal and oxidative lability. Indeed, most polymers mentioned so far are stable under oxidative conditions only at temperatures below 473 K, a temperature that is too low for industrial applications.

In contrast to the preceding examples, polybenzimidazole (PBI; **12a**) resins couple an outstanding thermooxidative stability with a pronounced affinity for the active Mo complexes (241–243).



As was demonstrated in thermogravimetric experiments, PBI and PBI–Mo are stable at temperature up to 673 K in an oxygen atmosphere. Immobilization of the Mo catalyst occurs by ligand exchange between $\text{MoO}_2(\text{acac})_2$ and the polymer refluxed in toluene for 72 h. The activity of the catalyst was first tested for the epoxidation of propylene with *t*-BuOOH (242):



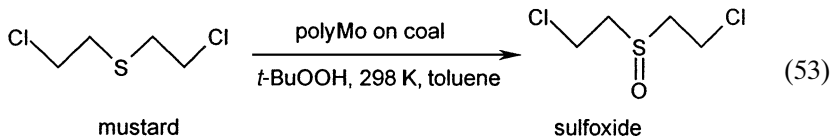
High propylene conversions can be obtained in combination with extremely high propylene oxide (PO) selectivities. Surprisingly, repeated use of the catalyst even improves the rate of PO production. The authors explained the improvement of the activity by changes of the morphology of the polymer (e.g., pore diameter and pore size distribution), in such a way that active sites become more accessible. Leaching of Mo (2–5%) was noticed only after the first run. Unfortunately, when the PBI–Mo catalyst was employed in the epoxidation of cyclohexene instead of propylene, an activity drop was found upon recycling. The latter behavior may be attributed to the formation of side products (e.g., from ring opening of the cyclohexene oxide which blocks the active Mo sites). The same PBI–Mo catalyst has also been used successfully in the epoxidation of many olefins in addition to cyclohexene and propylene (244, 245).

Because PBI is expensive, other thermostable polymers were explored and tested as catalysts (246). A cross-linked version of a polyimide (PI) support with incorporated triazole rings (**12b**) gave better results than PBI for the epoxidation of cyclohexene. Moreover, it can be reused in the cyclohexene epoxidation at least 10 times without any loss of activity (247). Even less expensive, but thermooxidatively stable materials include polysiloxane-based resins, which have also been used for incorporation of Ti (see Section II,A). In this case, the synthesis comprises the polymerization of TEOS and an oligomeric dimethyl silanol with the addition of functional trialkoxysilanes such as trimethoxysilyl-2-ethylpyridine instead of $\text{Ti}(\text{OiPr})_4$ (248). Preliminary results show that the activity per Mo atom is higher than that of PBI–Mo. Furthermore, the degree of leaching of Mo is very low. Thus, it is expected that the polysiloxane-based systems may soon find wide application in oxidation chemistry.

3. Porous Carbon Materials as Supports

Besides polymers and inorganic materials, commercially available porous carbons can be employed to immobilize Mo. For instance, the utility of Mo-impregnated carbon molecular sieves as epoxidation catalyst has been demonstrated by Gaffney *et al.* (249). For example, in a patent 1-octene

was epoxidized with *t*-BuOOH in the presence of Mo on activated carbon, with a conversion of 100% and a selectivity of about 70%. The catalyst was prepared by impregnating a commercial activated carbon with an aqueous solution of MoO₃. From the patent, one learns that a first conditioning run is always needed to ascertain the degree to which the catalyst remains anchored. Indeed, although considerable losses of Mo were found after the first run (>100 ppm), solubilization of Mo in subsequent runs was negligible. V and W catalysts were synthesized in the same way and their ability to epoxidize, for example, allyl alcohol and cyclohexene with *t*-BuOOH as the oxidant was evaluated (249). A Mo heteropoly acid H₅PV₂Mo₁₀O₄₀ was also supported on porous carbon materials and tested for the oxidation of thioethers (250). A particular objective was the selective conversion of the highly toxic mustard or bis(2-chloroethyl)sulfide into the corresponding nontoxic sulfoxide by using *t*-BuOOH as the source of oxygen:



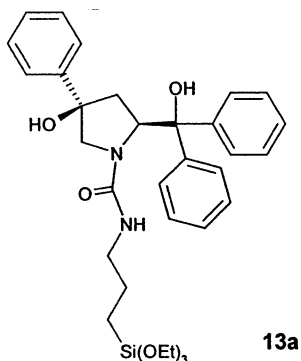
For example, in the presence of the aforementioned polyMo catalyst in toluene at 298 K under Ar, a model sulfide tetrahydrothiophene was 80% converted at >98% selectivity to the sulfoxide. Moreover, the authors claimed an excellent recoverability and reusability, but only when the reaction was performed in apolar solvents.

4. Hybrid Organosilica Catalysts

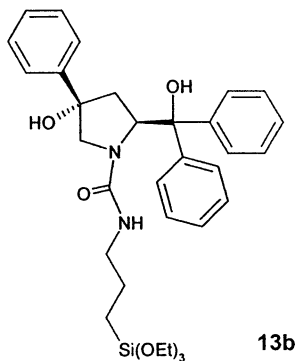
A useful strategy for combining the oxidative stability of inorganic materials with the strong complexation by organic ligands is the complexation of Mo onto appropriately functionalized silica surfaces.

Organonitrile-functionalized mesoporous silicas such as MCM-41 and MCM-48 have been used to immobilize dioxoMo(VI) complexes such as MoO₂X₂(THF)₂ (with X = Br or Cl) (218). The catalytic potential of these hybrid material was evaluated for the epoxidation of cyclooctene with *t*-BuOOH as the oxygen source. Notwithstanding the high activities claimed, pronounced Mo leakage was observed. Indeed, it was shown that cyclooctene continued to be converted after the solid catalyst was removed from the reaction mixture (218).

Chiral Mo complexes bearing ligands derived from a (2S,4R)- or (2S,4S)-4-hydroxyproline compound (**13a** and **13b**) have been tethered to the internal surface of a mesoporous zeolite USY (251). The supported asymmetric Mo catalyst was tested for the enantioselective epoxidation of allylic alcohols.



(2S,4R)-4-OH-proline adduct



(2S,4S)-4-OH-proline adduct

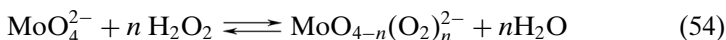
In the presence of the immobilized (2S,4S)-4-hydroxyproline Mo catalyst (**13b**), nerol and geraniol react selectively with *t*-BuOOH to form the 2,3-epoxide with ee values of 64 and 47%, respectively. Surprisingly, when Mo is complexed by the diastereomeric (2S,4R) form (**13a**), racemic epoxidation is observed. The enantioselective catalysis appears to be promoted by immobilization in the zeolite USY pores. Indeed, in the epoxidation of nerol, an ee of 10% was found for the homogeneous asymmetric Mo complex, whereas the supported catalyst favors the selective production of the (2S,3R)-epoxide (64% ee).

B. SUPPORTED MO CATALYST FOR OXIDATION WITH HYDROGEN PEROXIDE AS THE OXIDANT

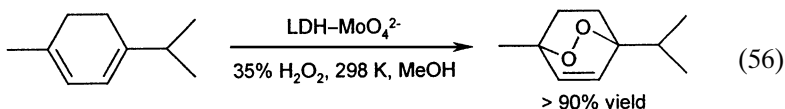
Since Mo preferentially forms negatively charged complexes in aqueous H_2O_2 , the majority of attempts to support catalysts discussed in this section deal with anion exchangers.

Tatsumi *et al.* (252) applied a LDH that is intercalated with anionic polyoxometallates for the epoxidation of 2-hexene, cyclohexene, and β -methylstyrene in tributyl phosphate using H_2O_2 as the oxidant. They observed that 2-hexene is epoxidized faster with $\text{LDH-Mo}_7\text{O}_{24}^{6-}$ than cyclohexene, whereas the opposite is true for the unsupported $(\text{NH}_4)_6\text{Mo}_7\text{O}_{24}$. The authors claimed that this intriguing reversal of the reactant selectivity was a result of shape selectivity imposed by the solid catalyst. However, Gardner and Pinnavaia (253) found that the original catalyst was not stable in the drying procedure prior to the reaction nor in the presence of peroxide. Moreover, since no pronounced microporosity was observed in the intercalated LDHs, the reactant selectivity cannot be an indication of molecular sieving.

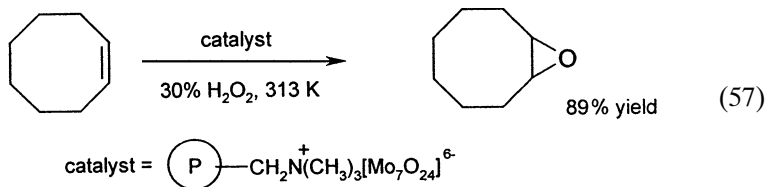
Monomeric molybdate has also been exchanged onto LDHs to give supported oxidation catalysts. LDH-MoO₄²⁻ decomposes H₂O₂ under ambient conditions in a controlled way. In contrast to what occurs with Fe, Mn, and Co catalysts, the decomposition of H₂O₂ produces excited state singlet oxygen rather than radicals (254). The key event in the decomposition is the formation of thermolabile peroxometal intermediates MoO_{4-n}(O₂)_n²⁻ (*n* = 2–4), which disproportionate into ¹O₂ and water (255):



Because singlet oxygen is an attractive reagent for the selective dioxygenation of unsaturated hydrocarbons, the development of new singlet oxygen generators is of great interest. The ¹O₂ produced by the LDH-H₂O₂ system has been successfully applied for the peroxidation of various olefins and aromatics (254, 256, 257). For instance, α -terpinene is fully converted into the corresponding endoperoxide at room temperature in dioxane or methanol:

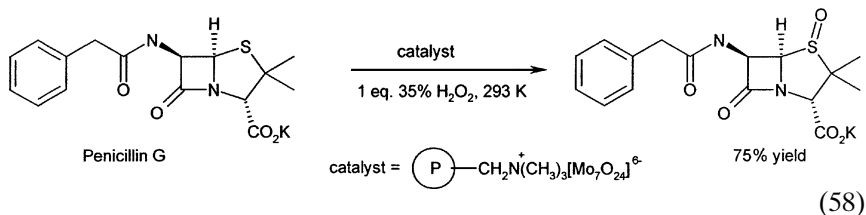


Irrespective of the concentration of H₂O₂, the decomposition rate with LDH-MoO₄²⁻ is higher than that with soluble MoO₄²⁻. Moreover, because the supported catalysts function under salt-free conditions, pure organic solvents may be applied. This allows the oxidation of highly concentrated apolar substrates. Surprisingly, the rate of peroxidation is affected by the composition of the LDH; for example, a change in the Mg to Al ratio from 2 to 5 led to an increase in the peroxidation rate by more than six times (255, 258). An analogous ¹O₂ generator has been synthesized from a cross-linked polystyrene anion exchange resin (259). However, the MoO₄²⁻-exchanged resin is much less effective for dioxygenation than the LDH catalytic system under comparable conditions. Srinivasan and Ford (260) reported polyoxomolybdate catalysts bound to cationic colloidal polymers for the epoxidation of various olefins by aqueous H₂O₂ in the absence of organic solvents. The colloidal polymer was a better support than the commercial cross-linked polystyrene resins. Mo₇O₂₄⁶⁻ catalysts were found to be more active than PMo₁₂O₄₀³⁻ catalysts. These anions are inferred to be only catalyst precursors, because they disintegrate into smaller oxoperoxo Mo anions upon reaction with H₂O₂ (261).



For example, with the $\text{Mo}_7\text{O}_{24}^{6-}$ -exchanged colloidal polymer, 90% of the cyclooctene was converted to >99% cyclooctene oxide by excess H_2O_2 in 24 h at 313 K. One advantage of working with the latex support in water is the higher epoxidation activity that results, relative to that of the free heptamolybdate. The authors attributed the activity increase to a higher local concentration of the apolar olefin in the latex than in the solution. Nevertheless, the material appears not to be very active because 1-octene did not react. Moreover, the activity clearly decreases upon recycling of the catalyst.

$(\text{NH}_4)_6\text{Mo}_7\text{O}_{24}$ supported on a cross-linked polystyrene has also been used for the selective oxidation of sulfur-containing compounds with H_2O_2 (209, 262). An example of interest is the selective conversion of penicillin G to the sulfoxide, an important intermediate for cephalosporin antibiotics:

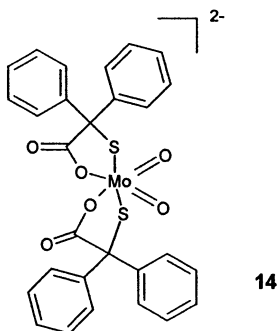


Mo was also fixed on active charcoal in the form of molybdenum blue (MoB), which is a mixed valence polyacid of Mo(V) and Mo(VI) prepared from Mo metal and H_2O_2 (263). The MoB-charcoal catalyst has been used to epoxidize several olefins in isopropanol at 323 K (264, 265). The epoxidation seems largely heterogeneous, since several batches of cyclohexene were oxidized with the same catalyst without significant loss of activity. However, a disadvantage of the system is that a large amount of H_2O_2 is decomposed into O_2 and water. This disadvantage can be overcome by the addition of organotin compounds; trimethyltin chloride seems to be the best choice. Poorly reactive olefins such as allyl chloride could not be converted (265). Molybdate and tungstate doped on porous carbon have also been used for sulfide oxidations with H_2O_2 (266).

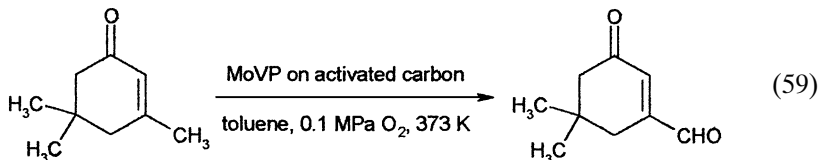
Benzene hydroxylation to give phenol has been performed with Mo-substituted mesoporous silicas and H_2O_2 in the absence of solvent (267). However, as explained earlier, reports of anchoring of Mo in an inorganic support must be treated with great caution, particularly if there is no clear concept for immobilizing both Mo and peroxy Mo. The same holds true for the Mo silicalite MoS-1, which has been used for sulfide oxidation with H_2O_2 (268).

C. SUPPORTED MO CATALYSTS WITH MOLECULAR OXYGEN AS THE OXIDANT

Anionic organic complexes of Mo have been immobilized on LDHs. For example, a Mo(VI)O_2 complex containing 2-mercapto-2,2-diphenylethanoate ligands (**14**) was supported on ZnAl LDH and used for the catalytic air oxidation of thiols (269–271). Although the homogeneous dioxoMo complex has some catalytic activity, it is rapidly deactivated as a result of the formation of dimers. By intercalation of the complex in an LDH structure, dimerization could be avoided, resulting in improved longevity.



An activated carbon supported molybdovanadophosphate (MoVP) oxidizes isophorone to 3-formyl-5,5-dimethyl-2-cyclohexen-1-one with O_2 as the oxidant (272):



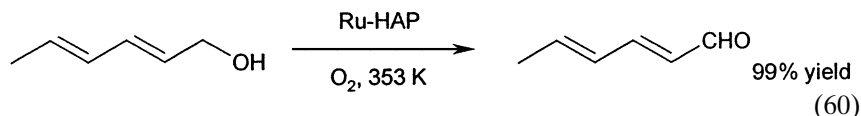
The regiochemistry of this reaction is remarkably different from that observed with most homogeneous catalysts, which produce the 1,4-diketone as the major product. This unusual selectivity was ascribed to pore size effects in the carbon support.

XII. Ruthenium

Ruthenium is one of the most versatile metal redox catalysts. It occurs frequently in all oxidation states between +3 and +8 (273). It can be used in reactions including hydroxylation or ketonization of alkanes (274), dehydrogenation of alcohols (275), and dihydroxylation or oxidative cleavage of olefins (276). Which of these reactions occurs depends on the initial valence of Ru, on its ligands, and particularly on the oxidants that are present. For example, alcohols can be ketonized with Ru^{3+} and molecular oxygen. However, in the presence of periodate, Ru^{3+} is converted into RuO_4 , which is capable of *cis* dihydroxylation or even cleavage of double bonds. Any attempt to anchor a Ru oxidation catalyst should provide binding positions for the initial Ru species and also for the active species in its highest oxidation state.

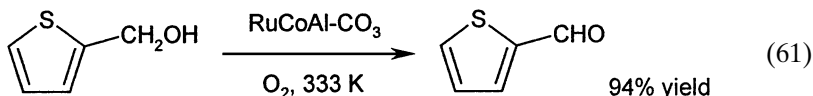
A. ALCOHOL OXIDATION CATALYSTS INCORPORATING Ru^{3+}

The group of Kaneda (277–279) proposed two methods for incorporating Ru^{3+} into a solid catalyst for air oxidation of alcohols. A first route is the incorporation of Ru^{3+} into materials with the hydrotalcite structure (277, 278). These LDHs consist of layers of octahedrally coordinated cations, (e.g., Mg and Al or Co and Al). When the hydroxides are prepared by precipitation in the presence of a small amount of trivalent Ru^{3+} , Ru^{3+} occupies lattice positions and is thus stably incorporated in the structure. The excess charge in the layers resulting from the trivalent Ru or Al is compensated by interlayer anions, resulting in materials denoted as RuCoAl-LDH-CO_3 or RuAlMg-LDH-CO_3 . A more original approach is the incorporation of Ru^{3+} into the mineral hydroxyapatite $\text{Ca}_{10}(\text{PO}_4)_6(\text{OH})_2$ (HAP). Ca^{2+} at certain lattice positions can be replaced with RuCl^{2+} , resulting in a material with the general formula $(\text{RuCl})_2\text{Ca}_8(\text{PO}_4)_6(\text{OH})_2$ (Ru-HAP). On the basis of X-ray photoelectron spectroscopy (XPS), energy dispersive X-ray analysis, and extended X-ray absorption fine structure analysis, it was proposed that Ru is surrounded by two phosphate anions and retains one Cl atom in its primary coordination sphere (279). With the Ru-LDH and Ru-HAP catalysts, more or less the same reactions can be performed, with O_2 as the oxidant:



Particularly, primary allylic and benzylic alcohol groups are converted into the corresponding aldehydes, with negligible formation of the acids. Simple

aliphatic alcohols such as 1- or 2-alkanols are transformed into the carbonyl compounds with selectivities >95%. Even oxidation-sensitive functions such as pyridine or thiophene rings are not attacked during alcohol oxidation:



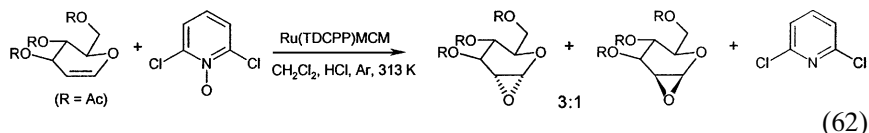
Under similar conditions, even benzylic C–H bonds of some hydrocarbons (xanthene and fluorene) are converted to the ketones (e.g., fluoren-9-one). Notwithstanding the parallel activities of the two catalysts, different mechanisms were tentatively proposed (277–279). Thus, for RuCoAl–LDH–CO₃, it was postulated that the presence of Co in the structure facilitated the formation of high-valent Ru(V)=O species. In contrast, for the Ru–HAP catalyst, it was proposed that after coordination of the reactant to Ru as an alcoholate, the carbonyl compound was eliminated, leaving a Ru–H compound, which in a next step is reoxidized by O₂. The basic nature of the HAP (or LDH) support may actually favor the latter route, with formation of an alcoholate. Filtration tests and elemental analyses confirm the stability of the supported species in both catalysts.

Catalysts with similar reactivities were prepared by anion exchange of perruthenate (RuO₄[−]) on materials with quaternary ammonium groups (e.g., cross-linked polystyrene beads or mesoporous siliceous molecular sieves of the MCM-41 type) (280–282). These MCMs were functionalized by silylation with $-(\text{CH}_2)_3\text{NMe}^+$ groups; because they are semiinorganic, they are inherently more stable than organic polymers. Reactions are best performed in toluene at 353 K with O₂. The range of reactants that can be used with these catalysts is strictly limited to benzylic and allylic primary alcohols; for instance, cyclohexanol and 2-cyclohexenol are unreactive. Results have been corroborated by satisfactory leaching tests and elemental analyses. Although the precise fate of the perruthenate in the reactions is unclear, it seems that RuO₂ is not formed (282). RuO₂ as well as Ru/C or Ru/CeO₂ are also catalysts for aerobic alcohol oxidation, but under much more drastic conditions (275). The same perruthenate-derived catalyst has also been used in the oxidation of hydroxylamines to give nitrones (283).

A material with nitrogen-coordinated Ru was obtained from a silica-linked 2-(phenylazo)pyridine ligand. Results for cyclobutanol oxidation with O₂ and the sacrificial oxidant isobutyraldehyde indicate that one- and two-electron oxidations occur simultaneously. The stability of the catalyst is not always guaranteed, probably because acids may be formed in oxidations of alcohols (284). Leaching problems are also encountered with a polymer-bound Ru Schiff base complex, used in oxidation of benzyl alcohol (285).

B. RU-CATALYZED EPOXIDATION

A modified MCM-41 was also used to immobilize Ru porphyrins such as Ru-*meso*-tetrakis(2,6-dichlorophenyl)porphyrin, [Ru(II)(TDCPP)(CO)(EtOH)] (286, 287). The grafted aminopropyl groups easily displace the ethanol ligand in the Ru(II) complex; efficient retention of the complex in the MCM-41 seems possible only if this coordinative bond is formed. When 2,6-dichloropyridine N-oxide is added to start the catalytic epoxidations, the Ru is presumably converted to a Ru(V) oxo species or a Ru(IV)-oxoporphyrin cation radical. During the reaction, the axial coordination of the tethered amino group on the Ru-porphyrin is probably preserved. Accordingly, this immobilized Ru-porphyrin has a reactivity that is distinguishable from that of a trans-dioxo Ru(VI)(TDCPP)O₂ complex (193). Most electron-rich olefins and even 1-octene are epoxidized in high yields:



HCl (30 mol%) is required for the reaction, and hence strictly anhydrous conditions are required to protect the epoxides. Although Ru-based numbers of turnover are quite high (up to 5000), the loading of the MCM with Ru-porphyrin is very low, and only 1.5–3.0 g of product is produced per gram of catalyst. Although many bulky olefins react smoothly, there are indications in the reaction of limonene, for example, that steric effects direct the regioselectivity. The catalyst is gradually deactivated, partly by leaching, since 5% of the Ru is lost in each run.

C. OLEFIN DIHYDROXYLATION

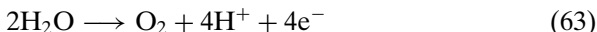
Polybenzimidazole-supported Ru seems to be a catalyst for the formation of cyclohexanediol from cyclohexene. However, the selectivity is low, and the stereochemistry and the stability of anchoring of the catalyst are unclear (37).

D. PARAFFIN HYDROXYLATION AND KETONIZATION

The immobilization of Ru-phthalocyanines follows routes similar to those employed for the analogous Fe complexes. Particularly, the perfluorinated Ru phthalocyanines were immobilized in zeolites by ship-in-a-bottle synthesis or by template synthesis, or in MCMs after surface modification. The materials display extremely high activities for the oxygenation of paraffins with *t*-BuOOH as the oxidant (128, 288).

E. CATALYSTS FOR OXIDATION OF WATER

Numerous Ru catalysts for oxidation of water were prepared by fixation of Ru cations to cation exchangers (289–296). This reaction has been investigated for its relevance to photosynthesis:

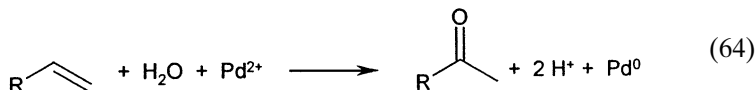


In model studies, the four electrons must be trapped, for example, by Ce^{4+} . Although this reaction is not of direct synthetic use, the investigations showed how the nuclearity—and consequently the reactivity—of Ru is critically influenced by the Ru precursor and by the ion exchanger. Support materials include montmorillonite and Nafion membranes. The actual catalytic center is probably an oligonuclear complex, but it is deactivated by bimolecular reaction with another catalyst entity. Consequently, if the Ru precursor is oligonuclear, such as the trinuclear compound Ru red ($[(\text{NH}_3)_5\text{Ru}(\text{III})-\text{O}-\text{Ru}(\text{IV})(\text{NH}_3)_4-\text{O}-\text{Ru}(\text{III})(\text{NH}_3)_5]^{6+}$), the immobilization drastically increases the activity per Ru atom since the deactivation is efficiently suppressed. In contrast, with mononuclear Ru precursors (e.g., $[\text{Ru}(\text{NH}_3)_5\text{Cl}]^{2+}$), the activity per Ru atom goes through a maximum as the Ru loading of the cation exchanger is increased; at low Ru loadings, an increasing Ru loading makes formation of an oligonuclear Ru compound more likely, but a Ru loading that is too high results in bimolecular deactivation.

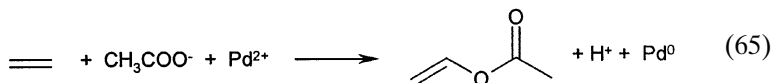
XIII. Palladium

A. Pd AS A WACKER-TYPE CATALYST

Textbook chemistry (297, 298) teaches that palladium is the preferred catalyst for aerobic oxidation of olefins. When water is the solvent, nucleophilic water addition to coordinated olefins is the key step in the so-called Wacker cycle. Wacker oxidation occurs regioselectively because a carbonyl group is formed at that carbon atom of the double bond where the nucleophile in a Markovnikov-like addition would enter. The Wacker reaction thus yields methylketones from primary alkenes:

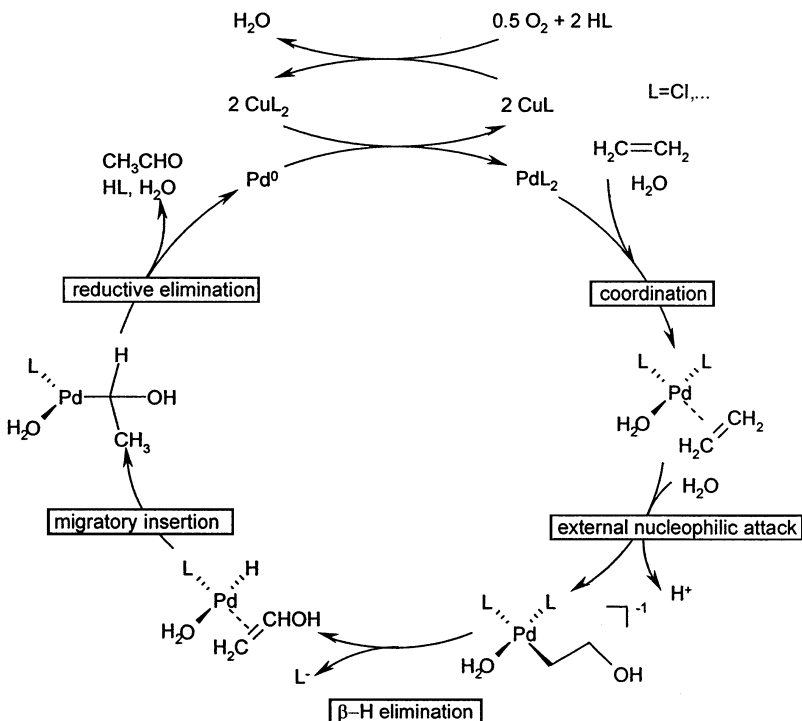


Electron-withdrawing substituents on the double bond direct the carbonyl group to the β position. In water-free acetic acid, (alkali) acetates are required as strong nucleophiles:



Both reactions were at the origin of the boom in palladium chemistry, scientifically as well as industrially. To render the previously cited reactions catalytic, the reduced form of Pd is reoxidized with the $\text{Cu}^{2+}/\text{Cu}^+$ redox couple, with the reduced form of copper finally being reoxidized with dioxygen. This chemistry is performed industrially with the chloride salts of Pd^{2+} and Cu^{2+} with ethylene as a feed, either in an aqueous or acetic acid medium. Products are acetaldehyde and vinyl acetate, respectively.

The Wacker catalytic cycle is known in detail due to the detailed work of several authors (298–301) and consists of linked elementary reactions known from organometallic chemistry (302). Even in a chloride medium there is firm evidence for the identity of the rate-determining step (303). The cycle, however, takes into account kinetic, spectroscopic, isotopic, and stereospecific evidence (Scheme 2).

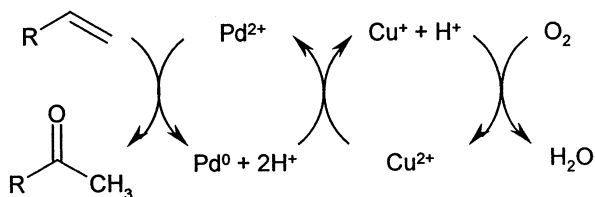


SCHEME 2

The main disadvantage of Wacker chemistry is the chloride medium in which the reaction occurs. It is corrosive and leads to formation of a significant number of chlorinated by-products; the yield of acetaldehyde is approximately 95% (304). For obvious reasons, attempts were reported to anchor a chloride-free variant of the traditional homogeneous Wacker catalyst.

1. Pd/Cu Ion-Exchanged Zeolites as “Green” Variants of the Wacker Catalyst

Taking into account the nature of the Wacker concept (305), it is evident that early work is available with Pd^{2+} and Cu^{2+} ion-exchanged zeolites (306–308). Because ion exchange was done with $\text{Pd}(\text{NH}_3)_4^{2+}$, it was not clear whether residual ammonia was an essential requirement for good catalyst selectivity and stability (Scheme 3).



SCHEME 3

Later, a more extensive comparison was made between homogeneous Wacker chemistry and the analogous version with Pd^{2+} and Cu^{2+} coexchanged on a Y zeolite (309, 310). A surprising parallel in properties was observed:

- The reactivities of the olefins decreased exponentially with their molecular weight, reflecting the susceptibility of the coordinated olefin to an external nucleophilic attack by water.
- Labeled oxygen atoms in dioxygen are not incorporated into the reactant, showing that product oxygen stems from water.
- The orders of reaction in olefin and Pd are 1 and 1, respectively.
- The absence of a reactant kinetic isotope effect indicates that C–H bond breaking is not part of the rate determining event.

The zeolite-based Wacker catalyst, however, shows the following characteristics:

- The variable order of reaction in oxygen suggests that the reoxidation of Pd^0 by Cu^{2+} or the reoxidation of Cu^+ with dioxygen are rate limiting at high or low partial pressures of O_2 , respectively.

- The formation and location of the active complex is obviously strongly dependent on the zeolite topology and composition; indeed, among the many zeolite structures examined, only the faujasite topology with the charge density of zeolite Y was found stabilize a maximum number of active sites.

It is clear that the Wacker cycle in a CuPdY zeolite incorporates the traditional features of the homogeneous catalysis combined with typical effects of a zeolite (303, 310). It also follows that whereas other cation exchangers in principle will show Wacker activity after cation exchange with Cu/Pd ions, the cage and pore architecture will probably be less suitable for Wacker chemistry than those of the faujasite structure. This is the case for fluorotetrasilicic mica, a synthetic layer silicate that swells under reaction conditions and allows access to the interlayer space (311).

Because most of this work has been done with an excess of oxygen, it is expected that cationic active species will not easily be released from the cation exchanger. Although long time-on-stream experiments have not been reported, the available data indicate acceptable stability (310).

2. Supported Redox Couples in Wacker Catalysis

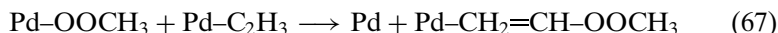
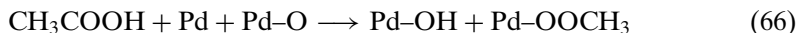
Besides the cupric/cuprous couple, reports show that a V^{4+}/V^{5+} couple is also able to reoxidize reduced Pd species under Wacker reaction conditions (312–316). In early work, a Pd salt was impregnated on a Ti-doped V_2O_5 phase supported on α -alumina (316) or on titania (315). The catalytic activity was reported to be proportional to the V^{4+} concentration ($g = 1.970$ in electron paramagnetic resonance). The latter can be increased by Mo doping of the supported V_2O_5 monolayer. An optimized version of this catalyst consists of $PdSO_4$ impregnated on an excess of V_2O_5 supported on titania (315, 316). The high order of the reaction in oxygen parallels that in CuPdY zeolites, suggesting that the reoxidation of V^{4+} is rate limiting. The stability of such a system has been examined for the 1-butene to butanone oxidation (315). After an initial phase of activity decline (60%), the activity was found to be steady for more than 700 h.

Heteropolyacids are possible substituents for Cu^{2+}/Cu^+ as the oxidant of Pd in Wacker chemistry (317). A Pd salt and molybdovanadophosphate impregnated on a high-surface-area support have been used as a Wacker catalyst for the oxidation of cyclopentene (318). In contrast to all other Wacker systems, which are not suitable for oxidation of higher olefins and cycloalkenes (319), this catalyst oxidizes cyclopentene to cyclopentanone, a starting material for a variety of pharmaceuticals and fragrances (e.g., jasmonates). Although during the first run good cyclopentanone yields were obtained, the leaching of Pd could only be limited to 1% in aqueous ethanol as the solvent.

B. ACETOXYLATION WITH SUPPORTED CATALYSTS

The industrially important acetoxylation consists of the aerobic oxidation of ethylene into vinyl acetate in the presence of acetic acid and acetate. The catalytic cycle can be closed in the same way as with the homogeneous Wacker acetaldehyde catalyst, at least in the older liquid-phase processes (320). Current gas-phase processes invariably use promoted supported palladium particles. Related fundamental work describes the use of palladium with additional activators on a wide variety of supports, such as silica, alumina, aluminosilicates, or activated carbon (321–324). In the presence of promoters, the catalysts are stable for several years (320), but they deactivate when the palladium particles sinter and gradually lose their metal surface area. To compensate for the loss of acetate, it is continuously added to the feed. The commercially used catalysts are Pd/Cd on acid-treated bentonite (montmorillonite) and Pd/Au on silica (320).

Several mechanistic proposals have been advanced, ranging from metal catalysis to redox cycles with Pd clusters or isolated Pd/PdO species (325–327). It is fair to assume that activation of ethylene occurs by hydrogen abstraction by palladium clusters, whereas H abstraction from acetic acid occurs on PdO (oxidized clusters):



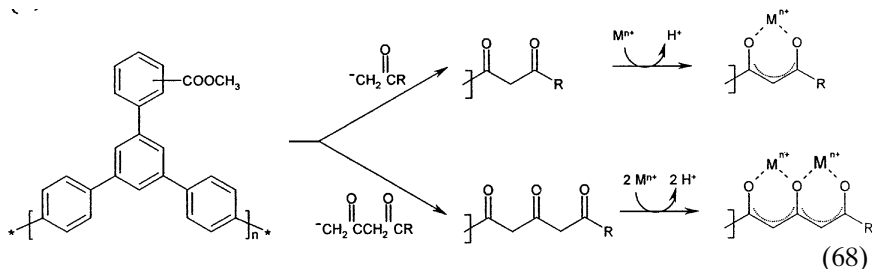
Alkali metal promoters seem to favor the formation of Pd-OOCCH₃ in the first reaction and facilitate the Pd-O bond rupture in the rate-limiting second reaction (320).

C. ALCOHOL OXIDATION WITH SUPPORTED Pd CATALYSTS

The classical Pd-on-carbon catalyst has been used occasionally in this context, specifically for the aerobic oxidation of glycerol into glyceric acid under alkaline conditions (328). This procedure in an aqueous medium is evidently limited to water-soluble reactants such as carbohydrates (329). Alternatively, a water-soluble (sulfonated) bathophenanthroline Pd(II) complex enables alcohol oxidation in a biphasic water-alcohol system (330).

Pd²⁺ chelated by a functionalized polymer was reported to be active for the aerobic oxidation of almost all types of alcohols, such as monohydric and polyfunctional alcohols, as well as unsaturated alcohols (331–333). In this work, mono- as well as binuclear catalysts were formed on a polymer support with β-di- and triketone surface ligands. For many reactants, a large increase in activity is observed in changing from the mono- to the binuclear

catalyst (333). Rate enhancements for simple alkanols and ethylene glycol are 5- and 30-fold, respectively. This enhancement is suggested to stem from a cooperative action of the two sites in a binuclear catalyst, with the first Pd^{2+} , for example, coordinating the reactant and the second one allowing its oxidation:



Whereas the use of “naked” supported metal clusters is well established in heterogeneous catalysis, the application of ligand-stabilized giant clusters, uniform in size, has only recently been implemented. For example, a support-immobilized five-shell Pd cluster $[\text{Pd}_5(\text{phen})]$ was shown to retain its original cluster size of 3.0 nm and the local ordering of the Pd atoms in the cluster when immobilized on a neutral titania surface (334, 335) (phen = 1,10-phenanthroline). The aerobic oxidation of primary allylic alcohols into α,β -unsaturated aldehydes with such an immobilized five-shell cluster was possible. Because the 1,10-phenanthroline ligands coordinate only edge and corner atoms, the other surface atoms must be protected, for example, by O_2^- . Highly reactive uncoordinated metal atoms may be generated *in situ* in the reactor. Understanding of the electronic and geometric properties of the Pd cluster surface is still in its infancy. In the same context, the preparation of supported surfactant-stabilized nanoclusters (of Pd) is noteworthy (336). The selective oxidation of D-glucose into gluconate is a current application of this catalytic material.

D. SUPPORTED LIQUID-PHASE Pd CATALYSTS

Supported liquid-phase catalysts (SLPCs) combine the salient features of both homogeneous and heterogeneous catalysis for enhanced catalytic and/or process efficiency (337). SLPC catalysts, in which a liquid-phase (homogeneous) catalyst is dispersed within a porous support, have been used in Wacker-type ethylene oxidation for acetaldehyde and vinyl acetate production (337, 338). In the former case, a traditional homogeneous Wacker catalyst (*vide supra*) consisting of a chlorinated solution of Pd and Cu chlorides retained on a support with monomodal pore size distribution

was found to function as a SLPC with a liquid loading of about 0.1 vol. homogeneous catalyst/volume of pores (338). On the other hand, the classical supported catalysts for vinyl acetate production (e.g., Pd/Au on silica) in plant conditions seem to function as SLPCs (339). Adsorbed acetic acid exists as a three-monolayer thick film, retained on the surface by palladium and alkali acetates. A layer of molten alkali acetate is assumed to be the foundational layer of liquid for the establishment of this SLPC (337). It is stressed that this rationalization of the behavior of a supported vinyl acetate catalyst is at variance with the one advanced earlier. With a SLPC aqueous Wacker catalyst on silica, long-chain olefins are oxidized aerobically to give ketones in low yields. The enhanced yields in isomeric olefins have been attributed to the slow reoxidation of Pd(0) as a consequence of low oxygen diffusion rates (340).

On the other hand, inverse phase transfer catalysis has been successfully applied for Wacker oxidation of 1-decene (341). In this approach (although outside the scope of this review), β -cyclodextrin functionalized with a polar substituent transfers the organophilic olefin adsorbed in its (organophilic) β cage into the aqueous phase containing a homogeneous Wacker catalyst, thus improving mass transfer between the aqueous and organic layers. The positive results have been correlated with the solubility of the functionalized cyclodextrins in water and the low stability of the host-guest inclusion complexes between the reactant and the organophilic cyclodextrin cage.

XIV. Cerium

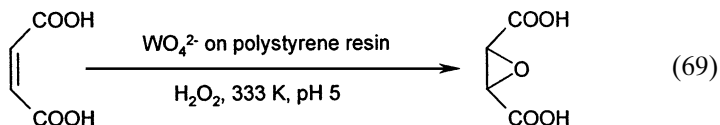
Ce^{4+} is easily exchanged on resins such as Nafion. Ce-Nafion catalyzed the oxidation of carveol to carvone with *t*-BuOOH as the oxidant; no data characterizing leaching were provided (59). CeO_2 on Al_2O_3 was used as a solid catalyst for the cooxidation of cyclohexane and cyclohexanone. Products are dibasic acids and ϵ -caprolactone. It was claimed that in water-free reaction conditions, Ce is not eluted from the solid (342).

XV. Tungsten

Tungsten is useful for oxidation catalysis, especially in combination with H_2O_2 as the oxygen donor. In analogy with Mo, the oxygenating species are often anionic peroxotungsten species, which are formed by the reaction

between oxotungstate and H_2O_2 . Although the activities of W and Mo are higher in the absence of coordinating molecules such as water and alcohols, the retarding effect of the solvent is less pronounced in the case of W catalysts. Thus, although Mo is an excellent oxidation catalyst only in an anhydrous nonalcohol environment, W catalysis can also be applied in aqueous and alcoholic solvents. Examples of commercial processes with homogeneous W/ H_2O_2 are the epoxidation of maleic acid (343), the epoxidation of allyl alcohol in water (344), and the oxidation of secondary amines (345).

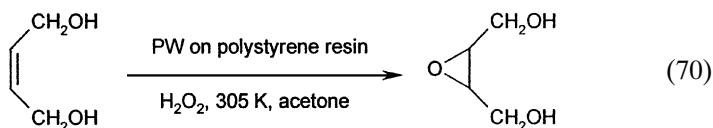
As a consequence of the similarities between Mo and W in catalysis with H_2O_2 , anchoring protocols for W closely parallel those for Mo. In many cases, organic, inorganic, or hybrid anion-exchanging supports are employed. For instance, tungstate immobilized on commercially available cross-linked polystyrene resins has been applied for the epoxidation of α,β -unsaturated acids and alcohols (346–348). For example, maleic acid is converted with aqueous H_2O_2 at 333 K at pH 5, yielding >90% of the corresponding *cis*-epoxysuccinate based on the oxidant:



However, particularly for the unsaturated acids, the epoxidation catalysis was not heterogeneous. Competitive anion exchange between the (peroxo)-tungstate and the carboxylate possibly causes leakage of W.

A major breakthrough in W catalysis was the discovery of heteronuclear peroxoW associations such as $\text{PW}_4\text{O}_{24}^{3-}$ (349–352). They are superior catalysts to W alone, for instance, because of their enhanced electrophilicity and oxidant efficiency. P–W catalysts were first anchored by Venturello *et al.* (353, 354) on a cross-linked polystyrene matrix containing quaternary ammonium groups. However, to optimize the catalytic results with supported P–W, fine tuning of the cross-linked polystyrene is necessary. For example, because most of the commercial resins are in the Cl form, two-electron oxidation of coexchanged chloride anions may occur, eventually resulting in chlorinated by-products. Hence, to perform selective oxidations, either the solid catalyst is fully exchanged with the P–W catalyst or the commercial material is completely converted into the nitrate form prior to the P–W catalyst exchange. The optimized P–W catalyst has been applied for the epoxidation of various olefins, including allylic alcohols (355). For example, *cis*-1,4-butene-diol is

converted with one equivalent of H_2O_2 into the corresponding *cis*-epoxide with 84% yield and 95% selectivity:



Moreover, the catalytic activity of a reused catalyst is completely preserved after several cycles, and the filtrate is catalytically inactive. This supported and reusable P–W catalyst has also been applied for the epoxidation of a series of terpene olefins (356). The productivity of the catalyst for the conversion of these bulky molecules is superior to that reported for Ti-MCM materials, for example. The stereochemical and regioselective characteristics of W catalysis are preserved in the supported P–W catalyst. For instance, geraniol is epoxidized at the 2,3 position, affording the *trans* product.

More thermostable variants contain quaternary ammonium groups that are linked to inorganic supports by hydrocarbon spacers. Silica-based hybrid anion exchangers have been applied to immobilize various oxoperoxoW anions, including $\text{W}_2\text{O}_{11}^{2-}$ and $\text{PW}_4\text{O}_{24}^{3-}$ (357). Polyoxometallates have been immobilized in a similar way (358). However, since these anions disintegrate upon contact with H_2O_2 into smaller active peroxyW anions, the eventual catalytically active W species are in principle identical. For example, $\text{PW}_4\text{O}_{24}^{3-}$ has been immobilized on a positively charged MCM-41 material and used for the production of various epoxides (359). The authors verified the heterogeneous behavior of the P–W on the cationic MCM-41 support and found no considerable dissolution of W in the epoxidation of cyclooctene.

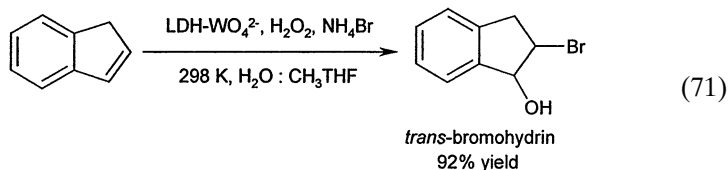
Neumann and Miller (360) reported catalytic epoxidations with analogous P–W materials in a triphasic mode. The activity in the solvent-free system is influenced by the length of the hydrocarbon spacer between the silica and the ammonium group. Cyclooctene, for example, is epoxidized with only 10% conversion when a trimethyl propyl ammonium salt is used, whereas a conversion of 45% can be obtained in the presence of an immobilized octyldimethyl benzyl ammonium salt. The enhanced conversion is probably the result of a nearly ideal hydrophilic–lipophilic balance at the active site.

LDHs have been intercalated with polymeric W anions such as $\text{H}_2\text{W}_{12}\text{O}_{40}^{6-}$ and $\text{W}_7\text{O}_{24}^{6-}$ (252, 253, 361). However, the W pillars disintegrate not only by the action of H_2O_2 but also because of drying prior to the catalytic oxidation. ZnAl-LDHs exchanged with the Keggin ion $\text{SiW}_{12}\text{O}_{40}^{4-}$ and the lacunary Keggin ion $\text{SiW}_9\text{O}_{39}^{8-}$, on the other hand, appear to be stable toward both treatments, with the lacunary W anion being more active than the Keggin structure (362). The ZnAl-LDH– $\text{SiW}_9\text{O}_{39}^{8-}$ material is capable of catalyzing

the epoxidation of cyclohexene with H_2O_2 in *t*-butyl phosphate. However, yields are low, and the epoxides are not fully stable in the reaction medium. In general, pillared LDHs have found only limited success in oxidation chemistry since a high catalytic activity of a pillar is often related to its partial degradation and hence an intrinsic destruction of the pillared material (363, 364).

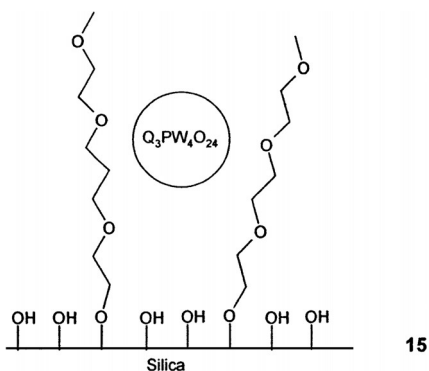
Besides polymeric W clusters, monomeric W has also been immobilized on LDHs. For example, LDH- WO_4^{2-} catalyzes the epoxidation of various olefins with H_2O_2 in methanol (365, 366). The anionic character of the intermediate peroxyW species under aqueous peroxidic conditions makes the LDH anion exchanger an excellent support. The results of leaching tests confirmed the strong electrostatic retention of all W species present during the catalytic cycle. The use of LDHs also allows simple modification of the microenvironment of tungstate. An apolar insoluble tungsten catalyst is readily prepared by exchanging WO_4^{2-} on the LDH in the presence of *p*-tosylate, for example. Reactions with hydrophilic and hydrophobic W-LDH catalysts demonstrate that the product yields are consistently better when there is a match between the polarities of the catalyst and the reactant. Moreover, regio-, stereo-, and chemoselectivity can be modified by manipulating the lipophilicity of the W environment. For example, the epoxidation of geraniol with H_2O_2 in the presence of the polar W catalyst gives mainly the 2,3-epoxide, whereas the 6,7-epoxide is formed preferentially with the *p*-tosylate material.

LDH- WO_4^{2-} has also been applied for oxidative bromination of unsaturated hydrocarbons (367). In a first step, W on LDH catalyzes the oxidation of Br^- with H_2O_2 . Subsequently, the resultant bromonium species (Br^+ , which could be equilibrated with species such as HOBr or Br_2) react rapidly with the target molecules. An advantage of the oxidative electrophilic bromination is that the active bromine is formed *in situ* in a controlled way; there is no direct contact with Br_2 . Moreover, the bromination is performed under mild conditions such as room temperature, atmospheric pressure, and near neutral pH. Indeed, the LDH- WO_4^{2-} -catalyzed bromination mimics the enzymatic activity of bromoperoxidases not only formally but also organizationally and mechanistically. For example, indene is bromohydroxylated almost quantitatively with NH_4Br and H_2O_2 in a water-2-methyltetrahydrofuran solvent mixture (368):



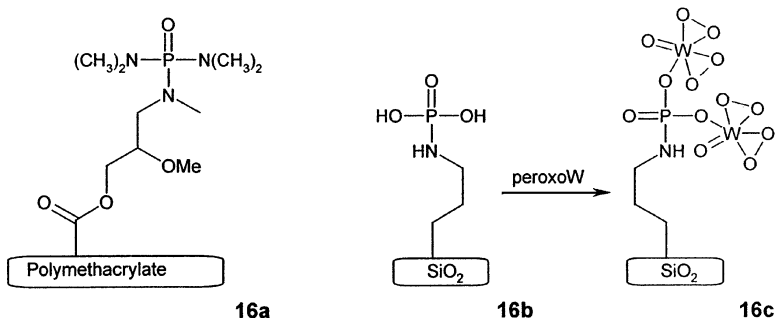
Supported W catalysts have also been prepared by using commercial activated carbon. For instance, in an old patent, the deposition of NaHWO_4 on charcoal is described. The W on charcoal appears to be active for the epoxidation of 1,4-butene-2-diol with H_2O_2 (369). Tungstate-doped porous carbons have been applied for sulfide oxidation (266). However, leaching of W from such materials seems unavoidable.

Neumann and Cohen (370) reported the sorption of neutral W catalysts such as $\text{Q}_3\text{PW}_4\text{O}_{24}$ (Q = tetrahexylammonium) in supported polyether phases (370). The catalyst (**15**) consists of polyoxyethylene or polyoxypropylene tails, which are covalently bound to a silica surface. The authors claimed an unchanged activity upon reuse of the catalyst.



There is also a series of reports on the incorporation of W in silica and MCM-41-type materials (371–375). The materials have been used in various reactions of olefins with aqueous H_2O_2 , such as epoxidation, formation of *trans* diols, and cleavage to dibasic acids. None of these papers presents a clear concept of how anionic peroxyW species are retained by the siliceous support during catalytic oxidation. As shown by Brégeault *et al.*, (372), W is leached out of the framework to a smaller or larger extent under aqueous H_2O_2 conditions. Similar problems are probably encountered for catalysts prepared by simple adsorption of $\text{H}_3\text{PW}_{12}\text{O}_{40}$ or $\text{H}_4\text{SiW}_{12}\text{O}_{40}$ on alumina (209, 262, 376).

A much more reliable concept is the formation of heteronuclear associations between tungstate and phosphorus species that are covalently attached to a support. This approach was pioneered by Gelbard *et al.* (377). For example, amino groups in a polymethacrylate matrix were phosphorylated to give grafted phosphoramides, such as **16a**. Alternatively, Hoegaerts *et al.* (359) phosphorylated silica-bound aminopropyl groups, leading to **16b**. Such immobilized P=O centers can form covalent bonds with peroxyW species; a possible structure is **16c**.



The resulting materials are particularly effective catalysts. Not only are the initial turnover frequencies high (up to 500 catalytic cycles per hour) but the stability of the anchored catalysts in such systems was also shown beyond doubt by two research teams (359, 377).

An analogous approach was followed by Duprey *et al.* (378), who grafted phosphate species on TS-1; these P groups can form covalent bonds with peroxoW. The resulting supported catalyst was capable of converting limonene to mainly the 1,2-epoxides. This is a strong demonstration that the W is the active species since limonene is too large to reach the Ti sites in the TS-1 micropores.

XVI. Rhenium

Re has recently come to the forefront in liquid phase oxidation catalysis, mainly as a result of the discovery of the catalytic properties of the alkyl compound CH_3ReO_3 [methyltrioxorhenium (MTO)]. MTO forms mono- and diperoxo adducts with H_2O_2 ; these species are capable of transferring an oxygen atom to almost any nucleophile, including olefins, allylic alcohols, sulfur compounds, amides, and halide ions (9). Moreover, MTO catalysis can be accelerated by coordination of N ligands such as pyridine (379–381). An additional effect of such bases is that they buffer the strong Lewis acidity of MTO in aqueous solutions and therefore protect epoxides, for example.

An obvious way to immobilize MTO would be by coordinative binding on a PVP resin. However, in our experience, peroxidized MTO is not efficiently retained on PVP. Two alternative approaches have been proposed. First, MTO was supported on Nb_2O_5 , and its activity was tested in the epoxidation of stilbenes and of styrenes (382). However, competitive metathesis and pronounced hydrolysis of the epoxides to the diols were observed. A second approach was suggested by Neumann and Wang (383). In a strategy similar to that for $\text{H}_5\text{PV}_2\text{Mo}_{10}\text{O}_{40}$ (370), they adsorbed MTO in a surface layer of

polyoxyethylene and polyoxopropylene chains on SiO₂. In neither of the two proposed immobilization routes is it clear how the MTO stays firmly bound to the surface.

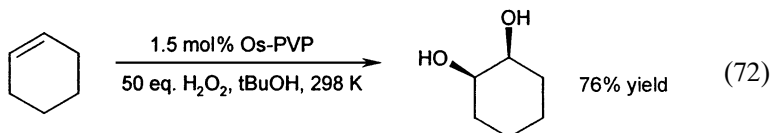
XVII. Osmium

The major application of Os to organic synthesis is the dihydroxylation of olefins to give *cis* diols. The dihydroxylations initially used stoichiometric OsO₄, but the reaction can be made catalytic by the addition of oxidants such as H₂O₂, *t*-BuOOH, amine N-oxides, metal chlorates, or even ferricyanide (384). These reoxidize Os(VI) to Os(VIII). Notwithstanding the high cost of Os, the reaction is a useful catalytic and highly selective alternative to the use of the stoichiometric permanganate reagent. A further step was the development of an enantioselective Os reaction by Kolb *et al.* (385). In this asymmetric dihydroxylation (AD), a chiral, cinchona-derived nitrogen base forms a coordinative bond with OsO₄. The ligand not only provides a chiral binding pocket around OsO₄, but also accelerates the addition of the Os *cis* dioxo group to the olefin (386). Hence, even if the equilibrium constant for binding of the ligand to Os is relatively low, the EE is still high since most dihydroxylations occur at ligand-bound Os centers. This situation also implies that under the optimum conditions of the AD, a considerable part of the Os is not bound to the ligand.

Attempts to anchor Os dihydroxylation catalysts are mainly fueled by the high cost of both Os and the chiral ligand and by the high toxicity and volatility of OsO₄. There are a multitude of reports on the anchoring of chiral ligands for the Os dihydroxylation. However, as explained previously, anchoring of the ligand does not imply that the Os is entirely anchored during catalysis since the binding is a dynamic process with a fairly small equilibrium constant (385). Experimental results show that reuse of a supported cinchona ligand necessitates supplementation with Os; the Os is subject to severe leaching in each run (387). Therefore, in the present context, we restrict the discussion to anchoring of the Os metal.

OsO₄ can coordinatively bind to PVP and other polymers with, for example, 1,4-diazabicyclo[2,2,2]octyl groups. This binding makes the compound much less volatile and hence safer. Cainelli *et al.* (388) noted that OsO₄ on PVP can be used with several oxidants. With H₂O₂, much of the ketol overoxidation product is formed. Better results are obtained with *t*-BuOOH for dihydroxylation of hindered olefins or with trimethylamine N-oxide for most other olefins. Herrmann *et al.* (389) used a similar material; however, when OsO₄ was immobilized on PVP in the presence of tetrahydrofuran solvent, the Os was reduced to the +VI state, as evidenced by XPS data (389).

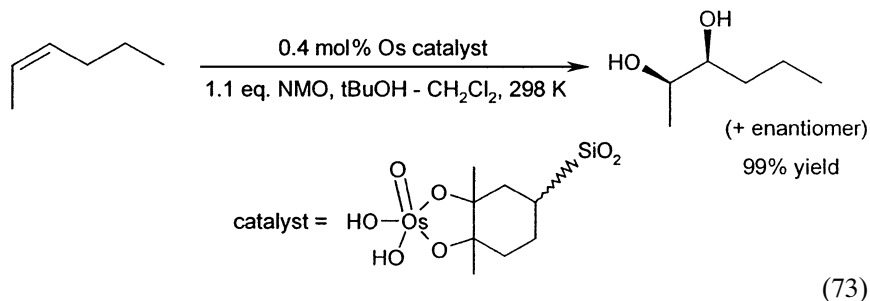
Moreover, XPS data also indicate that this Os reduction may be accompanied by oxidative degradation of the polymer. Not only the Os speciation but also the oxidant preference seem different for Herrmann's Os/PVP catalyst. Only H₂O₂ was an effective oxidant; even in this case, extreme oxidant excesses were applied to convert the olefins:



Neither Cainelli nor Herrmann reported a reliable test for stability of the anchoring (388, 389). Our experience indicates that Os massively leaches from PVP under oxidative conditions, and the filtrates are usually at least as active as the suspension. The suspension contains the base pyridine, which can retard the hydrolytic diol release from the Os(VI) glycolate complex (the latter step is often rate determining).

OsO₄ has also been entrapped in cross-linked polystyrene microspheres (390). Although this is an elegant approach, the concept by which Os is held inside the capsules is unclear. Moreover, the activity of the filtrate was not assessed.

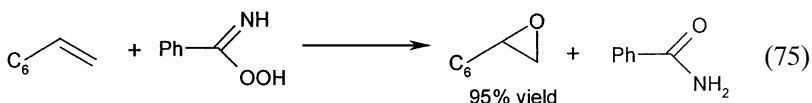
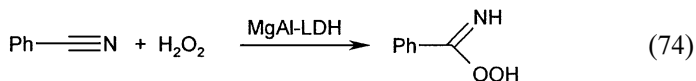
We recently immobilized an Os compound as a surface-bound, highly substituted diolate complex (391). It is well-known that the hydrolytic release of a diol from an Os–diolate complex becomes increasingly difficult with increasing substitution (392). Under well-defined conditions (e.g., with NMO as the oxidant in CH₂Cl₂–*t*-BuOH), tetrasubstituted diols and Os do not dissociate. Although the Os is bound on one side by the surface-anchored tetrasubstituted diolate, it is catalytically active on the other side. Most olefins can be dihydroxylated in very high yields with a stoichiometric amount of NMO (391):



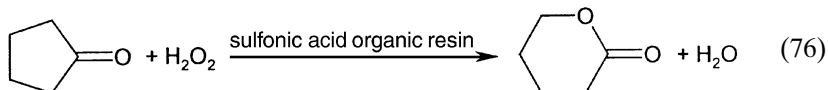
Most important, we have extensive evidence that in this case there is no catalytic activity in the filtrate.

XVIII. Metal-Free Oxidation Catalysts

Solid acids or bases often play a catalytic role in the activation of an oxidant such as H_2O_2 . Although this topic is not discussed in detail here, we nevertheless illustrate it with two examples. First, LDHs can function as solid bases to catalyze the conversion of aromatic nitriles to peroxy-imidic acids; the latter are excellent stoichiometric oxidants for olefin epoxidation (393):



Alternatively, acids can activate peroxides, for example, in the Baeyer-Villiger reaction (394):

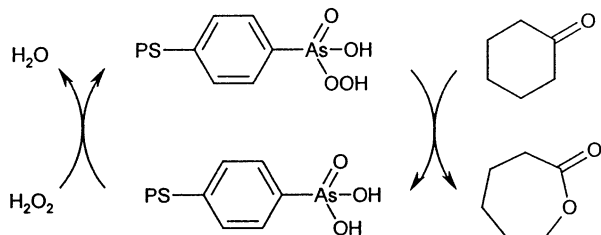


The remainder of this section is devoted to cases in which an immobilized oxidizing reagent can be regenerated by the action of a simple oxidant, such as a peroxide or O_2 . For instance, the flavin 10-ethyl-isoalloxazine was immobilized on organic polymers and used in the air oxidation of 1-benzyl-1,4-dihydronicotinamide (395). However, peracids, dioxiranes, and nitroxyl radicals are of much more synthetic importance.

A. PERACIDS

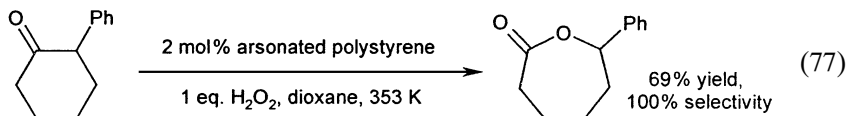
Organic percarboxylic acids have been immobilized on supports starting, for example, from silica-anchored cyanopropyl groups (396, 397). Subsequently, the nitriles are hydrolyzed to give acids, which are converted to peracids with H_2O_2 . The content of $-\text{COOOH}$ groups on a weight basis in the resulting reagent (3.5 mmol g^{-1}) is almost as much as in the widely used soluble *meta*-chloroperbenzoic acid, but because the reagent is a solid, it is much more readily recovered from the reaction mixture. However, regeneration of the percarboxylic acid is possible only by *ex situ* reaction with H_2O_2 and a strong acid, such as methanesulfonic acid.

In situ regeneration of a peracid, however, is possible if instead of a carboxylic acid, a phenylarsonic acid is used (398, 399). The catalytic cycle for the Baeyer-Villiger oxidation is given in Scheme 4.



SCHEME 4

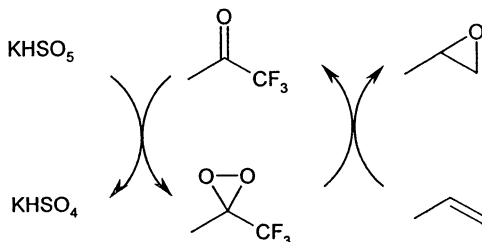
A cross-linked polystyrene-attached phenylarsonic acid was used as a Baeyer–Villiger and epoxidation catalyst in one or two liquid phases. For reactions in one liquid phase, dioxane is the preferred solvent, and highly concentrated H_2O_2 (90%) is used since protic solvents and water retard the formation of the perarsonic acid. Arylarsonic acids are relatively weak acids ($\text{p}K_a \sim 3\text{--}4$). Therefore, the hydrolysis of the lactone to give the ω -hydroxy acid, or of the epoxide to give the diol, can to some extent be avoided, even when the medium contains a high concentration of water at the end of the reaction. Consequently, high lactone yields can be obtained, even with stoichiometric H_2O_2 :



Alternatively, a liquid biphasic approach may be adopted for water-insoluble reactants such as estrone 3-methyl ether. Although the immobilization of the As undoubtedly improves its handling safety, the disposal of this toxic element remains a problem.

B. DIOXIRANES

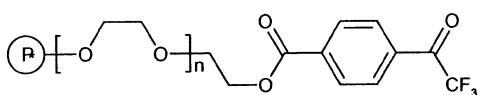
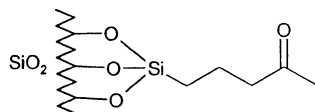
Ketones can be converted to dioxiranes by Oxone ($2\text{KHSO}_5 \cdot \text{KHSO}_4 \cdot \text{K}_2\text{SO}_4$) under slightly alkaline conditions (pH 7–8) (400). The dioxirane of 1,1,1-trifluoroacetone is a powerful yet selective oxidant under mild conditions, typically at temperatures below 313 K (10). Exemplary reactions are stereospecific olefin epoxidation and hydroxylation of tertiary C–H groups, or ketonization of CH_2 groups. With chiral ketones, even enantioselective reactions are possible (401). Although the reactions are often performed in excess ketone, it is actually possible to use the ketone in a catalytic fashion, for example, for 1,1,1-trifluoroacetone (Scheme 5).



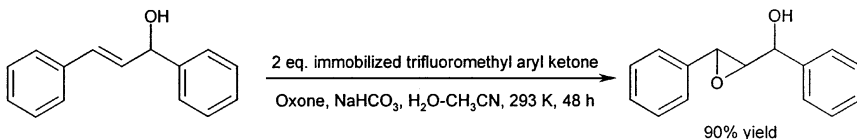
SCHEME 5

Highly fluorinated ketones such as hexafluoroacetone are oxidation catalysts even when H_2O_2 is used as an oxygen source. In this case, the reaction probably involves an α -hydroxyhydroperoxide, rather than a dioxirane, and the reactions require more drastic conditions (402, 403). Nevertheless, the observations demonstrate that fluorinated ketones are useful catalysts for activation of oxidants.

Several groups have attempted the anchoring of ketone catalysts for use in combination with Oxone (404–407). One of the incentives for anchoring the catalyst is that the most suitable ketone, 1,1,1-trifluoroacetone, is highly volatile. A solid-bound, nonvolatile ketone therefore offers obvious handling and cost advantages. In one approach, 4-(trifluoroacetyl)benzoic acid was anchored to a graft copolymer of polystyrene and polyoxyethylene (**17a**) (406); alternatively, aliphatic ketones were covalently bound to silica (**17b**) (405, 407).

**17a****17b**

Materials such as that shown in **17b** display a very low productivity in gram of product per gram of catalyst since the amount of immobilized ketone is relatively small (405); under homogeneous conditions, nonfluorinated ketones are mostly used in large, solvent-like amounts in order to achieve appreciable rates. In contrast, better results are achieved with **17a**; with two equivalents of supported ketone with respect to the olefin, more than a 90% yield is achieved with *trans*-chalcone (406):

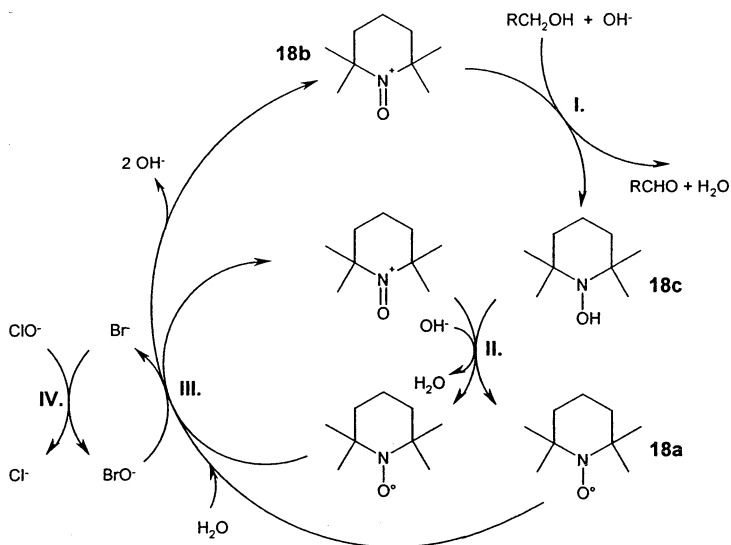


(78)

It is clear that this chemistry can benefit from the use of smaller amounts of more active ketones, possibly with H_2O_2 as the oxidant. Song *et al.* (407) covalently attached 1,1,1-trifluoro-2-oxododecyl groups to a SiO_2 surface. The site isolation (0.45 mmol g^{-1}) prevents formation of 1,2,4,5-tetraoxane structures and thus contributes to a higher stability of the trifluoroketones. However, even with this optimized material, 0.5 equivalent of ketone is needed, which amounts to 10 g of supported catalyst per gram of reactant.

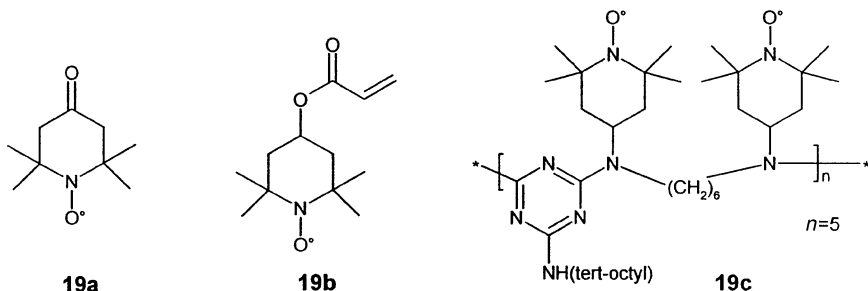
C. NITROXYL RADICALS

The nitroxyl radical TEMPO (**18a**) is an active catalyst for the selective oxidation of alcohols, with hypochlorite as the oxidant. The actual oxidizing species is the oxoammonium ion (**18b**), which in the alcohol oxidation (I in the structure) is reduced to the hydroxylamine (**18c**). A catalytic amount of bromide is used to generate BrO^- , which is capable of reoxidizing the hydroxylamine or the aminoxyl radical (**18a**) to the oxoammonium stage (408).

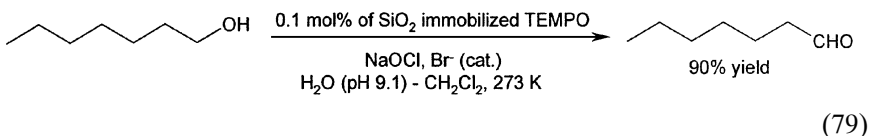


Numerous reports have described the covalent attachment of TEMPO-like groups to inorganic supports or polymers by several precursors (409–415). Typical strategies are reductive amination starting from 4-oxo-TEMPO (**19a**), amide formation with dicyclohexyl carbodiimide,

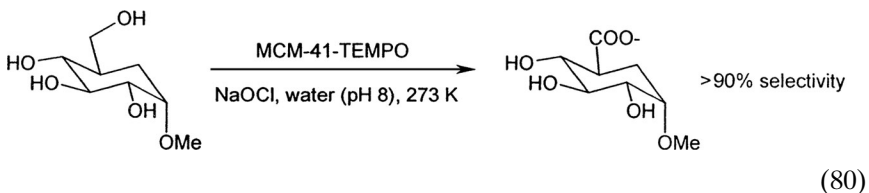
polymerization of a vinyl-bearing TEMPO-derivative (**19b**), or use of a commercially available oligomeric antioxidant (**19c**).



The chemical selectivity of reactions catalyzed by supported TEMPO closely resembles the patterns observed for homogeneous reactions. Primary alcohols are strongly preferred over secondary alcohols. Especially in liquid biphasic systems, high aldehyde yields can be achieved with as little as 0.1 mol% of the immobilized catalyst (412):



In contrast, if a single aqueous liquid phase is used, and if the aldehyde product has a tendency to be hydrated, the reaction proceeds smoothly to the carboxylic acid salt (413, 414). It is believed that the RC(OH)_2 hydration product of the aldehyde is the actual reagent. This reaction is highly useful for the selective oxidation of primary alcohol groups in sugars such as methyl- α -D-glucopyranoside to the uronic salt:



In this case, a less alkaline solution was used to prevent release of the organic groups from the MCM structure by alkaline hydrolysis. At pH 8 and 273 K, side reactions resulting from the presence of a small amount of HOCl can be avoided.

XIX. Conclusions

The research reviewed here reflects the intense activity of the preceding 30 years in the field of oxidation catalyst immobilization. Obviously, the literature contains many erroneous and unreliable results, particularly with respect to leaching of active metal components. Examples are the reactions with silica- or alumina-supported Mo, W, or Cr and organic peroxides as the oxidants. The majority of these reports simply deal with homogeneous catalysis. Nevertheless, many concepts have been proposed in which truly heterogeneous catalysis has been obtained. Examples include the Mopolybenzimidazole epoxidation catalyst (243), the Os-tetrasubstituted diolate catalyst for *cis*-dihydroxylation (391), the heteronuclear P-W epoxidation catalysts (359, 377), and the dioxirane systems (406, 407).

In many cases, the "black box" approach to anchoring of catalysts has been followed: A support and a metal compound are simply brought together, and it is hoped that the association between metal and support is persistent even under drastic oxidation conditions. However, this approach frequently leads to failure. It is preferable first to have a clear idea of all the chemical states of the catalyst that must be retained by the support. Thus, knowledge of the full catalytic cycle and of all metal species in the system is needed. Only then can a mechanism for catalyst immobilization be proposed. Although this is a demanding approach, it may often be the only one that is rewarding.

Stable anchoring of an oxidation catalyst can be promoted by reaction conditions, including the choice of solvents, catalytic species, and bases. For example, Fe- or Cu-exchanged materials have improved stability if they are used under alkaline conditions (138, 181). On the other hand, the presence of strong or complexing acids must be avoided since they induce metal leaching (162).

Immobilization often leads to much improved activity or lifetime of the catalyst. For example, the microenvironment of the catalytic center can be chosen to have the proper polarity, ionic strength, etc. for the catalytic activity (367). Prevention of bimolecular deactivation is the key to enhanced stability (115, 128). Unprecedented activities have been discovered by immobilization of catalytic centers, as is the case for Mn-catalyzed *cis* dihydroxylation (81). Another tantalizing reaction is the selective oxidation of primary carbon atoms, the industrial implementation of which is eagerly awaited (163).

ACKNOWLEDGMENT

Our research in heterogeneous liquid-phase catalysis has been supported by the Belgian federal government through an IUAP program "Supramolecular Chemistry and Catalysis."

REFERENCES

1. Van Rheenen, V., Kelly, R. C., and Cha, D. Y., *Tetrahedron Lett.* 1973 (1976).
2. Muzart, J., *Chem. Rev.* **92**, 113 (1992).
3. Sheldon, R. A., and Kochi, J. K., "Metal-Catalyzed Oxidations of Organic Compounds," Academic Press, New York, 1981.
4. Sheldon, R. A., and Kochi, J. K., *Adv. Catal.* **25**, 272 (1976).
5. Lyons, J. E., *Appl. Ind. Catal.* **3**, 131 (1984).
6. Parshall, G. W., "Homogeneous Catalysis: The Applications and Chemistry of Catalysis by Soluble Transition Metal Complexes," Wiley, New York, 1992.
7. Montanari, F., and Casella, L. (Eds.), "Metalloporphyrin Catalyzed Oxidations," Kluwer, Dordrecht, 1994.
8. Ojima, I., "Catalytic Asymmetric Synthesis," VCH, New York, 1993.
9. Herrmann, W. A., Fischer, R. W., and Marz, D. W., *Angew. Chem. Int. Ed. Engl.* **30**, 1638 (1991).
10. Mello, R., Fiorentino, M., Fusco, C., and Curci, R., *J. Am. Chem. Soc.* **111**, 6749 (1989).
11. Sheldon, R. A., and van Doorn, J. A., *J. Catal.* **31**, 427 (1973).
12. Clerici, M. G., and Ingallina, P., *J. Catal.* **140**, 71 (1993).
13. Murugavel, R., and Roesky, H. W., *Angew. Chem.* **109**, 491 (1997).
14. De Vos, D. E., Vanoppen, D., Buskens, P., Knops-Gerrits, P. P., and Jacobs, P. A., in "Comprehensive Supramolecular Chemistry," (T. Bein and G. Alberti, Eds.), Vol. 2, p. 647, Pergamon, Elmsford, NY, 1997.
15. Gao, Y., Hanson, R. M., Klunder, J. M., Ko, S. Y., Masamune, H., and Sharpless, K. B., *J. Am. Chem. Soc.* **109**, 5765 (1987).
16. Maschmeyer, T., Rey, F., Sankar, G., and Thomas, J. M., *Nature* **378**, 159 (1995).
17. Hutter, R., Mallat, T., and Baiker, A., *J. Catal.* **153**, 177 (1995).
18. Cativiela, C., Fraile, J. M., Garcia, J. I., and Mayoral, J. A., *J. Mol. Catal. A* **112**, 259 (1996).
19. Fraile, J. M., Garcia, J. I., Mayoral, J. A., Grazia Proietti, M., and Sanchez, M. C., *J. Phys. Chem.* **100**, 19484 (1996).
20. Fraile, J. M., Garcia, J. I., Mayoral, J. A., De Ménorval, L. C., and Rachdi, F., *J. Chem. Soc. Chem. Commun.*, 539 (1995).
21. Fraile, J. M., Garcia, J. I., Lazaro, B., and Mayoral, J. A. F., *J. Chem. Soc. Chem. Commun.*, 1807 (1998).
22. Fraile, J. M., Garcia, J. I., Mayoral, J. A., and Vispe, E., *J. Catal.* **189**, 40 (2000).
23. Coles, M. P., Lugmair, C. G., Terry, K. W., and Tilley, T. D., *Chem. Mater.* **12**, 122 (2000).
24. Ferreira, P., Goncalves, I. S., Kuhn, F. E., Pillinger, M., Rocha, J., Santos, A. M., and Thursfield, A., *Eur. J. Inorg. Chem.* **3**, 551 (2000).
25. Holmes, S. A., Quignard, F., Choplin, A., Teissier, R., and Kervennal, J., *J. Catal.* **176**, 173 (1998).
26. Holmes, S. A., Quignard, F., Choplin, A., Teissier, R., and Kervennal, J., *J. Catal.* **176**, 182 (1998).
27. Krijnen, S., Abbenhuis, H. C. L., Hanssen, R. W. J. M., van Hooff, J. H. C., and van Santen, R. A., *Angew. Chem. Int. Ed. Engl.* **37**, 356 (1998).
28. Krijnen, S., Mojet, B. L., Abbenhuis, H. C. L., van Hooff, J. H. C., and van Santen, R. A., *Phys. Chem. Chem. Phys.* **1**, 361 (1999).
29. Alder, K. I., and Sherrington, D. C., *J. Mater. Chem.* **10**, 1103 (2000).
30. Farrall, M. J., Alexis, M., and Trecarten, M., *Nouv. J. Chim.* **7**, 449 (1983).
31. Choudhary, B. M., Valli, V. L. K., and Durga Prasad, A., *J. Chem. Soc. Chem. Commun.*, 1186 (1990).
32. Choudhary, B. M., Rani, S. S., Rao, Y. V. S., Arntz, D., Kiricsi, I., Simons, K., Blackmond,

- D. G., Ratnasamy, P., Johnson, P., and Hoelderich, W., *Stud. Surf. Sci. Catal.* **75**, 1247 (1993).
33. Canali, L., Karjalainen, J. K., Sherrington, D. C., and Hormi, O. E. O., *Chem. Commun.*, 123 (1997).
34. Karjalainen, J. K., Hormi, O. E. O., and Sherrington, D. C., *Tetrahedron Asymmetry* **9**, 1563 (1998).
35. Karjalainen, J. K., Hormi, O. E. O., and Sherrington, D. C., *Tetrahedron Asymmetry* **9**, 2019 (1998).
36. Karjalainen, J. K., Hormi, O. E. O., and Sherrington, D. C., *Tetrahedron Asymmetry* **9**, 3895 (1998).
37. Sherrington, D. C., *Catal. Today* **57**, 87 (2000).
38. Linden, G. L., and Farona, M. F., *J. Catal.* **48**, 284 (1977).
39. Bhaduri, S., Ghosh, A., and Khwaja, H., *J. Chem. Soc. Dalton Trans.*, 447 (1981).
40. Sherrington, D. C., and Simpson, S., *J. Catal.* **131**, 115 (1991).
41. Rigutto, M. S., and van Bekkum, H., *J. Mol. Catal.* **81**, 77 (1993).
42. Whittington, B. I., and Anderson, J. R., *J. Phys. Chem.* **97**, 1032 (1993).
43. Reddy, J. S., Liu, P., and Sayari, A., *Appl. Catal. A* **7**, 148 (1996).
44. Knops-Gerrits, P. P., Trujillo, C. A., Zhan, B. Z., Li, X. Y., Rouxhet, P., and Jacobs, P. A., *Top. Catal.* **3**, 437 (1996).
45. Balkus, K. J. J., Khanmedova, A., Dixon, K. M., and Bedioui, F., *Appl. Catal.* **143**, 159 (1996).
46. Arends, I. W. C. E., and Sheldon, R. A., *Stud. Surf. Sci. Catal.* **110**, 1031 (1997).
47. Kozlov, A., Kozlova, A., Asakura, K., and Iwasawa, Y., *J. Mol. Catal. A* **137**, 223 (1999).
48. Choudary, B. M., Valli, V. L. K., and Durga Prasad, A., *J. Chem. Soc. Chem. Commun.*, 721 (1990).
49. Villa, A. L., De Vos, D. E., Verpoort, F., Sels, B. F., and Jacobs, P. A., *J. Catal.* **197**, (2001).
50. Ishida, M., Masumoto, Y., Hamada, R., Nishiyama, S., Tsuruya, S., and Masai, M., *J. Chem. Soc. Perkin Trans.* **2**, 847 (1999).
51. Das, S. K., Kumar, A., Nandrajog, S., and Kumar, A., *Tetrahedron Lett.* **36**, 7909 (1995).
52. Rohan, D., and Hodnett, B. K., *Appl. Catal. A* **151**, 409 (1997).
53. Joseph, R., Sasidharan, M., Kumar, R., Sudalai, A., and Ravindranathan, T., *Chem. Commun.*, 1341 (1995).
54. Chen, J. D., Dakka, J., Sheldon, R. A., and Neeleman, E., *Chem. Commun.*, 1379 (1993).
55. Chen, J. D., and Sheldon, R. A., *J. Catal.* **153**, 1 (1995).
56. Lempers, H. E. B., and Sheldon, R. A., *J. Catal.* **175**, 62 (1998).
57. Sheldon, R. A., Wallau, M., Arends, I. W. C. E., and Schuchardt, U., *Acc. Chem. Res.* **31**, 485 (1998).
58. Fréchet, J. M., Darling, P., and Farrall, M. J., *J. Org. Chem.* **46**, 1728 (1981).
59. Kanemoto, S., Saimoto, H., Oshima, K., and Nozaki, H., *Tetrahedron Lett.* **25**, 3317 (1984).
60. Ryan, O. B., Akporiaye, D. E., Holm, K. H., and Stöcker, M., *Stud. Surf. Sci. Catal.* **106**, 369 (1997).
61. Clark, J. H., Kybett, A. P., Landon, P., Macquarrie, D. J., and Martin, K., *J. Chem. Soc. Chem. Commun.*, 1355 (1989).
62. Takehira, K., Hayakawa, T., and Ishikawa, T., *J. Catal.* **66**, 267 (1980).
63. Chisem, I. C., Rafelt, J., Shieh, M. T., Chisem, J., Clark, J. H., Jachuck, R., Macquarrie, D. J., Ramshaw, C., and Scott, K., *Chem. Commun.*, 1949 (1998).
64. Choudhary, B. M., Durga Prasad, A., Swapna, V., Valli, V. L. K., and Bhuma, V., *Tetrahedron* **48**, 953 (1992).
65. Choudhary, B. M., Durga Prasad, A., Bhuma, V., and Swapna, V., *J. Org. Chem.* **57**, 5841 (1992).

66. Choudhary, B. M., Durga Prasad, A., and Valli, V. L. K., *Tetrahedron Lett.* **31**, 5785 (1990).
67. Choudhary, B. M., Lakshmi Kantam, M., and Lakshmi Santhi, P., *Catal. Today* **57**, 17 (2000).
68. Choudhary, B. M., Narender, N., and Bhuma, V., *Synth. Commun.* **26**, 631 (1996).
69. Samsel, E. G., Srinivasan, K., and Kochi, J. K., *J. Am. Chem. Soc.* **107**, 7606 (1987).
70. Koner, S., Chaudhari, K., Das, T. K., and Sivasanker, S., *J. Mol. Catal. A* **150**, 295 (1999).
71. Shen, Y. F., Zerger, P. R., De Guzman, R. N., Suib, S. L., Potter, D. I., and O'Young, C. L., *Science* **260**, 511 (1993).
72. Wang, J., Xia, G., Yin, Y., Suib, S. L., and O'Young, C. L., *J. Catal.* **176**, 275 (1998).
73. Tateiwa, J. I., Horiuchi, H., and Uemura, S., *J. Chem. Soc. Chem. Commun.*, 2567 (1994).
74. Staton, J. S., and Hu, P. C., U.S. Patent No. 4,731,196 to Ethyl Corporation (1988).
75. Bossek, U., Wieghardt, K., Nuber, B., and Weiss, J., *Inorg. Chim. Acta* **165**, 123 (1989).
76. Wieghardt, K., *Angew. Chem. Int. Ed. Engl.* **33**, 725 (1994).
77. Knops-Gerrits, P. P., De Vos, D. E., Thibault-Starzyk, F., and Jacobs, P. A., *Nature* **369**, 543 (1994).
78. Kim, S. S., Zhang, W. Z., and Pinnavaia, T. J., *Catal. Lett.* **43**, 149 (1997).
79. De Vos, D. E., Sels, B. F., Reynaers, M., Subba Rao, Y. V., and Jacobs, P. A., *Tetrahedron Lett.* **39**, 4909 (1998).
80. De Vos, D. E., and Bein, T., *Chem. Commun.*, 917 (1996).
81. De Vos, D. E., De Wildeman, S., Sels, B. F., Grobet, P. J., and Jacobs, P. A., *Angew. Chem. Int. Ed. Engl.* **38**, 1033 (1999).
82. Rao, Y. V. S., De Vos, D. E., Bein, T., and Jacobs, P. A., *Chem. Commun.*, 355 (1997).
83. De Vos, D. E., and Bein, T., *J. Am. Chem. Soc.* **119**, 9460 (1997).
84. De Vos, D. E., Meinershagen, J. L., and Bein, T., *Angew. Chem. Int. Ed. Engl.* **35**, 2211 (1996).
85. Sutra, P., and Brunel, D., *Chem. Commun.*, 2485 (1996).
86. Jacobsen, E. N., in "Comprehensive Organometallic Chemistry II" (E. W. Abel, F. G. A. Stone, and E. Wilkinson, Eds.), Vol. 12, p. 1097 (1995).
87. Canali, L., and Sherrington, D. C., *Chem. Soc. Rev.* **28**, 85 (1999).
88. Salvadori, P., Pini, D., Petri, A., and Mandoli, A., in "Chiral Catalyst Immobilization and Recycling" (D. E. De Vos, I. F. J. Vankelecom, and P. A. Jacobs, Eds.), p. 235. Wiley-VCH, New York, 2000.
89. De, B. B., Lohray, B. B., Sivaram, S., and Dhal, P. K., *Tetrahedron Asymmetry* **6**, 2105 (1995).
90. Minutolo, F., Pini, D., and Salvadori, P., *Tetrahedron Lett.* **37**, 3375 (1996).
91. Minutolo, F., Pini, D., Petri, A., and Salvadori, P., *Tetrahedron Asymmetry* **7**, 2293 (1996).
92. Canali, L., Cowan, E., Deleuze, H., Gibson, C. L., and Sherrington, D. C., *Chem. Commun.*, 2561 (1998).
93. Song, C. E., Roh, E. J., Yu, B. M., Chi, D. Y., Kim, S. C., and Lee, K., *Chem. Commun.*, 615 (2000).
94. Pini, D., Mandoli, A., Orlandi, S., and Salvadori, P., *Tetrahedron Asymmetry* **10**, 3883 (1999).
95. Janssen, K. B. M., Ph.D. thesis, Katholieke Universiteit Leuven (1999).
96. Kim, G. J., and Shin, J. H., *Tetrahedron Lett.* **40**, 6827 (1999).
97. Kureshy, R. I., Khan, N. H., Abdi, S. H. R., and Iyer, P., *React. Funct. Polym.* **34**, 153 (1997).
98. Sabater, M. J., Corma, A., Domenech, A., Fornes, V., and Garcia, H., *Chem. Commun.*, 1285 (1997).
99. Ogunwumi, S. B., and Bein, T., *Chem. Commun.*, 901 (1997).
100. Fraile, J. M., Garcia, J. I., Massam, J., and Mayoral, J. A., *J. Mol. Catal. A* **136**, 47 (1998).
101. Kim, G. J., and Kim, S. H., *Catal. Lett.* **57**, 139 (1999).

102. Piaggio, P., Langham, C., McMorn, P., Bethell, D., Bulman-Page, P. C., Hancock, F. E., Sly, C., and Hutchings, G., *J. Chem. Soc. Perkin Trans.* **2**, 143 (2000).
103. Piaggio, P., McMorn, P., Murphy, D., Bethell, D., Bulman-Page, P. C., Hancock, F. E., Sly, C., Kerton, O. J., and Hutchings, G., *J. Chem. Soc. Perkin Trans.* **2**, 2008 (2000).
104. Cooke, P. R., and Lindsay Smith, J. R., *J. Chem. Soc. Perkin Trans.* **1**, 1913 (1994).
105. Gilmartin, C., and Lindsay Smith, J. R., *J. Chem. Soc. Perkin Trans.* **2**, 243 (1995).
106. Miki, K., and Sato, Y., *Bull. Chem. Soc. Jpn.* **66**, 2385 (1993).
107. Battioni, P., Renaud, J. P., Bartoli, J. F., Reina-Artiles, M., Fort, M., and Mansuy, D., *J. Am. Chem. Soc.* **110**, 8462 (1988).
108. Battioni, P., Lallier, J. P., Barloy, L., and Mansuy, D., *J. Chem. Soc. Chem. Commun.*, 1149 (1989).
109. Barloy, L., Battioni, P., and Mansuy, D., *J. Chem. Soc. Chem. Commun.*, 1365 (1990).
110. Chen, S. M., *J. Mol. Catal. A* **112**, 277 (1996).
111. Lindsay Smith, J. R., and Lower, R. J., *J. Chem. Soc. Perkin Trans.* **2**, 2187 (1992).
112. Sorokin, A., and Meunier, B., *J. Chem. Soc. Chem. Commun.*, 1799 (1994).
113. Mirkhani, V., Tangestaninejad, S., and Mogdaham, M., *J. Chem. Res. S*, 722 (1999).
114. Labat, G., and Meunier, B., *J. Chem. Soc. Chem. Commun.*, 1414 (1990).
115. Chibwe, M., and Pinnavaia, T. J., *J. Chem. Soc. Chem. Commun.*, 278 (1993).
116. Battioni, P., Cardin, E., Loulodi, M., Schöllhorn, B., Spyroulias, G. A., Mansuy, D., and Traylor, T. G., *Chem. Commun.*, 2037 (1996).
117. van der Made, A. W., Smeets, J. W., Nolte, R. J. M., and Drenth, W., *J. Chem. Soc. Chem. Commun.*, 1204 (1983).
118. Tangestaninejad, S., and Mirkhani, V., *J. Chem. Res. S*, 788 (1998).
119. Ledon, H., and Brigandat, Y., *J. Organometallic Chem.* **165**, C25 (1979).
120. Sorokin, A. B., and Tuel, A., *Catal. Today* **57**, 45 (2000).
121. Parton, R. F., Neys, P. E., Jacobs, P. A., Sosa, R. C., and Rouxhet, P. G., *J. Catal.* **164**, 341 (1996).
122. Ernst, S., Glaser, R., and Selle, M., *Stud. Surf. Sci. Catal.* **105**, 1021 (1997).
123. Meyer, G., Wöhrle, D., Mohl, M., and Schulz-Ekloff, G., *Zeolites* **4**, 30 (1984).
124. Parton, R. F., Bezoukhanova, C. P., Casselman, M., Uytterhoeven, J., and Jacobs, P. A., *Nature* **370**, 541 (1994).
125. Parton, R. F., Bezoukhanova, C. P., Thibault-Starzyk, F., Reynders, R. A., Grobet, P. J., and Jacobs, P. A., *Stud. Surf. Sci. Catal.* **84**, 813 (1994).
126. Parton, R. F., Bezoukhanova, C. P., Grobet, J., Grobet, P. J., and Jacobs, P. A., *Stud. Surf. Sci. Catal.* **83**, 371 (1994).
127. Nakamura, M., Tatsumi, T., and Tominaga, H., *Bull. Chem. Soc. Jpn.* **63**, 3334 (1990).
128. Balkus, K. J. J., Eissa, M., and Lavado, R., *J. Am. Chem. Soc.* **117**, 10753 (1995).
129. Battioni, P., Iwanejko, R., Mansuy, D., Młodnicka, T., Poltowicz, J., and Sanchez, *J. Mol. Catal. A* **109**, 91 (1996).
130. Prado-Manso, C. M. C., Vidoto, E. A., Vinhado, F. S., Sacco, H. C., Ciuffi, K. J., Martins, P. R., Ferreira, A. G., Lindsay-Smith, J. R., Nascimento, O. R., and Iamamoto, Y., *J. Mol. Catal. A* **150**, 251 (1999).
131. Viana Rosa, I. L., Manso, C. M. C. P., Serra, O. A., and Iamamoto, Y., *J. Mol. Catal. A* **160**, 199 (2000).
132. Nakagaki, S., Xavier, C. R., Wosniak, A. J., Mangrich, A. S., Wypych, F., Cantao, M. P., Denicolo, I., and Kubota, L. T., *Coll. Surf. A* **168**, 261 (2000).
133. Valente, A. A., and Vital, J., *Stud. Surf. Sci. Catal.* **108**, 461 (1997).
134. Langhendries, G., Claessens, R., Baron, G. V., Parton, R. F., De Vos, D. E., and Jacobs, P. A., *Fundamentals Adsorption* **6**, 389 (1998).
135. Hampton, K. W., and Ford, W. T., *J. Mol. Catal. A* **113**, 167 (1996).

136. Medina, J. C., Gabriunas, N., and Paez-Mozo, E., *J. Mol. Catal. A* **115**, 233 (1997).
137. Alvaro, M., Ferrer, B., Garcia, H., and Sanjuan, A., *Tetrahedron* **55**, 11895 (1999).
138. Fajerweg, K., Foussard, J. N., Perrard, A., and Debellefontaine, H., *Water Sci. Technol.* **35**, 103 (1997).
139. Centi, G., Perathoner, S., Torre, T., and Verduna, M. G., *Catal. Today* **55**, 61 (2000).
140. Chou, S. S., and Huang, C. P., *Chemosphere* **38**, 2719 (1999).
141. Sakurada, H., *Nippon Kagaku Kaishi*, 1463 (1992).
142. Wang, D., Liu, Z., Liu, F., Ai, X., Zhang, X., Cao, Y., Yu, J., Wu, T., Bai, Y., Li, T., and Tang, X., *Appl. Catal. A* **174**, 25 (1998).
143. Dugal, M., Sankar, G., Raja, R., and Thomas, J. M., *Angew. Chem. Int. Ed. Engl.* **39**, 2310 (2000).
144. Raja, R., Sankar, G., and Thomas, J. M., *J. Am. Chem. Soc.* **121**, 11926 (1999).
145. Wöhrle, D., Buck, T., Hündorf, U., Schulz-Ekloff, G., and Andreev, A., *Makromol. Chem.* **190**, 961 (1989).
146. Iliiev, V., Andreev, A., Wöhrle, D., and Schulz-Ekloff, G., *J. Mol. Catal.* **66**, L5 (1991).
147. Rollmann, L. D., *J. Am. Chem. Soc.* **97**, 2132 (1975).
148. Buck, T., Wöhrle, D., Schulz-Ekloff, G., and Andreev, A., *J. Mol. Catal.* **70**, 259 (1991).
149. Fischer, H., Schulz-Ekloff, G., and Wöhrle, D., *Chem. Eng. Tech.* **20**, 624 (1997).
150. Iliiev, V., Ileva, A., and Bilyarska, L., *J. Mol. Catal. A* **126**, 99 (1997).
151. Perez-Bernal, E. M., Ruarno-Casero, R., and Pinnavaia, T. J., *Catal. Lett.* **11**, 55 (1991).
152. Chibwe, M., Perez-Bernal, M. E., Ruano-Casero, R., and Pinnavaia, T. J., Proceedings of the 10th International Clay Conference, p. 87 (1994).
153. Iliiev, V., Ileva, A. I., and Dimitrov, L. D., *Appl. Catal. A* **126**, 333 (1995).
154. Brouwer, W. M., Piet, P., and German, A. L., *J. Mol. Catal.* **29**, 347 (1985).
155. Alcaraz, J. J., Arena, B. J., Gillespie, R. D., and Holmgren, J. S., *Catal. Today* **43**, 89 (1998).
156. Hu, X., Huang, Z., Gu, G., Wang, L., and Chen, B., *J. Mol. Catal. A* **132**, 171 (1998).
157. Schipper, E. T., Pinckaers, R. P., Piet, P., and German, A. L., *Macromolecules* **28**, 2194 (1995).
158. Thibault-Starzyk, F., Van Puymbroeck, M., Parton, R. F., and Jacobs, P. A., *J. Mol. Catal. A* **109**, 75 (1996).
159. Hassanein, M., Abdel-Hay, F. I., and El-Hefnawy El-Esawy, T., *Eur. Polym. J.* **30**, 335 (1994).
160. Iwado, A., Mifune, M., Kato, J., Oda, J., Chikuma, M., Motohashi, N., and Saito, Y., *Chem. Pharm. Bull.* **48**, 1831 (2000).
161. Oudejans, J. C., and van Bekkum, H., *J. Mol. Catal.* **12**, 149 (1981).
162. Vanoppen, D. L., De Vos, D. E., Genet, M., Rouxhet, P. G., and Jacobs, P. A., *Angew. Chem.* **107**, 637 (1995).
163. Raja, R., Sankar, G., and Thomas, J. M., *Angew. Chem Int. Ed. Engl.* **39**, 2313 (2000).
164. Lin, S. S., and Weng, H. S., *Appl. Catal. A* **105**, 289 (1993).
165. Kraushaar-Czarnetski, B., Hoogervorst, W. G. M., and Stork, W. H. J., *Stud. Surf. Sci. Catal.* **84**, 1869 (1994).
166. Kulkarni, S., Alurkar, M., and Kumar, A., *Appl. Catal. A* **142**, 243 (1996).
167. Shen, H. C., and Weng, H. S., *Ind. Eng. Chem. Res.* **27**, 2246 (1988).
168. Shen, H. C., and Weng, H. S., *Ind. Eng. Chem. Res.* **27**, 2254 (1988).
169. Chen, L. C., and Chou, T. C., *Ind. Eng. Chem. Res.* **33**, 2523 (1994).
170. Maschmeyer, T., Oldroyd, R. D., Sankar, G., Thomas, J. M., Shannon, I. J., Klepetko, J. A., Masters, A. F., Beattie, J. K., and Catlow, C. R. A., *Angew. Chem.* **109**, 1713 (1997).
171. Fujiyama, H., Kohara, I., Iwai, K., Nishiyama, S., Tsuruya, S., and Masai, M., *J. Catal.* **188**, 417 (1999).
172. Kohara, I., Fujiyama, H., Iwai, K., Nishiyama, S., and Tsuruya, S., *J. Mol. Catal. A* **153**, 93 (2000).

173. Tadokoro, H., Nishiyama, S., Tsuruya, S., and Masai, M., *J. Catal.* **138**, 24 (1992).
174. Miyagi, A., Nishiyama, S., Tsuruya, S., and Masai, M., *J. Mol. Catal.* **55**, 379 (1989).
175. Okamura, J., Nishiyama, S., Tsuruya, S., and Masai, M., *J. Mol. Catal. A* **135**, 133 (1998).
176. Ohtani, T., Nishiyama, S., Tsuruya, S., and Masai, M., *Stud. Surf. Sci. Catal.* **75**, 1999 (1993).
177. Zhu, K., Liu, C., Ye, X., and Wu, Y., *Appl. Catal. A* **168**, 365 (1998).
178. Raja, R., and Ratnasamy, P., *J. Mol. Catal. A* **100**, 93 (1995).
179. Raja, R., and Ratnasamy, P., *Appl. Catal. A* **143**, 145 (1996).
180. Bahranowski, K., Gasior, M., Kielski, A., Podobinski, J., Servicka, E. M., Vartikian, L. A., and Wodnicka, K., *Clay Minerals* **34**, 79 (1999).
181. Auer, S. M., Wandeler, R., Gobel, U., and Baiker, A., *J. Catal.* **169**, 1 (1997).
182. Mantzavinos, D., Hellenbrand, R., Livingston, A. G., and Metcalfe, I. S., *Appl. Catal. B* **7**, 379 (1996).
183. Mantzavinos, D., Hellenbrand, R., Livingston, A. G., and Metcalfe, I. S., *Chem. Eng. Res. Des.* **75**, 87 (1997).
184. Alejandro, A., Medina, F., Rodriguez, X., Salagre, P., and Sueiras, J. E., *J. Catal.* **188**, 311 (1999).
185. Pintar, A., Bercic, G., and Levec, J., *Chem. Eng. Sci.* **52**, 4143 (1997).
186. Mantzavinos, D., Hellenbrand, R., Livingston, A. G., and Metcalfe, I. S., *Appl. Catal. B* **11**, 99 (1996).
187. Larache, F., Levesque, S., and Sayari, A., *J. Chem. Technol. Biotechnol.* **73**, 127 (1998).
188. Bunce, S., Cross, R. J., Farrugia, L. J., Kunchandy, S., Meason, L. L., Muir, K. W., O'Donnell, M., Peacock, R. D., Stirling, D., and Teat, S. J., *Polyhedron* **17**, 4179 (1998).
189. Raja, R., and Ratnasamy, P., *Stud. Surf. Sci. Catal.* **100**, 181 (1996).
190. Stojanova, M., Karshalykov, C., Price, G. L., and Kanazirev, V., *Appl. Catal. A* **143**, 175 (1996).
191. Mukaiyama, T., Yorozu, K., Takai, T., and Yamada, T., *Chem. Lett.*, 439 (1993).
192. Yorozu, K., Takai, T., Yamada, T., and Mukaiyama, T., *Chem. Lett.*, 1579 (1993).
193. Barf, G. A., and Sheldon, R. A., *J. Mol. Catal. A* **102**, 23 (1995).
194. Raja, R., Sankar, G., and Thomas, J. M., *Chem. Commun.*, 829 (1999).
195. Butterworth, A., Clark, J. H., Walton, P. H., and Barlow, S. J., *Chem. Commun.*, 1859 (1996).
196. Bouhleb, E., Laszlo, P., Levart, M., Montaufier, M. T., and Singh, G. P., *Tetrahedron Lett.* **34**, 1123 (1993).
197. Laszlo, P., and Levart, M., *Tetrahedron Lett.* **34**, 1127 (1993).
198. Chisem, J., Chisem, I. C., Rafelt, J. S., Macquarrie, D. J., and Clark, J. H., *Chem. Commun.*, 2203 (1997).
199. Wentzel, B. B., Leinonen, S. M., Thomson, S., Sherrington, D. C., Feiters, M. C., and Nolte, R. J. M., *J. Chem. Soc. Perkin Trans.* **1**, 3428 (2000).
200. Khenkin, A. M., Neumann, R., Sorokin, A. B., and Tuel, A., *Catal. Lett.* **63**, 189 (1999).
201. Kaneda, K., Ueno, S., and Imanaka, T., *J. Mol. Catal. A* **102**, 135 (1995).
202. Murahashi, S. I., Oda, Y., and Naota, T., *Tetrahedron Lett.* **33**, 7557 (1992).
203. Chisem, I. C., Chisem, J., and Clark, J. H., *New J. Chem.*, 81 (1998).
204. Dell'Anna, M. M., Mastroianni, P., and Nobile, C. F., *J. Mol. Catal. A* **108**, 57 (1996).
205. Kaneda, K., Ueno, S., and Imanaka, T., *Chem. Commun.*, 797 (1994).
206. Tuel, A., Gontier, S., and Teissier, R., *Chem. Commun.*, 651 (1996).
207. Quignard, F., Choplin, A., and Teissier, R., *J. Mol. Catal. A* **120**, L27 (1997).
208. Krohn, K., Knauer, B., K upke, J., Seebach, D., Beck, A. K., and Hayakawa, M., *Synthesis* 1341 (1996).
209. Wilson, S. L., and Jones, C. W., *Stud. Surf. Sci. Catal.* **110**, 603 (1997).
210. J orgensen, K. A., *Chem. Rev.* **89**, 431 (1989).
211. Haas, G. R., and Kolis, J. W., *Organometallics* **17**, 4454 (1998).

212. Deubel, D. V., Sundermeyer, J., and Frenking, G., *J. Am. Chem. Soc.* **122**, 10101 (2000).
213. Trifiro, F., Forzatti, P., Preite, S., and Pasquon, I., *J. Less Common Met.* **36**, 319 (1974).
214. Dai, P. E., and Lunsford, J. H., *J. Catal.* **64**, 173 (1980).
215. Dai, P. E., and Lunsford, J. H., *J. Catal.* **64**, 184 (1980).
216. Ward, M. B., Mizuno, K., and Lunsford, J. H., *J. Mol. Catal.* **27**, 1 (1984).
217. Sohn, J. R., and Lunsford, J. H., *J. Mol. Catal.* **32**, 325 (1985).
218. Ferreira, P., Gonçalves, I. S., Kühn, F. E., Lopes, A. D., Martins, M. A., Pillinger, M., Pina, A., Rocha, J., Romão, C. C., Santos, A. M., Santos, T. M., and Valente, A. A., *Eur. J. Inorg. Chem.* 2263 (2000).
219. Campestrini, S., Conte, V., Di Furia, F., Modena, G., and Bortolini, O., *J. Org. Chem.* **53**, 5721 (1988).
220. Thiel, W. R., and Eppinger, J., *Chem. Eur. J.* **3**, 696 (1997).
221. Ivanov, S. K., Boeva, R. S., and Tanielyan, S. K., *React. Kin. Catal. Lett.* **5**, 297 (1976).
222. Boeva, R. S., Kotov, S. V., and Jordanov, N., *React. Kin. Catal. Lett.* **24**, 239 (1984).
223. Ivanov, S., Boeva, R., and Tanielyan, S., *J. Catal.* **56**, 150 (1979).
224. Kotov, S. V., and Boneva, S., *J. Mol. Catal. A* **139**, 271 (1999).
225. Yokoyama, T., Nishizawa, M., Kimura, T., and Suzuki, T. M., *Bull. Chem. Soc. Jpn.* **58**, 3271 (1985).
226. Gil, S., Gonzalez, R., Mestres, R., Sanz, V., and Zapater, A., *React. Funct. Polym.* **42**, 65 (1999).
227. Bhaduri, S., and Khwaja, H., *J. Chem. Soc. Dalton Trans.*, 415 (1983).
228. Goto, M., and Goto, S., *React. Kin. Catal. Lett.* **39**, 267 (1989).
229. Kurusu, Y., Masuyama, Y., Saito, M., and Saito, S., *J. Mol. Catal.* **37**, 235 (1986).
230. Kurusu, Y., and Masuyama, Y., *J. Macromol. Sci.-Chem. A* **24**, 389 (1987).
231. Okamoto, Y., and Still, W. C., *Tetrahedron Lett.* **29**, 971 (1988).
232. Sobczak, J., and Ziolkowski, J. J., *J. Mol. Catal.* **3**, 165 (1977/78).
233. Sherrington, D. C., and Simpson, S., *Reactive Polym.* **19**, 13 (1993).
234. Arroyo, P., Gil, S., Muñoz, A., Palanca, P., Sanchis, J., and Sanz, V., *J. Mol. Catal. A* **160**, 403 (2000).
235. Cazaux, I., and Caze, C., *React. Polym.* **20**, 87 (1993).
236. Ferruti, P., Tempesti, E., Giuffrè, L., Ranucci, R., and Mazzocchia, C., *Stud. Surf. Sci. Catal.* **59**, 431 (1991).
237. Stamenova, R. T., Tsvetanova, R. T., Vassilev, K. G., Tanielyan, S. K., and Ivanov, S. K., *J. Appl. Polym. Sci.* **42**, 807 (1991).
238. Tempesti, E., Giuffrè, L., Di Renzo, F., Mazzocchia, C., and Modica, G., *J. Mol. Catal.* **45**, 255 (1988).
239. Filippov, A. P., and Polishchuk, O. A., *Kinet. Katal.* **25**, 1341 (1984).
240. Tempesti, E., Giuffrè, L., Mazzocchia, C., Gronchi, P., and Di Renzo, F., *J. Mol. Catal.* **55**, 371 (1989).
241. Miller, M. M., Sherrington, D. C., and Simpson, S., *J. Chem. Soc. Perkin Trans.* **2**, 2091 (1994).
242. Miller, M. M., and Sherrington, D. C., *J. Chem. Soc. Chem. Commun.*, 55 (1994).
243. Miller, M. M., and Sherrington, D. C., *J. Catal.* **152**, 377 (1995).
244. Olason, G., and Sherrington, D. C., *Macromol. Symp.* **131**, 127 (1998).
245. Leinonen, S., Sherrington, D. C., Sneddon, A., McLoughlin, D., Corker, J., Canevali, C., Morazzoni, F., Reedijk, J., and Spratt, S. B. D., *J. Catal.* **183**, 251 (1999).
246. Ahn, J. H., and Sherrington, D. C., *J. Chem. Soc. Chem. Commun.*, 643 (1996).
247. Ahn, J. H., Kim, J. C., Ihm, S. K., and Sherrington, D. C., *Stud. Surf. Sci. Catal.* **110**, 957 (1997).
248. Alder, K. I., and Sherrington, D. C., *Chem. Commun.*, 131 (1998).

249. Gaffney, A. M., Nandi, M. K., Pitchai, R., and Han, Y. Z., U.S. Patent No. 5319114 to Arco Chemical Technology (1994).
250. Gall, R. D., Hill, C. L., and Walker, J. E., *J. Catal.* **159**, 473 (1996).
251. Corma, A., Fuente, A., Iglesias, M., and Sanchez, F., *J. Mol. Catal. A* **107**, 225 (1996).
252. Tatsumi, T., Yamamoto, K., Tajima, H., and Tominaga, H., *Chem. Lett.*, 815 (1992).
253. Gardner, E., and Pinnavaia, T. J., *Appl. Catal. A* **167**, 65 (1998).
254. Sels, B. F., De Vos, D. E., Grobet, P. J., Pierard, F., Kirsch-De Mesmaeker, A., and Jacobs, P. A., *J. Phys. Chem. B* **103**, 11114 (1999).
255. Sels, B. F., De Vos, D. E., and Jacobs, P. A., *Chem. Eur. J.*, in press (2001).
256. Van Laar, F., De Vos, D. E., Vanoppen, D. L., Sels, B. F., Jacobs, P. A., Pierard, A., and Kirsch-DeMesmaeker, A., *Chem. Commun.*, 267 (1998).
257. De Vos, D. E., Sels, B. F., Van Rhijn, W. M., and Jacobs, P. A., *Stud. Surf. Sci. Catal.* **130**, 137 (2000).
258. van Laar, F., De Vos, D. E., Pierard, F., Kirsch-De Mesmaeker, A., Fiermans, L., and Jacobs, P. A., *J. Catal.* **197**, 139 (2001).
259. McGoran, E. C., and Wyborney, M., *Tetrahedron Lett.* **30**, 783 (1989).
260. Srinivasan, S., and Ford, W. T., *New J. Chem.* **15**, 693 (1991).
261. Aubry, C., Chottard, G., Platzner, N., Brégeault, J. M., Thouvenot, R., Chauveau, F., Huet, C., and Ledon, H., *Inorg. Chem.* **30**, 4409 (1991).
262. Brown, S. W., Johnstone, A., Jones, C. W., Lee, A. M., Oakes, S. C., and Wilson, S. L., *Recl. Trav. Chim. Pays Bas* **115**, 244 (1996).
263. Kurusu, Y., *Bull. Chem. Soc. Jpn.* **54**, 293 (1981).
264. Inoue, M., Itoi, Y., Enomoto, S., and Watanabe, Y., *Chem. Lett.*, 1375 (1982).
265. Itoi, Y., Inoue, M., Enomoto, S., and Watanabe, Y., *Chem. Pharm. Bull.* **32**, 418 (1984).
266. Drago, R. S., and Burns, D. S., *J. Catal.* **166**, 377 (1997).
267. Zhang, W., Wang, J., Tanev, P. T., and Pinnavaia, T. J., *Chem. Commun.*, 979 (1996).
268. Raghavan, P. S., Ramaswamy, V., Upadhyaya, T. T., Sudalai, A., Ramaswamy, A. V., and Sivasanker, S., *J. Mol. Catal. A* **122**, 75 (1997).
269. Cervilla, A., Corma, A., Fornés, V., Llopis, E., Palanca, P., Rey, F., and Ribera, A., *J. Am. Chem. Soc.* **116**, 1595 (1994).
270. Corma, A., Rey, F., Thomas, J. M., Sankar, G., Greaves, G. N., Cervilla, A., Llopis, E., and Ribeira, A., *Chem. Commun.*, 1613 (1996).
271. Corma, A., Fornes, V., Rey, F., Cervilla, A., Llopis, E., and Ribera, A., *J. Catal.* **152**, 237 (1995).
272. Hanyu, A., Sakurai, Y., Fujibayashi, S., Sakaguchi, S., and Ishii, Y., *Tetrahedron Lett.* **38**, 5659 (1997).
273. Griffith, W. P., *Chem. Soc. Rev.* **179** (1992).
274. Groves, J. T., Bonchio, M., Carofiglio, T., and Shalyaev, K., *J. Am. Chem. Soc.* **118**, 8961 (1996).
275. Sheldon, R. A., Arends, I. W. C. E., and Dijkstra, A., *Catal. Today* **57**, 157 (2000).
276. Shing, T. K. M., Tam, E. K. W., Tai, V., Chung, I. H. F., and Jiang, Q., *Chem. Eur. J.* **2**, 50 (1996).
277. Kaneda, K., Yamashita, T., Matsushita, T., and Ebitani, K., *J. Org. Chem.* **63**, 1750 (1998).
278. Matsushita, T., Ebitani, K., and Kaneda, K., *Chem. Commun.*, 265 (1999).
279. Yamaguchi, K., Mori, K., Mizugaki, T., Ebitani, K., and Kaneda, K., *J. Am. Chem. Soc.* **122**, 7144 (2000).
280. Hinzen, B., and Ley, S. V., *J. Chem. Soc. Perkin Trans.* **1**, 1907 (1997).
281. Hinzen, B., Lenz, R., and Ley, S. V., *Synthesis*, 977 (1998).
282. Bleloch, A., Johnson, B. F. G., Ley, S. V., Price, A. J., Shephard, D. S., and Thomas, A. W., *Chem. Commun.*, 1907 (1999).

283. Hinzen, B., and Ley, S. V., *J. Chem. Soc. Perkin Trans.* **1**, 1 (1998).
284. Jorna, A. M. J., Boelrijk, A. E. M., Hoorn, H. J., and Reedijk, J., *Reactive Functional Polymers* **29**, 101 (1996).
285. Dalal, M. K., Upadhyay, M. J., and Ram, R. N., *J. Mol. Catal. A* **142**, 325 (1999).
286. Liu, C. J., Li, S. G., Pang, W. Q., and Che, C. M., *Chem. Commun.*, 65 (1997).
287. Liu, C. J., Yiu, W. Y., Li, S. G., and Che, C. M., *J. Org. Chem.* **63**, 7364 (1998).
288. Ernst, S., and Selle, M., *Microporous Mesoporous Materials* **27**, 355 (1999).
289. Yao, G. J., Kira, A., and Kaneko, M., *J. Chem. Soc. Faraday Trans.* **1**, 4451 (1988).
290. Ramaraj, R., and Kaneko, M., *J. Chem. Soc. Chem. Commun.*, 579 (1993).
291. Yagi, M., Tokita, S., Nagoshi, K., Ogino, I., and Kaneko, M., *J. Chem. Soc. Faraday Trans.* **92**, 2457 (1996).
292. Yagi, M., Nagoshi, K., and Kaneko, M., *J. Phys. Chem. B* **101**, 5143 (1997).
293. Nagoshi, K., Yamashita, S., Yagi, M., and Kaneko, M., *J. Mol. Catal. A* **144**, 71 (1999).
294. Yagi, M., Sukegawa, N., Kasamastu, M., and Kaneko, M., *J. Phys. Chem. B* **103**, 2151 (1999).
295. Yagi, M., Kasamastu, M., and Kaneko, M., *J. Mol. Catal. A* **151**, 29 (2000).
296. Yamashita, S., Nagoshi, K., Yagi, M., and Kaneko, M., *J. Mol. Catal. A* **153**, 209 (2000).
297. Maitlis, P. M., "The Organic Chemistry of Palladium," Vol. 2, p. 128. Academic Press, New York, 1971, Tsuji, J., "Palladium Reagents and Catalysts, Innovations in Organic Synthesis." Wiley, New York, 1998.
298. Henry, P. M., "Palladium Catalyzed Oxidation of Hydrocarbons." Reidel, Dordrecht, 1980.
299. Smidt, J., Hafner, W., Jira, R., Sedlmeier, J., Sieber, R., Ruttinger, R., and Kojer, H., *Angew. Chem.* **71**, 176 (1959).
300. Moiseev, I. I., Levanda, O. G., and Vargaftik, M. N., *J. Am. Chem. Soc.* **96**, 1003 (1974).
301. Bäckvall, J. E., Akermark, B., and Ljunggren, S. O., *J. Am. Chem. Soc.* **101**, 2411 (1979).
302. Elsenbroich, C., and Salzer, A., "Organometallics," p. 425. VCH, Weinheim, 1989.
303. Jacobs, P. A., in "Handbook of Heterogeneous Catalysis" (G. Ertl, H. Knözinger, and J. Weitkamp, Eds.), Vol. 5, p. 2284. Wiley-VCH, New York, 1997.
304. Jira, R., in "Applied Homogeneous Catalysis with Organometallic Compounds" (B. Cornils and W. A. Herrmann, Eds.), p. 386 (1996).
305. Hosokawa, T., and Murahashi, S. I., *Acc. Chem. Res.* **23**, 49 (1990).
306. Elleuch, B., Nacchache, C., and Ben Taarit, Y., *Stud. Surf. Sci. Catal.* **35**, 139 (1984).
307. Kubota, T., Kumada, F., Tominaga, H., and Kunugi, T., *Int. J. Chem. Eng.* **13**, 539 (1973).
308. Arai, H., Yamashiro, T., Kubo, T., and Tominaga, H., *Bull. Jpn. Petrol. Inst.* **18**, 39 (1976).
309. Espeel, P. H., Tielen, M. C., and Jacobs, P. A., *J. Chem. Soc. Chem. Commun.*, 669 (1991).
310. Espeel, P. H., De Peuter, G., Tielen, M. C., and Jacobs, P. A., *J. Phys. Chem.* **98**, 11588 (1994).
311. Morikawa, Y., Ichikawa, S., Tanaka, H., and Ueda, W., in "Proceedings of the International Conference on Ion Exchange Processes," p. 139. Tokyo Inst. Technol. Press, Tokyo, 1991.
312. van der Heyde, E., Ammerlaan, J. A. M., Gerritsen, A. W., and Scholten, J. J. F., in "Proceedings of the 9th International Congress on Catalysis" Vol.4, p. 1648. Chemical Institute of Canada, 1988.
313. van der Heyde, E., Ammerlaan, J. A. M., Gerritsen, A. W., and Scholten, J. J. F., *J. Mol. Catal.* **55**, 320 (1989).
314. van der Heyde, E., Zwinkels, M., Gerritsen, A. W., and Scholten, J. J. F., *Appl. Catal. A* **86**, 181 (1992).
315. Stobbe-Kreemers, A. W., Makkee, M., and Scholten, J. J. F., *Appl. Catal. A* **156**, 219 (1997).
316. Evnin, A. B., Rabo, J. A., and Kasai, P. H., *J. Catal.* **30**, 109 (1973).
317. Matveev, K. I., *Kinet. Katal.* **18**, 862 (1977); Ogawa, H., Fujinami, H., and Taya K., *J. Chem. Soc. Chem. Commun.*, 1274 (1981).

318. Kishi, A., Higashino, T., Sakagushi, S., and Ishii, Y., *Tetrahedron Lett.* **41**, 99 (2000).
319. Tsuji, J., *Synthesis* **9**, 739 (1990).
320. Abel, R., Colling, P., Eichler, K., Nicolau, I., and Peters, D., in "Handbook of Heterogeneous Catalysis," (G. Ertl, H. Knözinger, and J. Weitkamp, Eds.), Vol. 5, p. 2295. Wiley-VCH, New York, 1997.
321. Nakamura, M., Fujiwara, Y., and Yasui, T., U.S. Patent No. 4087622 to Bayer (1978); Bartley, W. J., Jobson, S., Harkreader, G. G., Kitson, M. and Lemanski, M. F., U.S. Patent No. 5185308 to BP (1993).
322. Nicolau, I., Colling, P. M., and Johnson, L. R., U.S. Patent No. 5332710 to Hoechst Celanese (1994).
323. White, J. F., Slawski, B., and White, G., U.S. Patent No. 5347046 to Engelhard (1994).
324. Smith, D. W., Hanes, R. M., Scheben, J. A., and Augustine, S. M., U.S. Patent No. 5336802 to Quantum Chemical (1994).
325. Nakamura, S., and Jasui, T., *J. Catal.* **17**, 366 (1970).
326. Samanos, B., Boutry, P., and Montarnal, R., *J. Catal.* **23**, 19 (1971).
327. Ziemecki, S. B., and Jones, G. A., *J. Catal.* **95**, 621 (1985).
328. Abbadi, A., and van Bekkum, H., *Appl. Catal. A* **148**, 113 (1996).
329. Mallat, T., and Baiker, A., *Catal. Today* **19**, 247 (1994).
330. ten Brink, G. J., Arends, I., and Sheldon, R. A., *Science* **287**, 1636 (2000).
331. Zaw, K., and Henry, P. M., *J. Mol. Catal. A* **101**, 187 (1995).
332. Henry, P. M., Ma, X., Noronha, G., and Zaw, K., *Inorg. Chim. Acta* **240**, 205 (1995).
333. Noronha, G., and Henry, P. M., *J. Mol. Catal. A* **120**, 75 (1997).
334. Ebitani, K., Fijie, Y., and Kaneda, K., *Langmuir* **15**, 3557 (1999).
335. Schmid, G., Morun, B., and Malm, J. O., *Polyhedron* **7**, 2321 (1988).
336. Bönemann, H., Brijoux, W., Tilling, A. S., and Siepen, K., *Top. Catal.* **4**, 217 (1997).
337. Riley, C. R., and Lerou, J. J., *Catal. Today* **41**, 433 (1998).
338. Show, I. S., Dranoff, J. S., and Butt, J. B., *Ind. Eng. Chem. Res.* **27**, 935 (1988).
339. Crathorne, E. A., MacGowan, D., Morris, S. R., and Rawlinson, A. P., *J. Catal.* **49**, 254 (1994).
340. Arhancet, J. P., Davis, M. E., and Hanson, B. E., *Catal. Lett.* **11**, 129 (1991).
341. Monflier, E., Blouet, E., Barboux, Y., and Mortreux, A., *Angew. Chem. Int. Ed. Engl.* **33**, 2100 (1994).
342. Yao, C. S., and Weng, H. S., *Ind. Eng. Chem. Res.* **37**, 2647 (1998).
343. Payne, G. B., and Williams, P. H., *J. Org. Chem.* **24**, 54 (1959).
344. Kleeman, A., and Wagner, R., "Glycidol, Properties, Reactions, Applications," Alfred Hüttig Verlag, Basel, 1981.
345. Murahashi, S.-I., *Angew. Chem.* **107**, 2670 (1995).
346. Allan, G. G., U.S. Patent No. 3156709 to Du Pont (1964).
347. Allan, G. G., and Neogi, A. N., *J. Catal.* **16**, 197 (1970).
348. Allan, G. G., and Neogi, A. N., *J. Catal.* **19**, 256 (1970).
349. Venturello, C., Alneri, E., and Ricci, M., *J. Org. Chem.* **48**, 3831 (1983).
350. Ishii, Y., Yamawaki, K., Ura, T., Yamada, H., Yoshida, T., and Ogawa, M., *J. Org. Chem.* **53**, 3587 (1988).
351. Dengel, A. C., Griffith, W. P., and Parkin, B. C., *J. Chem. Soc. Dalton Trans.*, 2683 (1993).
352. Salles, L., Piquemal, J.-Y., Thouvenot, R., Minot, C., and Brégeault, J.-M., *J. Mol. Catal. A* **117**, 375 (1997).
353. Venturello, C., D'Aloisio, R., and Ricci, M., U.S. Patent No. 4562276 to Montedison (1985).
354. Venturello, C., D'Aloisio, R., and Ricci, M., U.S. Patent No. 4595671 to Montedison (1986).
355. Sels, B. F., Villa, A. L., Hoegaerts, D., De Vos, D. E., and Jacobs, P. A., *Top. Catal.* **13**, 223 (2000).

356. Villa, A. L., Sels, B. F., De Vos, D. E., and Jacobs, P. A., *J. Org. Chem.* **64**, 7267 (1999).
357. Soncini, P., and Bonsignore, S., U.S. Patent No. 5364951 to Eniricerche (1994).
358. Goetz, P., Wieland, S., Panster, P., Goor, G., and Siegmeier, R., U.S. Patent No. 5286885 to Degussa (1994).
359. Hoegaerts, D., Sels, B. F., De Vos, D. E., Verpoort, F., and Jacobs, P. A., *Catal. Today* **60**, 209 (2000).
360. Neumann, R., and Miller, H., *J. Chem. Soc. Chem. Commun.*, 2277 (1995).
361. Tatsumi, T., Tajima, H., Yamamoto, K., and Tominaga, H., *Stud. Surf. Sci. Catal.* **75**, 1703 (1993).
362. Watanabe, Y., Yamamoto, K., and Tatsumi, T., *J. Mol. Catal. A* **145**, 281 (1999).
363. Salles, L., Aubry, C., Thouvenot, R., Robert, F., Dorémieux-Morin, C., Chottard, G., Ledon, H., Jeannin, Y., and Brégeault, J. M., *Inorg. Chem.* **33**, 871 (1994).
364. Duncan, D. C., Chambers, R. C., Hecht, E., and Hill, C. L., *J. Am. Chem. Soc.* **117**, 681 (1995).
365. Sels, B. F., De Vos, D. E., and Jacobs, P. A., *Tetrahedron Lett.* **37**, 8557 (1996).
366. Sels, B. F., De Vos, D. E., and Jacobs, P. A., *Stud. Surf. Sci. Catal.* **110**, 1051 (1997).
367. Sels, B. F., De Vos, D. E., Buntinx, M., Pierard, F., Kirsch-De Mesmaeker, A., and Jacobs, P. A., *Nature* **400**, 855 (1999).
368. Sels, B. F., Ph.D. thesis, Katholieke Universiteit Leuven (2000).
369. Gable, C. M., U.S. Patent No. 2870171 to Shell (1959).
370. Neumann, R., and Cohen, M., *Angew. Chem.* **109**, 1997, 1810
371. Piquemal, J.-Y., Briot, E., Vennat, M., Brégeault, J. M., Chottard, G., and Manoli, J. M., *Chem. Commun.*, 1195 (1995).
372. Briot, E., Piquemal, J.-Y., Vennat, M., Brégeault, J. M., Chottard, G., and Manoli, J. M., *J. Mater. Chem.* **10**, 953 (2000).
373. Jin, R. H., Xia, X., Dai, W. L., Deng, J. F., and Li, H. X., *Catal. Lett.* **62**, 201 (1999).
374. Zhang, Z., Suo, J., Zhang, X., and Li, S., *Chem. Commun.*, 241 (1998).
375. Zhang, Z., Suo, J., Zhang, X., and Li, S., *Appl. Catal. A* **179**, 11 (1999).
376. Wilson, S. L., and Jones, C., World Patent No. 9421624 to Solvay Interox (1994).
377. Gelbard, G., Breton, F., Quenard, M., and Sherrington, D. C., *J. Mol. Catal. A* **153**, 7 (2000).
378. Duprey, E., Maquet, J., Man, P. P., Manoli, J. M., Delamar, M., and Brégeault, J.-M., *Appl. Catal. A* **128**, 89 (1995).
379. Villa, A. L., De Vos, D. E., Montes de C., C., and Jacobs, P. A., *Tetrahedron Lett.* **39**, 8521 (1999).
380. Rudolph, J., Reddy, K. L., Chiang, J. P., and Sharpless, K. B., *J. Am. Chem. Soc.* **119**, 6189 (1997).
381. Herrmann, W. A., Kratzer, R. M., Ding, H., Thiel, W. R., and Glas, H., *J. Organomet. Chem.* **555**, 293 (1998).
382. Zhu, Z. L., and Espenson, J. H., *J. Mol. Catal. A* **121**, 139 (1997).
383. Neumann, R., and Wang, T. J., *Chem. Commun.*, 1915 (1997).
384. Schröder, M., *Chem. Rev.* **80**, 187 (1980).
385. Kolb, H. C., Van Nieuwenhze, M. S., and Sharpless, K. B., *Chem. Rev.* **94**, 2483 (1994).
386. Berrisford, D. J., Bolm, C., and Sharpless, K. B., *Angew. Chem.* **107**, 1159 (1995).
387. Bolm, C., and Gerlach, A., *Eur. J. Org. Chem.*, 21 (1998).
388. Cainelli, G., Contento, M., Manescalchi, F., and Plessi, L., *Synthesis* 45 (1989).
389. Herrmann, W. A., Kratzer, R. M., Blümel, J., Friedrich, H. B., Fischer, R. W., Apperley, D. C., Mink, J., and Berkesi, O., *J. Mol. Catal. A* **120**, 197 (1997).
390. Nagayama, S., Endo, M., and Kobayashi, S., *J. Org. Chem.* **63**, 6094 (1998).
391. Severeys, A., De Vos, D. E., Fiermans, L., Verpoort, F., Grobet, P. J., and Jacobs, P. A., *Angew. Chem. Int. Ed. Engl.*, in press (2001).

392. Wai, J. S. M., Markó, I., Svendsen, J. S., Finn, M. G., Jacobsen, E. N., and Sharpless, K. B., *J. Am. Chem. Soc.* **111**, 1123 (1989).
393. Ueno, S., Yamaguchi, K., Yoshida, K., Ebitani, K., and Kaneda, K., *Chem. Commun.*, 295 (1998).
394. Fischer, J., and Hoelderich, W. F., *Appl. Catal. A* **180**, 435 (1999).
395. Schoo, H. F. M., Challa, G., Rowatt, B., and Sherrington, D. C., *React. Polymers* **16**, 125 (1992).
396. Elings, J. A., Ait-Meddour, R., Clark, J. H., and Macquarrie, D. J., *Chem. Commun.*, 2707 (1998).
397. Sankey, J. P., Wilson, S. L., and McAdam, J., World Patent No. 94/07855 to Solvay Interlox (1994).
398. Jacobson, S. E., Mares, F., and Zambri, P. M., *J. Am. Chem. Soc.* **101**, 6938 (1979).
399. Jacobson, S. E., Mares, F., and Zambri, P. M., *J. Am. Chem. Soc.* **101**, 6946 (1979).
400. Adam, W., Curci, R., and Edwards, J. O., *Acc. Chem. Res.* **22**, 205 (1989).
401. Frohn, M., and Shi, Y., *Synthesis*, 1979 (2000).
402. van Vliet, M. C. A., Arends, I. W. C. E., and Sheldon, R. A., *Chem. Commun.*, 263 (1999).
403. Ganeshpure, P. A., and Adam, W., *Synthesis*, 179 (1996).
404. Shiney, A., Rajan, P. K., and Sreekumar, K., *Polymer Int.* **41**, 377 (1996).
405. O'Connell, A., Smyth, T., and Hodnett, B. K., *Catal. Today* **32**, 273 (1996).
406. Boehlow, T. R., Buxton, P. C., Grocock, E. L., Marples, B. A., and Waddington, V. L., *Tetrahedron Lett.* **39**, 1839 (1998).
407. Song, C. E., Lim, J. S., Kim, S. C., Lee, K., and Chi, D. Y., *Chem. Commun.*, 2415 (2000).
408. de Nooy, A. E. J., Besemer, A. C., and van Bekkum, H., *Tetrahedron* **51**, 8023 (1995).
409. Osa, T., Akiba, U., Segawa, I., and Bobbitt, J. M., *Chem. Lett.*, 1423 (1988).
410. MacCorquodale, F., Crayston, J. A., Walton, J. C., and Worsfold, D. J., *Tetrahedron Lett.* **31**, 771 (1990).
411. Brunel, D., Lentz, P., Sutra, P., Deroide, B., Fajula, F., and Nagy, J. B., *Stud. Surf. Sci. Catal.* **125**, 237 (1999).
412. Bolm, C., and Fey, T., *Chem. Commun.*, 1795 (1999).
413. Verhoef, M. J., Peters, J. A., and van Bekkum, H., *Stud. Surf. Sci. Catal.* **125**, 465 (1999).
414. Ciriminna, R., Blum, J., Avnir, D., and Pagliaro, M., *Chem. Commun.*, 1441 (2000).
415. Dijkstra, A., Arends, I. W. C. E., and Sheldon, R. A., *Chem. Commun.*, 271 (2000).

Olefin Polymerization Catalyzed by Metallocenes

WALTER KAMINSKY

*Institute for Technical and Macromolecular Chemistry
University of Hamburg
20146 Hamburg, Germany*

Metallocene-catalyzed polymerization of olefins and diolefins, including styrene and selected polar vinyl monomers, is an important new technology that in recent years has started to make significant inroads into the polyolefin marketplace. Metallocenes have broadened our knowledge of the mechanistic understanding of Ziegler–Natta catalysis, stereospecific polymerization, and termination reactions. In contrast to classic Ziegler–Natta catalysis, the polymerization takes place at a defined transition metal center, which allows precise control of the monomer insertion and other reaction steps. Many titanocenes, zirconocenes, and hafnocenes with various symmetries have been synthesized and found to give tailored polymers of totally different structures. Methylalumoxane or other bulky cocatalysts are the main causes for the high activities of the metallocene catalysts. Single-site catalysts have the capability of permitting the user to control polymer tacticity, molecular weight, and molecular weight distribution more efficiently than in the

Abbreviations: Activity, polymerization activity (kg polymer/mol metallocene · h · monomer, pressure) or (kg polymer/mol metallocene · h · C_{monomer}); Al:Zr ratio, molar ratio of aluminum in MAO to zirconocene (mol/mol); Bz, benzyl; Cp, cyclopentadienyl; Cp*, pentamethylcyclopentadienyl; (E), ethylene concentration; En, ethylene bridge (–CH₂–CH₂–); EPDM, ethylene propene diene monomers (elastomer); Et, ethyl; Flu, fluorenyl; HDPE, high-density polyethylene; Ind, indenyl; IndH₄, tetrahydroindenyl; ^{iso}Pr, iso-propyl; λ , wavelength of light (nm); L, π complex bonded ligand to a metal; LDPE, low-density polyethylene; LLDPE, linear low-density polyethylene; MAO, methylalumoxane; Me, methyl; M_n , number average of molecular mass of polymers (g/mol)— $M_n = \sum_{i=1}^{\infty} n_i M_i / \sum_{i=1}^{\infty} n_i$, where n_i is the number of polymer chains formed by i monomers and M_i is the molecular weight of a polymer formed by i monomers; M_w , weight average of molecular mass of polymers (g/mol)— $M_w = \sum_{i=1}^{\infty} n_i M_i^2 / \sum_{i=1}^{\infty} n_i M_i$; MWD, molecular weight distribution (M_w/M_n); Ph, phenyl; PP, polypropylene; R, alkyl group; $r_{p,\text{max}}$, polymerization rate (mol propene/mol zirconocene · s); r_1 , copolymerization parameter [shows how much faster monomer 1 (M_1) is inserted into the polymer chain (P) than monomer 2 (M_2), if the last inserted unit was monomer 1]— $P-M_1 + M_1 \rightarrow P-M_1-M_1$ (rate constant = k_{11}), $P-M_1 + M_2 \rightarrow P-M_1-M_2$ (rate constant = k_{12}), $r_1 = k_{11}/k_{22}$; r_2 , copolymerization parameter (shows how much more slowly monomer 2 is inserted than monomer 1 if the last inserted unit was monomer 2)— $P-M_2 + M_2 \rightarrow P-M_2-M_2$ (rate constant = k_{22}), $P-M_2 + M_1 \rightarrow P-M_2-M_1$ (rate constant = k_{21}), $r_2 = k_{22}/k_{21}$; ^{tert}Bu, tert-butyl; T_g , glass transition temperature of polymer (°C); TIBA, triisobutylaluminum; T_m , melting point of polymer (°C); Tri, oligopropene formed by three propene units (2,4-dimethyl-1-heptene).

past, and they have allowed the synthesis of not just the homopolymers of ethylene and propylene but also new kinds of copolymers and elastomers. © 2001 Academic Press.

I. Introduction

A. TECHNOLOGICAL IMPORTANCE OF POLYOLEFINS

There is no catalytic process in the organic chemical industry with a commercial importance matching that of olefin polymerization catalyzed by organometallics (1–3). More than 10% of all profits in this area are made by these catalysts. The increase in the production of plastics worldwide indicates that the age of plastics began with the discovery of polyolefins, such as polyethylene, polypropylene, and copolymers of ethylene with other olefins. The increase started in the 1960s, when the Ziegler–Natta and Phillips catalysts were first applied. Plastics known before that time were too expensive, or their physical properties (e.g., melting points, flexibility, and processability) were insufficient to allow economic production on a large scale.

About 50% of all plastics produced today are polyolefins (4). These materials have become so widely used that it is difficult to imagine life without them. They are low in density, waterproof, stable in form, nontoxic, and resistant to corrosion; thus, they are the first choice for packaging materials, trash bags, pipes, films, bowls, fibers, toys, car interiors, and other applications. They have an immense number of applications ranging from simple products to high-module fibers and highly sophisticated capacitor films and CDs. Because they are thermoplastics, they can be easily processed. The basic building units, ethylene and propylene, which are linked together into long chains in the polymerization process, are easily and inexpensively obtained from the cracking of oil fractions. Polyolefins can be recycled or combusted with a gain in energy, and the only products are carbon dioxide and water (5). Therefore, it is clear that with increasing energy costs and the increasing importance of environmental concerns, polyolefin production will increase in the long term and polyolefins will replace materials that are produced at higher energy costs and with more pollution.

Table I shows the production of different kinds of polyolefins [high-density polyethylene (HDPE), low-density polyethylene (LDPE), isotactic polypropylene (PP), and linear low-density polyethylene (LLDPE)] (6). Apart from LDPE (discovered by workers at ICI), which has a highly branched structure and is produced in free radical reactions at ethylene pressures of 1000–3000 bar (1 bar = 10^5 Pa), the other polyolefins are synthesized at far lower pressures and in the presence of catalysts (7).

As Table I shows, there is expected to be a marked increase in the production of HDPE, LLDPE, and PP until the year 2005. An important point

TABLE I
Worldwide Production of Polyolefins^a

Year	Production rate of polymer			Percentage of plastics production
	Polyethylene LDPE	Polyethylene HDPE/LLDPE	Polypropylene	
1983	11.3	7.9	6.4	—
1990	14.0	16.1	12.6	43
1995	14.4	22.1	17.1	47
2005	15.8	36.1	27.7	55

^aLDPE, low-density polyethylene; HDPE, high-density polyethylene; LLDPE, linear low-density polyethylene (6).

in developing technology of polyolefins is the tailoring of the structure of the polymers and thereby their properties. Metallocene catalysts and other single-site catalysts open the way to this tailoring. It is estimated that from now until the Year 2010, every other new polyolefin plant will operate with these catalysts. In 1998, about 49 million tons of polyolefins were produced, which was 49% of the total production of plastics. In 2005, about 75 million tons of polyolefins are expected to be produced, amounting to 55% of the production of plastics.

Furthermore, metallocene and single-site catalysts offer the opportunity for a detailed understanding of the mechanism and the stereochemistry of olefin polymerization. Classical Ziegler catalysts are solids, with the polymerization taking place on dislocations and edges of the surface of TiCl_3 or mixtures of $\text{MgCl}_2/\text{TiCl}_4$ (8–10). Consequently, there are many different types of catalytically active sites, and the resulting polymer typically has a broad molecular weight distribution.

In research with Ziegler catalysts, Cossee (11) and Arlmann and Cossee (12) hypothesized that the insertion of propylene monomer takes place in a *cis* conformation into a titanium–carbon bond. Natta *et al.* (8) postulated that in the stereospecific polymerization, chiral centers on the surface are needed to produce isotactic polymers. These and other issues regarding the nature of the active sites have helped to increase the interest in investigations of homogeneous metallocene catalysis.

B. PROCESSES FOR POLYOLEFIN MANUFACTURE

The traditional catalysts for olefin polymerization were invented by Hogan *et al.* (their catalyst is the Phillips catalyst) (13–15) in 1952 and Ziegler *et al.* (16, 17) and Natta and Corradini (18, 19) in 1953. Commercialization of olefin polymerization with these catalysts provided the first linear polyethylene and the first isotactic polypropylene. Before these innovations,

commercial polyethylene had been made exclusively by free radical polymerization at extremely high pressures; the product was LDPE. The Phillips and Ziegler–Natta catalysts are licensed worldwide and account for most of the current production of HDPE and polypropylene.

There is a large market for LLDPE produced by the copolymerization of ethylene and an α -olefin, usually containing 1-butene, 1-hexene, or 1-octene. The density for LLDPE is between 0.915 and 0.925 kg/liter, whereas HDPE has a density of 0.960 kg/liter and LDPE a density of 0.91–0.93 kg/liter.

The heat of polymerization of ethylene is high (93.6 kJ/mol). Heat removal is thus a key issue in commercial polymerization processes. Polyolefins are produced primarily by suspension (slurry), gas-phase, or solution processes (20). Solution processes have been developed by various companies using hydrocarbons, such as heptane or cyclohexane, or hydrocarbon mixtures as solvents. The reaction temperature is in the range of 200–300°C. An advantage of these processes is that they readily accommodate a wide range of comonomer types and product densities. Like the high-pressure process, which is also a solution process, they are unable to accommodate highly viscous products.

In gas-phase processes, gaseous ethylene or propylene is contacted with solid catalysts, sometimes dispersed in dry polymer powder. The industry uses two different methods of carrying out this reaction, depending on the method of heat removal. In one class of processes, a fluidized bed is used, and in the other, a mechanically agitated dry powder bed is used with evaporative cooling in vertical and horizontal autoclaves. The advantage of a gas-phase process is that no solvent recovery is necessary so that the energy requirement is less.

HDPE is produced mainly by a suspension (slurry) process in various types of reactors and with various polymerization procedures. In these processes, a supported Ziegler–Natta catalyst system or a Phillips catalyst in a solvent is used. Because the temperature (80–100°C) is lower than the melting point of the polyethylene (140°C), the polymer produced is separated as a solid. This process is highly versatile and can be used to produce many kinds of polyethylenes.

C. CATALYSTS FOR POLYOLEFIN MANUFACTURE

1. *Ziegler Catalysts*

The Ziegler–Natta catalysts are mixtures of solid and liquid compounds containing a transition metal such as titanium or vanadium (16). The first catalyst used by Ziegler and coworkers for the polymerization of ethylene was a mixture of TiCl_4 and AlEt_3 . Each of these is soluble in hydrocarbon solvents, but when they are combined an olive-colored, highly sensitive

complex precipitates. The polymerization behavior is influenced by several experimental parameters, such as the Al : Ti ratio, temperature, time of mixing of the components, and the relative and absolute concentration of the reactants. After complexation, TiCl_4 is reduced by a process involving alkylation and dealkylative reduction to give titanium in the trivalent state. The actual TiCl_3 product is an alloy with small amounts of AlCl_3 and some chemisorbed AlEt_2Cl .

Instead of Et_3Al , other alkylaluminum compounds (including alkylaluminum halides) were used in the first-generation catalysts. These catalysts are used in the classic olefin polymerization process. In industry, however, the low activities of the catalysts required them to be present in high concentrations. Removal of catalyst residues from the colored polymer, by washing with HCl and alcohols, was also necessary (21).

The second-generation catalysts incorporating solid TiCl_3 and alkylaluminum were much more active than the first-generation catalysts. Even more highly active third-generation catalysts have been produced commercially by supporting the titanium compound on MgCl_2 , SiO_2 , or Al_2O_3 to increase the amount of active titanium from 0.1% to more than 5%. MgCl_2 , CoCl_2 , or other magnesium salts are used because the ionic radius of Mg^{2+} (0.066 nm) is almost the same as that of Ti^{4+} (0.068 nm). Currently, Ziegler-Natta catalysts are produced by ball milling MgCl_2 with about 5% of TiCl_4 . The cocatalyst is $\text{Al}(\text{C}_2\text{H}_5)_3$. The activity (approximately 10,000 g of HDPE per gram of catalyst) is high enough that the catalyst can remain in the polymer product. Only a small fraction of the titanium (1–20%) is active for the polymerization.

In propylene polymerization, internal and external electron-donor compounds such as ethyl benzoate, other aromatic esters, ethers, or silyl ethers are used to increase the activity of the catalyst and the yield of isotactic polypropylene. The role of the electron donors in the preparation of the support is to stabilize the very small MgCl_2 particles produced during the ball milling by adsorption on the freshly produced surfaces. Reaggregation of the crystallites is thereby minimized (22). During the treatment with TiCl_4 , ethyl benzoate is removed from the MgCl_2 surface by complexation with the Lewis acid TiCl_4 and substituted by TiCl_4 , which is then adsorbed on the surface vacancies.

2. Phillips Catalyst

The Phillips catalyst is usually made by impregnating a chromium compound onto a porous, high-surface-area silicate carrier and then calcining in dry air at 500–900°C (14) (Fig. 1). This latter step is an activation that converts the chromium into a hexavalent surface chromate or perhaps dichromate ester. Because each chromium atom is individually attached to the

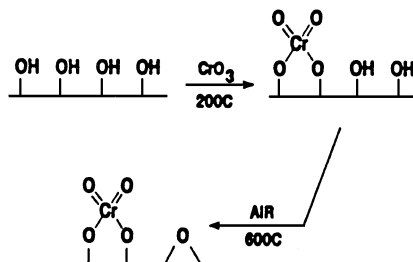
Cr OXIDE CATALYSTS

FIG. 1. Steps in the formation of an olefin polymerization catalyst. Chromium is thought to bind the high-surface-area carrier by reaction with hydroxyl groups. Activation is accomplished by calcining the support at a temperature of 600°C or higher, which removes much of the excess hydroxyl group population.

surface, the carrier is not inert but exerts a strong influence on the polymerization behavior of the site. Hexavalent chromium is reduced by ethylene or other hydrocarbons in the reactor, probably to Cr(II) or Cr(III), the catalytically active species. Because Cr(VI) is tetrahedrally coordinated, and the reduced species can be octahedral, the active site is thus coordinatively unsaturated and accepts olefin readily. However, this trait makes the catalyst very sensitive to low concentrations of polar impurities in the feed stream, such as alcohols, water, and amines. Commercial catalysts usually contain 0.5–1.0 wt% chromium, but only a small fraction of this (perhaps 10–20% or even less) is actually active for polymerization. This catalyst is not able to polymerize propylene to give an isotactic polymer.

3. *Why New Catalysts?*

The following are some of the characteristics of the Phillips and Ziegler–Natta catalysts that indicate possible improvements:

- The fraction of titanium or chromium forming active sites in the catalysts is low, only 1–20%.
- When a $\text{MgCl}_2/\text{TiCl}_4$ catalyst is used, 5–50 ppm chlorine remains in the polymer, responsible for some corrosion in the processing.
- Copolymerization with some α -olefins is possible but only in a small range. The comonomer is not randomly distributed over the whole polymer chain but instead is concentrated at the ends.
- The polymers contain small amounts (2–4%) of oligomers which can permeate out through the bulk.
- It is difficult to control the polymer microstructure.

Thus, there is a strong interest in new kinds of catalysts such as the metallocenes, in which all the transition metals are present in active sites, that have much higher activities than the classic catalysts, have very low amounts of chlorine, can produce all kinds of copolymers, produce no oligomers, allow tailoring of the microstructure of the polyolefin over a wide range, and which can be used in existing reactors.

4. *Metallocene Catalysts*

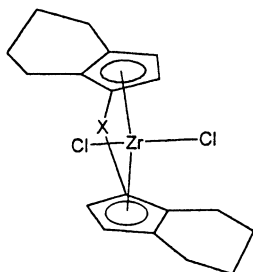
Metallocenes (Fig. 2) are sandwich structures, typically incorporating a transition metal such as titanium, zirconium, or hafnium in the center. The metal atom is linked to two aromatic rings with five carbon atoms and to two other groups—often chlorine or alkyl. The rings play a key role in the polymerization activity (23–27). Electrons associated with the rings influence the metal, modifying its propensity to attack carbon–carbon double bonds of the olefins. The activities of these metallocenes combined by aluminum alkyls, however, are too low to be of commercial interest. Activation with methylaluminoxane, however, causes them to become 10–100 times more active than Ziegler–Natta catalysts.

All the metallocenes shown in Fig. 2 polymerize ethylene; when they are used to polymerize polypropylene, however, they give various products. Unbridged compounds give atactic polypropylene, bridged bis-indenyl metallocenes give isotactic polypropylene, and bridged cyclopentadienyl-fluorenyl zirconocenes give syndiotactic polypropylene. Substitution of the rings influences the activity of the catalyst and the microstructure of the resulting polymer.

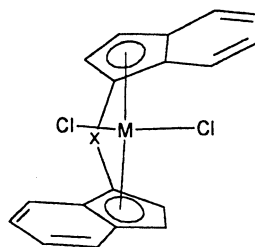
In addition to the metallocenes described previously, so-called half-sandwich compounds or constrained-geometry catalysts (Fig. 3) such as dimethylsilyl-*t*-butylamido cyclopentadienyl titanium dichloride are used. These catalysts are excellent for producing polyethylenes with long-chain branching and can incorporate high amounts of comonomers such as 1-octene.

5. *Other Catalysts*

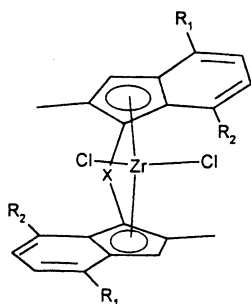
Recently, new families of catalysts have been discovered, including compounds of nickel, palladium, iron, and cobalt (28–31). Again, the cocatalyst is methylaluminoxane (MAO). The iron-containing catalyst (Fig. 4) incorporates a five-coordinated iron(II) center stabilized by a neutral 2,6-bis(imino)pyridine ligand. The molecular weight of the resulting polyethylene depends mainly on the aryl substitution of the ligand; *ortho* substitution by methyl groups yields oligomers, whereas substitution by *t*-butyl groups gives high-molecular-weight polyethylene. Similar complexes are able to copolymerize ethylene with methyl methacrylate, acrylonitrile, or methylvinyl ketone. Brookhart *et al.* (29, 30) described complexes of nickel(II) and of



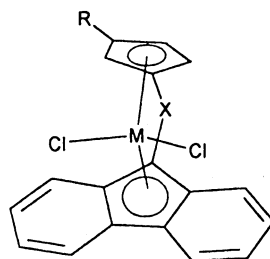
$X = C_2H_4, Me_2Si$



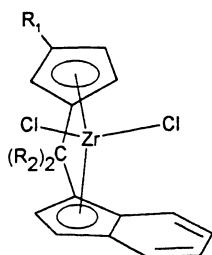
$M = Zr, Hf$
 $X = C_2H_4, Me_2Si$



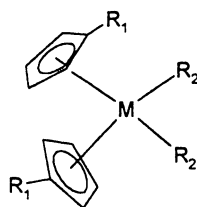
$X = C_2H_4, Me_2Si$
 $R_1 = Me, Ph, Naph$
 $R_2 = H, Me$



$M = Zr, Hf$
 $X = Me_2C, Ph_2C$
 $R = H, Me, t-Bu$



$R_1 = H, Me$
 $R_2 = Me, Ph$



$M = Ti, Zr, Hf$
 $R_1 = H, 5-Me, neomenthyl$
 $R_2 = Cl, Me$

Fig. 2. Structures of selected metallocenes used for polymerization of olefins.

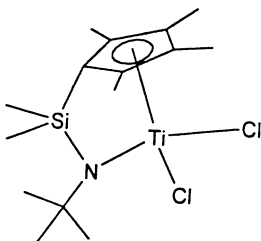


FIG. 3. Structure of dimethylsilylamido cyclopentadienyl titanium dichloride.

palladium(II) containing diimine ligands; these catalysts polymerize ethylene to give highly branched polymers. The polymerization of cyclic olefins such as cyclopentene or norbornene is also possible. The polymerization of propylene to give isotactic polymers is difficult, but syndiotactic polypropylene was observed at low temperatures and with chain end control. The development of these catalysts continues, and the practical potential is high.

D. HISTORY OF METALLOCENES

1. Kinetic Investigations

Metallocenes have been known for decades. In 1952, Wilkinson and Birmingham (32) and Fischer (33) solved the structure of ferrocene. For a long time this new class of compounds provided organometallic chemistry

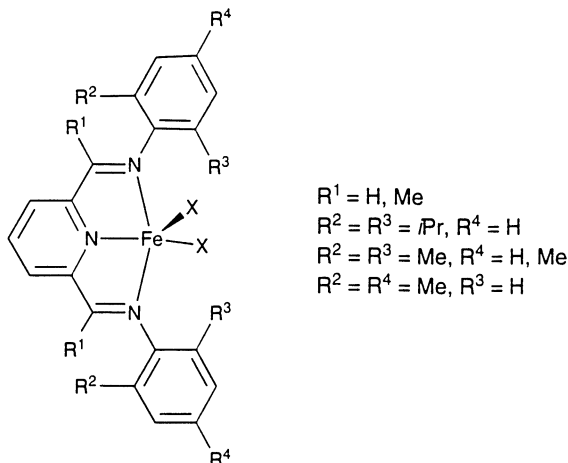


FIG. 4. Iron(II) complexes used for the polymerization of ethylene.

with versatility but failed to have an impact on industrial-scale applications. Soon after the important discovery by Ziegler and Natta, metallocenes were used by Natta *et al.* (34) and Breslow and Newburg (35) in combination with aluminum alkyls, such as triethylaluminum and diethylaluminum chloride, as catalysts for the polymerization of olefins. The activities of these catalysts were poor, and thus the metallocenes were only used for scientific, mainly mechanistic, studies, which were simpler with a hydrocarbon-soluble (homogeneous) catalyst than a solid Ziegler system (36–38).

Subsequent research on this and other systems with various alkyl groups was conducted by Natta (39), Belov *et al.* (40, 41), Patat and Sinn (42), Shilov *et al.* (43, 44), Chien (45), Adema (46), Clauss and Bestian (47), Henrici-Olivé and Olivé (48), Reichert and Schoetter (49), and Fink *et al.* (50, 51). Investigations of kinetics and various other methods have helped to define the nature of the active centers of some homogeneous catalysts, to explain aging effects of solid Ziegler catalysts, to establish the mechanism of the interaction of the catalyst with olefins, and to provide quantitative evidence of some elementary steps (10).

It is necessary to differentiate between the soluble homogeneous and solid polymerization catalyst systems. Unfortunately, although the well-defined bis(cyclopentadienyl)titanium is soluble, the system becomes heterogeneous when polyethylene is formed. This catalyst is also ineffective for propylene polymerization.

Table II is a summary of results obtained with soluble bis(cyclopentadienyl)titanium compounds as catalysts (52–56). The activity for polymerization increases in each run after a short induction period. After reaching a maximum, a continuous decrease in activity is observed as a consequence of rapid aging processes, such as alkyl exchange, hydrogen transfer, and reduction of the titanium. The average activity is 7–200 kg of PE

TABLE II
*Biscyclopentadienyltitanium Compounds and Aluminumalkyl as Catalysts
for the Polymerization of Ethylene*

Catalyst components	Ti: Al molar ratio	Temperature (°C)	Activity (kg PE) (mol Ti × h × bar) ⁻¹	Reference
Cp ₂ TiCl ₂ /AlMe ₂ Cl	1:2.5–1:6	30	40–200	Belov <i>et al.</i> (40), Agasaryan <i>et al.</i> (41)
Cp ₂ TiCl ₂ /AlMe ₂ Cl/H ₂ O	1:6:3	30	2000	Belov <i>et al.</i> (40)
Cp ₂ TiCl ₂ /AlEt ₂ Cl	1:2	15	7–45	Patat and Sinn (42), Dyachkovskii <i>et al.</i> (43)
Cp ₂ TiCl ₂ /AlMe ₃ Cl/H ₂ O	1:10 ⁵ :5 × 10 ²	20	3500	Borodko <i>et al.</i> (44)

(mol Ti · h · bar)⁻¹. The activity increases by the factor of 10 if traces of water are added.

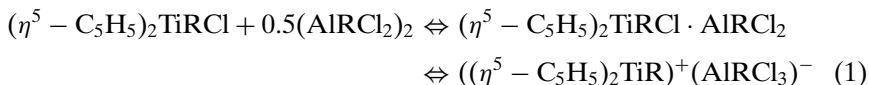
In all systems that contain at least one chlorine atom per pair of titanium–aluminum complexes, there is a fast complex formation which can be recognized by the intensification of color. If there are at least two chlorine atoms per titanium atom in the system, then besides a 1:1 titanium–aluminum complex, a 1:2 complex also exists, as shown by nuclear magnetic resonance (NMR) spectroscopy (50). A simple Ti–Cl→Al donor bond is present in these complexes. In agreement with this idea, no complex formation occurs with the halogen-free system (C₅H₅)₂TiMe₂–AlMe₃.

After formation of complex by combination of the titanocene dichloride and trialkyl aluminum, alkylation of the titanium component is presumed to take place.

2. Polymerization Mechanism

Breslow and Newburg (57) pointed out that polymerization takes place mainly when the titanocene exists as titanium(IV). According to Henrici-Olivé and Olivé (58), the rate of polymerization decreases with increasing intensity of the electron spin resonance signals of the developing titanium(III) compound.

Dyachkovskii *et al.* (43) were the first to postulate (on the basis of kinetics measurements) that the insertion takes place on a titanium cation. An ion of the type (C₅H₅)₂Ti⁺–R, derived from complexing and dissociation,

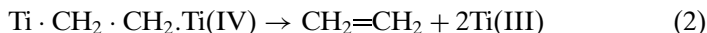


could be the active species for polymerization. In a series of solvents having increasing polarity (heptane, toluene, and CH₂Cl₂), titanium cations were detected by electroanalysis, with the activity for polymerization increasing with the polarity.

Sinn and Patat (59) drew attention to the electron-deficient character of those main group alkyls that afford complexes with the titanium compound. Fink *et al.* (51) showed by ¹³C NMR spectroscopy with ¹³C-enriched ethylene at low temperatures (when no alkyl exchange was observed) that, in the more highly halogenated systems, insertion of the ethylene takes place into a titanium–carbon bond of a titanium–aluminum complex.

The polymerization of α-olefins, accelerated by homogeneous Ziegler–Natta catalysts derived from bis(cyclopentadienyl)titanium(IV) or analogous zirconium compounds and aluminum alkyls, occurs simultaneously with

a series of other reactions that greatly complicate the interpretation of the kinetics of the polymerization process (Fig. 5). Concomitant with continued olefin insertion into the metal-carbon bond of the titanium-aluminum complex, alkyl exchange and hydrogen-transfer reactions occur. Whereas the normal reduction mechanism for transition metal-organic complexes is initiated by release of olefins with the formation of hydride followed by hydride transfer (60) to an alkyl group, in the case of some titanium and zirconium compounds a reverse reaction takes place. By the release of ethane, a dimetalloalkane is formed. In a second step, ethylene from the dimetalloalkane is evolved, and two reduced metal atoms remain (61):



Some of the aging processes that occur with soluble and solid Ziegler catalyst systems can be explained on the basis of these side reactions.

Most titanium(IV) alkyls tend to be reduced by aluminum alkyls in a complicated sequence of reactions accompanied by evolution of paraffin and olefin. The catalytic activity of the bis(cyclopentadienyl)titanium-aluminum complexes is associated with the titanium alkyl. Hence, it is important to characterize the mechanism of any reductive reaction. To investigate side reactions in the absence of polymerization, highly alkylated systems that are completely free of halogen are preferred. Moreover, the higher the alkyl group content of the added aluminum alkyl, the faster the reduction takes place.

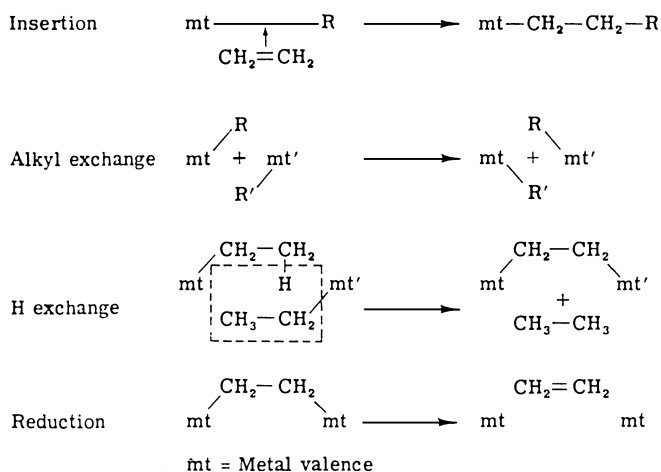


FIG. 5. Reactions with soluble titanocene catalysts, trialkyl-aluminum, and ethylene (56).

Similar intermediate steps have been elucidated for the soluble zirconocene system using aluminum alkyls as cocatalysts. Because of the much greater resistance of zirconium to reduction, the study of alkyl exchange and hydrogen transfer is more definitive than that for the titanium system. Figure 6 shows reaction pathways that were demonstrated by using gas-takeup techniques, NMR spectroscopy, mass-balance determinations, and the isolation of intermediate products (62, 63). The first step involves very fast complexation with AlEt_3 accompanied by alkylation of zirconium. The ethylation step is followed by further complexing by condensation, with subsequent β -hydrogen transfer, leading to compounds 4–6 in Fig. 6. The

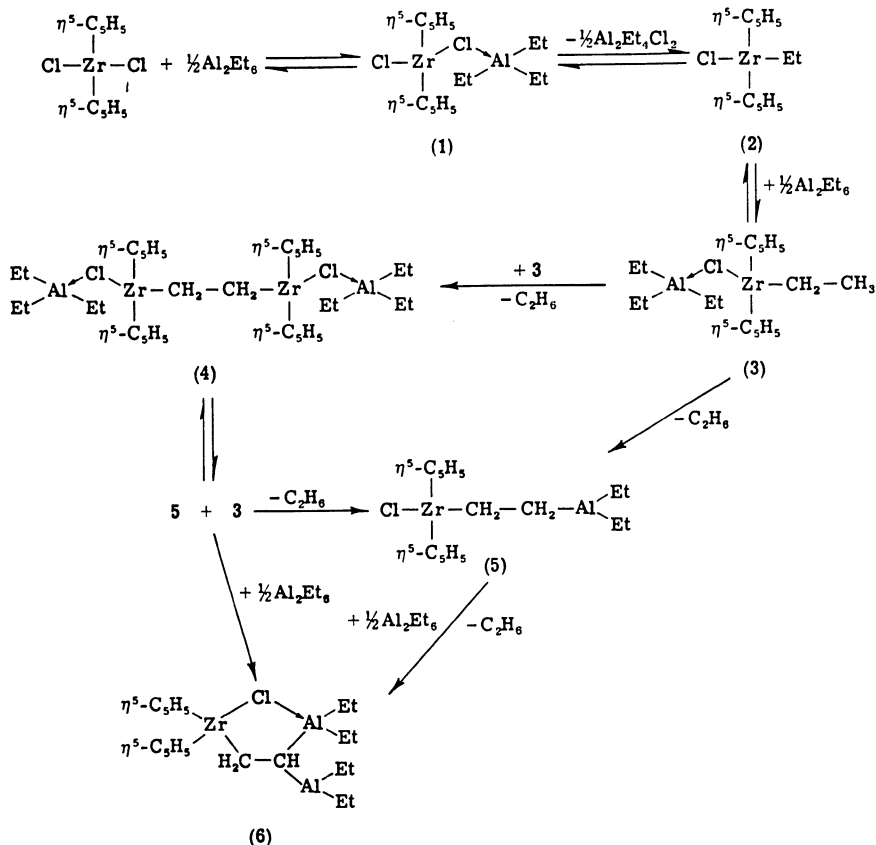


FIG. 6. Side reactions in the zirconocene system; biscyclopentadienyl zirconium dichloride, and triethyl aluminum at 20°C in toluene solvent (63).

reactions affording **6** are very slow and can only be observed at temperatures higher than 40°C.

The carbon-carbon bond angle of the Zr-CH₂-CH₂-Zr structure (compound **4**) is unusually narrow—only 76° (64). Compound **6** shows a similar carbon-carbon bond angle of 75° for the Zr-CH₂-CH-Al structure. β-Agostic hydrogen bonds can explain these angles and have been suggested to be a reason for the stabilization of the active site during the polymerization when methylaluminumoxane is used as a cocatalyst.

3. Increase of Activity

Relative to the titanocenes, the zirconocenes show negligible polymerization activity with aluminum alkyls as potential cocatalysts. Progress in increasing the activity was made by Reichert and Meyer (55) and Breslow and Newburg (57) by addition of small amounts of water to a system of titanocenes and alkylaluminum chlorides (Table II). The situation changed dramatically when, in 1975, at our Hamburg laboratory, water accidentally got into a test tube used for NMR measurements which contained bis(cyclopentadienyl)titaniumdimethyl, trimethylaluminum, and ethylene. Suddenly, the ethylene began to polymerize rapidly in a system that was regarded at the time to be inactive for olefin polymerization (65).

The intensive search for the active cocatalyst responsible for this activation led in 1977 to the isolation of MAO, a component in which aluminum and oxygen atoms are positioned alternately and free valences are saturated by methyl groups (65, 66). When metallocenes, especially zirconocenes, are combined with MAO, the resulting catalyst can polymerize olefins 10–100 times faster than those used in the most active Ziegler-Natta systems (67).

4. Advantage of Metallocene Catalysts

With the aid of metallocene catalysts, plastics can be made for the first time with a property profile that is precisely controllable and within wide limits. This precise control of properties such as temperature resistance, hardness, impact strength, and transparency had not been possible until recently because conventional Ziegler-Natta catalysts are generally solids on the surfaces of which relatively nonuniform catalytic action takes place. The nonuniformity of the surfaces results in corresponding nonuniformity in the resulting polymers.

Because the catalyst is insoluble, its active sites are hardly accessible for analytical purposes, and it has not been possible to improve it on a rational basis. In contrast, metallocene catalysts permit a polymerization in which the building blocks can be linearly joined at only a single kind of site. Propylene and long-chain olefins can be built up stereoregularly, with the building

blocks in the chain having a defined and constantly repetitive configuration. This configuration has significant influence on the properties of the resulting material. A variety of materials could very easily and for the first time be produced by the application of metallocene catalysts (68) as follows:

- Polyethylene with a narrow molecular weight distribution $M_w/M_n = 2$; Ziegler catalysts, in contrast, produce polyethylene with value of M_w/M_n of 5–10 because the nonuniformity of the active sites
- Polypropylenes with low amounts of oligomers; atactic, isotactic, isoblock, stereoblock, and syndiotactic
- Syndiotactic polystyrene with a melting point of 276°C
- Copolymers with a high proportion (5–30%) of a longer chain α -olefin
- Elastomers made of ethylene, propylene, and dienes (EPDM)
- Mono- and copolymerization of cycloolefins
- Cyclopolymerization of 1,5-hexadienes
- Polymerization in the presence of fillers

By using a (homogeneous) metallocene catalyst that is soluble in hydrocarbons, organic and inorganic particles (starches, cellulose, quartz grains, and metal powder) can be uniformly covered, and in the subsequent polymerization they can be coated with a film of polyolefins of variable thickness.

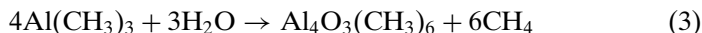
II. New Cocatalysts

Keys to the high polymerization activities of single-site catalysts are the cocatalysts. MAO is most commonly used and is synthesized by controlled hydrolysis of trimethyl aluminum. Other bulky anionic complexes which show a weak coordination, such as borates, also play an increasingly important role. One function of the cocatalysts is to form a cationic metallocene and an anionic cocatalyst species. Another function of MAO is the alkylation of halogenated metallocene complexes. In the first step, the monomethyl compound is formed within seconds, even at -60°C (69). Excess MAO leads to the dialkylated species, as shown by NMR measurements. For the active site to form, it is necessary that at least one alkyl group be bonded to the metallocene (70).

Other alkylaluminum oxanes (e.g., ethylaluminum oxane or isobutylaluminum oxane) were also used as cocatalysts instead of MAO (67) but show a much lower polymerization activity. The combination of zirconocenes with MAO is evidently optimal. The three-dimensional structure plays a role (there is a rough similarity to enzymes)—changing either the metal or the alkyl groups leads to lower activity, as does changing the amino acids in enzymes.

A. METHYLALUMOXANE

Alkylaluminum oxanes are prepared by a variety of methods, with the preferred being the reaction of trimethylaluminum with water (ice), a violent, highly exothermic reaction best carried out at low temperatures in an inert solvent (71, 72). Instead of water, hydrolysis of $\text{Al}_2(\text{SO}_4)_3 \cdot 16 \text{H}_2\text{O}$ can be used. In both cases the reaction is evidenced by the evolution of methane during hydrolysis:



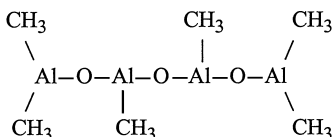
Unfortunately, this reaction is a gross oversimplification of the series of reaction steps that occur during the hydrolysis reaction. Hydrolysis has been shown to proceed via the formation of an alkylaluminum–water complex, which subsequently eliminates methane to form a dimethylaluminum hydroxide complex. This rapidly associates to give dimers or larger oligomers in solution. In the case of *t*-butylaluminum oxane, some of the intermediate species have been isolated and characterized structurally (73–76).

The structure of MAO is complex and has been investigated by cryoscopic measurements; hydrolysis reactions; infrared, ultraviolet, and NMR spectroscopies; and other methods (77). Equilibria are attained between the oligomers. The molecular weight, determined cryoscopically with samples in benzene, is between 1000 and 1500 g/mol. The work of Sinn (77) and Barron *et al.* (78, 79) has provided details of the structure of MAO and *t*-butylaluminum oxane. Among the different oligomers, the units shown in Scheme 1 are important.

These can associate, resulting in coordination of the unsaturated aluminum atoms. There are tri- and tetracoordinated aluminum atoms, of which the trivalent ones show extreme Lewis acidity. Four of the $\text{Al}_4\text{O}_3(\text{CH}_3)_6$ units can form a cage structure resembling a half-open dodecahedron ($\text{Al}_{16}\text{O}_{12}(\text{CH}_3)_{24}$) (Fig. 7) (77).

This cage is complexed with differing amounts of trimethylaluminum. The MAO complex can seize a methyl anion, a Cl anion, or another O anion from the metallocene, forming an AlL_4 anion that can distribute the negative charge over the whole cage, thus stabilizing the charged system.

There is strong evidence that the cationic species $\text{L}_2\text{M}(\text{CH}_3)^+$ is the active center in olefin polymerization. The appearance of cationic metallocene



SCHEME 1

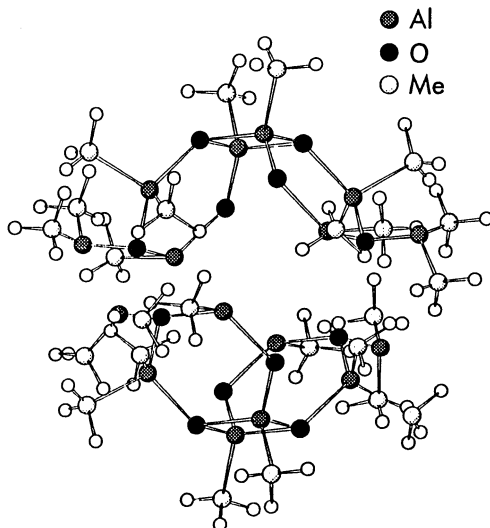


FIG. 7. Possible structures of methylalumoxane clusters (77).

complexes, $L_2M(CH_3)^+$, especially $Cp_2ZrCH_3^+$, in the presence of MAO-containing solutions was confirmed by ^{13}C NMR, ^{91}Zr NMR, and X-ray measurements (80, 81). The cation is stabilized by a weak coordination to Al–O units or by bridging CH_3 or Cl ligands (82).

B. PERFLUOROPHENYLBORANE AND -BORATE

Further evidence for the existence of cationic centers is given by the activation of metallocene catalysts for olefin polymerization by the use of anionic counterions such as tetraphenylborate ($C_6H_5)_4B^-$, carborane ($C_2B_9H_{12}$), or fluorinated borate. The use of $(C_6F_5)_4B^-$ counterions by Hlatky *et al.* (83), Sishta *et al.* (84), and Zambelli *et al.* (85) leads to highly active metallocene catalysts, which are formed by the reaction of a dealkylated zirconocene with dimethylaniliniumtetra(*bis*-perfluorophenyl)borate:



Cationic or dicationic metallocene complexes can also be formed by reactions of perfluorinated triphenylborane or trityltetrakis(pentafluorophenyl)borate (86).

Early investigations showed that even donor-stabilized metal alkyl cations are potent electrophiles which do not tolerate conventional anions such as BF_4^- and PF_6^- but form insoluble salts with $B(C_6H_5)_4^-$ (87–89). These investigations showed that the formation of cationic catalysts leads to a

complex equilibrium of various adducts of the highly electron-deficient $(\text{Cp}_2\text{ZrR})^+$ ion.

The amine liberated during the protolysis step, the counterion, and the solvent are capable of binding to the cationic metallocene. Under polymerization conditions this means that all these adducts are in competition for bonding with the active species for polymerization.

X-ray analysis of solid compounds such as $((\text{CH}_3)_2\text{C}_5\text{H}_3)_2\text{ZrCH}_3^+ + \text{H}_3\text{CB}(\text{C}_6\text{F}_5)_3$ (90) showed that a coordination bond still partly exists between the zirconocene and the borate. The olefin is π -complex bonded into this compound and then inserted into the zirconium–methyl bond.

A great advantage of the borates is that the ratio of borate to metallocene is about 1 to 1 and not 5000 to 1, as in the case of MAO for homogeneous systems. On the other hand, the borate system is highly sensitive to poisons and decomposition and must be stabilized by addition of aluminum alkyls such as triisobutylaluminum (TIBA); the necessary ratio of TIBA to zirconocene is in the range of 100–500.

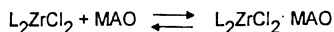
C. ROLE OF THE COCATALYST

The cocatalyst has various functions. The primary role of MAO as a cocatalyst for olefin polymerization with metallocenes is alkylation of the transition metal and the production of cation-like alkyl complexes of the type Cp_2MR^+ as catalytically active species (91). Indirect evidence that MAO generates metallocene cations has been furnished by the described perfluorophenylborates and by model systems (92, 93). Only a few direct spectroscopic studies of the reactions in the system $\text{Cp}_2\text{MCl}_2/\text{MAO}$ have been reported (94). The direct elucidation of the structure and of the function of MAO is hindered by the presence of multiple equilibria such as disproportionation reactions between oligomeric MAO chains. Moreover, some unreacted trimethylaluminum always remains bound to the MAO and markedly influences the catalyst performance (77, 95, 96). The reactions between MAO and zirconocenes are summarized in Fig. 8.

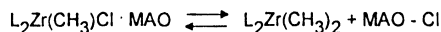
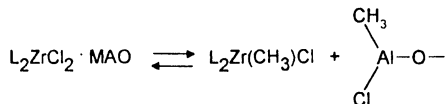
Even at -60°C , the metallocene and MAO form a complex, as shown by a new absorption maximum in the infrared spectrum (97). Following complexation, rapid alkylations and dissociation into an ion pair occur. An equilibrium is set up between the ion pair of the cationic metallocene and the anionic MAO and the resulting complexes (98). Both systems show polymerization activity, but the cationic complex is significantly more active. The two active centers show differences in the molecular weights of the resulting polymers (99).

An important side reaction is α -hydrogen transfer, which leads to the production of methane. Condensation of the metallocene and MAO takes

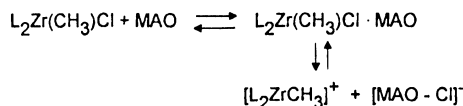
Complexation



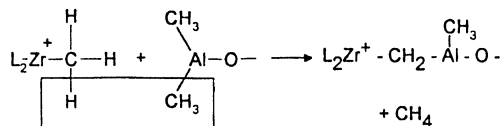
Methylation



Activation



Deactivation



Reactivation

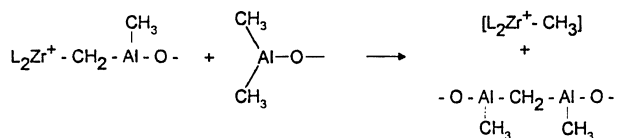


Fig. 8. Reactions of zirconocenes with MAO; L, π -bonded ligand (24).

place forming $Zr-CH_2-Al$ or $Zr-CH_2-Zr$ structures. These compounds are inactive, and their presence is one reason for the deactivation of metallocene catalysts (69).

The condensation rate depends on the structure of the zirconocene, the temperature, the Al:Zr ratio, and the concentration. Methane production is much faster with MAO than with the weaker Lewis acid trimethylaluminum. More than 2 mol of methane is eliminated per mole of zirconium in 15 min when high Al:Zr ratios are applied (Fig. 9). This is complicated by

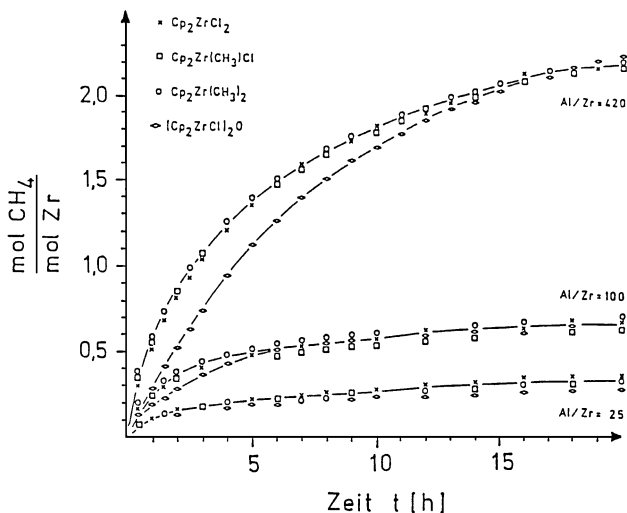


FIG. 9. Time dependence of rate of methane production in the reactions of zirconocenes with methylalumoxane at various Zr/Al ratios (94).

self-condensation of MAO. The high yield of methane and Zr-CH₂-Al structures means that the catalyst would have to be inactive after only minutes. Because the metallocene catalyst is active for hours or even days, there has to be a reactivation step. It was observed by dynamic ¹H-NMR measurements that inactive Zr-CH₂-Al structures could be activated by an excess of MAO, forming L₂ZrCH₃(Cl) and Al-CH₂-Al structures. When Cp₂ZrCl₂ was used, sharp signals were observed for the cyclopentadienyl rings, and these allowed differentiation of the chemical shifts of all the intermediates. The data show that an equilibrium was attained between deactivation and reactivation within 20–120 min.

Table III shows the relationship between polymerization activity and the evolution of methane as a function of reaction time. Nearly 15 min after mixing of the metallocene and MAO, the catalyst attains its maximum activity; the production of methane is low. After 2 h at 10°C, the equilibrium mentioned previously is reached. This corresponding activity is then nearly constant for 17 h. This result shows that another important function of MAO is the reactivation of inactive complexes formed by hydrogen-transfer reactions.

When perfluorophenylborate is used as a promoter, the side reactions are not known in detail. Unfluorinated borates show a fast interaction with the metallocenes. A substantial reduction in the cation-anion interaction was achieved with perfluorotetraphenylborate (B(C₆F₅)₄)⁻ as the counteranion.

TABLE III
*Polymerization of Propylene with Cp_2ZrCl_2/MAO after Various
 Prereaction Times^a*

Prereaction time (h)	Yield (moles of $CH_4 \cdot (\text{moles of Zr})^{-1}$)	$r_{p, \text{max}}$ (moles of propylene $\cdot (\text{moles of Zr})^{-1} \cdot \text{s}^{-1}$)
0.29	0.1	20.0
0.7	0.5	8.2
2.5	1.0	3.7
10.0	1.8	3.1
19.0	2.2	2.1

^aIndicated by the formation (yield) of methane. Polymerization conditions: 105 ml toluene, 37 ml propylene (3 bar), 10°C; concentrations: Zr, 10^{-5} mol liter⁻¹; MAO, 3.6×10^{-2} mol Al liter⁻¹; reaction time, 20 h. Prereaction: 50 ml of toluene, 10°C; concentrations: Zr, 4×10^{-3} mol liter⁻¹; MAO = 1.68 mol Al liter⁻¹ (94).

This borate is considerably less basic and less prone to phenyl transfer reactions than $(BPh_4)^-$ and can be used even at high polymerization temperatures. Because no alkylation is possible, the metallocenes must be dialkylated from the beginning, or an alkylaluminum has to be added (100–102). The use of $B(C_6F_5)_3$ with dimethylzirconocenes offers the advantage that the product is stabilized by methyl coordination and is relatively nonpolar and significantly soluble in toluene (103). In contrast to the reaction in the presence of methyl complexes, the reaction of zirconocene dibenzyls with $B(C_6F_5)_3$ gives only ionic products.

III. Metallocene-Catalyzed Ethylene Polymerization

A. HOMOPOLYMERIZATION

When bis(cyclopentadien)zirconium dichloride (Cp_2ZrCl_2) and MAO are used for ethylene polymerization, yields as high as 40×10^6 g of polyethylene (grams of zirconium \times h)⁻¹ are obtained.

Every zirconium atom forms an active complex, as shown by Tait (103) and Chien and Wang (104), producing about 46,000 polymer chains per hour. (This efficient use of the zirconium atoms is contrasted to Ziegler–Natta and Phillips polymerization, in which only a small fraction of the metal centers are active.) The insertion time of one ethylene unit is only 3×10^{-5} s. The rates are comparable to those observed for some enzymes catalyzing synthesis reactions. The analogy to enzymes is manifested in others ways as well—for example, the influence of substitution, regioselectivity, and stereospecificity.

Unbridged, bridged, substituted, and half-sandwich complexes have been used as metallocenes for ethylene polymerization (Figs. 1 and 2). To compare the activities and molecular masses, the polymerizations are carried out under the same conditions (30°C, 2 bar ethylene pressure, with toluene as a solvent) (105). Table IV shows the polymerization behavior of various metallocene/alumoxane catalysts. Generally, zirconium-containing catalysts are

TABLE IV

Homopolymerization of Ethylene at 30°C, 2.5 bar Ethylene Pressure, 6.25×10^{-6} mol/Liter Metalloocene Concentration, and Molar Ratio MAO/Metalloocene = 250^a

Catalyst	$10^{-4} \times$ activity (kg of PE) (moles of metallocene \cdot h \cdot C_{ethylene}) ^{-1b}	$10^{-5} \times$ molecular mass (g/mole)
Cp ₂ ZrCl ₂	6.09	6.2
Cp ₂ TiCl ₂	3.42	4.0
Cp ₂ HfCl ₂	0.42	7.0
Cp ₂ TiMeCl	2.70	4.4
Cp ₂ ZrMe ₂	1.40	7.3
Cp ₂ TiMe ₂	0.12	5.0
Cp ₂ ZrCl ₂ /EAO	0.25	5.5
Cp ₂ ZrCl ₂ /iBAO	0.54	3.9
(C ₅ Me ₅) ₂ ZrCl ₂	0.13	15
(NmCp) ₂ ZrCl ₂	1.22	10
(C ₅ Me ₄ Et) ₂ ZrCl ₂	1.88	8.0
(O(SiMeCp) ₂)ZrCl ₂	5.78	9.3
(O(SiMe ₂ tBuCp) ₂)ZrCl ₂	1.17	0.7
(En(Ind) ₂)ZrCl ₂	4.11	1.4
(En(Ind) ₂)HfCl ₂	0.29	4.8
(En(2,4,7)Me ₃ Ind) ₂)ZrCl ₂	7.80	1.9
(En(IndH ₄) ₂)ZrCl ₂	2.22	10
(Me ₂ Si(Ind) ₂)ZrCl ₂	3.69	2.6
(Ph ₂ (Ind) ₂)ZrCl ₂	2.02	3.2
(Bz ₂ Si(Ind) ₂)ZrCl ₂	1.22	3.5
(Me ₂ Si(2,4,7Me ₃ Ind) ₂)ZrCl ₂	11.19	2.5
(Me ₂ Si(IndH ₄) ₂)ZrCl ₂	3.02	9.0
(Me ₂ Si(2Me-4,6iPr-2Ind) ₂)ZrCl ₂	1.86	7.3
(Me ₂ Si(2Me-4Ph-Ind) ₂)ZrCl ₂	1.66	7.3
(Me ₂ Si(2Me-4,5BenzInd) ₂)ZrCl ₂	0.76	4.5
(Ph ₂ (Ind)(Cp))ZrCl ₂	0.333	0.18
(Me ₂ C(Ind)(Cp))ZrCl ₂	0.155	0.25
(Me ₂ (Ind)(3MeCp))ZrCl ₂	0.27	0.30
(Ph ₂ C(Fluo)(Cp))ZrCl ₂	0.289	6.3
(Me ₂ C(Fluo)(Cp))ZrCl ₂	0.20	5.0
(Me ₂ C(Fluo)(Cp))HfCl ₂	0.089	5.6
(En(Fluo) ₂)ZrCl ₂	4.0	4.0

^aEAO, ethylalumoxane; iBAO, triisobutylalumoxane (105). ^b C_{ethylene} is ethylene concentration in moles/liters.

more active than those containing hafnium or titanium (106). Partially substituted bisindenyl systems and bridged bisfluorenyl zirconocenes (107, 108) show high activities, exceeding those of the sterically less hindered Cp_2ZrCl_2 . In contrast, zirconocenes with bulky ligands such as neomentyl-substituted derivatives afford significantly lower productivities. This comparison indicates that electron-donating groups can enhance productivity, whereas steric crowding lowers it. Among the alumoxane cocatalysts, methylalumoxane is much more effective than ethyl- or isobutylalumoxane. The catalyst shows a long-lasting activity, even after more than 100 h of polymerization. The maximum activity is reached after 5–10 min; this period seems to be needed for the active site to form.

The concentrations of catalyst and cocatalyst and the partial pressure of ethylene influence the polymerization rate. A nearly linear dependence of the rate on the concentration of ethylene is observed. Polyethylenes produced by metallocene catalysts feature a molecular weight distribution (MWD) of $M_w/M_n = 2$, and the product incorporates 0.9–1.2 methyl groups per 1000 carbon atoms. Polyethylenes formed with various metallocene catalysts differ in their molecular weights by a factor of more than 50. Catalysts with a substituent in the cyclopentadienyl or in the 2 position of an indenyl ligand give polymers with relatively high molecular weights. Polyethylene produced with bis(pentamethyl-cyclopentadienyl)zirconium dichloride has a molecular weight of 1.5 million. Similar results are observed with tetrahydroindenyl compounds. The use of mixtures of more than one metallocene catalyst leads to bimodal distributions with values of MWD M_w/M_n in the range of 5–10. The molecular weight is easily lowered by increasing the temperature, raising the metallocene to ethylene ratio, or by adding small amounts of hydrogen (0.1–2 mol%).

At a reaction temperature of 10°C, polyethylene is formed by $\text{Cp}_2^*\text{ZrCl}_2$ with a molecular weight of 1.5×10^6 g/mol, whereas at 50°C this value is reduced to 180,000 g/mol and at 90°C to 90,000 g/mol. Raising the temperature to more than 100°C yields α -olefins with an even number of carbon atoms (109).

The molecular weight decreases nearly linearly with increasing zirconium concentration. This observation leads to the conclusion that chain transfer occurs via a bimetallic mechanism. Usually a β -hydrogen transfer from the growing polymer chain is responsible for the chain transfer. A metallocene hydride is formed along with polymer having a vinyl group at the chain end. In some cases the hydrogen can be transferred to the π -bonded ethylene, forming an ethyl–metallocene complex.

The molecular weight can also be influenced by the addition of hydrogen (110, 111). In contrast to Ziegler–Natta catalysis, in this case only traces of hydrogen are needed to lower the molecular weight over a wide range.

To reduce the molecular weight to about half the value obtained without hydrogen, the reactor needs to be fed with only 7.5 vol% H₂.

B. COPOLYMERS

Metallocenes are useful for copolymerization of ethylene with other olefins. Propylene, 1-butene, 1-pentene, 1-hexene, and 1-octene have been investigated as comonomers, forming linear low-density copolymers with polyethylene (LLDPE) (97-101) (Table V). The major part of the comonomer is randomly distributed over the polymer chain. The content of extractables is much less than in polymers synthesized with Ziegler catalysts. The copolymers have a great industrial potential and are formed at higher rates than the homopolymer. As a consequence of the short branches resulting from the incorporation of the α -olefin, the copolymers have lower melting points, lower crystallinities, and lower densities than the homopolymer. Films made of these materials more are flexible and more easily processed than those of polyethylene. Applications of the copolymers include packaging, shrink films with low steam permeabilities, elastic films that incorporate a high comonomer concentration, cable coatings used in the medical fields because of the low concentrations of extractables, and foams, elastic fibers, adhesives, etc.

The copolymerization parameter r_1 expresses how much faster an ethylene unit is incorporated into the growing polymer chain than an α -olefin, provided that the last-inserted monomer was an ethylene unit and is between 1 and 60, depending on the kind of comonomer and the catalyst. The

TABLE V
*Copolymerization Parameters for Ethylene/ α -Olefin Copolymerization
with Various Metallocene/MAO Catalysts^a*

Metallocene catalyst	Temperature (°C)	α -Olefin	r_1	r_2	$r_1 \times r_2$
Cp ₂ ZrMe ₂	20	Propylene	31	0.005	0.25
(En(Ind) ₂)ZrCl ₂	50	Propylene	6.61	0.06	0.40
(En(Ind) ₂)ZrCl ₂	25	Propylene	1.3	0.20	0.26
Cp ₂ ZrCl ₂	40	Butene	55	0.017	0.93
Cp ₂ ZrCl ₂	60	Butene	65	0.013	0.85
Cp ₂ ZrCl ₂	80	Butene	85	0.010	0.85
(En(Ind) ₂)ZrCl ₂	30	Butene	8.5	0.07	0.59
(En(Ind) ₂)ZrCl ₂	50	Butene	23.6	0.03	0.71
Cp ₂ ZrMe ₂	60	Hexene	69	0.02	1.38
(Me ₂ Si(Ind) ₂)ZrCl ₂	60	Hexene	25	0.016	0.40

^aTerms defined under Abbreviations (97).

copolymerization parameter r_2 is the analogous ratio for the α -olefin. The product $r_1 \times r_2$ is important in determining the distribution of the comonomer and is close to unity (indicating a randomly distributed comonomer) when C_2 -symmetric metallocenes are used as catalysts. This product is less than unity ($r_1 \times r_2 = 0.1$ – 0.4), and the polymer has a more alternating structure, when the catalysts are C_s symmetric (118).

Leclerc and Waymouth (119) and, independently, Arndt *et al.* (120) synthesized alternating copolymers of ethylene and propylene with zirconocene catalysts. The ethylene/propylene (EP) copolymerizations were carried out at 30 and 60°C for each of four metallocene catalysts ($Me_2C(3-R Cp)(Flu)ZrCl_2$ ($R = H, Me, ^{iso}Pr, ^{tert}Bu$)) (Fig. 10). As the size of the substituent increased, there were distinct changes in the copolymerization behavior and in the polymer microstructure.

However, the actual process of insertion could not be observed directly and has been the subject of speculation. Extensive studies of the reaction of the catalyst precursor with the cocatalyst showed that 14-electron species which have alkylzirconocenium ion character ($Cp_2Zr(\text{polymeryl})^+$) are reasonable models of the catalytically active species (121). Each of these complexes has a vacant coordination site suitable for olefin approach. Basically two types of mechanisms for insertion have been proposed (122, 123):

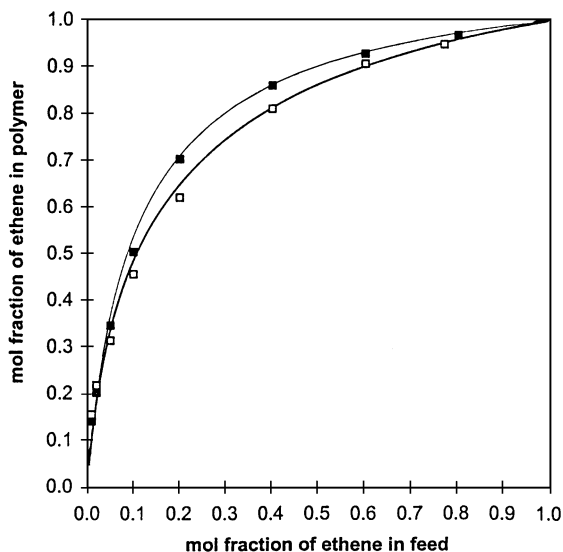


FIG. 10. Copolymerization diagrams for ethylene/propylene copolymerization carried out with ($Me_2C(3-^{tert}BuCp)(Flu)ZrCl_2$) at 30°C (□) and 60°C (■). (120).

1. The alternating mechanism involves a “migration” of the growing polymer chain during insertion and therefore, in the case of metallocenes with stereogenic transition metal centers, inversion of the configuration (the position formerly occupied by the polymer chain is available for the next olefin to approach, and the configuration of the metallocene alternates).

2. The retention mechanism in which the olefin always approaches the metallocene from the same direction and therefore, in the case of metallocenes with stereogenic transition metal centers, the configuration at the transition metal is retained.

The highest degree of alternating structure was observed with $(\text{Me}_2\text{C}(3\text{-}^{i\text{so}}\text{PrCp})(\text{Flu}))\text{ZrCl}_2$ (Fig. 11). The fraction of PEP trials (propene-ethylene-propene combinations in the polymer chain), or $(\text{CH}_2\text{-}\underset{\text{H}}{\text{C}}(\text{CH}_3)\text{-CH}_2\text{-CH}_2\text{-CH}_2\text{-}\underset{\text{H}}{\text{C}}(\text{CH}_3))$, measured by ^{13}C NMR spectroscopy is 40% at a molar fraction of 0.4 of ethylene in the copolymer. It is concluded that copolymerization proceeds via chain migratory insertion for $\text{R} = \text{H}$ or Me ,

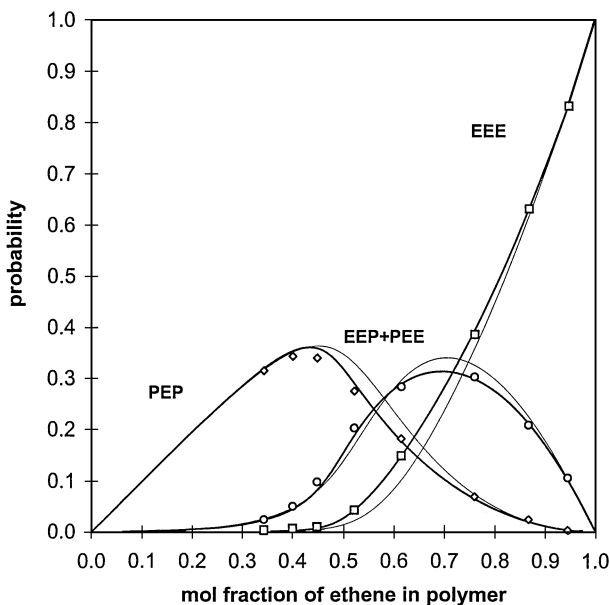


FIG. 11. Calculated and experimental distribution of ethylene-centered triads for ethylene/propylene copolymerization carried to with $(\text{Me}_2\text{C}(3\text{-}^{\text{tert}}\text{-BuCp})(\text{Flu}))\text{ZrCl}_2$ at 30°C : \square , EEE; \circ , EEP + PEE; \diamond , PEP. Copolymerization behavior fitted according to the terminal (—) and TSAM model (—) (120).

whereas a retention mechanism was found for $R = \text{tertBu}$. For $R = \text{isoPr}$, especially at 60°C , a defective alternating mechanism seems to be operative.

Under the same conditions, syndiospecific (C_s -symmetric) metallocenes are more effective in inserting α -olefins into an ethylene copolymer than isospecific (C_2 -symmetric) metallocenes or unbridged metallocenes. In particular, hafnocenes are more efficient than zirconocenes. An interesting effect is observed for the polymerization with ethylene(bisindenyl)zirconium dichloride and some other metallocenes. The catalytic activity for the homopolymerization of ethylene is very high, and it increases when copolymerization with propylene occurs (114) (Fig. 12). Muñoz-Escalona *et al.* (125) observed similar effects in the copolymerization of ethylene with 1-hexene.

The copolymerization of ethylene with other olefins is affected by the variation of the Al:Zr ratio, temperature, and catalyst concentration. These variables lead to changes in the molecular weight and the ethylene content. Higher temperatures lead to increases in the ethylene content and low molecular weights. Investigations of ethylene copolymerization with 1-butene

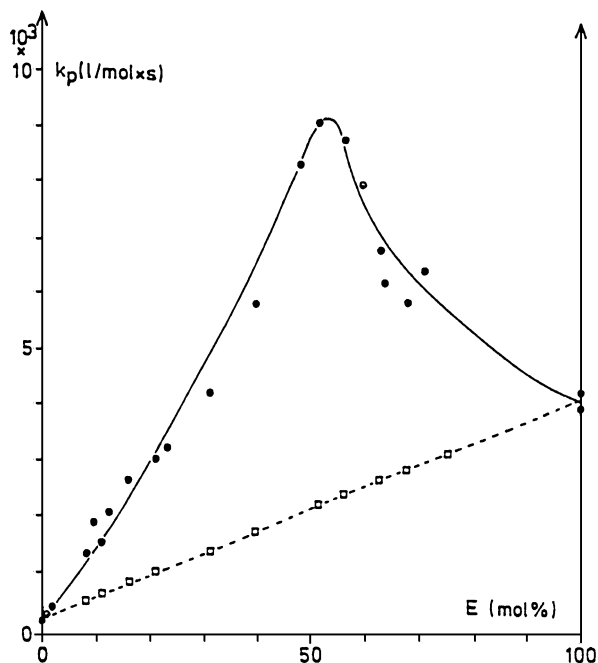


FIG. 12. Rate constant k_p of the ethylene/propylene copolymerization as a function of the ethylene concentration in the liquid phase at 37°C : dashed line, calculated; solid line, measured (114).

catalyzed by $\text{Cp}_2\text{ZrCl}_2/\text{MAO}$ indicated a decrease in the rate of polymerization with increasing comonomer concentration.

The copolymers of ethylene and propylene, with molar ratios in the range of 1 : 0.5–1 : 2, are of great industrial interest. These EP polymers have elastic properties; when the monomers are used together with 2–5 wt% of dienes as a third monomer, they produce elastomers (EPDM). Since it has no double bonds in the backbone of the polymer, this copolymer is less sensitive to oxidation reactions than polybutadiene. Ethylidene norbornene, 1,4-hexadiene, and dicyclopentadiene are also used as dienes. In most technological processes for the production of EP and EPDM rubber, soluble or highly dispersed vanadium components have been used. Similar elastomers, which are less highly colored, can be obtained with metallocene/MAO catalysts that have much higher activities (126). The regioselectivity of the metallocene catalysts toward propylene leads exclusively to the formation of head-to-tail enchainments. Ethylidene norbornene polymerizes via vinyl polymerization of the cyclic double bond, and the tendency for branching is low. The molecular weight distribution is narrow (about 2) (127).

In polymerization at low temperatures, the time required to form one polymer chain is long enough to consume one monomer fully and allow the subsequent addition of another one. Thus, it becomes possible to synthesize block copolymers, provided that the polymerization (especially when it is catalyzed by hafnocenes) starts with propylene and, after the propylene is nearly consumed, continues with ethylene.

Branching, which is caused by the incorporation of long-chain olefins into the growing polymer chain, has been observed by Stevens (128), Shapiro *et al.* (129), Okuda *et al.* (130), and others (131–134) with a new class of silyl bridged amidocyclopentadienyl titanium compounds (Fig. 3). These catalysts, used in combination with MAO or borates, incorporate oligomers with vinyl end groups which are formed during polymerization by β -hydrogen transfer, resulting in long-chain branched polyolefins; in contrast, linear polymers are obtained when the reactions are catalyzed by other metallocenes. Copolymers of ethylene with 1-octene are very flexible materials, provided that the comonomer content is less than 10% (135). When this value reaches 20%, the long-branched polymers have elastic properties.

IV. Metallocene-Catalyzed Polymerization of α -Olefins

A. REGIO- AND STEREOSPECIFICITY

The properties of polypropylenes depend mainly on the regio- and stereospecificity of the inserted propylene units which influence the microstructure. The microstructure of polypropylene in terms of the enchainment of

the monomer units and their configuration is determined by the regio- and stereospecificity of the insertion of the monomer. Depending on the orientation of the monomer during insertion into the transition metal–polymeryl bond, primary (1,2) and secondary (2,1) insertions are possible (Fig. 13). Consecutive regiospecific insertion results in regioregular head-to-tail enchainment (1,3-branching) of monomer units, whereas regioirregularities cause the formation of head-to-head (1,2-branching) and tail-to-tail (1,4-branching) structures (136, 137).

Generally, metallocenes favor consecutive primary insertions as a consequence of their bent sandwich structures. Secondary insertion also occurs to an extent determined by the structure of the metallocene and the experimental conditions (especially temperature and monomer concentration). Secondary insertions cause an increased steric hindrance to the next primary insertion. The active center is blocked and therefore regarded as a resting state of the catalyst (138). The kinetic hindrance of chain propagation by another insertion favors chain termination and isomerization processes. One of the isomerization processes observed in metallocene-catalyzed polymerization of propylene leads to the formation of 1,3-enchained monomer units (Fig. 14) (139–142). The mechanism originally proposed to be of an elimination–isomerization–addition type is now thought to involve transition metal-mediated hydride shifts (143, 144).

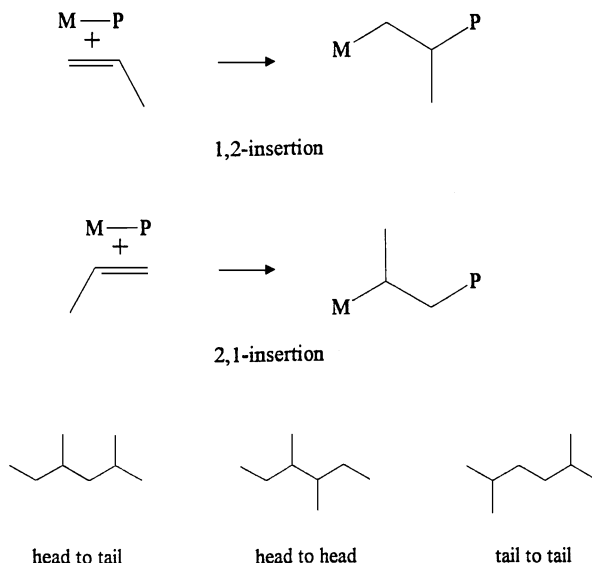


FIG. 13. Primary (1,2) and secondary (2,1) insertion in propylene polymerization.

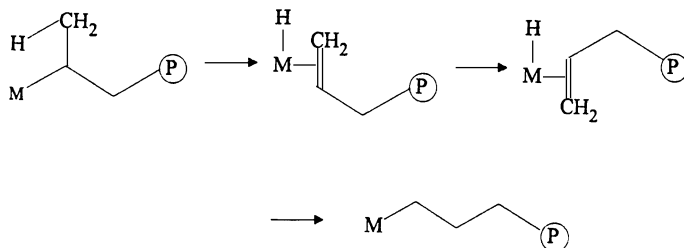


FIG. 14. Elimination, isomerization, and addition mechanism for the formation of 1,3-enchainment in polypropylene.

B. MICROSTRUCTURES OF POLYPROPYLENES

Another type of steric isomerism observed in polypropylene is related to the facts that propylene and other α -olefins are prochiral and that polymers have pseudochiral centers at every tertiary carbon atom of the chain. The regularity of the configuration of successive pseudochiral centers determines the tacticity of the polymer. If the configuration of two neighboring pseudochiral centers is the same, this "diad" is said to have a meso arrangement of the methyl groups. If the pseudochiral centers are enantiomeric, the diad is called *racemic*. A polymer containing only meso diads is called *isotactic*, whereas a polymer consisting of racemic diads only is called *syndiotactic*. Polypropylene in which meso and racemic diads are randomly distributed is called atactic (Fig. 15). The tacticity has a major influence on the properties of the polymer. Atactic polypropylene is a liquid with a high viscosity, whereas isotactic and syndiotactic polypropylenes are solids and partially crystalline. Each of these microstructures can be produced in a

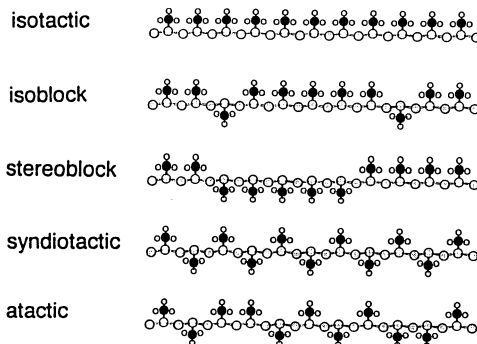


FIG. 15. Microstructures of polypropylenes of various tacticities; modified Fischer projections.

high purity by metallocene catalysis, whereas Ziegler–Natta catalysts give mixtures.

A single step of the polymerization is analogous to a diastereoselective synthesis. Thus, to achieve a certain level of chemical stereocontrol, chirality of the catalytically active species is necessary. In metallocene catalysis, chirality may be associated with the transition metal, the ligand, or the growing polymer chain (e.g., the terminal monomer unit). Therefore, two basic mechanisms of stereocontrol are possible (145, 146): (i) catalytic site control (also referred to as *enantiomorphic site control*), which is associated with the chirality at the transition metal or the ligand; and (ii) chain-end control, which is caused by the chirality of the last inserted monomer unit. These two mechanisms cause the formation of microstructures that may be described by different statistics; in catalytic site control, errors are corrected by the (nature (chirality) of the catalytic site (Bernoullian statistics), but chain-end controlled propagation is not capable of correcting the subsequently inserted monomers after a monomer has been incorrectly inserted (Markovian statistics).

1. *Atactic Polypropylenes*

Atactic polypropylenes are produced in catalysis by C_{2v} -symmetric metallocenes that are achiral, such as Cp_2MCl_2 or $(Me_2Si(FLu)_2)ZrCl_2$. The only stereocontrol observed is both of the chain-end type and low because the chiral center of the terminal monomer unit of the growing chain is in the β position as a consequence of the 1,2 insertion of the monomers. A significant influence on the tacticity is observed only at low temperatures, being much more pronounced for titanocenes and hafnocenes than zirconocenes as a consequence of their shorter $M-C_\alpha$ bonds, bringing the chiral β -carbon closer to the active center (147, 148).

2. *Isotactic Polypropylenes*

The first metallocene/MAO catalysts for the isotactic polymerization of propylene were described in 1984. Ewen (146) found that Cp_2TiPh_2/MAO produced isotactic polypropylene at low temperatures by the chain-end control mechanism (giving a stereoblock structure). When he used a mixture of racemic and meso $(En(Ind)_2)TiCl_2$ in combination with MAO, he obtained a mixture of isotactic and atactic polypropylene, with the isotactic polymer having a microstructure in accord with catalytic site control (an isoblock structure). The use of pure racemic $(En(Ind)_2)ZrCl_2$ yielded the first pure isotactic polypropylene formed by metallocene/MAO catalysis (149–151). These investigations were the beginning of rapid development in the area of metallocene-catalyzed polymerization of propylene, resulting

in the invention of tailor-made metallocenes for different microstructures based on the mechanistic understanding of stereocontrol.

Depending on the structure of the metallocene, different polymer microstructures are formed. Generally, among the rigid metallocenes, different structures may be distinguished (152, 153), and there are also metallocenes that have fluctuating structures.

Table VI provides a comparison of the catalytic activities of various zirconocenes and one hafnocene measured under the same conditions, along with the product molecular weight, isotacticity, and melting point. The bisindenyl compounds show high activity, but the activities of the hafnocene and the mixed (indenyl)cyclopentadienyl compounds are significantly lower. The ligand in the bridge is also influential. Replacement of the methyl group with a phenyl increases the activity, whereas replacement with benzyl

TABLE VI
Polymerization of Propylene with Metallocene Catalysts in Toluene^a

Catalyst	Activity [kg PP/(moles of metallocene × h × C _{monomer})] ^b	Molecular weight [g(mol) ⁻¹]	Isotacticity (mmmm%)
Cp ₂ ZrCl ₂	140	2,000	7
(NmCp) ₂ ZrCl ₂	170	3,000	23
(C ₅ Me ₄ Et) ₂ ZrCl ₂	290	200	5
(O(SiMe ₂ Cp) ₂)ZrCl ₂	230	300	24
(En(Ind) ₂)ZrCl ₂	1,690	32,000	91
(En(Ind) ₂)HfCl ₂	610	446,000	85
(En(2,4,7Me ₃ Ind) ₂)ZrCl ₂	750	418,000	99
(En(IndH ₄) ₂)ZrCl ₂	1,220	24,000	90
(Me ₂ Si(Ind) ₂)ZrCl ₂	1,940	79,000	96
(Ph ₂ Si(Ind) ₂)ZrCl ₂	2,160	90,000	96
(Bz ₂ Si(Ind) ₂)ZrCl ₂	270	72,000	86
(Me ₂ Si(2,4,7Me ₃ Ind) ₂)ZrCl ₂	3,800	192,000	95
(Me ₂ Si(IndH ₄) ₂)ZrCl ₂	7,700	44,000	95
(Me ₂ Si(2Me-4,6iPr-2Ind) ₂)ZrCl ₂	6,100	380,000	98
(Me ₂ Si(2Me-4PhInd) ₂)ZrCl ₂	15,000	650,000	99
(Me ₂ Si(2Me-4,5BenzInd) ₂)ZrCl ₂	6,100	380,000	98
(Ph ₂ C(Ind)(Cp))ZrCl ₂	170	2,000	19
(Me ₂ C(Ind)(Cp))ZrCl ₂	180	3,000	19
(Me ₂ (Ind)(3MeCp))ZrCl ₂	400	4,000	34
(Ph ₂ C(Fluo)(Cp))ZrCl ₂	1,980	729,000	0.4
(Me ₂ C(Fluo)(Cp))ZrCl ₂	1,550	159,000	0.6
(Me ₂ C(Fluo)(Cp))HfCl ₂	130	750,000	0.7
(Me ₂ C(Fluo)(3-t-BuCp))ZrCl ₂	1,045	52,000	89
(Ph ₂ SiH(2,3,5Me ₃ -Cp))ZrCl ₃	150	5,600	6

^aUnder the following conditions: temperature, 30°C; propylene partial pressure, 2.5 bar; metallocene concentration, 6.25×10^{-6} mol/liter; MAO/metallocene molar ratio, 250 (24).
^bC_{monomer} is monomer concentration (mol/liter).

decreases it. The (indenyl)zirconocene is more active than the (tetrahydroindenyl)zirconocene. The activity increases with increasing temperature. The molecular weights of the polymers catalyzed by the C_s -symmetric compounds are high, especially when there are phenyl groups in the bridge.

Spaleck *et al.* (154) reported a large number of chiral zirconocenes with different bridges and substitutions on the indenyl ligand (Table VII). Some C_2 -symmetric metallocenes give polypropylenes with a high melting point (162°C) and tacticities (mmmm pentades) of 97–99%, measured by ^{13}C -NMR spectroscopy (155, 156).

Systematic investigations of bis(indenyl)zirconocenes as catalysts showed that the main chain termination reaction is β -hydrogen transfer with the monomer (157, 158). This reaction is very effectively suppressed by substituents (Me and Et) in position 2 of the indenyl ring (159, 160). Substituents in position 4 also cause an enhancement in molecular weight by reducing 2,1 misinsertions, which preferentially result in chain termination by β -hydrogen elimination. Because primary insertion is sterically hindered after a regioerror occurs, and therefore the catalyst is in a resting state after a 2,1 insertion, suppression of this type of misinsertion also leads to enhanced activities. Aromatic substituents in position 4 result in additional electronic effects. Thus, the most active catalysts incorporate a methyl or ethyl group in position 2 and an aromatic group in position 4 of the indenyl rings.

TABLE VII

Comparison of the Productivity, Molecular Weights, Melting Point, and Isotacticity Obtained in Polymerization Experiments with Various Zirconocene/MAO Catalysts^a

Metallocene catalyst	Productivity [kg of PP (mmol of Zr \times h) ⁻¹]	$10^{-3} \times$ molecular weight (g mol ⁻¹)	Melting point (°C)	Isotacticity (% mmmm)
(En(Ind) ₂)ZrCl ₂	188	24	132	78.5
(Me ₂ Si(Ind) ₂)ZrCl ₂	190	36	137	81.7
(Me ₂ Si(2Me-Ind) ₂)ZrCl ₂	99	195	145	88.5
(Me ₂ Si(2Me-4iPr-Ind) ₂)ZrCl ₂	245	213	150	88.6
(Me ₂ Si(2Me-4,5BenzInd) ₂)ZrCl ₂	403	330	146	88.7
(Me ₂ Si(2Me-4Ph-Ind) ₂)ZrCl ₂	755	729	157	95.2
(Me ₂ Ge(2Me-4Ph-Ind) ₂)ZrCl ₂	750	1135	158	
(Me ₂ Si(2Me-4Naph-Ind) ₂)ZrCl ₂	875	920	161	99.1
(Me ₂ Si(2Et-4Naph-Ind) ₂)ZrCl ₂	825	990	162	
(Me ₂ C(Fluo)(Cp))ZrCl ₂	180	90		0.82
(Ph ₂ C(Fluo)(Cp))ZrCl ₂	3138	478	133	0.87

^aConditions: bulk polymerization in 1 liter of liquid propylene at 70°C, Al/Zr molar ratio = 15000. The results illustrate the broad range of attainable product properties (155).

Besides the bis(indenyl) ansa compounds, C_2 -symmetric bridged bis(cyclopentadienyl) metallocenes of zirconium and hafnium were found to produce isotactic polypropylene (161). The keys to high isotacticity are substituents in positions 2, 4, 3', and 5', which surround the transition metal similar to the one in bis(indenyl) metallocenes. In this type of metallocenes the chirality is a consequence of the chirality of the ligand, and the two chlorine atoms (e.g., the position of the growing chain and the coordinating monomer) are homotopic. According to a model of Pino *et al.* (162–165), and Corradini *et al.* (166–171), the conformation of the growing polymer chain is determined by the structure of the incoming monomer and is forced into a distinct orientation by steric interactions of its side chain with the polymer chain (Fig. 16) (the relative topicity of this reaction was found to be similar). As a consequence of the C_2 symmetry and the homotopicity of the coordination vacancies, isotactic polymer is produced (Fig. 17).

Isotactic polypropylene synthesized by metallocene catalysis has properties different from those of conventional polypropylene produced by Ziegler–Natta catalysis. With approximately the same melting points and molecular weights, the metallocene PP shows a 30% higher E -modulus (Young's modulus), a much more narrow molecular weight distribution, and only a 10th of the content of extractables, which could be important in packaging or medicinal applications. The differences arise from the single-site character of the metallocene catalysts relative to the multisite character of the Ziegler–Natta catalyst.

3. Syndiotactic Polypropylene

In 1988, Ewen and Razavi developed a catalyst for the syndiotactic polymerization of propylene based on C_s -symmetric metallocenes (Table VI)

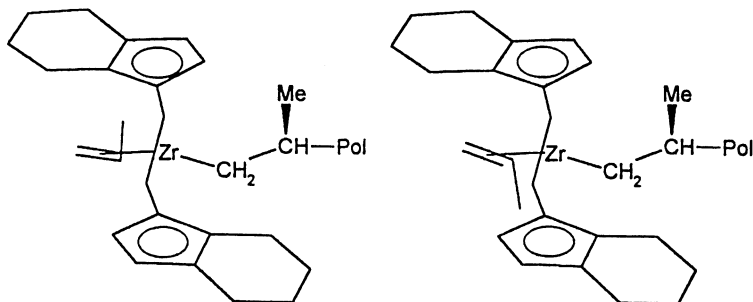


FIG. 16. Origin of the stereospecificity of C_2 symmetric bis(indenyl) zirconocene catalysts. The orientation shown on the right is favored over the one shown on the left because of nonbonding interaction of the approaching monomer and the ligand.

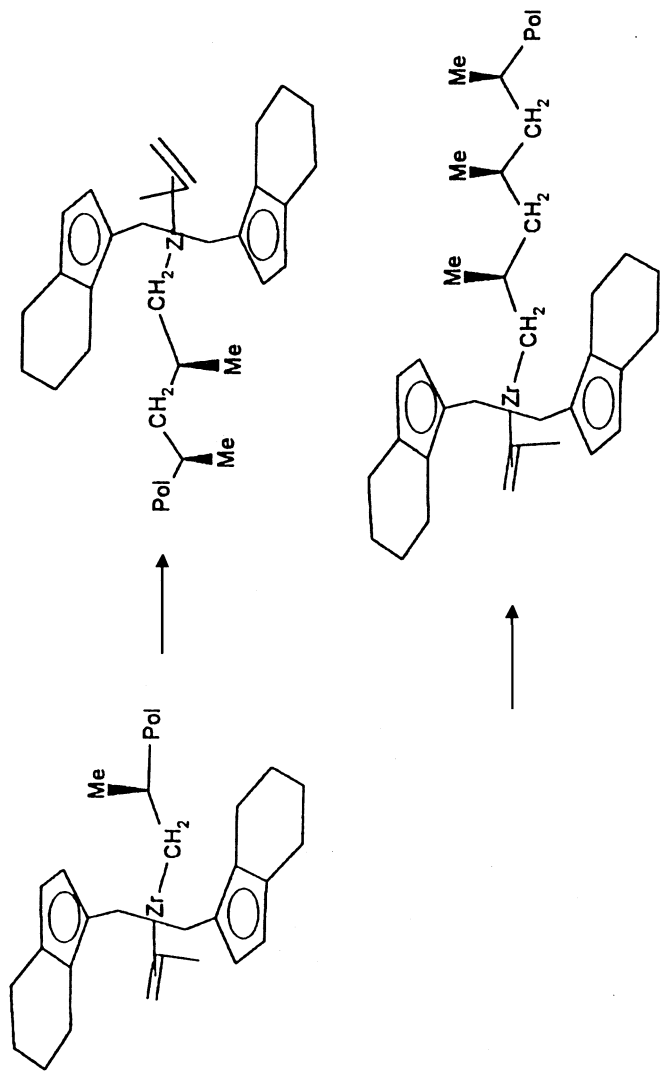


Fig. 17. Mechanism of the isotactic polymerization of propylene involving an alkylzirconocenium ion generated from a C₂ symmetric bis(indenyl) zirconocene.

(172, 173). The syndiotactic polypropylene has a melting point up to 133°C (174). $(\text{Me}_2\text{C}(\text{Flu})(\text{Cp}))\text{ZrCl}_2$ and similar metallocenes, in combination with MAO or other perfluorinated borates, can produce chiral metallocenium ions in which chirality is centered at the transition metal. Because of the flipping of the polymer chain, the metallocene alternates between the two enantiomeric configurations and produces a syndiotactic polymer (172, 175). It had not previously been possible to produce such pure syndiotactic polymer.

Modifications of C_s -symmetric metallocenes may lead to C_1 -symmetric metallocenes (Fig. 8). If a methyl group is introduced at position 3 of the cyclopentadienyl ring, stereospecificity is disturbed at one of the reaction sites so that every second insertion is random; a hemiisotactic polymer is produced (176, 177). If steric hindrance is greater (e.g., if a *t*-butyl group replaces the methyl group), stereoselectivity is inverted, and the metallocene catalyzes the production of isotactic polymers (178–180).

The microstructures described previously are associated with chain migratory insertion. Although in the case of a C_2 - or C_{2v} -symmetric metallocene, as a consequence of the homotopic nature of the potentially active sites chain stationary insertion or migratory insertion followed by site isomerization would result in the same microstructure as chain migratory insertion, in the case of C_s -symmetric catalysts the result is isotactic blocks. C_1 -symmetric metallocenes are able to produce new microstructures if consecutive insertions take place on the same active site in addition to chain migratory insertion. Polypropylenes containing blocks of atactic and isotactic sequences are produced, with the block lengths depending on the rate of chain stationary insertion or site isomerization vs chain migratory insertion (181–185). Thus, hemiisotactic polypropylene represents a special case, having a chain stationary:chain migratory ratio of 1 : 1.

4. Stereoblock Polypropylenes

Polymers with atactic and isotactic blocks in the same chain are obtained if unbridged substituted metallocenes having a significant rotational isomerization barrier are used as catalysts (Fig. 18). Early attempts focused on substituted cyclopentadienyl and indenyl compounds (186–188). Efforts by Coates and Waymouth (189) and others (190, 191) have shown that 2-phenylindenyl groups are well suited for this purpose. They oscillate between the enantiomeric and meso arrangements, giving rise to a stereoblock polypropylene containing atactic (produced by the meso rotamer) and isotactic (produced by the chiral rotamer) sequences. The block length is strongly dependent on the temperature. The polymer has elastomeric properties. Only metallocenes offer the possibility for tailoring the microstructure

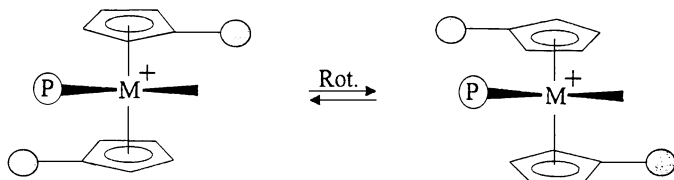


FIG. 18. Oscillating metalocene; by rotation of the cyclopentadienyl rings, the metalocene epimerizes.

of the polypropylenes by changing the ligands in the aromatic rings of the sandwich compound catalysts.

V. Mechanism of Stereospecificity

A. INSERTION OF OLEFINS

Natta postulated that for the stereospecific polymerization of propylene with Ziegler–Natta catalysts, chiral active sites are necessary; he was not able to verify this hypothesis. However, the metallocene catalysts now provide evidence that chiral centers are the key to isotacticity. On the basis of the Cossee–Arman mechanism, Pino *et al.* (164, 165) proposed a model to explain the origin of stereoselectivity: The metallocene forces the polymer chain into a particular arrangement, which in turn determines the stereochemistry of the approaching monomer. This model is supported by experimental observations of metallocene-catalyzed oligomerization.

One way of controlling the molecular weights of polymers produced by Ziegler–Natta catalysis is through the addition of hydrogen, which causes chain termination by hydrogen transfer; at high hydrogen concentrations, oligomers are produced. If an enantiomerically pure metallocene such as (S)-(En(IndH₄))ZrCl₂ is used as the catalyst, optically active oligomers are formed. From measurements of the optical rotation of these oligomers, the topology of insertion may be determined, as can the enantiomeric excess.

Alternatively, one may investigate the stereorigidity of the C₂-symmetric metallocenes. The isotacticity of the polymer increases with decreasing flexibility of the ligands. The effect could be calculated by molecular modeling. Bulk polymerizations of propylene were carried out with rac-(En-(2,4,7-Me₃-Ind)₂)ZrCl₂ (192) as well as with their dimethylsilylene-bridged analogs at various temperatures for comparison with results obtained with the unsubstituted bis(indenyl)zirconocenes. The trimethyl-substituted zirconocenes gave no detectable amounts of regiospecific errors. Only rac-(Me₂Si(2,4,7-Me₃-Ind)₂)ZrCl₂ gave 0.7% of 2,1 insertions at 60°C.

Tetrahydroindenyl and substituted bisindenyl compounds have a low tendency for racemo 1,2 insertion following 2,1 insertion. In the case of the more flexible tetrahydroindenyl catalysts the 2,1 insertion is changed to a 1,3 insertion by an allylic intermediate (193).

The isotacticity measured by the mmmm pentads of polypropylene prepared by $\text{En}(2,4,7\text{-Me}_3\text{-Ind})_2\text{ZrCl}_2$ is surprisingly high in comparison with that prepared by the dimethylsilylene-bridged analogs. At 0°C , this complex gives polypropylenes with the highest melting points of up to 165°C (Fig. 19). Even when the polymerization is carried out at 60°C , the melting point of the resulting polymer is quite high, whereas polymers made with other catalysts show a stronger decrease of the melting point with an increase in polymerization temperature.

Leclerc and Brintzinger (194) investigated the nature of the stereoselectivity by using α -deuterated propylene as a monomer. The observation of CH_2D instead of CH_3 groups in the mrrm stereo mistakes shows that these mistakes arise mainly in isomerization of the chain end. Highly active zirconocenes with a high stereoselectivity are more efficient in suppressing this isomerization relative to the propagation step.

Another method for investigating the decrease of regio- and stereospecificity in polymerization at elevated temperatures is to increase the flexibility of the ligand. To investigate the effects of this flexibility, molecular mechanics

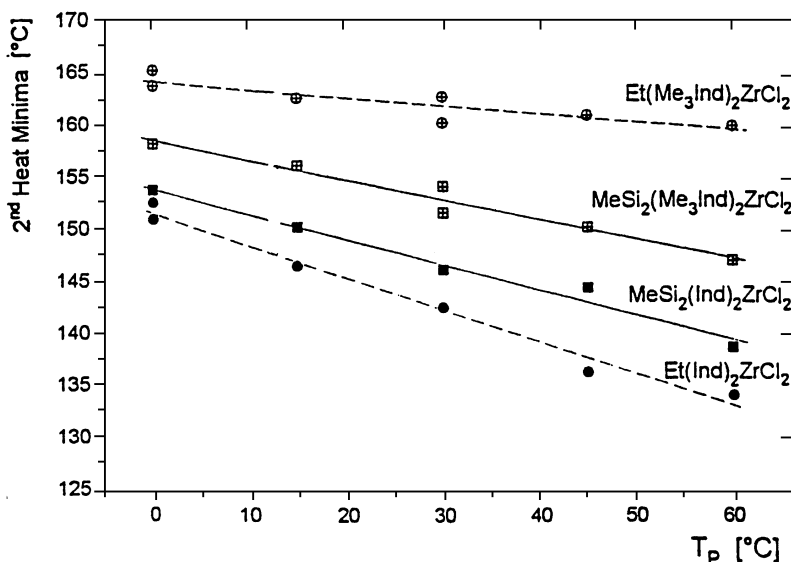


FIG. 19. Melting points of polypropylenes (192).

calculations were performed by using a modified valence force field and combining the results with those of ^1H NMR spectroscopy of the complex in solution (195). The zirconium-centroid torsion angles were forced to adopt certain angles with high force constants, whereas the energy of the remainder of the molecule in the two-dimensional energy maps of conformational flexibility displayed in Fig. 20 was minimized; the calculations were carried out for two different metallocenes. The calculations show two distinct minimum surfaces corresponding to the δ and λ conformations, separated by a low-energy barrier of only $1.5 \text{ kcal mol}^{-1}$ for $\text{rac}(\text{En}(\text{Ind})_2)\text{ZrCl}_2$ (Fig. 20a). To enhance the rigidity of the system, methyl substituents were introduced in positions 2,2' and 7,7' of the indenyl ligand. They are expected to increase the steric bulk around the bridge, thus hindering an exchange between the two conformers. An additional methyl group was introduced in position 4,4' to prevent the formation of stereoisomers during synthesis and to enhance the regiospecificity. The molecular structure of $\text{En}(2,4,7\text{-Me}_3\text{-Ind})_2\text{ZrCl}_2$ determined by X-ray diffraction shows a λ conformation of the bridge, and the molecular mechanics calculations of the potential energy surface make clear that the δ conformation cannot be adopted by this compound (Fig. 20b).

The horizontal extension of the minima can be regarded as a measure of the ease with which chlorine atoms adopt certain positions along the lateral extension angle. This model can be applied to alkyl-olefin complexes to describe the conformational space available to the olefin and alkyl groups. It has been stated that the transition states for β -hydrogen elimination via transfer to the metal center or transfer to the olefin, causing a chain termination, are sterically more demanding than those in the actual olefin insertion process (196–198). For a π -coordinated propylene instead of a chlorine atom, molecular mechanics calculations show that for a 1,2 insertion, the value of the total potential energy $\Delta(\text{re-si coordination of the olefin; Fig. 21})$ is more in favor of mm enchainments in the case of substituted bis(indenyl)zirconocenes. The olefin is unstrained and remains in a favorable position for 1,2 insertion. This high rigidity is a major influence accounting for the high stereospecificity.

B. STABILITIES OF METALLOCENES

Many ansa zirconocenes are sensitive to light (199, 200). An interconversion into the C_s -symmetric meso form is observed until an equilibrium is reached between the two diastereomers. The final rac/meso proportion and the interconversion rate depend on the structures of the different metallocenes (Table VIII, p. 130). The colorless tetrahydroindenyl compounds are stable, but the substituted bis(indenyl)zirconocenes, which are the most

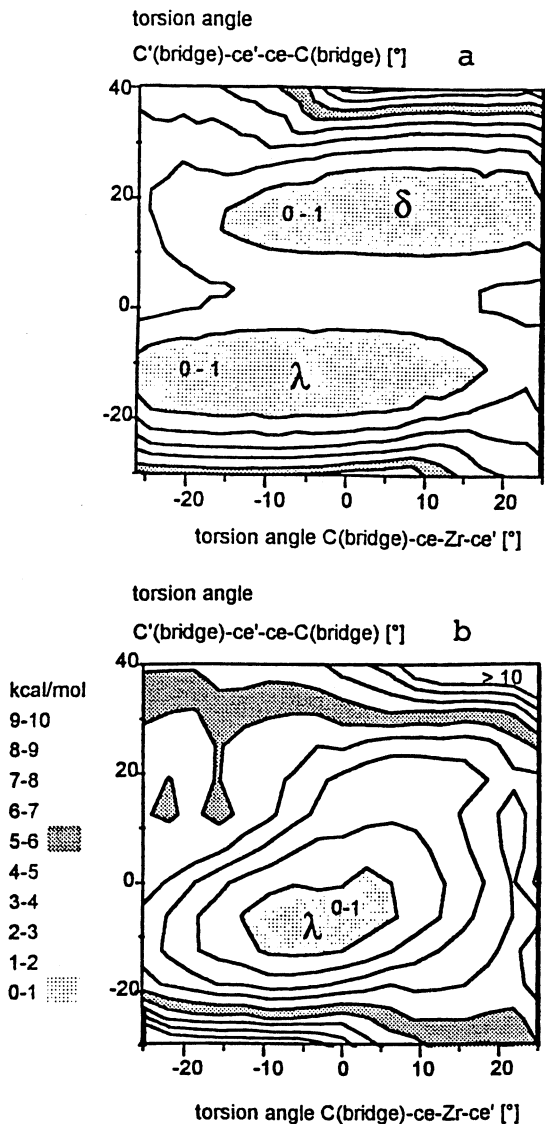


FIG. 20. Flexible geometry contour map of the total potential energy above the minimum conformation of $(\text{En}(\text{Ind})_2)\text{ZrCl}_2$ (a) and $(\text{En}(2,4,7\text{-Me}_3\text{-Ind})_2)\text{ZrCl}_2$ (b) calculated by relaxing the entire molecule while systematically sampling the torsion angles C(bridged)-ce-Zr-ce-Zr-ce which were restrained with 1000 kcal/mol. The energy is contoured in 1-kcal (mol)⁻¹ intervals as a function of C(bridge)-ce-Zr-ce and C'(bridge)-ce-ce-C(bridge) torsion angles; ce refers to the centroid of five-membered ring and C(bridged) to the carbon atom of the five-membered ring substituted with the bridging group. Force field parameters were estimated with a modified CFF91-Discover R_{2,9} and Insight R_{II}, V2, 3.0 (Biosym Technologies, 9685 Scranton Road, San Diego, CA 92121-4778, USA) and were optimized by a fitting procedure to 30 zirconocenes (192).

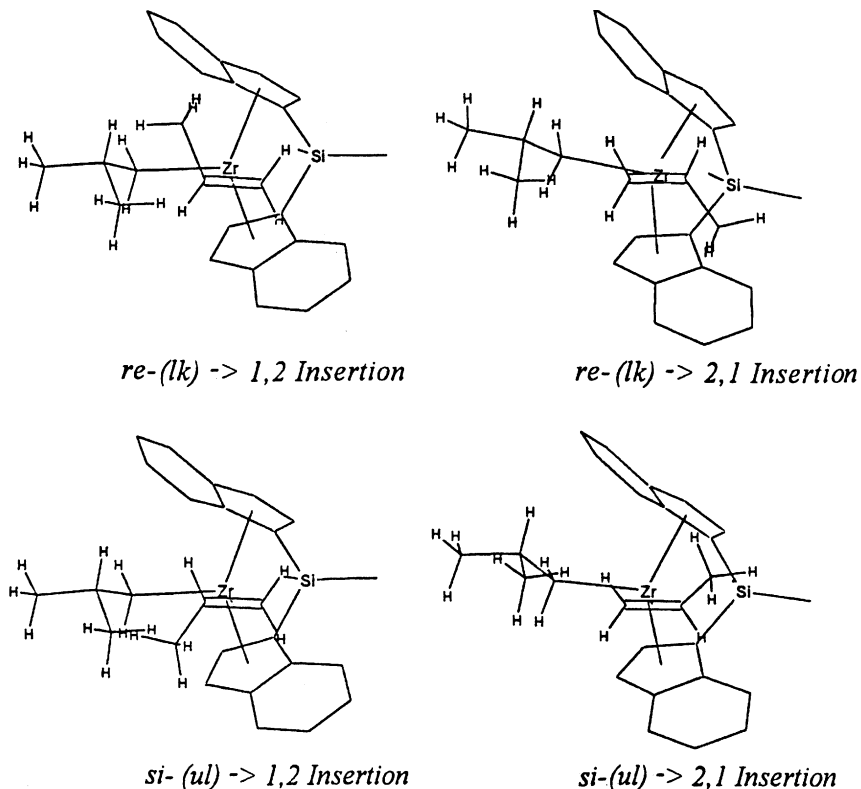


FIG. 21. Possible coordination of propylene on $\text{Me}_2\text{Si}(R,R(\text{Ind})_2)\text{ZrCl}_2$ at the active sites in the 2,1 position or the 1,2 position, with the methyl group to the top or to the bottom (24).

active, change mainly into the meso form. Results of α -olefin polymerization catalyzed by meso- and racemo-rich $(\text{Me}_2\text{Si}(2\text{Me}-4,6\text{-iPr}-2\text{-Ind})_2)\text{ZrCl}_2$ are reported in Table IX. The meso form produces atactic polymers with relatively low molecular weights, whereas the racemo catalyst gives isotactic polymers. On the basis of these data, the activities can be calculated for the pure racemo and meso catalysts (Table X). For propylene polymerization, the racemo forms are more active than the meso form. The opposite is true for α -olefins with longer chains. Surprisingly, the meso form shows the higher activity.

C. OLIGOMERIZATION OF OLEFINS

Another way to improve the regio- and stereospecificity in the conversion of α -olefins is to carry out oligomerization with metallocene catalysts. Under

TABLE VIII
*Rac: meso Ratios of Several Zirconocenes after 4 Weeks
of Irradiation by Daylight^a*

Zirconocene	Rac : meso
(Me ₂ Si(2-Me-4,6-iPr ₂ Ind) ₂)ZrCl ₂	0.11
(Me ₂ Si(2-Me-4-PhInd) ₂)ZrCl ₂	0.25
(Me ₂ Si(2-Me-4,5-BzoInd) ₂)ZrCl ₂	0.35
(Me ₂ Si(Ind) ₂)ZrCl ₂	1.2
(Me ₂ Si(IndH ₄) ₂)ZrCl ₂	1.6
(En(Ind) ₂)ZrCl ₂	1.7
(En(Ind) ₂)HfCl ₂	5.1
(En(IndH ₄) ₂)ZrCl ₂	∞
(En(S-H ₄ -Ind) ₂)Zr(OOC-R-C*(H)(Ph)OCOCH ₃) ₂	∞

^aAdapted from Kaminsky *et al.* (200).

particular conditions, such as low monomer concentrations, high metallocene concentrations, and high temperatures, oligomers are formed instead of polymers. Much experience has shown that the influence of the growing chain on tacticity is low (chain-end control) (201). This makes it possible to synthesize purely atactic polypropylene or other polyolefins with C₁-symmetric zirconocenes.

The main reason for isospecificity is enantiomorphic site control, which means a chiral active center is necessary. To measure the influence of

TABLE IX
*Polymerization Results Obtained with (Me₂Si(2-Me-4,6-*i*-Pr₂Ind)₂)ZrCl₂
for Propylene, Pentene, Hexene, and Octene Monomers^a*

Run ^b	Polymer	Activity ^c	M _n ^d	MWD ^e	I ^f	T _m ^g	T _g ^h
1a	PP	8160	382	2.0	98	154	
1b	PP	1380	166	3.9	64	153	
2a	PPE	132	88	2.3	33		-18
2b	PPE	421	51	1.8	12		-16
3a	PHex	171	107	2.1	33		34
3b	PHex	662	63	1.7	9		-30
4a	PO	145	141	1.7	28		-57
4b	PO	583	78	1.7	8		Not detected

^aCocatalyst, MAO; A1 : Zr molar ratio, 7800; temperature, 30°C; propylene partial pressure, 2 bar; concentration of zirconium complex, 10⁻⁶ mol liter⁻¹ (200). ^bRac : meso ratio = 13 : 1 for runs 1a, 2a, 3a, and 4a; rac : meso ratio = 1 : 9 for runs 1b, 2b, 3b, and 4b. ^cIn units of (kg of polymer/mol of Zr × h × C_{monomer}). ^dIn g/mol. ^eMWD (molecular weight distribution) = M_w/M_n. ^fIsotacticity in % mmmm. ^gMelting point in °C. ^hT_g, glass transition in °C.

TABLE X
Activity Ratios of Racemo and Meso
(Me₂Si(2-Me-4,6-iPr₂Ind)₂)ZrCl₂/MAO
for Olefin Polymerization^a

Olefin	Activity [(kg of polymer) (moles of Zr × h × C _{monomer})] ^b		
	Rac	Meso	Ratio rac : meso
Propylene	7980	560	14.3
Pentene	105	461	0.23
Hexene	125	729	0.17
Octene	103	650	0.16

^aConditions: Cocatalyst, MAO; Al:Zr molar ratio, 5000; temperature, 30°C (200). ^bC_{monomer} is monomer concentration in moles/liter.

chiral active centers, optically active metallocenes were prepared using the method of Schäfer *et al.* (202) by separation of (En(IndH₄)₂)ZrCl₂ using *S*-binaphthol or *O*-acetyl-*R*-mandelate. In these reactions, diastereomers are obtained in pure forms. *S*-zirconocene forms a complex with *S*-binaphthol, which crystallizes, whereas the other diastereomer remains in solution. *O*-acetyl-*R*-mandel acid reacts only with the *S*-zirconocenes. This complex was separated from the remaining compounds (Fig. 22). The oligomerization starts when an olefin undergoes insertion into a transition metal hydrogen or methyl bond, with the latter formed by methylation with methylaluminoxane.

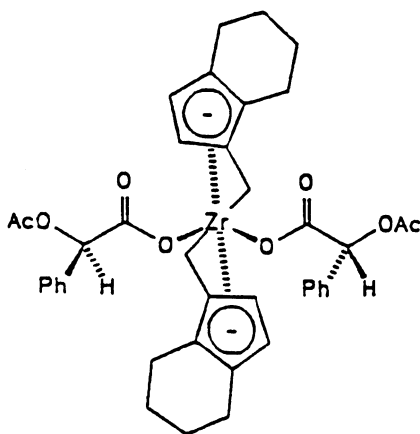


FIG. 22. Structural formula of (*S*)-(1,1-ethylenebis(4,5,6,7-tetrahydroindenyl))-zirconium-bis(*O*-acetyl-*R*-mandelate) (204).

Subsequent insertions lead to chain growth. Chain termination takes place by β -hydrogen transfer to the transition metal atom or to a complex-bound olefin, resulting in formation of the hydride or alkyl transition metal compound in addition to the oligomer. The former allows new insertion steps to occur. The dimers formed do not contain a chiral carbon atom. Optical activity is observed first in trimers and higher oligomers (203, 204).

Ethylene-bis(tetrahydroindenyl)zirconiumbis(*O*-acetyl(*R*)-mandelate) was used for the oligomerization of propylene. To obtain sufficient amounts of the product using a low propylene feed rate of 2.5–20 ml/min, the reaction time had to be extended to between 15 and 24 h; the temperature was varied from 20 to 70°C. The products were found to contain oligopropylenes of various degrees of oligomerization. Oligopropylenes from dimers up to hexamers were detected by gas chromatography.

In the various oligopropylene fractions, many by-products (isomers) are formed apart from the main component. Table XI gives the product distributions according to their differing degrees of oligomerization; this table not only shows a shift of distribution maxima with varying temperatures but also makes clear that the oligomerization conditions can be chosen so that mainly trimers through heptamers are formed. The propylene oligomers consist predominantly of 1-olefins, because these are formed by 1,2 insertion, and isomeric by-products. The main component of the dimers is 2-methyl-1-pentene. The composition of the trimers varies with reaction temperature and monomer concentration (Table XII).

At 30°C and a propylene feed rate of 10 ml/min, 99% of the trimer fraction consists of 2,4-dimethyl-1-heptene (Tri₁), which is formed by 1,2 insertions; this result shows that even under these oligomerization conditions the regioselectivity is still very high. A marked decrease in the relative concentration

TABLE XI
Compositions of Mixtures of Propylene Oligomers Obtained in Propylene Conversion at Various Temperatures^a

Temperature (°C)	wt% of the oligomer in the product mixture						Sum (Di–Hep)
	Di	Tri	Tet	Pen	Hex	Hep	
30	0.1	2.0	3.2	4.5	4.3	4.1	18.1
40	1.3	5.2	6.9	8.3	8.4	7.3	37.4
50	2.4	8.9	11.5	12.2	11.3	9.4	55.7
60	4.0	14.4	18.8	17.2	12.7	9.4	76.5
70	3.5	11.5	17.1	16.2	14.5	11.5	74.3

^aCatalyst, (*S*)-En(IndH₄)₂Zr(C₁₀H₈O₄)₂ at a concentration of 5×10^{-4} mol liter⁻¹; MAO concentration, 4.2×10^{-2} moles of Al liter⁻¹. Reaction time, 24 h; (low rate of propylene, 10 ml/min at 2.2 bar pressure (204)).

TABLE XII

Distribution of Isomers in the Trimer Fraction of the Propylene Oligomerization Product as a Function of Temperature and Propylene Flow Rate^a

Temperature (°C)	Propylene flow rate [ml (min) ⁻¹]	wt% of oligomer in product				
		Tri ₁	Tri ₂	Tri ₃	Tri ₄	Tri ₅
30	10	99.3	—	—	—	0.7
40	10	96.5	1.3	0.4	—	0.9
50	2.5	85.4	5.9	5.9	1.1	2.0
50	5	87.3	5.5	3.3	1.1	2.1
50	10	88.2	4.7	1.9	0.9	2.2
50	15	89.2	4.7	1.3	—	2.2
50	20	91.8	4.3	1.2	—	2.2
60	10	80.2	7.3	4.3	1.5	5.2
70	10	71.1	10.2	6.9	2.3	6.5

^aCatalyst, (S)-En(IndH₄)₂Zr(C₁₀H₈O₄)₂; concentration, 5×10^{-4} mol liter⁻¹; MAO concentration, 4.2×10^{-2} moles of Al liter⁻¹; reaction time, 24 h (204).

of this main component is observed at higher oligomerization temperatures as well as at lower monomer feed rates (lower monomer concentrations). Simultaneously, other isomers that are formed by double bond migration, 2,1 insertion, and 1,3 insertion gain in significance. Figure 23 shows the structures assigned to the individual isomers.

The trimer Tri₂ is different from Tri₁ in the location of the double bond. The migration reaction becomes increasingly important at higher temperatures. Tri₃ is formed by an initial 2,1 insertion followed by a 1,3 insertion, which in turn results from rearrangement of another 2,1 insertion after the first

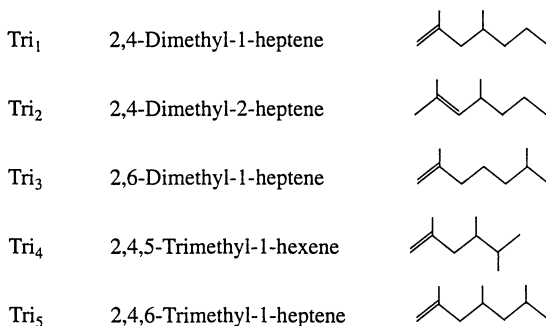
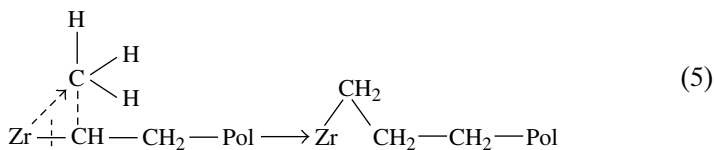


FIG. 23. Asymmetric oligomerization of propylene. Isomers of trimeric propylene were detected by gas chromatography/mass spectrometry (204).

one and migration of the zirconium CH-carbon bonds to the methyl carbon bond (2) by hydrogen transfer as follows:



where \vdots indicates bond forming and \vdash indicates bond breaking. This order of events becomes plausible when one considers that a regular 1,2 enchainment is sterically hindered after a 2,1 insertion, thus favoring another 2,1 insertion. This steric hindrance between two adjacent methyl groups in a 2,1-1,2 sequence is responsible for the relatively low concentration of Tri₄, which contains an initial 2,1 enchainment followed by two insertions with 1,2 orientation. Finally, Tri₅ is formed in the same way that Tri₁ is formed—by three consecutive 1,2 insertions. In this case, however, the initial propylene unit is inserted into a Zr-methyl bond formed in a reaction of zirconocene with methylalumoxane as opposed to a Zr-hydrogen bond resulting from the common β -hydride transfer.

The optical activities of the chiral oligopropylenes were determined at various wavelengths. Polarimetric measurements were only made for product mixtures from oligomerizations performed with various monomer concentrations and at various reaction temperatures and also for individual fractions of dimers, trimers, and tetramers. The product mixtures were fractionated by distillation over a split tube column (Table XIII).

The propylene oligomers, starting with the trimers, are dextrorotatory.

TABLE XIII
Specific Optical Rotation (α)²⁵ of the Propylene Trimers, Tetramers, and Mixed Oligomers at Various Wave lengths (λ) and Various Reaction Temperatures^a

Temperature (°C)	Wavelength, λ (nm)	Trimer (α) ²⁵ (°/mol · 10 cm)	Tetramer (α) ²⁵ (°/mol · 10 cm)	Oligomer (α) ²⁵ (°/mol · 10 cm)
40	589	+ 1.7	+ 3.5	+ 3.0
40	365	+ 6.5	+ 11.8	+ 9.2
50	589	+ 0.9	+ 2.8	+ 2.6
50	365	+ 3.0	+ 8.7	+ 7.6
60	589	+ 0.4	+ 2.2	+ 2.2
60	365	+ 1.5	+ 6.6	+ 6.8
70	589	+ 0.08	+ 1.8	+ 1.9
70	365	+ 0.14	+ 5.6	+ 5.6

^aAdapted from Kaminsky *et al.* (204).

As expected, the achiral dimer does not show any optical activity. The trimer, 2,4-dimethyl-1-heptene, which was produced with the catalyst (*S*)-En(IndH₄)₂Zr(C₁₀H₈O_n)₂/MAO, is inferred to have *S* configuration, since a specific optical rotation (α)_D²⁴ of 6,1 was determined for the R enantiomer (205).

With increasing reaction temperatures, the specific optical rotation of each of the oligomers decays. This result demonstrates that the stereoselectivity of the organometallic catalyst decreases at higher temperatures.

The optical activity of the tetramers is higher than that of the trimers. This difference is caused not only by the additional chiral carbon atom but also by an increased stereoselectivity in the catalysis associated with the longer alkyl chain attached to the active center. This difference is particularly significant at elevated temperatures. Although the specific optical rotation of the trimer is lowered by a factor of 20 as the reaction temperature is reduced from 40 to 70°C, it is only reduced by a factor of 2 for the tetramer.

The extent of stereoselectivity in the chiral synthesis can be checked by determining the enantiomeric excess of the optically active olefins in the products. The optical purity was determined by gas chromatographic resolution of enantiomers by means of an optically active column. Thermostable substituted cyclodextrins are well suited as asymmetric phases (206). The trimer, 2,4-dimethyl-1-heptene, was resolved into its enantiomers by capillary gas chromatography with an octakis(6-*O*-methyl-2,3-*d*-*O*-pentyl)- λ -cyclodextrine phase.

At low temperatures (20°C), the formation of the first chiral center proceeds with the high selectivity of 97.6%, leading to an enantiomeric excess of 95.3%. At higher temperatures, the *ee* value decreases to 23.8% at 50°C and to 2.5% at 70°C. As expected, the *ee* value of the trimer produced with the racemic catalyst is 0 (Fig. 24).

It is evident that at high oligomerization temperatures the isotacticity of the trimers formed is low (23.8% at 50°C). At the same temperature, it is higher for the tetramers (38.1%) than for the trimers. The calculated hypothetical *ee* value of isotactic polypropylene prepared at 50°C is 87.5%, calculated for the *mm* triads. At a higher monomer concentration, the results show that the isotacticity increases during the polymerization after three insertion steps (23.8%) four steps (38.1%), and up to many steps 87.5%. The growing chain has an influence on the stereospecificity. The influence of the monomer concentration is described by Busico *et al.* (207). To achieve high isotacticity, a chiral metallocene is needed. The first insertion steps show low stereospecificity, which increases with the growing polymer chain and the polymerization rate. The polymerization rate *r* depends on the monomer concentration C_{monomer} ($r = k_P \cdot C_{\text{monomer}} \cdot C_{\text{catalyst}}$).

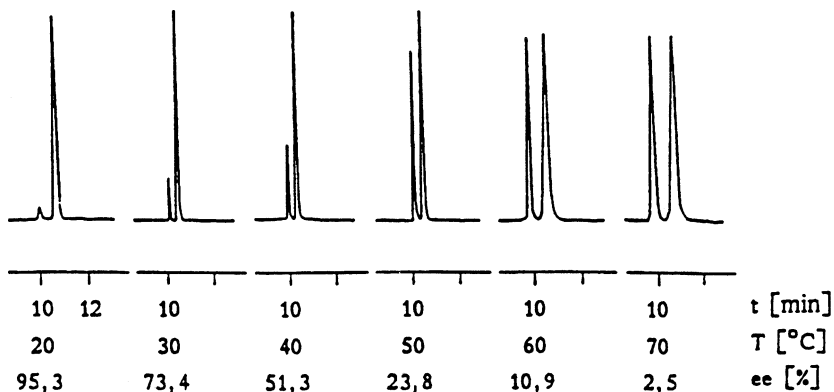


FIG. 24. Asymmetric oligomerization of propylene at various temperatures: gas-chromatographic separation of 2,4-dimethyl-2-heptene (trimer) in a capillary column coated with octakis(6-*O*-methyl-2,3-di-*O*-pentyl)cyclodextrin (204).

VI. Anchoring of Metallocene Catalysts to Supports

In only a few polymerization processes are metallocene catalysts used in a soluble form. Supported metallocene catalysts are preferred for the production of polyethylene or isotactic polypropylene on an industrial scale, especially in the slurry and gas-phase processes. To use them in existing technological processes (drop-in technology) as replacements for the conventional Ziegler–Natta catalysts, the metallocenes have to be anchored to an insoluble powder support, including silica, alumina, and magnesium dichloride (208–217). Various methods of anchoring catalysts to supports are possible (Fig. 25):

1. Initial absorption of MAO on the support with subsequent addition to metallocenes in a second step; this is the procedure most commonly used. The washed catalysts are used in combination with additional MAO or other aluminum alkyls in polymerization (208–210).
2. A mixture of the metallocene and MAO is adsorbed on the support. In this case, the prereaction time plays an important role (213).
3. Absorption and immobilization of the metallocene on the support surface first; then, after addition of MAO, this catalytic is used in the polymerization process (213, 214).
4. The metallocene can be bonded directly to the support by a spacer and an anchor group, resulting in effective immobilization (211).

Each of these procedures affords a different catalyst, and each in turn produces polyolefins with different properties. As a result of supporting a

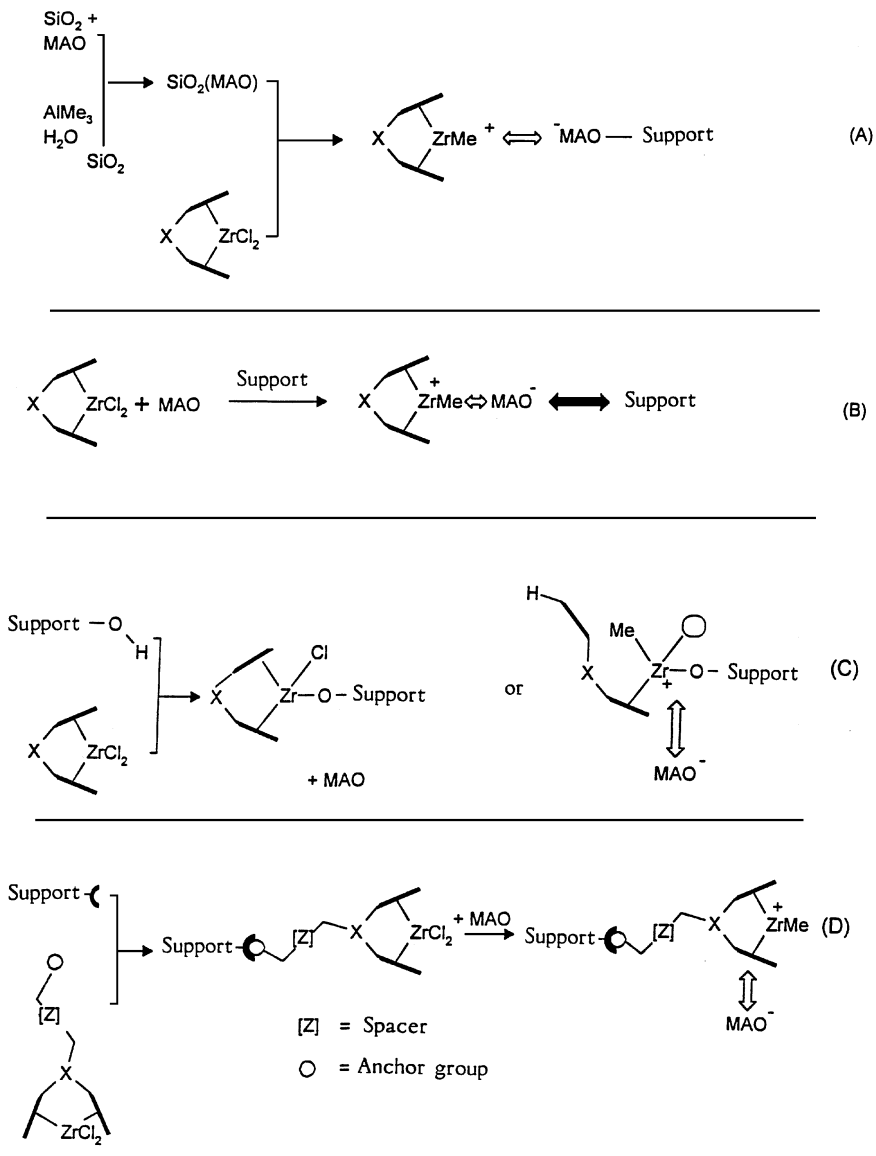


FIG. 25. Methods for supporting metallocenes (221).

metallocene catalysts, the energy of the transition state is increased, leading in most cases to a decrease in the catalytic activity. On the other hand, the steric hindrance and the rigidity increase, which can change the tacticity of the product polypropylene.

The polymers obtained with catalysts made by method 1 are very similar to those obtained with the homogeneous system. Each metallocene on the support forms an active center and thus the starting point of the growth of a polymer chain. Because the active sites on the surface of each catalyst grain are virtually identical, all chains grow uniformly, resulting in polymers with the same microstructures and very narrow molecular weight distributions. Molecular weight and isotacticity are similar to those of the homogeneous system, but the activity is about two times lower because one side of the active site is blocked by the support. On the other hand, some deactivation steps are also hindered by this blocking, which means that the large excess of MAO that is necessary to achieve good activity in solution can be decreased from the range of 3000–10,000 molar ratio $\text{Al}_{\text{MAO}} : \text{Zr}$ (homogeneous) to 100–500 $\text{Al} : \text{Zr}$ (heterogeneous). For ethylene polymerization, Fink *et al.* (218, 219) showed that the method of supporting the metallocene on porous silica has a substantial influence on the progress of polymerization. Fragmentation of catalyst particles by the growing polymer can be circumvented so that the catalytic activity can be maintained.

If the metallocene is linked to the support first, bonding occurs on various adsorption sites, giving nonuniform supported species and much broader molecular weight distributions in the polymer product than those obtained in the corresponding homogeneous catalysis. Furthermore, a large part of the metallocene may be destroyed by acidic centers of the support; then the activity of the supported catalyst is much lower than in the case of the homogeneous system.

Table XIV shows the results of the polymerization of propylene with various supported metallocenes and a comparison with the homogeneous system; silica grade 952 was used as the support (214). The molecular weights of the polypropylene obtained with the supported catalysts are 15–30 times higher than those obtained with the homogeneous ones; the isotacticity, determined by the concentration of mmmm pentads, is also greater. On the other hand, the activities are much lower. The molar ratio $\text{Al} : \text{Zr}$ for an active system was decreased to 150 : 1 from 5000 : 1. Surprisingly, the nature of the tacticity changes when a catalyst is supported; when a metallocene that gave syndiotactic polymer was anchored to a support, the mmmm pentads, measured by ^{13}C NMR spectroscopy increased from 0.4 to 96%, representing an isotactic polymer. The melting points of polypropylene produced by supported metallocenes can reach 163°C, whereas the homogeneous catalysts under the same conditions produce only low-melting polymers (with melting points of about 122°C).

TABLE XIV
*Comparison of the Polymerization of Propene with Homogeneous and Silica-Supported
 [End(Ind)₂]Zr Cl₂(I) or [Me₂C(FluoCp)]ZrCl₂(II)^a*

Catalyst	Al:Zr molar ratio	Activity in kg [PP/(mol Zr · h)]	M _n (g/mol)	Melting point (°C)	Tacticity mmmm (%)
I/MAO-homo	4000	1690	20,000	122	74
Silica/I/MAO	150	26	520,000	157	94
Silica/I/MAO	200	18	640,000	158	96
Silica/II/MAO	200	6	335,000	163	98
II/MAO-homo	5900	1500	47,000	131	0.4
Silica/II/MAO	180	20	350,000	158	96

^aCocatalyst, 300–400 mg MAO in 100 ml toluene; temperature, 50°C; [Zr]SiO₂ = 3–5 × 10⁻⁵ mol/liter, [Zr]homo = 1 × 10⁻⁶ mol/liter. Adapted from Kaminsky and Remmer (214).

The most common industrial method of producing a supported metallocene catalyst is to treat the support with MAO first and then adsorb the metallocene on it. Many procedures for such preparations have been reported. The properties of the support provide some control of the morphology of the polymer produced; the polymer particles are often replicates of the catalyst particles (220).

The adsorbed metallocene can be prereacted with additional MAO, and the prereaction time plays a role. Scavengers can be used, which react with poisons such as oxygen, alkynes, and sulfur compounds. During the prereaction, the active site is formed faster by higher concentrations of the compounds. The supported catalyst is washed to remove the excess MAD.

To demonstrate changes in the tacticity of the product polypropylene as a consequence of anchoring the catalyst to a carrier, Me₂C(CpFlu)Zr Cl₂ was supported on MAO–SiO₂ (221). Triisobutylaluminum (TIBA) was added to the reaction mixture as scavenger. The zirconocene is not very strongly adsorbed on the silica surface, and it can be washed out, especially if MAO is used as an additional cocatalyst and scavenger in the solvent (Table XV). When the supported catalyst is washed with TIBA (ratio TIBA to Zr = 500), the filtrate shows no polymerization activity, even when additional TIBA is added. However, if some MAO is added to the same filtrate, a weak polymerization activity is observed (0.21 g of polymer), showing that small amounts of Me₂C(CpFlu)ZrCl₂ are extracted into solution, and these are activated not by TIBA but by MAO. The extracted catalyst is evidently not destroyed—it produces syndiotactic polypropylene. On the other hand, polymerization activity of the filtrate is high if the supported catalyst is washed with MAO, which has a stronger Lewis acidity than TIBA. The amount of catalyst extracted by MAO is about 20 times greater than that extracted with TIBA.

TABLE XV
*Removable Amount of Zirconocene by Washing of
 $\text{Me}_2\text{C}(\text{CpFlu})\text{ZrCl}_2/\text{MAO}-\text{SiO}_2$ Measured by Polymerization Activity
of Propene*

Leaching by	Scavenger used	Filtrate is polymerization active	Yield (g of PP)
TIBA (1 : 500)	TIBA (1 : 500)	No	—
TIB (1 : 500)	MAO (1 : 3000)	Yes, sPP	0.21
MAO (1 : 3500)	TIBA (1 : 500)	Yes, sPP	4.26

This difference shows that when additional MAO is used as scavenger, a supported metallocene catalyst in a slurry process gives a mixture of polymers, some produced on the supported catalyst and some in the homogeneous phase.

The tacticities are also different, depending on whether the metallocene is supported. The homogeneous $\text{Me}_2\text{C}(\text{CpFlu})\text{ZrCl}_2/\text{MAO}$ catalyst gives a higher yield of syndiotactic polypropylene than the supported catalyst (Fig. 26).

The dependence of the catalyst performance on temperature is nearly the

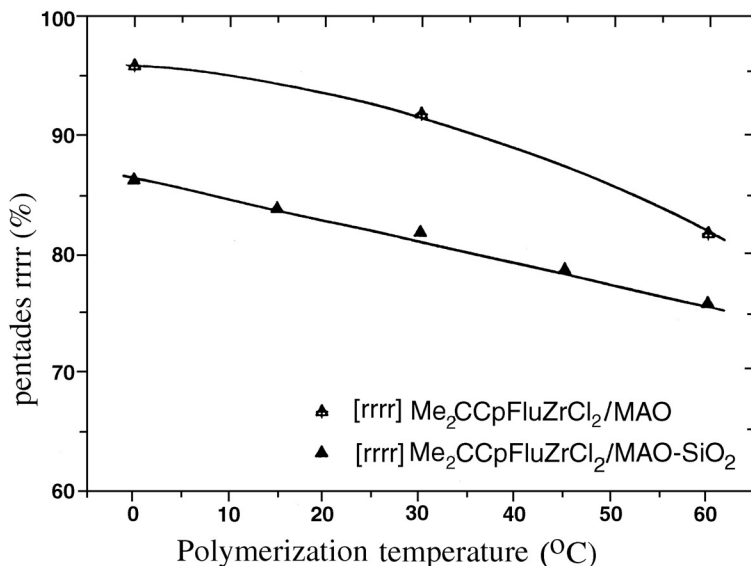


FIG. 26. ^{13}C -NMR measured rrrr pentads in dependence of the polymerization temperature (221).

TABLE XVI
*Influence of Propene Concentration on the Microstructure (¹³C-NMR Measured Pentades) of Polypropenes by Supported
 and Unsupported Catalysts*

Propene (moles/liter)	mmmm (%)	mmmr (%)	rmmr (%)	mmrr (%)	rmrr/mrmm (%)	mmr (%)	rrrr (%)	rrrm (%)	mrmm (%)
Me₂CpFluZrCl₂/MAO-SiO₂									
0.06	0.0	0.0	2.1	4.0	10.4	0.0	69.7	13.7	0.0
0.29	0.0	0.0	2.2	4.3	8.3	0.0	74.3	10.9	0.0
1.29	0.0	0.0	1.7	3.8	5.2	0.0	81.8	7.5	0.0
3.27	0.0	0.0	1.8	3.9	3.2	0.0	85.1	5.9	0.0
6.2	0.0	0.0	1.9	3.4	2.9	0.0	86.8	5.1	0.0
Me₂CpFluZrCl₂									
0.06	0.0	0.0	0.5	2.1	8.6	0.8	75.7	12.2	0.0
0.29	0.0	0.0	0.9	1.8	3.5	1.2	87.5	5.2	0.0
1.29	0.0	0.0	1.2	2.4	1.8	0.0	91.7	2.9	0.0
3.29	0.0	0.0	1.1	1.5	0.8	0.0	95.4	1.3	0.0

^a Adapted from Kaminsky and Winkelbach (22f).

same for the soluble and supported catalysts. Similar values observed for the rmmr pentads indicate that there is no loss of the enantiomorphic site control resulting from anchoring of the catalyst.

The dependence the polymer microstructure on the propylene concentration in the reactor is shown in Table XVI. By varying the monomer concentration in operation with the supported catalyst, one can obtain polypropylenes with relatively low concentration of rrrr pentads. At low propylene concentrations, it is possible that m insertions are formed by epimerization. The yield of these isolated m diads is significantly increased when the catalyst is supported. Similar effects were shown by catalysts producing isotactic polymer.

VII. Metallocenes for Polymerization of Particular Monomers

A. CYCLOOLEFIN HOMOPOLYMERIZATION

Strained cyclic olefins, such as cyclobutene, cyclopentene, and norbornene, can be used as monomers and comonomers to synthesize a wide variety of polymers. Generally, they can be polymerized by ring-opening polymerization (ROMP), giving elastomeric materials (223–225), or by double bond opening (vinyl polymerization). Homopolymerization of cyclic olefins by double bond opening is achieved by several transition metal catalysts, including palladium (226–231) and metallocene catalysts (Fig. 27). Ziegler–Natta and Phillips catalysts are not able to polymerize cyclic olefins.

The polymers include two chiral centers per monomer unit and therefore

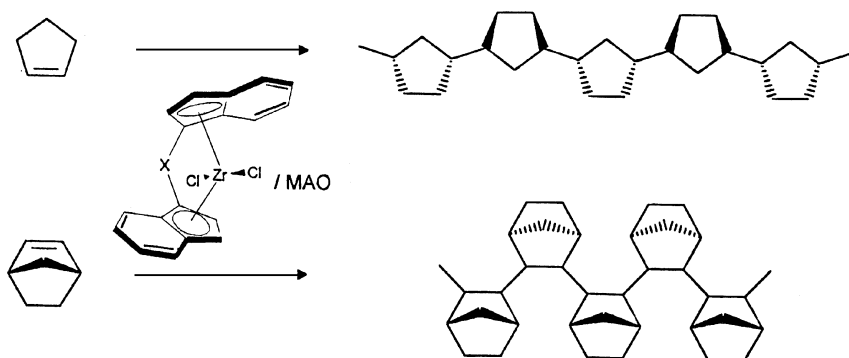


FIG. 27. Vinyl polymerization of cyclopentene and norbornene is possible using metallocene/MAO catalysts (137).

TABLE XVII
Polymerization of Cyclopentene by Metallocene/MAO Catalysts^a

Metallocene	Activity (gPC/mmolZr · h)	% <i>trans</i>	M_n (g/mol)
[En(Ind) ₂]ZrCl ₂	6.0	<2	360
[En(IndH ₄) ₂]ZrCl ₂	11.0	36	880
Cp ₂ ZrCl ₂	5.0	3	560
[En(Cp) ₂]ZrCl ₂	4.0	<1	460
[En(3MeCp) ₂]ZrCl ₂	18.0	38	470
[En(3iPrCp) ₂]ZrCl ₂	5.0	66	1100
Ind ₂ ZrCl ₂	0.7	27	800

^a Toluene, 45 ml; cyclopentene, 5 ml; Zr = 0.5 mmol/liter; MAO = 100 mmol/liter; 25°C, 24 h.

are ditactic. Whereas polymers produced by achiral palladium catalysts seem to be atactic, chiral metallocene catalysts produce highly tactic crystalline materials, with extraordinarily high melting points (in some cases above the decomposition temperature) and extreme chemical resistance.

The microstructures of these polymers have been investigated by using oligomers as models. Norbornene was shown to polymerize via *cis* exo-insertion (232, 233), whereas cyclopentene was shown to give quite unusual *cis* and *trans*-1,3 enchainment of the monomer units (234–236).

Cyclopentene polymerization has been catalyzed by several metallocenes (Table XVII). In each case, the homopolymers were found to contain no 1,2 enchainments. Whereas a mechanism similar to that proposed for the formation of 1,3 enchainments in polypropylene is reasonable, there is no plausible explanation for the formation of *trans* structures.

Polymers produced at high catalyst concentrations have low molecular weights, consistent with melting over a broad temperature range (150–350°C). At low catalyst concentrations, crystalline polymers (which do not melt even at temperatures as high as about 400°C) may be produced if the catalyst is a chiral metallocene. Another important property of a polymer is the glass transition temperature, which is the temperature at which the polymer becomes flexible. The glass transition temperature of poly(cyclopentene) is about 65°C.

Polymerization of norbornene catalyzed by chiral metallocenes results in insoluble polymers exhibiting a glass transition temperature of about 210°C. Although the oligomers have been shown to be tactic, no melting at temperatures as high as 500°C has been observed. Wide-angle X-ray scattering shows two amorphous halos and, for some samples, additional sharp reflexes at small angles, so it is not clear whether these polymers are crystalline (237).

B. CYCLOOLEFIN COPOLYMERS

Although homopolymerization of cyclopentene results in 1,3 enchainment of the monomer units in copolymerization, blocks of cyclic monomer units are rarely observed as a consequence of the unfavorable copolymerization parameters. The isolated cyclopentene units may be incorporated in a *cis*-1,2 or *cis*-1,3 fashion, with their ratio dependent on the catalyst used (238–240). Thus, ethylene compensates for the steric hindrance at the α carbon atom of the growing chain after insertion of the cyclopentene.

The homopolymers of cycloolefins such as norbornene or tetracyclododecene are not processable because of their high melting points and their insolubility in common organic solvents. By copolymerization of these cyclic olefins with ethylene or α -olefins, cycloolefin copolymers are produced, and these represent a new class of thermoplastic amorphous materials (241–248). Early attempts to produce such copolymers were made with solid $\text{TiCl}_4/\text{AlEt}_2\text{Cl}$ catalysts. In the 1980s, vanadium catalysts were applied in these copolymerizations, but real progress was not made until metallocene catalysts were used for this purpose. They are about 10 times more active than vanadium catalysts and, with proper choice of the metallocene, allow variation of the comonomer distribution from statistical to alternating. Statistical copolymers are amorphous if more than 12–15% of cycloolefin is incorporated in the polymer chain. The glass transition temperature can be varied over a wide range (Fig. 28) by choice of the cycloolefin and the amount of cycloolefin incorporated in the polymer chain.

In the reaction of ethylene and norbornene, it is also possible to produce copolymers with molecular weight distributions M_w/M_n in the range of 1.1–1.4 by controlling the polymerization conditions (249). This “pseudo-living polymerization” enables the production of block copolymers by changes in the feed composition. Statistical copolymers are transparent because of their amorphous character, colorless, and show a high optical anisotropy (Table XVIII). Because of the high carbon to hydrogen ratio, these polymers have a high refractive index (1.53 for ethylene/norbornene copolymers at 50 mol% incorporation of each monomer). Their resistance to hydrolysis and chemical degradation in combination with their stiffness and very good processability make them potentially valuable materials for optical applications, for example, in compact discs, lenses, and optical fibers (250).

The alternating copolymers are characterized both by a glass transition temperature (130°C for ethylene/norbornene copolymers) and a melting point (295°C for the totally alternating copolymer). The melting point and the crystallinity of these copolymers may be influenced by choice of the metallocene and the conditions of polymerization. Compared with the statistical copolymers, the alternating structures show better resistance to nonpolar

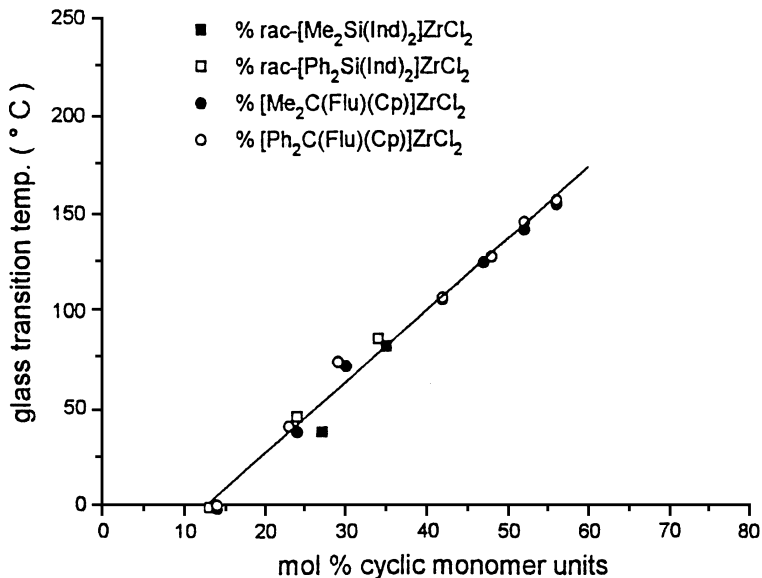


FIG. 28. Dependence of the glass transition temperature of ethylene/norbornene copolymers produced by various metallocene/MAO catalysts on the incorporation of norbornene (24).

solvents. The crystallite diameter is about 50 nm, and thus these copolymers are transparent. Thermoplastic processing is possible at temperatures of 30–330°C.

Similar alternating structures are obtained by ROMP of multicycle polyolefins followed by hydrogenation of the unsaturated polymer.

TABLE XVIII
*Properties of a Random Ethene Norbornene Copolymer
Containing 52 mol% Norbornene^a*

Mechanical properties	
Density (g/cm ³)	1.02
Glass transition temperature (°C)	150
e modulus, ISO 527 (MPa)	3100
Tensile strength, ISO 527 (MPa)	66
Elongation until break, ISO 527 (%)	2–3
Optical properties	
Clarity	White, clear
Anisotropy	Very low
Refractive index	1.53

^aAdapted from Land (250).

C. STYRENE

In 1985, the first pure syndiotactic polystyrene was synthesized by Idemitsu Kosan with transition metal compounds and MAO as the catalyst and cocatalyst (251, 252). Since then, other catalysts have been discovered, and work on technological applications of syndiotactic polystyrene has been carried out (253–262). This material has a melting point of 270°C, which is among the highest of most polymers made from single monomers. Its properties range from good resistance to chemicals, water, and steam to good rigidity and electronic properties.

Some half-sandwich titanium compounds with cyclopentadienyl ligands have been shown to be the most active catalysts for synthesis of these polymers. Fluorinated half-sandwich metallocenes, synthesized by Roesky *et al.* (263), have activities of up to a factor of 30 greater than those of chlorinated compounds. Polymerization has been carried out within a temperature range of 10–70°C (264).

Figure 29 provides a comparison of the polymerization activities of Cp^*TiCl_3 and Cp^*TiF_3 at various temperatures and Al:Ti ratios. At all temperatures investigated, the fluorinated compound is more active than the chlorinated one. Although an increase of the Al:Ti ratio to 900 enhances the activity of Cp^*TiCl_3 , the opposite is observed with Cp^*TiF_3 . The higher activity of the latter complex was found at a usefully low Al:Ti ratio of 300. Table XIX provides a summary of the results.

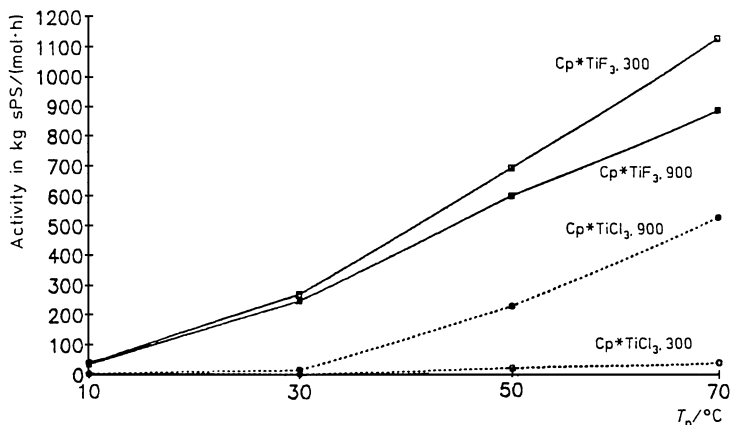


FIG. 29. Polymerization of styrene by Cp^*TiCl_3 and Cp^*TiF_3 /MAO catalysts at various temperatures and Al/Ti ratios. $\text{Cp}^*\text{TiCl}_3 = 6.3 \times 10^{-4}$ mol/liter; $\text{Cp}^*\text{TiF}_3 = 6.3 \times 10^{-5}$ mol/liter (24).

TABLE XIX

Synthesis of Syndiotactic Polystyrene Using Metallocene/MAO Catalysts^a

Catalyst	Temperature (°C)	Activity (kgPS/molM · h)	T_m (°C)	M_w (kg/mol)	M_w/M_n
CpTiCl ₃	10	109	267	390	3.6
	30	477	263	230	2.2
(C ₅ Me ₅)TiCl ₃	30	3.5	277	186	2.3
	50	15.4	275	169	3.6
(C ₅ Me ₅)ZrCl ₃	30	0.01	249	20	2.2
(C ₅ Me ₅)TiCl ₃	50	690	275	660	2.0
CpTiF ₃	30	2400	261	380	1.8
	50	1700	257	100	2.0

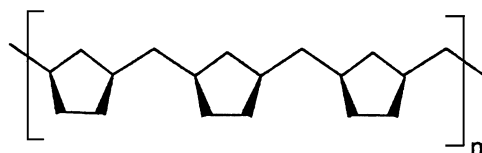
^aAdapted from Kaminsky (24).

The highest melting point (275°C) can be obtained with pentamethylcyclopentadienyltitanium compounds. The fluorinated complex gives a significantly higher molecular weight (660 kDa at 50°C), than the chlorinated complex (169 kDa), and it is more stable, being used at a polymerization temperature of 70°C. The best catalytic activities are obtained with CH₃C₅H₄TiF₃. This compound gives syndiotactic polystyrene with a melting point of 267°C.

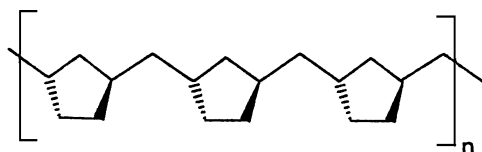
D. DIENES

Metallocenes catalyze polymerization of nonconjugated and conjugated dienes. A new type of cyclopolymerization affording ring structures interspaced by CH₂ groups of nonconjugated dienes was observed by Waymouth *et al.* (265–267), who used 1,5 dienes as monomers. A 1,2 insertion of the terminal double bond into the zirconium–carbon bond is followed by an intramolecular cyclization forming a ring (Fig. 30) (268). The microstructure and properties of the polymer depend on the *cis*:*trans* ratio of the ring bonding and on the stereochemistry of the structures between the rings. Poly(methylene-1,3-cyclopentane) obtained by copolymerization with 1,5-hexadiene includes four different structures, of which the *trans* isotactic structure is predominant, when simple bicyclopentadienyl compounds are the catalysts. More highly substituted (pentamethyl) zirconocenes yield mainly *cis*-connected polymers, which are highly crystalline and have melting points up to 190°C.

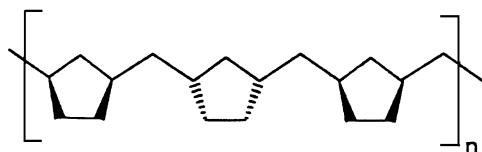
Optically active ansa metallocenes (R-En(IndH)₂ZrCl₂) polymerize the diene to give optically active *trans*-isotactic polymers, whereas only optically active oligomers and inactive polymers are obtained with olefins.



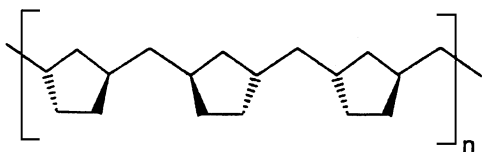
cis-isotactic



trans isotactic



cis syndiotactic



trans syndiotactic

FIG. 30. Possible microstructures of poly(methylenecyclopentane) produced by metallocene/MAO catalysts from 1,5-hexadiene (137).

Cyclopolymerizations of functionalized 1,6 dienes such as 4-trimethylsilyoxy-1,6-heptadiene are also possible, with $B(C_6F_5)_3$ as cocatalyst and bis-(pentamethylcyclopentadienyl)zirconocenes as catalysts. Hydrolysis of the product with HCl gives polymethylene-3-hydroxycyclohexane. With the same catalyst, Kesti *et al.* (269) succeeded in polymerizing 5-*N,N*-diisopropyl-amino-1-pentene and 4-*tert*-butyldimethylsiloxy-1-pentene.

Another possibility in the functionalization of polyolefins results from the copolymerization of olefins with boran monomers. Chung and Rhubrigut

(270) and Chung (271) polymerized 5-hexenyl-9-borabicyclo(3,3,1)nonane together with various α -olefins, such as ethylene, propylene, and 1-butene, using both solid catalysts ($\text{TiCl}_3/\text{AlEt}_2\text{Cl}$) and soluble metallocene catalysts such as Cp_2ZrCl_2 and $\text{En}(\text{ind})_2\text{ZrCl}_2$ with MAO as the cocatalyst.

The homogeneous catalysts were much more effective. The high-molecular-weight polymers contain 1 or 2 mol% of the organoborane units, which were subsequently converted in ionic reactions with $\text{NaOH}/\text{H}_2\text{O}_2$ reagents. The borane groups were completely converted to the corresponding hydroxyl groups. These functional groups as well as vinyl groups can be used, to make graft and block copolymers. Some interesting polymers, such as PE-PMMA, PE-polycaprolactone, PP-PMMA, and PP-polyvinyl acetate, have been synthesized and used as components in polymer blends (272).

Block copolymers of olefins and acrylates or vinyl esters can be obtained with lanthanoid compounds as catalysts. Living polyethylene-biscyclopentadienyl samarium systems can continue the polymerization of cyclooctone monomers by ROMP (273, 274).

As was found for the polymerization of styrene, $\text{CpTiCl}_3/\text{MAO}$ and similar half-sandwich titanocenes are active catalysts for the polymerization of conjugated 1,3 dienes (Table XX) (275). Butadiene, 1,3-pentadiene, 2-methyl-1,3-pentadiene, and 2,3-dimethylbutadiene yield polymers with different *cis*-1,4, *trans*-1,4, and 1,2 structures, depending on the polymerization temperature. A change in the stereospecificity as a function of polymerization temperature was observed by Ricci *et al.* (276). At 20°C, polypentadiene with mainly *cis*-1,4 structures was obtained, whereas at -20°C a crystalline, 1,2- syndiotactic polymer was produced. This temperature effect is attributed to a change in the mode of coordination of the monomer to the metallocene, which is mainly *cis*- η^4 at 20°C and *trans*- η^2 at -20°C.

TABLE XX
Polymerization of Dienes Using $\text{CpTiCl}_3/\text{MAO}$ at 20°C, 2 ml Monomer,
16 ml Toluene^a

Monomer	Time (h)	Conversion (%)	<i>cis</i>	1,2	<i>trans</i>	T_m (°)
Butadiene	0.75	42.9	80	18	2	—
(<i>E</i>)-1,3-pentadiene	1	57.1	43	57	0	—
(<i>Z</i>)-1,3-pentadiene	100	35	>99	—	—	Waxy
2,3-Dimethylbutadiene	1.2	85.3	>99	—	—	120
(<i>E</i>)-2-methylpentadiene	18	14.7	>99	—	—	136
4-Methylpentadiene	0.1	100	—	99	—	95
(<i>E,E</i>)-2,4-hexadiene	17	100	—	70	30	—

^a[Ti] = 10^{-5} mol/liter; [MAO] = 10^{-2} mol/liter. Adapted from Porri *et al.* (275).

E. METHYL METHACRYLATE

The substitution of methylaluminumoxane by other Lewis acid cocatalysts such as tetraphenylborates leads to catalysts which may tolerate functional groups in the monomer. Okuda *et al.* (277) reported the polymerization of *t*-butylacrylate or acrylonitrile. Collins *et al.* (278, 279) investigated the polymerization of methylmethacrylate by two-component catalysts consisting of a metallocenedimethyl and a methylmetallocenium ion with tetraborate as the counterion. They obtained polymethyl methacrylate and, in the case of chiral metallocene (En(IndH₄)₂ZrCl₂), highly isotactic polymer. On the basis of investigations of the kinetics, a mechanism was proposed involving an intermolecular Michael addition of a neutral enolate with a complexed monomer. On the basis of the narrow MWD (1.2–1.5), the polymerization seems to have a living character. Deng *et al.* (280) investigated the polymerization of methyl methacrylate initiated by chiral zirconocenedimethyl combined with (Ph₃C)(B(C₆F₅)₄) and found highly isotactic polymers when an aluminum or zinc alkyl was added as a third component (Table XXI). Investigations of the microstructure showed that the catalysts work by enantiomeric site control. Without the third component, no activity was observed. The authors proposed a mechanism similar to the one given by Yasuda *et al.* (274) for polymerization of methyl methacrylate by lanthanocenes (which are isoelectronic with alkylzirconium ions). The role of the third component in this mechanism is not known.

Palladium catalysts are used for the copolymerization of ethylene and methylacrylate (281). The copolymers contain both alkyl and ester side chains.

TABLE XXI
Polymerization of Methylmethacrylate Using Chiral Zirconocenedimethyl Complexes
in Combination with Trityltetrakis(pentafluorophenyl) Borate and Zincalkyls^a

Metallocene	ZnR ₂	Conversion			M _n		M _w /M _n
		(%)	mm ^b	mr	rr	(kg/mol)	
[En(Ind) ₂]ZrMe ₂	CH ₂ Me	33	96.5	2.5	1.0	393	1.43
	(CH ₂) ₃ Me	82	94.5	3.5	2.0	600	1.30
	(CH ₂) ₂ CH=CH ₂	48	98.0	1.3	0.7	599	1.30
[En(IndH ₄) ₂]ZrMe ₂	CH ₂ Me	79	94.4	3.7	1.9	320	1.32
	(CH ₂) ₃ Me	68	95.1	3.7	1.2	405	1.30
	(CH ₂) ₂ CH=CH ₂	64	95.5	3.3	1.2	339	1.25
[Me ₂ Si(Ind) ₂]ZrMe ₂	CH ₂ Me	25	86.8	5.8	7.4	114	1.71
	(CH ₂) ₃ Me	38	84.6	7.5	7.9	371	1.41
	(CH ₂) ₂ CH=CH ₂	34	91.4	5.3	2.3	345	1.34

^aAdapted from Deng *et al.* (280). ^bmm, mr, and rr triads measured by ¹³C-NMR.

Polymerization of polar monomers by metallocene catalysts is an open field of research in which investigations are just beginning.

VIII. Conclusions

Metallocene catalysts are poised to make a great step forward in synthesis and production of polyolefins, polystyrene, and copolymers. Some polymers, such as syndiotactic polypropylene, syndiotactic polystyrene, cycloolefin copolymers, optically active oligomers, and polymethylenecycloolefins, can be produced on a technological scale only by metallocene catalysts. It is possible to tailor the microstructures of polymers by changing the ligand structure of the metallocene. The influence of the ligands can increasingly be predicted and understood by molecular modeling and other calculations.

It is estimated that by the Year 2010, nearly every other new polyolefin plant will run with metallocene catalysts. Many polymer manufacturers are working to use mainly supported metallocene catalysts in their existing plants—so-called “drop-in” technology; others build plants especially designed for these new types of catalysts. New organometallic complexes of the late transition metals are opening up new possibilities for long-chain branching, the copolymerization of olefins together with polar monomers, and styrene- or diene-containing polymers. These investigations are just beginning and have great potential.

Appendix

NOTES ON STEREOCHEMISTRY, THREE-DIMENSIONAL STRUCTURES OF POLYMERS

Regiospecific: The insertion of an olefin in the same position in the growing polymer chain. In the case of propene the CH_2 group is inserted nearest to the metal catalyst (1,2 insertion); if the $\text{CH}(\text{CH}_3)$ group is the nearest bond to the metal (2,1 insertion) (see Fig. 13).

Stereospecific: Inserting propene or other α -olefins into a metal carbon bond, a chiral carbon* is formed by the tertiary carbon atom $\text{M}-\text{CH}_2-\text{CH}(\text{CH}_3)-\text{R}$. There are two enantiomers (configuration) possible (by Fischer projection: methyl group to the top or to the bottom). Different catalysts can synthesize the different configurations (see Fig. 15).

Tacticity: The regularity of monomer units within a polymer produced by stereospecific catalysts.

Atactic: Polymers with a statistically random configuration at their tertiary carbon atoms (see Fig. 15). They have an amorphous structure.

Isotactic: Polymers with the same relative configuration at their tertiary carbon atoms (see Fig. 15). They are partially crystalline.

Syndiotactic: Polymers with an alternating configuration at their tertiary carbon atoms (see Fig. 15). They are partially crystalline.

Diads (triads, pentads): View of two (three, five) combined monomer units at any position in a polymer chain and investigating (e.g., by ^{13}C NMR spectroscopy) the configuration of the tertiary carbon atoms. The term *meso* is used if they have the same configuration; the term *racemo* is used if they have the opposite configuration.

Isotacticity: The part of all meso (mmmm) pentads (diads, triads) in relation to the whole number of pentads (diads, triads). This value shows the isotacticity of a polymer.

REFERENCES

1. Böhm, L. L., Berthold, J., Enderle, H. F., and Fleissner, M., in "Metalorganic Catalysts for Synthesis and Polymerization" (W. Kaminsky, Ed.), p. 3. Springer, Heidelberg, 1999; Galli, P., Cecchin, G., Chadwick, J. C., Del Duca, D., and Vecellio, G., *ibid.*, p. 14.
2. Clayfield, T. E., *Kunststoffe-Plast. Eur.* **85**, 305 (1995).
3. Thayer, A. M., *C & EN*, p. 15 (1995, September 11).
4. Foxley, D., *Chem. Ind.*, 305 (1998, April 20).
5. Brandrup, J., Bittner, M., Michaeli, W., and Menges, G. (Eds.), *Recycling and Recovery of Plastics*, Hanser, Munich, 1996.
6. Kaminsky, W., *J. Chem. Soc. Dalton Trans.*, 1413 (1998).
7. Gibson, R. O., Fawcett, E. W., and Perrin, M. W., *Proc. R. Soc.* **150**, 223 (1935).
8. Natta, G., Pino, P., Mazzanti, G., and Lanzo, R., *Chim. Ind. (Paris)* **197**, 3907 (1996).
9. Boor, J., *Ziegler-Natta Catalysts and Polymerizations*, Academic Press, New York, 1979.
10. Keii, T., *Kinetics of Ziegler-Natta Polymerization*, Kodansha/Chapman & Hall, Tokyo/London, 1972.
11. Cossee, P., *Tetrahedron Lett.* **12**, 17 (1960).
12. Arlmann, E. J., and Cossee, P., *J. Catal.* **3**, 99 (1964).
13. Hogan, J. P., and Banks, R. L. (Phillips Petroleum), US Patent No. 2825721 (1958).
14. Clark, A., Hogan, J. P., Banks, R. L., and Lanning, W. C., *Ind. Eng. Chem.* **48**, 1152 (1956).
15. Hogan, J. P., *J. Polymer Sci. Part A-1* **8**, 2637 (1970).
16. Ziegler, K., Holzkamp, E., Breil, H., and Martin, H., *Angew. Chem.* **67**, 541 (1955).
17. Ziegler, K., *Angew. Chem.* **76**, 545 (1964).
18. Natta, G., and Corradini, P., *Atti Accad. Naz. Lincei Mem. Cl. Sci. Fis. Mat. Nat. Sez. II-5* **73**, 393 (1955).
19. Natta, G., *Angew. Chem.* **68**, 393 (1956).
20. Whiteley, K. S., Heggs, T. G., Koch, H., Mawer, R. L., and Immel, W., in "Ullmann's Encyclopedia of Industrial Chemistry," Vol. A21, p. 487. VCH, Weinheim, 1992.
21. Böhm, L. L., *Chem. Eng. Technol.* **56**, 674 (1984).
22. Locher, F. W., and Seebach, H. M. V., *Ind. Eng. Chem. Process Res. Dev.* **11**, 190 (1972).
23. Brintzinger, H. H., Fischer, D., Mülhaupt, R., Rieger, B., and Waymouth, R., *Angew. Chem. Int. Ed. Eng.* **107**, 1255 (1995).

24. Kaminsky, W., *Macromol. Chem. Phys.* **197**, 3907 (1996).
25. Gupta, V. K., Satish, S., and Bhardwaj, I. S., *Macromol. Chem. Phys. C* **34**, 439 (1994).
26. Bochmann, M., *J. Chem. Soc. Dalton Trans.* 255 (1996).
27. Hlatky, *Coordination Chem. Rev.* **181**, 243 (1999).
28. Britovsek, J. P., Gibson, V. C., and Wass, D. F., *Angew. Chem. Int. Ed.* **38**, 428 (1999).
29. Brookhart, M., Grant, B., and Volpe, A. F., *Organometallics* **11**, 3920 (1992).
30. Small, B. L., Brookhart, M., and Bennett, A. M. A., *J. Am. Chem. Soc.* **120**, 4049 (1998).
31. Small, B. L., and Brookhart, M., *Macromolecules* **32**, 2120 (1999).
32. Wilkinson, G., and Birmingham, I. M., *J. Am. Chem. Soc.* **76**, 4281 (1954).
33. Fischer, E. O., *Angew. Chem.* **22**, 620 (1952).
34. Natta, G., Pino, P., Corradini, P., Danusso, F., Mantica, E., Mazzanti, G., and Moraglio, G., *J. Am. Chem. Soc.* **77**, 1708 (1955).
35. Breslow, B. S., and Newburg, N. R., *J. Am. Chem. Soc.* **79**, 5072 (1957).
36. Dyachkovskii, F. S., Shilova, A. K., and Shilov, A. E., *J. Polym. Sci.* **16**, 2333 (1967).
37. Patat, F., and Sinn, H., *Angew. Chem.* **70**, 496 (1958).
38. Fink, G., Rottler, R., Schnell, D., and Zoller, W., *J. Appl. Polym. Sci.* **20**, 2779 (1976).
39. Natta, G., *J. Nucl. Inorg. Chem.* **49**, 1855 (1955).
40. Belov, G. P., Kuznetsov, V. I., Solovyeva, T. I., Chiikov, N. M., and Ivanchev, S. S., *Makromol. Chem.* **140**, 213 (1970).
41. Agasaryan, A. B., Belov, G. P., Davtyan, S. P., and Eritsyan, M. L., *Eur. Polym. J.* **11**, 549 (1975).
42. Patat, F., and Sinn, H., *Angew. Chem.* **70**, 496 (1958).
43. Dyachkovskii, F. S., Shilova, A. K., and Shilov, A. E., *J. Polym. Sci.* **16**, 2333 (1967).
44. Borodko, Yu. G., Kyashina, E. F., Panov, V. B., and Shilov, A. E., *Kinet. Katal.* **14**, 255 (1973).
45. Chien, J. C. U., "Coordination Polymerization." Academic Press, New York, 1975.
46. Adema, E. H., *J. Polym. Sci.* **16**, 3643 (1969).
47. Claus, K., and Bestian, H., *Justus Liebigs Ann. Chem.* **654**, 8 (1962).
48. Henrici-Olivé, G., and Olivé, S., *J. Organomet. Chem.* **16**, 339 (1969).
49. Reichert, K. H., and Schoetter, E., *Z. Phys. Chem. (N.F.)* **57**, 74 (1968).
50. Fink, G., *Polymer Prep. Am. Chem. Soc. Div. Polym. Chem.* **13**, 443 (1972).
51. Fink, G., Rottler, R., Schnell, D., and Zoller, W., *J. Appl. Polym. Sci.* **20**, 2775 (1976).
52. Long, W. P., and Breslow, D. S., *Justus Liebigs Ann. Chem.* 463 (1975).
53. Chien, J. C. W., *J. Am. Chem. Soc.* **81**, 86 (1959).
54. Breslow, D. S., and Newburg, N. R., *J. Am. Chem. Soc.* **81**, 81 (1959).
55. Reichert, K. H., and Meyer, K. R., *Makromol. Chem.* **169**, 163 (1973).
56. Sinn, H., and Kaminsky, W., *Adv. Organomet. Chem.* **18**, 99 (1980).
57. Breslow, D. S., and Newburg, N. R., *J. Am. Chem. Soc.* **79**, 5072 (1957).
58. Henrici-Olivé, G., and Olivé, S., *Angew. Chem.* **79**, 764 (1967).
59. Sinn, H., and Patat, F., *Angew. Chem.* **75**, 805 (1963).
60. Chatt, J., and Shaw, B. L., *J. Chem. Soc.*, 5075 (1962).
61. Heins, E., Hinck, H., Kaminsky, W., Oppermann, G., Raulinat, P., and Sinn, H., *Makromol. Chem.* **134**, 1 (1970).
62. Kaminsky, W., Vollmer, H.-J., Heins, E., and Sinn, H., *Makromol. Chem.* **175**, 443 (1974).
63. Kaminsky, W., and Sinn, H., *Justus Liebigs Ann. Chem.*, 424 (1975).
64. Kaminsky, W., Kopf, J., and Thirase, G., *Justus Liebigs Ann. Chem.*, 1531 (1974).
65. Andresen, A., Cordes, H. G., Herwig, J., Kaminsky, W., Merck, A., Mottweiler, R., Pein, J., Sinn, H., and Vollmer, H. J., *Angew. Chem.* **15**, 630 (1976).
66. Sinn, H., Kaminsky, W., Vollmer, H. J., and Woldt, R., *Angew. Chem.* **92**, 396 (1980).
67. Kaminsky, W., Miri, M., Sinn, H., and Woldt, R., *Makromol. Chem. Rapid Commun.* **4**, 417 (1983).

68. Kaminsky, W., and Sinn, H. (Eds.), "Transition Metals and Organometallics as Catalysts for Olefin Polymerisation." Springer, Berlin, 1988.
69. Kaminsky, W., and Steiger, R., *Polyhedron* **7**, 2375 (1988).
70. Tritto, I., Li, S., Sacchi, C., and Zannoni, G., *Macromolecules* **26**, 7112 (1993).
71. Winter, H., Schnuchel, W., and Sinn, H., *Makromol. Symp.* **97**, 119 (1995).
72. Storr, A., Jones, K., and Laubengayer, A. W., *J. Am. Chem. Soc.* **90**, 3173 (1968).
73. Harlan, C. J., Gillan, E. G., Bott, S. G., and Barron, A. R., *Organometallics* **15**, 5479 (1996).
74. Storre, J., Klemp, A., Roesky, H. W., Schmidt, H.-G., Noltemeyer, M., Fleischer, R., and Stalke, D., *J. Am. Chem. Soc.* **118**, 1380 (1996).
75. Boleslawski, M., and Serwatowski, J., *Organomet. Chem.* **255**, 259 (1983).
76. Harlan, C. J., Mason, M. R., and Barron, A. R., *Organometallics* **13**, 2957 (1994).
77. Sinn, H., *Makromol. Symp.* **97**, 27 (1995).
78. Barron, A. R., *Macromol. Symp.* **97**, 15 (1995).
79. Kiode, Y., Bott, S. G., and Barron, A. R., *Organometallics* **15q**, 2213 (1996).
80. Eisch, J. J., Pombrick, S. I., and Zheng, G. X., *Organometallics* **12**, 3856 (1993).
81. Gassmann, P. G., and Callstrom, M. R., *J. Am. Chem. Soc.* **108**, 1718 (1986).
82. Jordan, R. F., Dasher, W. E., and Echols, S. F., *J. Am. Chem. Soc.* **108**, 1718 (1986).
83. Hlatky, G. G., Upton, D. J., and Turner, H. W., US Patent No. 459921; *Chem. Abstr.* **115**, 256897v (1991).
84. Sishta, C., Hathorn, R. M., and Marks, T. J., *J. Am. Chem. Soc.* **114**, 1112 (1992).
85. Zambelli, A., Luongo, P., and Grassi, A., *Macromolecules* **22**, 2186 (1989).
86. Green, M. L. H., and Saßmannshausen, J., *Chem. Commun.*, 115 (1999).
87. Bochmann, M., Wilson, L. M., Hursthouse, M. B., and Motevalis, M., *Organometallics* **7**, 1148 (1988).
88. Jordan, R. F., Bajgur, C. S., Willet, R., and Scott, B., *J. Am. Chem. Soc.* **108**, 7410 (1986).
89. Bigpost, E. A., Zuidefeld, M. A., Meetsma, A., and Teuben, J. H., *J. Organomet. Chem.* **551**, 159 (1998).
90. Yang, X., Stern, C. L., and Marks, T. J., *J. Am. Chem. Soc.* **116**, 10015 (1994).
91. Eisch, J. J., Pombrick, S. I., and Li, S., *Macromol. Rapid Commun.* **15**, 217 (1994).
92. Tritto, J., Sacchi, M. C., and Locatelli, P., *Macromol. Symp.* **97**, 101 (1995).
93. Bochmann, M., Green, M. L. H., Powell, A. K., Saßmannshausen, J., Triller, M. U., and Wocadlo, S., *J. Chem. Soc. Dalton Trans.*, 43 (1999).
94. Kaminsky, W., Bark, A., and Steiger, R., *J. Mol. Catal.* **74**, 109 (1992).
95. Howie, M. S., Proceedings of MetCon 93, May 26, 1993 Houston TX, p. 253.
96. Tritto, I., Sacchi, M. C., and Li, S., *Macromol. Rapid Commun.* **15**, 217 (1994).
97. Kaminsky, W., *Macromol. Symp.* **97**, 79 (1995).
98. Mülhaupt, R., Duschek, T., Fischer, D., and Setz, S., *Polym. Adv. Technol.* **4**, 2235 (1993).
99. Breck, S., and Brintzinger, H. H., *Inorg. Chim. Acta* **270**, 376 (1998).
100. Bochmann, M., Lancaster, S. J., Hursthouse, M. B., and Malik, K. M. A., *Organometallics* **13**, 2235 (1994).
101. Piers, W. E., *Chem. Eur. J.* **4**, 13 (1998).
102. Yano, A., Sone, M., Yamada, S., Hasegawa, S., and Akimoto, A., *Macromol. Chem. Phys.* **200**, 917 (1999).
103. Tait, P., in "Transition Metals and Organometallics as Catalysts for Olefin Polymerisation." (W. Kaminsky and H. Sinn, Eds.), p. 309. Springer, Berlin, 1988.
104. Chien, J. C. W., and Wang, B. P., *J. Polym. Sci. Part A* **27**, 1539 (1989).
105. Kaminsky, W., Engehausen, R., Zoumis, K., Spaleck, W., and Rohrmann, J., *Makromol. Chem.* **193**, 1643 (1992).
106. Herwig, J., and Kaminsky, W., *Polymer Bull.* **9**, 464 (1983).
107. Alt, H. G., Milius, W., and Palackal, S. J., *J. Organomet. Chem.* **472**, 113 (1994).

108. Naga, N., and Mizunuma, K., *Makromol. Chem. Phys.* **199**, 113 (1998).
109. Quirk, R. P., and Kaminsky, W., in "Transition Metal Catalyzed Polymerisation," p. 225. Harwood, New York, 1983.
110. Kaminsky, W., and Lüker, H., *Makromol. Chem. Rapid Commun.* **5**, 225 (1989).
111. Blom, R., and Dahl, I. M., *Macromol. Chem. Phys.* **200**, 442 (1999).
112. Erwart, S. W., Sarsfield, M. J., Jeremic, D., Tremblay, T. L., Williams, E. F., and Baird, M. C., *Organometallics* **17**, 1502 (1998).
113. Suhm, J., Maier, R.-D., Kressler, J., and Mülhaupt, R., *Acta Polymer* **49**, 80 (1998).
114. Kaminsky, W., *Catal. Today* **20**, 257 (1994).
115. Kaminsky, W., and Schlobohm, M., *Makromol. Chem. Makromol. Symp.* **4**, 103 (1986).
116. Rossi, A., Zhang, J., and Odian, G., *Macromolecules* **29**, 2331 (1996).
117. Peeters, M., Goderis, B., Reynaers, H., and Mathot, V., *J. Polym. Sci., Part B Phys.* **37**,
118. Herfert, N., and Fink, G., *Makromol. Chem.* **193**, 1359 (1992).
119. Leclerc, M. K., and Waymouth, R. M., *Angew. Chem.* **110**, 964 (1998).
120. Arndt, M., Kaminsky, W., Schauwienold, A.-M., and Weingarten, U., *Macromol. Chem. Phys.* **199**, 1135 (1998).
121. Jordan, R. F., *Adv. Organomet. Chem.* **32**, 325 (1991).
122. Farrina, M., DiSilvestro, G., and Terragni, A., *Macromol. Chem. Phys.* **196**, 353 (1996).
123. van der Leek, Y., Angermund, K., Reffke, M., Kleinschmidt, R., Goetzki, R., and Fink, G., *Chem. Eur. J.* **4**, 585 (1997).
124. Kaminsky, W., and Drögemüller, H., in "Polymer Reaction Engineering" (K. H. Reichert and W. Geiseler, Eds.), p. 372. VCH, Berlin, 1989.
125. Cruz, V. L., Muñoz-Escalona, A., and Martinez-Salazar, J., *J. Polym. Sci. Part A* **36**, 1157 (1998).
126. Kaminsky, W., and Miri, M., *J. Polym. Sci. Chem. Ed.* **23**, 2151 (1985).
127. Chien, J. C. W., and He, D., *J. Polym. Sci. Part A* **29**, 1585 (1991).
128. Stevens, J., *Proc. MetCon Houston*, May 26–28, p. 157 (1993).
129. Shapiro, P. J., Bunel, E., Schaefer, W. P., and Bercaw, J. E., *Organometallics* **9**, 867 (1990).
130. Okuda, J., du Plooy, K. E., Massa, W., Kang, H.-C., and Rose, U., *Chem. Berlin* **129**, 5275 (1996).
131. Gomes, P. T., Green, M. L. H., and Martins, A. M., *J. Organomet. Chem.* **551**, 133 (1998).
132. Barnhart, R. W., and Bazan, G. C., *J. Am. Chem. Soc.* **120**, 1082 (1998).
133. Yan, D., Wang, W. J., and Zhu, S., *Polymer* **40**, 1737 (1999).
134. Akpalu, Y., Kielhorn, L., Hsiao, B. S., Stein, R. S., Russell, T. P., v. Egmond, J., and Muthukumar, M., *Macromolecules* **32**, 765 (1999).
135. Suhm, J., Chaier, R.-D., Kressler, J., and Mülhaupt, R., *Acta Polymer* **49**, 80 (1998).
136. Busico, V., Cipullo, R., and Talarico, G., *Macromolecules* **31**, 2387 (1998).
137. Kaminsky, W., and Arndt, M., *Adv. Polym. Sci.* **127**, 143 (1997).
138. Busico, V., Cipullo, R., and Corradini, P., *Makromol. Chem.* **14**, 97 (1993).
139. Grassi, A., Zambelli, A., Resconi, L., Albizzati, E., and Mazzocchi, R., *Macromolecules* **21**, 617 (1989).
140. Soga, K., Shiono, T., Takemura, S., and Kaminsky, W., *Makromol. Chem. Rapid Commun.* **8**, 305 (1987).
141. Cheng, H. N., and Ewen, J. A., *Makromol. Chem.* **190**, 1931 (1989).
142. Rieger, B., Mu, X., Mallin, D. T., Rausch, M. D., and Chien, J. C. W., *Macromolecules* **23**, 3559 (1990).
143. Schupfner, G., and Kaminsky, W., *J. Mol. Catal. A Chem.* **102**, 59 (1995).
144. Busico, V., and Cipullo, R., *J. Am. Chem. Soc.* **117**, 1652 (1994).
145. Sheldon, R. A., Fueno, T., Tsuntsugu, T., and Kurukawa, J., *J. Polym. Sci. Part B* **3**, 23 (1965).

146. Ewen, J. A., *J. Am. Chem. Soc.* **106**, 6355 (1984).
147. Resconi, L., Piemontesi, F., Camurati, I., Sudmeijer, O., Nifant'ev, I. E., Ivehenko, P. V., and Kuz'ming, L. G., *J. Am. Chem. Soc.* **120**, 2308 (1998).
148. Resconi, L., Abis, L., and Franciscano, G., *Macromolecules* **25**, 6814 (1992).
149. Kaminsky, W., and Arndt, M., in "Catalysis Design for Tailor-Made Polyolefins" (K. Soga and M. Terano, Eds.), p. 179. Kodansha, Tokyo, 1994.
150. Kaminsky, W., Külper, K., Brintzinger, H. H., and Wild, F. R. W. P., *Angew. Chem.* **97**, 507 (1985).
151. Kaminsky, W., Külper, K., and Niedoba, S., *Makromol. Chem. Makromol. Symp.* **3**, 377 (1986).
152. Farina, M., DiSilvestro, G., and Terragni, A., *Makromol. Chem. Phys.* **196**, 353 (1995).
153. Xu, J., and Feng, L., *Eur. Polym. J.* **35**, 1289 (1999).
154. Spaleck, W., Aulbach, M., Baxhmann, B., Küber, F., and Winter, A., *Makromol. Symp.* **89**, 237 (1995).
155. Spaleck, W., Antberg, M., Aulbach, M., Bachmann, B., Dolle, V., Haftka, S., Küber, F., Rohrmann, J., and Winter, A., in "Ziegler Catalysts." (G. Fink, R. Mülhaupt, and H. H. Brintzinger, Eds.), p. 83. Springer-Verlag, Berlin, 1994.
156. Spaleck, W., Küber, F., Winter, A., Rohrmann, J., Bachmann, B., Kiprf, P., Behn, J., and Herrmann, W. A., *Organometallics* **13**, 954 (1994).
157. Jüngling, S., Mülhaupt, R., Stehling, U., Brintzinger, H. H., Fischer, D., and Langhauser, F., *Macromol. Symp.* **97**, 205 (1995).
158. Resconi, L., Fait, A., Pietmontesi, F., Colonesi, M., Rychlicki, H., and Ziegler, R., *Macromolecules* **28**, 6667 (1995).
159. Spaleck, W., Antberg, A., Rohrmann, J., Winter, A., Bachmann, B., Kiprof, P., Behn, J., and Herrmann, W. A., *Angew. Chem.* **104**, 1373 (1992).
160. Stehling, U., Diebold, J., Kirsten, R., Röhl, W., Brintzinger, H. H., Jüngling, S., Mülhaupt, and Langhauser, F., *Organometallics*, **13**, 964 (1994).
161. Mise, T., Miya, S., and Yamazaki, H., *Chem. Lett.*, 1853 (1989).
162. Pino, P., Cioni, P., Wei, J., Rotztinger, B., and Arizzi, S., in "Transition Metal Cataly. Polymerisations." (R. P. Quirk, Eds.), p. 1. Cambridge Univ. Press, Cambridge, UK, 1988.
163. Pino, P., Cioni, P., and Wei, J., *J. Am. Chem. Soc.* **109**, 6189 (1987).
164. Waymouth, R., and Pino, P., *J. Am. Chem. Soc.* **112**, 4911 (1990).
165. Pino, P., and Galimberti, M., *J. Organomet. Chem.* **370**, 1 (1989).
166. Corradini, P., and Guerra, G., in "Transition Metal Catalyzed Polymerization" (R. P. Quirk, Ed.), p. 553. Cambridge Univ. Press, Cambridge, UK, 1988.
167. Corradini, P., Busico, V., and Guerra, G., in "Transition Metals and Organometallics as Catalysts for Olefin Polymerisation." (W. Kaminsky and H. Sinn, Eds.), p. 337. Springer-Verlag, Berlin, 1987.
168. Corradini, P., Guerra, G., Vacatello, M., and Villani, V., *Gazz. Chim. Ital.* **118**, 173 (1988).
169. Venditto, V., Guerra, G., Corradini, P., and Fusco, R., *Polymer* **31**, 530 (1991).
170. Corradini, P., and Guerra, G., *Progr. Polym. Sci.* **16**, 239 (1991).
171. Corradini, P., *Makromol. Chem. Makromol. Symp.* **66**, 11 (1993).
172. Ewen, J. A., Jones, R. L., Razavi, A., and Ferrara, J., *J. Am. Chem. Soc.* **110**, 6255 (1988).
173. Ewen, J. A., Elder, M. J., Jones, R. L., Curtis, S., and Cheng, H. N., in "Catalytic Olefin Polymerization." (T. Keii and K. Soga, Eds.), p. 439. Kodansha, Tokyo, 1991.
174. Ewen, J. A., Elder, M. J., Jones, R. L., Haspeslagh, L., Atwood, J. L., Bott, S. G., and Robinson, K., *Polym. Prepr. Am. Chem. Soc.* **32**, 469 (1991).
175. Razavi, A., Nafpliotis, L., Vereecke, D., DenDauw, K., Atwood, J. L., and Thewald, U., *Macromol. Symp.* **89**, 345 (1995).
176. Farina, M., DiSilvestro, G., and Sozzani, P., *Macromolecules* **26**, 946 (1993).

177. Herfert, N., and Fink, G., *Makromol. Chem. macromol. Symp.* **66**, 157 (1993).
178. Ewen, J. A., *Macromol. Symp.* **89**, 181 (1995).
179. Spaleck, W., Aulbach, M., Bachmann, B., Küber, F., and Winter, A., *Macromol. Symp.* **89**, 237 (1995).
180. Ewen, J. A., and Elder, M. J., in "Ziegler Catalysts," (G. Fink, R. Mülhaupt, and H. H. Brintzinger, Eds.), p. 99. Springer-Verlag, Berlin, 1995.
181. Mallin, D. T., Rausch, M. D., Lin, G. Y., Dong, S., and Chien, J. C. W., *J. Am. Chem. Soc.* **112**, 2030 (1990).
182. Chien, J. C. W., Llinas, G. H., Rausch, M. D., Lin, G. Y., and Winter, H. H., *J. Am. Chem. Soc.* **113**, 8569 (1991).
183. Llinas, G. H., Day, R. O., Rausch, M. D., and Chien, J. C. W., *Organometallics* **12**, 1283 (1993).
184. Llin, G. Y., Mallin, D. T., Chien, J. C. W., and Winter, H. H., *Macromolecules* **24**, 850 (1991).
185. Gauthier, W. J., Corrigan, J. F., Taylor, N. J., and Collins, S., *Macromolecules* **28**, 3771 (1995).
186. Erker, G., *Pure Appl. Chem.* **64**, 393 (1992).
187. Erker, G., Aulbach, M., Wingbergmühle, D., Krüger, K., and Werner, S., *Chem. Berlin* **126**, 755 (1993).
188. Erker, G., Aulbach, M., Knickmeier, M., Wingbergmühle, D., Krüger, K., Nolte, M., and Werner, S., *J. Am. Chem. Soc.* **115**, 4590 (1993).
189. Coates, G. W., and Waymouth, R. M., *Science* **267**, 217 (1995).
190. Bravakis, A. M., Bailey, L. E., Pigeon, M., and Collins, S., *Macromolecules* **31**, 1000 (1998).
191. Hu, Y., Carlson, E. D., Fuller, G. G., and Waymouth, R. M., *Macromolecules* **32**, 3334 (1999).
192. Kaminsky, W., Rabe, O., Schauwienold, A. M., Schupfner, G. U., Hanss, J., and Kopf, J., *J. Organomet. Chem.* **497**, 181 (1995).
193. Soga, K., Shino, T., Takemura, S., and Kaminsky, W., *Makromol. Chem. Rapid Commun.* **8**, 305 (1987).
194. Leclerc, M., and Brintzinger, H. H., *J. Am. Chem. Soc.* **117**, 1651 (1995).
195. Schupfner, G., and Kaminsky, W., *J. Catal.* **102**, 559 (1995).
196. Burge, P., Hortmann, K., and Brintzinger, H. H., *Makromol. Chem. Macromol. Symp.* **66**, 127 (1993).
197. Guerra, G., Cavallo, L., Venditto, V., Vacatello, M., and Corradini, P., *Makromol. Chem. Macromol. Symp.* **69**, 237 (1993).
198. Stehling, U., Diebold, J., Kirsten, R., Röhl, W., Brintzinger, H. H., Jüngling, S., Mühlhaupt, R., and Langhauser, F., *Organometallics* **13**, 964 (1994).
199. Hollis, P. K., Rheingold, L., Robinson, N. P., Whelan, J., and Bosnich, B., *Organometallics* **11**, 1869 (1992).
200. Kaminsky, W., Freidanck, F., and Schauwienold, A. M., *J. Mol. Catal. A Chem.* **112**, 37 (1996).
201. Kaminsky, W., and Arndt, M., in "Catalyst Design for Tailor-Made Polyolefins" (K. Soga, Ed.), p. 179. Kodansha, Tokyo, 1994.
202. Schäfer, A., Karl, E., Zsolnai, L., Huttner, G., and Brintzinger, H. H., *J. Organomet. Chem.* **328**, 87 (1987).
203. Kaminsky, W., Ahlers, A., and Möller-Lindenhof, N., *Angew. Chem.* **101**, 1304 (1989); *Int. Ed. Eng.* **28**, 1216 (1989).
204. Kaminsky, W., Ahlers, A., Rabe, O., and König, W., in "Organic Synthesis via Organometallics," (D. Enders, H.-J. Gais, and W. Keim, Eds.), p. 151. Vieweg, Braunschweig, 1993.

205. Pino, P., Cioni, P., and Wei, J., *J. Am. Chem. Soc.* **109**, 6189 (1987).
206. König, W. A., Lutz, S., and Wenz, G., *Angew. Chem.* **100**, 989 (1988).
207. Busico, V., Caporaso, L., Cipullo, R., and Landriani, L., *J. Am. Chem. Soc.* **118**, 2105 (1996).
208. Kaminaka, M., and Soga, K., *Makromol. Chem. Rapid Commun.* **12**, 367 (1991).
209. Soga, K., and Kaminaka, M., *Makromol. Chem. Rapid Commun.* **13**, 221 (1992).
210. Chien, J. C. W., and Hen, D., *J. Polym. Sci. Part A Polym. Chem.* **29**, 1603 (1991).
211. Lee, B. Y., and Oh, J. S., *J. Organomet. Chem.* **552**, 313 (1998).
212. Sacchi, M. C., Zucchi, D., Tritto, P., and Locatelli, P., *Macromol. Chem. Rapid Commun.* **16**, 581 (1995).
213. Hlatky, G. G., and Upton, D. J., *Macromolecules* **29**, 8019 (1996).
214. Kaminsky, W., and Renner, F., *Macromol. Chem. Rapid Commun.* **14**, 239 (1993).
215. Collins, S., Kelly, W. M., and Holden, D. A., *Macromolecules* **25**, 1780 (1992).
216. Kitagawa, T., Uozumi, T., and Soga, K., *Polymer* **3**, 615 (1997).
217. Sensarma, S., and Sivaram, S., *Macromol. Chem. Phys.* **200**, 323 (1999).
218. Goretzki, R., Fink, G., Tesche, B., Steinmetz, B., Rieger, R., and Uzick, W., *J. Polym. Sci. Part A Polym. Chem.* **37**, 677 (1999).
219. Przybyla, C., and Fink, G., *Acta Polym.* **50**, 77 (1999).
220. Abbenhuis, H. C. L., *Angew. Chem. Ind. Ed.* **38**, 1058 (1999).
221. Kaminsky, W., and Winkelbach, H., *Topics Catal.* **7**, 61 (1999).
222. Booth, B. L., Ofunne, G. C., Stacey, C., and Tait, P. J., *J. Organomet. Chem.* **315**, 143 (1986).
223. Calderon, N., *J. Macromol. Sci. Rev. Macromol. Sci.* **C7**, 105 (1972).
224. Ivin, K. J., "Olefin Metathesis." Academic Press, New York, 1983.
225. Novak, B. M., Risse, W., and Grubbs, R. H., *Adv. Polym. Sci.* **102**, 47 (1992).
226. Schultz, R. G., *Polym. Lett.* **4**, 451 (1966).
227. Tanielian, C., Kienneman, A., and Osparuch, T., *Can. J. Chem.* **57**, 2022 (1979).
228. Sen, A., and Lai, T. W., *Organometallics* **359**, 415 (1982).
229. Sen, A., Lai, T. W., and Thomas, R. R., *J. Organomet. Chem.* **359**, 569 (1988).
230. Mehler, C., and Risse, W., *Makromol. Chem. Rapid Commun.* **12**, 255 (1991).
231. Breuning, S., and Risse, W., *Makromol. Chem.* **193**, 2915 (1992).
232. Arndt, M., Engehausen, R., Kaminsky, W., and Zoumis, K., *J. Mol. Catal. A Chem.* **101**, 171 (1995).
233. Arndt, M., and Kaminsky, W., *Macromol. Symp.* **97**, 225 (1995).
234. Collins, S., and Kelly, W. M., *Macromolecules* **25**, 233 (1992).
235. Kelly, W. M., Taylor, N. J., and Collins, S., *Macromolecules* **27**, 447 (1995).
236. Arndt, M., and Kaminsky, W., *Macromol. Symp.* **95**, 167 (1995).
237. Arndt, M., Grimm, B., Kaminsky, W., and Zachmann, H. G., *Europhys. Conf. Abstr.* **19F**, 42 (1995).
238. Kaminsky, W., and Spiehl, R., *Makromol. Chem.* **190**, 515 (1989).
239. Arndt, M., PhD thesis, University of Hamburg. Verlag Shaker Aachen.
240. Jershow, A., Ernst, E., Herrmann, W., and Müller, N., *Macromolecules* **28**, 7095 (1995).
241. Kaminsky, W., Bark, A., and Arndt, M., *Makromol. Chem. Macromol. Symp.* **47**, 83 (1991).
242. Kaminsky, W., and Noll, A., *Polym. Bull.* **31**, 175 (1993).
243. Arndt, M., Kaminsky, W., and Schupfner, G. U., "Proceedings of the International Congress on Metallocene Polymers Metallocene '95," p. 403. Schotland Business Research, Brussels, 1995.
244. Kaminsky, W., and Noll, A., in "Ziegler Catalysts" (G. Fink, R. Mülhaupt, and H. H. Brintzinger, Eds.), p. 14. Springer-Verlag, Berlin, 1995.
245. Benedikt, G. M., Goodall, B. L., Marchant, N. S., and Rhodes, L. F., *New J. Chem.* **18**, 105 (1994).

246. Benedikt, G. M., Goodall, B. L., Marchant, N. S., and Rhodes, L. F., "Proceedings of the Worldwide Metallocene Conference MetCon '94." Catalyst Consultant, Houston, 1994.
247. Kaminsky, W., Engehausen, R., and Kopf, J., *Angew. Chem.* **107**, 2469 (1995).
248. Rische, T., Waddon, A. J., Dickinson, L. C., and Macknight, W. J., *Macromolecules* **31**, 1871 (1998).
249. Cherdron, H., Brekner, M. J., and Osan, F., *Angew. Makromol. Chem.* **223**, 121 (1994).
250. Land, H. T., "Proceedings of the International Congress on Metallocene Polymers Metallocenes '95," p. 217. Scotland Business Research, Brussels, 1995.
251. JP 0392 345, Idemitsu Kosan Co. Ltd., Inventor; Nakano, A., *Chem. Abstr.* **115**, 51539 (1991).
252. Ishihara, N., Kuromoto, M., and Uol, M., *Macromolecules* **21**, 3356 (1988).
253. Zambelli, A., Olivia, L., and Pellecchia, C., *Macromolecules* **22**, 2129 (1989).
254. Chien, J. C. W., and Dong, S., *Polym. Bull.* **29**, 515 (1992).
255. Kucht, H., Kucht, A., Chien, J. C. W., and Rausch, M. D., *Appl. Organomet. Chem.* **8**, 393 (1994).
256. Pellecchia, C., Pappalardo, D., Oliva, L., and Zambelli, A., *J. Am. Chem. Soc.* **117**, 6593 (1995).
257. Wang, Q., Quyoum, R., Gillis, D. J., Tudoret, M.-J., Jeremie, D., Hunter, B. K., and Baird, M. C., *Organometallics* **15**, 693 (1996).
258. Kaminsky, W., and Lenk, S., *Macromol. Chem. Phys.* **195**, 2093 (1994).
259. Okuda, J., and Masoud, E., *Macromol. Chem. Phys.* **199**, 543 (1998).
260. Po, R., Cardì, N., and Abis, L., *Polymer* **39**, 959 (1998).
261. Xu, J., Zhao, J., Fan, Z., and Feng, L., *Eur. Polym. J.* **35**, 127 (1999).
262. Liu, J., Ma, H., Juang, J., Qian, Y., and Chan, A. S. C., *Eur. Polym. J.* **35**, 543 (1999).
263. Herzog, A., Liu, F. Q., Roesky, H. W., Demsar, A., Keller, K., Noltemeyer, M., and Pauer, F., *Organometallics* **13**, 1251 (1994).
264. Kaminsky, W., Lenk, S., Scholz, V., Roesky, H. W., and Herzog, A., *Macromolecules* **30**, 7647 (1997).
265. Resconi, L., and Waymouth, R. M., *J. Am. Chem. Soc.* **112**, 4953 (1990).
266. Resconi, L., Coates, G. W., Mogstad, A., and Waymouth, R. M., *J. Macromol. Sci. Chem. Ed.* **A28**, 1255 (1991).
267. Kesti, M. R., and Waymouth, R. M., *J. Am. Chem. Soc.* **114**, 3565 (1991).
268. Coates, G. W., and Waymouth, R. M., *J. Am. Chem. Soc.* **115**, 91 (1993).
269. Kesti, M. R., Coates, G. W., and Waymouth, R. M., *J. Am. Chem. Soc.* **114**, 9679 (1992).
270. Chung, T. C., and Rhubright, D., *Macromolecules* **26**, 3019 (1993).
271. Chung, T. C., *Macromol. Symp.* **89**, 151 (1995).
272. Rösch, J., and Mülhaupt, R., *Macromol. Chem. Rapid Commun.* **14**, 503 (1993).
273. Yasuda, H., Yamamoto, H., Yokota, K., Miyaka, S., and Nakamura, A., *J. Am. Chem. Soc.* **114**, 4908 (1992).
274. Yasuda, H., Yamamoto, H., Yamashita, K., Yokato, K., Nakamura, A., and Miyada, S., *Macromolecules* **26**, 7134 (1993).
275. Porri, L., Giarrusso, A., and Ricci, G., *Prog. Polym. Sci.* **16**, 405 (1991).
276. Ricci, G., Porri, L., and Giarrusso, A., *Macromol. Symp.* **89**, 383 (1995).
277. Hultzsch, K. C., Spaniol, T. P., and Okuda, J., *Angew. Chem.* **111**, 163 (1999).
278. Collins, S., and Ward, D. G., *J. Am. Chem. Soc.* **114**, 5460 (1992).
279. Collins, S., Ward, D. G., and Suddaby, K. H., *Macromolecules* **27**, 7222 (1994).
280. Deng, H., Shiono, T., and Soga, K., *Macromolecules* **28**, 3067 (1995).
281. Heinemann, J., Mülhaupt, R., Brinkmann, P., and Luinstra, G., *Macromol. Chem. Phys.* **200**, 384 (1999).

Kinetics of Heterogeneous Catalytic Reactions: Analysis of Reaction Schemes

R. D. CORTRIGHT AND J. A. DUMESIC

*Department of Chemical Engineering
University of Wisconsin
Madison, Wisconsin 53706*

A wide variety of techniques are usually employed in investigations of heterogeneous catalysis. These investigations typically involve one or more of the following experimental approaches: (i) synthesis and testing of catalytic materials, (ii) characterization of bulk and surface properties, (iii) evaluation of surface adsorptive properties and chemical reactivity, and (iv) assessment of catalyst performance. The recent advances in

Abbreviations: a_i , thermodynamic activity of component i ; A_i , preexponential factor for rate constant i ; A_I , chemical affinity for the step I ; C° , concentration at standard state conditions; C_{sites} , surface concentration of sites; CSTR, continuous-flow stirred tank reactor; E_i , activation energy; F , molecular flow rate of feed to reactor; $F_{s,i}$, molecular site velocity for species i in a flow reactor; F_i'' , number of gas-phase molecule colliding with a surface per unit area per unit time; F_{loc} , fraction of gaseous local entropy; ΔG , change of Gibbs free energy; h , Planck's constant; ΔH , change of enthalpy; I_1, I_2, I_3 , moments of inertia about the principal axes; k_B , Boltzmann constant; $k_{i,\text{for}}$, k_i , forward rate constant for reaction i ; $k_{i,\text{rev}}$, k_{-i} , reverse rate constant for reaction i ; K , $K_{i,\text{eq}}$, equilibrium constant for reaction i ; m , mass of a molecule; N_C , number of carbon atoms in surface species; N_i , number of molecules of species i in the reactor; N_g , number of gas-phase molecules; N_{sat} , number of adsorbed molecules at saturation; N_{site} , number of catalytic sites; $N_{s,i}$, number of gaseous molecules for species i per site in a batch reactor; P_i , partial pressure of species i ; PFR, plug flow reactor; P_{tot} , total pressure; r_i , rate of the chemical reaction i or elementary step i ; r_i''' , rate per unit reactor volume; \bar{r}_i , forward rate of elementary step i ; R_i , rate of production of species i ; R , gas constant; SA, surface area of active sites; ΔS , change of entropy; $S_{\text{trans,3D}}^\circ$, translational entropy of species with three degrees of translation freedom; $S_{\text{trans,2D}}^\circ$, translational entropy of species with two degrees of translation freedom; S_{rot} , rotational entropy; S_{vib} , vibrational entropy; S_R , number of catalytic sites in the reactor; $X_{RC,i}$, degree of rate control for step i ; V , volume; V_R , volume of reactor; Z_i , reversibility of step i ; α_H , linear variation of the adsorption heat with carbon number; ϕ_i , dimensionless sensitivity of the overall rate with respects to k_i ; $\Phi_{i,\text{tot}}$, total sensitivity with respect to k_i ; γ , activity coefficient; ν_i , vibrational frequency; ν^\ddagger , frequency factor; ν_{ij} , stoichiometric coefficient for the j reactant and i elementary step; σ_r , rotational symmetry number; σ , sticking coefficient, symmetry number of a molecule; σ_i , stoichiometric coefficient of the linear combination of step i that leads to an overall stoichiometric reaction; τ , space time; Ω_i , turnover frequency of reaction i ; Ω , number of distinguishable configurations of a compound; $^\circ$, standard state, degrees, inlet condition; \ddagger , activated complex.

quantum chemical techniques, combined with improved computer performance, make it possible to conduct quantum chemical calculations to represent more realistic models of active sites and more complex reaction schemes. Since these experimental and theoretical investigations are conducted under different conditions and on a variety of related materials, it is useful to conduct analyses of appropriate reaction schemes to consolidate the results. An important consequence of conducting reaction kinetics analysis in conjunction with results from quantum chemical calculations and experimental studies is that quantitative knowledge about the catalytic process is built at the molecular level into the kinetic model. This process of extracting fundamental knowledge provides a molecular-level basis for comparisons between catalyst systems and provides unifying principles for the design of new catalyst systems. This review provides an introduction to methods for analyses of reaction schemes that describes the results from both experimental and theoretical investigations. Several case studies are provided to illustrate different analysis methods. © 2001 Academic Press.

I. Introduction

A major aspect of research and development in industrial catalysis is the identification of catalytic materials and reaction conditions that lead to effective catalytic processes. The need for efficient approaches to facilitate the discovery of new solid catalysts is particularly timely in view of the growing need to expand the applications of catalytic technologies beyond the current chemical and petrochemical industries. For example, new catalysts are needed for environmental applications such as treatment of noxious emissions or for pollution prevention. Improved catalysts are needed for new fuel cell applications. The production of high-value specialty chemicals requires the development of new catalytic materials. Furthermore, new catalysts may be combined with biochemical processes for the production of chemicals from renewable resources. The catalysts required for these new applications may be different from those in current use in the chemical and petrochemical industries.

The discovery and optimization of catalytic processes can be approached by using chemical intuition and experience with related catalytic processes. Catalytic materials are selected and/or synthesized, followed by the testing in catalytic reactors and characterization by various physical, chemical, and spectroscopic techniques. At some point in the research and development process, it also becomes useful to supplement these experimental studies with quantitative analyses of the reaction kinetics to compare and/or extrapolate the performance of different catalytic materials at various reaction conditions.

In a previous publication (1), the term *microkinetics* was defined to denote reaction kinetics analyses that attempt to incorporate into the kinetic model

the basic surface chemistry involved in the catalytic reaction. Accordingly, the kinetic model is based on a description of the catalytic process in terms of information and/or assumptions about the active sites and the nature of the elementary steps that comprise the reaction scheme. Such a kinetic model can be a convenient tool for the consolidation of fundamental information about a catalytic process and for extrapolation of this information to other reaction conditions and to other catalytic reactions involving related reactants, reaction intermediates, and/or products. The kinetic model is then used to describe the observed experimental results (e.g., reaction kinetics data, spectroscopic observations, microcalorimetric measurements, and TPD spectra) by conducting analyses of the appropriate reaction schemes.

In contrast to so-called microkinetic analyses, an important aspect of chemical reaction engineering involves the use of semiempirical rate expressions (e.g., power law rate expressions) to conduct detailed analyses of reactor performance, incorporating such effects as heat and mass transport, catalyst deactivation, and reactor stability. Accordingly, microkinetic analyses should not be considered to be more fundamental than analyses based on semiempirical rate expressions. Instead, microkinetic analyses are simply conducted for different purposes than analyses based on semiempirical rate expressions. In this review, we focus on reaction kinetics analyses based on molecular-level descriptions of catalytic processes.

Catalytic processes on surfaces take place through sequences of elementary reactions (steps) involving adsorbed reactants, products, and reaction intermediates associated with active sites on the catalyst surface. Although in the most general case it is desirable to determine preexponential factors and activation energies for each of these elementary steps, there is usually not sufficient information to extract the values of all kinetic parameters. Accordingly, there is an information deficit that requires a compromise between the desire to include chemical detail in the reaction scheme and the realization that the observed reaction kinetics is controlled by a limited number of kinetic parameters. In this respect, several issues are important. For example, how many kinetic parameters are required in the most general case to calculate the overall rate from a reaction scheme? What species are most abundant on the catalyst surface under reaction conditions? For the reaction conditions and kinetic parameters of interest, does the reaction scheme include a rate-determining step? In general, only a few of the kinetic parameters are significant; however, it may be difficult at the outset to anticipate which kinetic parameters, in fact, control the overall rate of the catalytic process. Therefore, initial estimates must be made for more kinetic parameters than will ultimately be needed in the final description of the catalytic process.

In the preceding several years, significant advances have been made in the applications of quantum chemical techniques to identify the geometries and energetics of chemical species interacting with catalytic sites consisting of clusters or periodic arrangements of atoms (2, 3). These recent advances in quantum chemical techniques, combined with improved computer performance, make it possible to conduct such calculations to represent more realistic models of active sites and more complex reaction schemes. Furthermore, considerable information about the properties of chemical species on catalyst surfaces is available from experimental studies (4, 5). Therefore, improved results from quantum chemical calculations, combined with an increasing amount of experimental information, make it possible to carry out reaction kinetics analyses with more realistic reaction schemes and with better initial estimates for kinetic parameters. Various researchers (2, 6–18) have applied quantum chemical techniques to mechanistic investigations of heterogeneous catalysis. Accordingly, results from reaction kinetics analyses based on molecular-level descriptions of catalytic processes are becoming more reliable, and it is believed that the applications of these analyses in catalysis research will become more widespread.

Considerable attention is currently being given to the applications of combinatorial chemistry and high-throughput screening methodologies toward the discovery of solid catalysts (19–22). A significant strength of these techniques is that they can be applied without comprehensive knowledge of the details of the catalytic process. Accordingly, the discovery process is not confined by preconceived limitations imposed by the researcher. However, this discovery process does not necessarily take full advantage of intuition gained from the literature and experience accumulated during research.

In combination with data-based techniques using combinatorial chemistry and high-throughput screening, it seems appropriate to employ knowledge-based techniques in heterogeneous catalysis research to guide the discovery process. As the range of reaction conditions becomes broader and the types of catalytic materials become more diverse, it becomes more important to identify fundamental similarities between catalytic systems to be able to extrapolate from the performance of existing systems to predict the behavior of new systems. Specifically, one of the difficulties typically encountered when trying to use experimental information about a particular catalyst system to assist in the development of another catalyst system is that a common basis for comparison between the systems cannot be identified. For example, the active sites may have different structures, the reaction schemes may involve different reaction intermediates, and the surface coverage regimes may be different. Without a means to account for the key

differences between the catalyst systems, it is not possible to take advantage of the similarities that these systems may possess. However, by extracting information about catalyst systems at the molecular level, it may be possible to identify common properties that control the nature and strength of the chemical bonding in these catalyst systems. Indeed, since combinatorial chemistry and high-throughput screening techniques are capable of rapid generation of large amounts of data, sufficient time may be available to operate these approaches in both discovery modes and elucidation modes. In the latter modes of operation, experimental results are generated with the goal of providing fundamental knowledge that may be used to guide further research and/or development. This more facile collection of reaction kinetics data over a wide range of catalysts and reaction conditions opens new opportunities for conducting extensive kinetic analyses based on molecular-level descriptions of catalytic processes.

Here, we review the basic principles used to conduct reaction kinetics analyses of reaction schemes consisting of elementary steps. Several case studies are presented to illustrate how such analyses can be used to consolidate results from experimental and theoretical investigations, with the aim of interpreting the kinetics of overall reactions in terms of contributions from individual elementary steps.

II. Formulation of the Kinetic Model

A. CHOICE OF REACTION SCHEME

Catalytic processes on solid surfaces take place through combinations of elementary reactions involving adsorbed reactants, products, and reaction intermediates associated with active sites on the catalyst surface. Detailed descriptions at a molecular level are not generally available for catalytic reactions occurring on solid surfaces. Accordingly, the strategy used in reaction kinetics analyses is to formulate a reaction scheme that captures the essential chemistry taking place on the catalyst surface. This reaction scheme is based on a series of conjectures that must be reconciled with experimental and theoretical results, and this scheme is generally revised as necessary when new information becomes available.

It is important that different reaction schemes can lead to the same apparent rate expression. Thus, even if reaction kinetics data were collected without experimental errors, the reaction scheme still would not be determined by fitting the data to various rate expressions. In other words, the rate expression can be determined from the reaction scheme, but the

reaction scheme cannot be determined from the rate expression. Stoltze (23) highlighted this aspect of reaction kinetics analyses. This unidirectional condition is the reason why research in chemical kinetics does not focus entirely on measurements of reaction rates but also involves the collection of spectroscopic, theoretical, and other results to give information about adsorbed intermediates and the nature of the important steps in the reaction scheme.

A feasible reaction scheme includes all the reactants and products, and it generally includes a variety of reaction intermediates. The validity of an elementary step in a reaction sequence is often assessed by noting the number of chemical bonds broken and formed. Elementary steps that involve the transformation of more than a few chemical bonds are usually thought to be unrealistic. However, the desire to formulate reaction schemes in terms of elementary processes taking place on the catalyst surface must be balanced with the need to express the reaction scheme in terms of kinetic parameters that are accessible to experimental measurement or theoretical prediction. This compromise between molecular detail and kinetic parameter estimation plays an important role in the formulation of reaction schemes for analyses. The description of a catalytic cycle requires that the reaction scheme contain a closed sequence of elementary steps. Accordingly, the overall stoichiometric reaction from reactants to products is described by the summation of the individual stoichiometric steps multiplied by the stoichiometric number of that step, σ_i .

The strategy in most kinetic studies is to probe the form of the reaction scheme by attempting to analyze the available reaction kinetics data by using values of kinetic rate constants that are constrained within physically realistic limits. As shown later, it is possible to make reasonable initial estimates of preexponential factors by using collision theory and/or by making assumptions about the mobilities of the surface species involved in the reaction scheme. Information about activation energies and heats of reaction for the various steps is generally more difficult to obtain. However, recent advances in quantum chemical calculations make it possible to estimate the energetic properties of molecular species and transition states for clusters or periodic arrangements of atoms, and these theoretical calculations have sufficient accuracy that they can be used to complement the available experimental information for initial estimation of kinetic parameters. Importantly, accurate values are not needed for all the kinetic parameters in the reaction scheme because many of these parameters are eventually shown to be kinetically insignificant. On the other hand, we cannot know at early stages of analysis which parameters are kinetically important. Thus, studies must begin with the best possible estimates of all kinetic parameters.

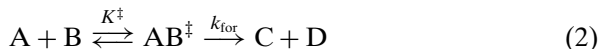
B. RATE CONSTANT ESTIMATION

1. *Transition State Theory*

Transition-state theory allows details of molecular structure to be incorporated approximately into rate constant estimation. The critical assumption of transition-state theory is that quasi-equilibrium is established between the reactants and an activated complex, which is a reactive chemical species that is in transition between reactants and products. The application of transition-state theory to the estimation of rate constants can be illustrated by the bimolecular gas-phase reaction



The potential energy diagram for this reaction is a multidimensional surface representing the potential energy of the system as a function of the atomic coordinates of the reactants and products. A reaction coordinate can be defined as a variable that describes the progress of the reaction as the atomic coordinates of species A and B are changed smoothly to produce species C and D. The path of the reaction along the reaction coordinate passes through a saddle point corresponding to the lowest energy barrier that must be surmounted during the conversion of reactants to products. The molecular configuration of the reactive species at this saddle point is defined as the transition state, and chemical species corresponding to this molecular configuration is the activated complex, AB^\ddagger . Accordingly, we write the forward reaction as



where k_{for} is the rate constant for the forward reaction. The quasi-equilibrium constant, K^\ddagger , for production of the activated complex AB^\ddagger from A and B is defined as

$$K^\ddagger = \frac{a_{AB^\ddagger}}{a_A a_B} \quad (3)$$

where a_i are the thermodynamic activities of species i . The macroscopic formulation of transition-state theory is obtained by writing K^\ddagger in terms of the standard free energy change, $\Delta G^{\circ\ddagger}$, or in terms of the changes of standard entropy, $\Delta S^{\circ\ddagger}$, and enthalpy, $\Delta H^{\circ\ddagger}$, for the formation of activated complex AB^\ddagger from A and B:

$$K^\ddagger = \exp\left(-\frac{\Delta G^{\circ\ddagger}}{k_B T}\right) = \exp\left(\frac{\Delta S^{\circ\ddagger}}{k_B}\right) \exp\left(-\frac{\Delta H^{\circ\ddagger}}{k_B T}\right) \quad (4)$$

The rate of the chemical reaction per unit volume, r_{AB} , is equal to the concentration of activated complex multiplied by a frequency factor equal to $k_B T/h$, where h is Planck's constant. The thermodynamic activity of the activated complex is equal to

$$a_{AB^\ddagger} = \gamma^\ddagger \frac{C_{AB^\ddagger}}{C^\circ} \quad (5)$$

where C_{AB^\ddagger} is the concentration of the activated complex, C° is its concentration at the standard state conditions, and γ^\ddagger is the activity coefficient of the activated complex. The expression for r_{AB} thus becomes

$$r_{AB} = \frac{C^\circ k_B T}{\gamma^\ddagger h} K^\ddagger a_A a_B \quad (6)$$

The structure of the activated complex, and thus γ^\ddagger may depend on the nature of the solvent for liquid-phase reactions. Here, we focus on gas-phase reactions; therefore, we assume that γ^\ddagger is unity in subsequent analyses and replace the activity a_i by the partial pressure P_i for an ideal gas. The rate r_{AB} thus becomes

$$r_{AB} = \frac{k_B T}{h} \exp\left(\frac{\Delta S^\circ^\ddagger}{k_B}\right) \exp\left(-\frac{\Delta H^\circ^\ddagger}{k_B T}\right) P_A P_B \quad (7)$$

The units of this rate are molecules per unit volume per unit time, and the corresponding rate constant is equal to

$$k_{AB} = \frac{k_B T}{h} \exp\left(\frac{\Delta S^\circ^\ddagger}{k_B}\right) \exp\left(-\frac{\Delta H^\circ^\ddagger}{k_B T}\right) \quad (8)$$

The principal dependence of the rate constant on temperature is incorporated in the exponential term including the enthalpy of activation. Thus, we may assume that the rate constant is approximately equal to a product of a preexponential factor, A'_{AB} , and a term involving the activation energy E_{AB} :

$$k_{AB} = A'_{AB} \exp\left(-\frac{E_{AB}}{k_B T}\right) \quad (9)$$

where A'_{AB} and E_{AB} are given by

$$A'_{AB} = \frac{k_B T_{ave}}{h} \exp\left(\frac{\Delta S_{ave}^\circ^\ddagger}{k_B}\right) \quad (10)$$

$$E_{AB} = \Delta H_{ave}^\circ^\ddagger \quad (11)$$

The subscript "ave" corresponds to the quantity evaluated at the average temperature of the reaction kinetics data set.

The standard entropy change, $\Delta S^{\circ\dagger}$ for the formation of the activated complex AB^\ddagger from A and B is as follows:

$$\Delta S^{\circ\dagger} = S_{AB^\ddagger}^{\circ} - (S_A^{\circ} + S_B^{\circ}) \quad (12)$$

where $S_{AB^\ddagger}^{\circ}$, S_A° , and S_B° are the total standard entropies of the individual species. The total standard entropy (S_{tot}°) of a gas-phase species is a summation of contributions from translational ($S_{\text{trans,3D}}^{\circ}$), rotational (S_{rot}°), and vibrational (S_{vib}°) modes within the molecule or activated complex. The expression for the standard translational entropy of a gaseous molecule is

$$S_{\text{trans,3D}}^{\circ} = R \left[\ln \left(\frac{(2\pi mk_B T)^{3/2}}{h^3} \right) + \ln \left[\frac{V}{N_g} \right] + \frac{5}{2} \right] \quad (13)$$

where m is the mass of the molecule, R is the gas constant, and V/N_g is the volume per molecule in the standard state. The standard rotational entropy of a nonlinear gaseous molecule is

$$S_{\text{rot}} = R \left[\ln \left(\frac{8\pi^2 \sqrt{8\pi^3 I_{x1} I_{x2} I_{x3}} (k_B T)^{3/2}}{\sigma_r h^3} \right) + \frac{3}{2} \right] \quad (14)$$

where I_{x1} , I_{x2} , and I_{x3} are the three moments of inertia about the principal axes and σ_r is the rotational symmetry number. The standard rotational entropy of a linear gaseous molecule is

$$S_{\text{rot}}(\text{linear}) = R \left[\ln \left(\frac{8\pi^2 I_{\text{linear}} (k_B T)}{\sigma_r h^2} \right) + 1 \right] \quad (15)$$

where I_{linear} is the moment of inertia of the linear molecule. The standard vibrational entropy of a molecule is

$$S_{\text{vib}} = R \sum_i^{\# \text{ of modes}} \left(\frac{x_i}{e^{x_i} - 1} - \ln(1 - e^{-x_i}) \right) \quad (16)$$

where x_i for each vibrational mode is defined in terms of the vibrational frequency, ν_i , as

$$x_i = \frac{h\nu_i}{k_B T} \quad (17)$$

The number of vibrational modes is equal to $3N_i - 5$ or $3N_i - 6$ for a linear or nonlinear molecule, respectively, where N_i is the number of atoms in the molecule.

For adsorbed species and activated complexes on surfaces, the translational and rotational modes are replaced by vibrational modes corresponding

to frustrated translation and rotation on the surface. Accordingly, the entropy of the adsorbed species is given by S_{vib} based on $3N_i$ vibrational modes. The frequencies of these frustrated modes may be estimated from experimental vibrational spectra and/or quantum chemical calculations of the appropriate stable adsorbed species or activated complex.

In the limiting case for which the species is mobile on the surface, we may assume to a first approximation that it behaves as a two-dimensional gas and maintains the full rotational and vibrational modes of the corresponding gaseous species. The entropy contribution for the two degrees of surface mobility is given by

$$S_{\text{trans,2D}}^{\circ} = R \left[\ln \left(\frac{(2\pi mk_{\text{B}}T)}{h^2} \right) + \ln \left[\frac{\text{SA}}{N_{\text{sat}}} \right] + 2 \right] \quad (18)$$

where, SA/N_{sat} is the area occupied per adsorbed molecule at the standard state conditions. We generally assume that the standard state is monolayer coverage, and SA/N_{sat} thus equals the reciprocal of the surface concentration of sites, C_{sites} . For this choice of standard state, the activity of the adsorbed species i is equal to the fractional surface coverage, θ_i .

For example, we now use transition state theory to estimate the rate constant for an adsorption process. From transition state theory, the adsorption of species A is expressed by the reaction



The quasi-equilibrium between the surface-activated complex and the gaseous reactant is given by

$$K^{\ddagger} = \frac{\theta_{A^{\ddagger*}}}{a_A \theta_*} \quad (20)$$

The rate of adsorption per surface area, r_A , is equal to the surface concentration of activated complexes, leading the following expression:

$$r_A = \frac{C_{\text{sites}} k_{\text{B}} T}{h} \exp \left(\frac{\Delta S^{\circ\ddagger}}{k_{\text{B}}} \right) \exp \left(-\frac{\Delta H^{\circ\ddagger}}{k_{\text{B}} T} \right) a_A \theta_* \quad (21)$$

If we assume that the activated complex is mobile on the surface and that the rotational and vibrational modes of the activated complex are the same as those of the gaseous species A, then the standard entropy change of adsorption is equal to

$$\Delta S^{\circ\ddagger} = S_{\text{trans,2D}}^{\circ} - S_{\text{trans,3D}}^{\circ} \quad (22)$$

Substitution of the previous expressions for translational entropies leads to the following:

$$\Delta S^{\circ\dagger} = R \left[\ln \left(\frac{\frac{h}{k_B T}}{(2\pi m k_B T)^{1/2}} \left(\frac{SA}{N_{\text{sat}}} \right) P^\circ \right) - \frac{1}{2} \right] \quad (23)$$

In Eq. (23), we have used the ideal gas law:

$$\frac{N_g}{V} = \frac{P^\circ}{k_B T} \quad (24)$$

where P° is the standard state pressure (i.e., 1 atm). The rate of adsorption can now be written as

$$r_A = \frac{C_{\text{sites}} k_B T}{h} \frac{\frac{h}{k_B T}}{(2\pi m k_B T)^{1/2}} \frac{SA}{N_{\text{sat}}} P^\circ \exp\left(-\frac{1}{2}\right) \exp\left(-\frac{\Delta H^{\circ\dagger}}{k_B T}\right) a_A \theta_* \quad (25)$$

Note that $C_{\text{sites}} = (N_{\text{sat}}/SA)$ and $a_A = P_A/P^\circ$, leading to the following expression for r_A :

$$r_A = \frac{P_A}{(2\pi m k_B T)^{1/2}} \exp\left(-\frac{(\Delta H^{\circ\dagger} + \frac{k_B T}{2})}{k_B T}\right) \theta_* \quad (26)$$

For a species having n degrees of translational freedom, the translational energy is equal to $n k_B T/2$. Since the activated complex has two degrees of translational freedom, and gaseous A has three, we write

$$\Delta H^{\circ\dagger} + \frac{k_B T}{2} = \Delta E^{\circ\dagger}(T = 0 \text{ K}) \quad (27)$$

where $\Delta E^{\circ\dagger}(T = 0)$ is the value of $\Delta E^{\circ\dagger}$ evaluated at $T = 0$ K. This leads to the final result for r_A :

$$r_A = \frac{P_A}{(2\pi m k_B T)^{1/2}} \exp\left(-\frac{\Delta E^{\circ\dagger}(T = 0 \text{ K})}{k_B T}\right) \theta_* \quad (28)$$

Another convenient limit regarding the mobility of a species follows from the assumption that the activated complex is immobile on the surface and that it retains some fraction of its rotational and vibrational entropy from the gas phase. Accordingly, we define the local entropy, S_{loc} , of a gaseous species as

$$S_{\text{loc}} = S_{\text{rot}} + S_{\text{vib}} = S_{\text{tot}}^\circ - S_{\text{trans,3D}}^\circ \quad (29)$$

The entropy change of activation for the adsorption process is thus given by

$$\Delta S^{\circ\dagger} = F_{\text{loc}} S_{\text{loc}} - (S_{\text{trans,3D}}^\circ + S_{\text{loc}}) = (F_{\text{loc}} - 1) S_{\text{loc}} - S_{\text{trans,3D}}^\circ \quad (30)$$

where F_{loc} is the fraction of the gaseous local entropy retained by the activated complex.

2. Collision Theory

Collision theory can be used to define rate constants for adsorption processes in terms of the number of gas-phase molecules colliding with a surface per unit area per unit time, F_i'' :

$$F_i'' = \frac{P_i}{\sqrt{2\pi m_A k_B T}} \quad (31)$$

The rate of adsorption per unit area, r_A , is then defined as F_i'' multiplied by the sticking coefficient, σ , which is the probability that collision with the surface leads to adsorption:

$$r_A = F_i'' \sigma \quad (32)$$

The sticking coefficient depends on fractional surface coverage, θ , and temperature. For example, σ may be expressed as the product of its value on a clean surface, $\sigma^\circ(T)$ (a function of temperature in some cases) multiplied by a function of surface coverage, $f(\theta)$. The expression for the rate of adsorption then becomes

$$r_A = F_i'' \sigma^\circ(T) f(\theta) = \frac{P_i \sigma^\circ(T) f(\theta)}{\sqrt{2\pi m_A k_B T}} \quad (33)$$

The corresponding expression for the rate constant is

$$k_A = \frac{\sigma^\circ(T)}{\sqrt{2\pi m_A k_B T}} \quad (34)$$

Setting the value of $\sigma^\circ(T)$ equal to 1 gives an upper limit for the rate constant and for the preexponential factor for adsorption.

The expression for the rate of adsorption obtained from collision theory with $\sigma^\circ(T) = 1$ is the same as that obtained from transition state theory for a mobile activated complex with $\Delta E^{\circ\dagger}(T=0) = 0$.

3. Thermodynamic Consistency

The values of the activation enthalpies and activation entropies for the forward (for) and reverse (rev) rate constants of an elementary step are constrained by two thermodynamic relationships:

$$\Delta H_{i,\text{rev}}^{\circ\dagger} = \Delta H_{i,\text{for}}^{\circ\dagger} - \Delta H_i^\circ \quad (35)$$

$$\Delta S_{i,\text{rev}}^{\circ\dagger} = \Delta S_{i,\text{for}}^{\circ\dagger} - \Delta S_i^\circ \quad (36)$$

where ΔH_i° and ΔS_i° are the changes in standard enthalpy and entropy, respectively, for step i . Accordingly, the rate constants in the forward and reverse directions of elementary step i in the reaction scheme satisfy the

following relationship of microscopic reversibility:

$$K_{i,\text{eq}} = \frac{k_{i,\text{for}}}{k_{i,\text{rev}}} = \exp\left(\frac{\Delta S_i^\circ}{k_B}\right) \exp\left(-\frac{\Delta H_i^\circ}{k_B T}\right) \quad (37)$$

where $K_{i,\text{eq}}$ is the equilibrium constant for step i .

Since the values of ΔH_i° and ΔS_i° are generally easier to estimate than the values of the forward and reverse activation entropies and activation energies, it is usually desirable to define the kinetic parameters for step i in terms of $K_{i,\text{eq}}$ and then choose either $k_{i,\text{for}}$ or $k_{i,\text{rev}}$.

Any linear combination of steps in the reaction scheme that leads to an overall stoichiometric reaction that converts reactants and products gives rise to a relationship of thermodynamic consistency. Specifically, if σ_i are the stoichiometric coefficients of the linear combination of steps i that lead to an overall stoichiometric reaction, then the values of ΔH_i° and ΔS_i° for these steps are related by the following equations:

$$\sum_i \sigma_i \Delta H_i^\circ = \Delta H_{\text{tot}}^\circ \quad (38)$$

$$\sum_i \sigma_i \Delta S_i^\circ = \Delta S_{\text{tot}}^\circ \quad (39)$$

where the subscript “tot” refers to the overall stoichiometric reaction. Alternatively, the statement of thermodynamic consistency can be written in terms of the equilibrium constants for steps i :

$$\prod_i K_{i,\text{eq}}^{\sigma_i} = \prod_i \left(\frac{k_{i,\text{for}}}{k_{i,\text{rev}}}\right)^{\sigma_i} = K_{\text{tot}} \quad (40)$$

where K_{tot} is the equilibrium constant for the overall stoichiometric reaction. Alternatively, the activation enthalpies and activation entropies for the forward and reverse directions of step i are related by the following:

$$\sum_i \sigma_i (\Delta H_{i,\text{for}}^{\circ\dagger}) - \sum_i \sigma_i (\Delta H_{i,\text{rev}}^{\circ\dagger}) = \Delta H_{\text{tot}}^\circ \quad (41)$$

$$\sum_i \sigma_i (\Delta S_{i,\text{for}}^{\circ\dagger}) - \sum_i \sigma_i (\Delta S_{i,\text{rev}}^{\circ\dagger}) = \Delta S_{\text{tot}}^\circ \quad (42)$$

Since the thermodynamic properties of the reactants and products are known, it is essential to ensure that the kinetic model is constructed so that it is consistent with these properties. Depending on how the model is parameterized (e.g., in terms of $k_{i,\text{for}}$ and $K_{i,\text{eq}}$, in terms of $k_{i,\text{rev}}$ and $K_{i,\text{eq}}$, or in terms of $k_{i,\text{for}}$ and $k_{i,\text{rev}}$), one of the previous equations of thermodynamic consistency must be used for each linear combination of steps that leads to an overall stoichiometric reaction.

4. Reactor Descriptions

Catalytic reactors are generally described in terms of the following types of ideal reactors: batch reactor, continuous-flow stirred tank reactor (CSTR), and plug flow reactor (PFR). In the batch reactor the key assumption is that the reactor contents are well mixed; that is, the concentration of any species in the reactor is uniform spatially (but varies with time). The CSTR is also assumed to be perfectly mixed so that the concentration of any species is that in the effluent stream. In contrast, longitudinal mixing in the PFR is assumed to be negligible, whereas mixing in the radial direction is complete; a concentration gradient along the length of the reactor is thereby established.

The batch reactor is characterized by its volume, V_R , and the holding time, t , that the fluid has spent in the reactor. Flow reactors are usually characterized by reactor volume and space time, τ , with the latter defined as the reactor volume divided by the volumetric flow rate of feed to the reactor. The physical significance of τ is the time required to process a volume of fluid corresponding to V_R . For catalytic reactions, the space time may be replaced by the site time, τ_ρ , defined as the number of catalytic sites in the reactor, S_R , divided by the molecular flow rate of feed to the reactor, F . The physical interpretation of τ_ρ is the time required to process many molecules equal to the number of active sites in the reactor.

The three ideal reactors form the building blocks for analysis of laboratory and commercial catalytic reactors. In practice, an actual flow reactor may be more complex than a CSTR or PFR. Such a reactor may be described by a residence time distribution function $F(t)$ that gives the probability that a given fluid element has resided in the reactor for a time longer than t . The reactor is then defined further by specifying the origin of the observed residence time distribution function (e.g., axial dispersion in a tubular reactor or incomplete mixing in a tank reactor).

The governing equations for each of the three ideal reactors are material balances for reactants and products of the reaction. In general, one material balance equation must be written for each independent reaction taking place in the reactor. For a group of N_{sp} species (i.e., reactants and products) in the reactor consisting of N_{el} elements, the number of independent chemical reactions typically is equal to $(N_{sp} - N_{el})$.

The material balance for species i in a general flow reactor is given by

$$F_i^\circ + R_i = F_i + \left\{ \frac{dN_i}{dt} \right\} \quad (43)$$

where F_i° is the molecular flow rate of species i into the reactor, F_i is the analogous flow rate leaving the reactor, R_i is the rate of production of species

i , and N_i is the number of molecules of species i in the reactor. For a batch reactor, the molecular flow rates are equal to zero, and the material balance equation takes the following form:

$$\frac{dN_i}{dt} = V_R r_i''' = S_R \Omega_i \quad (44)$$

where r_i''' represents the rate per unit reactor volume and S_R is the number of sites in the reactor; Ω_i is the turnover frequency, defined as the number of reaction events per active site per second.

For a CSTR operating at steady state, the accumulation term, dN_i/dt , is equal to zero, and the material balance equation has the following form:

$$F_i - F_i^\circ = V_R r_i''' = S_R \Omega_i \quad (45)$$

The material balance equation for a PFR is obtained by considering a differential longitudinal section of the reactor, followed by integration of the differential balance over the length of the reactor. This procedure gives the following result for a PFR operating at steady state:

$$F_i - F_i^\circ = \int r_i''' dV_R = \int \Omega_i dS_R \quad (46)$$

The previous equations are particularly useful for numerical analyses of the general case in which multiple reactions take place with the number of moles changing upon reaction.

For complex catalytic reactions requiring numerical analyses, it is useful to write the material balance equations for flow reactors in terms of molecular flow rates per active site ($F_{s,i} = F_i/S_R$), which are denoted as molecular site velocities. For batch reactors, the number of gaseous molecules per active site ($N_{s,i} = N_i/S_R$) is used. (These normalized quantities are typically of the order of unity.) The batch reactor, CSTR, and PFR material balance equations become the following:

$$\text{Batch: } \frac{dN_{s,i}}{dt} = \Omega_i \quad (47)$$

$$\text{CSTR: } F_{s,i} - F_{s,i}^\circ = \Omega_i \quad (48)$$

$$\text{PFR: } F_{s,i} - F_{s,i}^\circ = \frac{1}{S_R} \int \Omega_i dS_R \quad (49)$$

The sum of inlet molecular flow rates per site for a flow reactor, $\sum(F_{s,i}^\circ)$, is equal to the reciprocal of the site time, $1/\tau_\rho$, which may be defined as the overall inlet site velocity, F_s° .

Another reactor equation useful in reaction kinetics analyses represents the transient CSTR. This situation is encountered in temperature-programmed desorption and isotope tracer experiments. The material balance for the transient CSTR operating at constant total pressure for an ideal gas is

$$\frac{dF_{s,i}}{dt} = (F_{s,i}^{\circ} - F_{s,i} + \Omega_i) \frac{F_s}{N_s} + \frac{F_{s,i}}{F_s} \frac{dF_s}{dt} - \frac{F_{s,i}}{N_s} \frac{dN_s}{dt} \quad (50)$$

where $F_s = \sum F_{s,i}$ and $N_s (= \sum N_{s,i})$ is equal to the number of gas-phase molecules per active site in the CSTR. If the change in the number of moles upon reaction is negligible and the reactor is isothermal, then F_s is equal to F_s° and the last two terms in Eq. (50) are negligible. The material balance equation for the transient CSTR then becomes

$$\frac{dF_{s,i}}{dt} = (F_{s,i}^{\circ} - F_{s,i} + \Omega_i) \frac{F_s}{N_s} \quad (51)$$

F_s/N_s is typically of the order of 1 s^{-1} .

The rate expressions, Ω_i , in the material balance equations depend on the partial pressures, P_i , of reactants and products. For reactions involving ideal gases at constant total pressure, P_{tot}° , the partial pressure P_i can be related to $F_{s,i}$ or $N_{s,i}$ as follows:

$$\text{Flow reactors: } P_i = \frac{F_{s,i}}{F_s} P_{\text{tot}}^{\circ} \quad (52)$$

$$\text{Batch reactor: } P_i = \frac{N_{s,i}}{N_s^{\circ}} P_{\text{tot}}^{\circ} \quad (53)$$

where $N_s^{\circ} (= \sum N_{s,i}^{\circ})$ is the initial number of molecules per active site in the batch reactor.

III. Significance of Kinetic Parameters

Here, we outline several simple principles for assessing the kinetic significance of various steps in a reaction scheme. We show how these principles lead to well-known limiting cases. For example, the kinetic parameters are generally not kinetically significant for steps that are quasi-equilibrated under reaction conditions, and the rate constants are typically not important for steps involving reactive intermediates that are produced in preceding irreversible steps. Generally, we identify the maximum number of kinetic parameters needed to describe a reaction scheme. We show how these parameters can be expressed in terms of quasi-equilibria involving the transition states

of the reaction scheme. In addition, one additional kinetic parameter is required for each species that becomes abundant on the catalyst surface, i.e., for each species that is involved in occupying surface sites. We show that the dimensionless sensitivities for the forward and reverse rate constants of an elementary step are related by the reversibility of the step. Moreover, the sum of the dimensionless sensitivities for the forward and reverse rate constants for all the steps of the reaction scheme is equal to unity. This conservation of sensitivity suggests that potential confusion in the use of the concept of a rate-determining step might be eliminated by denoting a step as being the “maximum sensitivity step” of a reaction scheme.

A. PARAMETERIZATION OF THE KINETIC MODEL IN TERMS OF TRANSITION STATES

Consider the following three-step reaction scheme for the reversible conversion of A to D ($A \rightleftharpoons D$):



where species B and C are reaction intermediates, and k_i and k_{-i} are rate constants for the forward and reverse directions of step i .

At steady state, the net rates of the three steps are equal, leading to the following expression for the net rate, r , of the overall reaction:

$$r = \frac{k_1 k_2 k_3 a_A \left(1 - \frac{a_D}{K_{\text{eq}} a_A}\right)}{k_2 k_3 + k_{-1} k_3 + k_{-1} k_{-2}} \quad (57)$$

where a_i is the activity of species i (equal to the partial pressure of species i for an ideal gas), and K_{eq} is the equilibrium constant for the overall reaction, equal to

$$K_{\text{eq}} = \frac{k_1 k_2 k_3}{k_{-1} k_{-2} k_{-3}} \quad (58)$$

The rate expression can be rearranged into the following form in terms of three lumped kinetic parameters, K_{TS_1} , K_{TS_2} , and K_{TS_3} :

$$r = \frac{K_{\text{TS}_1} K_{\text{TS}_2} K_{\text{TS}_3} \left(1 - \frac{a_D}{K_{\text{eq}} a_A}\right)}{K_{\text{TS}_1} K_{\text{TS}_2} + K_{\text{TS}_1} K_{\text{TS}_3} + K_{\text{TS}_2} K_{\text{TS}_3}} \quad (59)$$

These lumped kinetic parameters are defined by the following relationships:

$$\begin{aligned} K_{\text{TS}_1} &= k_1 \\ K_{\text{TS}_2} &= \frac{k_1 k_2}{k_{-1}} = K_{1,\text{eq}} k_2 \\ K_{\text{TS}_3} &= \frac{k_1 k_2 k_3}{k_{-1} k_{-2}} = K_{1,\text{eq}} K_{2,\text{eq}} k_3 \end{aligned} \quad (60)$$

where $K_{i,\text{eq}}$ is the equilibrium constant for step i ($K_{i,\text{eq}} = k_i/k_{-i}$).

Often, the rate constant k_i can be expressed approximately in terms of transition state theory:

$$k_i = \nu^\ddagger K_i^\ddagger = \nu^\ddagger \exp\left(\frac{\Delta S_i^{\circ\ddagger}}{R} - \frac{\Delta H_i^{\circ\ddagger}}{RT}\right) \quad (61)$$

where ν^\ddagger is a frequency factor (equal to $k_B T/h$ and possibly containing an activity coefficient for the activated complex), K_i^\ddagger is the quasi-equilibrium constant for the formation of the activated complex from the reactants of step i , and $\Delta S_i^{\circ\ddagger}$ and $\Delta H_i^{\circ\ddagger}$ are the corresponding standard changes in entropy and enthalpy, respectively.

The expressions for K_{TS_i} can now be written as follows:

$$K_{\text{TS}_1} = \nu^\ddagger K_1^\ddagger \quad (62)$$

$$K_{\text{TS}_2} = \nu^\ddagger K_{1,\text{eq}} K_2^\ddagger \quad (63)$$

$$K_{\text{TS}_3} = \nu^\ddagger K_{1,\text{eq}} K_{2,\text{eq}} K_3^\ddagger \quad (64)$$

These products of equilibrium constants indicate that the kinetic parameters K_{TS_i} can be related to quasi-equilibrium constants for the following overall reactions to form each of the three transition states TS_i from reactant A:



We now reach the important conclusion that the net rate of the overall reaction can be expressed in terms of kinetic parameters K_{TS_i} , that depend only on the properties of the transition states for the elementary steps relative to the reactants (and possibly the products) of the overall reaction, i.e., the

net rate of the overall reaction does not depend on the properties of the stable reaction intermediates B and C.

B. IDENTIFICATION OF KINETIC PARAMETERS FROM DE DONDER RELATIONS

The previous result that the net rate of the overall reaction can be expressed in terms of kinetic parameters that depend only on the properties of the transition states can be demonstrated more generally by using De Donder relationships (24–28). According to the formulation of De Donder, the net rate, r_i , of elementary step i is expressed in terms of the forward rate of the step, \bar{r}_i , and the affinity for the step, A_i :

$$r_i = \bar{r}_i \left[1 - \exp\left(\frac{-A_i}{RT}\right) \right] \quad (68)$$

where the affinity is equal to the change in the Gibbs free energy with respect to the extent of reaction (i.e., equal to the difference in the Gibbs free energies of the reactants and products of the elementary step at the reaction temperature and at the corresponding partial pressure for each reactant, product, and reaction intermediate). In general, the affinity, A_i , is expressed in terms of the standard state Gibbs free energies, G_j° , and the activities, a_j , of the j reactants and products of the step:

$$A_i = - \sum_j \nu_{ij} G_j = - \sum_j \nu_{ij} [G_j^\circ + RT \ln(a_j)] \quad (69)$$

where ν_{ij} are the stoichiometric coefficients for the j reactants and products of step i . This expression can be written in terms of the equilibrium constant for the step, $K_{i,\text{eq}}$:

$$\exp\left(\frac{-A_i}{RT}\right) = \frac{\prod_j a_j^{\nu_{ij}}}{K_{i,\text{eq}}} \quad (70)$$

since the equilibrium constant is determined by the change in the standard state Gibbs free energies:

$$K_{i,\text{eq}} = \exp\left[\frac{-\sum_j \nu_{ij} G_j^\circ}{RT}\right] \quad (71)$$

For convenience, we define a dimensionless variable, z_i , equal to the exponential of $-A_i/RT$:

$$z_i = \exp\left(\frac{-A_i}{RT}\right) = \frac{\prod_j a_j^{\nu_{ij}}}{K_{i,\text{eq}}} \quad (72)$$

The value of z_i approaches zero as step i becomes irreversible, and it approaches unity as step i becomes quasi-equilibrated. Therefore, the value of z_i may be termed the reversibility of step i . The value of z_i remains bounded between 0 and 1, provided that step i proceeds in the forward direction.

For the three-step reaction scheme of this example, the values of z_i are as follows:

$$z_1 = \frac{a_B}{K_{1,\text{eq}}a_A} \quad (73)$$

$$z_2 = \frac{a_C}{K_{2,\text{eq}}a_B} \quad (74)$$

$$z_3 = \frac{a_D}{K_{3,\text{eq}}a_C} \quad (75)$$

However, only two of these values are independent because the product of the three values of z_i is controlled by the overall reversibility of the reaction, z_{total} :

$$z_{\text{total}} = z_1 z_2 z_3 = \frac{a_D}{K_{\text{eq}}a_A} \quad (76)$$

This result follows from the relationship that

$$A_{\text{total}} = A_1 + A_2 + A_3 \quad (77)$$

where A_{total} is the total change in affinity for the overall reaction, given by

$$A_{\text{total}} = -RT \ln \left[\frac{a_D}{K_{\text{eq}}a_A} \right] \quad (78)$$

The activities of intermediates B and C are now expressed in terms of z_i as follows:

$$a_B = K_{1,\text{eq}}a_A z_1 \quad (79)$$

$$a_C = K_{1,\text{eq}}K_{2,\text{eq}}a_A z_1 z_2 \quad (80)$$

and the net rates of the three reactions are given by

$$r_1 = k_1 a_A (1 - z_1) \quad (81)$$

$$r_2 = K_{1,\text{eq}}k_2 a_A z_1 (1 - z_2) \quad (82)$$

$$r_3 = K_{1,\text{eq}}K_{2,\text{eq}}k_3 a_A z_1 z_2 \left(1 - \frac{z_{\text{total}}}{z_1 z_2} \right) \quad (83)$$

The unknown values of z_1 and z_2 are determined by the requirement that the net rates of steps 1–3 are equal. Therefore, the net rate of the overall

reaction is again controlled by three lumped kinetic parameters, K_{TS} :

$$r_1 = K_{TS_1} a_A (1 - z_1) \quad (84)$$

$$r_2 = K_{TS_2} a_A z_1 (1 - z_2) \quad (85)$$

$$r_3 = K_{TS_3} a_A z_1 z_2 \left(1 - \frac{z_{\text{total}}}{z_1 z_2} \right) \quad (86)$$

In summary, it can be seen for the three-step reaction scheme of this example that the net rate of the overall reaction is controlled by three kinetic parameters, K_{TS} , that depend only on the properties of the transition states for the elementary steps relative to the reactants (and possibly the products) of the overall reaction. The reaction scheme is represented by six individual rate constants k_i and k_{-i} , the product of which must give the equilibrium constant for the overall reaction. However, it is not necessary to determine values for five linearly independent rate constants to determine the rate of the overall reaction. We conclude that the maximum number of kinetic parameters needed to determine the net rate of overall reaction is equal to the number of transition states in the reaction scheme (equal to three in the current case) since each kinetic parameter is related to a quasi-equilibrium constant for the formation of each transition state from the reactants and/or products of the overall reaction. To calculate rates of heterogeneous catalytic reactions, an additional kinetic parameter is required for each surface species that is abundant on the catalyst surface. Specifically, the net rate of the overall reaction is determined by the intrinsic kinetic parameters K_{TS_i} , as well as by the fraction of the surface sites, θ_* , available for formation of the transition states; furthermore, the value of θ_* is determined by the extent of site blocking by abundant surface species.

C. SENSITIVITIES OF THE NET RATE TO INDIVIDUAL RATE CONSTANTS

It was previously shown that calculation of the net rate for the three-step reaction scheme can be reduced from determining values for five linearly independent rate constants to determining values for three lumped kinetic parameters. However, it is generally found that not all these parameters are kinetically significant. For example, the kinetic parameter involving a transition state for a quasi-equilibrated step is not significant. Furthermore, the kinetic parameter involving a transition state for a step including an intermediate formed in a preceding irreversible step is not significant. These situations for which kinetic parameters become insignificant are identified systematically by sensitivity analyses.

We again consider the three-step reaction scheme discussed previously. The net rates for the three steps are given in the De Donder form:

$$r_1 = k_1 a_A (1 - z_1) \quad (87)$$

$$r_2 = \frac{k_1}{k_{-1}} k_2 a_A z_1 (1 - z_2) \quad (88)$$

$$r_3 = \frac{k_1}{k_{-1}} \frac{k_2}{k_{-2}} k_3 a_A z_1 z_2 \left(1 - \frac{k_{-1} k_{-2} k_{-3}}{k_1 k_2 k_3} \frac{a_D}{z_1 z_2 a_A} \right) \quad (89)$$

The sensitivity of the net rate with respect to k_1 is determined by first taking the derivatives of r_1 , r_2 , and r_3 with respect to k_1 :

$$\left(\frac{\partial r_1}{\partial k_1} \right)_{k_j} = \left(\frac{\partial r_1}{\partial k_1} \right)_{k_j, z_i} + \left(\frac{\partial r_1}{\partial z_1} \right)_{k_i, z_2} \left(\frac{\partial z_1}{\partial k_1} \right)_{k_j} \quad (90)$$

$$\left(\frac{\partial r_2}{\partial k_1} \right)_{k_j} = \left(\frac{\partial r_2}{\partial k_1} \right)_{k_j, z_i} + \left(\frac{\partial r_2}{\partial z_1} \right)_{k_i, z_2} \left(\frac{\partial z_1}{\partial k_1} \right)_{k_j} + \left(\frac{\partial r_2}{\partial z_2} \right)_{k_i, z_1} \left(\frac{\partial z_2}{\partial k_1} \right)_{k_j} \quad (91)$$

$$\left(\frac{\partial r_3}{\partial k_1} \right)_{k_j} = \left(\frac{\partial r_3}{\partial k_1} \right)_{k_j, z_i} + \left(\frac{\partial r_3}{\partial z_1} \right)_{k_i, z_2} \left(\frac{\partial z_1}{\partial k_1} \right)_{k_j} + \left(\frac{\partial r_3}{\partial z_2} \right)_{k_i, z_1} \left(\frac{\partial z_2}{\partial k_1} \right)_{k_j} \quad (92)$$

where k_j refers to all rate constants except k_1 , k_i refers to all rate constants, and z_i refers to z_1 and z_2 .

At steady state, the three net rates r_i are equal to the overall rate, r . Therefore, we write

$$\left(\frac{\partial r_1}{\partial k_1} \right)_{k_j} = \left(\frac{\partial r_2}{\partial k_1} \right)_{k_j} = \left(\frac{\partial r_3}{\partial k_1} \right)_{k_j} = \left(\frac{\partial r}{\partial k_1} \right)_{k_j} \quad (93)$$

which allows determination of the partial derivatives of z_1 and z_2 with respect to k_1 :

$$\left(\frac{\partial z_1}{\partial k_1} \right)_{k_j} = \frac{(k_2 k_3 + k_3 k_{-1} + k_{-1} k_{-2}) z_1 - k_{-1} (k_3 + k_{-2})}{k_1 (k_2 k_3 + k_3 k_{-1} + k_{-1} k_{-2})} \quad (94)$$

$$\left(\frac{\partial z_2}{\partial k_1} \right)_{k_j} = \frac{-(k_3 + k_{-2}) z_2 + k_{-1} k_{-2}}{k_1 (k_2 k_3 + k_3 k_{-1} + k_{-1} k_{-2}) z_1} \quad (95)$$

We now define the dimensionless sensitivity, ϕ_1 , of the overall rate with respect to k_1 as

$$\phi_1 = \left(\frac{\partial r}{\partial k_1} \right)_{k_j} \frac{k_1}{r} \quad (96)$$

Substitution of the relationships for $(\frac{\partial z_1}{\partial k_i})_{k_j}$ and $(\frac{\partial z_2}{\partial k_i})_{k_j}$ into any of the expressions for the partial derivatives of r_i with respect to k_I gives the sensitivity ϕ_1 :

$$\phi_1 = \frac{k_2 k_3}{(k_2 k_3 + k_3 k_{-1} + k_{-1} k_{-2})(1 - z_1)} \quad (97)$$

Similarly, we derive an expression for the dimensionless sensitivity, ϕ_{-1} , of the overall rate with respect to k_{-1} as follows:

$$\phi_{-1} = \left(\frac{\partial r}{\partial k_{-1}} \right)_{k_j} \frac{k_{-1}}{r} = \frac{-k_2 k_3 z_1}{(k_2 k_3 + k_3 k_{-1} + k_{-1} k_{-2})(1 - z_1)} \quad (98)$$

The following expressions for ϕ_2 , ϕ_{-2} , ϕ_3 , and ϕ_{-3} are derived according to the steps outlined previously:

$$\phi_2 = \frac{k_2 k_3 z_1}{(k_2 k_3 + k_3 k_{-1} + k_{-1} k_{-2})(1 - z_1)} \quad (99)$$

$$\phi_{-2} = \frac{-k_2 k_3 z_1 z_2}{(k_2 k_3 + k_3 k_{-1} + k_{-1} k_{-2})(1 - z_1)} \quad (100)$$

$$\phi_3 = \frac{k_2 k_3 z_1 z_2}{(k_2 k_3 + k_3 k_{-1} + k_{-1} k_{-2})(1 - z_1)} \quad (101)$$

$$\phi_{-3} = \frac{-k_2 k_3 z_{\text{total}}}{(k_2 k_3 + k_3 k_{-1} + k_{-1} k_{-2})(1 - z_1)} \quad (102)$$

It is now apparent that ϕ_{-1} , ϕ_{-2} , and ϕ_{-3} are related to ϕ_1 , ϕ_2 , and ϕ_3 as follows:

$$\phi_{-1} = -z_1 \phi_1 \quad (103)$$

$$\phi_{-2} = -z_2 \phi_2 \quad (104)$$

$$\phi_{-3} = -z_3 \phi_3 \quad (105)$$

The previous relationships are specific cases of the general result for any elementary step i :

$$\phi_{-i} = -z_i \phi_i \quad (106)$$

This result indicates that the sensitivity of the overall rate to the reverse rate constant for a step depends on the reversibility of the step. For example, the sensitivity of the overall rate to the reverse rate constant is equal to zero for an irreversible step ($z_i = 0$) and to the negative value of the sensitivity of the overall rate to the forward rate constant for a quasi-equilibrated step ($z_i = 1$).

In this case, we also see that

$$\phi_2 = z_1\phi_1 \quad (107)$$

$$\phi_3 = z_2\phi_2 \quad (108)$$

Accordingly, the sensitivity of the overall rate to the forward rate constant for step 2 depends on the reversibility of step 1 that produces the intermediate in step 2. Similarly, the sensitivity of the overall rate to the forward rate constant for step 3 depends on the reversibility of step 2 that produces the intermediate in step 3. In these cases, the sensitivity of the overall rate to the forward rate constant for a step approaches zero as the preceding step that produces the reaction intermediate becomes irreversible ($z_i = 0$). In contrast, the sensitivity of the overall rate to the forward rate constant for a step remains nonzero as the preceding step that produces the reaction intermediate becomes reversible ($z_i > 0$).

In general, the sensitivity of the overall rate to the forward rate constant for step i is always proportional to the reversibility of the preceding step that produces the reaction intermediate in step i ; however, the proportionality constant depends on the stoichiometric coefficients for the formation and consumption of the reactive intermediates. For example, if the reactive intermediate is consumed once in step i and produced twice in the preceding step j , then $\phi_i = 2 Z_j \phi_j$.

D. CONSERVATION OF SENSITIVITY

The previous relationships suggest a conservation of sensitivity for the forward and reverse rate constants of a reaction scheme that leads to a single overall reaction. Consider the following sum of sensitivities for the three-step reaction scheme:

$$\sum_{i=1,3} (\phi_i + \phi_{-i}) = [(1 - z_1) + z_1(1 - z_2) + z_1 z_2(1 - z_3)]\phi_1 \quad (109)$$

which leads to the result that

$$\sum_{i=1,3} (\phi_i + \phi_{-i}) = (1 - z_1 z_2 z_3)\phi_1 \quad (110)$$

The sensitivity ϕ_1 was expressed in terms of $(1 - z_1)$, and the value of $(1 - z_1)$ at steady state is equal to

$$(1 - z_1) = \frac{k_1 k_2 k_3 a_A - k_{-1} k_{-2} k_{-3} a_D}{k_1 a_A (k_2 k_3 + k_3 k_{-1} + k_{-1} k_{-2})} \quad (111)$$

Thus, the sensitivity ϕ_1 can be written as

$$\phi_1 = \frac{k_1 k_2 k_3 a_A}{k_1 k_2 k_3 a_A - k_{-1} k_{-2} k_{-3} a_D} \quad (112)$$

Furthermore,

$$z_1 z_2 z_3 = z_{\text{total}} = \frac{a_D}{k_{\text{eq}} a_A} = \frac{k_{-1} k_{-2} k_{-3} a_D}{k_1 k_2 k_3 a_A} \quad (113)$$

Therefore,

$$\sum_{i=1,3} (\phi_i + \phi_{-i}) = \left(1 - \frac{k_{-1} k_{-2} k_{-3} a_D}{k_1 k_2 k_3 a_A}\right) \frac{k_1 k_2 k_3 a_A}{k_1 k_2 k_3 a_A - k_{-1} k_{-2} k_{-3} a_D} = 1 \quad (114)$$

A more general demonstration of this conservation of sensitivity is based on the following use of De Donder relationships for the net rates of the three-step reaction scheme:

$$r_1 = k_1 F(z_1) \quad (115)$$

$$r_2 = k_2 F(z_1, z_2) G(K_{1,\text{eq}}) \quad (116)$$

$$r_3 = k_3 F(z_1, z_2) G(K_{1,\text{eq}}, K_{2,\text{eq}}) \quad (117)$$

where $F(z_i)$ and $G(K_{i,\text{eq}})$ are functions of z_i and $K_{i,\text{eq}}$. For a given step i , the sum of ϕ_i and ϕ_{-i} is equivalent to the sensitivity caused by increasing k_i while maintaining $K_{i,\text{eq}}$ constant. Consider the sensitivity for step 1:

$$\frac{\phi_1 + \phi_{-1}}{k_1/r_1} = \left(\frac{\partial r_1}{\partial k_1}\right)_{k_j, z_i, K_{i,\text{eq}}} + \left(\frac{\partial r_1}{\partial z_1}\right)_{k_i, z_2, K_{i,\text{eq}}} \left(\frac{\partial z_1}{\partial k_1}\right)_{k_j, K_{i,\text{eq}}} \quad (118)$$

$$\begin{aligned} \frac{\phi_1 + \phi_{-1}}{k_1/r_1} &= \left(\frac{\partial r_2}{\partial k_1}\right)_{k_j, z_i, K_{i,\text{eq}}} + \left(\frac{\partial r_2}{\partial z_1}\right)_{k_i, z_2, K_{i,\text{eq}}} \left(\frac{\partial z_1}{\partial k_1}\right)_{k_j, K_{i,\text{eq}}} \\ &+ \left(\frac{\partial r_2}{\partial z_2}\right)_{k_i, z_1, K_{i,\text{eq}}} \left(\frac{\partial z_2}{\partial k_1}\right)_{k_j, K_{i,\text{eq}}} \end{aligned} \quad (119)$$

$$\begin{aligned} \frac{\phi_1 + \phi_{-1}}{k_1/r_1} &= \left(\frac{\partial r_3}{\partial k_1}\right)_{k_j, z_i, K_{i,\text{eq}}} + \left(\frac{\partial r_3}{\partial z_1}\right)_{k_i, z_2, K_{i,\text{eq}}} \left(\frac{\partial z_1}{\partial k_1}\right)_{k_j, K_{i,\text{eq}}} \\ &+ \left(\frac{\partial r_3}{\partial z_2}\right)_{k_i, z_i, K_{i,\text{eq}}} \left(\frac{\partial z_2}{\partial k_1}\right)_{k_j, K_{i,\text{eq}}} \end{aligned} \quad (120)$$

where k_i refers to all forward rate constants, k_j refers to forward rate constants other than k_1 , $K_{i,\text{eq}}$ refers to all equilibrium constants, and z_i refers to z_1 and z_2 .

Furthermore,

$$\left(\frac{\partial r_1}{\partial k_1}\right)_{k_j, z_i, K_{i,eq}} = \frac{r_1}{k_1} \quad (121)$$

$$\left(\frac{\partial r_2}{\partial k_1}\right)_{k_j, z_i, K_{i,eq}} = 0 \quad (122)$$

$$\left(\frac{\partial r_3}{\partial k_1}\right)_{k_j, z_i, K_{i,eq}} = 0 \quad (123)$$

Since the net rates of the three steps are equal to each other at steady state, these three equations are solved to determine the values of $(\partial z_1/\partial k_1)_{k_j, K_{i,eq}}$ and $(\partial z_2/\partial k_1)_{k_j, K_{i,eq}}$, and substitution of these values into any one of the three expressions for $(\phi_1 + \phi_{-1})$ gives

$$\phi_1 + \phi_{-1} = \frac{\left(\frac{\partial r_2}{\partial z_1}\right)\left(\frac{\partial r_3}{\partial z_2}\right) - \left(\frac{\partial r_2}{\partial z_2}\right)\left(\frac{\partial r_3}{\partial z_1}\right)}{\left(\frac{\partial r_1}{\partial z_1}\right)\left(\frac{\partial r_2}{\partial z_2}\right) - \left(\frac{\partial r_2}{\partial z_2}\right)\left(\frac{\partial r_3}{\partial z_1}\right) - \left(\frac{\partial r_1}{\partial z_1}\right)\left(\frac{\partial r_3}{\partial z_2}\right) + \left(\frac{\partial r_2}{\partial z_1}\right)\left(\frac{\partial r_3}{\partial z_2}\right)} \quad (124)$$

where all the partial derivatives are evaluated at constant $k_i, K_{i,eq}$, and either z_1 or z_2 , as appropriate.

Similar derivations lead to analogous expressions for steps 2 and 3:

$$\phi_2 + \phi_{-2} = \frac{-\left(\frac{\partial r_1}{\partial z_1}\right)\left(\frac{\partial r_3}{\partial z_2}\right)}{\left(\frac{\partial r_1}{\partial z_1}\right)\left(\frac{\partial r_2}{\partial z_2}\right) - \left(\frac{\partial r_2}{\partial z_2}\right)\left(\frac{\partial r_3}{\partial z_1}\right) - \left(\frac{\partial r_1}{\partial z_1}\right)\left(\frac{\partial r_3}{\partial z_2}\right) + \left(\frac{\partial r_2}{\partial z_1}\right)\left(\frac{\partial r_3}{\partial z_2}\right)} \quad (125)$$

$$\phi_3 + \phi_{-3} = \frac{\left(\frac{\partial r_1}{\partial z_1}\right)\left(\frac{\partial r_2}{\partial z_2}\right)}{\left(\frac{\partial r_1}{\partial z_1}\right)\left(\frac{\partial r_2}{\partial z_2}\right) - \left(\frac{\partial r_2}{\partial z_2}\right)\left(\frac{\partial r_3}{\partial z_1}\right) - \left(\frac{\partial r_1}{\partial z_1}\right)\left(\frac{\partial r_3}{\partial z_2}\right) + \left(\frac{\partial r_2}{\partial z_1}\right)\left(\frac{\partial r_3}{\partial z_2}\right)} \quad (126)$$

Summing these three equations leads to the result

$$(\phi_1 + \phi_{-1}) + (\phi_2 + \phi_{-2}) + (\phi_3 + \phi_{-3}) = 1 \quad (127)$$

In summary, the sum of the sensitivities for the forward and reverse rate constants of a reaction scheme is equal to unity for a reaction scheme that leads to a single overall reaction:

$$\sum_{i=1,3} (\phi_i + \phi_{-i}) = 1 \quad (128)$$

Furthermore, the sum of the sensitivities for the forward and reverse rate constants of a particular step i is equal to

$$\phi_i + \phi_{-i} = (1 - z_i)\phi_i \quad (129)$$

Therefore, the sum of the sensitivities for the forward and reverse rate constants of a particular step i is equal to zero for a quasi-equilibrated step ($z_i = 1$). Since the sum of sensitivities for all steps is equal to unity, the sensitivity of a quasi-equilibrated step is passed on to the subsequent steps in the reaction sequence. Similarly, the sum of the sensitivities for the forward and reverse rate constants of a particular step i is equal to the sensitivity for the forward rate constant for an irreversible step ($z_i = 0$). Since the sum of sensitivities for all steps is equal to unity, the sensitivity of an irreversible step is not passed on to the subsequent steps in the reaction sequence. Accordingly, the sensitivities of the rate constants for a step approach zero as the preceding steps that produce the reaction intermediates become irreversible.

We emphasize that this conservation of sensitivity applies in general to reaction schemes for which the stoichiometric numbers of the individual steps are not all equal to unity.

E. CAMPBELL'S DEGREE OF RATE CONTROL

Campbell (29) suggested that the kinetic importance of a particular step in a reaction scheme can be ascertained by computing the effect on the overall rate of increasing the forward and reverse rate constants for that step while maintaining the same value of the equilibrium constant for the step. According to Campbell, the degree of rate control for step i , $X_{RC,i}$ is equal to

$$X_{RC,i} = \frac{k_i}{r} \left(\frac{\delta r}{\delta k_i} \right)_{K_{i,eq}, k_j} \quad (130)$$

where the equilibrium constant for step i ($K_{i,eq}$) and all other rate constants are held constant.

We now compute Campbell's degree of rate control in terms of the sensitivities for the forward and reverse rate constants. We compute the change in the overall rate, δr , resulting from a change in k_i by δk_i and a change in k_{-i} by $\delta k_{-i}/K_{i,eq}$ to maintain the same equilibrium constant:

$$\delta r = \left(\frac{\partial r}{\partial k_i} \right)_{k_j} \delta k_i + \left(\frac{\partial r}{\partial k_{-i}} \right)_{k_j} \frac{\delta k_{-i}}{K_{i,eq}} \quad (131)$$

where k_j are all rate constants other than k_i or k_{-i} , as appropriate.

We compute Campbell's degree of rate control as follows:

$$X_{RC,i} = \frac{k_i}{r} \left(\frac{\delta r}{\delta k_i} \right)_{K_{i,eq}, k_j} = \frac{k_i}{r} \left[\left(\frac{\partial r}{\partial k_i} \right)_{k_j} + \left(\frac{\partial r}{\partial k_{-i}} \right)_{k_j} \frac{k_{-i}}{k_i} \right] \quad (132)$$

which leads to the following relationship:

$$X_{RC,i} = \phi_i + \phi_{-i} \quad (133)$$

Furthermore,

$$X_{RC,i} = (1 - z_i)\phi_i \quad (134)$$

Since we previously showed that the sum of the sensitivities for the forward and reverse rate constants of a reaction scheme is equal to unity for a reaction scheme that leads to a single overall reaction, we now see that the sum of $X_{RC,i}$ for the steps is also conserved:

$$\sum_i X_{RC,i} = 1 \quad (135)$$

In the previous example of a three-step reaction scheme, the values of $X_{RC,i}$ are equal to the following:

$$X_{RC,1} = (1 - z_1)\phi_1 \quad (136)$$

$$X_{RC,2} = z_1(1 - z_2)\phi_1 \quad (137)$$

$$X_{RC,3} = z_1 z_2(1 - z_3)\phi_1 \quad (138)$$

$$\sum_{i=1,3} X_{RC,i} = (1 - z_1 z_2 z_3)\phi_1 = 1 \quad (139)$$

Therefore, Campbell's degree of rate control, $X_{RC,i}$, provides an excellent measure of the sensitivity of the overall reaction rate to the kinetic parameters for each step. The value of $X_{RC,i}$ approaches zero as step i becomes quasi-equilibrated, and the value of $X_{RC,i}$ becomes small as the preceding steps that produce the reaction intermediates for step i become irreversible.

Finally, we note that some confusion exists regarding the concept of a rate-determining step. For the three-step reaction scheme of this example, consider the case for which step 1 is quasi-equilibrated and steps 2 and 3 are irreversible:



This case leads to the following values for $X_{RC,i}$:

$$X_{RC,1} = (1 - z_1)\phi_1 = 0 \quad (143)$$

$$X_{RC,2} = z_1(1 - z_2)\phi_1 = \phi_1 = 1 \quad (144)$$

$$X_{RC,3} = z_1 z_2(1 - z_3)\phi_1 = 0 \quad (145)$$

Clearly, step 2 controls the rate of the overall reaction. However, the net rates of all three reactions are equal to the rate of the overall reaction. Therefore, it is not proper to say that the rate of the overall reaction is equal to the rate of the rate-determining step, whereas the rates of the remaining steps are high; that is, it is not proper to denote the rate-determining step as the slow step and the remaining steps as fast steps.

This potential confusion in using the concept of a rate-determining step might be eliminated by denoting a step as being the maximum sensitivity step. In the previous example, although the net rates of steps 1–3 are all equal to the overall rate, the sensitivities of steps 1 and 3 are equal to zero, whereas the sensitivity of step 2 approaches the maximum value of 1.

IV. Case Studies

The desire to formulate reaction schemes in terms of molecular processes taking place on a catalyst surface must be balanced with the need to express the reaction scheme in terms of kinetic parameters that are accessible to experimental measurement or theoretical prediction. This compromise between mechanistic detail and kinetic parameter estimation plays an important role in the use of reaction kinetics analysis to describe the reaction chemistry for a catalytic process. Here, we discuss four case studies in which different compromises are made to develop an adequate kinetic model that describes the available observations determined experimentally and/or theoretically. For convenience, we selected these examples from our work in this field; however, this selection is arbitrary, and many other examples could have been chosen from the literature.

The first case deals with the reversible dehydrogenation of isobutane on PtSn-containing catalysts at elevated temperatures. This example was selected as a case for which the reaction scheme is well established (i.e., the Horiuti–Polanyi reaction scheme) and for which sufficient experimental results are available to identify a rate-limiting step. Accordingly, the general reaction scheme represented by 14 kinetic parameters can be reduced to an analytical rate expression containing 6 kinetically significant parameters. This strategy of starting with a general reaction scheme and justifying approximations to simplify the scheme is the basis for essentially all reaction kinetics analyses. Here, the general case is simple, such that the justifiable approximations lead to an analytical rate expression.

The second case considered in this review deals with ethane hydrogenolysis on Pt-containing catalysts. We illustrate the advantages of lumping quasi-equilibrated steps (i.e., hydrogenation–dehydrogenation steps). An important advantage of using lumped kinetic coefficients to conduct analyses of reaction schemes is that these coefficients minimize complications

from unintentional compensation effects; furthermore, the use of the proper lumped kinetic coefficients provides a more direct approach for identifying the factors controlling the kinetics of the catalytic process. We show that this lumping of quasi-equilibrated steps is appropriate for stable adsorbed species as well as transition states. This example also illustrates the use of theoretical methods [DFT calculations representing Pt(111) and Pt(211) slabs] to generate initial guesses for kinetic parameters. We expect that this strategy of combining theoretical calculations with experimental results to guide analyses of reaction schemes will become widespread.

The third case deals with the conversions of ethanol, acetic acid, and ethyl acetate on Cu-containing catalysts. This case illustrates analyses of reaction schemes leading to multiple reaction products. This situation is commonly encountered in industry, in which the factors controlling product selectivity are often more important than the factors controlling catalytic activity. We illustrate the effective strategy of combining reaction kinetics data obtained by feeding reactants as well as products to the catalytic reactor to probe various aspects of the reaction scheme. This case also continues the trend of combining experimental results with results of theoretical calculations [DFT calculations representing Cu(111) and Cu(211) slabs as well as Cu₁₃ clusters] to generate initial guesses for kinetic parameters. Results from this case suggest that the kinetic parameters for elementary steps may be applied to systems with similar chemistry and coverage regimes.

The final case of this review deals with the conversion of isobutane on solid acid catalysts. This case illustrates the use of a catalytic probe reaction, based on well-defined surface chemistry which displays selectivity patterns that reflect the properties of the active sites. Although the kinetic model is based on well-established "carbenium-ion transition state" chemistry, the reaction scheme includes 312 steps because many combinations of oligomerization and β -scission processes take place involving various olefins and adsorbed species. Furthermore, the model must take into account isomerization steps (that interconvert various adsorbed species) and hydride transfer steps (that lead to the formation of alkane products). Therefore, this example represents the situation in which a kinetic model is needed to help interpret the information contained in an apparently complex product distribution. Furthermore, it illustrates a strategy for parameterizing a kinetic model for a complex reaction scheme, starting with an analysis of the thermodynamic properties of all species, followed by an identification of reaction families into which all steps can be categorized. We speculate that this case might anticipate the use of reaction kinetics analyses to assist the discovery process driven by combinatorial chemistry and high-throughput screening techniques. In particular, we envision that the kinetic model would be used with these approaches to extract information about catalyst systems at the molecular level to identify

common properties that control the reactivities. To be an effective tool in this respect, the kinetic model may need to be based on a complex reaction scheme; furthermore, the model must be consistent with known thermodynamic properties and be based on a limited number of parameters designed to capture the essential surface chemistry.

The four cases described here do not explicitly build into the analyses any effects of surface nonuniformity or surface coverage. (Effects of surface coverage are addressed implicitly in the case of isobutane dehydrogenation.) It is emphasized that these non-Langmuirian effects can easily be included in kinetic models since analyses can be conducted by using numerical methods to solve the reactor and surface coverage equations (i.e., reaction kinetics analyses are not limited to cases for which analytical rate expressions must be derived). Moreover, with recent advances in electronic structure calculations (e.g., DFT methods), it is possible to estimate adsorbate binding energetics on different sites (i.e., surface nonuniformity effects) and to estimate adsorbate binding energetics on surfaces having different coverages and different coadsorbed species (i.e., surface coverage effects). Monte Carlo simulations can then be conducted to predict surface coverages and reaction kinetics for various temperatures and pressures, on the basis of the interaction energies predicted from theoretical calculations (13, 30–32). The results of these Monte Carlo simulations can be used directly to describe the observed reaction kinetics. Alternatively, the Monte Carlo simulation results can be used to develop polynomials in terms of kinetic parameters and pressures that describe the predicted surface coverages and reaction rates over a wide range of conditions, and these polynomials can then be employed in additional analyses by using the techniques outlined in this article. Therefore, although we do not address in detail the effects of surface nonuniformity and surface coverage in the case studies, the methods outlined are directly applicable when these effects may need to be included in the reaction kinetics analyses (e.g., when the reaction conditions are varied so widely that the surface coverage regime changes dramatically).

A. ISOBUTANE DEHYDROGENATION ON SUPPORTED Pt/Sn

The first case study involves isobutane dehydrogenation catalyzed by Pt/Sn-containing materials. Supported Pt/Sn catalysts are highly selective for isobutane dehydrogenation (33, 35). The combined results of adsorption microcalorimetry, steady-state kinetic studies, and Mössbauer spectroscopy have shown that tin interacts with platinum to form Pt/Sn alloy particles, leading to decreases in the size of the surface Pt ensembles and inhibition of the formation of highly dehydrogenated surface species required for the competing isomerization, hydrogenolysis, and coking reactions (36). Subsequent

investigations have shown that the addition of potassium to Pt/Sn/SiO₂ catalysts further increases the selectivity for isobutane dehydrogenation and enhances the rate of isobutane dehydrogenation (37, 38). Furthermore, supporting tin and platinum on the potassium form of zeolite LTL produces a unique material that exhibits high dehydrogenation activity and selectivity (38–41).

The dehydrogenation of isobutane at elevated temperatures (e.g., 700 K) is a reversible reaction. Accordingly, information is obtained from kinetic investigations in which both isobutane dehydrogenation and isobutylene hydrogenation occur. The reaction kinetics analyses of this system involve consolidating experimental results from kinetic investigations of isobutane dehydrogenation and isobutylene hydrogenation, deuterium tracing studies of both the dehydrogenation and hydrogenation reactions, and microcalorimetric measurements of the adsorption of hydrogen and of isobutylene on tin-modified platinum surfaces. These analyses are based on the simple four-step Horiuti–Polanyi reaction scheme:



As written, this reaction scheme incorporates steps that initially are all assumed to be reversible. Accordingly, 14 kinetic parameters would be required to account for the conversions at various temperatures and reaction conditions. The approach to analyze this system involved first analyzing the combined experimental results obtained with silica-supported Pt/Sn catalysts. Fortunately, in this case there is a large amount of information that allows the prediction of many of the desired kinetic parameters (36, 38, 40, 42). Reaction kinetics analysis of the data obtained with Pt/Sn/SiO₂ allows identification of the kinetically important elementary steps and the sensitive parameters. As shown later, this analysis suggests that steps 2–4 are quasi-equilibrated at the conditions of the kinetic studies. Accordingly, a rate expression may be derived for the case for which the first step is rate limiting, and this expression requires only 6 kinetically significant parameters. The rate expression and parameters are then used for analyses of data representing the three investigated catalysts. It was concluded from these analyses that the higher reaction rates on Pt/Sn/KLTL zeolite are caused by stabilization of the activated complex for isobutane dissociation on the small Pt/Sn clusters in the zeolitic micropores and/or stabilization by the presence of potassium (40).

This case is an example of the situation for which a large amount of information at the molecular level can be extracted about the investigated Pt/Sn-containing materials on the basis of analyses of experimental results. It was possible to identify factors that control the nature and the strength of the interaction of the important transition state with a specific catalytic site. A summary of the analyses of isobutane dehydrogenation on Pt/Sn-containing catalysts is provided next.

1. *Experimental Result*

Kinetic studies were conducted to determine reaction rates and kinetic orders for isobutane dehydrogenation and isobutylene hydrogenation on Pt/Sn/SiO₂, Pt/Sn/K/SiO₂, and Pt/Sn/KLTL zeolite catalysts at 673, 723, and 773 K. Typical results are shown in Figs. 1 and 2. Details of the catalyst preparation and the kinetic investigations are given elsewhere (38, 40). Sieved catalyst fractions (80–120 mesh) were mixed with Cab-O-Sil silica at a dilution ratio greater than 19:1 to ensure that the rates were not influenced by transport limitations (43–45). All the data were collected at conversions lower than 15% of the equilibrium values. The product formation rates are reported as turnover frequencies based on the number of surface platinum atoms determined from saturation hydrogen uptakes at 403 K (22 μmol of surface Pt/g, 38 μmol of surface Pt/g, and 4 μmol of surface Pt/g for Pt/Sn/SiO₂, Pt/Sn/K/SiO₂, and Pt/Sn/KLTL zeolite, respectively). The rates of deactivation during isobutane dehydrogenation and isobutylene hydrogenation on Pt/Sn/SiO₂ are low. Accordingly, reaction kinetics data may be obtained for these reactions on relatively clean surfaces.

Figures 1a and 1b show the isobutylene production rates for the three catalysts at 773 K versus the hydrogen and isobutane pressures. These figures show that the addition of potassium to Pt/Sn/SiO₂ nearly doubles the dehydrogenation rate, and the dehydrogenation rates are more than an order of magnitude higher on Pt/Sn/KLTL zeolite than on Pt/Sn/SiO₂ or Pt/Sn/K/SiO₂. Figure 1a shows a negative hydrogen pressure dependence for the dehydrogenation reaction on each of the three catalysts. Figure 1b shows a positive isobutane pressure dependence for the dehydrogenation reaction rate. At the low conversions of this investigation the reaction orders with respect to isobutane pressure were found to be nearly 1 for each of the three catalysts. Figures 2a and 2b show isobutane production rates at 723 K for the three catalysts. Regarding the dehydrogenation reaction, these figures show that the addition of potassium increases the rate of the hydrogenation reaction, and Pt/Sn/KLTL zeolite exhibits hydrogenation reaction rates more than an order of magnitude higher than those observed for Pt/Sn/SiO₂ or Pt/Sn/K/SiO₂. Figure 2a shows a positive hydrogen pressure dependence for

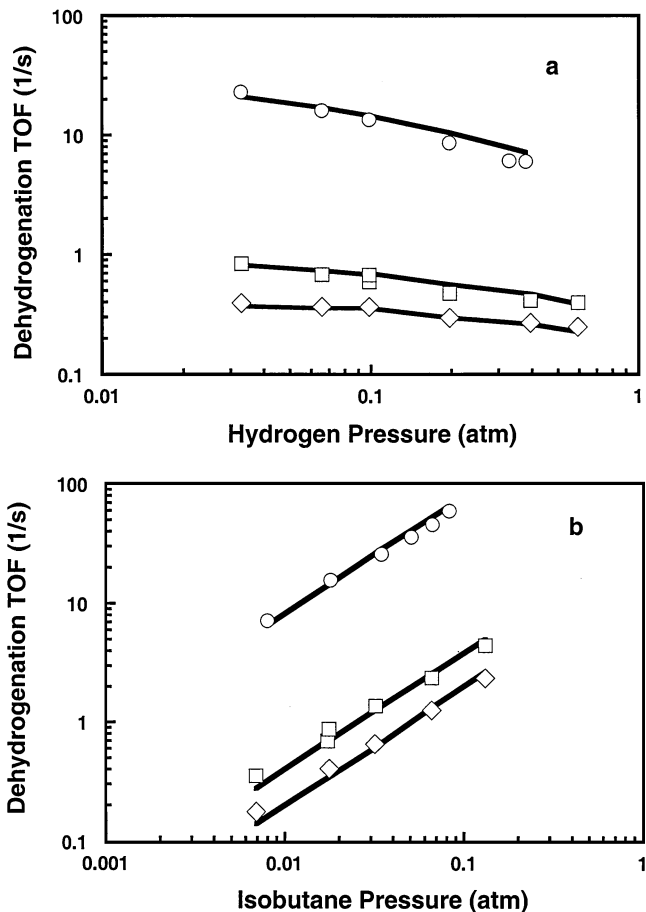


FIG. 1. Turnover frequencies for isobutylene production at 773 K and 0.016 atm isobutane pressure (a) and 0.099 atm hydrogen pressure (b) for reaction catalyzed by Pt/Sn/SiO₂ (\diamond), Pt/Sn/K/SiO₂ (\square), and Pt/Sn/K-L (\circ). Adapted from (40). Solid lines represent the fit for each set of data using the Horiuti-Polanyi mechanism.

the hydrogenation reaction. The hydrogen kinetic orders increased from 0.5 to 1 with increasing temperature. Over the range of isobutylene pressures the isobutylene kinetic orders were observed to vary between 0.7 and unity for each of the three catalysts.

Differential enthalpy changes of hydrogen and isobutylene adsorption were measured, as described elsewhere (36, 42). Figure 3 shows differential heat versus adsorbate coverage for hydrogen and isobutylene adsorption on Pt/Sn/SiO₂. Values of the differential enthalpy changes of adsorption,

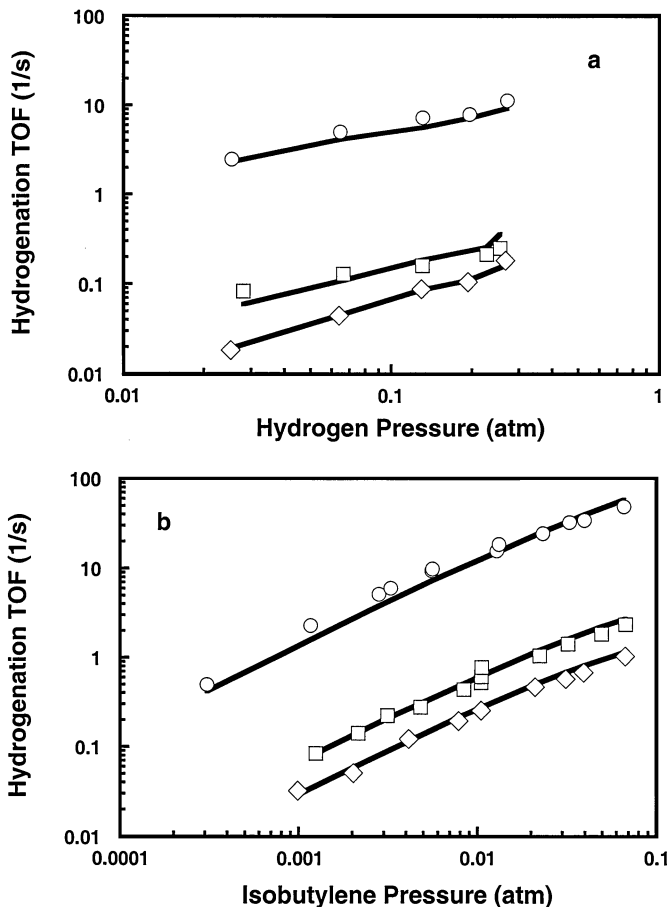


FIG. 2. Turnover frequencies for isobutane production of 723 K and 0.0033 atm isobutylene pressure (a) and 0.13 atm hydrogen pressure (b) for reaction catalyzed by Pt/Sn/SiO₂ (\diamond), Pt/Sn/K/SiO₂ (\square), and Pt/Sn/K-L (\circ). Adapted from (40). Solid lines represent the fit for each set of data using the Horiuti-Polanyi mechanism.

ΔH_{ads} , are negative, and it is convenient to define the heat of adsorption as being equal to $-\Delta H_{\text{ads}}$. Figure 3 shows initial heats for hydrogen and isobutylene adsorptions of 95 and 125 kJ/mol, respectively. In both cases, the heats of adsorption decrease with increasing coverage. The observed heat of isobutylene adsorption has been attributed to the formation of either di- σ -bonded or π -bonded olefin on the tin-modified platinum surface (46). Recent microcalorimetric and infrared spectroscopic measurements characterizing adsorption of ethylene indicate that the addition of tin to

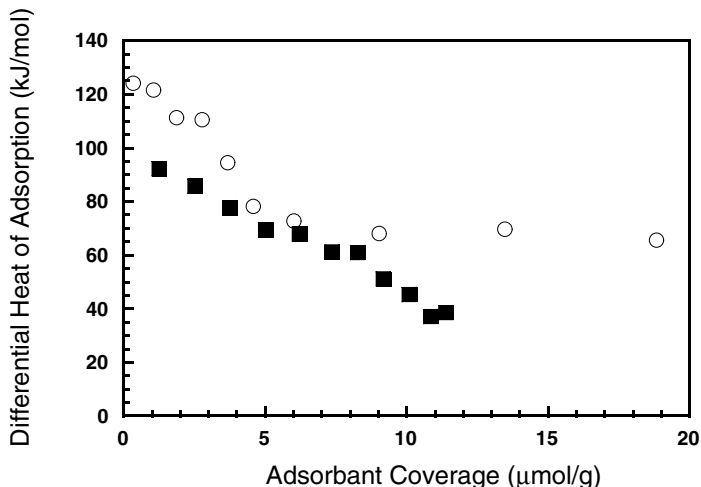


FIG. 3. Differential heats of hydrogen adsorption (■) at 403 K and isobutylene adsorption (○) at 303 K on silica-supported Pt/Sn. Adapted from (40).

supported platinum suppresses the formation of ethylidyne and that significant amounts of π -bonded and di- σ -bonded ethylene are formed on Pt/Sn-containing materials (46). Furthermore, results of a recent theoretical investigation of ethylene adsorption show that the binding energies of π -bonded ethylene, di- σ -bonded ethylene, and ethylidyne are weaker on Pt₃Sn(111) than on Pt(111) by 21, 31, and 50 kJ/mol, respectively (47). It was concluded that the electronic effect of Sn on the adsorption of ethylene depends on the type of adsorption site, with adsorption on threefold sites weakened more than adsorption on twofold and onefold sites.

Deuterium tracing studies were conducted to determine the extent of deuterium incorporation into isobutane and isobutylene during isobutane dehydrogenation and isobutylene hydrogenation reactions. Details of these deuterium tracing experiments are described elsewhere (38). Table I presents the results of deuterium tracing studies for isobutane dehydrogenation on Pt/Sn/SiO₂ at 723 K, 0.20 atm deuterium pressure, and 0.033 atm isobutane pressure. The isobutane conversion was 2.6%, and the equilibrium conversion under these conditions is 14.2%. The amount of deuterium incorporated into isobutylene was also determined for isobutylene hydrogenation on Pt/Sn/SiO₂ at 723 K, 0.91 atm deuterium pressure, and 0.091 atm isobutylene pressure. Table I shows that perdeuterated isobutylene is the predominant species, and the average number of deuterium atoms (M_8) incorporated into an isobutylene molecule is greater than six for isobutane dehydrogenation on the Pt/Sn catalyst. Table I also shows that little deuterium is incorporated

TABLE I
Isobutylene Deuterium Distributions, M_8 and M_{10} ^a

Catalyst reaction conversion	Pt/Sn/SiO ₂ dehydrogenation isobutane 2.6%		Pt/Sn/SiO ₂ hydrogenation isobutylene 12.3%	
	Exp.	Sim.	Exp.	Sim.
d0 (mol%)	0.0	2.0	21.6	22.8
d1 (mol%)	4.8	2.3	13.6	8.0
d2 (mol%)	3.1	2.6	10.6	8.6
d3 (mol%)	2.5	3.0	9.0	9.6
d4 (mol%)	7.7	3.7	8.9	10.9
d5 (mol%)	1.4	4.8	9.4	12.6
d6 (mol%)	3.8	7.6	11.1	13.1
d7 (mol%)	26.1	18.9	10.9	10.3
d8 (mol%)	50.6	55.2	5.0	4.1
M_8 ^b	6.7	6.7	3.3	3.4
M_{10} ^c	1.4	1.0	—	—

^a Adapted from Cortright *et al.* (38). ^b M_8 is the average number of deuterium atoms incorporated into isobutylene. ^c M_{10} is the average number of deuterium atoms incorporated into isobutane.

into isobutane, as indicated by the small value of M_{10} (the average number of deuterium atoms incorporated into isobutane) during the dehydrogenation reaction, and the observed deuterated isobutane contained eight or more deuterium atoms per molecule.

2. Reaction Kinetics Analysis

a. *Reaction Scheme.* The Horiuti–Polanyi reaction scheme was used to describe the combined results from steady-state kinetic studies, deuterium tracing, and temperature-programmed desorption for ethylene hydrogenation on Pt/SiO₂ at temperatures between 248 and 333 K (1, 48). Regarding ethylene hydrogenation, in this case it is desired to develop a reaction scheme with a reasonable set of kinetic parameters that is consistent with microcalorimetric measurements and that describes the observed steady-state reaction kinetics data and deuterium tracing results for isobutane dehydrogenation and isobutylene hydrogenation.

The Horiuti–Polanyi reaction scheme shows that in the case of isobutane, the reaction scheme involves isobutyl and adsorbed olefin intermediates. Cremer *et al.* (49) identified 2-propyl, π -bonded propylene, and di- σ -bonded propylene surface species on platinum during propylene hydrogenation.

These investigators implicated the 2-propyl and π -bonded propylene species as reaction intermediates.

b. *Model Equations and Parameterization.* Reaction kinetics analysis of the steady-state data on the basis of the previous four-step scheme requires the simultaneous solution of three steady-state equations for reactive adsorbed species (H^* , $C_4H_9^*$, and $C_4H_8^{**}$) and the site balance for catalyst surface sites. Furthermore, this kinetic model requires three CSTR equations to describe the molecular flow rates of the gas-phase products. The parameters in these equations are standard entropy and enthalpy changes for the formation of the activated complexes for the forward and reverse reactions of each step (Table II). A general regression analysis was performed to determine a consistent set of parameters to describe the steady-state hydrogenation/dehydrogenation data for the Pt/Sn/SiO₂ catalyst. The model was constrained to maintain overall thermodynamic consistency, to reflect that hydrogen and isobutylene adsorptions are nonactivated, and to maintain heats of adsorption that are consistent with the measured heats of hydrogen and isobutylene adsorption on supported Pt/Sn catalysts (Fig. 3). Over the range of reaction conditions investigated, the average fraction of free sites was found to be 0.65 (38). This value was used to estimate average heats of isobutylene and hydrogen adsorption of 118 and 78 kJ/mol, respectively.

c. *Reaction Kinetics Analyses of Deuterium Tracing Result.* The use of isotopic tracing to elucidate reaction pathways on catalyst surfaces is well established (50). In the analyses of the deuterium tracing data shown in Table I, the approach was to develop a consistent kinetic model that describes both the deuterium tracing results and the steady-state kinetics results for

TABLE II
Kinetic Parameters for the Horiuti–Polanyi Reaction Scheme for Isobutane Dehydrogenation and Isobutylene Hydrogenation

Step	$\Delta S_{\text{for}}^{\ddagger}$ [J/(mol K)]	E_{for} (kJ/mol)	$\Delta S_{\text{rev}}^{\ddagger}$ [J/(mol K)]	E_{rev} (kJ/mol)	$\Delta S_{\text{rx}}^{\circ}$ [J/(mol K)]	ΔH_{rx} (kJ/mol)
1	-166 ± 1	42 ± 1	-20^a	85^a	-146	-43
2	-25 ± 3	42 ± 5	-75 ± 3	72 ± 5	50	-30
3	-22 ± 1	118^b	-167 ± 1	0^c	145	118
4	-141 ± 1	0^c	-48 ± 1	78^b	-93	-78
Total reaction					141	122

^aParameters adjusted to maintain thermodynamic consistency for the overall reaction. ^bConstrained to listed value to be consistent with results from microcalorimetry. ^cAssumption of nonactivated adsorption for both isobutylene and hydrogen.

the dehydrogenation and hydrogenation reactions. This approach is similar to that applied to ethylene hydrogenation on platinum (1, 48). In the current case, the analysis of the deuterium tracing data requires solution of the material balance equation for 23 isotopic gas-phase and 21 isotopic surface species.

d. *Results of Reaction Kinetics Analyses.* Table II shows values of the kinetic parameters that describe the essential aspects of the deuterium tracing and steady-state hydrogenation/dehydrogenation kinetics on Pt/Sn/SiO₂. The reaction kinetics data employed in this fitting procedure consisted of more than 72 steady-state reaction kinetics data points at various pressures of hydrocarbon and hydrogen for both the hydrogenation and dehydrogenation reactions at 673, 723, and 773 K. The rectification plot shown in Fig. 4 indicates good agreement between the observed reaction rates and fitted reaction rates predicted from the Horiuti–Polanyi reaction scheme for both isobutane dehydrogenation and isobutylene hydrogenation on the Pt/Sn catalyst. Furthermore, Table I shows that the reaction scheme simulates closely the amounts and distributions of deuterium incorporation into isobutylene and isobutane for the D₂/isobutane experiments with the catalyst as well as the amount of deuterium incorporated into isobutylene for the D₂/isobutylene study.

e. *Sensitivity Analysis of the Kinetic Model.* The kinetically significant elementary steps may be deduced by using the concepts introduced previously based on De Donder analysis and the values of the fitted kinetic

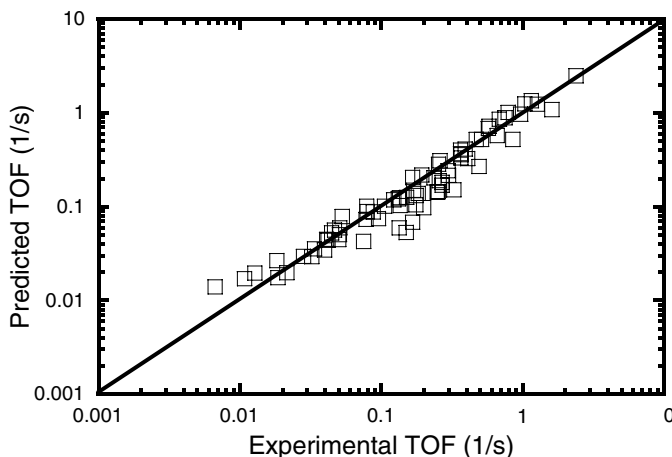


FIG. 4. Rectification plot for isobutane dehydrogenation and isobutylene hydrogenation kinetic data over Pt/Sn/SiO₂. Adapted from (38).

parameters shown in Table II. As an example of typical reaction conditions for isobutylene hydrogenation, consider the case for which the reaction temperature is 673 K and the partial pressures of H_2 , C_4H_8 , and C_4H_{10} are 0.6, 0.2, and 0.2 atm, respectively. For these conditions, the values of z_i can be determined to be the following: $z_1 = 0.0125$, $z_2 = 0.9977$, $z_3 = 0.9962$, $z_4 = 0.9993$, and $z_{total} = 0.0124$.

The fraction of the platinum surface that is free of adsorbed species, θ_* , is equal to 0.084 under these conditions. The most abundant surface intermediates are adsorbed H^* and $C_4H_8^*$, indicating that the only significant kinetic parameters in the expression for θ_* are K_{3eq} and K_{4eq} . It is clear from these values of z_i that steps 2–4 are quasi-equilibrated ($z_i \sim 1$ or $A_i \sim 0$) and step 1 is rate determining ($z_1 \sim z_{tot}$ or $A_1 \sim A_{total}$) under these reaction conditions.

The deuterium tracing results show that isobutylene is highly deuterated during the dehydrogenation reaction, and the small amount of isobutane that becomes deuterated is highly deuterated. These observations are a result of the slow dissociative adsorption of isobutane proceeding simultaneously with the faster removal of hydrogen from the adsorbed isobutyl species. Furthermore, the heats of adsorption determined from the microcalorimetric measurements indicate that the adsorption/desorption steps should be relatively fast at the reaction temperatures of the kinetic studies. The observation that the dissociative adsorption of the isobutane is rate limiting has also been suggested by Lok *et al.* (128) in their investigation of isobutane dehydrogenation on alumina-supported Pt/Sn catalysts.

3. Reaction Kinetics Analyses Based on a Simplified Rate Expression

Since steps 2–4 are quasi-equilibrated under the conditions of the kinetic studies, the following simplified rate expression may be derived to describe the hydrogenation/dehydrogenation reactions:

$$r_{DH} = k_1 \theta_*^2 \left[P_{C_4H_{10}} - \frac{P_{C_4H_8} P_{H_2}}{K_{eq}} \right] \quad (150)$$

where r_{DH} is the net dehydrogenation rate, k_1 is the rate constant for the dissociative adsorption of isobutane, K_{eq} is the overall equilibrium constant for isobutane dehydrogenation, and θ_* is the fraction of sites free of adsorbed species. Previous reaction kinetics analyses indicated that the fractional coverage of isobutyl species is less than 10^{-5} under the reaction conditions of this kinetic study (38). Accordingly, the value of θ_* is dependent only on the adsorption/desorption equilibria for hydrogen and isobutylene and can be determined from the following expression:

$$\theta_* = \frac{-K_3}{4P_{C_4H_8}} \left[1 + \sqrt{K_4 P_{H_2}} - \sqrt{1 + 2\sqrt{K_4 P_{H_2}} + K_4 P_{H_2} + \frac{8P_{C_4H_8}}{K_3}} \right] \quad (151)$$

where K_3 is the equilibrium constant for isobutylene desorption (step 3), and K_4 is the equilibrium constant for hydrogen adsorption (step 4).

The combination of Eqs. (150) and (151) provides a rate expression for the dehydrogenation/hydrogenation reactions that is dependent on the values of k_1 , K_3 , and K_4 (as well as the overall equilibrium constant, K_{eq}). Estimates of these kinetic parameters can be made in terms of physically meaningful quantities such as entropies and enthalpy changes. Transition state theory gives the following expression for k_1 :

$$k_1 = \frac{k_B T}{h} e^{(\Delta S_1^{\ddagger}/R)} e^{(-\Delta H_1^{\ddagger}/RT)} \quad (152)$$

where ΔS_1^{\ddagger} and ΔH_1^{\ddagger} are the standard entropy change and the standard enthalpy change, respectively, for formation of the transition state from gaseous isobutane. Similarly, the equilibrium constants may be described in terms of standard entropy changes (ΔS_3° and ΔS_4°) and enthalpy changes (ΔH_3° and ΔH_4°) for adsorption of isobutylene and hydrogen. These standard entropy changes can be expressed in terms of known gaseous entropies and entropies of the three surface species: adsorbed H atoms, adsorbed isobutylene, and the activated complex for step 1. Accordingly, a quantitative description of the hydrogenation/dehydrogenation reactions may be determined for a given catalyst in terms of six parameters: $S_1^{\circ\ddagger}$, S_{H^*} , $S_{iC_4H_8^*}$, $\Delta H_1^{\circ\ddagger}$, ΔH_3° , and ΔH_4° .

a. *Application of Analyses to Distinguish between Different Catalysts.* The previous rate expression (Eq. 150), and set of parameters allow for the isobutane dehydrogenation and isobutylene hydrogenation reactions to be used as probe reactions to elucidate the effects of catalyst properties on the rate-limiting elementary step. Such analyses were performed to investigate the effects of potassium on the reactivity of silica-supported Pt/Sn as well as platinum and tin supported in the potassium form of LTL zeolite. The values of the kinetic parameters were determined for each of the Pt/Sn catalysts by using a general regression analysis of the apparent rate expression combined with CSTR design equations to fit the combined results of the isobutane dehydrogenation and isobutylene hydrogenation kinetic studies. The number of adjustable parameters was reduced to four by fixing the heats of isobutylene and hydrogen adsorption (ΔH_3° and ΔH_4°) at 118 and 78 kJ/mol, respectively.

The solid lines in Figs. 1 and 2 represent the turnover frequencies predicted by using the previous rate expression and the fitted parameters listed in Table III, which is a list of the values of the fixed and fitted parameters, the 95% confidence limits for the fitted parameters, and the overall relative error of the fitted reaction kinetics data. Figures 1 and 2 show that the kinetic

TABLE III
Fitted Parameter Table for Isobutane Dehydrogenation and Isobutylene Hydrogenation on Pt/Sn-Containing Materials^a

Catalyst	Step 1: forward activation		Step 3: quasi-equilibrium		Step 4: quasi-equilibrium		Relative error (%)	Sticking coefficient
	S_1^\ddagger (J/mol/K)	$\Delta H_1^{\ddagger\dagger}$ (kJ/mol)	$S_{C_3H_8^*}$ (J/mol/K)	ΔH_3° (KJ/mol)	S_{H^*} (J/mol/K)	ΔH_4° (KJ/mol)		
Pt/Sn/silica	273.7 ± 9.3	60.9 ± 7.6	253.6 ± 3.9	118 fixed	22.9 ± 7.0	-78 fixed	12.9	4.0×10^{-3}
Pt/Sn/K/silica	256.9 ± 8.4	41.9 ± 7.1	256.5 ± 3.5	118 fixed	26.4 ± 4.2	-78 fixed	16.0	5.0×10^{-4}
Pt/Sn/LTL zeolite	265.4 ± 7.7	24.3 ± 7.1	262.2 ± 4.9	118 fixed	35.1 ± 5.5	-78 fixed	14.4	1.5×10^{-3}

^aAdapted from Cortright *et al.* (40).

model provides a good fit of the data for the three Pt/Sn catalysts, with average relative errors being between 13 and 16% (Table III).

Table III shows the best fit for parameters that describe the forward rate constant of step 1. Similar fits could be obtained by using different sets of values for S_1^\ddagger and ΔH_1^\ddagger because of the compensation effect caused by the limited temperature range of this investigation. However, the fitted values of the entropies for the transition state correspond to sticking coefficients between 5.0×10^{-4} and 4.0×10^{-3} . These sticking coefficients are within the range of values reported for isobutane dissociation on Pt (110)-(1 × 2) (51).

Table IV is a list of values of entropies (52) for gaseous atomic hydrogen, molecular hydrogen, isobutane, and isobutylene at 723 K and 1 atm. This table also includes the entropies when these species have zero degrees of translational freedom (S_{loc}), one degree of translational freedom ($S_{\text{loc}+1\text{D}}$), and two degrees of translational freedom ($S_{\text{loc}+2\text{D}}$). The values of $S_{\text{loc}+1\text{D}}$ and $S_{\text{loc}+2\text{D}}$ were calculated by assuming surface densities of $(10^{15})^{0.5} \text{ cm}^{-1}$ and 10^{15} cm^{-2} , respectively. Comparison of the fitted entropies of Table III with the calculated entropies of Table IV provides information about the mobility of the various surface species. The fitted entropies for the transition state of step 1 are between the values of S_{loc} and $S_{\text{loc}+1\text{D}}$, indicating a relatively immobile transition state. Tables III and IV show that the entropies of adsorbed isobutylene are also between the values of S_{loc} and $S_{\text{loc}+1\text{D}}$ for each of the three catalysts, and adsorbed hydrogen atoms are more mobile than adsorbed isobutylene. Furthermore, the entropies of adsorbed isobutylene and atomic hydrogen on the various catalysts appear to increase in the following order: Pt/Sn/KLTL zeolite > Pt/Sn/K/SiO₂ > Pt/Sn/SiO₂. These results suggest that adsorbed isobutylene and hydrogen are least mobile on Pt/Sn/SiO₂ and most mobile on Pt/Sn/KLTL zeolite.

The parameters of Table III suggest that the higher reaction rates on Pt/Sn/KLTL zeolite and Pt/Sn/K/SiO₂ may be attributed to the stabilization of adsorbed species on the small Pt/Sn clusters within the zeolite micropores and/or stabilization by the presence of potassium. For example, equilibrium constants for hydrogen adsorption at the average temperature of

TABLE IV
Gas-Phase Entropies of Different Species at 723 K and 1 atm^a

Species	S_{total}° (J/mol/K)	S_{loc} (J/mol/K)	$S_{\text{loc}+1\text{D}}$ (J/mol/K)	$S_{\text{loc}+2\text{D}}$ (J/mol/K)
H	133.0	0.0	25.6	43.0
H ₂	156.6	20.8	49.3	69.5
<i>i</i> C ₄ H ₁₀	420.6	242.8	285.3	319.5
<i>i</i> C ₄ H ₈	404.7	227.4	269.8	303.8

^aFrom Cortright *et al.* (40) and Stull *et al.* (52).

723 K appear to be 2.3 and 19 times greater for adsorption on Pt/Sn/K/SiO₂ and Pt/Sn/KLTL zeolite, respectively, than for Pt/Sn/SiO₂. Furthermore, the equilibrium constants for isobutylene adsorption at 723 K are 1.4 and 2.8 times greater for adsorption on Pt/Sn/K/SiO₂ and Pt/Sn/KLTL zeolite, respectively, than for adsorption on Pt/Sn/SiO₂. Moreover, the free energy change to form the activation complex for step 1 at 723 K decreases in the following order:

$$\begin{array}{ccccc} \text{Pt/Sn/SiO}_2 & > & \text{Pt/Sn/K/SiO}_2 & > & \text{Pt/Sn/KLTL zeolite} \\ (167 \text{ kJ/mol}) & & (160 \text{ kJ/mol}) & & (136 \text{ kJ/mol}) \end{array} \quad (153)$$

This trend suggests that the activated complex of step 1 is also stabilized on Pt/Sn/K/SiO₂ and Pt/Sn/KLTL zeolite relative to Pt/Sn/SiO₂.

Langmuirian kinetics on a uniform surface were used to analyze the results of this kinetic investigation. The successful application of the proposed rate expression based on the four-step Horiuti–Polanyi reaction scheme is attributed to the relatively clean surface at the reaction conditions investigated ($0.45 < \theta_* < 0.75$). Furthermore, the fitted entropy values shown in Table III are appropriate for the indicated heats of adsorption, and similar fits could be achieved by using different entropy values with different heats of adsorption according to the compensation effect. However, the heats of adsorption are relatively constant over the coverage regime of this investigation (36–39, 42) (i.e., ΔH_4^\ddagger increases from 70 to 85 kJ/mol as θ_* increases from 0.45 to 0.75). Accordingly, the heats of adsorption used for this analysis (Table III) are representative for the conditions of this study.

B. ETHANE HYDROGENOLYSIS ON SILICA-SUPPORTED PLATINUM

Currently, quantum chemical techniques are being applied to identify the geometries, energetics, and vibrational modes of species interacting with catalytic sites consisting of clusters or periodic arrangements of atoms (2, 3). In this case study, quantum chemical calculations are first applied to probe the nature and energetics of various stable adsorbed C₂H_x species on platinum (53, 54). These theoretical results are then used to help interpret the experimental results from combined spectroscopic and microcalorimetric studies (46, 53). These same quantum chemical techniques are then applied to predict the nature and energetics of reactive surface species that cannot be observed experimentally. For example, these theoretical methods allow prediction of the structures and energetics of the transition states involved in the C–C bond cleavage for various C₂H_x species adsorbed on platinum (53, 55).

As outlined later, the combined results of experimental and theoretical investigations are used to develop a potential energy diagram for the interactions of various C₂H_x species adsorbed on platinum. This potential

energy diagram is then used to make initial estimates of kinetic parameters representing the hydrogenolysis of ethane on platinum (53, 55). Ethane hydrogenolysis has been used as a bellwether probe reaction of the catalytic properties of various supported metals and alloys. The results of our analyses based on the potential energy diagram from DFT calculations suggest that the most abundant surface species during ethane hydrogenolysis are adsorbed atomic hydrogen and highly dehydrogenated hydrocarbon species (e.g., ethylidyne). However, the DFT results indicate that the primary reaction pathways for cleavage of the C–C bond on platinum take place through transition states that are more highly hydrogenated (e.g., adsorbed C_2H_5 and $CHCH_3$ species). Importantly, results of our DFT calculations indicate that adsorbed C_2H_x species and transition states interact more strongly with stepped Pt(211) surfaces than with flat Pt(111) surfaces, in agreement with the known structure sensitivity of ethane hydrogenolysis on platinum catalysts (53, 55).

1. Experimental Results

a. *Reaction Kinetics Data for Ethane Hydrogenolysis on Platinum.* Reaction rates and partial pressure dependencies characterizing ethane hydrogenolysis were measured with a silica-supported platinum catalyst at 573, 623, and 673 K. Details of the catalyst preparation and the kinetic studies are given elsewhere (56). These data were collected with the catalyst in a substantially clean state by using techniques similar to those employed by Bond and Cunningham (57) and Sinfelt *et al.* (58–61). The procedure consisted of reducing the catalyst at 723 K for 1 h in flowing hydrogen. The reactant gases were allowed to pass over the catalyst for a period of 1 min, at which time the reactant effluent was sampled. The catalyst was treated in flowing hydrogen for 15 min at the reaction temperature before the next experimental point was collected.

Figures 5 and 6 show the experimentally measured rates of ethane hydrogenolysis on Pt/SiO₂. These figures show the change of the methane production rate with respect to the ethane and hydrogen pressures at 573, 623, and 673 K. Tests were conducted under replicate conditions to track possible changes in catalytic activity (e.g., deactivation). Data points for these replicate tests are shown in Figs. 5 and 6. The experimental error determined from these points was less than 6%. Figure 5 shows a negative hydrogen pressure dependence at higher hydrogen pressures and lower temperatures. Furthermore, this figure shows that the kinetic order in hydrogen becomes less negative at lower hydrogen pressures and higher temperatures. Figure 6 shows that the ethane pressure dependence decreases from approximately 1 to 0 as the temperature increases from 573 to 673 K for a hydrogen pressure

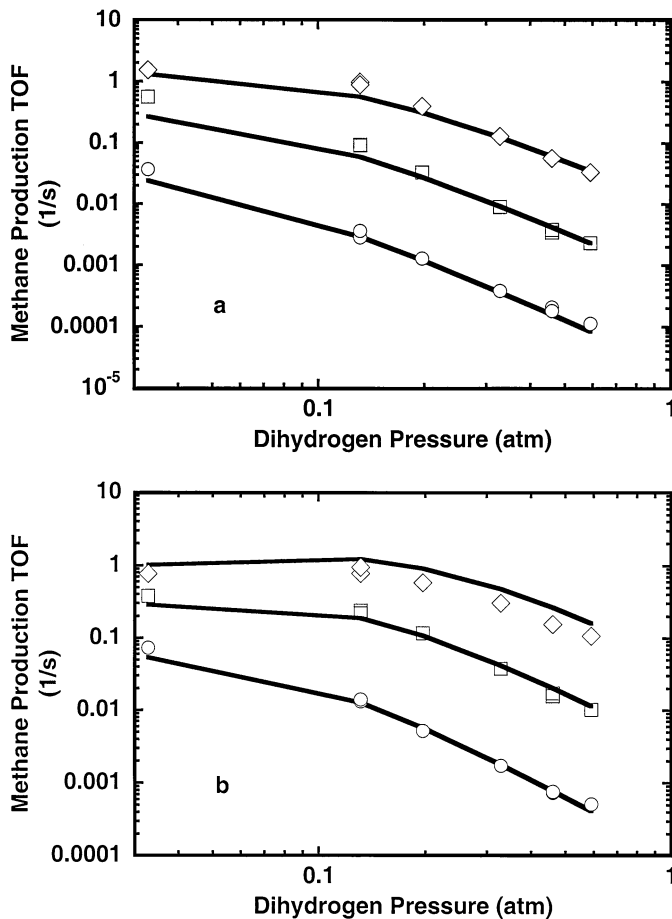


FIG. 5. Dihydrogen pressure dependencies for ethane hydrogenolysis at 0.0066 (a) and 0.033 (b) atm ethane pressures (experimental results: \circ , 573 K; \square , 623 K; and \diamond , 673 K). Predicted rates given by solid lines. Adapted from (55).

of 0.13 atm. In contrast, this figure shows that the ethane kinetic order is near unity at all temperatures at the higher hydrogen pressure of 0.46 atm.

2. Theoretical Results

Quantum chemical calculations employing density functional theory were performed to investigate the interactions of various C_2H_x species adsorbed on flat Pt(111) and stepped Pt(211) slabs (53). These calculations primarily used two-layer slabs of Pt(111) and Pt(211), periodically repeated in a

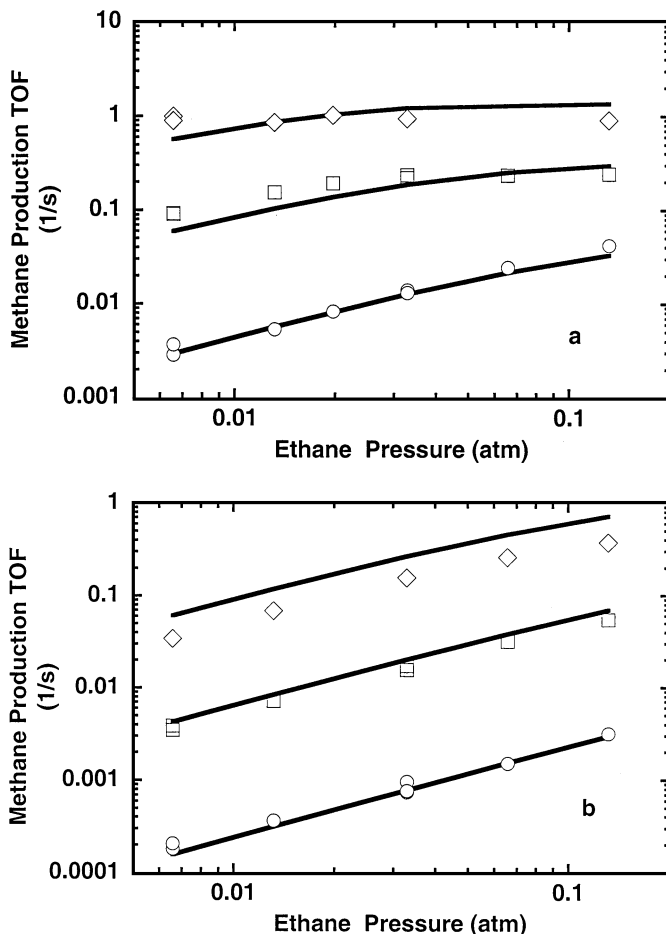


FIG. 6. Ethane pressure dependencies for ethane hydrogenolysis at 0.13 (a) and 0.46 (b) atm dihydrogen pressure (experimental results: ○, 573 K; □, 623 K; and ◇, 673 K). Predicted rates given by solid lines. Adapted from (55).

supercell geometry with four equivalent layers of vacuum between any two successive metal slabs. These slabs are shown in Fig. 7. Three-layer slabs were also investigated to determine the effect of the slab thickness on the calculated binding energies for several adsorbates. The calculated equilibrium lattice constant was 4.00 Å. A 2×2 unit cell was used to study the adsorption of various species, corresponding to one-fourth monolayer coverage. Adsorption occurs on one side of the slab to avoid errors originating from the spurious interactions of adsorbates through the slab. In most calculations,

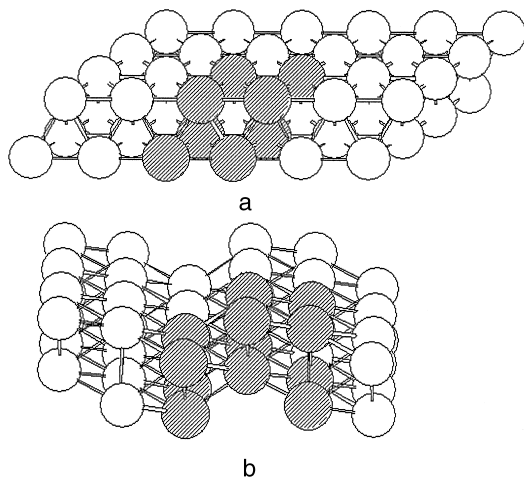


FIG. 7. Models of platinum slabs: (a) Pt(111) slab, (b) Pt(211) slab. Shaded atoms illustrate the supercell used for slab calculations. Adapted from (53).

the adsorbate atoms were allowed to relax, and the surface layer was kept fixed; however, the effects of surface atom relaxations were also investigated in several cases. Ionic cores are described by ultra-soft pseudopotentials (62), and the Kohn–Sham one-electron valence states are expanded in a basis of plane waves with kinetic energies less than 25 Ry. The surface Brillouin zone is sampled at 18 special k points. The exchange–correlation energy and potential are described by the generalized gradient approximation (PW-91) (34, 63). The self-consistent PW-91 density is determined by iterative diagonalization of the Kohn–Sham Hamiltonian, Fermi population of the Kohn–Sham states ($k_B T = 0.1$ eV), and Pulay mixing of the resulting electronic density (64). All the reported binding energies are calculated using the PW-91 functional, and these energies have been extrapolated to $k_B T = 0$. The calculated values for the energetics of various species adsorbed on Pt(111) and Pt(211) are summarized in Table V.

a. *Adsorption of Hydrogen on Pt(111) and Pt(211)*. DFT calculations predict that hydrogen atoms adsorb on threefold sites on the Pt(111) surface (53). The calculated energies for dissociative adsorption of a dihydrogen molecule for one-fourth monolayer and full monolayer coverages are -85 and -81 kJ/mol, respectively. Hence, there appear to be minimal adsorbate/adsorbate interactions between hydrogen atoms on Pt(111). The experimental value of the heat of H_2 dissociation is -90 kJ/mol for supported platinum catalysts and platinum powder (36, 65, 66). In the same

TABLE V
Summary of DFT Calculation Results for Reactions of Ethane on Pt(111) and Pt(211)^{a,b}

Step	Reaction	$\Delta E_{\text{electronic}}$ (kJ/mol)		ΔH° (kJ/mol)		ΔS° (J/mol/K)	ΔG° (kJ/mol)	
		(111)	(211)	(111)	(211)		(111)	(211)
S1	$\text{C}_2\text{H}_6 + \text{*} \rightleftharpoons \text{*C}_2\text{H}_5 + 0.5 \text{H}_2$	51	6	46	1	-92	103	58
S2	$\text{C}_2\text{H}_6 + \text{*} \rightleftharpoons \text{*C}_2\text{H}_4 + \text{H}_2$	70	-1	53	-18	-43	80	9
S3	$\text{C}_2\text{H}_6 + \text{*} \rightleftharpoons \text{*CHCH}_3 + \text{H}_2$	104	19	77	-8	-33	98	13
S4	$\text{C}_2\text{H}_6 + \text{*} \rightleftharpoons \text{*CHCH}_2 + 1.5 \text{H}_2$	128	80	97	49	18	86	38
S5	$\text{C}_2\text{H}_6 + \text{*} \rightleftharpoons \text{*CCH}_3 + 1.5 \text{H}_2$	58	45	30	17	35	8	-5
S6	$\text{C}_2\text{H}_6 + \text{*} \rightleftharpoons \text{*CCH}_2 + 2 \text{H}_2$	157	138	119	100	86	65	46
S7	$\text{H}_2 + 2 \text{*} \rightleftharpoons 2\text{H}^*$	-85	-146	-91		-119	-17	
T1	$\text{C}_2\text{H}_6 + \text{*} \rightleftharpoons \text{*C}_2\text{H}_5^\ddagger + 0.5 \text{H}_2$	224	108	213	97	-107	280	164
T2	$\text{C}_2\text{H}_6 + \text{*} \rightleftharpoons \text{*C}_2\text{H}_4^\ddagger + \text{H}_2$		192		168		-40	193
T3	$\text{C}_2\text{H}_6 + \text{*} \rightleftharpoons \text{*CHCH}_3^\ddagger + \text{H}_2$	210	182	187	159	-43	214	186
T4	$\text{C}_2\text{H}_6 + \text{*} \rightleftharpoons \text{*CHCH}_2^\ddagger + 1.5 \text{H}_2$	288	241	253	206	16	242	196

^aThermodynamic properties (ΔH° , ΔS° , and ΔG°) determined at 623 K and 1 atm. Adapted from Watwe *et al.* (53). ^bThe calculated standard entropies (1 atm, 623 K) for gaseous ethane and dihydrogen are 278 and 152 J/mol/K, respectively.

investigation, DFT calculations showed that hydrogen adsorbs on a twofold site on the step edge of Pt(211) with an energy change of -146 kJ/mol for dissociative adsorption of dihydrogen.

b. *Adsorption of Ethylene on Pt(111)*. Various theoretical studies have addressed the adsorption of ethylene on platinum (53, 54, 67, 68). Figure 8a shows the adsorption of di- σ -bonded ethylene having the symmetrical structure with the C-C axis oriented parallel to the Pt(111) surface. The binding energy of this molecularly adsorbed ethylene was calculated to be -101 kJ/mol. Stuck *et al.* (69) reported that the heat of ethylene adsorption to form di- σ -bonded ethylene is -136 kJ/mol on a Pt(110)(2×1) surface at room temperature. Microcalorimetric results for ethylene adsorption on platinum powders at 173 K show a heat of -120 kJ/mol (65), conditions for which di- σ -bonded ethylene species are predominant on the surface (46).

Studies of the interactions of ethylene with Pt(111) at temperatures higher than 280 K indicate that ethylene adsorbs dissociatively and rearranges such that the C-C axis is oriented perpendicular to the surface (70). The resulting ethylidyne species prefers the threefold site on Pt(111), as shown in Fig. 8b. DFT calculations for adsorbed ethylidyne at threefold hollow sites give an

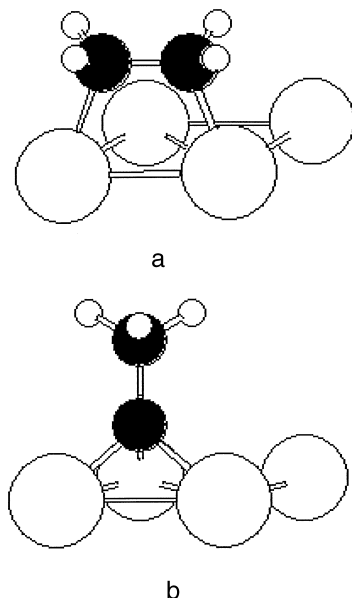


FIG. 8. Adsorption of (a) di- σ -bonded ethylene on bridge site and (b) ethylidyne species on Pt(111). Adapted from (53).

energy change for the formation of ethylidyne from gas-phase ethylene (with the liberation of gas-phase dihydrogen) of -113 kJ/mol. Since the energy of H_2 adsorption on Pt(111) is calculated to be -85 kJ/mol, the energy change for ethylene adsorption with the formation of ethylidyne and hydrogen on the surface is -156 kJ/mol. Stuck *et al.* (69) reported a heat of -174 kJ/mol for adsorption of ethylene on Pt(111), which was attributed to the formation of ethylidyne and coadsorbed H atoms. Microcalorimetric measurements showed a heat of -160 kJ/mol for ethylene interacting with platinum powder at 303 K (65). DFT calculations were performed to study the effect of slab thickness and adsorption-induced surface relaxation (53). These calculations predicted the formation of ethylidyne on a three-layer Pt(111) slab, for which the upper layer was allowed to relax. These calculations showed an energy change for the formation of ethylidyne from gas-phase ethylene with the liberation of gas-phase dihydrogen of -97 kJ/mol, which is more endothermic by 16 kJ/mol than the value predicted for the two-layer, fixed slab.

DFT calculations were also performed to predict the structure and energies for the formation of adsorbed C_2H_5 , $CHCH_3$, $CHCH_2$, and CCH_2 on Pt(111) (53). Table V shows the energy changes to form adsorbed C_2H_x species from gas-phase ethane with the liberation of gas-phase dihydrogen.

c. *Adsorption of Ethylene on Pt(211)*. DFT calculations were performed to determine the structures and energies of C_2H_x species adsorbed on a stepped Pt(211) surface (53). Figure 9b shows the optimized geometry of di- σ -bonded ethylene adsorbed on the step edge of Pt(211). A step-edge platinum atom has a coordination number of 7, and a terrace platinum atom has a coordination number of 9. The calculated binding energy of ethylene on Pt(211) is -172 kJ/mol, and the binding is stronger than that of ethylene on Pt(111) by 71 kJ/mol. Figure 9d shows the optimized geometry of adsorbed ethylidyne on Pt(211). The energy change for the formation of ethylidyne on Pt(211) from gas-phase ethylene with the liberation of gas-phase dihydrogen is -126 kJ/mol; the reaction is more exothermic than that on Pt(111) by only 13 kJ/mol.

The optimized geometries of adsorbed C_2H_5 , $CHCH_3$, and $CHCH_2$ on Pt(211) are shown in Figs. 9a, 9c, and 9e. These species bind more strongly on Pt(211) than on Pt(111) by 45, 85, and 48 kJ/mol, respectively. DFT calculations were also performed to investigate the adsorption of ethyl species on a three-layer Pt(211) slab, with the upper Pt layer free to relax. The calculated energy change for the formation of ethyl species on the surface from gas-phase ethane with the liberation of gas-phase dihydrogen is 7 kJ/mol, which is similar to the corresponding energy change of 6 kJ/mol for the

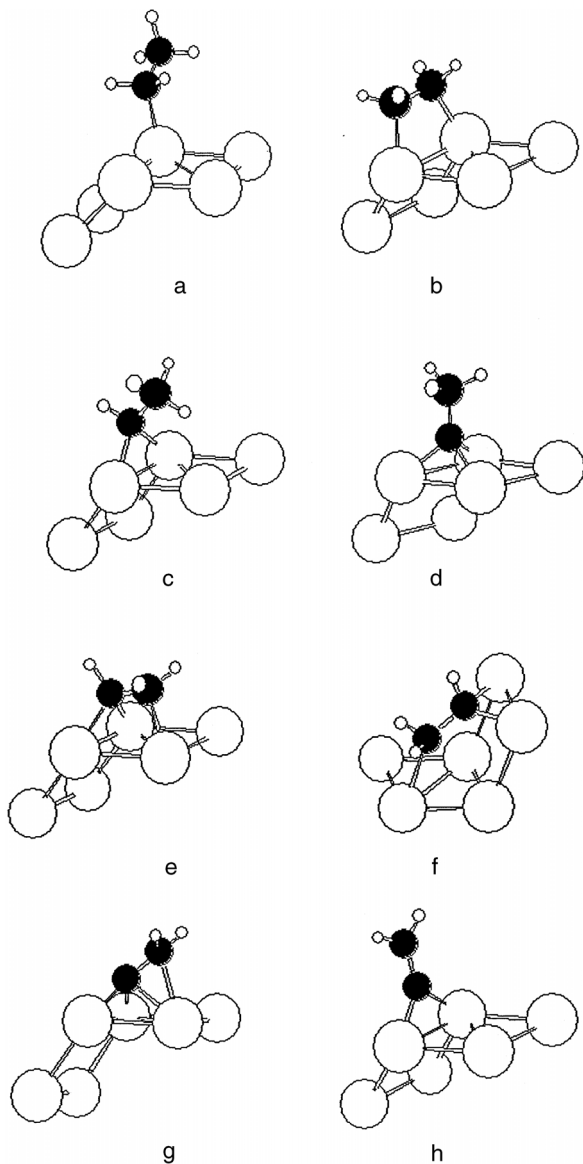


FIG. 9. Adsorption of ethyl species (a), di- σ -bonded ethylene (b), ethylidene species (c), ethynylidyne species (d), vinyl species on step edge (e), vinyl species on the special site (f), di- σ / π vinylidene species (g), and μ_2 -vinylidene species on Pt(211) (h). Adapted from (53).

two-layer Pt(211) slab. The platinum atom bonded to the ethyl species moves upward by 0.01 Å and the neighboring platinum atom on the step edge moves downward by 0.17 Å as a result of surface relaxation.

Also investigated was a different form of CHCH₂ adsorbed on the step, as shown in Fig. 9f. This species is bonded to platinum atoms on step edges as well as on different (111) terraces. This species is less stable than the adsorbed CHCH₂ species of Fig. 9e (by 92 kJ/mol). Whereas one carbon atom in this species forms two bonds with the step edge, having bond length of 2.05 Å, the other carbon atom near the (111) terrace is at a longer distance of 2.49 Å from a platinum atom. The rationale behind studying such a species is to investigate the effect of the specific geometry available at the step edge for C–C bond dissociation.

Figure 9g shows the di-σ/π vinylidene species adsorbed on the step edge of Pt(211). The calculated energy of acetylene adsorption to form this species is –254 kJ/mol, in agreement with results of a microcalorimetric study of acetylene on Pt(211) showing an initial heat of adsorption of –270 ± 10 kJ/mol (71). Figure 9h shows the μ₂ form of the vinylidene species on Pt(211), for which the C–C bond length is 1.34 Å, corresponding to a C=C double bond. The energy of acetylene adsorption to form this species is –237 kJ/mol. Hence, the di-σ/π form of the vinylidene species is slightly more stable than the μ₂ form of the vinylidene species on Pt(211).

d. *C–C Bond Activation on Pt(111) and Pt(211).* Constrained geometry optimizations were conducted to map the potential energy surface for cleavage of the C–C bond for adsorbed C₂H₅, CHCH₃, and CHCH₂ (53). In particular, the value of the C–C bond length was fixed at various values, and the geometry of the constrained adsorbate on the Pt(111) and Pt(211) surfaces was optimized. After a series of such calculations, an approximate maximum was located in the plot of energy versus C–C bond length. The forces on the carbon atoms were also monitored for the various intermediate structures represented in this plot, and it was confirmed that the slope of these forces changes its sign at the energy maximum, verifying that the structure at this maximum is close to a transition state connecting the reactants and products.

The approximate transition state structures for C–C bond dissociation of ethyl, di-σ-bonded ethylene, ethylidene, and vinyl on Pt(211) are shown in Fig. 10. Two transition states for C–C cleavage of ethylidene were identified (adsorbed CHCH₃; Figs. 10c and 10d), as were two transition states for C–C cleavage of vinyl (adsorbed CHCH₂; Figs. 10e and 10f). The configuration of the ethylidene activated complex shown in Fig. 10c is more stable than the configuration shown in Fig. 10d (by 10 kJ/mol) since the former species has more bonds with the step edge atoms. The configuration of the vinyl

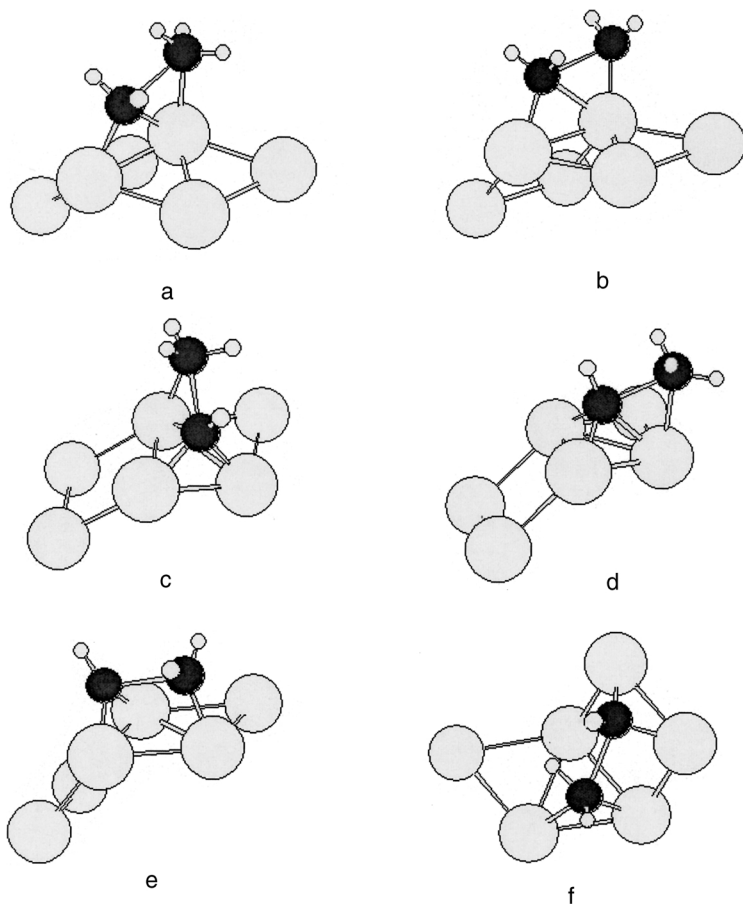


FIG. 10. Adsorption of activated ethyl species (a), di- σ -bonded ethylene (b), ethylidene species (c and d), vinyl species on the step edge (e), and vinyl species on the special site of Pt(211) (f). Adapted from (53).

activated complex shown in Fig. 10e is more stable than the configuration shown in Fig. 10f (by 17 kJ/mol).

The results of the DFT calculations for various stable C₂H_x species and transition states on Pt(111) and Pt(211) are summarized in Table V, which also shows entropy changes for the various steps, as estimated from DFT calculations of the vibrational frequencies of the various adsorbed C₂H_x species and transition states on 10-atom platinum clusters (53). Table V also includes estimates of the standard Gibbs free energy changes for the formation of stable C₂H_x surface species and activated complexes responsible for C–C bond cleavage at 623 K. These estimates were made by combining

the energetic information obtained from DFT calculations involving C_2H_x species on platinum slabs, with entropic information obtained from DFT calculations involving C_2H_x species on platinum clusters. The results of Table V show that the processes with the most favorable changes in Gibbs free energies are steps S7 and S5—that is, the formation of atomic hydrogen and ethylidyne (CCH_3) on platinum. In contrast, the lowest Gibbs free energy barrier for cleavage of the C–C bond is through the activated complex based on ethyl species (C_2H_5). Furthermore, Table V shows that the calculated values of the activation barriers are significantly lower on Pt(211) than on Pt(111), illustrating the structure sensitivity of ethane hydrogenolysis on platinum.

3. Reaction Kinetics Analysis

The results of DFT calculations summarized in Table V provide an initial estimate of the potential energy surface involved in the formation and reaction of various C_2H_x species adsorbed on platinum. Results of this table predict that the principal pathways for C–C bond cleavage involve activated complexes that are more highly hydrogenated (e.g., adsorbed $CHCH_3$ and C_2H_5) than the most abundant surface intermediates (e.g., CCH_3). Accordingly, the reactive C_2H_x species that are responsible for C–C bond cleavage are not necessarily the most abundant surface intermediates that can be observed spectroscopically. However, the most abundant surface intermediates (e.g., atomic hydrogen and CCH_3) still play an important role in the reaction kinetics by determining the fraction of the surface available for catalytic reaction (i.e., they participate in site blocking).

In view of the accuracy of today's quantum chemical calculations, it is typically necessary to adjust the initial estimates of the potential energy surface to describe the observed kinetics of a catalytic process. Accordingly, the theoretical results presented in Table V provide only initial guesses for the entropies and enthalpies of the stable species and reactive intermediates involved in ethane hydrogenolysis on platinum.

a. *Reaction Scheme for Ethane Hydrogenolysis.* On the basis of the results of DFT calculations shown in Table V, the reaction scheme shown in Table VI was used to describe the reaction kinetics data for ethane hydrogenolysis on platinum shown in Figs. 5 and 6. This reaction scheme incorporates the quasi-equilibrated formation of adsorbed C_2H_x species with $2 \leq x \leq 5$ and C–C bond cleavage of adsorbed C_2H_x species with $3 \leq x \leq 5$. Consistent with the manner in which the DFT results are reported in Table V, the surface coverages by stable C_2H_x species and activated complexes for C–C cleavage are expressed in terms of quasi-equilibrium coefficients and partial pressures of ethane and dihydrogen.

TABLE VI
Fitted Parameters for Ethane Hydrogenolysis on Pt/SiO₂ at 623 K^a

Step	Reaction	ΔS° (J/mol/K)	ΔH° (kJ/mol)	ΔG° (kJ/mol)	ΔG° difference (kJ/mol) ^b
S1	C ₂ H ₆ + * ⇌ *C ₂ H ₅ + 0.5 H ₂	-47 ^c	1 ^d	30	28
S2	C ₂ H ₆ + * ⇌ *C ₂ H ₄ + H ₂	-9 ^c	-4 ± 6	2	7
S5	C ₂ H ₆ + * ⇌ *CCH ₃ + 1.5 H ₂	69 ^c	-44 ± 11	1	-6
S6	C ₂ H ₆ + * ⇌ *CCH ₂ + 2 H ₂	110 ^c	100 ^d	31	15
S7	H ₂ + 2* ⇌ 2H*	-68 ^a (constrained) ^e	-54 ± 6.4	-12	-5
T1	C ₂ H ₆ + * ⇌ *C ₂ H ₃ [‡] + 0.5 H ₂	-120 ^f	82 ± 14	159	5
T3	C ₂ H ₆ + * ⇌ *CHCH ₃ [‡] + H ₂	-55 ^f	109 (constrained) ^g	143	43
T4	C ₂ H ₆ + * ⇌ *CHCH ₂ [‡] + 1.5 H ₂	7 ^f	156 (constrained) ^g	151	44

^aAdapted from Cortright *et al.* (55). ^bDifference between theoretical ΔG° (see Table V) and the fitted ΔG° of this table. ^cFitted parameter is the ratio of surface entropy to the DFT-predicted entropy for the adsorbed species. The value of this parameter was found to be 1.4 ± 0.15. ^dParameters maintained at values predicted by DFT calculations (see Table V). ^eValue constrained such that adsorbed hydrogen does not exceed two degrees of translational mobility. ^fFitted parameter is the ratio of surface entropy of the activated complex to the DFT-predicted entropy of that activated complex. The value of this parameter was found to be 0.86 ± 0.13. ^gValue constrained to be within 50 kJ/mol of the theoretical value.

Importantly, the results from De Donder analyses of a general reaction scheme for ethane hydrogenolysis indicate that the rate of the overall reaction can be described in terms of a series of lumped reaction steps involving the formation of stable adsorbed C_2H_x species and transition states from gas-phase ethane and dihydrogen (55). On platinum catalysts, these lumped reactions that form stable C_2H_x species are quasi-equilibrated, an inference drawn from the results of deuterium tracing experiments showing that exchange reactions between ethane and deuterium that yield deuterated ethane occur at rates higher than that of the hydrogenolysis reaction. In particular, Zaera and Somorjai (72) showed that the deuterium exchange rates were three orders of magnitude higher than the rate of ethane hydrogenolysis on Pt(111) at temperatures between 475 and 625 K.

An important advantage of using lumped equilibrium to conduct analyses of reaction schemes is that the resulting equilibrium constants eliminate complications from unintentional compensation effects (55). If the kinetic model had been formulated in terms of the individual rate coefficients for the elementary steps, then it would appear that the rates of specific steps might depend on the strength of interaction of atomic hydrogen with the surface. Accordingly, the use of the proper lumped kinetic coefficients provides a more direct approach for identifying the factors controlling the kinetics of the catalytic process.

Another unintentional compensation effect would be introduced into the kinetic model by expressing the activation barrier for cleavage of the C–C bond in terms of the energy of the corresponding stable, adsorbed C_2H_x species. If this species remains at a low concentration on the surface, then one recognizes from the De Donder relationships that the kinetic parameters controlling the surface coverage by this species are not significant. However, the kinetic parameters that control the coverage by this species can be significant if the properties of the kinetically significant transition state are defined in terms of the properties of the stable adsorbed species (55).

b. *Parameterization of the Kinetic Model.* Table VI shows the values of the parameters used to describe the observed reaction kinetics of ethane hydrogenolysis on platinum (55). The entropies of surface species were adjusted by two parameters: (i) a multiplicative factor applied to the DFT-predicted entropies for stable adsorbed C_2H_x species and (ii) a multiplicative factor applied to the DFT-predicted entropies of activated complexes. Furthermore, the enthalpy changes of the eight quasi-equilibrated steps shown in Table VI were varied. For the stable adsorbed species, the energetic properties corresponding to the most favorable Gibbs free energy for a given stoichiometry were used. For example, the surface coverage by di- σ -bonded ethylene species (adsorbed C_2H_4) was considered instead of that

by vinylidene species (adsorbed CHCH_3). However, the transition state for cleavage of the C–C bond in adsorbed C_2H_4 has a higher Gibbs free energy than the transition state for cleavage of adsorbed CHCH_3 . Therefore, C–C bond cleavage proceeding via the activated vinylidene was used rather than that via the activated di- σ -bonded ethylene (55).

c. *Results of the Reaction Kinetics Analysis.* Values of the fitted parameters were determined by using Athena Visual Workbench (73). This software employs a general regression analysis of the reaction kinetics data, with the reactor treated as a CSTR. All values of the parameters were estimated at the average reactor temperature of 623 K.

Figures 5 and 6 show comparisons of the predicted rates (depicted by the solid lines) with experimentally observed rates of ethane hydrogenolysis on Pt/SiO₂. Table VI includes the values of the fixed and fitted parameters, along with 95% confidence limits for the latter. The surface coverages of the stable adsorbed C_2H_5 and CCH_2 species are predicted to be low; therefore, the overall rate was not sensitive to the enthalpy changes characterizing the formation of these surface species, and the values of these enthalpy changes were maintained at the theoretically predicted values. In this simulation, the entropy of adsorbed hydrogen was constrained not to exceed a value corresponding to two degrees of translational freedom (mobile adsorption). The resulting enthalpy change for hydrogen adsorption was constrained to a value of -54 kJ/mol. The analyses predict that the surface should be largely covered by atomic hydrogen (fractional coverage of 0.55). Results of microcalorimetric studies of hydrogen adsorption on silica-supported platinum indicate that the fitted standard entropy and enthalpy changes are reasonable at this average coverage (36, 65, 66). Furthermore, Table VI shows comparisons of the theoretically predicted and the fitted free energy changes. This free energy comparison shows good agreement between the predicted and the fitted values for the adsorption of hydrogen. Similarly, Table VI shows good agreement between theoretical and fitted values for the free energy changes involved in the formation of stable adsorbed CCH_3 and C_2H_4 species. The results shown in Table VI suggest that the mobilities of the stable adsorbed C_2H_x species are higher than the predicted values since the value of the multiplicative factor applied to the standard surface entropies of these stable species was found to be 1.41 ± 0.15 . This factor results in fitted values for the surface entropies of the stable species that correspond to species with one degree of translational freedom on the surface. Table VI also indicates that the fit of the reaction kinetics data leads to slightly lower entropies for the transition states than theoretical predictions since the multiplicative factor applied to the standard surface entropies of these transition states was found to be 0.86 ± 0.13 . These results suggest that the transition states are essentially immobile.

The major differences between the theoretical predictions and the results of the reaction kinetics analysis are in the enthalpy changes for formation of the transition states from gas-phase ethane. The theoretically predicted enthalpy changes for the formation of C_2H_x transition states were too large to account for the measured rate of ethane hydrogenolysis. Accordingly, these enthalpy changes were allowed to decrease, but they were constrained to remain within 50 kJ/mol of the theoretical values. The results of the DFT calculations predict that the preferred pathway for cleavage of the C–C bond involves adsorbed C_2H_5 species, whereas the results of these analyses suggest that the preferred reaction pathway involves adsorbed $CHCH_3$. Importantly, the results of DFT calculations and the reaction kinetics analyses agree that C–C bond cleavage takes place via adsorbed C_2H_x species that are more highly hydrogenated than the most abundant C_2H_x species on the surface.

The previous analysis shown that the initial values of most of the kinetic parameters obtained from DFT calculations provide a good description of the reaction kinetics data collected over a wide range of conditions. The principal difference between the values of the final kinetic parameters used in the model and the initial values obtained from DFT calculations is that the fitted enthalpy changes for the formation of C_2H_x transition states involved in cleavage of the C–C bond are lower than the initial values predicted from DFT calculations. This difference may be explained by the structure sensitivity of the system and/or by the inherent error of the DFT calculations.

The analyses of this example provide a description at the molecular level of the catalytic chemistry involved in ethane hydrogenolysis on platinum, and this description may be useful for further studies of hydrocarbon reactions on various metal surfaces.

C. REACTIONS OF ETHANOL, ETHYL ACETATE, AND ACETIC ACID ON Cu/SiO_2

The previous two cases illustrate situations in which a specific reactant proceeds to a single specific product. More commonly, many products are formed. Accordingly, it is desired to develop quantitative kinetic models that incorporate the necessary elementary reaction pathways to account for the observed products. Furthermore, it is desired to parameterize the elementary steps so that these steps may be applied to related reaction systems under similar conditions.

The reactions of ethanol, ethyl acetate, and acetic acid in the presence of hydrogen on silica-supported copper were chosen to illustrate kinetic analyses of reaction schemes leading to multiple reaction products. Copper-containing catalysts are extremely important for the reduction of oxygenated compounds, such as alcohols, esters, and carboxylic acids. Such materials

typically exhibit high selectivities for the conversion of esters and carboxylic acids to alcohols (74).

Experimental results show that ethanol reacts to form acetaldehyde and ethyl acetate, whereas ethyl acetate reacts to form acetaldehyde and ethanol. The major products formed from acetic acid are acetaldehyde, ethanol, water, and ethyl acetate. These results suggest that there are common reaction pathways for the reactions of ethanol, ethyl acetate, and acetic acid. The reactions of ethyl acetate and ethanol may be described by using the first six elementary steps listed in Table VII. Furthermore, the reactions of acetic acid may be described by using these same six elementary steps plus three others shown in Table VII.

This case also continues the trend of combining experimental and theoretical results. Regarding ethane hydrogenolysis, the theoretical results are used to develop a potential energy diagram for the interactions of various adsorbed oxygenated species with copper. The resulting potential energy diagram is then used to make initial estimates of kinetic parameters involved in the reactions of ethanol, ethyl acetate, and acetic acid on copper (75, 76).

1. *Experimental Results*

Samples containing 5 wt% copper were prepared by ion exchange on silica (Cab-O-Sil) with aqueous $\text{Cu}(\text{NO}_3)_2$. Approximately $19 \pm 2\%$ of the total copper atoms were present as metallic surface atoms, as determined by N_2O decomposition experiments. Subsequent adsorption studies of CO on this catalyst suggest that little if any oxidized copper was present. Details of the catalyst preparation and characterization are given elsewhere (75, 76). Before reaction kinetics measurements, the catalyst was treated with flowing hydrogen at 600 K for more than 8 h. Dandekar and Vannice (77) reported characterization and kinetic studies of copper on a variety of supports, including SiO_2 . These investigators employed the dissociative adsorption of N_2O to determine the number of metallic copper surface atoms and CO adsorption to determine the number of surface Cu^+ sites. Their results suggest that a combination of metallic and Cu^+ sites was present on the catalyst surface after reduction in hydrogen at 573 K, depending on the type of support. Of particular interest is that these investigators showed by infrared spectra of CO adsorbed on a 5.1 wt% Cu/SiO_2 reduced at 573 K that copper is almost completely reduced to the metallic state. These results thus suggest that the copper on the silica-supported catalyst used in our kinetic studies was essentially completely reduced.

Details of our experimental procedures are given elsewhere (75, 76). The reactions of ethanol were conducted over a temperature range of 453–513 K, a hydrogen pressure range of 0.2–0.8 atm, and an ethanol pressure range of 0.02–0.17 atm (Fig. 11). Figure 11 shows that the major products were

TABLE VII
Parameters of the Kinetic Model Used to Describe the Reduction of Ethanol, Ethyl Acetate, and Acetic Acid
on 5 wt% Cu/SiO₂^a

Step	Reaction	ΔS° (J/mol K)	ΔH° (kJ/mol)	E_{for} (kJ/mol)	E_{rev} (kJ/mol)
1	$\text{CH}_3\text{COOC}_2\text{H}_5 + 2^* \rightleftharpoons \text{CH}_3\text{C}^*\text{O} + \text{C}_2\text{H}_5\text{O}^*$	-31 ^b	-28 ^b	42 ± 3 ^c	70
2	$\text{CH}_3\text{C}^*\text{O} + \text{H}^* \rightleftharpoons \text{CH}_3\text{CHO}^* + ^*$	-2	0 ^d	105 ± 6 ^e	105
3	$\text{CH}_3\text{CHO}^* \rightleftharpoons \text{CH}_3\text{CHO} + ^*$	118 ^f	61 ± 2	61	0 ^g
4	$\text{CH}_3\text{CHO}^* + \text{H}^* \rightleftharpoons \text{C}_2\text{H}_5\text{O}^* + ^*$	38 ^b	-14 ^b	35 ^d	49
5	$\text{C}_2\text{H}_5\text{O}^* + \text{H}^* \rightleftharpoons \text{EtOH} + 2^*$	103 ^f	30 ± 1	30	0 ^g
6	$\text{H}_2 + 2^* \rightleftharpoons 2\text{H}^*$	-145 ± 7	-27 ± 3	30 ^h	57
7	$\text{CH}_3\text{COOH} + 2^* \rightleftharpoons \text{CH}_3\text{C}^*\text{O} + \text{HO}^*$	-65 ^b	-41 ^b	47 ± 3 ^c	88
8	$\text{HO}^* + \text{H}^* \rightleftharpoons \text{H}_2\text{O} + 2^*$	129 ^f	30 ± 1	30	0 ^g
9	$\text{CH}_3\text{COOH} + 2^* \rightleftharpoons \text{CH}_3\text{C}^*\text{OO}^* + 1/2\text{H}_2$	-19 ^f	-43 ± 3	0 ^g	43

^aAdjustable parameters are provided with 95% confidence limits. ^bChanges in enthalpy and entropy set to maintain thermodynamic consistency for gas-phase reactions. ^cActivation energy for acetic acid adsorption is constrained to be at least 5 kJ/mol greater than the activation energy for ethyl acetate adsorption. Change in entropy is based on an immobile activated complex. ^dChange in enthalpy is not sensitive. ^eChange in standard entropy to form the activated complex for step 2 was fitted to be -27 ± 12 J/mol K. ^fAdsorbed species assumed to be mobile. Entropy of surface species equivalent to $S_{\text{loc}} + S_{2D}$. ^gNonactivated adsorption is assumed for these steps, and a sticking coefficient of 1.0 is assumed. ^hHydrogen adsorption step is assumed activated with an activation energy of 30 kJ/mol.

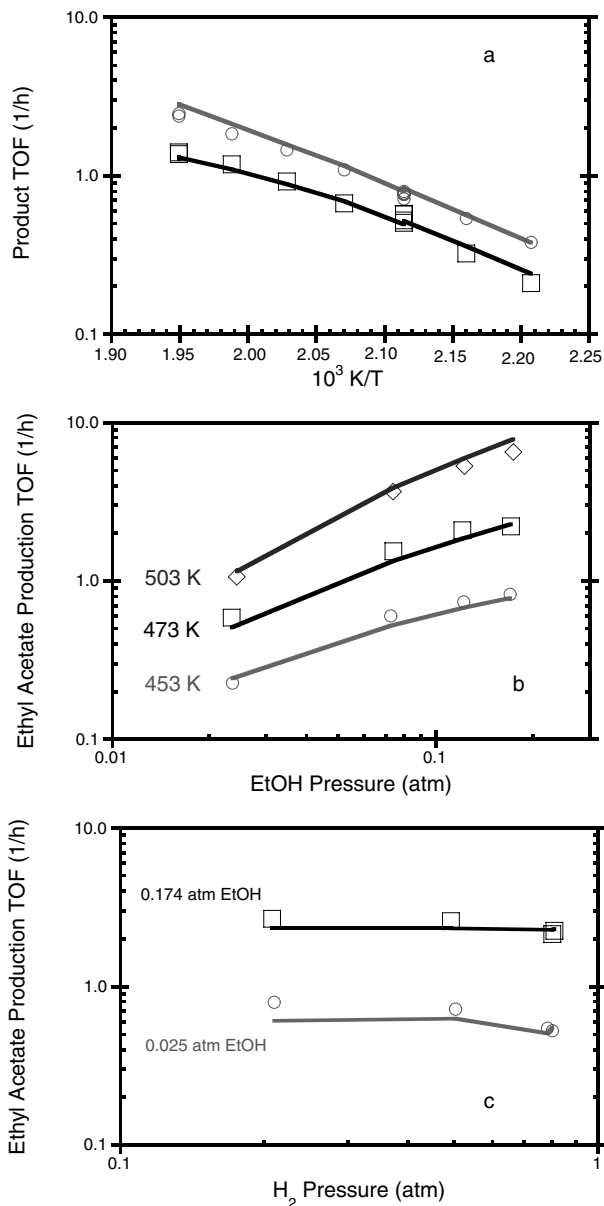


FIG. 11. (a) Turnover frequencies (TOF) for production of acetaldehyde (AcH) and ethyl acetate (EA) as a function of $1/T$ at 0.023 atm ethanol (EtOH) and 0.8 atm hydrogen (H_2): (○) AcH, (□) EA. (b) TOF for production of EA at 0.8 atm H_2 : (○) 453 K, (□) 473 K, (◇) 503 K. (c) TOF for production of EA at 473 K: (○) 0.025 atm EtOH, (□) 0.174 atm EtOH.

acetaldehyde and ethyl acetate and that acetaldehyde formed in equilibrium with ethanol. In a similar investigation, support effects were noted by Iwasa and Takezawa (78) for the reactions of ethanol on supported copper. The support plays a significant role in the formation of ethyl acetate on zirconia-supported copper, whereas the formation of ethyl acetate occurs on the copper alone when the support is silica.

Kinetic results for the reduction of ethyl acetate and acetic acid on similarly prepared 5 wt% Cu/SiO₂ catalysts are shown in Figs. 12 and 13 (75). The experiments were performed at 570 K at various partial pressures of hydrogen and oxygenated compounds. Measurements were also made at temperatures from 500 to 580 K (Figs. 12 and 13). It was observed that ethyl acetate reacts to form only acetaldehyde and ethanol, in equilibrium with each other (75). Figure 12 shows the effects of reaction conditions on the formation of ethanol when ethyl acetate is converted on Cu/SiO₂.

Acetic acid reacts on Cu/SiO₂ to form acetaldehyde, ethanol, and ethyl acetate. Acetaldehyde and ethanol were found to be equilibrated with each other in the reactions of both ethyl acetate and acetic acid (75). Figure 13 shows the effects of reaction conditions on the formation of ethanol and ethyl acetate when acetic acid reacts on Cu/SiO₂. The reduction of ethyl acetate occurs at a higher rate than the reduction of acetic acid on this catalyst.

2. Theoretical Results

Copper atoms in these catalysts may be distributed between bulk metallic particles and oxide patches associated with the silica support. However, as mentioned previously, spectroscopic evidence suggests that little if any oxidized copper is present on a 5 wt% Cu/SiO₂ catalyst reduced at 573 K. Furthermore, the reduction of esters and carboxylic acids is believed to occur predominantly on metallic copper (74). Accordingly, the conjecture of these analyses is that the reaction occurs on metallic copper.

As in the investigations of the interactions of C₂H_x species on platinum quantum chemical calculations employing density functional theory were performed to characterize the interactions of various CH_xO species with flat Cu(111) and stepped Cu(211) slabs (76) [typically represented as three-layer slabs of Cu(111) and Cu(211)]. Details are given elsewhere (76).

A 3 × 3 × 3 unit cell was used to represent the interactions of CH_xO with a flat Cu(111) surface (Fig. 14). The binding energies and site preferences of methoxy species (CH₃O), adsorbed formaldehyde (CH₂O), formyl species (CHO), carbon monoxide, and hydrogen atoms were determined for the Cu(111) surfaces. The calculations were performed with one-ninth ML coverage of the adsorbate. Table VIII is a summary of the changes in electronic

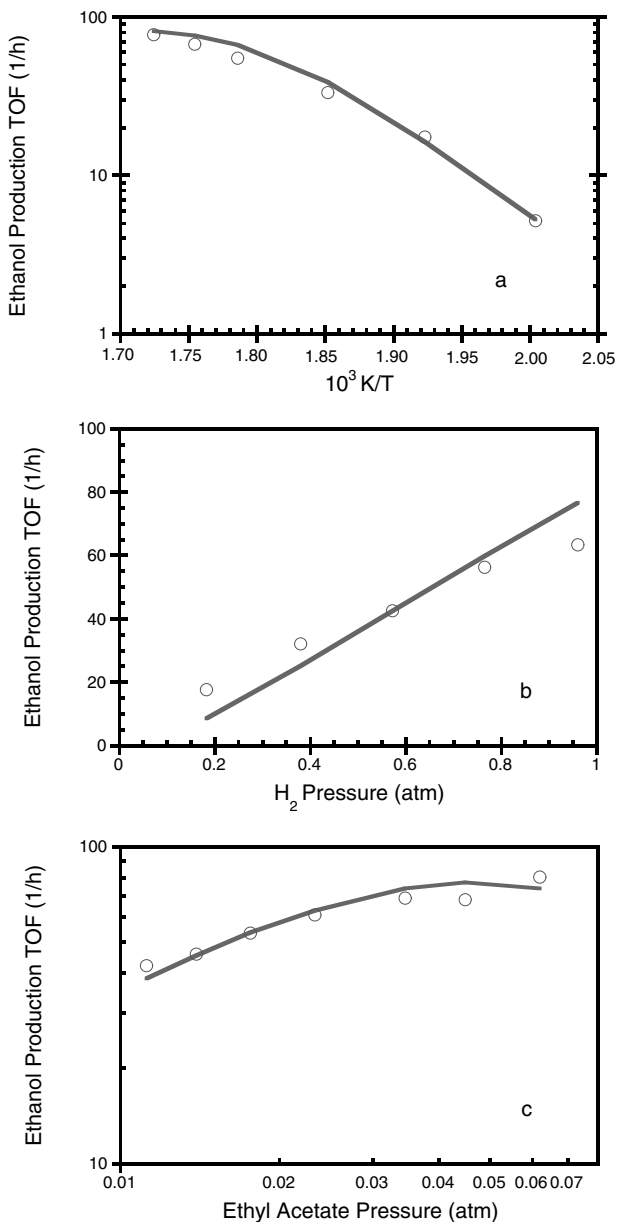


FIG. 12. Turnover frequencies (TOF) for ethanol production (a) as a function of $1/T$ at 0.04 atm EA and 0.96 atm H_2 , (b) as a function of H_2 pressure at 570 K and 0.04 atm EA, and (c) as a function of EA pressure at 570 K and 0.945 atm H_2 .

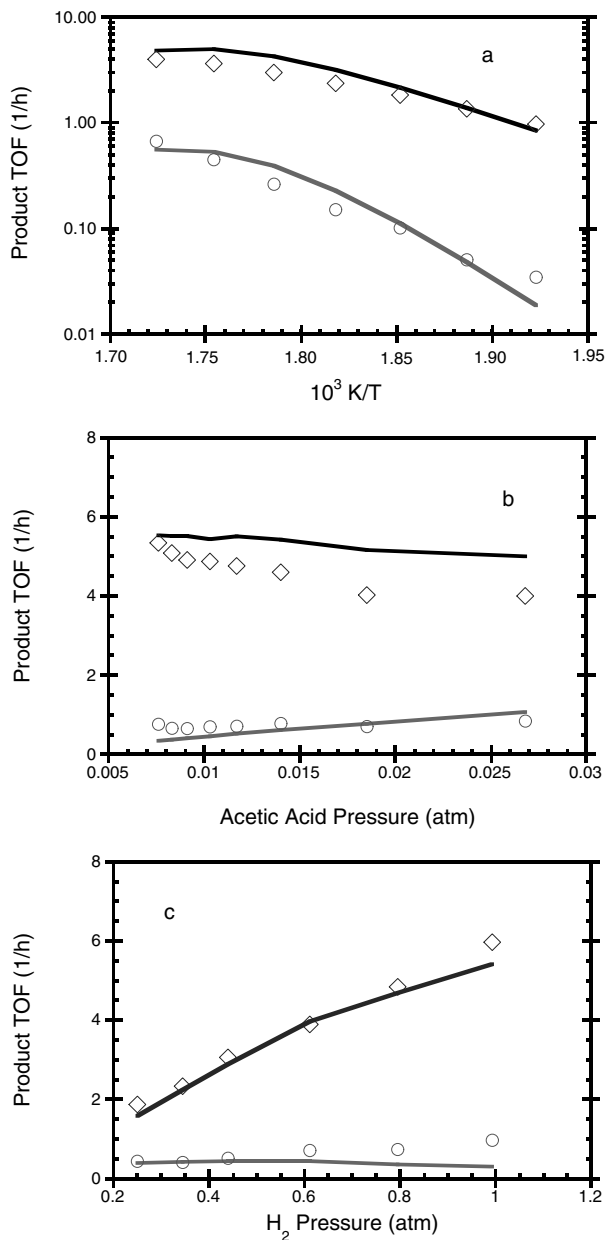


FIG. 13. Turnover frequencies (TOF) for production of ethyl acetate (○) and ethanol (◇) (a) as a function of $1/T$ at 0.027 atm acetic acid (AcOH) and 0.97 atm H_2 , (b) as a function of AcOH pressure at 570 K and 0.975 atm of H_2 , and (c) as a function of H_2 pressure at 570 K and 0.007 atm of AcOH.

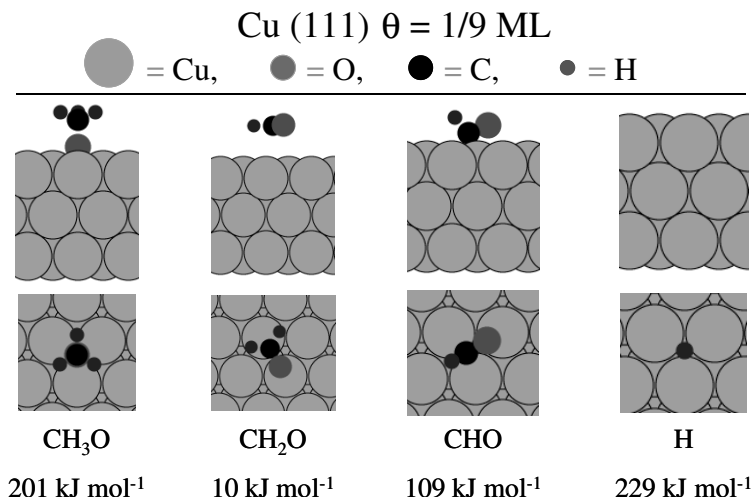


FIG. 14. Front and top view of the optimized structure of CH_xO and H species on Cu(111). Most adsorbates have at least one approximately degenerate configuration.

energies based on these calculations for C_1 oxygenates for elementary steps similar to those shown in Table VII for C_2 oxygenates. Table VIII shows that the molecular adsorption of formaldehyde on Cu(111) is mildly exothermic and that the dissociative adsorption of methanol to form methoxy species and adsorbed hydrogen is endothermic.

A $2 \times 3 \times 3$ unit cell was used to calculate the interactions of adsorbed CH_xO species and atomic hydrogen with the edge site of the stepped Cu(211)

TABLE VIII
DFT Predictions of Energetics (kJ mol^{-1}) for Various Elementary Reactions of C_1 Oxygenates on Cu(211) and Cu(111) and for Carbonyl-Containing Organic Molecules on Cu_{13}

Elementary reaction	Surface or cluster		
	Cu(211) (kJ mol^{-1})	Cu(111) (kJ mol^{-1})	Cu_{13} (kJ mol^{-1})
$\text{CHO}^* + \text{H}^* \rightleftharpoons \text{CH}_2\text{O}^* + ^*$	-26	-54	—
$\text{CH}_2\text{O}^* \rightleftharpoons \text{CH}_2\text{O} + ^*$	55	9	—
$\text{CH}_2\text{O}^* + \text{H}^* \rightleftharpoons \text{CH}_3\text{O}^* + ^*$	-79	-93	—
$\text{CH}_3\text{O}^* + \text{H}^* \rightleftharpoons \text{CH}_3\text{OH} + 2^*$	53	-9	90
$\text{H}_2 + 2^* \rightleftharpoons 2\text{H}^*$	-47	-17	—
$\text{CH}_3\text{O}^* \rightleftharpoons [\text{CH}_3\text{O}^*]^\ddagger$	—	137	—
$\text{CH}_3\text{COOC}_2\text{H}_5 + ^* \rightleftharpoons [\text{CH}_3\text{COOC}_2\text{H}_5^*]^\ddagger$	—	—	50–60
$\text{CH}_3\text{COOH} + ^* \rightleftharpoons [\text{CH}_3\text{COOH}^*]^\ddagger$	—	—	90–100

surface (Fig. 15). The calculations were performed with one-sixth ML coverage of the adsorbate. It was found that the binding energies depend strongly on the geometry of the surface. For example, methoxy species are bonded more strongly (by 47 kJ/mol) at the step edge of Cu(211) than on Cu(111). Formyl species are bonded more strongly (by 58 kJ/mol) at the step edge. Table VIII provides summary of these results; they suggest that the reductions of carboxylic acids and esters should be structure-sensitive reactions on copper.

Acetic acid and ethyl acetate can dissociate on copper through cleavage of the C–X bond adjacent to the carbonyl group, where X represents either hydroxyl or alkoxy. The chemical behavior of supported copper was simulated by using a 13-atom copper cluster resembling an icosahedron (75). All the surface atoms in this cluster have the same coordination number of six (Fig. 16). Quantum chemical calculations within the cluster approximation depend on the number of surface and bulk atoms incorporated in the model; therefore, results of these calculations should be used only to deduce trends in bonding and reactivity for various species adsorbed on copper.

A schematic representation of the transition states and the corresponding activation energies are included in Fig. 16. Activation energies are reported as a range of values because the first-order saddle points on the corresponding potential energy surfaces were not located rigorously. These calculations suggest that the activation energy for dissociative adsorption decreases as the reactant is changed from acetic acid to ethyl acetate. These results and the energetics listed in Table VIII are applied to establish an initial estimate

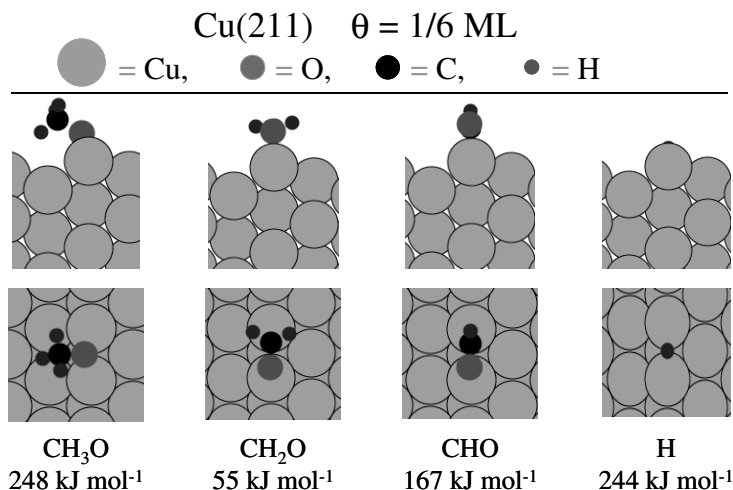


FIG. 15. Front and top view of the optimized structure of CH_xO and H species on Cu(211).

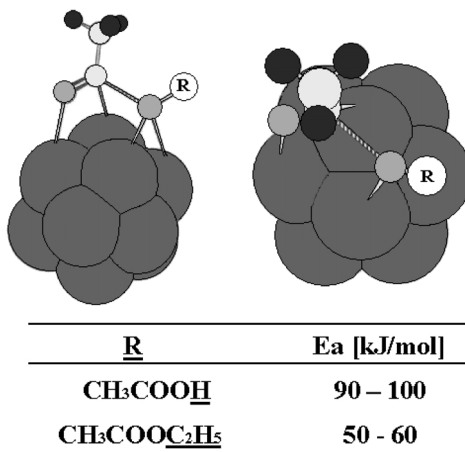
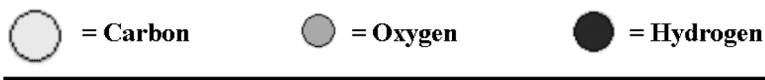


FIG. 16. Transition states and activation energies for dissociative adsorption of carbonyl-containing organic molecules on Cu_{13} .

of the potential energy surface of the interactions of C_2 oxygenated species with copper.

3. Reaction Kinetics Analysis

a. *Reaction Scheme.* The elementary steps listed in Table VII are employed to describe the catalytic reaction schemes for the reactions of ethanol, ethyl acetate, and acetic acid on Cu/SiO_2 . Steps 1–6 describe the reaction scheme necessary for the reversible reactions between ethanol and ethyl acetate. The kinetic model for the reduction of acetic acid involves the reaction steps related to reduction of ethyl acetate (steps 1–6) and additional steps to describe the dissociative adsorption of acetic acid on copper (step 7), the hydrogenation of hydroxyl species to give water (step 8), and the equilibrated formation of acetate species on the surface (step 9). The formation of acetate species is not included for the cases of ethyl acetate reduction since ethane was not detected in our experiments. However, it should be easier to break the $\text{CH}_3\text{COO}-\text{H}$ bond for acetic acid than the $\text{CH}_3\text{COO}-\text{R}$ bonds in the esters; therefore, the formation of acetate species is included in the kinetic model for acetic acid reduction. This reaction scheme consists of dissociative adsorption of reactants and products and surface hydrogenation reactions.

b. *Parameterization of the Kinetic Model.* To test the feasibility of this reaction scheme to describe the reaction kinetics data, it is necessary to quantify thermodynamic and kinetic parameters associated with each step. The equilibrium constants describing the formation of stable surface species are expressed in terms of the appropriate standard entropy changes and enthalpy changes. Values for standard entropies and enthalpies for the gas-phase species were obtained from the compilation of Yaws (79). The standard state pressure is 1 atm.

In this reaction kinetics analysis the following assumptions were employed: The surface entropies of oxygenated species were linked together, assuming that these species exhibit similar mobility on the surface. Accordingly, the surface entropies of oxygenated species were described in terms of a factor that multiplied the local surface entropies of these species, where the local entropy, S_{loc} , for a species is defined as the vibrational and rotational entropy associated with the species in the gas phase.

The enthalpy changes for adsorption of acetaldehyde (step 3), ethanol (step 5), hydrogen (step 6), water (step 8), and acetic acid to form adsorbed acetate (step 9) were adjusted in the reaction kinetics analysis. The initial estimates of the heats of adsorption of acetaldehyde, ethanol, and hydrogen were obtained from the DFT predictions for these species on Cu(211) (Table VIII). The heat of adsorption of water was constrained to be equal to the heat of adsorption of ethanol in these analyses. The steps involving adsorption of ethanol, acetaldehyde, water, and the step in which acetic acid forms the surface acetate species were all assumed to be nonactivated.

The standard entropy and enthalpy changes for the dissociative adsorption of ethyl acetate (step 1), acetic acid (step 7), and the hydrogenation of adsorbed acetaldehyde to form ethoxy species (step 4) were constrained to maintain thermodynamic consistency for the appropriate overall gas-phase reactions.

The activation energies for the dissociative adsorption of ethyl acetate and acetic acid were adjusted in the analysis. To be consistent with the DFT results shown in Table VIII, the activation energy for the dissociative adsorption of ethyl acetate was constrained to be less than the activation energy for the dissociative adsorption of acetic acid. The standard entropy changes for these steps were constrained such that the activated complexes were immobile species. The standard entropy and enthalpy changes to form the activated complex for step 2 were adjusted.

The activation energy for adsorption of hydrogen on copper was set at 30 kJ mol^{-1} , in agreement with the literature (80). A sticking coefficient of unity was assumed for this step. Furthermore, the entropy of the adsorbed surface hydrogen was adjusted in the analysis.

The results of the DFT calculations outlined previously provide initial estimates of activation energies and enthalpy changes associated with various

steps of the reaction scheme. Values of the adjusted parameters were determined by using Athena Visual Workbench (73). This software employs a general regression analysis of the reaction kinetics data with the reactor treated as a PFR. All values of the parameters were estimated at a reactor temperature of 483 K.

The optimized parameters for the kinetic model used to describe the catalytic reactions of the three oxygenates are listed in Table VII. In this analysis, eight parameters were found to be sensitive, and the 95% confidence limits are given for these parameters in Table VII. The solid curves in Figs. 11–13 represent predictions of the kinetic model under various reaction conditions. Good agreement is achieved between the predictions of the model and the experimental reaction kinetics for all three reactions.

4. *Conclusions from Reaction Kinetics Analysis*

The results of the reaction kinetics analyses suggest that adsorption steps for acetaldehyde (step 3), ethanol (step 5), hydrogen (step 6), and water (step 8) and the formation of the acetate species (step 9) are quasi-equilibrated. Furthermore, the hydrogenation of the adsorbed formaldehyde to form ethoxy species (step 4) was also found to be quasi-equilibrated. The dissociative adsorption steps for ethyl acetate (step 1) and acetic acid (step 7) appear to be slower, and these are reversible under most of the conditions investigated. Furthermore, the hydrogenation of the acyl species to form adsorbed acetaldehyde (step 2) is also slow but reversible. The model predicts that the surface is highly covered (fractional coverages higher than 80%), with the acyl species being the most abundant surface species when the reactant is either ethanol or ethyl acetate. Acetate is predicted to be the major surface species when acetic acid is the reactant.

The entropy values shown in Table VII suggest that all the oxygenated adsorbed species are mobile. As noted previously, the enthalpy changes for the adsorption of ethanol and water (steps 4 and 7) were constrained to be equal. The fitted heats for the adsorption of acetaldehyde, ethanol, and hydrogen were within 25 kJ/mol of the DFT predictions when the catalyst was Cu(211). The adjusted activation energy for the dissociative adsorption of acetic acid is greater than the activation energy for the dissociative adsorption of ethyl acetate. This trend is in agreement with DFT predictions for a Cu₁₃ cluster (Table VIII). The fractional coverage of the copper surface is predicted to be similar for both cases when ethyl acetate and acetic acid react on copper. Accordingly, the lower activity noted for the reaction of acetic acid compared to ethyl acetate may be attributed to the higher activation barrier for the dissociative adsorption of acetic acid.

The results of the analyses for the reactions of oxygenates on silica-supported copper suggest that reaction schemes based on reactions occurring

on metallic copper are feasible. DFT predictions suggest that these reactions may be structure sensitive since stronger interactions of the adsorbed species are predicted for a stepped Cu(211) surface than for the flat Cu(111).

In this case study, nine elementary steps were invoked to construct reaction schemes that describe the reactions of three different reactants, with six of the elementary steps common to the three reactions. The success of these analyses suggests that the parameters for these elementary steps may be applied to systems with similar chemistry (i.e., reduction of oxygenates) at similar coverage regimes.

D. REACTIONS OF ISOBUTANE ON SOLID ACID CATALYSTS

Solid acid catalysts are used extensively in the chemical and petrochemical industries for hydrocarbon conversion processes. For example, acidic zeolite-containing catalysts are used in fluid catalytic cracking processes, and acid sites are used in combination with metal sites for bifunctional isomerization of alkanes. Extensive research has been conducted with the aim of relating the performance of solid acid catalysts to the strengths of the acidic sites. These sites can be characterized, for example, by their interactions with basic probe molecules, determined by temperature-programmed desorption, microcalorimetry, and spectroscopic techniques such as infrared and nuclear magnetic resonance. The quantification of catalyst performance can be defined in terms of the target catalytic process, and it is also desirable to use relatively simple catalytic probe reactions. The following are attributes of an effective probe reaction: (i) It proceeds via well-defined surface chemistry, (ii) it displays stable catalytic activity or controlled catalyst deactivation, (iii) it displays selectivity patterns that reflect the properties of the active sites, and (iv) it can be conducted over a wide range of reaction conditions. For example, the selectivity for the conversion of 2-methyl-2-pentene has been used effectively as a probe of solid acid strength (81–84), where by the formation of 2-methyl-3-pentene via a double-bond shift is catalyzed by all acidic sites, the formation of 3-methylpentenes via a methyl shift is catalyzed by stronger acid sites, and the formation of 2,3-dimethylbutenes via branching rearrangement is catalyzed only by the strongest acidic sites. The cracking and/or isomerization of alkanes have also been used as probe reactions to characterize the acidic properties of the catalytic materials (85–99). The conversion of isobutane has been investigated extensively (100–112), and the reaction kinetics are addressed in the following example.

1. *Reaction Scheme*

The surface chemistry involved in the conversion of isobutane on solid acids is shown schematically in Fig. 17. The conversion takes place according to a surface chain reaction scheme involving initiation, propagation, and

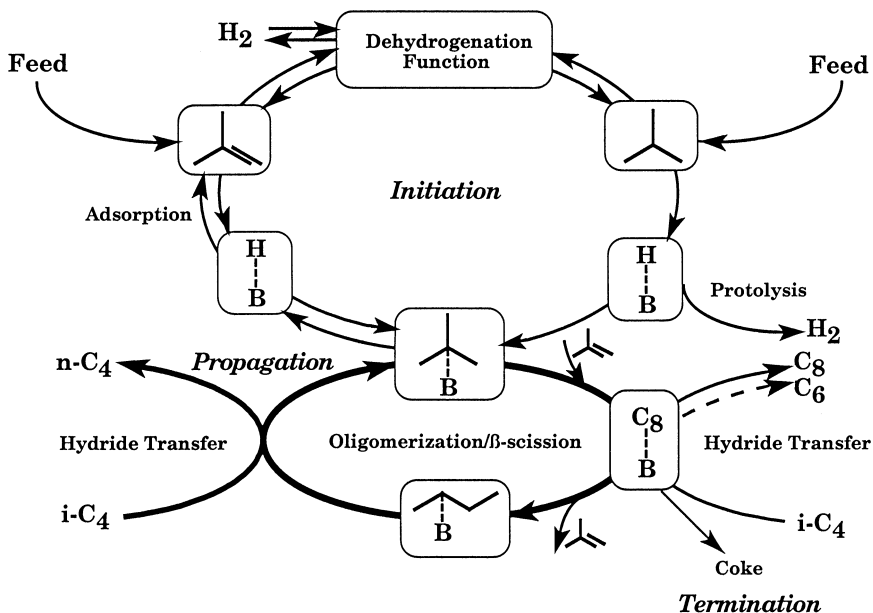
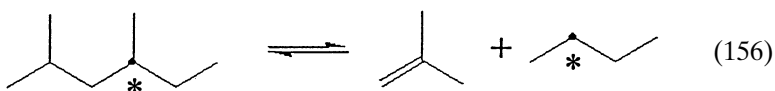
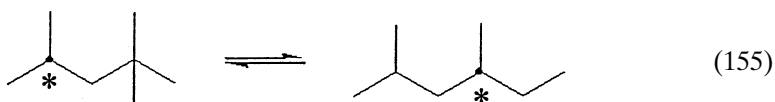


FIG. 17. Schematic representation of surface chain reaction scheme for isobutane conversion on solid acid catalysts (99).

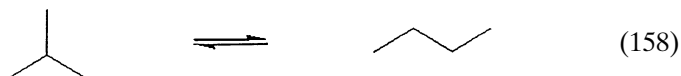
termination steps. The reaction can be initiated, for example, by adsorption of isobutylene on Brønsted acid sites to form surface isobutyl species. The isobutylene can be formed by dehydrogenation of isobutane (e.g., on sulfated zirconia catalysts), or it can be added to the reactor feed (e.g., with zeolite catalysts). Alternatively, the surface chain reaction can be initiated by activation of isobutane to form adsorbed isobutyl species and gaseous H_2 or by activation of isobutane to form adsorbed propyl species and gaseous CH_4 . These activation processes may take place via protolysis steps (102, 113), or they may involve radical species. It is well established that the adsorbed species formed in the initiation processes are surface alkoxy species rather than surface carbenium ions (10, 114–118). In contrast, the subsequent reactions of these neutral surface alkoxy species take place via either carbenium or carbonium ion transition states (10, 114–118), and these explain why the selectivity patterns in the reactions of hydrocarbons on solid acid catalysts are controlled by the relative stabilities of carbocations.

Isobutyl species formed on the catalyst in the initiation steps do not react in unimolecular processes since such reactions (e.g., the formation of *n*-butyl species) involve primary carbenium ion transition states. Therefore, propagation steps in the conversion of isobutane include oligomerization reactions

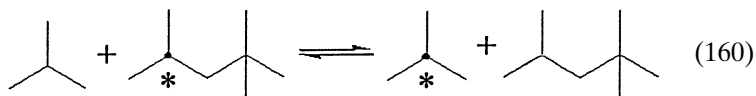
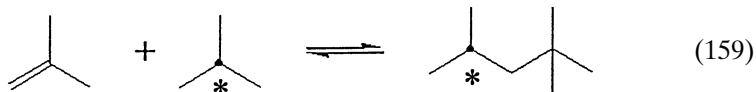
of adsorbed species with olefins, β -scission processes of adsorbed species to give smaller adsorbed species and olefins (i.e., the reverse of oligomerization), nonbranching isomerization reactions of adsorbed species involving hydrogen shifts and methyl shifts, branching isomerization reactions of adsorbed species, and hydride transfer reactions of adsorbed species with isobutane in which an adsorbed species is converted to an alkane as an isobutyl species is regenerated on the site. In the following steps, it can be seen that once a surface isobutyl species has been formed in an initiation step, this intermediate can first be converted to *n*-butane and then regenerated, without further consumption of isobutylene:



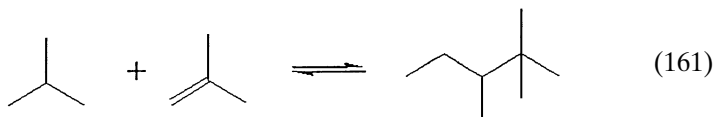
The overall effect of summing these four propagation steps is the conversion of isobutane to *n*-butane:



The surface chain reaction is terminated by processes that consume olefins. For example, hydride transfer between isobutane and heavy adsorbed species leads to consumption of isobutylene, as illustrated in the following reactions:

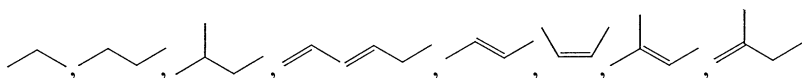


where the overall effect of these reactions is the reaction of isobutane with isobutylene to form octane:



Other termination steps include desorption of species as olefins (which leave the reaction system in the reactor effluent) and the conversion of adsorbed species to coke.

In general, we have outlined how the conversion of isobutane on solid acid catalysts takes place according to well-established carbenium ion transition state chemistry. The difficulty with using isobutane conversion as a probe of catalyst performance is that many combinations of oligomerization/ β -scission processes with isomerization steps are possible, resulting in a wide variety of adsorbed species and observable reaction products. For example, the following products are observed from isobutane conversion in the presence of ultrastable Y zeolite at temperatures near 520 K (where the reaction is initiated by the addition of isobutylene to the feed):



The olefinic products can be formed in β -scission steps involving C_8^* adsorbed species (Fig. 18). In Fig. 18 $\sim\text{Me}$ represents a methyl shift, Δ represents a branching rearrangement through a cyclopropyl transition state, β_A is a β -scission step in which a tertiary species gives a smaller tertiary species, β_{B1} is a β -scission step converting a secondary species to a tertiary species, β_{B2} is a β -scission step converting a tertiary species to a secondary species, and β_C is a β -scission step converting a secondary species to another secondary species. Furthermore, the observed olefinic reaction products can be produced in β -scission steps involving other C_n^* adsorbed species. The paraffinic products are formed in various hydride transfer reactions of adsorbed C_n^* species with isobutane.

To build a kinetic model for isobutane conversion, we must first specify the adsorbed C_n^* species to be included. Under the conditions employed in our kinetic studies (i.e., temperatures between 523 and 573 K, total pressure of 1 atm, isobutylene feed contents near 50–400 ppm, and isobutane concentrations of 20 and 80%), the primary olefins observed in the reactor effluent are isobutylene, 1-butene, *cis*- and *trans*-2-butene, propene, and smaller amounts of isopentenes. Accordingly, the following adsorbed species

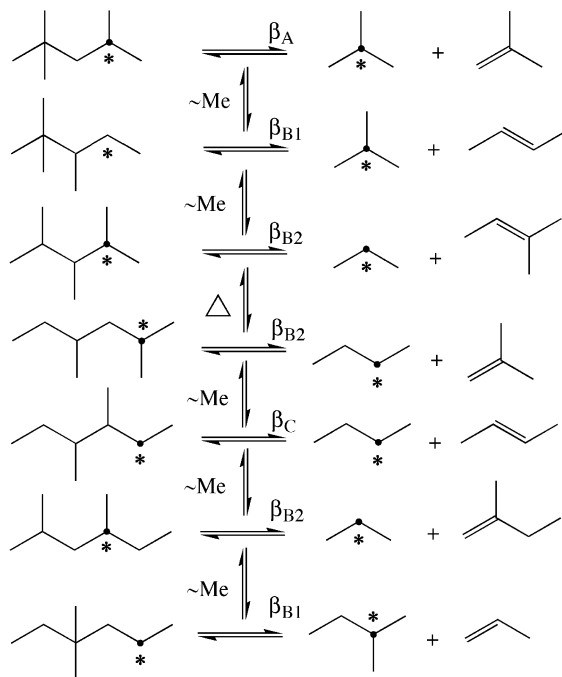
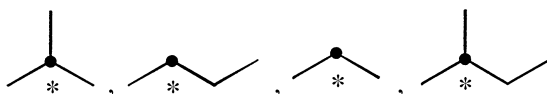
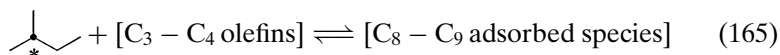
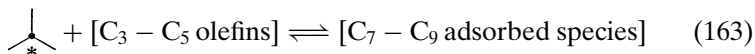
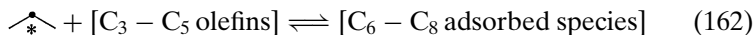


FIG. 18. β -Scission and isomerization processes of adsorbed C_8^* species.

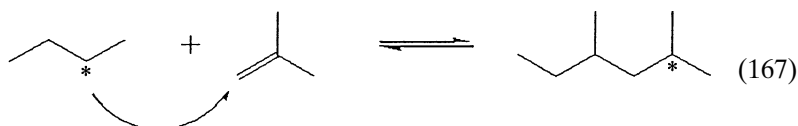
are formed from the adsorption of these olefins:



Next, we allow these adsorbed species to undergo oligomerization by reacting with the primary olefins observed in the reactor effluent, leading to the following species:

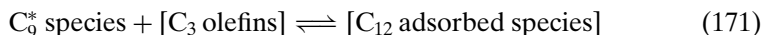
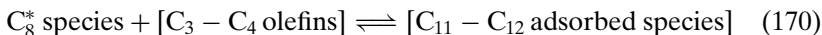
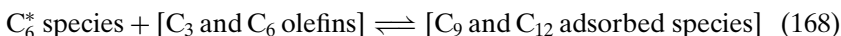


These oligomerization steps are written in accord with Markovnikov's rule (119), as illustrated here:



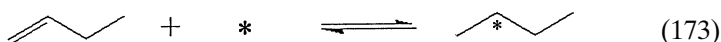
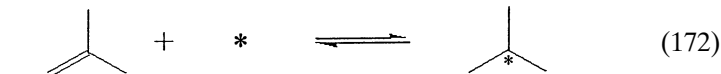
In this strategy for generating surface species, we have not included the reaction of adsorbed C_5^* species with C_5 olefins because the concentrations of these olefins are much lower than the concentrations of C_3 and C_4 olefins.

The previous strategy gives C_9 species as the heaviest hydrocarbons on the catalyst. However, we may expect surface species as heavy as C_{12} , resulting from the oligomerization of three C_4 species since the C_4 species are the most abundant olefins in the reactor. Therefore, we added the following types of oligomerization steps, truncating all possible adsorbed species at 12 carbon atoms:



The arguments outlined previously lead to 88 steps for oligomerization and β -scission processes involving 74 adsorbed hydrocarbon species. Although the choice of these steps is arbitrary, we later show that relatively few of them are kinetically significant.

The reaction scheme for isobutane conversion is expanded by allowing each adsorbed species to be formed from adsorption of the corresponding olefin on a Brønsted acid site, as illustrated here for isobutyl and *n*-butyl species:

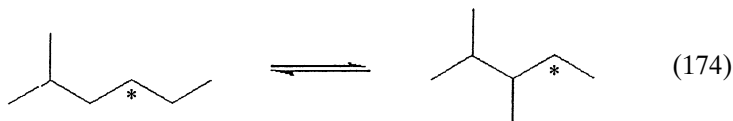


The 74 species lead to the addition of 78 adsorption/desorption steps (i.e., three C_4 olefins are generated from adsorbed *n*-butyl species; we have

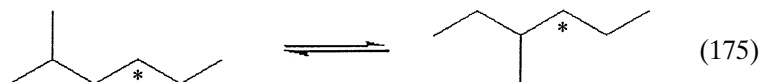
allowed two C₅ olefins to be formed from adsorbed isopentyl species, and we have allowed two C₆ olefins to be formed from adsorbed isohexyl species).

The 74 adsorbed hydrocarbon species can be interconverted via isomerization steps. We have included 71 representative isomerization steps to allow interconversion between the various C_{*n*}* isomers. We categorize each of these steps as a nonbranching rearrangement (involving hydrogen and methyl shifts) or a branching rearrangement:

Branching rearrangement:

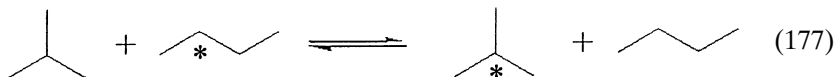
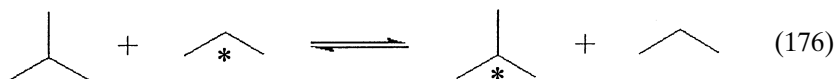


Nonbranching rearrangement:



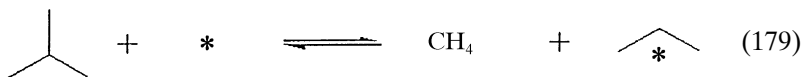
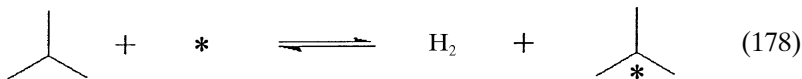
In general, we anticipate that the rate constants for branching rearrangements should be less than those for nonbranching rearrangements.

The reaction scheme for isobutane conversion also includes 73 steps representing hydride transfer for each surface species (with the exception of isobutyl species) with isobutane:



Hydride transfer steps leading to the formation of propane, *n*-butane, and isopentane are involved in propagation cycles of the surface chain reactions, whereas hydride transfer steps that produce heavier alkanes lead to termination of surface chain reactions.

Finally, the reaction scheme is expanded to include two initiation steps representing activation of isobutane to form surface isobutyl species or surface propyl species:



In summary, our kinetic model for the carbenium ion transition state chemistry involved in isobutane conversion on solid acid catalysts under the conditions of our studies contains 312 steps, which combine to form surface chain reaction cycles. This reaction scheme involves two initiation steps for isobutane activation, 78 steps for olefin adsorption/desorption processes (one of these adsorption steps gives rise to initiation of isobutane conversion by adsorption of isobutylene from the reactor feed), 88 steps for oligomerization and β -scission involving olefins and adsorbed species, 71 isomerization steps for interconversion of adsorbed C_n^* isomers (via branching and non-branching rearrangements), and 73 hydride transfer reactions of adsorbed species with isobutane (leading to propagation and termination of surface chain reactions).

2. Parameterization of the Kinetic Model

The first step in parameterizing the kinetic model is to consider the reaction thermodynamics of the system. Our strategy is first to estimate the absolute entropies and the enthalpies of formation for all gaseous olefins and alkanes in their standard states (i.e., at 1 atm and the reactor temperature). These values can be found in standard references for the lighter hydrocarbons (e.g., C_n species with $n < 7$). For the heavier hydrocarbons, we use Benson's group contribution methods (120–123). By basing the kinetic model on well-established thermodynamic values for gaseous species (including the reactants and the observed products), we ensure that the kinetic parameters of the model will be thermodynamically consistent.

We next estimate the thermodynamic properties of all surface species in terms of standard entropy changes and enthalpy changes of adsorption for all gaseous olefins. In particular, the kinetic model contains 78 steps for olefin adsorption/desorption, and we use these steps to relate the thermodynamic properties of all adsorbed species to the known thermodynamic properties of gaseous olefins. Actually, this strategy of relating the thermodynamic properties of adsorbed species to the known thermodynamics of gaseous species is used generally in building kinetic models, even when the adsorbed species do not necessarily desorb as stable molecular species. In these cases, the thermodynamic properties of a particular adsorbed species are related to the known thermodynamic properties of a gaseous radical or ion.

We first consider the parameterization of the enthalpy changes of adsorption. It has been established that the heats of adsorption of various paraffins in zeolites vary linearly with carbon number (124–126). Therefore, we define the enthalpy of formation for a surface species as

$$H_{\text{surface}} = H_{\text{olefin}}^{\circ} + \Delta H_3^{\circ} + \alpha_H (N_C - 3) \quad (180)$$

where H_{surface} and $H_{\text{olefin}}^{\circ}$ are the enthalpies of formation of the surface species and the corresponding olefin, ΔH_3° is the enthalpy change of adsorption for propene, N_C is the number of carbon atoms in the surface species, and α_H is the slope of the linear variation of the adsorption heat with carbon number. Therefore, we have defined the enthalpies of all surface species in terms of two parameters, ΔH_3° and α_H .

Estimation of standard entropies for all surface species is based on the local entropies of gaseous olefins and the changes in symmetry that occur upon adsorption. As noted in Section II, the local entropy, S_{loc} , of a gaseous species is calculated by subtracting the gaseous translational entropy, $S_{\text{trans,3D}}$, from the total entropy (leaving the entropy contributions from vibrational and rotational degrees of freedom). To account for changes in symmetry upon adsorption, we again use Benson's method to estimate standard entropies for unknown species in terms of values for known species. This method has been used extensively by Froment (127) in detailed analyses of hydrocarbon reactions on various catalysts. The basis for these effects of symmetry is outlined here.

The absolute entropy, S , of a molecule is given by

$$S = R \ln \Omega \quad (181)$$

where Ω is the number of distinguishable configurations of the compound. In this expression, the rotational entropy contributions must be corrected to account for the indistinguishable configurations of the molecule due to symmetry. Thus a term ($R \ln \sigma_s$) must be subtracted from the previous entropy expression, where σ_s is the symmetry number of the molecule. In addition, if the molecule has optical isomers (contains one or more asymmetric carbon atoms), then the number of spatial orientations is increased, and the entropy is increased by a term ($R \ln 2^n$), where n is the number of chiral carbon atoms. Therefore, the absolute entropy for the species is given by

$$S = R \ln \Omega' + R \ln(2^n/\sigma_s) \quad (182)$$

where Ω' is the number of configurations of the compound without regard to symmetry.

We now use the previous expression to relate the entropy of an adsorbed species, S_{surface} , to the entropy of a corresponding gaseous species, S_{gas} :

$$S_{\text{surface}} = F_{\text{loc}} \left\{ (S_{\text{gas}}^{\circ} - S_{\text{trans,3D}}) + R \ln \left(\frac{2^{n_{\text{surface}}}}{\sigma_{\text{surface}}} \right) - R \ln \left(\frac{2^{n_{\text{gas}}}}{\sigma_{\text{gas}}} \right) \right\} \quad (183)$$

where the subscripts "surface" and "gas" refer to the symmetry numbers and the numbers of chiral centers in the surface species and the gaseous olefin, respectively. As noted in Section II, the term F_{loc} corresponds to the fraction

of the local entropy in the gaseous molecule that is retained by the gaseous species. We have now defined the entropies of all surface species in terms of one parameter, F_{loc} .

The standard entropy and enthalpy changes for each of the 312 steps of the reaction sequence (ΔS_i° and ΔH_i°) can now be calculated from the thermodynamic properties of the gaseous and surface species, followed by calculation of equilibrium constants ($K_{i,\text{eq}}$) for each step:

$$K_{i,\text{eq}} = \exp\left(\frac{\Delta S_i^\circ}{R} - \frac{\Delta H_i^\circ}{RT}\right) \quad (184)$$

The next step in the reaction kinetics analysis is to choose for each family of reactions (i.e., adsorption/desorption, oligomerization/ β -scission, isomerization, and hydride transfer) whether to parameterize the kinetic model in terms of either the forward or the reverse rate constant ($k_{i,\text{for}}$ or $k_{i,\text{rev}}$) since the ratio of the forward and the reverse rate constants must equal the known value of $K_{i,\text{eq}}$:

$$\frac{k_{i,\text{for}}}{k_{i,\text{rev}}} = K_{i,\text{eq}} \quad (185)$$

For parameterization of the adsorption/desorption steps, we choose the adsorption direction. Accordingly, we define the adsorption rate constant from collision theory as

$$k_{\text{ads}} = \frac{\exp\left(-\frac{E_{\text{ads}}}{RT}\right)}{\sqrt{2\pi m_A k_B T} N_{\text{sat}}} \quad (186)$$

where E_{ads} is the activation energy for adsorption and N_{sat} is the saturation number of sites per unit area (i.e., 10^{15} sites/cm²). Typical values of E_{ads} estimated from DFT calculations are near 50 kJ/mol. As noted previously, we then use the equilibrium constant for the step to calculate the desorption rate constant. We use the same value of E_{ads} for all adsorption processes. The units of the rate constant are atm⁻¹ s⁻¹ (since we have chosen the standard state for gaseous species to be 1 atm).

We calculate the two rate constants, k_{init} , for initiation of the reaction by activation of isobutane (to produce adsorbed isobutyl and adsorbed propyl) in the same manner as the adsorption steps (i.e., using collision theory for the forward direction):

$$k_{\text{init}} = \frac{\exp\left(-\frac{E_{\text{init}}}{RT}\right)}{\sqrt{2\pi m_A k_B T} N_{\text{sat}}} \quad (187)$$

where E_{init} is the activation energy for the initiation reaction. We use a slightly different value of E_{init} for the initiation reaction to form adsorbed isobutyl

and H_2 ($E_{\text{init,H}_2}$) than for the reaction to form adsorbed propyl species and CH_4 ($E_{\text{init,CH}_4}$). The units of the rate constant are $\text{atm}^{-1} \text{s}^{-1}$.

For parameterization of the oligomerization/ β -scission steps, we choose to calculate the rate constant for the β -scission direction. Since the reaction in this reaction does not involve gaseous species, we write the rate constant for β -scission, k_β , as

$$k_\beta = 10^{13} \exp\left(-\frac{E_\beta}{RT}\right) \quad (188)$$

where E_β is the activation energy for β -scission. The value of E_β depends on the nature of the β -scission process. Specifically, we expect the following order for values of E_β :

$$E_{\beta,\text{ss}} > E_{\beta,\text{st}} > E_{\beta,\text{tt}}$$

where $E_{\beta,\text{ss}}$ corresponds to the activation energy for β -scission of a secondary species to form another secondary species, $E_{\beta,\text{st}}$ corresponds to β -scission of a secondary species to form a tertiary species or β -scission of a tertiary species to form a secondary species, and $E_{\beta,\text{tt}}$ corresponds to β -scission of a tertiary species to form another tertiary species. Accordingly, we parameterize the rate constants for the 88 β -scission steps in terms of three kinetic parameters: $E_{\beta,\text{ss}}$, $E_{\beta,\text{st}}$, and $E_{\beta,\text{tt}}$. The units of the β -scission rates constants are s^{-1} .

The rate constants for isomerization steps are similar in the forward and the reverse directions. For convenience, we choose to parameterize the kinetic model in terms of the forward rate constants. In this respect, we use the concept of single-event rate coefficients developed by Froment (127). According to Froment, the rate constant for a particular step is obtained by multiplying a single-event rate coefficient by the number of single events, n_e , possible for the reactant. The expression for n_e is

$$n_e = (\sigma_r/2^{n_r})/(\sigma^\ddagger/2^{n^\ddagger}) \quad (189)$$

where σ_r is the symmetry number of the reactant, σ^\ddagger is the symmetry number of the activated complex, n_r is the number of chiral centers in the reactant, and n^\ddagger is the number of chiral centers in the activated complex. We assumed that the transition state for isomerization is a three-membered carbon ring within the molecule. The rate constants for isomerization steps are now written as follows:

$$k_{\text{iso}} = n_e 10^{13} \exp\left(-\frac{E_{\text{iso}}}{RT}\right) \quad (190)$$

where E_{iso} is the activation energy for the isomerization step. We next categorize all isomerization steps as being branching or nonbranching

rearrangements, and the activation energies for these two classes of isomerization steps are defined as $E_{\text{iso,b}}$ and $E_{\text{iso,nb}}$, respectively. In general, we expect branching rearrangements to be more difficult than nonbranching rearrangements, leading to

$$E_{\text{iso,b}} > E_{\text{iso,nb}}$$

Accordingly, we parameterize the rate constants for the 71 isomerization steps in terms of two kinetic parameters, $E_{\text{iso,b}}$ and $E_{\text{iso,nb}}$. The units of the rate constants are s^{-1} .

We parameterize the hydride transfer steps in the direction of the reaction with isobutane. Accordingly, we define the hydride transfer rate constant, k_{H} , from collision theory as

$$k_{\text{H}} = \frac{\exp\left(\frac{\Delta S^{\ddagger}}{R} - \frac{E_{\text{H}}}{RT}\right)}{\sqrt{2\pi m_{\text{A}}} k_{\text{B}} T N_{\text{sat}}} \quad (191)$$

where E_{H} is the activation energy for hydride transfer and ΔS^{\ddagger} is the entropy change in changing from a mobile transition state to the actual transition state. This definition of the entropy change derives from the result that a sticking coefficient of unity corresponds to a mobile transition state (i.e., a species with the full local entropy of the gas phase and having two degrees of surface translation). We have included this entropy change as a kinetic parameter since the values of k_{H} have high sensitivity in the reaction kinetics analysis. Therefore, we are not able to achieve a proper value of k_{H} and also describe properly the temperature dependence of k_{H} with a single kinetic parameter, E_{H} . In our reaction kinetics analysis, we allow different values of E_{H} and ΔS^{\ddagger} for hydride transfer of isobutane with propyl species, *n*-butyl species, isopentyl species, and all heavier species. Therefore, we parameterize the rate constants for the 73 hydride transfer steps in terms of eight kinetic parameters: E_{C_3} , E_{C_4} , E_{C_5} , $E_{\text{C}_{6+}}$, $\Delta S_{\text{C}_3}^{\ddagger}$, $\Delta S_{\text{C}_4}^{\ddagger}$, $\Delta S_{\text{C}_5}^{\ddagger}$, and $\Delta S_{\text{C}_{6+}}^{\ddagger}$. The units of the rate constants are $\text{atm}^{-1} \text{s}^{-1}$.

In summary, we have parameterized our kinetic model for isobutane conversion (containing 312 steps, 78 olefins, 73 paraffins, and 74 surface species) in terms of the following 19 parameters: ΔH_3° , α_{H} , F_{loc} , E_{ads} , $E_{\text{init,H}_2}$, $E_{\text{init,CH}_4}$, $E_{\beta,\text{ss}}$, $E_{\beta,\text{st}}$, $E_{\beta,\text{tt}}$, $E_{\text{iso,b}}$, $E_{\text{iso,nb}}$, E_{C_3} , E_{C_4} , E_{C_5} , $E_{\text{C}_{6+}}$, $\Delta S_{\text{C}_3}^{\ddagger}$, $\Delta S_{\text{C}_4}^{\ddagger}$, $\Delta S_{\text{C}_5}^{\ddagger}$, and $\Delta S_{\text{C}_{6+}}^{\ddagger}$. Not all of these parameters will be kinetically significant in the final reaction kinetics analysis.

The reaction scheme outlined previously leads to a kinetic model containing 226 unknowns (i.e., 151 gaseous molecular flow rates, 74 surface species, and the fraction of free sites). We assumed that the reactor operates as a PFR. Therefore, we solve 151 differential equations for the gaseous

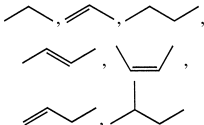
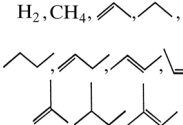
molecular flow rates versus reactor length combined with 74 steady-state equations for the fractional surface coverages by adsorbed species and one site-balance equation.

3. Results of the Reaction Kinetics Analysis

The kinetic model was used in an attempt to reconcile two data sets collected under different reaction conditions. Specifically, isobutane conversion data were collected at low temperatures (from 523 to 573 K) as the reaction was initiated by isobutylene added to the feed (at concentrations from 50 to 400 ppm); separately, isobutane conversion was investigated at higher temperatures (from 733 to 773 K) as the reaction was initiated by activation of isobutane to form isobutyl species and H₂ and to form propyl species and CH₄. These two sets of reaction conditions are summarized in Table IX. The values of the kinetic parameters used to describe the reaction kinetics data under the two sets of reaction conditions are summarized in Table X. Values of the fitted parameters were determined with Athena Visual Workbench (73). Table X also gives the 95% confidence limits for the parameters. The kinetic model contains 19 parameters, but it was found that the following parameters showed low sensitivity, and they were therefore set at reasonable values: E_{ads} , $E_{\text{iso,b}}$, and $E_{\text{iso,nb}}$. Accordingly, the kinetic model contains 16 parameters that are kinetically significant.

Figures 19–23 show the trends for the effluent concentrations of *n*-butane, propane, isopentane, propene, and butenes (the sum of isobutylene, 1-butene, *cis*- and *trans*-2-butenes) versus isobutylene feed concentration at

TABLE IX
Reaction Conditions and Products Observed for Isobutane Conversion on Ultrastable Y Zeolite at Low (523–573 K) and High (733–773 K) Temperatures^a

Feed and product properties	Reaction conditions	
	Low temperature (523–573 K)	High temperature (733–773 K)
Isobutane in feed %	20, 80	25
Isobutylene in feed (ppm)	50–400	0
Space velocity (mol g ⁻¹ h ⁻¹)	0.32, 1.27	0.062–0.19
Conversion of isobutane (%)	<0.1	10–40
Observed products		

^aCatalyst was calcined at 798 K for 2 h. High-temperature data from Yaluris *et al.* (129).

TABLE X
*Values and Confidence Limits of Kinetic Parameters Used
 to Describe Isobutane Conversion at Both Low (523–573 K)
 and High (733–773 K) Temperatures*

Parameter	Units	Value	95% Confidence interval	
			Lower	Upper
α_H	—	–2.7	–2.8	–2.7
Δ_{H_3}	kJ mol^{-1}	–107.5	–108.4	–107.4
F_{loc}	—	1.121	1.121	1.129
E_{ads}	kJ mol^{-1}	48.2	0.000	64.1
E_{init,H_2}	kJ mol^{-1}	155.9	155.9	157.2
E_{init,CH_4}	kJ mol^{-1}	155.4	154.8	156.2
$E_{\beta,tt}$	kJ mol^{-1}	122.2	122.2	122.6
$E_{\beta,st}$	kJ mol^{-1}	130.7	130.5	131.0
$E_{\beta,ss}$	kJ mol^{-1}	130.7	130.5	131.0
$E_{iso,b}$	kJ mol^{-1}	116.6	93.9	129.6
$E_{iso,nb}$	kJ mol^{-1}	90.981	—	—
E_{C_3}	kJ mol^{-1}	83.7	83.3	84.0
E_{C_4}	kJ mol^{-1}	88.6	87.6	88.7
E_{C_5}	kJ mol^{-1}	80.8	80.8	83.0
$E_{C_{6+}}$	kJ mol^{-1}	75.8	75.7	76.1
$\Delta S^{\circ \ddagger}_{C_3}$	$\text{J mol}^{-1} \text{K}^{-1}$	–12.0	–12.4	–11.6
$\Delta S^{\circ \ddagger}_{C_4}$	$\text{J mol}^{-1} \text{K}^{-1}$	–24.0	–25.9	–22.1
$\Delta S^{\circ \ddagger}_{C_5}$	$\text{J mol}^{-1} \text{K}^{-1}$	–16.6	–17.3	–15.9
$\Delta S^{\circ \ddagger}_{C_{6+}}$	$\text{J mol}^{-1} \text{K}^{-1}$	–28.3	–28.7	–27.9

low temperatures and versus space velocity and temperature at the higher temperatures. Figure 24 also shows trends for the effluent concentrations of H_2 , CH_4 , and isopentene versus space velocity and versus temperature at the higher temperatures (these products were not observed in significant amounts at lower temperatures). The solid lines in these figures represent predictions of the kinetic model. The kinetic model describes the trends for all the products at both sets of reaction conditions. Therefore, the surface chain reaction scheme is able to bridge the gap between the kinetics of isobutane conversion at low and high temperatures by accounting for the change in the nature of the initiation steps as the propagation and termination steps remain the same.

4. Sensitivity Analysis of the Kinetic Model

We next consider the sensitivity of the kinetic model to various steps in the reaction scheme. As indicated in Section II, we define the dimensionless

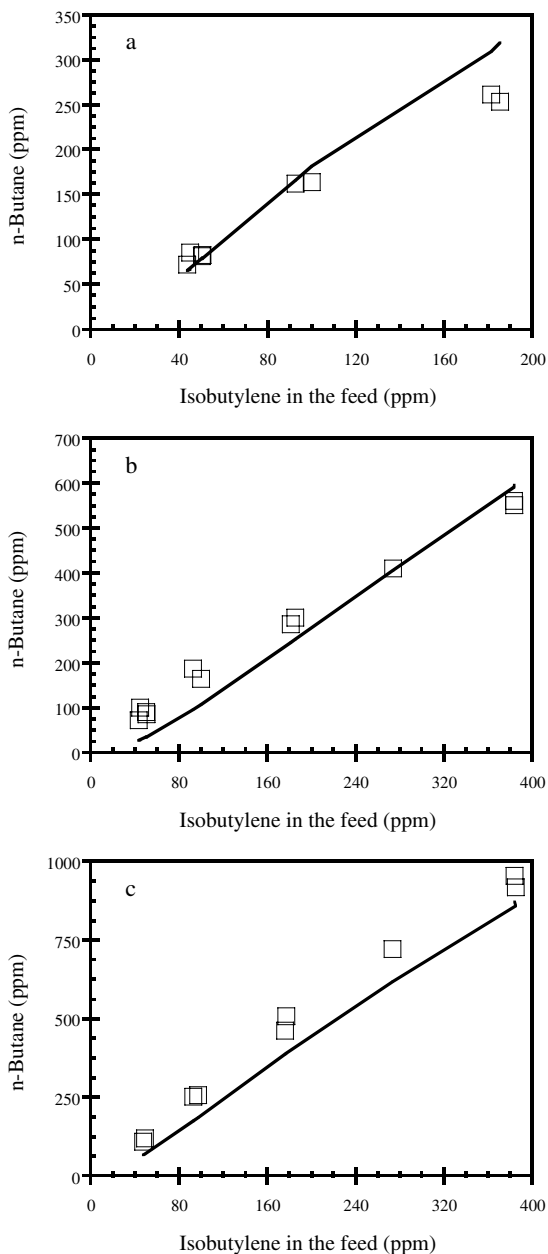


FIG. 19. Effluent concentration of *n*-butane as a function of isobutylene feed concentration at low temperatures (a–d) and as a function of temperature and space velocity at higher temperatures (e, f). (a) iC_4 in the feed $\sim 20\%$, $T = 523$ K; (b) iC_4 in the feed $\sim 20\%$, $T = 573$ K; (c) iC_4 in the feed $\sim 80\%$, $T = 523$ K; (d) iC_4 in the feed $\sim 80\%$, $T = 573$ K; (e) iC_4 in the feed $\sim 25\%$, $SV = 0.062 \text{ mol g}^{-1} \text{ h}^{-1}$; (f) iC_4 in the feed $\sim 25\%$, $T = 773$ K.

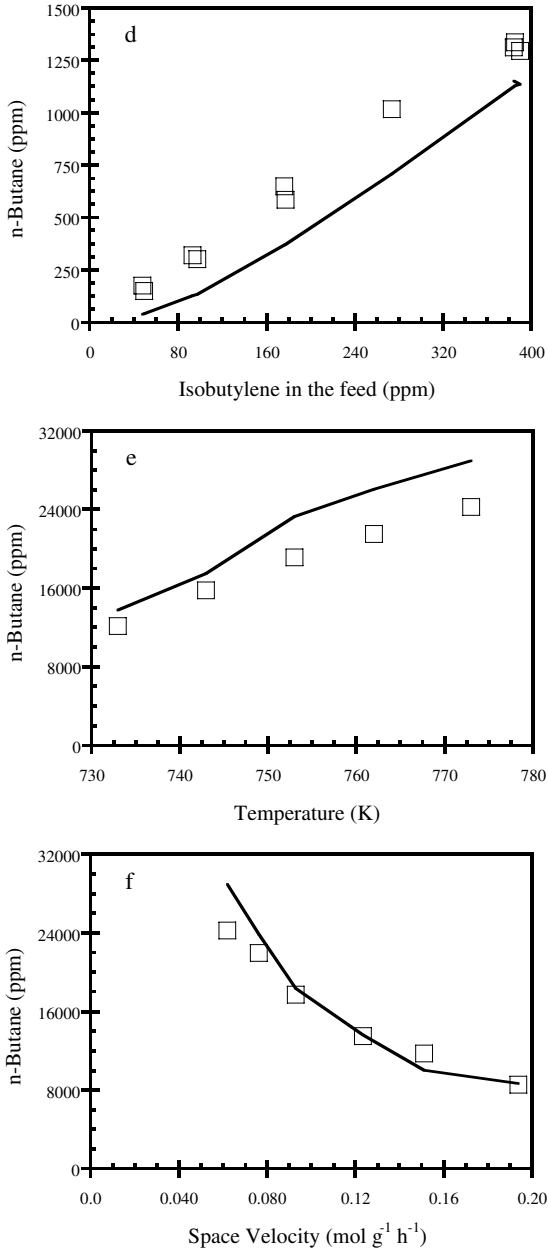


FIG. 19. (continued)

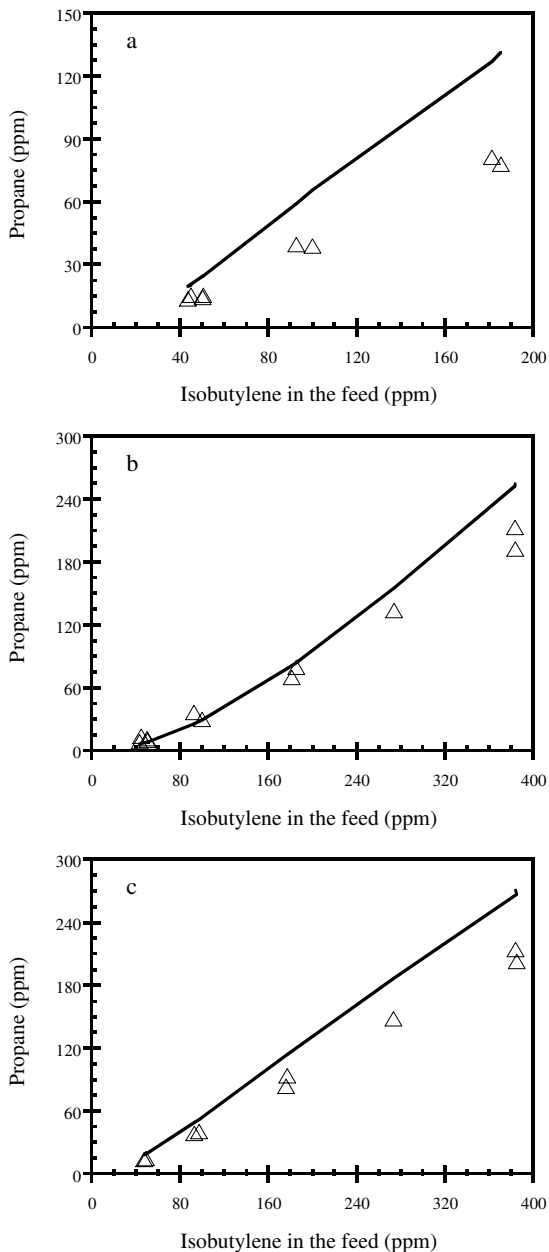


FIG. 20. Effluent concentration of propane as a function of isobutylene feed concentration at low temperatures (a–d) and as a function of temperature and space velocity at higher temperatures (e, f). (a) iC_4 in the feed $\sim 20\%$, $T = 523$ K; (b) iC_4 in the feed $\sim 20\%$, $T = 573$ K; (c) iC_4 in the feed $\sim 80\%$, $T = 523$ K; (d) iC_4 in the feed $\sim 80\%$, $T = 573$ K; (e) iC_4 in the feed $\sim 25\%$, $SV = 0.062 \text{ mol g}^{-1} \text{ h}^{-1}$; (f) iC_4 in the feed $\sim 25\%$, $T = 773$ K.

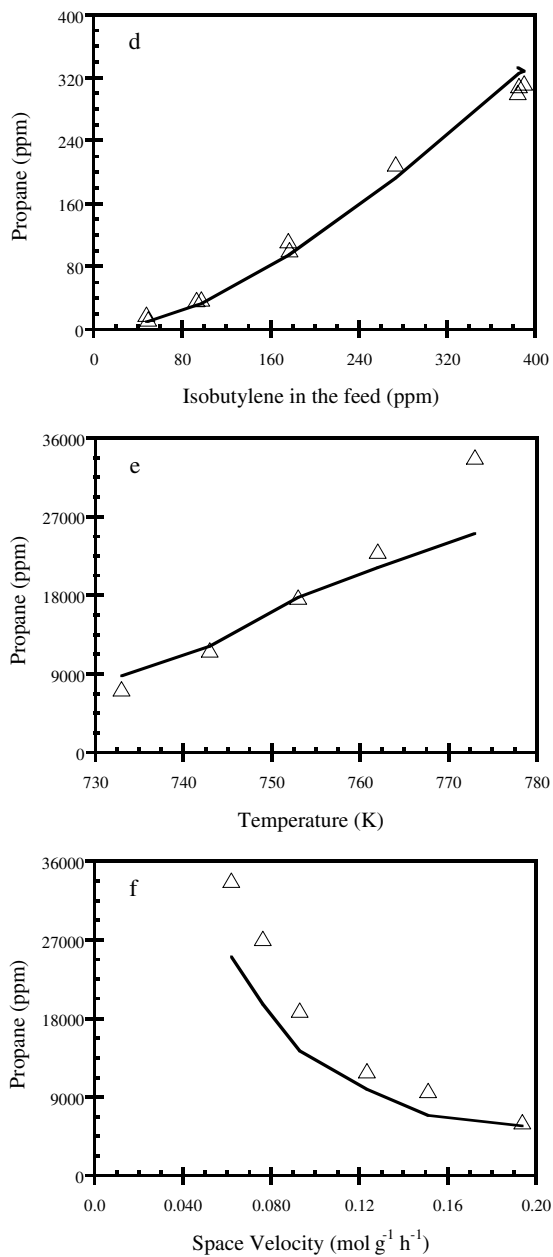


FIG. 20. (continued)

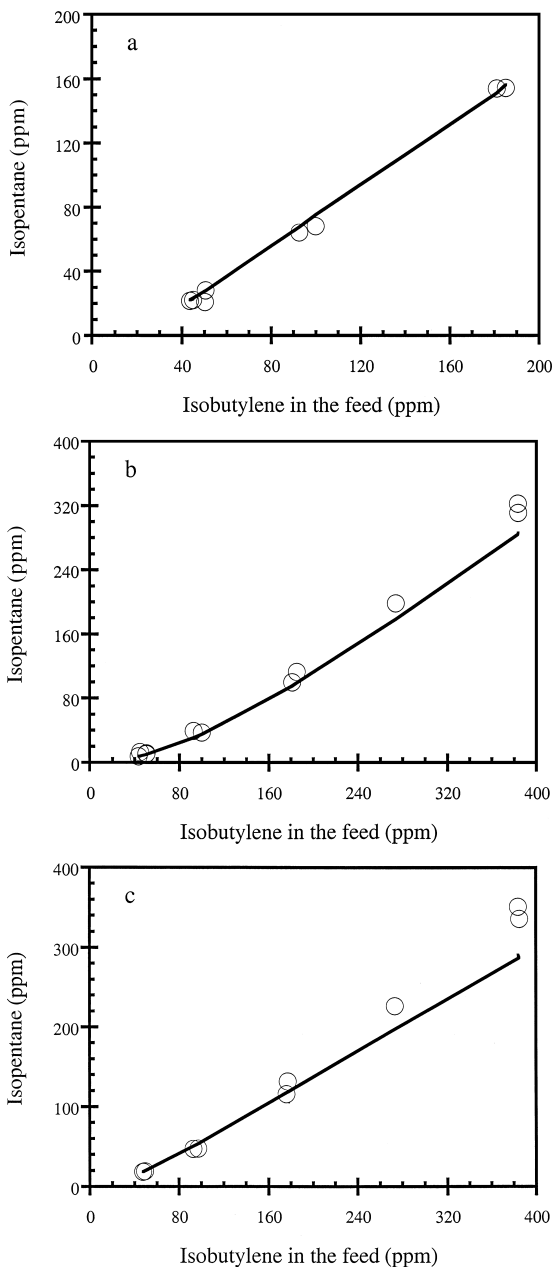


FIG. 21. Effluent concentration of isopentane as a function of isobutylene feed concentration at low temperatures (a–d) and as a function of temperature and space velocity at higher temperatures (e, f). (a) iC_4 in the feed $\sim 20\%$, $T = 523$ K; (b) iC_4 in the feed $\sim 20\%$, $T = 573$ K; (c) iC_4 in the feed $\sim 80\%$, $T = 523$ K; (d) iC_4 in the feed $\sim 80\%$, $T = 573$ K; (e) iC_4 in the feed $\sim 25\%$, $SV = 0.062 \text{ mol g}^{-1} \text{ h}^{-1}$; (f) iC_4 in the feed $\sim 25\%$, $T = 773$ K.

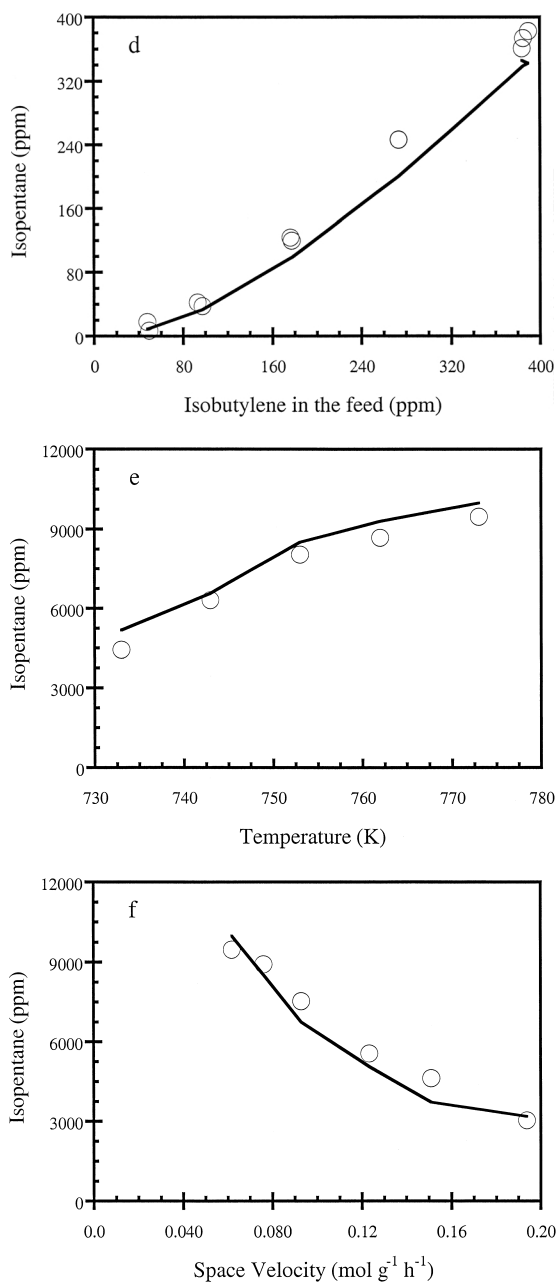


FIG. 21. (continued)

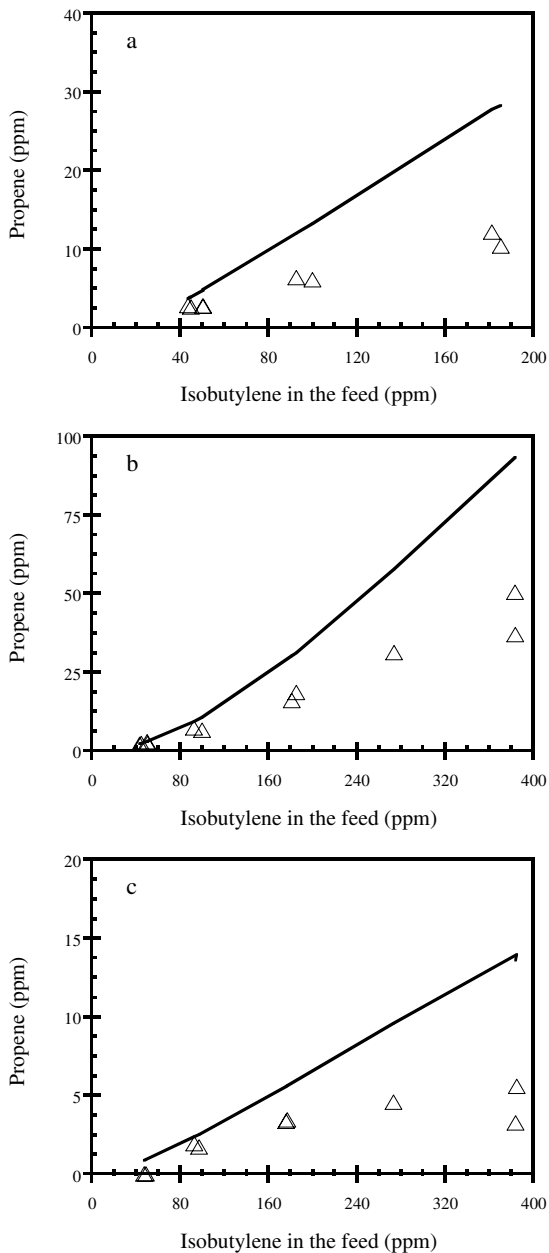


FIG. 22. Effluent concentration of propene as a function of isobutylene feed concentration at low temperatures (a–d) and as a function of temperature and space velocity at higher temperatures (e, f). (a) iC_4 in the feed $\sim 20\%$, $T = 523$ K; (b) iC_4 in the feed $\sim 20\%$, $T = 573$ K; (c) iC_4 in the feed $\sim 80\%$, $T = 523$ K; (d) iC_4 in the feed $\sim 80\%$, $T = 573$ K; (e) iC_4 in the feed $\sim 25\%$, $SV = 0.062 \text{ mol g}^{-1} \text{ h}^{-1}$; (f) iC_4 in the feed $\sim 25\%$, $T = 773$ K.

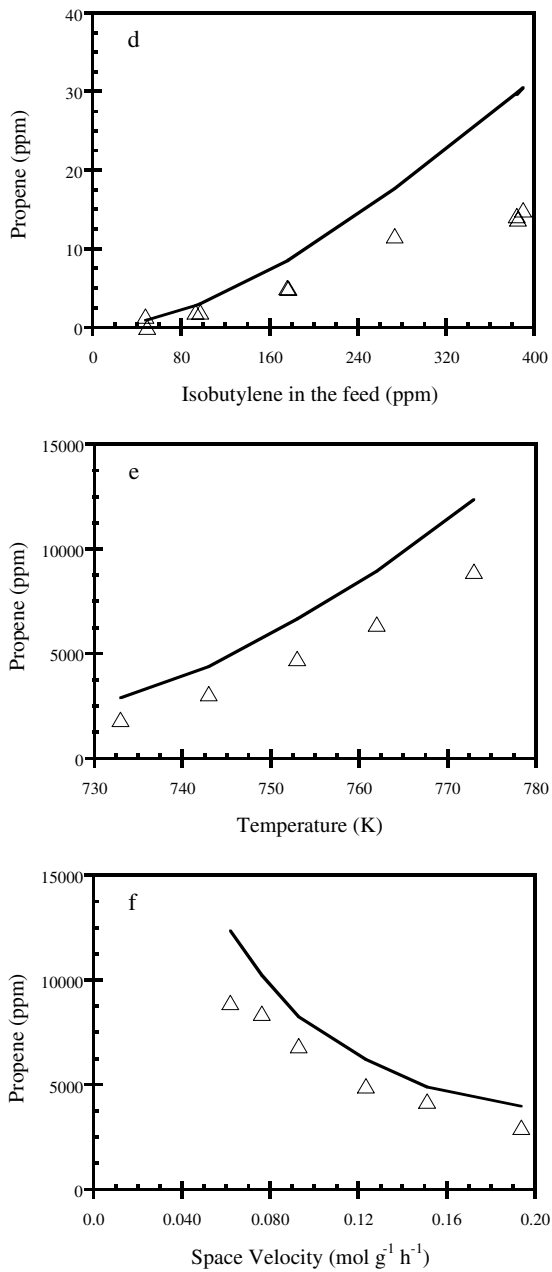


FIG. 22. (continued)

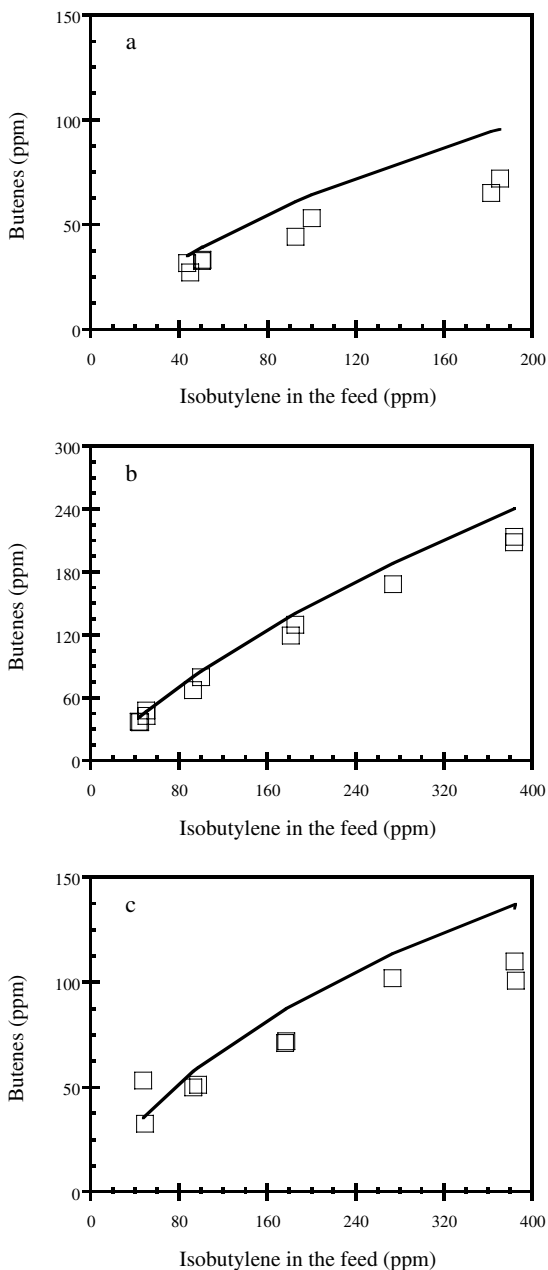


FIG. 23. Effluent concentration of butenes as a function of isobutylene feed concentration at low temperatures (a–d) and as a function of temperature and space velocity at higher temperatures (e, f). (a) iC_4 in the feed $\sim 20\%$, $T = 523$ K; (b) iC_4 in the feed $\sim 20\%$, $T = 573$ K; (c) iC_4 in the feed $\sim 80\%$, $T = 523$ K; (d) iC_4 in the feed $\sim 80\%$, $T = 573$ K; (e) iC_4 in the feed $\sim 25\%$, $SV = 0.062 \text{ mol g}^{-1} \text{ h}^{-1}$; (f) iC_4 in the feed $\sim 25\%$, $T = 773$ K.

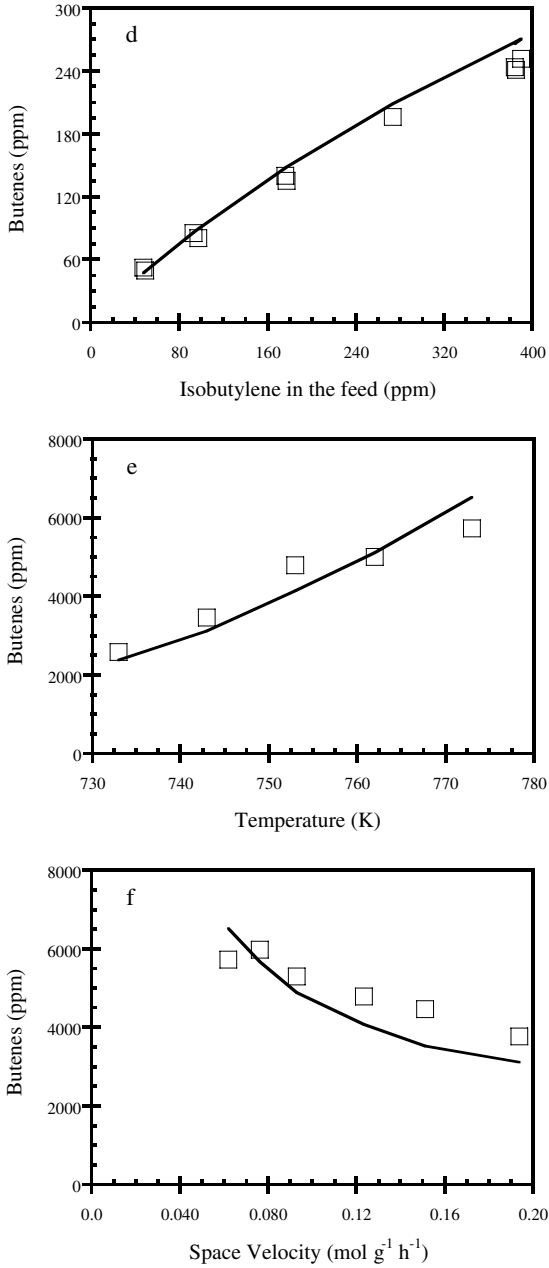


FIG. 23. (continued)

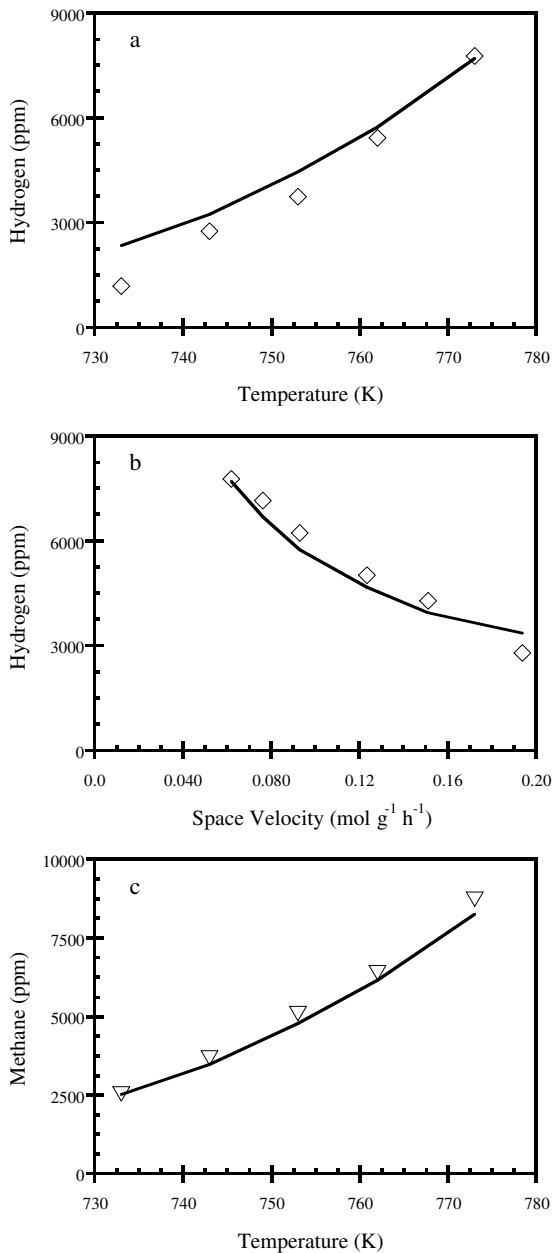


FIG. 24. Effluent concentration of hydrogen, methane, and 2-isopentene as a function of temperature and space velocity at higher temperatures. (a, c, e) iC_4 in the feed $\sim 25\%$, $SV = 0.062 \text{ mol g}^{-1} \text{ h}^{-1}$; (b, d, f) iC_4 in the feed $\sim 25\%$, $T = 773 \text{ K}$.

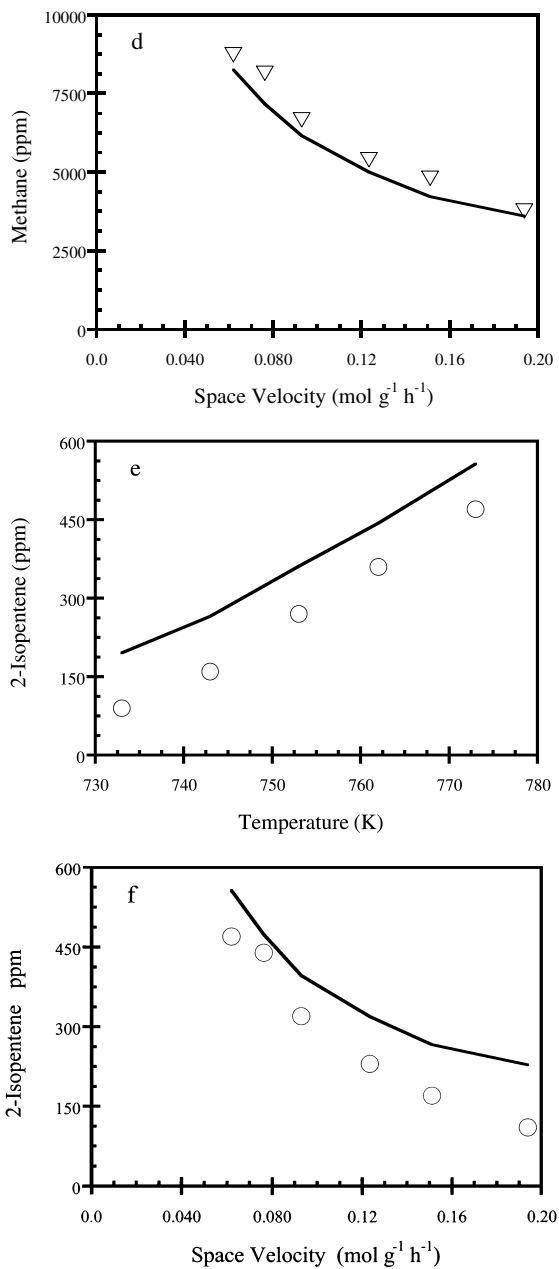


FIG. 24. (continued)

sensitivity, ϕ_i , of the overall rate with respect to k_i as

$$\phi_i = \left(\frac{\partial r}{\partial k_i} \right)_{k_j} \frac{k_i}{r} \quad (192)$$

Since we have multiple products, we define the total sensitivity, $\Phi_{i,\text{tot}}$, with respect to k_i as

$$\Phi_{i,\text{tot}} = \sum_k \left| \left(\frac{\partial r_k}{\partial k_i} \right)_{k_j} \frac{k_i}{r_k} \right| \quad (193)$$

where r_k refers to the rate of production of species k . We use the absolute value in this sum since a given kinetic parameter may have a positive sensitivity for a given product and a negative sensitivity for another product. Accordingly, although the parameter would not affect the overall conversion, it would change the product selectivity. Finally, we note again that Campbell's (29) degree of rate control is given by

$$X_{\text{RC},i} = \Phi_{i,\text{tot}} + \Phi_{-i,\text{tot}} \quad (194)$$

Table XI shows the steps with the highest degree of rate control for representative points at low and high temperatures. The most sensitive steps involve hydride transfer of surface species with isobutane and oligomerization/ β -scission steps involving predominantly adsorbed C_8 and C_7 species.

Finally, we note that the two steps for isobutane activation are kinetically significant under the high-temperature reaction conditions. The kinetic model was used to calculate the predicted surface coverage under reaction conditions. Approximately 96% of the surface sites are free under the low-temperature reaction conditions, whereas more than 99% of the sites are free at the higher temperatures. The most abundant surface species are predicted to be adsorbed $C_3^* - C_5^*$. The most abundant heavy species are predicted to be $C_6^* - C_9^*$. The fractional surface coverage by adsorbed $C_{10}^* - C_{12}^*$ is very low (e.g., 10^{-8}), consistent with our decision to neglect surface species heavier than C_{12}^* .

V. Conclusions

It is well established that the formulation of an effective catalyst involves the optimization of various physical and chemical phenomena. For example, the catalyst must bind the reactants and/or reaction intermediates sufficiently strongly to activate them for subsequent chemical reactions; however, the catalyst must not bind surface species too strongly, such that they block surface sites for further reaction. Furthermore, a selective catalyst must be

TABLE XI
Steps with the Highest Degree of Rate Control ($X_{RC,i}$)

Step	$X_{RC,i}$	
	Low temperatures	High temperatures
	—	4.0
	—	4.0
	2.5	1.3
	1.8	0.30
	1.2	0.35
	1.2	—
	1.2	2.8
	1.2	0.52
	0.88	—
	0.83	—
	0.78	—
	0.78	—
	0.44	0.37
	0.40	—
	0.31	—
	0.29	0.14

(continued)

TABLE XI (continued)

Step	$X_{RC,i}$	
	Low temperatures	High temperatures
	0.24	—
	0.20	—
	0.13	0.10
	0.13	—
	0.13	—
	0.12	—
	0.10	—
	—	0.88
	—	0.57

sufficiently active for production of desired products while being sufficiently inactive for production of undesired products. Similarly, a stable catalyst must be sufficiently inactive for production of species (such as coke precursors) that lead to catalyst deactivation. Furthermore, the optimization of catalyst performance depends on reaction conditions since the relative rates of competing surface reactions depend on temperature and the partial pressures of reactants and products.

An effective approach to help address the issues involved in controlling catalyst performance is to formulate and analyze reaction schemes that describe the essential chemistry taking place on the catalyst surface. This approach has been used successfully in catalysis research for many years. We suggest that this approach will see increased use in catalysis research. Specifically, continuing improvements in computer capabilities allow rapid analysis of complex reaction schemes for all common reactor configurations (e.g., reactors operating at steady state as well as under transient reaction conditions and nonisothermal reactors). Moreover, recent advances in quantum

chemical techniques, combined with improved computer performance, make it possible to use theoretical methods to calculate initial estimates for potential energy diagrams involved in reactions on realistic models of active sites. Results of these calculations can be used to probe the reactivities of sites with different coordination environments and to probe interactions between coadsorbed species, allowing effects of surface nonuniformity and effects of surface coverage to be included in reaction kinetics analyses (e.g., by use of Monte Carlo techniques). Moreover, important advances are being made in the applications of combinatorial chemistry and high-throughput screening methods to generate large amounts of reaction kinetics data for various catalytic materials. The improvements in computer capabilities, combined with recent advances in theoretical methods (e.g., DFT calculations) and experimental techniques (e.g., combinatorial chemistry and high-throughput screening), therefore allow analyses of reaction schemes to be conducted (i) more routinely, (ii) with better initial estimates of kinetic parameters, (iii) for more realistic kinetic models, and (iv) with more complete sets of reaction kinetics data.

Our objectives in writing this review were to provide a brief introduction to simple methods that are useful for analyses of reaction schemes and to provide several case studies that illustrate different scenarios for the applications of these analysis methods. Finally, we stress that analyses of reaction schemes are not used to “prove” reaction schemes. Instead, these analyses may be used first to test the feasibility of reaction schemes that have been formulated from chemical experience, intuition, and theoretical methods; these analyses may then be used to consolidate and extrapolate the information contained in kinetic models of reaction schemes to help guide the search for better catalytic materials and/or more favorable reaction conditions.

ACKNOWLEDGMENTS

We acknowledge the financial support for this work by the National Science Foundation, Department of Energy, and the National Center for Clean Industrial and Treatment Technologies. We acknowledge the help of Professor Manos Mavrikakis in discussions of DFT techniques. We also thank Marco A. Sanchez-Castillo for helping us in the preparation of the manuscript and Nitin Agarwal for help on the final case study.

REFERENCES

1. Dumesic, J. A., Rudd, D. F., Aparicio, L. M., Rekoske, J. E., and Treviño, A. A., “The Microkinetics of Heterogeneous Catalysis.” American Chemical Society, Washington, DC, 1993.
2. Neurock, M., and van Santen, R. A., *Catal. Today* **50**, 445 (1999).
3. Nørskov, J. K., *Stud. Surf. Sci. Catal.* **122**, 3–10 (1999).

4. Somorjai, G. A., "Introduction to Surface Chemistry and Catalysis," Wiley, New York, 1994.
5. Masel, R. I., "Principles of Adsorption and Reaction on Solid Surfaces." Wiley, New York, 1996.
6. van Santen, R. A., and Niemantsverdriet, J. W., "Chemical Kinetics and Catalysis," Plenum, New York, 1995.
7. van Santen, R. A., and Neurock, M., *Catal. Rev.-Sci. Eng.* **37**, 557 (1995).
8. van Santen, R. A., in "Chemisorption and Reactivity on Supported Clusters and Thin Films (Sicily)," NATO ASI Series E, p. 371. Kluwer, Dordrecht, 1997.
9. Sautet, P., *Topics Catal.* **13**, 213 (2000).
10. van Santen, R. A., *Catal. Today* **50**, 511 (1999).
11. Nicholas, J. B., *Topics Catal.* **4**, 157 (1997).
12. Nicholas, J. B., *Topics Catal.* **9**, 181 (1999).
13. Hansen, E. W., and Neurock, M., *Chem. Eng. Sci.* **54**, 3411 (1999).
14. Byskov, L. S., Norskov, J. K., Clausen, B. S., and Topsøe, H., *J. Catal.* **187**, 109 (1999).
15. Mavrikakis, M., Stoltze, P., and Nørskov, J. K., *Catal. Lett.* **64**, 101 (2000).
16. Gomes, J. R. B., and Gomes, J. A. N. F., *J. Electroanalytical Chem.* **483**, 180 (2000).
17. Barbosa, L. A., and van Santen, R. A., *J. Catal.* **191**, 200 (2000).
18. Broadbelt, L. J., *Appl. Catal. A* **200**, 23 (2000).
19. Maxwell, I. E., *Nature* **394**, 325 (1998).
20. Pescarmona, P. P., van der Wall, J. C., Maxwell, I. E., and Maschmeyer, T., *Catal. Lett.* **63**, 1 (1999).
21. Mirodatos, C., *Actualite Chim.* **9**, 35 (2000).
22. Gennari, F., Seneci, P., and Miertus, S., *Catal. Rev.-Sci. Eng.* **42**, 385 (2000).
23. Stoltze, P., *Prog. Surf. Sci.* **65**, 65 (2000).
24. De Donder, T., "L' Affinite." Gauthier-Villiers, Paris, 1927.
25. Boudart, M., "Kinetics of Chemical Processes." Prentice Hall, Englewood Cliffs, NJ, 1968.
26. Boudart, M., "Physical Chemistry: An Advanced Treatise," Vol. 7. Academic Press, New York, 1975.
27. Boudart, M., *J. Phys. Chem.* **87**, 2786 (1983).
28. Dumesic, J. A., *J. Catal.* **185**, 496 (1999).
29. Campbell, C. T., *Topics Catal.* **1**, 353 (1994).
30. Duca, D., Botar, L., and Vidoczy, T., *J. Catal.* **162**, 260 (1996).
31. Neurock, M., *Topics Catal.* **9**, 135 (1999).
32. Neurock, M., and Hansen, E. W., *Comp. Chem. Eng.* **22**, S1045 (1998).
33. Miller, S. J., *US Patent No. 4,727,216* (1986)
34. Perdew, J. P., Chevary, J. A., Vosko, S. H., Jackson, K. A., Pederson, M. R., Singh, D. J., and Fiolhais, C., *Phys. Rev. B* **46**, 6671 (1992).
35. Brinkmeyer, F. M., and Rohr, D. F. J., US Patent No. 4,866,211 (1987).
36. Cortright, R. D., and Dumesic, J. A., *J. Catal.* **148**, 771 (1994).
37. Cortright, R. D., *J. Catal.* **157**, 576 (1995).
38. Cortright, R. D., Bergene, E., Levin, P., Natal-Santiago, M., and Dumesic, J. A., *Proc. 11th Int. Cong. Catal.* **101**, 1185 (1996).
39. Cortright, R. D., and Dumesic, J. A., *Appl. Catal. A* **129**, 101 (1995).
40. Cortright, R. D., Levin, P. E., and Dumesic, J. A., *Ind. Eng. Chem. Res.* **37**, 1717 (1998).
41. Hill, J. M., Cortright, R. D., and Dumesic, J. A., *Appl. Catal. A* **168**, 9 (1998).
42. Natal-Santiago, M. A., Podkolzin, S. G., Cortright, R. D., and Dumesic, J. A., *Catal. Lett.* **45**, 155 (1997).
43. Anderson, J. B., *Chem. Eng. Sci.* **18**, 147 (1963).
44. Mears, D. E., *J. Catal.* **20**, 127 (1971).

45. Mears, D. E., *Ind. Eng. Chem. Process Des. Develop.* **10**, 541 (1971).
46. Shen, J., Hill, J. M., Watwe, R. M., Spiewak, B. E., and Dumesic, J. A., *J. Phys. Chem. B* **103**, 3923 (1999).
47. Watwe, R. M., Cortright, R. D., Mavrikakis, M., Nørskov, N. K., and Dumesic, J. A., *J. Chem. Phys.* **114**, 4663 (2001).
48. Goddard, S. A., Cortright, R. D., and Dumesic, J. A., *J. Catal.* **137**, 186 (1992).
49. Cremer, P. S., McIntyre, B. J., Salmeron, M., Shen, Y. R., and Somorjai, G. A., *Catal. Lett.* **34**, 11 (1995).
50. Ozaki, A. (Ed.), "Isotopic Studies of Heterogeneous Catalysis." Academic Press, New York, 1977.
51. Weinberg, W. H., and Sung, Y., *Surf. Sci. Lett.* **277**, L39 (1992).
52. Stull, D. R., Westrum, J. E. F. Jr., and Sinke, G. C., "The Chemical Thermodynamics of Organic Compounds." Wiley, New York, 1969.
53. Watwe, R. M., Cortright, R. D., Nørskov, J. K., and Dumesic, J. A., *J. Phys. Chem. B* **104**, 2299 (2000).
54. Watwe, R. M., Spiewak, B. E., Cortright, R. D., and Dumesic, J. A., *J. Catal.* **180**, 184 (1998).
55. Cortright, R. D., Watwe, R. M., and Dumesic, J. A., *J. Mol. Catal.* **63**, 91 (2000).
56. Cortright, R. D., Watwe, R. M., Spiewak, B. E., and Dumesic, J. A., *Catal. Today* **53**, 395 (1999).
57. Bond, G. C., and Cunningham, R. H., *J. Catal.* **163**, 328 (1996).
58. Sinfelt, J. H., Taylor, W. F., and Yates, D. J. C., *J. Phys. Chem.* **69**, 95 (1965).
59. Sinfelt, J. H., and Yates, D. J. C., *J. Catal.* **8**, 82 (1967).
60. Sinfelt, J. H., *J. Catal.* **27**, 468 (1972).
61. Sinfelt, J. H., *Adv. Catal.* **23**, 91 (1973).
62. Vanderbilt, D. H., *Phys. Rev. B* **41**, 7892 (1990).
63. White, J. A., and Bird, D. M., *Phys. Rev. B* **50**, 4954 (1994).
64. Kresse, G., and Furthmüller, J., *Comput. Mat. Sci.* **6**, 15 (1996).
65. Spiewak, B. E., Cortright, R. D., and Dumesic, J. A., *J. Catal.* **176**, 405 (1998).
66. Sharma, S. B., Miller, J. T., and Dumesic, J. A., *J. Catal.* **148**, 198 (1994).
67. Paul, J. F., and Sautet, P., *J. Phys. Chem. B* **102**, 1578 (1998).
68. Ge, Q., and King, D. A., *J. Chem. Phys.* **110**, 4699 (1999).
69. Stuck, A., Wartnaby, C. E., Yeo, Y. Y., and King, D. A., *Phys. Rev. Lett.* **74**, 578 (1995).
70. Shepard, N., and De La Cruz, C., *Adv. Catal.* **41**, 1 (1996).
71. Brown, W. A., Kose, R., and King, D. A., *Chem. Rev.* **98**, 797 (1998).
72. Zaera, F., and Somorjai, G. A., *J. Phys. Chem.* **89**, 3211 (1985).
73. Caracotsios, M. C., and Stewart, W. A., Athena Visual Workbench 5.0 (2000).
74. Turek, T., Trimm, D. L., and Cant, N. W., *Catal. Rev.-Sci. Eng.* **36**, 645 (1994).
75. Natal-Santiago, M. A., Sánchez-Castillo, M. A., Cortright, R. D., and Dumesic, J. A., *J. Catal.* **193**, 16 (2000).
76. Cortright, R. D., Sanchez-Castillo, M. A., Greeley, J. P., Mavrikakis, M., and Dumesic, J. A., Manuscript in preparation (2001).
77. Dandekar, A., and Vannice, M. A., *J. Catal.* **178**, 621 (1998).
78. Iwasa, N., and Takezawa, N., *Bull. Chem. Soc. Jpn.* **64**, 2619 (1991).
79. Yaws, C. L., "Chemical Properties Handbook." McGraw-Hill, New York, 1999.
80. Hammer, B., and Nørskov, J. K., *Nature* **376**, 238 (1995).
81. Kramer, G. M., McVicker, G. B., and Ziemiak, J. J., *J. Catal.* **92**, 355 (1985).
82. Beyerlein, R. A., McVicker, G. B., Yacullo, L. N., and Ziemiak, J. J., *Preprints. Am. Chem. Soc. Div. Pet. Chem.* **31**, 90 (1986).

83. Soled, S., McVicker, G., Miseo, S., Gates, W., and Baumgartner, J., *Proc. 11th Int. Congr. Catal.* **101**(A), 563 (1996).
84. Natal-Santiago, M. A., Alcalá, R., and Dumesic, J. A., *J. Catal.* **181**, 124 (1999).
85. Hattori, H., Takahashi, O., Takagi, M., and Tanabe, K., *J. Catal.* **68**, 132 (1981).
86. Fogash, K. B., Larson, R. B., Gonzalez, M. R., Kobe, J. M., and Dumesic, J. A., *J. Catal.* **163**, 138 (1996).
87. Cortright, R., Dumesic, J. A., and Madon, R. J., *Topics Catal.* **4**, 15 (1997).
88. Yaluri, G., Madon, R. J., and Dumesic, J. A., *J. Catal.* **165**, 205 (1997).
89. Babitz, S. M., Kuehne, M. A., and Kung, H. H., *Ind. Eng. Chem. Res.* **36**, 3027 (1997).
90. Hong, Z., Fogash, K. B., Watwe, R. M., Kim, B., Masqueda-Jimenez, B. I., Natal-Santiago, M. A., Hill, J. M., and Dumesic, J. A., *J. Catal.* **178**, 489 (1998).
91. Brait, A., Seshan, K., Weinstabl, H., Ecker, A., and Lercher, J. A., *Appl. Catal. A* **169**, 313 (1998).
92. Brait, A., Seshan, K., and Lercher, J. A., *Appl. Catal. A* **169**, 299 (1998).
93. Tran, M. T., Gnep, N. S., Szabo, G., and Guisnet, M., *Appl. Catal. A* **170**, 49 (1998).
94. Babitz, S. M., Williams, B. A., Miller, J. T., Snurr, R. Q., Haag, W. O., and Kung, H. H., *Appl. Catal. A* **179**, 71 (1999).
95. Williams, B. A., Babitz, S. M., Miller, J. T., Snurr, R. Q., and Kung, H. H., *Appl. Catal. A* **177**, 161 (1999).
96. Kung, H. H., Williams, B. A., Babitz, S. M., Miller, J. T., and Snurr, R. Q., *Catal. Today* **52**, 91 (1999).
97. Baburek, E., and Novakova, J., *Appl. Catal. A* **185**, 123 (1999).
98. Matsuhashi, H., Shibata, H., Nakamura, H., and Arata, K., *Appl. Catal. A* **187**, 99 (1999).
99. Hong, Z., Fogash, K. B., and Dumesic, J. A., *Catal. Today* **51**, 269 (1999).
100. McVicker, G. B., Kramer, G. M., and Ziemiak, J. J., *J. Catal.* **83**, 286 (1983).
101. Beyerlein, R. A., McVicker, G. B., Yacullo, L. N., and Ziemiak, J., *J. Phys. Chem.* **92**, 1967 (1988).
102. Lombardo, E. A., and Hall, W. K., *J. Catal.* **112**, 565 (1988).
103. Kramer, G. M., and MacVicker, G. B., *J. Catal.* **115**, 608 (1989).
104. Hall, W. K., Lombardo, E. A., and Engelhardt, J., *J. Catal.* **115**, 611 (1989).
105. Engelhardt, J., *J. Catal.* **125**, 472 (1990).
106. Stefanadis, C., Gates, B. C., and Haag, W. O., *J. Mol. Catal.* **67**, 363 (1991).
107. Umansky, B., Engelhardt, J., and Hall, W. K., *J. Catal.* **127**, 128 (1991).
108. Engelhardt, J., and Hall, W. K., *J. Catal.* **151**, 1 (1995).
109. Engelhardt, J., Onyestyak, G., and Hall, W. K., *J. Catal.* **157**, 721 (1995).
110. Engelhardt, J., *J. Catal.* **164**, 449 (1996).
111. Fogash, K. B., Hong, Z., Kobe, J. M., and Dumesic, J. A., *Appl. Catal. A* **172**, 107 (1998).
112. Fogash, K. B., Hong, Z., and Dumesic, J. A., *J. Catal.* **173**, 519 (1998).
113. Haag, W. O., and Dessau, R. M., *Proc. 8th Int. Congr. Catal. Berlin*, 305 (1984).
114. Kazansky, V. B., Frash, M. V., and van Santen, R. A., *Catal. Lett.* **48**, 61 (1997).
115. Kazansky, V. B., *Catal. Today* **51**, 419 (1999).
116. Haw, J. F., Nicholas, J. B., Song, W. G., Deng, F., Wang, Z. K., Xu, T., and Heneghan, C. S., *J. Am. Chem. Soc.* **122**, 4763 (2000).
117. van Santen, R. A., *Catal. Today* **38**, 377 (1997).
118. Natal-Santiago, M. A., Alcalá, R., and Dumesic, J. A., *J. Catal.* **181**, 124 (1999).
119. Morrison, R. T., and Boyd, R. N., "Organic Chemistry," 6th ed. Prentice Hall, Englewood Cliffs, NJ, 1992.
120. Benson, S. W., "Thermochemical Kinetics." Wiley, New York, 1968.
121. Benson, S. W., and Buss, J. H., *J. Chem. Phys.* **29**, 546 (1969).

122. Benson, S. W., Cruickshank, F. R., Golden, D. M., Haugen, G. R., O'Neal, H. E., Rodgers, A. S., Shaw, R., and Walsh, R., *Chem. Rev.* **69**, 279 (1969).
123. Reid, R. C., Prausnitz, J. M., and Poling, B. E., "The Properties of Gases and Liquids," 4th ed. McGraw-Hill, New York, 1987.
124. Haag, W. O., in "Zeolites and Related Microporous Materials: State of the Art" (J. Weitkamp, H. G. Karge, H. Pfeifer, and W. Hölderich, Eds.), Vol. 84, p. 1375. Elsevier, Amsterdam, 1994.
125. Eder, F., Stockenhuber, M., and Lercher, J. A., *J. Phys. Chem. B* **101**, 5414 (1997).
126. van Well, W. J. M., Janchem, J., de Haan, J. W., and van Santen, R. A., *J. Phys. Chem. B* **103**, 1841 (1999).
127. Froment, G. F., *Catal. Today* **52**, 153 (1999).
128. Lok, L. K., Gaidai, N. A., Gudkov, B. S., Kiperman, S. L., and Kogan, S. B., *Kinet. Katal.* **27**, 1365 (1986).
129. Yaluris, G., Rekoske, J. E., Aparicio, L. M., Madon, R. J., and Dumesic, J. A., *J. Catal.* **153**, 54 (1995).

Surface Structures of Oxides and Halides and Their Relationships to Catalytic Properties

A. ZECCHINA, D. SCARANO, S. BORDIGA, AND G. SPOTO

*Department of Inorganic, Physical, and Material Chemistry
University of Turin
I-10125 Turin, Italy*

AND

C. LAMBERTI

*Department of Inorganic, Physical, and Material Chemistry
University of Turin
I-10125 Turin, Italy
and
INFN U.d.R di Torino Università*

In this review, the relationships between structure, morphology, and surface reactivity of microcrystals of oxides and halides are assessed. The investigated systems we discuss include alkali halides, alkaline earth oxides, NiO, CoO, NiO–MgO, CoO–MgO solid solutions, ZnO, spinels, cuprous oxide, chromia, ferric oxide, alumina, lanthana, perovskites, anatase, rutile, and chromia/silica. A combination of high-resolution transmission electron microscopy with vibrational spectroscopy of adsorbed probes and of reaction intermediates and calorimetric methods was used to characterize the surface properties. A few examples of reactions catalyzed by oxides are also reported. © 2001 Academic Press.

Abbreviations: $A(hkl)$, surface area of the simulation cell in atomistic approaches (m^2); a_{AM} , lattice parameter of an AM oxide (\AA); A_{5c}^{n-} , fivefold coordinated, n -valent anion; A_{4c}^{n-} , fourfold coordinated, n -valent anion; A_{3c}^{n-} , threefold coordinated, n -valent anion; ABX_3 , general formula for perovskite-type structure: A, large cation; B, small transition metal or main group ion; and X, an oxygen or an halide; AFM, atomic force microscopy; bcc, body-centered cubic; BE, binding energy (kJ/mol); d_{hkl} , distance between the (hkl) planes (\AA); E , electric field (V/nm); $E_{total}(hkl)$, total energy in atomistic simulations (J); $E_{boundary}(hkl)$, boundary energy in atomistic simulations (J); $E_{crystal}(hkl)$, crystal energy in atomistic simulations (J); EELS, electron energy loss spectroscopy; EPR, electron paramagnetic resonance; F^+ , positively charged bulk F center consisting of one electron trapped in anion vacancy in oxides; F , neutral bulk F center consisting of two electrons trapped in anion vacancy in oxides; F_s^+ , positively charged surface F center consisting of one electron trapped in anion vacancy in oxides; F_s , neutral surface F center consisting of two electrons trapped in anion vacancy in oxides; FTIR, Fourier transform infrared; FWHM, full-width at half maximum; HREELS, high-resolution electron

I. Introduction

Although oxides and chlorides represent some of the most important and widely employed classes of solid catalysts, either as active phases or supports, investigations of the surface properties of oxide and chloride single crystals with the classical methods of surface science fall short of what the practical importance of the materials should merit. The lack is partially a consequence of the insulating character of most of these solids, which prevents the straightforward application of classical electron spectroscopies such as high-resolution electron energy loss spectroscopy (HREELS) to single crystal faces. This obstacle is now gradually being overcome by investigations of films (mostly of oxides) grown epitaxially on single-crystal metal faces, both by spectroscopic and surface science methods; the conducting properties of the underlying metals help to alleviate the experimental difficulties (1–7). As such investigations progress, the knowledge of the surface properties of oxides and halides is expected to become comparable to that of metallic surfaces. This conclusion is reinforced by the fact that the intensive application of *ab initio* and force field-based computational methods to model systems (simulating the oxide surfaces) is providing additional valuable characterization of the surface properties of this class of solids (8, 9).

Although investigations of well-defined (single-crystal) oxide and chloride surfaces started only a few years ago, dispersed materials have received much more attention because of their closer connection to practical catalytic materials. The number of publications in this field (particularly concerning the application of spectroscopic and calorimetric methods) is extremely large (10–21). However, notwithstanding their close similarity to supported catalysts (in contrast to single crystals), dispersed materials suffer from poor surface definition; consequently, investigations of surface properties of these

energy loss spectroscopy; HRTEM, high-resolution transmission electron microscopy; IR, infrared; LEED, low-energy electron diffraction; M_{5c}^{n+} , fivefold coordinated, n -valent cation; M_{4c}^{n+} , fourfold coordinated, n -valent cation; M_{3c}^{n+} , threefold coordinated, n -valent cation; NEXAFS, near-edge X-ray absorption fine structure; NMR, nuclear magnetic resonance; $r(M^{n+})$, ionic radius of n -valent cations (Å); SEM, scanning electron microscopy; STM, scanning tunneling microscopy; TDS, thermal desorption spectroscopy; UPS, ultraviolet photoelectron spectroscopy; UV–VIS, ultraviolet and visible; x , relative fraction of a cation in a solid solution: $0 \leq x \leq 1$ (e.g., $Mg_xNi_{1-x}O$); XPS, X-ray photoelectron spectroscopy; XRD, X-ray diffraction; ΔH_{ads} , differential heats of adsorption (kJ/mol); α_e , electronic polarizability (Å^3); α_v , vibrational polarizability (Å^3); $\Delta\alpha_v$, variation of vibrational polarizability (Å^3); ϵ_{CO} , extinction coefficient of the C–O stretching mode; $\bar{\nu}$, wavenumber (cm^{-1}); $\bar{\nu}_0(\text{CO})$, stretching frequency of the unperturbed CO molecule (2143 cm^{-1}); $\Delta\bar{\nu}$, wavenumber shift (cm^{-1})—normally computed with respect to the frequency of the corresponding mode in the unperturbed molecule; $\Delta\bar{\nu}_{dyn}$, dynamical wavenumber shift (cm^{-1}); $\Delta\bar{\nu}_{stat}$, static wavenumber shift (cm^{-1}); $\bar{\nu}_0$, singleton frequency (cm^{-1}) (i.e., the frequency at $\theta \rightarrow 0$); $\bar{\nu}_{asym}$, asymmetric stretching mode (cm^{-1}); $\bar{\nu}_{sym}$, symmetric stretching mode (cm^{-1}); $\gamma(\text{hkl})$, energy of the (hkl) surface in atomistic simulations (Jm^{-2}); θ , surface coverage ($0 < \theta < 1$); Σ_0 , direct dipolar sum (Å^{-3}); ν , surface electron trap.

materials have often been considered as a branch of science substantially separated from surface science.

However, in recent years it has been shown that single crystals and dispersed materials are not so different as to hinder fruitful comparisons of results from the separate fields (22, 23). It has been shown that when proper synthesis and sintering procedures are adopted, oxide and chloride microparticles are obtained that can assume the crystalline habits of very well-defined polyhedra and consequently can expose facelets with regularity not significantly different from that of single crystals (22, 23).

The method we refer to as progressive sintering has allowed preparation of samples of oxides and chlorides with a wide range of surface properties, virtually spanning the range between highly dispersed samples and single crystals. Characterization data representing samples having controlled morphology represent a link between dispersed catalytic materials, on the one hand, and single crystals and epitaxial films on the other hand.

Thus, this review is concerned with the following topics:

1. Crystallography and bonding of the main classes of bulk oxides and chlorides, including those with the rock salt structure (e.g., MgO and NaCl), the wurtzite structure (ZnO), the Cu₂O structure, the corundum structure (α -Cr₂O₃, α -Fe₂O₃, and α -Al₂O₃), the hexagonal structure (La₂O₃), the spinel and perovskite structure, and also TiO₂ and amorphous silica (both pure and with supported metal ions).
2. The use of high-resolution transmission electron microscopy (HRTEM) and scanning tunneling microscopy (STM) to investigate the morphologies of oxides and chlorides and to compare the surface characteristics of dispersed materials, films, and single crystals.
3. Spectroscopic methods for investigation of oxide and chloride surfaces.
4. Electrostatic fields at the surface of oxides and halides.
5. Acidity and basicity of surfaces.
6. Redox properties of oxide surfaces and their relationships to catalytic activity.

The review continues with case studies of the surface reactivities of a few representative crystalline oxides and chlorides (as single crystals, ordered films, or dispersed materials) with simple probe molecules. The systems are essentially those indicated in topic 1.

In these case studies, in addition to a brief discussion of the catalytic applications, representative reactions are discussed with the aim of illustrating in detail the relationships between surface structures (as inferred from investigations with probe molecules) and catalytic activity. The following topics are discussed in detail: (i) MgO as a model catalyst for base-catalyzed reactions; (ii) the mechanism of ethene hydrogenation on ZnO; (iii) Cu₂O as an oxidation catalyst for the conversion of methanol to formaldehyde, with

consideration of the activities of the different surface planes; (iv) α -Cr₂O₃ as a hydrocarbon dehydrogenation catalyst; (v) perovskites as hydrocarbon total oxidation catalysts; and (vi) Cr²⁺/SiO₂ and its activity for ethene polymerization.

Finally, on the basis of all the results illustrated for the case studies, the problem of quantification of the acid strengths of the surface sites is discussed.

II. The Simplest Classes of Oxides and Chlorides: Structure and Bonding

Here, information about the structures of the most commonly encountered classes of oxides and halides is given. This brief description is intended to facilitate understanding of the following sections and to help the reader understand the geometrical properties that determine the structure and reactivity of the most commonly exposed faces of oxides and halides.

A. OXIDES AND HALIDES WITH ROCK SALT STRUCTURE

MgO and NaCl are the best examples of this class of ionic solids, which includes NiO, CoO, CaO, BaO, and LiF (24). The morphologies of these solids are represented in Fig. 1, in which the local geometric structures of low-index (100), (010), and (001) faces on edges and corners are illustrated schematically. The morphologies of the microparticles represented in Fig. 1 have been determined on the basis of results obtained experimentally and with computer modeling techniques.

In the bulk, cations and anions are sixfold coordinated. The total energy of the crystal is nearly completely given by the Madelung (electrostatic) energy. On the surfaces of the microcrystals, different local coordinations are encountered, with coordination numbers varying from five on the (100), (010), and (001) faces to four on edges and steps and three on corners. Threefold coordinated ions are also present on reconstructed (111) faces.

As a consequence of the identical crystallographic structure and the very similar ionic radii, MgO and NiO or CoO form uniform solid solutions Mg_(1-x)M_xO ($0 \leq x \leq 1$), where *M* is Ni or Co (25). Real crystals are often covered by strongly adsorbed water and carbon dioxide, and thermal treatments *in vacuo* are needed to clean the surfaces and create the surface coordinative unsaturation mentioned previously (in particular the fourfold and threefold coordinated sites are cleaned only at very high temperatures). In this connection, it is evident that the surface chemistry of clean surfaces is primarily determined by the presence of these

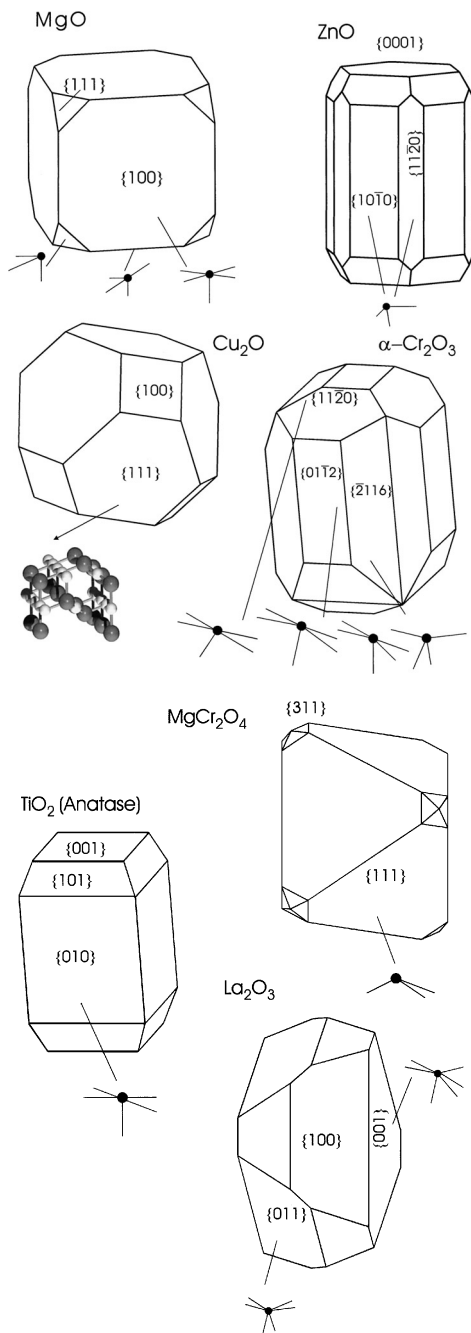


FIG. 1. Representation of particle morphologies as obtained by the combined use of HRTEM and computer modeling.

coordinatively unsaturated sites, the relative abundance of which is influenced by the surface morphology.

B. OXIDES AND HALIDES WITH THE WURTZITE STRUCTURE

In these systems, the metal and oxygen or halogen ions are fourfold coordinated. ZnO and CuCl are the best examples of this group of solids. The tetrahedral coordination is usually associated with a substantial degree of covalency, and consequently the positive and negative centers do not carry the full charge (half of the value is considered a good approximation in many cases).

Electron microscopy results and surface energy calculations show that typical microcrystals of ZnO expose preferentially the $(10\bar{1}0)$ and $(11\bar{2}0)$ faces (Fig. 1), where the ions are threefold coordinated; this is a situation only rarely encountered with systems having the rock salt structure. Ions in still lower coordination state can potentially be found on edges, steps, and corners. However, such highly coordinatively unsaturated sites cannot really be found on microcrystals of stoichiometric ZnO because hydroxyl groups permanently saturate these coordinative vacancies. These groups cannot be eliminated even under the most severe thermal treatments *in vacuo* without altering the stoichiometry of the crystals (26). For this reason, these highly defective structures will not be considered in the case studies for the wurtzite structure.

C. CUPRITE (Cu_2O) STRUCTURE

Because of the importance of cuprous oxide and cuprous-based systems in catalysis, the most common shape of the microcrystals of Cu_2O , as determined experimentally and theoretically, is reported in Fig. 1. Several investigations of Cu_2O single crystals have been reported, and these are particularly valuable for purposes of this review.

The cuprite structure consists of a body-centered cubic (bcc) array of oxygen atoms, and the copper atoms occupy centers of four of the eight cubes into which the bcc cell may be divided. In this partially covalent structure, copper has a linear coordination and oxygen a tetrahedral coordination.

D. OXIDES WITH THE CORUNDUM STRUCTURE

The corundum structure is assumed by three oxides of primary importance in catalysis, namely, $\alpha\text{-Cr}_2\text{O}_3$, $\alpha\text{-Al}_2\text{O}_3$, and $\alpha\text{-Fe}_2\text{O}_3$ (which, *inter alia*, form solid solutions in the complete compositional range) (21, 27). The three-dimensional arrangement of the ions in this hexagonal structure consists of a hexagonal close-packed array of anions with the cations occupying two-thirds of the octahedral interstices.

The shape of the microparticles is reported in Fig. 1. Although bulk cations are six-fold coordinated, the ions on regular low-index faces can assume five-fold [(11 $\bar{2}$ 0), (01 $\bar{1}$ 2), and ($\bar{2}$ 116) faces] and fourfold [($\bar{2}$ 116) face] coordination. Higher coordinative unsaturation is encountered only at edges, steps, and corners (usually saturated by hydroxyl groups). Because the radius to charge ratios of Al³⁺ and Cr³⁺ are small, there are only small deviations from full ionicity. For the same reason, the effective charges present on the positive and negative ions are smaller than the formal ones.

E. OXIDES WITH HEXAGONAL STRUCTURE: La₂O₃

Among the oxides with hexagonal structure (La₂O₃, Y₂O₃, and Ce₂O₃), which find application mostly as ceramic materials, lanthanum oxide is the one with the most thoroughly investigated surface structure. Both experimental results (analysis of the surface profile images of the microcrystals by HRTEM) (28) and theoretical results are available (29). Consequently, we focus on La₂O₃.

In this structure, each La ion is surrounded by seven oxygen ions—four in tetrahedral and three in octahedral coordination. This coordination is associated with the large radius of the lanthanum ion. Experimental and theoretical investigations (28, 29) show that the most stable surfaces are the (001) and the (011) faces; the stability of the (001) face is greater than that of the (011) face. On this basis, it is inferred that the most plausible shape of the microcrystals of well-crystallized La₂O₃ can be represented as in Fig. 1.

F. SPINELS

Spinel form a large class of compounds that are important in catalysis. The structure of “normal” spinels is related to that of MgAl₂O₄, the unit cell of which contains 32 oxygen atoms in a nearly perfect cubic array (30, 31). The Mg and Al cations occupy tetrahedral and octahedral sites, respectively.

In addition to Mg, other divalent cations, including Co, Ni, and Cu, can be incorporated in the spinel structure. Al can be replaced by Ga, In, Cr, and other trivalent ions. In addition to normal spinels, so-called inverse structures are also possible in which half the trivalent cations occupy the octahedral sites, with the other trivalent cations and all the divalent cations in tetrahedral positions. Several factors influence whether a given spinel will adopt the normal or inverse structure, including the following: (i) the relative ionic radii, (ii) the Madelung constants of the normal and inverse structures, (iii) the crystal field stabilization energy of the transition metal ions, and (iv) polarization or covalency effects. Defective spinel structures are also known as acidic supports in catalysts, such as γ -Al₂O₃ and δ -Al₂O₃ (32).

A variety of coordination states (threefold and fivefold) exist on the low-index surfaces (Fig. 1), depending on (i) the local structure of the bulk site

(tetrahedral or octahedral) from which the surface site has originated and (ii) the face index. Because of the structural complexity of these systems, more details are given in the following sections, in which special cases are considered.

G. PEROVSKITES

Oxides with the perovskite-type structure constitute an important class of inorganic solids having the general formula ABX_3 , in which A (the large cation) may be an alkali, alkaline earth, or rare earth ion; B represents a small transition metal or main group ion; and X is commonly oxygen or a halide. The perfect structure is cubic and shows a network of corner-sharing BX_6 octahedra, centered on the transition metal ions B. All the oxygen atoms are in topologically equivalent 2-coordinate positions, bridging the two adjacent B sites. The dodecahedral interstices of the anionic sublattice are occupied by a second cation A, and the cationic charge can be distributed in different ways between octahedral and dodecahedral sites so as to ensure electroneutrality. Examples are $KNbO_3$ (K^+ , Nb^{5+}), $CaTiO_3$ (Ca^{2+} , Ti^{4+}), and $LaCrO_3$ (La^{3+} , Cr^{3+}).

Regarding the morphology, a polyhedron terminated by the (001) face is expected for cubic II–IV perovskites, i.e., ABO_3 perovskites in which A and B are divalent and tetravalent, respectively. In these perovskites, two non-polar (001) surface terminations are possible (AO and BO_2). On an $A-O$ terminated surface, the cation A is octa-coordinated, whereas on the BO_2 terminated surface the cation B is penta-coordinated. III–III perovskites, bulk structures with lower symmetry, are more stable (orthorhombic or rhombohedral) than II–IV perovskites, and the nonpolar low-index faces are more complex and show a different coordinative environment for both A and B cations.

More than 90% of the natural metallic elements of the periodic table form perovskites; the wide range of cations, the possibility of partial substitution of A or B cation sites, and the remarkable capacity to accommodate a multitude of different kinds of defects result in a wealth of properties of these solids leading to applications ranging from superconductors (33) to oxidation catalysts (34).

H. OXIDES WITH THE AB_2 STRUCTURE: TiO_2

TiO_2 is an important oxide with a broad range of applications in catalysis (as a catalyst or a support) (6), photocatalysis (35, 36), and sensor technology; it is also used as a pigment. Of the three titanium dioxide polymorphs (rutile, anatase, and brookite), rutile and anatase have been most widely investigated; they are the only ones reviewed here.

Both rutile and anatase crystallize in a tetragonal lattice, and their bulk structure can be described basically in terms of a three-dimensional arrangement of TiO_6 octahedra. The two polymorphs differ by the degree of distortion of each octahedral unit and by the manner in which the TiO_6 building blocks are spatially assembled. The structural differences described previously result in different physicochemical properties, such as density (4.250 g cm^{-3} for rutile and 3.894 g cm^{-3} for anatase) and stability (rutile is more stable than anatase by about 4.9 kJ mol^{-1}).

Most of the data available for polycrystalline TiO_2 concern the anatase modification, for which correlations of adsorption properties with the microcrystal morphology (as determined by electron microscopy) have been realized. It has been shown (37) that TiO_2 obtained by flame hydrolysis of TiCl_4 (anatase containing 25% rutile, Titanoxid P25 from Degussa) is made of well-shaped hexagonal prisms, with crystallite dimensions in the 10–50-nm range, predominantly exposing the (010) face and, to a lesser extent, the (101) and (001) faces. A simplified model illustrating the morphology of the anatase P25 microcrystals is represented in Fig. 1. The (010) (or the isostructural (100)) and the (101) (or the isostructural (011)) terminations have also been found to be predominant on TiO_2 samples prepared by other routes; (110), (111), (112), and (113) faces have been also observed, although to a lesser extent (38, 39).

As shown in Fig. 1, on both the (010) and (001) faces the exposed Ti^{4+} ions are fivefold coordinated. Molecular dynamics calculations (40) indicate the occurrence of some relaxation of the (001) surface, which does not, however, change the coordination of the metal ions. Unlike the (010) and (001) terminations, the (101) face is polar in nature, and extensive surface reconstruction is therefore to be expected.

We mention that the surface of prepared polycrystalline TiO_2 samples is strongly hydrated because of the presence of both surface hydroxyl groups and coordinated molecular water, and that small amounts of residual OH groups are still present even after outgassing *in vacuo* at temperature as high as 973 K (38, 39, 41).

I. AMORPHOUS SiO_2 WITH AND WITHOUT TRANSITION METAL IONS

Silicas are amorphous materials formed by irregularly corner-linked rigid tetrahedra $[\text{SiO}_4]$ forming flexible rings and chains. The $[\text{SiO}_4]$ unit, which is the building block of all siliceous materials, is able to form a peculiar Si–O–Si bond with other $[\text{SiO}_4]$ moieties characterized by Si–O–Si angles ranging from 130 to 180° with very low energy cost (42), as shown by calculations adopting different basis sets (43). Because of this flexibility, various models of amorphous silica have been constructed as networks

of SiO_4 building blocks with a random distribution of the Si–O–Si angle centered around 140° .

On the external surfaces, valences are saturated by hydrogen forming hydroxyl groups. In addition to siloxane bridges, four types of surface hydroxyl groups are distinguished: isolated, geminal, vicinal, and interacting. ^{29}Si CP/magic angle spinning nuclear magnetic resonance (NMR) spectra confirm this picture, showing three silicon signals (bulk silicon, silicon carrying one hydroxyl, and silicon linked to two hydroxyls) (44). Surface hydroxyl groups are widely used to anchor foreign species (transition metal ions) that are highly dispersed reactive species. One of the silica-based systems most widely investigated, because of its importance as an ethene polymerization catalyst (Phillips or Union Carbide processes), is represented by Cr^{III} grafted on silica (45). We describe this system in detail later. The surface properties of amorphous silica are not reviewed here because they have already been described extensively (46).

III. Surface Characterization of Oxides and Halides

A. THE USE OF HRTEM AND SCANNING ELECTRON MICROSCOPY TO INVESTIGATE THE MORPHOLOGY OF OXIDES AND CHLORIDES: COMPARISON OF THE SURFACE DEFINITION OF DISPERSED MATERIALS, FILMS, AND SINGLE CRYSTALS

For catalytic applications, the oxides and halides described so far are usually prepared as microcrystalline powders, with the dimensions of the microcrystals varying from 10 to 100 nm. To investigate the surface properties of these oxides and correlate them with properties of well-defined surface structures, we have to answer the following questions:

1. Which types of faces do the microcrystals expose (or, alternatively, what are their morphologies)?
2. What is the relative fraction of atoms on faces, edges, steps, corners, and other surface defects?
3. How flat and regular are the faces defining the morphologies of the microcrystals?
4. What methods can be used to alter selectively the morphologies of the microcrystals to tailor the surface properties?

Topics 1–3 can be addressed by the combined use of electron microscopy [HRTEM and scanning electron microscopy (SEM)] (47) and methods that probe the surfaces at the atomic level (e.g., by analyzing the modifications induced in the vibrational spectra of simple probe molecules adsorbed on the different coordinatively unsaturated sites (22, 23).

The morphological information contained in the electron micrographs of polycrystalline materials (constituted by a multitude of variably shaped polyhedra) is difficult to extract and does not give straightforward and unambiguous information about the shapes of the microcrystals. In the images obtained with HRTEM only the two-dimensional (2D) projections of the single 3D polyhedra in various orientations relative to the electron beam are obtained.

Fortunately, the images obtained at high resolution do not provide only the projected contours of the microcrystals. When one or more crystal planes are parallel to the electron beam, plane fringes are observed in the micrograph which are superimposed on the 2D projection of the microcrystal.

From the measured distances between individual fringes it is possible to determine the crystallographic indices of the responsible planes. In the planar projections of the randomly oriented microcrystals, only one type of plane fringes is usually observable, and this is still not sufficient to solve the morphological problems mentioned previously. In a few cases, corresponding to favorably oriented microcrystals, two sets of plane fringes are simultaneously present in the planar projection of the same object; this information is sufficient to single out the direction of the electron beam (which corresponds to the intersection of the planes) and consequently to infer the orientation of the planes of the polyhedron. On the basis of this information, it is possible to project polyhedra of reasonably selected shapes along the direction determined by the crossing plane fringes and to determine whether the measured plane angles do indeed correspond to the angles between the faces of the selected polyhedron.

Strictly speaking, the procedure described previously only allows the determination of the shapes of those (few) microcrystals which show at least two types of intersecting fringes. However, the observations made for these relatively rare (suitably oriented) crystals can be extended with some confidence to the others. All the considerations mentioned previously hold only for samples consisting of well-defined single microcrystals (which require low-surface-area samples). Very low-surface-area ($\leq 10 \text{ m}^2 \text{ g}^{-1}$) crystalline materials, although usually made up of well-defined polyhedra, cannot be studied with this method because the single microcrystals are too thick to give planar fringes. In this case, SEM images are more suitable to provide information about the particle morphology.

In high-surface-area samples ($50\text{--}200 \text{ m}^2 \text{ g}^{-1}$), the particles form ill-defined agglomerates of undefined contours, and the previously mentioned method cannot be applied. The crossing fringes (when observed) arise preferentially from different particles of the agglomerates, and the measured angles do not contain valuable morphological information. Notwithstanding this difficulty, good (although indirect) morphological information can also be obtained in these cases. In the following sections we show that this information

arises from the infrared (IR) spectra of adsorbed diatomic molecules used as probes of the surface structures.

B. VIBRATIONAL SPECTROSCOPIES FOR INVESTIGATIONS OF OXIDE AND CHLORIDE SURFACES

1. *Modification of Vibrational Spectra of Diatomic Molecules Induced by the Adsorption on Oxide and Halide surfaces: A method for Probing the Structures of the Adsorption Sites and the Surface Morphologies of Sintered Materials*

The nondissociative adsorption of diatomic molecules (CO, N₂, NO, and H₂) on the surface ions of oxides and halides is accompanied by distinct perturbations of the vibrational spectra. This statement is documented in detail for CO in this review. At this stage of the discussion, it is sufficient to mention the following points.

First, diatomic molecules are usually adsorbed on cations (some exceptions to this empirical rule are mentioned in the case studies). The type of interaction and the resulting vibrational perturbation (purely electrostatic or with some orbital overlap contribution) depend on the charge carried by the cation and by the anions in nearest-neighbor positions and on the electronic structure of the cation (with or without *d* electrons). As a typical example of the effect of a purely electrostatic perturbation on the stretching mode of a diatomic molecule, we mention the classic case of CO adsorbed on Na⁺ exposed on NaCl (100) (Fig. 2), in which it is clearly shown that the frequency of adsorbed CO is distinctly blue shifted with respect to that of CO gas (2143 cm⁻¹) (48). More general considerations concerning the role of the electrostatic field in perturbing the adsorbed molecules are discussed elsewhere (12–15, 21–23).

Second, at low coverages, the vibrational perturbation induced by adsorption on cationic sites located on different faces of the same microcrystal is primarily determined by the coordinative unsaturation of the cation (which in turn is a complex function of the structure of the face). This statement implies that the vibrational spectra of diatomic molecules adsorbed on low-surface-area materials (in which the crystallites exhibit only a few dominant faces) are usually characterized by the presence of a small number of narrow peaks—one for each exposed face. Therefore, vibrational spectra of adsorbed species provide morphological information that can be compared with information derived from HRTEM and SEM studies of the same microcrystals.

Third, at low coverages the band half-widths of the species adsorbed on the different faces depend strictly on inhomogeneous broadening effects. The half-width thus provides information about the extension and regularity of

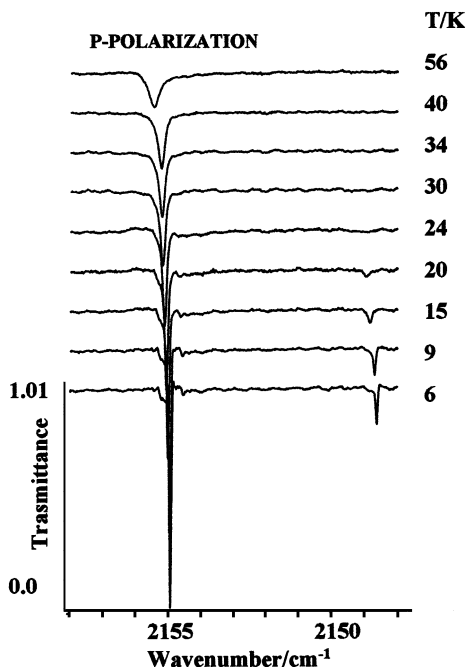


FIG. 2. Monolayer transmittance spectra of the adsorbate ^{12}CO on NaCl (100) at various temperatures (angle of incidence $50 \pm 1^\circ$) [adapted from Heidberg *et al.* (48) with permission of Elsevier Science Publishers].

the faces. To illustrate this point, the IR spectra of CO adsorbed on the (100) face of a single crystal of NaCl and of CO adsorbed on a film of NaCl (annealed and unannealed) are compared in Fig. 3 (49). The peak representing CO adsorbed on a film is significantly broader than that of CO on the flat single crystal. Hence, the experimental observations contain valuable morphological information that cannot be obtained easily by other experimental methods.

Fourth, the vibrational frequency of the adsorbed species undergoes coverage-dependent shifts $\Delta\bar{\nu}$ as a consequence of dynamic and static effects (see Section IV.A.4). The shift depends on the type of bonding and the density of cationic centers on the face. Several examples of coverage effects of this type are reported in the following. It will be shown later that this information also has morphological implications because different faces can be characterized by different bonds and cation densities (and hence by different static and dynamic shifts of the vibrational frequency).

Finally, probe molecules adsorbed on highly coordinatively unsaturated defects (e.g., corners and edges) are usually more strongly perturbed than

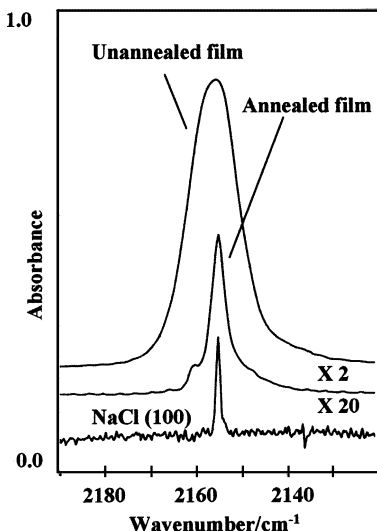


FIG. 3. IR spectra of CO on NaCl (100) and NaCl films. The absorbance scale factors reflect the available number of adsorption sites of the substrates [adapted with permission from Richardson and Ewing (49). Copyright 1987 American Chemical Society].

those adsorbed on flat faces (the associated adsorption energy is also stronger). These effects provide qualitative information about the defect structures of surfaces on the atomic scale and, hence, morphological information that could not be obtained otherwise. A good example is represented by the spectrum of CO adsorbed on an annealed NaCl film (Fig. 3), where the peak of CO adsorbed on Na^+ ions of steps is clearly visible at 2162 cm^{-1} .

2. Relations between the Vibrational Spectra of Adsorbed Probes and the Surface Morphology of High-Surface-Area Solids

On the basis of the considerations developed so far, the progressive sintering method (22, 23) provides information about the morphologies of poorly defined (high-surface-area) samples relative to samples with better defined morphologies.

The progressive sintering method is based on the following observations: First, when proper synthesis and sintering conditions are adopted, oxide and chloride microparticles assume all types of morphologies between those characterizing high-surface-area materials (very small and ill-defined microcrystals clustered in the form of disordered aggregates) and those typical of sintered or highly sintered solids (well-shaped microcrystals exposing a few flat low-index faces).

Second, the IR spectra of probe molecules adsorbed on progressively sintered materials (often characterized by specific surface areas decreasing progressively by about one order of magnitude) develop continuously from a very complex appearance (characterizing the contribution of the spectroscopic components associated with probe molecules adsorbed on intrinsic defects and on planar faces and terraces of low extension) to simple features (characterizing the most stable low-index faces). This continuous evolution of the spectra provides invaluable assistance for the assignment of bands to low-index faces and terraces of limited extension present at the surfaces of the microcrystals (the remaining bands characterize defect sites). It is emphasized that only this laborious comparative method permits a detailed and unambiguous assignment of the individual bands present on high-surface-area samples.

C. PREDICTING MICROCRYSTAL MORPHOLOGY: INTRODUCTION TO GEOMETRIC, FORCE FIELD, AND *Ab Initio* MODELING APPROACHES

1. *Geometric Methods*

The morphology of a microcrystal depends in a complex way on the thermodynamics and kinetics that determine the stabilities of the faces and their growth. Currently, an exhaustive theory of crystal growth in different atmospheres is not available; nevertheless, a reasonable prediction of surface morphology based on the bulk crystalline structure of the solid is possible in many cases.

The simplest method is based on the consideration that the faces characterized by the highest interplanar distances d_{hkl} grow at the lowest rate. Because the faces that are growing faster tend to disappear during the growth, the morphology can be predicted simply with the following rule: The polyhedron describing the shape of the crystal is made of terminating faces characterized by the highest d_{hkl} (the Donnay–Harker rule) (50–52).

The relationship between the growth rate and d_{hkl} can be explained easily if it is considered that the faces with highest d_{hkl} also show the highest concentration of chemical and/or electrostatic bonds within the plane of the face and the minimal density of bonds in the direction perpendicular to the plane of the face. When oxides and halides are considered, the previous rule can also be formulated in the following way: Faces exposing ions with the lowest coordinative unsaturation are the most stable and least reactive and hence determine the final morphology of the microcrystals under thermodynamic equilibrium conditions.

It is evident from the previous considerations that this approach is based exclusively on the knowledge of the cell parameters and of the space group and that the forces involved at the atomic level are totally ignored; therefore, this approach is called *geometric*.

2. Force Field and Ab Initio Methods

The more modern methods of predicting the morphologies of crystals are based on the calculation of the energies of the various faces. The methods are based on the intuitive consideration that the closed polyhedron describing the shape of the crystal is determined by the faces with the lowest surface free energy and that the extension of these faces is inversely proportional to the respective surface free energy.

The surface energy $\gamma(\text{hkl})$ can be defined as the energy needed to create a unit surface area by cutting the infinite crystal into two parts and by allowing surface relaxation to occur. We recall the definition given by Gay and Rohl (53) in a force field-based approach:

$$\gamma(\text{hkl}) = [E_{\text{total}}(\text{hkl}) - E_{\text{boundary}}(\text{hkl}) - n E_{\text{crystal}}(\text{hkl})] / A(\text{hkl}) \quad (1)$$

where n is the number of unit cells in the relaxed region and $A(\text{hkl})$ is the surface area of the simulation cell (53). The surface energy can also be calculated by means of *ab initio* methods.

D. ELECTROSTATIC FIELDS AT SURFACES OF OXIDES AND HALIDES

As summarized previously, knowledge of surface structures at the atomic level allows one to evaluate a few important properties of the surface ions (coordinative unsaturation and accessibility) that play an important role in surface reactivity and catalysis. A further important property that merits quantification is the electrostatic potential in the space just above the surface plane. Potential energy maps provide quantitative descriptions of the distributions of the electrostatic fields and hence (indirectly) of the strengths of the adsorption sites. However, the problem of the calculation of the electrostatic field at a given point caused by the an infinite distribution of point charges is not straightforward. Because of the $1/r$ dependence of the potential, the coulombic sum of a semiinfinite point charge distribution does not readily converge. This difficulty is overcome by using the Ewald sum. The electrostatic potential maps which are reported later in the discussion of the case studies have been calculated by using the Ewald method in the context of the CRYSTAL code (54). Details of the computational method are not reported here. Only the most general conclusions are briefly summarized as follows.

First, the electric fields at surface cations and anions are positive and negative, respectively, as shown in Fig. 4 for the (100) face potential map of NaCl, used as prototype.

Second, the strength of the electric field E on cationic sites located on a flat face of an oxide or halide is strongly influenced by the charge and by the radius of the cation (cations with high charge and small radius give rise to the greatest positive fields). Because the radii of the cations of common oxides

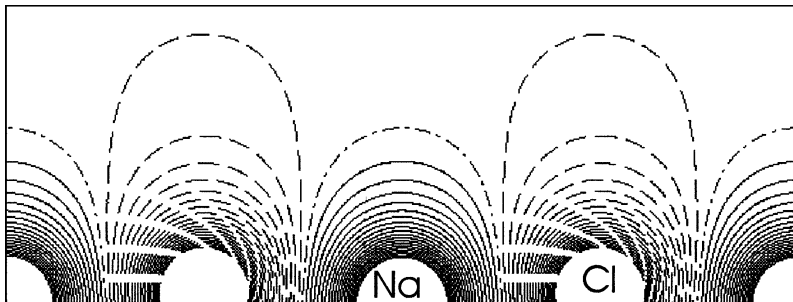


FIG. 4. Potential map generated by a distribution of cations and anions on the (100) face of NaCl: solid, dot-dashed, and dashed lines represent positive, zero, and negative equipotential surfaces, respectively.

and halides are usually smaller than those of the oxide and halide ions, it follows that, on flat surfaces, the positive electric field at the cationic center is larger than that generated at the negative anionic center and that this positive field plays the decisive role in the initial stages of the adsorption process (the long-range electrostatic forces are sensed by the approaching molecules at distances longer than those involved in real chemical bond formation). The net value of the electric field at a given cationic position (being, to a first approximation, the sum of contributions of the cation and of the anions in nearest-neighbor positions) depends on the 2D structure of the surface. Furthermore, the equilibrium distance between the adsorbed molecule and the surface cation is determined not only by the net attractive force but also by the Pauli repulsive force of the anions in nearest-neighbor positions.

Third, the greatest electric fields are created by ionic sites located on edges (steps) and corners, respectively. This result (which is to be documented thoroughly for systems with the rock salt structure e.g., NaCl and MgO) indicates that these ions are expected to be the most polarizing (and hence the most reactive) toward adsorbate molecules and to show the strongest Lewis acidic and basic character.

Finally, the perturbation induced on the stretching mode of adsorbed CO (expressed as the difference $\Delta\tilde{\nu}$ between the stretching frequency of CO in the gas phase and CO in the adsorbed state) is proportional to the electric field E at the equilibrium distance from the adsorbing site (55, 56). It will be shown that the $\Delta\tilde{\nu}(\text{CO}) \propto E$ relationship can be used to establish a spectroscopic scale of the polarizing tendencies of the positive centers at surfaces of ionic solids and, indirectly, to construct a reasonable scale of their acidic strengths. The spectrum of CO adsorbed on NaCl films (Fig. 3), consisting of several bands, can be used to show that fourfold coordinated Na^+ ions on steps have enhanced polarizing character toward CO.

It will be shown in the case studies that similar perturbations are induced on other molecules, such as H_2 , N_2 , and CH_4 .

E. CALORIMETRIC METHODS

Adsorption microcalorimetry applied to high-surface-area samples plays an important role in the quantitative characterization of site densities and of adsorption energies because it allows the simultaneous determination of the amounts of a suitable probe molecule that are adsorbed and of the evolved heat as the surface coverage increases (17, 18, 57–59). This technique has been recently reviewed by Ge *et al.* (59). Here, we only briefly mention some of the advantages associated with the combined use of IR spectroscopy and microcalorimetry. This approach provides both qualitative and quantitative information concerning the nature, population, and strengths of adsorption sites (60–62). The combined use of IR and microcalorimetry, on the one hand, and of microscopy, on the other hand, allows the development of correlations between the surface properties and the micromorphologies of the particles and, in particular, elucidation of the adsorption properties of the preferentially exposed (hkl) faces and of the structural defects (steps, kinks, terraces, edges, etc.) (63–69).

A dose-by-dose procedure is usually adopted, and equilibrium data are obtained, leading to the differential heats of adsorption (ΔH_{ads}) as a function of both coverage and equilibrium pressure. ΔH_{ads} can give good estimates of bonding energies between the probe molecule and the adsorbing site. The surface heterogeneity (structural, chemical, and/or induced) can be monitored by processing the overall set of combined volumetric and calorimetric data.

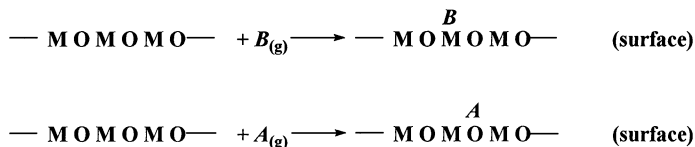
F. ACIDIC AND BASIC PROPERTIES OF OXIDE AND HALIDE SURFACES

More than 130 acid–base catalysts are known, many of which are currently used in industrial processes (70). The estimation of strength, structure, and concentration of acidic and basic sites at the surface of such catalysts is consequently a topic of primary interest (15, 71, 72).

The surface of an ionic oxide in its fully dehydroxylated form can be considered as a 2D and rigid array of Lewis acidic and basic sites (Scheme 1; M, cationic sites with vacant orbitals; O, O^{2-} ions with available electron pairs). In flat faces, M and O sites normally occupy equivalent positions. Of course, this is not the case for defect sites (e.g., on edges and corners). Furthermore,



SCHEME 1



SCHEME 2

besides centers with Lewis acidic and basic character, partially hydroxylated surfaces contain OH groups with Brønsted acidic and/or basic character.

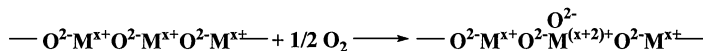
All these often coexisting surface species can react with Lewis bases (B) and acids (A) to give surface acid–base adducts (Scheme 2). Following these simple considerations, the analogy with acid–base reactions under homogeneous conditions (following the Lewis and Brønsted definitions) seems to be obvious. However, this analogy is not entirely correct. Acidic and basic surface sites can never be considered to be independent of each other, and it is not possible to react one of them (e.g., the acidic site) with basic species from the gas-phase without more or less perturbing the basic sites located in adjacent positions. This perturbation weakens the analogy between liquid solutions and solid surfaces and renders the evaluation of the strength of the surface species conceptually more problematic. For this reason, the evaluation of the acidic and basic properties of oxides is a very broad and complex subject that merits a more exhaustive and separate contribution in its own right. Consequently, it is not treated extensively in this review, although a few considerations are discussed in Section XII.

G. REDOX PROPERTIES OF OXIDES AND HALIDES

In addition to the acidic and basic properties mentioned previously, oxides and halides can possess redox properties. This is particularly true for solids containing transition metal ions because the interactions with probe molecules such as CO, H₂, and O₂ can lead to electron transfer from the surface to the adsorbed species and to the modification of the valence state of the metal centers. An important role in surface redox processes involving CO is played by the most reactive oxygen ions on the surface (e.g., those located at the most exposed positions such as corners), which can react with CO as follows:



These reactions lead to the formation of surface carboxylate and carbonate-like species and to electrons that can reduce transition metal ions located in



SCHEME 3

nearest-neighbor positions (as verified on NiO). On oxidic surfaces that do not contain transition metal ions, redox reactions accompanied by electron transfer from the surface to the adsorbed molecule (or vice versa) are much less probable or even impossible. Nevertheless (as will be shown in the discussion of MgO), redox-type surface reactions can still be observed when the electron transfer occurs between adsorbed molecules.

Hydrogen is also a species that can produce surface reduction of transition metal oxides by attacking the most reactive surface oxygen species, with formation of water and reduced metal centers.

Important oxidation processes involving the metal centers can occur at the surfaces of transition metal oxides (e.g., α -Cr₂O₃) upon dissociative oxygen adsorption (Scheme 3). In some cases the (nondissociative) adsorption of oxygen can lead to the formation of superoxide O₂⁻ or peroxide O₂²⁻ species with simultaneous oxidation of surface metal cation centers.

IV. Oxides and Halides with the Rock Salt Structure: Surface Structure, Reactivity, and Catalytic Activity

Many systems belong to this class of solids; typical representatives are MgO, CaO, SrO, NiO, CoO, NaCl, LiF, KI, and KCl. These solids can be prepared in the form of very high-surface-area polycrystalline samples, which exhibit high densities of highly reactive step, edge, and corner sites. Because of their simple crystal structures and because the (001) face is the most abundant terminating surface plane, they represent an ideal family of solids for the investigation of the surface properties of both cations (Mg²⁺, Ni²⁺, Ca²⁺, Co²⁺, Li⁺, Na⁺, or K⁺) and anions (O²⁻, F⁻, Cl⁻, I⁻) in different local environments. For both cations (Mⁿ⁺) and anions (Aⁿ⁻) we can distinguish among regular 5-coordinated sites (M_{5c}ⁿ⁺ and A_{5c}ⁿ⁻) on flat (001) faces, 4-coordinated sites (M_{4c}ⁿ⁺ and A_{4c}ⁿ⁻) on steps and edges and 3-coordinated sites (M_{3c}ⁿ⁺ and A_{3c}ⁿ⁻) on corners. Figure 5a shows schematically the modifications of the morphology induced by sintering, and Fig. 5b shows model surfaces with anions and cations in different coordination states.

From Fig. 5, it can be inferred that even for this class of structurally simple solids, the surface of a real high-surface-area solid is so complex that IR spectra of the adsorbed species cannot be decoded straightforwardly. Fortunately, by the progressive sintering method, samples can be virtually

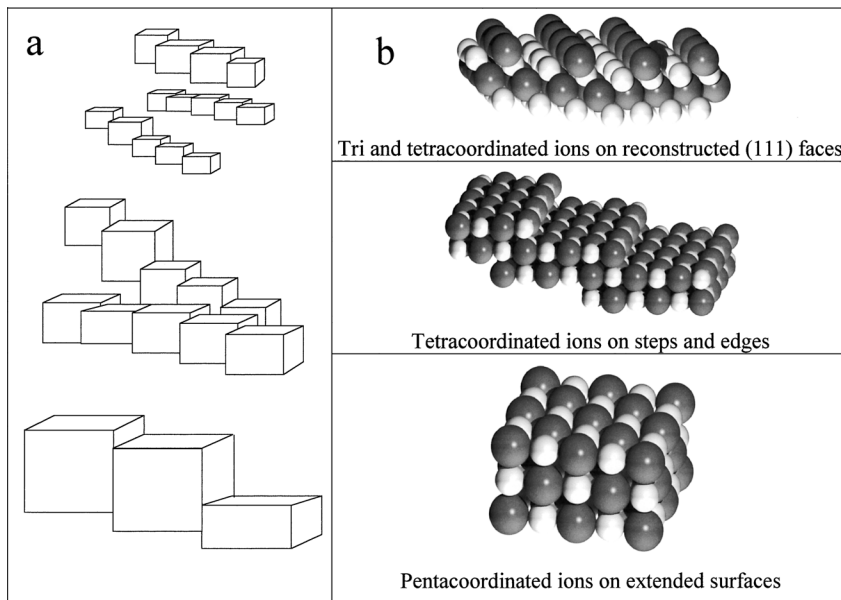


FIG. 5. (a) Effect of sintering on particle dimensions. (111) facelets are omitted. (b) (Top) Representation of MgO structure: reconstructed (111) facelet with tricoordinated oxygen; (middle) terraced surface with steps and edges, where ions are tetra-coordinated; (bottom) (001) flat surface with pentacoordinated species (Mg^{2+} ions are white and O^{2-} ions are gray).

prepared with wide ranges of surface areas starting from the values typical for practical catalysts to the values approaching those typical of single crystals (10, 22, 23, 73–75). Because of the progressive simplification of the surface site distribution induced by sintering, the IR spectra also undergo a progressive simplification. Consequently, comparison of the IR spectra of probe molecules adsorbed on progressively sintered samples provides the key to the assignment of all the vibrational spectra of the adsorbed species.

Cubic oxides and halides are important not only for experimental studies but also for theoretical investigations. The high symmetry of adsorption sites is ideal for *ab initio* calculations of large clusters using the most complete basis sets (8, 76). Moreover, because of the high symmetry of the sites, the preferential orientation of adsorbed molecules may be easily identified, a fact that has been of great help in both *ab initio* and atomistic simulations (54, 77–79). Another advantage associated with the ionic solids having the rock salt structure, at least with regard to the regular (001) face, is that the surface relaxation effects are negligible. This fact has been used to simplify markedly the first *ab initio* calculations, since the complex study of the

relaxation process could be neglected, to a first approximation. Furthermore, the high ionicity of solids with the rock salt structure permits the Mulliken charges of both cations and anions to be approximated well by the formal charges. This approximation has allowed the elimination of one degree of freedom in the atomistic simulations (77, 78).

An additional interesting property of cubic oxides is their ability to form solid solutions (25) that maintain the original cubic structure. In these solids the cation sites can be shared between the two competitive cations over a wide range of compositions. This is the case for the NiO–MgO system, for which the $\text{Mg}_x\text{Ni}_{1-x}\text{O}$ solid solution can be prepared with $0 \leq x \leq 1$ because of the very similar ionic radii of the cations [$r(\text{Mg}^{2+}) = 0.72 \text{ \AA}$ and $r(\text{Ni}^{2+}) = 0.69 \text{ \AA}$]. Another relevant case is CoO–MgO.

A. MgO CASE STUDY

Magnesium oxide is an ideal case study because it is by far the most extensively investigated and most representative oxide on both theoretical and experimental grounds. Regarding theory, the case study character of MgO relates to the fact that among all binary oxides with the cubic structure (all being strongly basic and with definite ionic character), MgO has the smallest number of electrons in its asymmetric unit (Mg–O) (the lighter BeO crystallizes in the hexagonal structure). Regarding experiments, the cleavage of MgO single crystals in ultrahigh vacuum can in principle yield (001) faces of high perfection, which can be characterized with the typical surface science methods (1–3, 80–83). On the other hand, regarding polycrystals, MgO is particularly useful since its morphological changes upon thermal treatments [investigated by electron microscopy (84–88)] are very well-known. The modifications of the surface properties of this oxide upon increasing the dimension and the perfection of the microcrystals have therefore been widely investigated.

1. IR Spectroscopy of the CO/MgO System

IR spectra of CO adsorbed on polycrystalline MgO were first reported in the 1970s (89–91). Pioneering studies were performed with samples activated at moderate temperatures and still covered by a relatively high density of OH groups (89, 90). Under these conditions, CO is adsorbed as a carbonate-like species only if O_2 is present. Investigations of fully dehydrated samples (85–88, 91, 92) in the absence of O_2 showed that CO chemisorption leads to the formation of peculiar, highly colored, anionic polymeric species.

High-surface-area MgO is usually prepared by decomposition of brucite, $\text{Mg}(\text{OH})_2$, at 520–550 K *in vacuo*. The hexagonal platelets of brucite are topotactically transformed into linear aggregates of cubes preferentially

exposing (001) faces, as shown schematically in Fig. 5. The average edge length of these cubes is ~ 7 nm (in agreement with the high value of the surface area, $200 \text{ m}^2 \text{ g}^{-1}$); this means that the average area of the cubic faces of the microcrystals is $\sim 50 \text{ nm}^2$. It has been calculated (87) that on this type of sample the percentages of surface atoms (either Mg or O) in corner, edge, and face positions are ~ 1 , ~ 15 , and $\sim 84\%$, respectively, far from the distribution of an ideal infinite and perfect single-crystal (001) face. Once formed at 520–550 K, the surface is fully covered by hydroxyl groups and can be fully cleaned only by outgassing under high vacuum at $T \geq 1100$ K. When, after this treatment, the surface of highly dispersed MgO is probed by CO at room temperature (RT), a complicated IR spectrum is observed which has been the subject of many detailed investigations (85–88, 91–96). The surface species formed at RT derive only from the interaction of CO with the O_{3c}^{2-} anions located at corners; the remaining oxygen anions at edges and (001) faces are not reactive. For short contact times, the reaction path is represented by a series of steps shown schematically as follows:



with formation of negatively charged monomeric, dimeric, and polymeric (conjugated) species characterized by a complex (but nevertheless fully understood) IR spectrum (see Fig. 6, in which the evolution of the spectra of adsorbed CO with decreasing MgO surface area is reported). The CO_2^{2-} (carbonite which has a bidentate structure), the precursor of the dimeric and oligomeric species, has a transient character, and maximum concentrations are detected in the initial stages of the chemisorption process. The formation of carbonite species on CO contact with the surface can be considered as the fingerprint of the O_{3c}^{2-} sites having a strongly basic character. The negatively charged polymeric and conjugated species have also been characterized by electron paramagnetic resonance (EPR) (97–99) and ultraviolet and visible (UV–VIS) (100–102) spectroscopies. As a consequence of the extensive π -type conjugation, some of the oligomeric compounds are strongly colored (100–102), thus allowing direct visualization of the high reactivity of low-coordinated O^{2-} anions. Very strong interactions of CO with only few highly reactive surface sites have been demonstrated by Huzimura *et al.* (103) by ^{18}O -isotopic exchange between CO and MgO. Some of the species originate from the interaction of CO with O_{3c}^{2-} pairs in corner position, a situation which is likely associated with vicinal O_{3c}^{2-} ions of reconstructed (111) faces. [The nonneutrality of the (111) face

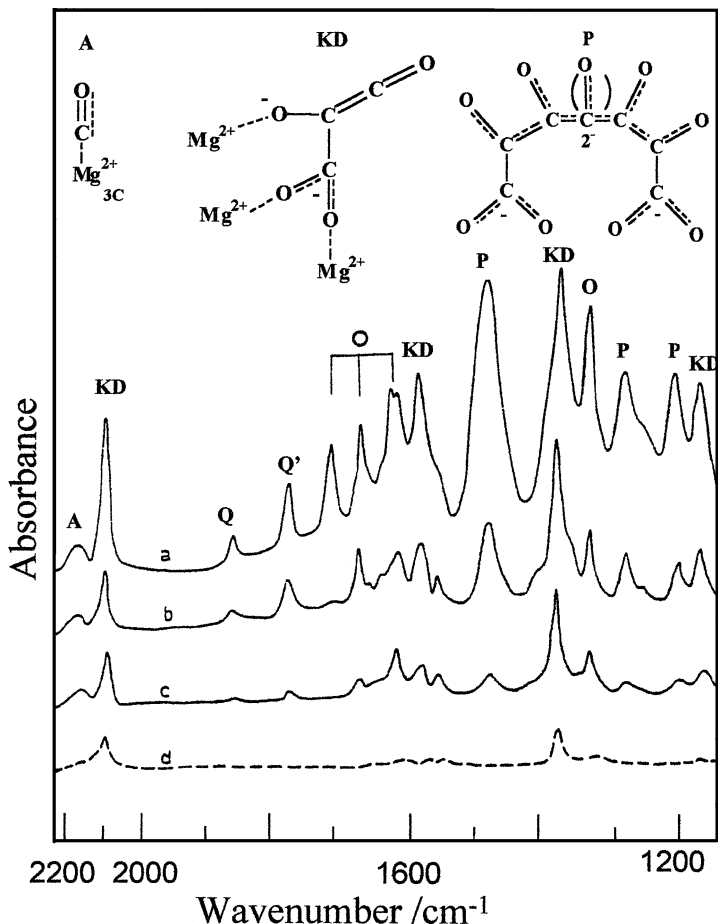


FIG. 6. Effect of sintering temperature on the IR spectra of ^{12}CO adsorbed at 298 K (5.33 kPa) on (a) high-surface-area MgO, (b and c) progressively sintered MgO samples, and (d) MgO smoke. KD (trimeric) and P (polymeric) species evolve with time through fragmentation in O (oxidized, carbonate-like groups) and (Q, Q') reduced counterparts [reprinted from Zecchina *et al.* (22) with permission of Elsevier Science Publishers].

implies a reconstruction.] For longer contact times, a disproportionation reaction also occurs, leading to oxidized (carbonate-like) and to reduced $\text{C}_n\text{O}_n^{2-}$ species.

That the $\text{O}_{3\text{c}}^{2-}$ species play a key role in determining the complex chemistry illustrated previously can be easily demonstrated by comparing the IR spectra of CO adsorbed on progressively sintered samples (Fig. 6). Inspection of

Fig. 6 shows clearly that the anionic species formed at threefold coordinated sites are preferentially affected by the morphological modifications induced by the sintering and resulting from a dramatic decrease in the abundance of surface O_{3c}^{2-} anions as the dimension and perfection of the microcrystals gradually increase (Fig. 5). Of course, on the nearly perfect microcrystals of MgO smoke, anionic species were not observed.

At RT, CO molecules probe not only the O_{3c}^{2-} anions but also the Mg_{3c}^{2+} ions at corner positions. Stable $Mg_{3c}^{2+} \cdots CO$ adducts characterized by a very weak $\tilde{\nu}(CO)$ band at 2200 cm^{-1} are observed upon CO adsorption (Fig. 7). This $\tilde{\nu}(CO)$ frequency, 57 cm^{-1} higher than that of gaseous CO, is explained by the polarization effects caused by the high positive electric field centered at the threefold coordinated Mg_{3c}^{2+} center (93). To probe in addition the less coordinatively unsaturated cationic sites, the temperature must be decreased to about 77 K. Only at low temperatures can the less reactive fourfold and fivefold coordinated Mg^{2+} sites located at edges, on steps, and at the (001) faces and terraces form sufficiently stable CO adducts to be observed by IR spectroscopy (bands at 2159 and 2148 cm^{-1} , respectively; Fig. 7). To assign these bands, the evolution of the IR spectra of CO adsorbed on MgO samples with decreasing surface area has been of great help. Figure 7 is a summary of the IR spectra of the $\tilde{\nu}(CO)$ region characterizing the $Mg^{2+} \cdots CO$ adducts

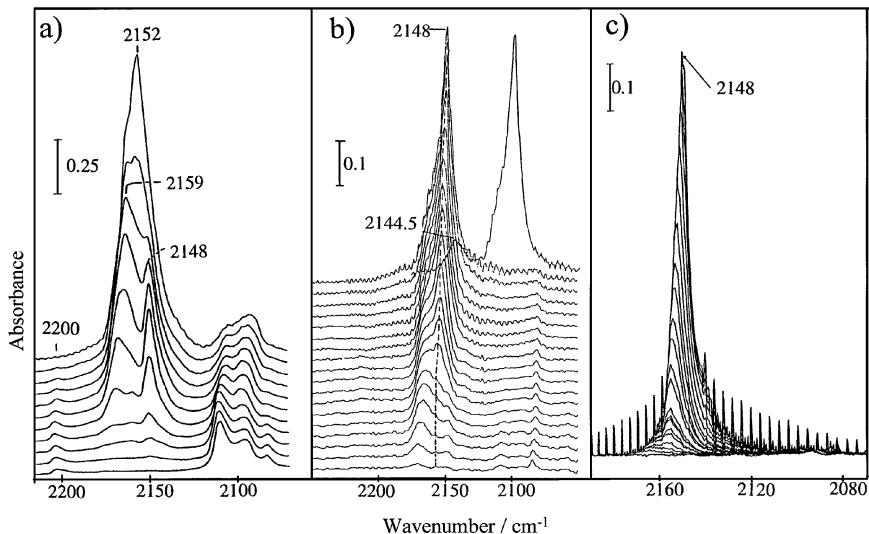


FIG. 7. IR spectra of ^{12}CO adsorbed at 77 K at coverages ranging from $\theta = 1$ (5.33 kPa) to $\theta \rightarrow 0$ on (a) high-surface-area MgO; (b) sintered MgO [the spectrum of ^{12}CO : ^{13}CO (15 : 85) isotopic mixture at $\theta = 1$ is also reported; and (c) MgO smoke, where $\theta = 1$ corresponds to 2.67 kPa [reprinted from Zecchina *et al.* (22) with permission of Elsevier Science Publishers].

(CO was adsorbed on MgO samples with surface areas of about 200, 35, and $10 \text{ m}^2 \text{ g}^{-1}$ in Figs. 7a–7c, respectively).

From these spectra it can easily be inferred that the $\text{Mg}_{4c}^{2+} \cdots \text{CO}$ complexes absorb in the $2175\text{--}2159 \text{ cm}^{-1}$ interval. A simple IR spectrum (Fig. 7) indicating a simple surface structure is obtained for MgO smoke (as clearly shown in Fig. 5). The only relevant $\tilde{\nu}(\text{CO})$ band found for CO on MgO smoke is observed at 2148 cm^{-1} for $\theta = 1$ and at 2157 cm^{-1} for $\theta \rightarrow 0$ (Fig. 7c). This band clearly corresponds to the stretching mode of CO polarized through the carbon end on Mg_{5c}^{2+} ions exposed on the (001) faces (86, 104–106). Figure 7c also shows that not only the frequency of the peak shifts but also the full-width at half maximum (FWHM) changes with coverage from 4.5 cm^{-1} at $\theta = 1$ to $\sim 12 \text{ cm}^{-1}$ at $\theta \rightarrow 0$. Both the half-width and the frequency changes are associated with adsorbate–adsorbate interactions (mainly of the dipole–dipole type), which gradually build up with coverage. These effects, typically observed when an overlayer is formed by aligned and perpendicular oscillators on a flat surface, are discussed more extensively in Sections IV.A.3 and IV.A.4, respectively. Here, it is noted that coverage-induced shifts are indicative of the presence of flat surfaces and terraces of extended areas.

From all these observations, we conclude that CO is an excellent probe for exploring the electric fields at cationic sites and, indirectly, for investigating the relative Lewis acid strengths, which follow the sequence $\text{Mg}_{3c}^{2+} > \text{Mg}_{4c}^{2+} > \text{Mg}_{5c}^{2+}$. Also, flat faces of MgO are unreactive and reactive sites with distinct acidic and basic character can be found only at defective positions such as corners, reconstructed (111) faces, edges, and steps.

2. (CO) Frequencies and Heats of Adsorption of CO Adsorbed on Mg_{5c}^{2+} , Mg_{4c}^{2+} , and Mg_{3c}^{2+} Sites in the $\theta \rightarrow 0$ Limit: Comparison with Theoretical Studies

To avoid the spectroscopic effects induced by adsorbate–adsorbate interactions (frequency shifts and FWHM variations), we deal only with low-coverage spectra ($\theta \rightarrow 0$ limit) here. The effect of adsorbate–adsorbate interactions (both static and dynamic) is discussed briefly in Section IV.A.4.

At very low coverages ($\theta < 0.1$), the frequency of CO (singleton) adsorbed through the carbon end on Mg_{5c}^{2+} , Mg_{4c}^{2+} , and Mg_{3c}^{2+} is blue shifted with respect to the frequency of CO gas by 14, 27, and 60 cm^{-1} , respectively ($\tilde{\nu}(\text{CO}) = 2157, 2170, \text{ and } 2202 \text{ cm}^{-1}$). This shift is the typical result of the Stark effect associated with the positive electric field of the cation. Following Hush and Williams (55) and Pacchioni *et al.* (56), the shift is proportional to the strength of the moderate electric field sensed by CO when no *d*-electrons are involved, in agreement with the intuitive concept that to a first approximation the effective field sensed by CO adsorbed on a cationic site is the

result of the contribution of the part associated with the cation and of an opposite part associated with the O^{2-} ions in the first coordination sphere. When the number of anions surrounding a given Mg^{2+} ion decreases (as at corners, edges, and steps), the negative contribution to the electric field decreases, and hence the effective positive field sensed by CO increases. To demonstrate this idea, recall that CO interacting with the low-coordinated Mg^{2+} of the MgF_2 molecule isolated in an argon matrix (106) absorbs at $\tilde{\nu}(\text{CO}) = 2205 \text{ cm}^{-1}$ [$\Delta\tilde{\nu}(\text{CO}) = 62 \text{ cm}^{-1}$]. Of course, because the electrostatic effects can be classified as long-range effects, small inhomogeneities in the distribution of the anionic and cationic sites (face borders, steps, kinks, etc.) surrounding a given isolated CO molecule on an extended face can have a small influence on the singleton absorption frequency; this explains why, even at very low coverages, the CO peak still shows a remarkable width (see Section IV.A.3).

Experimentally determined binding energies of CO on MgO are important. A brief review of the early data for Mg_{5c}^{2+} sites on (001) faces and terraces of MgO powder samples indicates that these energies exhibit variations between 13 and 42 kJ mol^{-1} (92, 107–110), which are systematically lower than those obtained for CO on thin MgO films (111–113). Paukshtits *et al.* (107–109) calculated a binding energy (BE) of 15 kJ mol^{-1} from the integrated intensities of the IR spectra of CO adsorbed on MgO powders at various pressures and temperatures. Comparable values (in the 13–22 kJ mol^{-1} range) were reported by Zaki and Knözinger (92) and Furuyama *et al.* (110) for CO on MgO powders. Henry *et al.* (111), using a kinetic model for the interpretation of experiments representing diffusion of CO on a single crystal (001) surface covered with Pd particles, deduced a BE in the 29–38 kJ mol^{-1} range. Goodman *et al.* (112, 113) reported BE values as high as 42 kJ mol^{-1} (isosteric heat) and 2178 and 2201 cm^{-1} $\tilde{\nu}(\text{CO})$ frequencies (as measured by IR reflection absorption spectroscopy) for CO adsorbed on a thin MgO film supported on Mo(100) at 90 K. Possible explanations for these discrepancies between data obtained with powder samples (92, 107–110) and single crystals (111) or films (112, 113) that are (i) the presence of Pd particles on the MgO(001) surface investigated by Henry *et al.* (111) influenced the CO/Mg_{5c}^{2+} BE values and (ii) the thin films investigated by He *et al.* (112, 113) were far from perfect and were consequently dominated by the properties of defective Mg_{4c}^{2+} and Mg_{3c}^{2+} surface sites. This interpretation is consistent with the observed 2178 and 2201 cm^{-1} $\tilde{\nu}(\text{CO})$ frequencies, which are very close to the values reported by Zecchina *et al.* (86, 93) for high-surface-area polycrystalline MgO and which were attributed to $Mg_{4c}^{2+} \cdots \text{CO}$ and $Mg_{3c}^{2+} \cdots \text{CO}$ adducts, respectively. Wichtendahl *et al.* (114, 115) performed thermal desorption spectroscopy (TDS) experiments with a MgO(001) single crystal cleaved under high-vacuum conditions starting at temperatures as low as 20 K. At low coverages, the TDS data exhibit

a well-defined desorption peak centered around 57 K and a much broader peak at about 76 K. The former, corresponding to a BE of about 12.5 kJ mol^{-1} [as estimated from the Redhead equation (116)], has been attributed to the desorption of CO from regular Mg_{5c}^{2+} surface sites, and the latter has been attributed to the desorption of CO from defective surface sites. The observation of the 57 K peak agrees well with the low-energy electron diffraction (LEED) evidence presented by Audibert *et al.* (117), who observed ordered CO superstructures on MgO(001) only at temperatures lower than 56 K, and with the helium scattering study of Gerlach *et al.* (118) reporting ordered CO in the 36–59 K range. The experiment of Wichtendahl *et al.* (114, 115) explains why Goodman *et al.* (113) were not able to observe CO adsorbed on regular 5-coordinated surface sites; at the pressures used in the experiment, the temperatures were not low enough to stabilize $\text{Mg}_{5c}^{2+} \cdots \text{CO}$ adducts. The reported data must then be attributed to CO adsorbed on Mg_{4c}^{2+} and Mg_{3c}^{2+} surface defect sites. Heidberg *et al.* (119) reported an IR investigation of a MgO(001) single crystal, but working at lower temperatures (32–56 K), they observed bands attributed to the $\text{Mg}_{5c}^{2+} \cdots \text{CO}$ adduct at $2150.5\text{--}2151.2 \text{ cm}^{-1}$ [i.e., a value very close to that observed for CO on polycrystalline MgO by Zecchina *et al.* (86, 93)]. An interesting comparison between CO/MgO(001) and CO/NiO(001) systems is also reported in Refs. (114, 115).

On the basis of the data discussed previously it is concluded that the correct BE values for $\text{Mg}_{5c}^{2+} \cdots \text{CO}$ adducts are in the range $13\text{--}20 \text{ kJ mol}^{-1}$ and that the Mg_{5c}^{2+} ions on flat (001) faces and terraces behave as very weak Lewis acidic sites. Furthermore, only cations in lower coordination sites give more stable adducts with CO.

The CO/MgO system is interesting not only because of the abundant and accurate spectroscopic and energetics data but also for the extensive theoretical work (120–127). A brief overview of the theoretical aspects was published recently (128). The results of the calculations are relevant to the interpretation of the IR spectra discussed so far.

In conclusion, the combined experimental and theoretical results provide a firm understanding of the interactions of CO with Mg_{5c}^{2+} , Mg_{4c}^{2+} , and Mg_{3c}^{2+} surface sites of MgO. The weak interactions are mainly electrostatic, and the corresponding BE and $\tilde{\nu}(\text{CO})$ values increase progressively on passing from Mg_{5c}^{2+} through Mg_{4c}^{2+} to Mg_{3c}^{2+} . The prototypical character of MgO is emphasized; it has allowed major refinements of both the experimental and theoretical methods.

3. Widths of Carbonyl Bands of $\text{Mg}^{2+} \cdots \text{CO}$ Adducts

We comment on the variation of the FWHM of the main peak on passing from high specific-surface-area samples (for which the extension of the faces is $\sim 50 \text{ nm}^2$) to very low-surface-area smoke samples (for which the

extension of the faces and terraces is 10^3 – 10^4 nm²). We have noticed that, on increasing the dimension and the perfection of the adsorbent faces, the FWHM gradually decreases from ~ 18 to ~ 4.5 cm⁻¹ (data obtained in the $\theta \rightarrow 1$ limit). This observation clearly indicates that the FWHM is determined mainly by inhomogeneous broadening effects. In other words, the half-width of the $\tilde{\nu}(\text{CO})$ peak provides indirect information about the regularity of the face on which the CO molecule is adsorbed.

To be more quantitative, the following question must be answered: What is the intrinsic FWHM of the $\tilde{\nu}(\text{CO})$ of an isolated CO molecule adsorbed on a Mg_{5c}²⁺ site located on infinite and perfect (001) faces? The answer is not straightforward, and more information, based on single-crystal data, is needed. Contributions by Heidberg *et al.* (119, 129) indicate that the FWHM of CO adsorbed on MgO(001) single crystals cut *in vacuo* is greater than 1 cm⁻¹ a value somewhat high in comparison with the FWHM of about 0.25 cm⁻¹ reported by Noda *et al.* (130, 131) and Disselkamp *et al.* (132) for CO adsorbed on NaCl(001) at 30 K. Comparison with the CO/NaCl(001) system is appropriate because the interaction is electrostatic and the $\tilde{\nu}(\text{CO})$ (2154.5 cm⁻¹) values are very similar. From this comparison it is concluded that although electron micrographs of the microcrystals of the smoke suggest that only regular (001) faces are exposed, the exposed faces must still be quite inhomogeneous at the atomic level (e.g., because of the presence of steps one or two atomic layers thick and of kinks that escape detection by electron microscopy). This inhomogeneity is probably caused by the preparation procedure. Because the MgO smoke is prepared by burning a Mg ribbon in air (which contains H₂O vapor; see Section IV.A.1), the surface can be heavily contaminated by OH groups, and their elimination upon outgassing *in vacuo* creates stepped surfaces (133–135). Atomic force microscopy (AFM) indicated surface roughness of MgO(001). Therefore, even the surfaces of single crystals are not ideal and perfect as previously supposed.

4. Adsorbate–Adsorbate Interactions on MgO(001) Faces: Dependence of the Shift and the Intensity of the $\tilde{\nu}(\text{CO})$ Peak on Coverage

As briefly mentioned in Section IV.A.1, the main peak of CO on MgO(001) gradually shifts from 2157 cm⁻¹ (at $\theta = 0$) to 2148 cm⁻¹ (at $\theta = 1$), and this behavior has been ascribed to changes in lateral interactions. As discussed by many authors (22, 23, 73, 136–140), in overlayers formed by very weakly adsorbed diatomic species the interactions among the oscillators are essentially of the “through space” type. These interactions occur among the static and dynamic dipoles of the diatomic species. For this reason, the shift $\Delta\tilde{\nu}$ is the sum of two contributions, $\Delta\tilde{\nu} = \Delta\tilde{\nu}_{\text{stat}} + \Delta\tilde{\nu}_{\text{dyn}}$. When the interaction energies become larger than those characteristic of simple physisorption

processes, other static effects must be considered which are more appropriately classified as chemical. These effects, being transmitted through the solid, are also called through solid effects. Two types of chemical effects can be proposed: inductive and relaxation effects (which are not always independent). The first is associated with electronic density changes at a given site induced by adsorption at a neighboring site. This effect is absent when overlap forces are not operative [as for CO on MgO(001), for which electrostatic polarization forces are predominant]. The relaxation effect is a through solid effect associated with changes in surface relaxation caused by the formation of adlayers. Upon adsorption at a given cationic position, the positive ions move toward energetically more favorable positions, as do the negative ions in nearest-neighbor and more distant positions. Although the effect dies away within the distance of a few lattice constants, it is evident that adsorption at a given site modifies the structural situation in a small but nonnegligible circular area around the adsorption center, thus perturbing the adsorptive properties of other cationic sites within this area. This effect is always present and is expected to be of relatively great importance for chemisorption, particularly for the CO/ZnO system (because of the tetrahedral coordination of zinc and oxygen) and for CO on high index faces of other oxides exposing ions in low coordination sites.

The relative value of $\Delta\tilde{\nu}_{\text{stat}}$ and $\Delta\tilde{\nu}_{\text{dyn}}$ can be evaluated by means of diluted isotope mixtures suggested by Hammaker *et al.* (136) which remove the dynamic coupling between $^{12}\text{CO}^{13}\text{CO}$ oscillators in diluted $^{12}\text{CO}^{13}\text{CO}$ (15:85) mixtures. In the CO/MgO system the observed shifts are $\Delta\tilde{\nu}_{\text{dyn}} = 3.5 \text{ cm}^{-1}$ and $\Delta\tilde{\nu}_{\text{stat}} = -11.3 \text{ cm}^{-1}$. Following the modified Hammaker equation (136), $\Delta\tilde{\nu}_{\text{dyn}}$ is related to the dynamic polarizability α_v of the CO molecule by the relationship

$$(\tilde{\nu}/\tilde{\nu}_0)^2 = 1 + (\theta\alpha_v\Sigma_0)/(1 + \theta\alpha_e\Sigma_0) \quad (7)$$

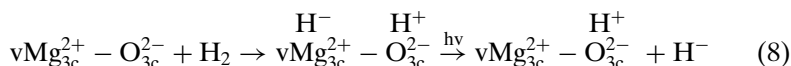
where $\tilde{\nu}$ is the stretching frequency at $\theta = 1$ (in the absence of static effects), $\tilde{\nu}_0$ is the singleton frequency, α_e is the electronic polarizability [$\alpha_e = 1.98 \text{ \AA}^3$ (138)], and Σ_0 is the direct dipolar sum. From this relationship, a value of $\alpha_v = 0.031 \text{ \AA}^3$ is obtained, which is not much different from that usually accepted for free CO ($\alpha_v = 0.057 \text{ \AA}^3$), as expected in view of the weakness of the perturbation (141). The α_v value fully confirms the picture emerging from the experimental and theoretical investigations discussed in Section IV.A.2.

5. Interaction of MgO with Other Simple Molecules

The adsorption of H_2 at RT on high-surface-area MgO sintered at 1073 K leads to heterolytic dissociation of the molecule on a few acid–base sites,

as shown by IR (142–144), UV–VIS (145), and TPD data (96). The results demonstrate that H₂ is a probe for acid–base pair sites of enhanced acid–base strength. These pairs are likely located at corners and on reconstructed (111) faces. Low-temperature experiments ($T < 77$ K), to the best of our knowledge, are still missing, and consequently the spectroscopy of hydrogen on flat (001) surfaces is still unknown. Paganini *et al.* (146) provided evidence for the combined action of a surface electron trap (v) and adjacent low-coordinated cations and anions in the heterolytic dissociation of H₂ on MgO.

The following hypothetical pathway has been proposed:



A mechanism was proposed (142) for the interaction of O₂ with preadsorbed H₂ concerning the electron transfer process from H[−] ions to oxygen molecules with formation of the paramagnetic O₂[−], as evidenced by UV–VIS and EPR data (147). The formation of surface O₂[−] species has also been observed by EPR spectroscopy upon dosing of O₂ onto pyridine-pretreated MgO (148).

The monolayer structure of N₂ molecules adsorbed on highly homogeneous MgO powders has been investigated in the 10–60 K range by Trablesi *et al.* (149), who used neutron diffraction techniques; the results are comparable to those obtained by Angot and Suzanne (150) by LEED.

The NO/MgO system has been investigated by means of IR (151–153) and EPR (154) spectroscopies. The results show that NO reacts on the surface of MgO to give NO₂[−] and N₂O₂^{2−} (153). However, the surface coverage obtained with NO is greater than that observed with CO. This result indicates that the higher reactivity of NO allows it to probe a larger fraction of O^{2−} Lewis basic sites (not only the corner sites). The coadsorption of CO and NO was investigated by UV–VIS spectroscopy (155). The IR and EPR study of Garrone *et al.* (156, 157) showed that the reaction of CO with NO on MgO gives CO₂ + N₂. The presence of paramagnetic CNO₂[−] species, formed on the more unsaturated surface ions, has been tentatively proposed. In a subsequent EPR study, supported by molecular orbital calculations, the same group reassigned the observed radical ion as CNO₃^{2−} (158). The interaction of both N₂O and propene on MgO with preadsorbed CO has been investigated by IR and UV–VIS spectroscopies (159); a comparison with parallel experiments carried out with CaO was also reported.

Busca *et al.* (160) performed an IR investigation of the adsorption of CO₂ on MgO, reporting shifts of 42, −17, and 21 cm^{−1} for the $\tilde{\nu}_1$, $\tilde{\nu}_2$, and $\tilde{\nu}_3$ modes of CO₂, respectively. A combined low-temperature IR and TPD study in the temperature range 100–1000 K (after adsorption of CO₂ at 27 Pa at liquid nitrogen temperature) was also reported (96).

The molecular (161) and dissociative (162, 163) adsorption of NH_3 on MgO was investigated by IR and UV–VIS spectroscopies (157). The results show that a small fraction of ammonia undergoes heterolytic dissociation on adjacent low-coordinated Mg^{2+} and O^{2-} ions to form NH_2^- and OH^- groups. The reaction of CO with the NH_2^- and OH^- has been characterized by IR emission spectroscopy (164). Formaldehyde and formates are formed first; they react to give isocyanate derivatives, and decomposition at high temperatures yields simple $(\text{NCO})^-$ ions (164). Garrone *et al.* (165) reported the interaction of N_2O with irreversibly preadsorbed ammonia to yield surface azid (N_3^-) species. The interaction of O_2 with preadsorbed NH_3 on MgO was described by Martra *et al.* (166), who used IR spectroscopy; the oxidized species N_2^- , N_3^- , NO^- , NO_2^- , and NO_3^- were detected.

The interaction of H_2O with oxide surfaces is of particular relevance to the understanding of several fundamental phenomena (167, 168). In particular, H_2O undergoes heterolytic dissociation through a nucleophilic attack by the basic O^{2-} anions; hence, the MgO surface becomes immediately covered by a full layer of hydroxyl groups, as demonstrated by IR investigations (169–171). The contributions of Echterhoff and Knözinger (172) and Knözinger *et al.* (173) together with some theoretical contributions (174–181) are noteworthy. Scamehorn *et al.* (176, 177) reported two stable configurations for H_2O molecules physisorbed on Mg(001); H_2O either forms bifurcate hydrogen bonds with the O^{2-} ions of the surface or an oxygen-down configuration on top of a Mg^{2+} ion. Experiments with MgO(001) single crystals were carried out by Ferry *et al.* (182, 183), who used elastic helium scattering and LEED. A combined LEED and IR study (with a polarized IR source) was reported by Heidberg *et al.* (184); at 150 K, a broad polarization-dependent band was observed in the 3050–3650 cm^{-1} range, which was assigned as the symmetric and antisymmetric H_2O stretching vibrations $\tilde{\nu}_1$ and $\tilde{\nu}_2$. From an evaluation of the integrated intensities for p- and s-polarized radiation, it was inferred that the molecular plane is nearly parallel to the MgO(001) surface. The observed frequencies suggest a strong $\text{O}-\text{H} \cdots \text{O}$ hydrogen bond among nearest-neighbor water molecules. In ordered H_2O monolayers, no dangling OH groups were observed, but a p-polarized absorption at 3680 cm^{-1} was attributed to hydroxyl species absorbed on steps. The hydroxyl groups formed on low-coordinated sites of MgO(001), after dissociative adsorption of water, were characterized by Coustet and Jupille (185, 186) in a combined HREELS and X-ray photoelectron spectroscopy (XPS) study. The authors observed a $\tilde{\nu}(\text{OH})$ band at 3685 cm^{-1} (at maximum OH coverage), in agreement with the HREELS data reported by Xu *et al.* (187). The most recent findings of the Jupille group on this topic have been reported by Abriou and Jupille (188). The picture emerging from all these investigations is that regular 5-coordinated surface sites are not able to dissociate H_2O and that the

process occurs only on 4- and 3-coordinated sites. Finally, Xu and Goodman (189) reported a combined TPD, IRAS, and LEED study of D_2O adsorbed on thin $MgO(001)$ films grown on a $Mo(001)$ substrate. They concluded that for the first chemisorbed layer, 0.62 D_2O molecules are absorbed on surface Mg^{2+} cation sites.

Adsorption of CH_4 on MgO has been studied both experimentally (15, 190–194) and theoretically. We mention the IR and theoretical study by Knözinger (15) and Ferrari *et al.* (195). The IR spectrum is reproduced in Fig. 8.

The spectra reported in Fig. 8, being unaffected by coadsorption of CO , are attributed to CH_4 adsorbed on anions at low temperature. The methane molecule forms a weak $CH \cdots O_{3c}^{2-}$ bond, which reduces its symmetry from T_d to C_{3v} . At elevated temperatures, methyl radical formation was reported (190–192). Ito *et al.* (192) reported a TPD study in the 220–600 K range of

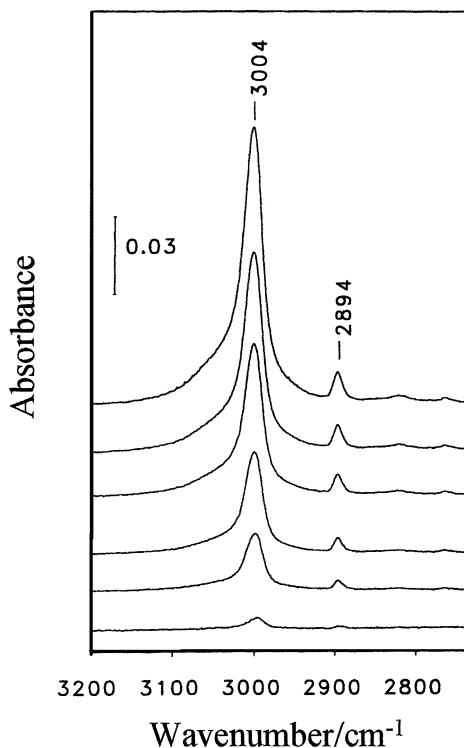
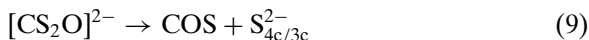


FIG. 8. IR spectra in the C–H stretching region of methane adsorbed on MgO at 80 K (MgO pretreated in O_2 at 773 K, followed by evacuation at 773 K) [reproduced from Knözinger (15) with permission of VCH].

CH₄ on MgO (adsorption was carried out at RT; the sample was subsequently cooled to 220 K). Pelmenshikov *et al.* (196) reported a combined IR and computational *ab initio* study of the adsorption of CD₃CN on bare (MgO)_n clusters ($n = 4, 6, 10, \text{ and } 12$).

Our group reported IR and UV-VIS spectra characterizing the adsorption of CS₂ on MgO (197). Substitution of surface O²⁻ ions by S²⁻ was observed, resulting in a tailored modification of the basicity of the surface. The CS₂ molecules adsorb on the low-coordinated oxygen anions, O_{4c/3c}²⁻ + CS₂ → [CS₂O]²⁻. The [CS₂O]²⁻ surface species are decomposed *in vacuo* at 650 K



thus generating low-coordinated surface S²⁻ species. The surface basicity of S-doped MgO is drastically modified, as shown by the result that the formation of negatively charged (C_nO_{n+1})²⁻ species is totally suppressed upon interaction with CO (197).

The interaction of acetylene with Mg(001) was investigated by LEED (198–200). At 88 K, C₂H₂ molecules lie almost parallel to the surface, and neither molecule nor substrate distortions have been observed, indicating that only a weak physisorption occurs. Calculations with semiempirical potentials confirm the structure determined by LEED (199). The isomerization of *cis*-2-butene on MgO has been reported (201). The dissociation of cyclopentadiene on a few active acid–base pair sites of totally dehydrated MgO was followed by IR spectroscopy, and the formation of surface hydroxyl groups and C₅H₅⁻ species was proposed (202). Methanol decomposition (203) and ethanol decomposition (204, 205) have been reported.

From this review, we conclude that the (001) faces are relatively unreactive and that the preferential chemisorption sites are always located at defects.

6. Metal-Doped MgO: Structure and Catalytic Properties

A high activity in the oxidative coupling of methane has been reported for Li-doped MgO (192, 206, 207). Ruckenstein and Khan (208) also found alkali-promoted MgO to be a promising catalyst for this reaction. It has been shown that the breaking of a C–H bond plays a key role on these catalysts (209). The problem of the oxidative coupling of methane has been discussed from a theoretical point of view by Børve and Pettersson (210), who approached the problem of hydrogen abstraction from CH₄ on the undoped MgO(001) surface by using clusters of increasing size with point ion embedding. They concluded that the perfect (001) surface of MgO is not active. Børve (211) extended the study to defective Mg_{4c}²⁺ and Mg_{3c}²⁺ sites, concluding that oxygen ions at steps are inactive, whereas those at corners (showing

an O^- character) can dissociate methane. These results are in agreement with recent results of Ferrari *et al.* (195), who performed more sophisticated quantum mechanical calculations and showed that CH_4 adsorption occurs on undoped MgO only at corner sites. Johnson *et al.* (212) reported an *ab initio* embedded cluster study to elucidate the mechanism of methane coupling on Li-doped MgO. They showed that several surface defects, such as $[Li^+O^-]$, $[Li^+O^-]O_2$, and $[Li^+O^-]O$, may abstract hydrogen from CH_4 . Wu *et al.* (213–215) investigated methane activation on Li-promoted MgO(100)/Mo(100) films by combined surface science techniques and kinetics measurements at high pressures; EELS measurements identified peaks at 1.6, 3.6, and 5.33 eV, attributed to $[Li^+O^-]$, F aggregates, and F centers, respectively. The authors found that the ethane formation rate correlates well with the F center concentration but not with that of $[Li^+O^-]$ centers. Therefore, they concluded that the role of lithium could be to promote F-center formation. The high C_2 yield on Li-doped MgO is probably related to the increase of surface basicity of the catalysts as a result of the promotion with the alkali cation. To achieve this objective, several groups doped MgO with other electropositive elements, such as Na (216), Cs (217, 218), Ba (218–220), or Y (218, 221); segregated Ca ions in Ca-rich MgO/CaO solid solutions were also investigated (222). Li- and Na-trapped hole centers in MgO have been characterized with the CRYSTAL code (223). EPR data provide evidence of the paramagnetic ionic cluster Li_3^{2+} in Li-doped MgO (224).

7. Reactivity of Electron-Rich MgO Surfaces: Role of F_S , F_S^+ , and F_S^{2+} Centers

Surface anion vacancies in highly ionic crystals exhibit high reactivities and have been postulated to be the active sites for many catalytic reactions (76, 213); this section is dedicated to this topic. Anion vacancies were first observed as bulk defects. A bulk F center in MgO or in other systems with cubic structure consists of one (F^+) or two (F) electrons trapped in an anion vacancy surrounded by six cations in octahedral symmetry. If the anionic vacancy is located at the surface, it represents an accessible electronic trap, in which electrons can be captured from a donor molecule A, stored, and ultimately transferred to an acceptor molecule B. The anion vacancy can thus play a catalytic role. Following the nomenclature introduced by Tench and Nelson (225), a suffix “S” is added to denote the surface nature of the defect; we are thus dealing with F_S^+ (paramagnetic) or with F_S (diamagnetic) centers. F-centers (bulk or surface) are also called color centers because they are responsible for the typical blue color assumed by MgO powder. The removal of an oxygen ion implies the appearance of a new electronic state in the energy gap, about midway between the bottom of the empty

Mg $3s$ and $3p$ conduction band and the top of the filled O $2p$ valence band. The optical properties of F-centers in MgO have been investigated since the early 1970s (226, 227). The original model of surface color centers proposed by Tench and Nelson (225) consists of the elimination of a O_{3c}^{2-} ion from the MgO(001) surface resulting in a defect with C_{4v} symmetry. The presence of defects originating from the elimination of low-coordinated ions such as O_{4c}^{2-} or O_{3c}^{2-} has also been found (142, 146); there are defects with lower symmetry but higher reactivity. Paganini *et al.* (146) proposed that an electron at an O_{3c}^{2-} vacancy at the vertex of a microcube on a polar MgO(111) face can be stabilized by the three adjacent Mg^{2+} ions. The origin of these surface defects can be associated with the physico-chemical processes occurring on MgO surfaces during the dehydration process at high temperature (87), through elimination of surface OH groups (see Section IV.A.1), as shown by UV-VIS (155, 228) and IR spectra (85, 142). Experimental (146, 229–232) and theoretical (229, 233–236) work has been performed to characterize the magnetic properties of the surface color centers.

The concentration of surface electrons trapped in anion vacancies can be considerably increased by doping the MgO surface with metals with low ionization energies, such as alkali metals (230, 237) or Mg (230, 238–240).

O_2 is able to abstract an electron from an F_S^+ center, giving the surface superoxide O_2^- species. This process has been investigated by EPR spectroscopy (238, 241–243); it may play an important role in many catalytic oxidation reactions (244–248). The formation of the superoxide species via the reaction $F_S^+ + O_2 \rightarrow F_S^{2+} + O_2^-$ (146, 243) is of course favored on metal-doped MgO surfaces. In a combined EPR and IR study, Giamello *et al.* (240) demonstrated that CO is able to abstract an electron from a surface F center to form novel dimeric species produced by $C_2O_2^{2-}$. CO^- radical anions have also been reported (237).

B. OTHER ALKALINE EARTH OXIDES WITH CUBIC STRUCTURE

The chemistry of CO adsorbed on CaO and on SrO has been investigated by IR spectroscopy (249) and compared with that occurring on MgO. It was concluded that the CO interacts irreversibly with O^{2-} surface ions with the formation of CO_2^{2-} (carbonite) and oligomeric species and that a strong electrostatic interaction between the negative species and the surface cations accounts for the marked dependence of the IR signals on the lattice parameter of the solid, $a_{MgO} < a_{CaO} < a_{SrO}$. The increasing basicity in the series (MgO < CaO < SrO) causes a marked increase in this series of the total adsorption capacity, an increase of the relative population of negatively charged CO polymers with respect to dimers, and an increase

in importance of a Boudouard-like reaction upon desorption (leading to oxidized and reduced species).

IR spectroscopy was used to follow the molecular and the dissociative adsorption of NH_3 on MgO , CaO , and SrO (162). A comparative UV-VIS investigation of the interaction of ammonia with the three systems was reported (157).

Che *et al.* observed the formation of surface O_2^{2-} species by EPR upon dosing ^{17}O -enriched O_2 molecules on pyridine-pretreated CaO (250), MgO , and SrO (148). For the three oxidic systems the splitting of the $2p\pi^*$ orbitals by the surface crystal field has been measured from the g_{zz} component of the \mathbf{g} tensor, and a dependence on the polarizing tendency of the surface cation (q/r) was found (148). It was inferred that the donor sites producing the O_2^{2-} molecular ions are the coordinatively unsaturated surface O^{2-} ions. F_S -centers in CaO have been investigated by EPR (251).

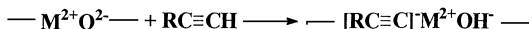
Nakamura *et al.* (252) reported an IR investigation of the adsorption of N_2O on CaO . The work was stimulated by the fact that CaO is a much more active catalyst than MgO for the decomposition of N_2O into N_2 and O_2 (253, 254).

Pacchioni *et al.* (255) performed *ab initio* cluster calculations to characterize the chemisorption of CO_2 and SO_2 on CaO and compared the results with those obtained for MgO . They concluded that, whereas both molecules interact strongly with the oxygen anions of the $\text{CaO}(001)$ surface, only weak bonds are formed on the $\text{MgO}(001)$ surface. The authors explained the results by considering that the large lattice parameter of CaO ($a_{\text{CaO}} = 2.4 \text{ \AA}$ compared to $a_{\text{MgO}} = 2.1 \text{ \AA}$) implies that a surface oxygen anion experiences a Madelung potential that is lower in CaO than in MgO . In CaO , this results in a reduced energy cost for using the charge of surface O^{2-} to form chemical bonds. These considerations also explain the higher activity of CaO (with respect to MgO) in the decomposition of N_2O .

C. ADDITIONAL EXAMPLES OF THE SURFACE REACTIVITY OF ALKALINE EARTH OXIDES

In addition to the reactions of basic oxides with H_2 , CO , and NH_3 described in the previous sections, it is worth mentioning the reactivity of MgO , CaO , and SrO surfaces toward more complex molecules. Among the numerous reactions described in the literature, the following are highlighted:

1. $\text{M}^{2+} \text{O}^{2-}$ ($\text{M} = \text{Mg}, \text{Ca}, \text{Sr}$) coordinatively unsaturated pairs are able to abstract a hydrogen ion from acetylenic hydrocarbons following the reaction path shown in Scheme 4 (—, surface plane; R, alkyl group), with formation



SCHEME 4

of hydroxyl groups and negative species (256). The negative groups can react further with oxygen to give surface (EPR-active) O_2^- species. The reaction of oxygen with the negative species represents an example of electron transfer between adsorbed molecules.

2. The most active acid–base pairs of the surface (presumably those exposed on edges, steps, and corners) are able to abstract hydrogen from olefinic hydrocarbons (257) with formation of hydroxyl groups (detected by IR) and allyl anionic species (detected by UV/VIS spectroscopy). Subsequent contact with O_2 leads to the formation of superoxide O_2^- ions (revealed by EPR spectroscopy). A similar interaction with cyclopentadiene leads to surface Cp^- and OH^- groups (202).

3. A small number of surface sites are able to abstract hydrogen even from benzene and toluene. The occurrence of this surface process is revealed only by the subsequent interaction with oxygen to produce a small number of superoxidic species (257).

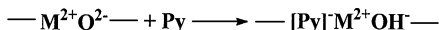
4. Hydrogen ions can be abstracted from acetone leading to the formation of hydroxyl groups and highly colored negatively charged species of undefined structure (258).

5. Coordinatively unsaturated surface pairs abstract hydrogen ions from the α position of pyridine as shown in Scheme 5. The $[\text{Py}]^-$ can then further react with excess Py to give bipyridyl radical anions (259). As usual, these negatively charged species can then react with oxygen to give superoxidic anion radicals.

D. REACTIONS CATALYZED BY BASES

Among the various reactions catalyzed by bases, we have selected (i) the polymerization of ethylene oxide catalyzed by MgO (260), (ii) the closely related reaction of ethylene oxide with alcohols on basic hydrotalcites to give polyoxyethylene polymer (the Henkel process), (iii) the phenol alkylation with methanol on MgO (General Electric and BASF processes) (261), and (iv) phenol amination to give aniline on MgO (the USS process) (262).

These choices are justified not only because the reactions are applied industrially but also because they seem to involve a common mechanism based on anionic intermediates formed at basic oxygen sites.



SCHEME 5

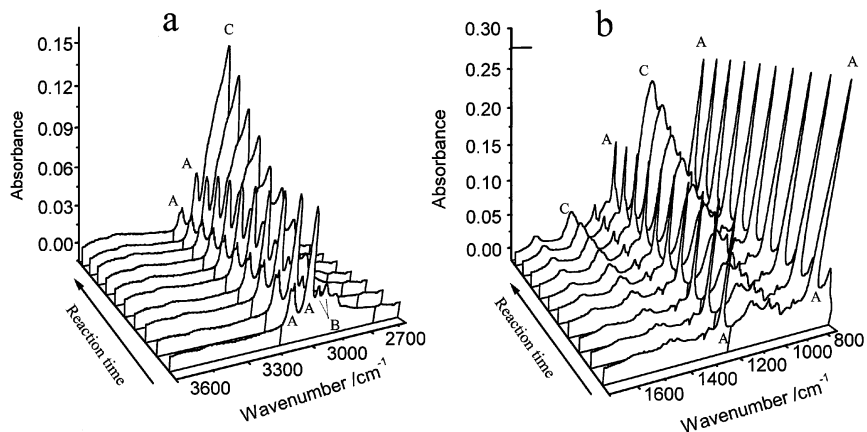
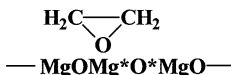


FIG. 9. IR spectra of increasing doses of ethylene oxide adsorbed at 298 K on fully dehydrated MgO [experiment repeated on the basis of Zecchina and Stone (259)].

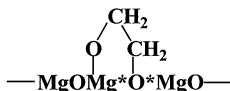
1. Ethylene Oxide Oligomerization

When the surface of fully dehydrated MgO is contacted with ethylene oxide at RT (260), the first surface product formed is the σ adduct between the ethylene oxide molecules and the most coordinatively unsaturated Mg^{2+} ions of the surface, presumably localized on edges, steps, and corners (hereafter Mg^*) (Fig. 9: IR bands labeled A) (Scheme 6). This first step is not unexpected since ethylene oxide, with its medium base strength, acts as a surface probe for the most reactive Lewis acid sites (three- and fourfold coordinated Mg^{2+} ions). This precursor species transforms at RT into a truly chemisorbed species, leading to the formation of a structure plausibly suggested to be the cyclic structure represented below (bands B in Fig. 9) because of the nucleophilic attack of the basic coordinatively unsaturated oxygen ion (O^*) in adjacent position on the CH_2 group (Scheme 7).

In the presence of excess ethylene oxide, species A and B transform into polymeric species (C bands) via insertion of ethylene oxide. It has been speculated that these species may have cyclic structures (260). It has also been ascertained that these species have a "living" character and can be displaced from the surface by water with formation of $\text{HOCH}_2(\text{CH}_2\text{OCH}_2)_n\text{CH}_2\text{OH}$ and surface hydroxyl groups.



SCHEME 6



SCHEME 7

2. Synthesis of Polyoxoethylene Polymers

The same mechanism can be postulated for the reaction of ethylene oxide and an alcohol ROH (as in the Henkel process) (261), leading to the catalytic formation of the polymeric $\text{RO}(\text{CH}_2\text{CH}_2\text{O})_n\text{H}$ (with a narrow molecular weight range). In this case it is the alcohol molecule (instead of water) that displaces the polymer from the surface and gives the final product.

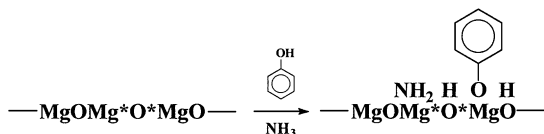
3. Phenol Alkylation

Although not studied in detail, the mechanism of phenol alkylation with methanol can be formulated on similar grounds by assuming that the initial interaction of phenol and methanol with MgO gives surface phenoxide and methoxide ions and OH groups [these species are known to be formed separately on MgO (263)]. This initial reaction is then followed by elimination of H_2O and formation of trialkyl phenol.

4. Phenol Amination

The mechanism of phenol amination on MgO can be formulated in an identical way since it is known that ammonia also dissociates heterolytically on the most unsaturated Mg^*O^* pairs (264) located at edges, steps, and corners, with formation of surface NH_2^- and OH^- species (see Section IV.A.5). Since phenol (an acidic molecule) is adsorbed on all surface $\text{Mg}^{2+}\text{O}^{2-}$ pairs, the most plausible adsorption interaction mechanism is that shown in Scheme 8. The densely packed negatively charged OH, phenoxide, and amino groups are then expected to readily react at the reaction temperature with elimination of aniline and water.

In conclusion, the major role in these examples is played by the *basic oxygen ions*, which can display nucleophilic reactivity and abstract hydrogen ions from methanol, phenol, and even ammonia to form reactive negatively charged intermediates (264).



SCHEME 8

E. NiO

NiO is a cubic oxide characterized by ionicity and lattice parameters very similar to those of MgO. Furthermore, the preparation procedures of the two oxides may be similar: (i) Stoichiometric high-surface-area NiO is prepared (as is MgO) from the hydroxide precursor by decomposition under vacuum and (ii) low-surface-area materials are obtained by progressive sintering at high temperatures. The evolution of the microcrystal morphology on passing from high- to low-surface-area (sintered) NiO is also similar to that for MgO, as demonstrated by Escalona Platero *et al.* (73, 265, 266); the final habit of the microcrystals is represented by nearly perfect cubes predominantly defined by atomically flat (001) faces and terraces.

1. IR Spectroscopy of the Co/NiO System: Comparison with Results of Other Techniques

The vibrational spectra of CO adsorbed on NiO samples (22, 73, 265, 266) characterized by decreasing surface area and correspondingly increased surface perfection are represented in Fig. 10 for $\theta \approx 1$, where only the 2200- to 2000- cm^{-1} interval is illustrated for simplicity. Figure 10 shows the progressive simplification of the spectra and the continuous decrease of the FWHM (the final narrow band at 2136 cm^{-1} has a FWHM = 3.7 cm^{-1}) as a function

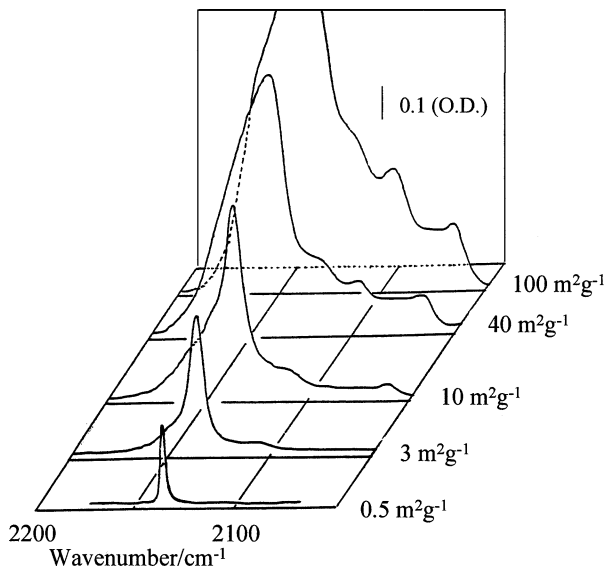
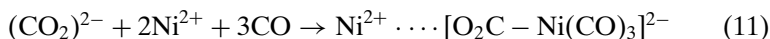
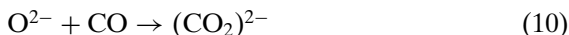


FIG. 10. IR spectra of ^{12}CO adsorbed at 77 K on NiO samples with crystallites of increasing perfection [adapted from Zecchina *et al.* (22) with permission of Elsevier Science Publishers].

of the decreasing surface area (265). These simple spectra obtained for the most highly sintered samples suggest that the majority of the adsorbed CO molecules occupy crystallographically identical surface sites with similar environments. Moreover, the remarkably small FWHM suggests that inhomogeneous broadening effects are very small and that the adsorption of CO on such NiO microcrystals can be compared with that on single crystals. A parallel SEM, AFM, and HRTEM study suggested that the surface termination is mainly represented by the (001) faces; (111) faces are also present on sintered NiO (265). However, they do not play a role in CO chemisorption because they are permanently covered by OH groups. For the reasons already discussed for MgO, the main peak at 2136 cm^{-1} must be assigned to CO adsorbed in end-on configuration on regular Ni_{3c}^{2+} ions located on (001) faces and terraces. The remarkably narrow width of this band shows that these faces and terraces are extended and without significant defects. The adsorption in the 2100 to 2050-cm^{-1} range, present only on high-surface-area samples, is associated with reduced nickel species, either generated during the activation procedure or formed following the reaction path



with formation of a species which can be identified as $\text{Ni}(\text{CO})_4$ adsorbed on a $\text{Ni}^{2+}\text{O}^{2-}$ pair. The first step of this reaction, which is initiated by the oxygen ions with lowest coordination number, located at corners and (probably) edges, is analogous to the first step observed on MgO; only the final products are different in the two cases, owing to the presence of the reducible transition metal ion in NiO (267). By analogy with MgO, the less resolved high-frequency shoulders at $\tilde{\nu} > 2150\text{ cm}^{-1}$ correspond to CO adsorbed on Ni_{4c}^{2+} and Ni_{3c}^{2+} ions located at edge, step, and corner positions. The utility of the method of progressive sintering in assigning the individual components appearing in the complex spectra of CO adsorbed on a high-surface-area material is again obvious. A complex morphology of the sample is not the only source of spectroscopic complexity; nonstoichiometry can also play a role. This is the case for NiO, for which traces of hydrocarbon can lead to sample reduction during the outgassing procedure, with the subsequent appearance of reduced species.

Figure 11 Shows the evolution of the IR spectra of CO adsorbed on low-surface-area NiO crystals as a function of coverage. The single narrow peak, observed on highly sintered NiO at 2136 cm^{-1} ($\theta \approx 1$), belongs to the reversibly formed $\text{Ni}_{3c}^{2+} \dots \text{CO}$ species. Also in this case, a progressive frequency shift is observed upon decreasing the coverage, from 2136 to 2152 cm^{-1} in the $\theta \rightarrow 0$ limit. On the basis of the discussion of the

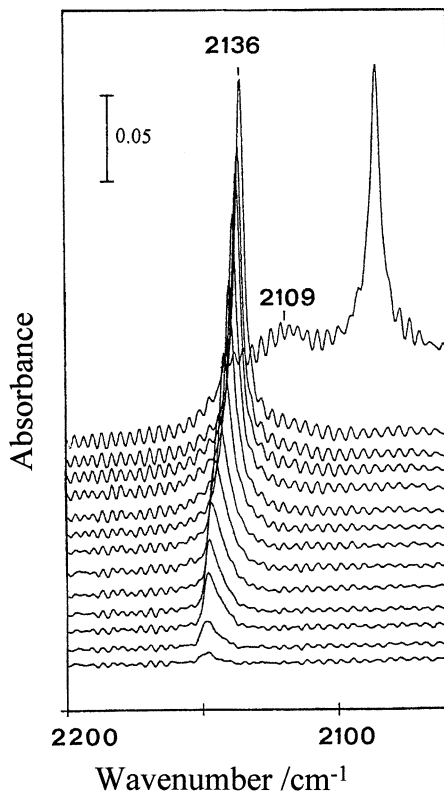


FIG. 11. IR spectra of ^{12}CO adsorbed at 77 K on highly sintered NiO samples at coverages ranging from $\theta = 1$ (5.33 kPa) to $\theta \rightarrow 0$ and of $^{12}\text{CO}^{13}\text{CO}$ (15 : 85) isotopic mixture at $\theta = 1$ [reproduced from Zecchina *et al.* (22) with permission of Elsevier Science Publishers].

MgO/CO system (Section IV.A.4), we know that this shift is associated with the changes of the adsorbate–adsorbate (static and dynamic) interactions occurring when the coverage changes from 0 to 1. With the aid of the isotopic substitution method, Escalona Platero *et al.* (265) calculated $\Delta\tilde{\nu}_{\text{dyn}} = +27\text{cm}^{-1}$, $\Delta\tilde{\nu}_{\text{st}} = -43\text{cm}^{-1}$, and $\alpha_v = 0.256\text{Å}^3$. All these values are higher than those found for CO on MgO; therefore, both the permanent and the dynamic dipoles and the associated charge oscillations from the adsorbate to the surface and vice versa during the stretching vibration [which have direct influence on α_v (141)] are substantially increased upon adsorption on NiO. This in turn indicates that the $\text{Ni}^{2+} \cdots \text{CO}$ bond does not have a purely electrostatic character (as in the $\text{Mg}^{2+} \cdots \text{CO}$ case) and that some $d-\pi$ overlap forces play a small but definite role (87). The quantification of

the chemical contribution in the $\text{Ni}^{2+} \cdots \text{CO}$ bond is difficult to make on the basis of the IR results alone. However, modest enhancement of α_ν and the completely reversible character of the CO species even at low temperature suggest that chemical forces still play only a minor role. Therefore, the assumption that the static shift is mainly due to dipole–dipole (through space) effects can still be considered to be a valid approximation. The presence of a small backdonation also explains why the frequency of the CO peak is lower than that observed for CO on MgO. The interaction of CO with Ni^{2+} ions has been studied by means of *ab initio* methods by Pacchioni *et al.* (268) and Neyman and Rösch (269). Both groups emphasized the predominant role of electrostatic forces, whereas opposite conclusions were reached regarding the minor contribution of d – π overlap.

The bond energy of CO on regular Ni_{5c}^{2+} sites of NiO(001) is significantly higher than that of CO on Mg_{5c}^{2+} of MgO, in agreement with IR results. Klier (270) reported a value of 29 kJ mol^{-1} for powdered crystals. TDS has been used to measure the bond energy, and values of 31 and 41 kJ mol^{-1} were reported by Cappus *et al.* (271) and Veaecky *et al.* (272), respectively. Wichtendahl *et al.* (114, 115) reported improved TDS data, basically confirming their previous results (29 kJ mol^{-1}). Pacchioni *et al.* (268, 273) calculated, at the SCF level, bond energy of a 23 kJ mol^{-1} (but a high shift $\Delta\tilde{\nu}$ (CO) of 38 cm^{-1}), in fair agreement with the experimental values.

The discussion about the possible presence of a small contribution of d – π overlap forces at the surface of NiO is of interest because it may occur with Ni^{2+} interacting with adsorbates with π -acceptor characteristics, such as CO, NO (Section IV.I.2), and O_2 . IR spectra of O_2 adsorbed at 77 K on progressively sintered NiO samples (274) follow a trend similar to that observed for CO. In particular, on high-surface-area samples, O_2^- species formed at edge, step, and corner sites are predominant, whereas on progressively more sintered samples “neutral” species adsorbed in side-on configuration on Ni^{2+} of the (001) faces become the only species detectable by IR spectroscopy.

2. IR Spectroscopy of the NO/NiO System: Comparison with Results of Other Techniques

Electronic surface states are responsible for adsorptive and catalytic processes occurring at the surfaces of solids. Therefore, the catalytic behavior of the simple transition metal oxides such as NiO and CoO (Section IV.F) led to extensive experimental and theoretical investigations of the corresponding $3d$ surface states (115, 275–283). Whereas the role of d – π overlap is quite modest in the $\text{Ni}^{2+} \cdots \text{CO}$ surface complexes, the same does not necessarily hold for the $\text{Ni}^{2+} \cdots \text{NO}$ complexes formed upon interaction of NiO(001) with the stronger π -acceptor NO ligand. This is shown by the formation of

$\text{Ni}^{2+} \cdots \text{NO}$ complexes on $\text{NiO}(001)$ faces (284), which are stable at room temperature. These complexes are characterized by a coverage-dependent $\tilde{\nu}(\text{NO})$ stretching frequency in the 1805–1799 cm^{-1} range. A $\tilde{\nu}(\text{NO})$ value lower than that of NO gas [$\tilde{\nu}_o(\text{NO}) = 1876 \text{ cm}^{-1}$] and the stability at RT imply that $d-\pi$ overlap contributions must be substantial. The spectra of the NO/NiO system are illustrated in Fig. 12. As was observed for CO, the $\tilde{\nu}(\text{NO})$ band gradually shifts with coverage because of the static and dynamic dipole–dipole interactions ($\Delta\tilde{\nu}_{\text{dyn}} = 32 \text{ cm}^{-1}$ and $\Delta\tilde{\nu}_{\text{st}} = -26 \text{ cm}^{-1}$) (284).

A combined IR, microcalorimetric, and volumetric study of NO adsorbed on $\text{NiO}(001)$ by Escalona Platero *et al.* (285) gave a constant molar heat of adsorption of 81 kJ mol^{-1} in the $0 < \theta < 0.2$ coverage range. At higher coverages, adsorbate–adsorbate interactions progressively reduced the molar heat of adsorption to 69 kJ mol^{-1} (285). Figure 12 also shows a comparison between the volumetric and the spectroscopic isotherms.

Kuhlenbeck *et al.* (275, 276) and Bäumer *et al.* (283) investigated the adsorption of NO on thin $\text{NiO}(001)$ layers deposited on $\text{Ni}(001)$ and on vacuum-cleaved $\text{NiO}(001)$ single-crystal surfaces with variety of techniques. By means of XPS, angle-resolved ultraviolet photoelectron spectroscopy (UPS), near-edge X-ray absorption fine structure (NEXAFS), and HREELS, the authors showed that the surfaces of both samples have similar occupied and unoccupied states. The single band at 1800 cm^{-1} observed by HREELS, is very close to the value observed by IR spectroscopy for NO on microcrystalline samples (284) and indicates that there is only one adsorbed NO species. NEXAFS data indicate that the NO axis is tilted by 45° relative to the $[001]$ vector, and TDS measurements yield a bond energy of about 50 kJ mol^{-1} . The latter value has been essentially confirmed (55 kJ mol^{-1}) in a TDS study by the same group (115) and is in qualitative agreement with the value obtained by Escalona Platero *et al.* (285) for NO on NiO powders.

Bandara *et al.* (286) studied the adsorption of NO on thin $\text{NiO}(111)$ films grown on $\text{Ni}(111)$. A $\tilde{\nu}(\text{NO})$ value of 1800 cm^{-1} was reported. The influence of the presence of surface OH groups on the adsorption properties of $\text{NiO}(001)/\text{Ni}(100)$ films was characterized by EELS and *ab initio* calculations (277, 287). In agreement with previous results, Polcik *et al.* (288) presented a nitrogen 1s scanned energy-mode photoelectron diffraction study of NO on $\text{NiO}(001)$ (supported by a full multiple scattering simulation), concluding that the NO molecule is bonded through the N atom atop a surface Ni^{2+} ion, with the N–O axis tilted from the $[001]$ direction by 59° .

F. CoO

The results obtained for CO on sintered CoO are quite similar to those found for the CO/NiO and CO/MgO systems, the main difference being

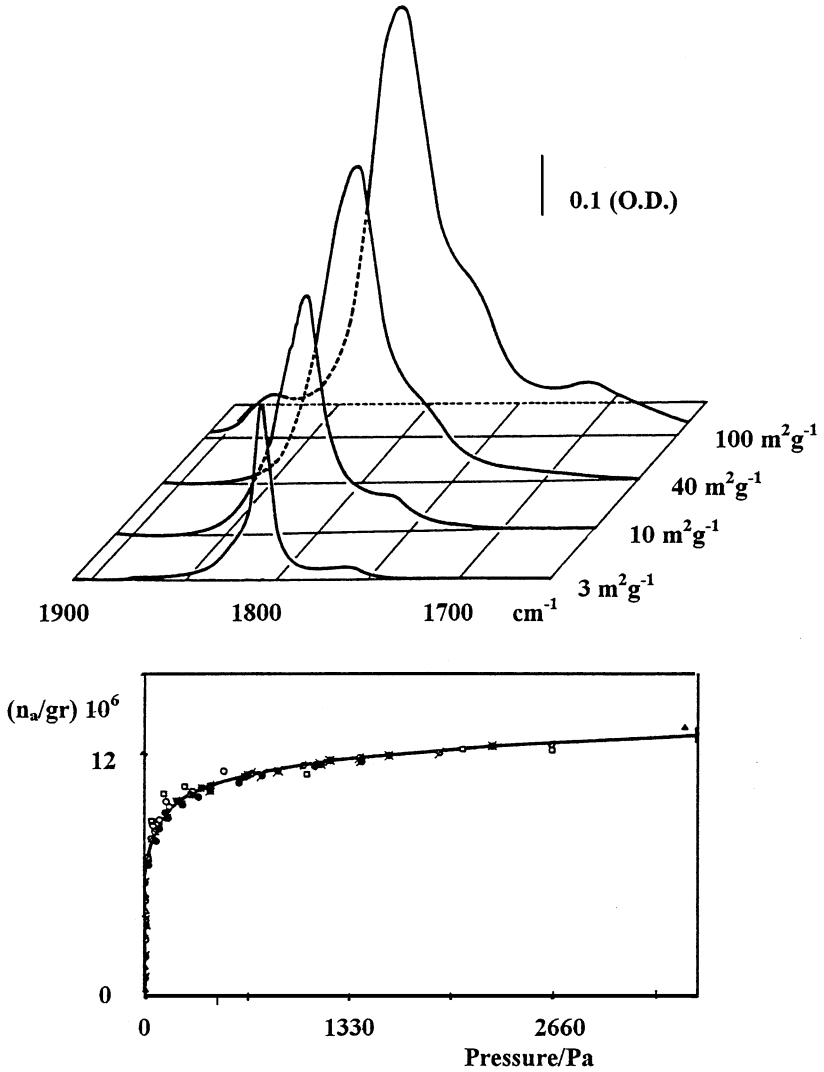


FIG. 12. IR spectra of NO adsorbed at 300 K on NiO samples sintered at progressively higher temperatures (the spectra correspond to $\theta \approx 0.5$) and volumetric [number of adsorbed moles of NO per gram of NiO ($1.5 \text{ m}^2 \text{ g}^{-1}$)] and spectroscopic (integrated IR intensity) isotherms. The two sets of data have been normalized to coincide at $P_{\text{NO}} = 16 \text{ Torr}$ [adapted from Escalona Platero *et al.* (285) with permission of Elsevier Science Publishers].

caused by the greater imperfection of the CoO microcrystals, even after severe sintering. Therefore, the FWHM of the CO band at 2136 cm^{-1} ($\theta = 1$) is larger than that observed for CO on NiO. Nonetheless, a simple interpretation of the spectra is possible (87).

Adsorption of both CO and NO on nonpolar CoO(001) and polar CoO(111) epitaxial films has been investigated by Schönnenbeck *et al.* (289) with HREELS and NEXAFS. Comparison with results for NiO(001) and NiO(111) surfaces was also reported. On all these oxide surfaces, NO exhibited stretching frequencies that were red shifted, whereas the $\nu(\text{CO})$ band is very close to that of the free molecule.

G. HALIDES WITH THE CUBIC STRUCTURE

Pioneering IR studies of the interaction of CO with NaCl microcrystals were performed by Gevitzman *et al.* (290, 291) in the late 1960s and early 1970s, IR-transparent NaCl films, characterized by high specific surface areas, were made by sublimation of NaCl onto a cold (77 K) NaCl plate. This preparation method can be successfully adopted in the preparations of LiF, KCl, or NaI films (73, 290–292). In the mid-1980s, Zecchina *et al.* (73, 293) and Heidberg *et al.* (294) extended this research. Comparing the spectra obtained for adsorbates on low- and high-area NaCl films, Zecchina *et al.* (73, 293) assigned the CO bands at 2159 and 2175 cm^{-1} ($\theta \rightarrow 0$) to the $\tilde{\nu}(\text{CO})$ of molecules adsorbed on Na_{5c}^+ and Na_{4c}^+ sites, respectively. The FWHM of the former band was found to be coverage dependent, increasing from 15 to 20 cm^{-1} as θ increased from 0 to θ_{max} . In the spectra obtained with high-area NaCl films, the 2175 cm^{-1} band is clearly visible at low θ , whereas at high θ it is totally superimposed by the IR band of the much more abundant $\text{Na}_{5c}^+ \cdots \text{CO}$ adducts (shifted to 2156 cm^{-1} by adsorbate–adsorbate interactions; Section IV.A.4). Zecchina *et al.* (293) estimated the relative importance of the static and dynamic effects by using $^{12}\text{CO}^{13}\text{CO}$ mixtures, and a value of α_v of 0.0235 \AA^{-3} was calculated from the Hammaker (136) equation (see Section IV.A.4). The experimental approach was extended to LiF (73), KCl (73, 295, 296), and NaI (73) films, and the corresponding spectroscopic results are summarized in Table I, in which the corresponding values for MgO and NiO are reported for comparison.

The spectroscopy of CO on NaCl single crystals has been investigated in detail by Ewing *et al.* (49, 130–132, 297–299) and Heidberg *et al.* (48, 300, 301). The structure of CO on NaCl(001) was also investigated by means of helium scattering (302, 303) and fluorescence spectroscopy (304); thermodynamic investigations (305, 306) were also reported.

The group of Heidberg also performed an IR study of the adsorption of NH_3 (307), CO_2 (308), and H_2 (309) on NaCl, and the group of Ewing

TABLE I
IR Frequency, $\Delta\bar{\nu}_{\text{dyn}}$, $\Delta\bar{\nu}_{\text{stat}}$, and α_v Characterizing Interactions of ^{12}CO and $^{12}\text{CO}/^{13}\text{CO}$ Isotopic Mixtures Dosed onto LiF, NaCl, KCl, NaI, MgO, and NiO^a

System	$^{12}\text{CO}/^{13}\text{CO}$ (99 : 1) ($\bar{\nu}/\text{cm}^{-1}$)		$^{12}\text{CO}/^{13}\text{CO}$ (10 : 90) ($\bar{\nu}/\text{cm}^{-1}$)	$\Delta\bar{\nu}_{\text{dyn}}(\text{cm}^{-1})$	$\Delta\bar{\nu}_{\text{stat}}(\text{cm}^{-1})$	$\alpha_v(\text{\AA}^3)$
	$\theta \rightarrow 0$	$\theta \rightarrow \theta_{\text{max}}$	$\theta \rightarrow \theta_{\text{max}}$			
LiF	2155	2150	2148	2.2	7.2	0.017
NaCl	2159	2156	2153	3.0	6.0	0.023
KCl	2153	2149	2147	2.3	6.0	0.024
NaI	2159	2157	2154	2.5	5.0	0.026
MgO	2157	2151	2148	3.5	-11.3	0.031
NiO	2152	2136	2109	27.0	43.0	0.256

^aData from Escalona Platero *et al.* (73).

investigated CO_2 (310), H_2 (311), CH_4 (312), and H_2O (313) on NaCl. The adsorption of N_2O on NaCl(001) was investigated by IR, LEED, and helium scattering (314).

We summarize a few reports of the catalytic properties of halides. The photochemical properties of alkali halides were investigated by several groups (315–322). Berg and Ewing (316) reported that the photodissociation ($\lambda = 185$ nm) of $\text{C}_2\text{H}_2\text{CO}$ on NaCl gives the CH_2 radical and CO with a quantum efficiency similar to that of the gas phase reaction. The photochemical reactions of acetylene C_2H_2 and C_2D_2 to give C_2HO on NaCl were reported to occur with quantum efficiencies an order of magnitude greater than in the gas phase (317, 319). Polanyi *et al.* (315, 321) showed that the photodissociation ($\lambda = 222$ nm) of carbonyl sulfide catalyzed by the LiF surface has a quantum efficiency three orders of magnitude greater than that in the gas phase.

H. SOLID SOLUTIONS OF CUBIC SYSTEMS

1. General Considerations

In this section, a few general statements about solid solutions are given, followed by a discussion of specific solid solutions of cubic crystals. The solid solutions formed from MO and AO oxides are denoted the MO–AO system, with AO being considered as the host matrix and M the dopant cation. The mole fraction of M is indicated by subscript x (e.g., $\text{M}_x\text{A}_{1-x}\text{O}$).

Metal oxide solid solutions have attracted the interest of many research groups since the 1950s (323–329), for two reasons. First, solid solutions have been used to investigate the effect that a guest cation (M) has on the

properties of the host matrix (AO). They are also useful for studying the effect that the crystal field of the surrounding ions of AO has on the electronic states of M. Second, solid solutions permit one to probe the role of the local structure of the active sites (in contrast to collective properties) on the activities and selectivities of catalytic reactions (324, 325). This approach readily showed that the activity of a M ion in the MO–AO system can be very different from that observed for M in the pure MO oxide and that it can be greatly influenced by the degree of dilution of M in AO.

It also became evident that a great variety of catalysts, potentially exhibiting a large flexibility, could be prepared via solid solutions. Three different degrees of freedom can be varied in a controlled fashion: the chemical nature of the host matrix AO, the chemical nature of the guest cation M, and the dopant concentration x . Furthermore, solid solutions can be formed not only by cubic oxides but also by alumina, titania, zirconia, and others. Thus, another degree of freedom is added, namely, the different crystal structures.

Dilute solutions ($x \leq 0.05$) are particularly interesting since, in these solids, M cations can be considered as virtually isolated in the AO matrix, and mutual $M \cdots M$ interactions are absent. Therefore, the intrinsic catalytic behavior of isolated centers M can be singled out (25). The catalytic behavior can be compared for M in matrices of the same symmetry but different ionicity (e.g., AO = MgO, CaO, NiO, or SrO) or those also differing in symmetry (e.g., AO = NiO or ZnO). For example, it has been shown that the activity for N_2O decomposition of both Ni^{2+} and Co^{2+} ions is lower when the ions are hosted in ZnO than in MgO (330). A progressive increase of x allows one to follow the insulator to semiconductor transition of the $M_xA_{1-x}O$ system in a controlled way without changing the local structure of M as surface active centers.

In host matrices with cubic structure (e.g., AO = MgO, CaO, NiO, or SrO), the coordination number of the guest cation is 6 when substituting, for example, for bulk Mg^{2+} ions but M_{5c} , M_{4c} , and M_{3c} dopant cations are obtained when the substitution occurs with surface Mg^{2+} or Ca^{2+} ions located on terraces, steps, or corners (1, 25, 331). As has been mentioned, at low x values M cations are isolated in the matrix, but increasing x leads to pairs, triplets, etc. (25, 332).

Several factors influence the x range in which the $M_xA_{1-x}O$ solid solution can be obtained without segregation of the MO and AO phases. Large x values are tolerated for isovalent ions: M^{2+} dopants in MgO, CaO, NiO, ZnO, etc.; M^{3+} ions hosted in Cr_2O_3 or Al_2O_3 ; or M^{4+} ions in ZrO_2 . A high solubility is also expected when the size and the preferred coordination of the host and guest cations are the same. These considerations explain why NiO (or CoO) and MgO form solid solutions $Ni_xMg_{1-x}O$ (or $Co_xMg_{1-x}O$)

over the entire range ($0 < x < 1$) and why the solubility of Ni^{2+} in CaO is limited—there is a disparity of cation sizes. The solubilities of Zn^{2+} in MgO (difference of symmetry, resulting in $x < 0.25$) and of Cu^{2+} in MgO (coordination constraint attributed to Jahn–Teller effect of Cu^{2+}) are also limited (25). The occurrence of $\text{M}_x\text{A}_{1-x}\text{O}$ solid solutions, the absence of segregated phases, and the precise determination of the x values were assessed by X-ray diffraction (XRD) crystallography (25, 333–336). Accurate determinations of the lattice parameters a_x by XRD lead to the determination of x since ideal $\text{M}_x\text{A}_{1-x}\text{O}$ solid solutions obey the virtual crystal approximation law: $a_x = x a_{\text{MO}} + (1 - x) a_{\text{AO}}$. A nonlinear change of the lattice parameter with solute concentration indicates the presence of nonidealities (25). Of course, the determination of a_x by XRD leads to a measure of the average x value of the bulk. Since the catalytic properties of a material are dictated by surface ions, it must be carefully checked that neither kinetics constraints during the preparation (337) nor surface energy effects (338) result in a compositional gradient from the surface to the bulk inferior. The x value determined by XRD must be confirmed by surface-sensitive techniques such as XPS, Auger, or ion scattering spectroscopies. In a classical experiment, Cimino *et al.* (339) demonstrated that diluted Zn^{2+} solutions in MgO show a systematic surface enrichment in zinc. In contrast, in both NiO–MgO and CoO–MgO solid solutions, only very small differences between bulk and surface composition were detected (333, 334, 338, 340–342). If the check of surface versus bulk x is missing, misleading results may be obtained.

In addition to XRD (25, 333–336), other techniques can also be applied to monitor the structural quality of a solid solution (i.e., the absence of clustering effects leading to segregation). Calorimetric measurements (25, 331, 343), temperature programmed reduction (344), and IR (345, 346), electronic, and magnetic techniques, when applicable, are also sensitive methods for revealing interactions between solute ions. If M is a paramagnetic ion, such as Cu^{2+} , the presence of M pairs or triplets can be monitored by EPR because of spin–spin interactions (347, 348); the occurrence of clustering leads to a quenching of the intensity and a loss in resolution of the EPR spectra (349). Measurements of the electronic conductivity allow the determination of the insulator-to-semiconductor transition as x is increased (25, 350). UV–VIS spectroscopy has also been used (340). The atomic selectivity of Extended X-ray absorption fine structure (EXAFS) and X-ray absorption near edge structure (XANES) techniques and their ability to probe the local environment of a selected atom have been used to investigate the dispersion of Ni in MgO (351).

Zeolites and related materials prepared by isomorphous substitution of lattice atoms can also be considered as solid solutions and yield specifically designed micro- and mesoporous catalysts.

2. NiO–MgO/CO

The surfaces of NiO–MgO solid solutions have been investigated by IR spectroscopy with CO as a probe (345); the effect of sample pretreatment with H₂ has also been reported (346). Pacchioni *et al.* (268) proposed the hypothesis that the lower stretching frequency observed for CO adsorbed on NiO (compared to MgO) could simply be associated with the lower ionicity of NiO. If the positive charge localized on Ni²⁺ is decreased, the strength of the electrostatic field centered on Ni²⁺ ions is also decreased, resulting in a smaller blue shift of the CO stretching frequency. However, this hypothesis still leaves the observed frequency (lower than that of CO gas) and the observed increments of dynamic and static shifts (together with the anomalous value of α_v) unexplained. Scarano *et al.* (87) designed an experiment which should, in principle, allow the estimation of the role of ionicity. These authors investigated the adsorption properties of NiO–MgO (5% NiO) solid solutions toward CO. The relative roles played by d – π overlap forces and ionicity (with the related polarizing field) in determining the CO stretching frequency should be detectable for these solids because the Ni²⁺ ions located on the (001) faces are diluted in the MgO matrix and should therefore experience an environment and an ionicity very similar to those of Mg²⁺ ions on the same face. If chemical interactions are absent, the frequencies of CO on Mg²⁺ and on Ni²⁺ of solid solutions are expected to be identical, because the two ions, having the same radius and the same charge, should also have the same polarizing tendency. The experimental results summarized in Fig. 13 show in contrast, a distinctly lower frequency for CO adsorbed on Ni²⁺ than on Mg²⁺ ions. The intensity of the CO band on Ni²⁺ is higher than expected on the basis of the stoichiometry, which is an indirect indication that α_v increased.

Note that shift of the Ni²⁺ \cdots CO peak, $\Delta\tilde{\nu} = -14\text{ cm}^{-1}$, observed upon changing the coverage is entirely static, since the CO oscillators on Mg²⁺ and Ni²⁺ are dynamically independent. These results provide further experimental evidence that the d – π contribution cannot be ignored in the interaction of CO with Ni²⁺ ions. This spectroscopic evidence agrees well with the experimental differences of the bond energy (114, 115) for the formation of the Mg_{5c}²⁺ \cdots CO and Ni_{5c}²⁺ \cdots CO complexes in MgO(001) and NiO(001) [13.5 vs 29 kJ mol⁻¹ for CO adsorbed on MgO and NiO (001) faces, respectively].

3. NiO–MgO/NO

Whereas the d – π overlap is modest in the Ni²⁺ \cdots CO surface complexes, this is not necessarily true when a stronger π -acceptor ligand such as NO is used to probe the surface Ni²⁺ ions located on (001) faces of NiO or

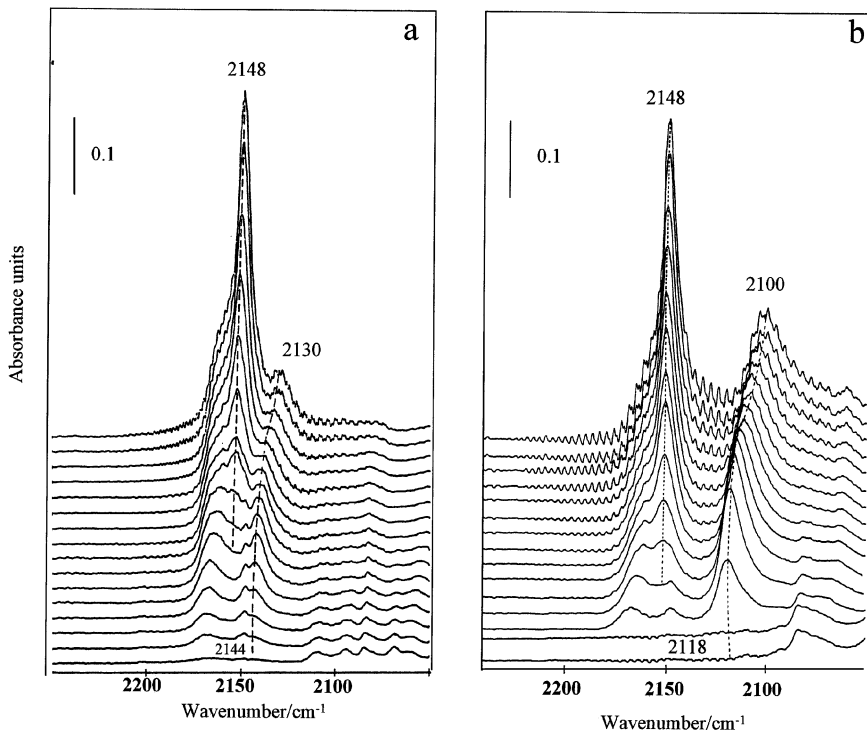


FIG. 13. (a) IR spectra of ^{12}CO adsorbed at 77 K on sintered NiO/MgO solid solutions for coverages ranging from $\theta = 1$ (5.33 kPa) to $\theta \rightarrow 0$, (b) IR spectra of ^{12}CO adsorbed at 77 K on sintered CoO/MgO solid solutions for coverages ranging from $\theta = 1$ (5.33 kPa) to $\theta \rightarrow 0$ [reproduced from Scarano *et al.* (87) with permission of the Royal Society of Chemistry].

NiO–MgO solid solutions. The interaction of NO with Mg^{2+} ions exposed on the (001) faces of MgO and NiO–MgO solid solutions remains weak since only polarization forces are involved (because of the absence of d -orbitals of suitable energy centered at the adsorbing Mg^{2+} ion). It is therefore expected that a probe molecule with greater d - π acceptor ability, such as NO, could provide further information about the propensity of the d -orbitals to participate in bond formation at the transition metal centers (because it is able to amplify the d - π effects). The experimental results confirm this view: (i) On MgO and on Ni^{2+} -free portions of the NiO–MgO solid solution, the NO is so weakly bonded to the surface centers that (at 77 K) it gives preferentially lateral interaction products (dimerization with formation of *cis*- N_2O_2 species); (ii) on Ni^{2+} ions, in contrast, $\text{Ni}^{2+} \cdots \text{NO}$ complexes are stable at room temperature. The stability of this complex, together with its

stretching frequency (lower than that of NO gas), can be understood only if d -orbitals are substantially involved.

4. NiO–MgO System as Catalyst

The N_2O decomposition into N_2 and O_2 on the NiO–MgO system was investigated (352, 353). This reaction has been reviewed by Cimino and Stone (25), who compared the catalytic behavior of several $3d$ transition metal ions, such as Cr^{3+} (354), Mn^{4+} (355), Mn^{3+} (355), Mn^{2+} , Fe^{3+} , Fe^{2+} , Co^{2+} (356), Ni^{2+} (352, 353), and Cu^{2+} , each hosted in MgO. All these oxides have been found to be active for N_2O decomposition, and a general reaction path has been proposed (25): $2N_2O + 2e^-$ (from the catalyst) $\rightarrow 2N_2 + 2O_{ads}^- \rightarrow 2N_2 + O_2 + 2e^-$ (to the catalyst).

It has been shown that pure MgO is inactive and most of these solid solutions are those containing Mn^{3+} (d^4) and Co^{2+} (d^7). Mn^{2+} and Fe^{3+} (both in d^5 configuration) are less active, and Ni^{2+} (d^8) and Mn^{4+} (d^3) are intermediate in activity (25). The activity of the solid solution decreases in all cases with increasing x values (25). The results clearly indicate that a localized electron transfer, with the electron retained in a surface complex centered on an isolated transition metal ion, favors the activity (25, 357).

The catalytic activity of the NiO–MgO solid solutions for hydrogenation of CO and of CO_2 and for steam reforming (358, 359) has been attributed to the high efficiency of NiO–MgO in inhibiting carbon decomposition, which could not be avoided on the other Ni-containing catalysts (360, 361). Diluted NiO–MgO solid solutions ($x_{Ni} = 0.03$), reduced in H_2 at about 1100 K, are remarkable catalysts that permit carbon-free operation at 1123 K in the reforming of CH_4 with CO_2 , with lifetimes greater than 3000 h (362–367). On the basis of XRD, electron microscopy, dispersion measurements, and IR investigations of the catalyst, Cheng *et al.* (368) concluded that the excellent coking resistance in the CO_2 reforming of methane on the reduced $Ni_{0.03}Mg_{0.97}O$ solid solution catalyst is caused by the high dispersion of the Ni species, the basicity of the support, and the Ni–MgO interaction (368). These authors also reported that interactions between CO and CO_2 molecules on $Ni_xMg_{1-x}O$ samples also occur. Hu and Ruckenstein (369) presented a TPD study of CO desorption from the surfaces of NiO–MgO solid solutions for the entire composition range ($0 \leq x \leq 1$); the effect of reduction in H_2 was also discussed. The following results were obtained for reduced samples: (i) In the temperature range 323–473 K, two overlapping CO peaks (attributed to CO adsorbed molecularly on slightly different Ni surface species) were observed; (ii) in the temperature range 473–973 K (depending on x), both CO and CO_2 were detected. The author, inferred that CO was dissociatively adsorbed on Ni, with some CO

converted into CO₂, as follows: 2CO → 2C + 2O → CO₂ + C. The same group (370) reported a programmed reaction mass spectrometry investigation of the activation of CH₄ reacting with CO and CO₂ on NiO–MgO.

5. CoO–MgO

UV–VIS and IR spectroscopies was used in combination to investigate the electronic and vibrational transitions in CoO–MgO solid solutions in the entire composition range ($0 \leq x \leq 1$) (371).

The adsorption of ¹⁶O₂ and ¹⁸O₂ on a sintered CoO–MgO solid solution was reported (372) and later investigated by IR and EPR spectroscopies (373, 374). IR spectra of CO on CoO–MgO solid solutions were also reported (375–377). Experiments performed at liquid nitrogen temperature with Co-diluted samples indicate the formation of both σ -bonded Mg²⁺ ... CO and σ - π -bonded Co²⁺ ... CO adducts on (001) faces (375). The latter are characterized by a significantly lower stretching frequency than CO gas ($\tilde{\nu}(\text{CO}) = 2118 \text{ cm}^{-1}$, $\Delta\tilde{\nu} = 39 \text{ cm}^{-1}$ at $\theta \rightarrow 0$) and by a remarkable static shift as a function of θ ($\Delta\tilde{\nu}_{\text{stat}} = -18 \text{ cm}^{-1}$), in line with the hypothesis that d - π overlap is significant (Fig. 13).

CO molecules adsorbed on Mg²⁺ ions on (001) faces of sintered CoO–MgO solid solutions exhibit a dipole–dipole coupling similar to that found for CO on bare MgO, whereas CO molecular adsorbed on Co²⁺ are decoupled but interact with adjacent Mg²⁺ ... CO species *via* static effects (375). The intensity of the $\nu(\text{CO})$ peak of the Co²⁺ ... CO complex is greater than expected on the basis of the stoichiometry; this result is in agreement with the fact that the peak intensity is proportional to α_{ν} (141).

The room-temperature chemistry of high-surface-area CoO–MgO solid solutions is dominated by the adsorption of CO on edges and steps. Coordinatively unsaturated Co²⁺ and O²⁻ ions react primarily as O²⁻Co²⁺O²⁻ triplets with formation of [(CO)₂CoCO]²⁻ species. In samples with high Co contents, the large amounts of clustered cobalt guest species are easily reduced by CO, even at room temperature, with formation of Co(CO)₄⁻ and carbonate-like species (377). The formation of polymeric radical anions of CO on high-surface-area CoO–MgO solid solution has also been reported (378).

The disproportionation of NO into N₂O and surface nitrates was investigated for CoO–MgO and NiO–MgO solid solutions by IR and EPR techniques (379). The heterolytic dissociation of H₂ on Co²⁺ and O²⁻ pairs present at edges and steps of CoO–MgO cubes to generate hydride and hydroxyl species has been shown by IR spectroscopy (380). The decomposition of N₂O was also investigated (356).

An IR and UV–VIS investigation of the interaction of NH₃, ND₃, and pyridine with CoO–MgO solid solutions with low Co contents has also been

reported (381). Subsequent interaction of NH_2^- and molecularly adsorbed NH_3 with CO gives adsorbed HCONH^- species preferentially located on the Mg-rich part of the surface. An investigation of the interaction of O_2 with NH_3 at the surfaces of CoO–MgO solid solutions by IR spectroscopy (382) showed that oxidized species, NO_2^- and NO_3^- , are formed preferentially.

The reactions of ethene, propene, *trans*-2-butene, and toluene with O_2 on CoO–MgO (5% CoO) were investigated (383, 384, 385) by IR and EPR techniques. A surface superoxide species was found to be the oxidizing agent. The oxidation follows essentially the same path as that on MgO (dissociative adsorption of the hydrocarbon, formation of a carbanion, charge transfer to a surface oxygen atom yielding the superoxide, and insertion of the oxygen species into the organic chain). However, the rate is much higher than on MgO, yielding acetates, formates, and benzoates. EPR data indicate that surface Co^{2+} ions coordinate O_2 molecules much as natural oxygen carriers do.

CoO–MgO solid solutions have also been shown to be active for CO oxidation. The activity for the reaction on $\text{Co}_x\text{Mg}_{1-x}\text{O}$ is the same over the entire composition range ($0 < x < 1$) (386).

6. Less-Common Solid Solutions

The surfaces of MgO–ZnO solid solutions enriched in Zn^{2+} ions were investigated by IR spectroscopy with both CO and H_2 used as probes (387). Scarano *et al.* (388) reported an IR investigation of the adsorption of CO on CoO–ZnO ($x_{\text{Co}} = 0.05$); a comparison with the interaction of CO with the CoO–MgO was repeated. The interaction of O_2 with a FeO–MgO solid solution ($x_{\text{Fe}} = 0.05$) was investigated by IR spectroscopy (389); the formation of $\text{Fe}^{3+}\text{O}_2^-$ species was proposed.

V. Oxides and Halides with the Wurtzite Structure: Surface Structures, Reactivity, and Catalytic Activity

A. ZnO CASE STUDY

ZnO exhibits varied catalytic properties, being active for hydrogenation and dehydrogenation reactions, dehydration of alcohols, methanol synthesis, and other reactions. ZnO is a wide-band *n*-type semiconductor with surface states present in the band gap. It can be doped with cations, and defects can be generated by treatment under oxidizing or reducing conditions (which change the availability of electrons at the surface).

Because of these properties, ZnO has been considered to be an ideal material for testing the electronic theories of catalysis, specifically the band model (based on the collective properties of the solid) or the localized site

model (based on the reactivities of sites with atomically defined structures (390). These theories are beyond the scope of this review (391, 392). We state only that recently the localized site model has gained credibility, whereas the band model and the direct correlation between catalytic activity and semiconducting properties have been discounted.

The semiconducting properties of ZnO have nevertheless proved to be advantageous because they permit the extensive application of modern surface spectroscopies (such as XPS, UPS, EELS, and LEED) for the investigation of the surface structures since the charging problems that are usually encountered with oxides are avoided (393). For this reason, ZnO is one of the most thoroughly investigated oxides.

ZnO can be prepared as single crystals or microcrystalline powders. The single crystals often have needle-like shapes and preferentially expose prismatic (10 $\bar{1}$ 0) and (11 $\bar{2}$ 0) faces. When examined by LEED, these neutral faces appear unreconstructed (393). In contrast the Zn and oxygen-rich positively and negatively charged (0001) faces prepared by cleavage of single crystals show a distinct tendency toward extensive reconstruction and accumulation of metal impurities.

Highly dispersed powders can be prepared in several ways. When prepared by combustion of metallic zinc, the resulting very pure ZnO (with $\sim 10 \text{ m}^2 \text{ g}^{-1}$ specific surface area) is constituted of microcrystals characterized by well-defined elongated prismatic habits (Fig. 14) exposing preferentially unreconstructed (10 $\bar{1}$ 0) and (11 $\bar{2}$ 0) faces (394). When prepared by decomposition of ZnCO₃, the resulting high-surface-area powder ($\sim 50 \text{ m}^2 \text{ g}^{-1}$) is constituted of very small microcrystals with ill-defined shapes.

Because of the high purity, the excellent morphological definition, and the good optical properties of the microcrystals, the surface and catalytic properties of ZnO powders prepared by Zn combustion have been investigated extensively by spectroscopic techniques. The results of these investigations are well suited to comparison with results obtained with single crystals and less well-defined samples.

On the virgin sample, the surfaces of the microcrystals are fully covered by adsorbed water and CO₂; consequently, they do not show any adsorption by diatomic molecules such as CO and H₂.

Activation at temperatures near 673 K is sufficient to clean the prismatic faces, whereas the sites located on the other (high index) faces, edges, steps, and corners remain covered by adsorbed impurities (mainly hydroxyl group). For this reason, the samples activated at 673 K can be considered as ideal for investigation of the properties of the (10 $\bar{1}$ 0) and (11 $\bar{2}$ 0) faces of ZnO, the abundance of which is on the order (10 $\bar{1}$ 0) > (11 $\bar{2}$ 0). Samples treated at higher temperatures *in vacuo* have been less thoroughly investigated because ZnO has a tendency to lose oxygen and become nonstoichiometric.

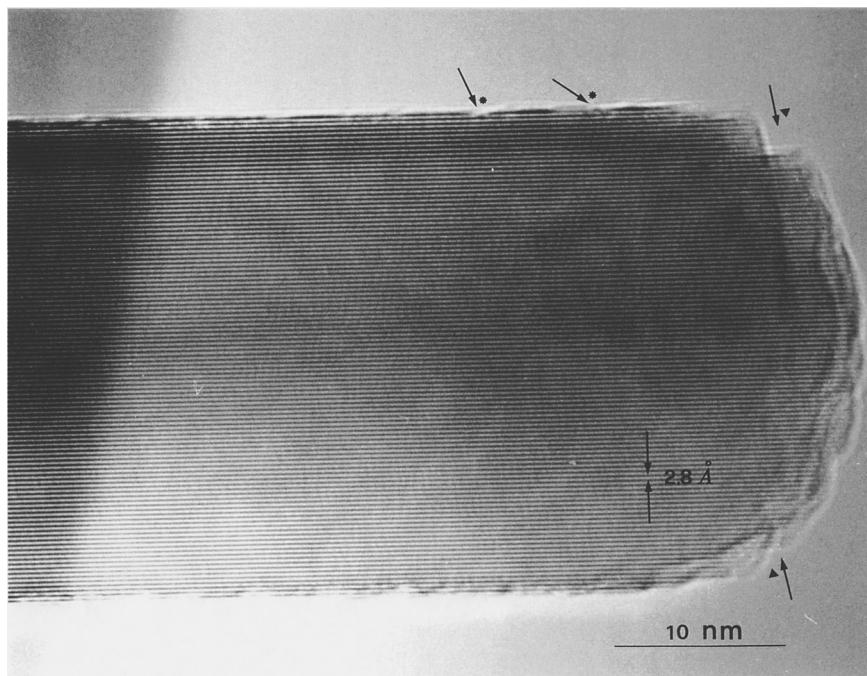


FIG. 14. HRTEM image of a ZnO microcrystal, where $(10\bar{1}0)$ planes are evident. The arrows show the presence of terraces and steps along the prismatic direction and many small facets (having the same symmetry as the predominant one) at the prism terminations [reproduced from Scarano *et al.* (394) with permission of Elsevier Science Publishers].

To a first approximation, the $(10\bar{1}0)$ surface can be considered as a 2D square array of threefold coordinated zinc as shown schematically in Fig. 15a. The structure of the $(11\bar{2}0)$ face is very similar (Fig. 15b).

1. ZnO/CO

The IR spectra of increasing doses of CO adsorbed at 77 K on ZnO pretreated at 673 K under vacuum are illustrated in Fig. 16a. These spectra are characterized by strong absorptions in the 2195- to 2165- cm^{-1} range (395). These absorptions, centered at frequencies higher than that of CO gas, correspond to polarized CO species σ bonded at the carbon end on Zn sites (394). In this review we comment only on the most important features of the spectra. For details, the reader is referred to Gay *et al.* (396).

Figure 16a shows that the spectrum of adsorbed CO changes gradually with coverage. In particular, at $\theta \rightarrow 0$ a single peak (probably due to the

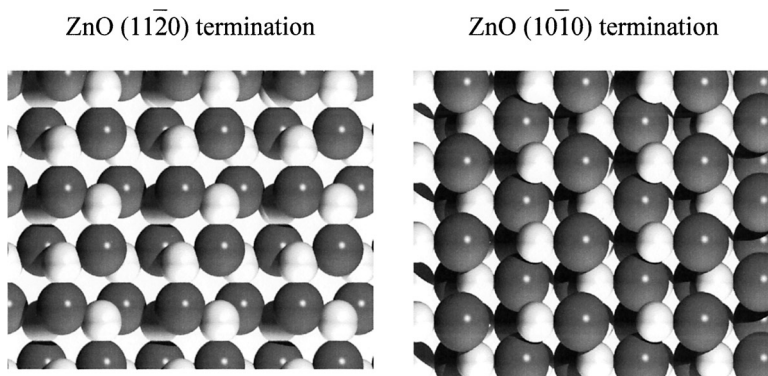


FIG. 15. Representation of the structure of (10 $\bar{1}$ 0) and (11 $\bar{2}$ 0) faces of ZnO. On both faces threefold coordinated Zn²⁺ species are exposed. Zn²⁺ are white; O²⁻ are gray.

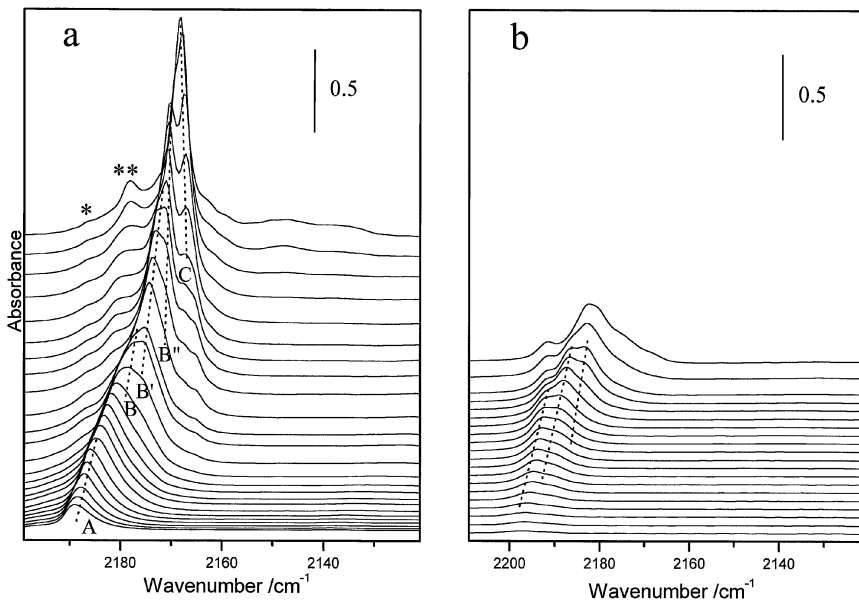


FIG. 16. (a) IR spectra of CO adsorbed at 77 K on ZnO samples; species A are dominant in the $0 \leq \theta \leq 0.25$ coverage interval; species C corresponds to the complete occupation of the vacant Zn²⁺ sites ($\theta = 1$); and species B, B', and B'' are dominant at $\theta \cong 0.5, 0.7$, and 0.9 , respectively. Weak bands labeled with one or two asterisks correspond to Zn²⁺-CO complexes located on edges and corners. (b) IR spectra of CO adsorbed at 77 K on hydrogen-precovered ZnO samples. All spectra were collected according to the procedure described in Scarano *et al.* (394).

superposition of two unresolved components), tailing into the low-frequency region, is observed at 2190 cm^{-1} (peak A). With increasing CO coverage, peak A gradually shifts to lower frequencies and then declines as new bands (B, B', and B'') appear and disappear in succession. For $\theta \rightarrow 1$, a single narrow component at 2168 cm^{-1} (C band) dominates. Like peak A, the C band is a composite, as can be seen at intermediate coverages, for which two components are detected. In our opinion, the composite structure of peaks A and C reflects the presence of two types of structurally similar Zn^{2+} sites located on the $(10\bar{1}0)$ and $(11\bar{2}0)$ faces, respectively. The stepwise evolution of the spectra of adsorbed CO as a function of coverage is a unique characteristic of ZnO.

The five bands arise from the stepwise occupation of the surface Zn^{2+} sites and correspond to different surroundings of the CO molecules.

Species A is dominant in the $0 \leq \theta \leq 0.25$ coverage interval, and species C corresponds to the complete filling of the vacant Zn^{2+} sites ($\theta = 1$). Species B, B', and B'' are dominant at coverages $\theta \cong 0.5, 0.7$, and 0.9 , respectively.

At the lowest coverages, the frequency of adsorbed CO (singleton frequency) is observed at 2190 cm^{-1} (A band), i.e., shifted by 47 cm^{-1} with respect to CO gas. This is in agreement with results of high-resolution electron energy loss vibrational studies (397). This large upward shift [when compared with that observed for the only other divalent ion without d electrons that has been investigated (Mg^{2+})], can be explained in terms of the strong polarizing electrostatic field associated with the threefold coordinated Zn^{2+} ions present on the $(10\bar{1}0)$ and $(11\bar{2}0)$ faces. On the basis of UPS results characterizing CO on single-crystal faces (396), the presence of a σ -type orbital overlap involving the 5σ -orbital of CO and an empty dangling sp^3 hybrid with acceptor character centered on Zn^{2+} must be considered as well. As documented by Gay *et al.* (396), the CO axis is slightly tilted with respect to the surface plane. Direct support for the presence of a σ bond derives from the experimental adsorption enthalpy at zero coverage ($\sim 50\text{ kJ mol}^{-1}$) (396), which is definitely higher than that observed for CO on MgO ($15\text{--}20\text{ kJ mol}^{-1}$), for which the electrostatic interaction plays the determining role (see Section IV.A.2).

An increase in the coverage from 0 to 1 shifts the peak downwards from 2190 to 2168 cm^{-1} because lateral interactions between the adsorbed CO species increase. The total shift observed for the full monolayer ($\Delta\tilde{\nu}_{\text{tot}} = -22\text{ cm}^{-1}$) is the sum of two types of dipole-dipole interactions, static and dynamic. By using the method of the diluted isotopic mixtures (see Section IV.A.2), it has been determined that the total shift is the sum of two contributions ($\Delta\tilde{\nu}_{\text{total}} = \Delta\tilde{\nu}_{\text{dynamic}} + \Delta\tilde{\nu}_{\text{static}}$ where $\Delta\tilde{\nu}_{\text{dynamic}} = 6\text{ cm}^{-1}$ and $\Delta\tilde{\nu}_{\text{static}} = -28\text{ cm}^{-1}$).

In comparing the shifts observed for CO on MgO and on NiO, we note that both the dynamic and static parts are intermediate between those observed for CO on MgO (3.5 and -11.3 cm^{-1}) and on NiO (27 and -43 cm^{-1}). This observation suggests that the dynamic and static shifts are minimal when the CO–surface interactions are purely electrostatic and increase with increasing σ - and π -orbital overlap contributions to the adsorbate–adsorbent bond (the largest shifts are found for CO on metals with partially filled d bands, for which π -overlap contributions are maximum). It is difficult to establish whether the static shift arises only from through-space effects (dipole–dipole interactions) or whether through-solid effects operate as well. A distinct and gradual decrease of the isosteric heat of adsorption with coverage of CO on prismatic faces has been ascribed to repulsive adsorbate–adsorbate interactions (396).

IR spectra of CO adsorbed on prismatic faces of ZnO show that the apparent half-widths of peaks A and C are ~ 4 and $\sim 1.5\text{ cm}^{-1}$, respectively. The decrease of the half-width with coverage [also clearly observed for CO on NaCl (100)] reflects the increasing collective character of the vibration observed on moving from low to high coverage, which becomes increasingly less influenced by inhomogeneous broadening effects associated with the presence of surface defects that interrupt the surface periodicity. The half-width of peak A (dominant at the lowest coverages) is larger than that observed for CO on NaCl (100) (see Section IV.C). This result can be accounted for both by the presence of a chemical bond between CO and Zn sites (which influences the lifetime of the excited states) and by inhomogeneous broadening caused by site heterogeneity. The relative weights of the two contributions are not known.

The weak bands labeled with one or two asterisks in Fig. 16 are also noteworthy. These bands are observed at 2178 (shoulder) and 2184 cm^{-1} for θ_{\max} , and their frequencies move gradually to a common position at 2190 cm^{-1} as the coverage is decreased. We assign these two bands to Zn^{2+} –CO complexes formed on the same prismatic faces (therefore, both bands shift to the common 2190 cm^{-1} frequency at zero coverage) but located near edges and corners (which explains the reduced shifts induced by increasing adsorbate–adsorbate interactions because the dipolar effects near the edges and corners are approximately one-half and one-fourth of the total effect characteristic of the sites located at the centers of the faces) (394). If this assignment is correct, the intensity ratio between the main peak and the peaks at 2178 and 2184 cm^{-1} (at full coverage) may provide a qualitative estimate of the real extension of the flat portions of the prismatic faces and terraces (qualitative but not quantitative because the intensity of the high-frequency bands could be influenced by intensity borrowing effects, as found for metallic surfaces). Note that the intensity ratio of the bands at 2184 and 2178 cm^{-1} relative to the main peak is larger for ZnO ex-carbonate, in agreement with

its more disordered morphology compared to ZnO microcrystals resulting from combustion of metallic zinc. These considerations indicate again that the IR spectra of adsorbed probes may provide information about the surface morphology. It also becomes evident that surface inhomogeneity has a strong influence on the frequencies and shapes of the IR peaks of adsorbed probe molecules.

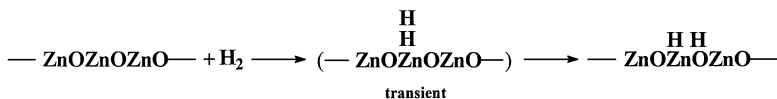
In conclusion, CO is an excellent probe molecule for the properties of coordinatively unsaturated surface Zn^{2+} sites, both isolated sites or those grouped into 2D patches. It is also emphasized that the prismatic faces also expose coordinatively unsaturated oxygen ions; their presence, however, is indirectly detected only via their influence on the electrostatic field at the Zn^{2+} center.

2. ZnO/H_2

When H_2 is used to probe ZnO surface sites, hydrides and hydroxyl groups are formed at temperatures as low as 80 K, as indicated by the immediate appearance of two medium strong bands at 3500 cm^{-1} (OH groups) and 1710 cm^{-1} (ZnH groups) (398–400). These bands are asymmetric on the low- and on the high-frequency side and are probably composed of several contributions. The formation of these bands is a clear indication that Zn ions and coordinatively unsaturated oxygen ions participate in the adsorption process. Presumably, the species formed initially is a polarized form of molecular hydrogen adsorbed on top of the coordinatively unsaturated Zn^{2+} ions. This species is transient in the 77–273 K temperature range (400) because it is sufficiently polarized to undergo a nucleophilic attack by the unsaturated oxygen ions in adjacent positions (heterolytic dissociation), as shown in Scheme 9. This reaction leads to formation of a hydride–hydroxyl pair. A Lewis acid–base pair operates in the dissociative adsorption of H_2 . It is thus evident that CO is suitable for probing the Lewis acidity, whereas H_2 detects acid–base pairs. Because of the similarities of C–H and H–H bonds (both of the σ type), it is expected that ZnO can activate not only hydrogen but also alkanes (398, 401).

3. Model of Adsorption Sites for CO and H_2 on ZnO

In the preceding discussion it was implicitly assumed that the sites that are reactive for hydrogen chemisorption are the same ones that adsorb CO



SCHEME 9



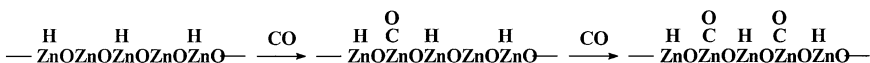
SCHEME 10

(located on the prismatic faces). If the sites located on the prismatic faces are involved in both hydrogen and CO adsorption it would be expected that adsorption of CO on prismatic faces precovered by hydrogen would be at least partially inhibited. The result of an experiment to test this possibility is illustrated in Fig. 16b, which shows that (i) the overall intensity of adsorbed CO is greatly reduced; (ii) the spectrum of adsorbed CO changes with coverage whereas at $\theta \cong 0$ the $\tilde{\nu}(\text{CO})$ is observed at 2197 cm^{-1} and the value at the maximum coverage is 2183 cm^{-1} ; and (iii) the spectrum of adsorbed CO is complex (with at least three components clearly detected and intensities that depend on coverage).

Although the distinct reduction of the CO intensity caused by preadsorption of hydrogen demonstrates beyond doubt that prismatic faces are reactive for both CO and hydrogen adsorption, the complex (coverage-dependent) structure of the residual band of CO after preadsorption of hydrogen needs further consideration. First, we infer that hydrogen does not block the Zn sites completely and that a fraction of sites remain coordinatively unsaturated. The coordinatively unsaturated ZnO pairs on the prismatic faces are all structurally equivalent. It must therefore be postulated that the presence of ZnH and OH groups formed by dissociative adsorption of H_2 creates repulsive forces that limit further H_2 adsorption, thus leaving a fraction of the Zn sites (one-half in our model) unoccupied. This postulate accounts partially for the low coverage ($\sim 10\%$) observed by Dent and Kokes (399). Furthermore, the frequency of adsorbed CO at zero coverage (2196 cm^{-1} ; i.e., higher than the 2190 cm^{-1} observed for CO on clean ZnO) suggests that the residual reactive Zn sites have acquired an enhanced tendency to polarize CO.

A plausible structure of the adsorbed hydrogen phase is characterized by rows of ZnHOH groups separated by rows of empty ZnO sites. In this ordered structure, each ZnH of the original ZnHOH pair has two empty Zn sites in nearest-neighbor positions along a perpendicular row, as shown in Scheme 10. These unoccupied sites are available for further adsorption of CO, as shown in Scheme 11.

In conclusion, three ZnH hydride species can be distinguished which differ from each other in the number of CO molecules (0, 1, or 2) adsorbed in nearest-neighbor positions. An analogous situation occurs for the OH



SCHEME 11

groups. Moreover, as the CO groups are aligned in rows, three arrangements of the CO molecules (with 0, 1, or 2 CO molecules in nearest-neighbor positions) can be distinguished, the relative amounts of which change with coverage. Figure 17 demonstrates the effect of CO adsorption on the $\tilde{\nu}(\text{ZnH})$ mode. The $\tilde{\nu}(\text{ZnH})$ frequency shifts downward upon CO dosage in two clear and well-defined steps, a result that closely fits the scheme illustrated previously. An opposite but smaller shift has been simultaneously observed for the $\tilde{\nu}(\text{OH})$. The physical reasons for the opposite signs of the frequency shifts of the $\tilde{\nu}(\text{ZnH})$ and $\tilde{\nu}(\text{OH})$ modes have been discussed (140, 402, 403). The observations are consistent with the shift of the C–O vibration in the two steps, as shown in Fig. 16b.

B. EXAMPLES OF REACTIONS CATALYZED BY ZnO

Dent and Kokes (404) investigated the hydrogenation of ethylene catalyzed by ZnO; the available data were reviewed by Gates (405). Interest in this reaction is motivated by the relative simplicity of its mechanism and the possibility to detect kinetically relevant intermediates spectroscopically. When the reaction is carried out with D_2 , the sole product is $\text{CH}_2\text{DCH}_2\text{D}$. This result is in contrast to what is observed with metallic catalysts. However, since ZnO and other active oxides (e.g., $\alpha\text{-Cr}_2\text{O}_3$) behave similarly, it

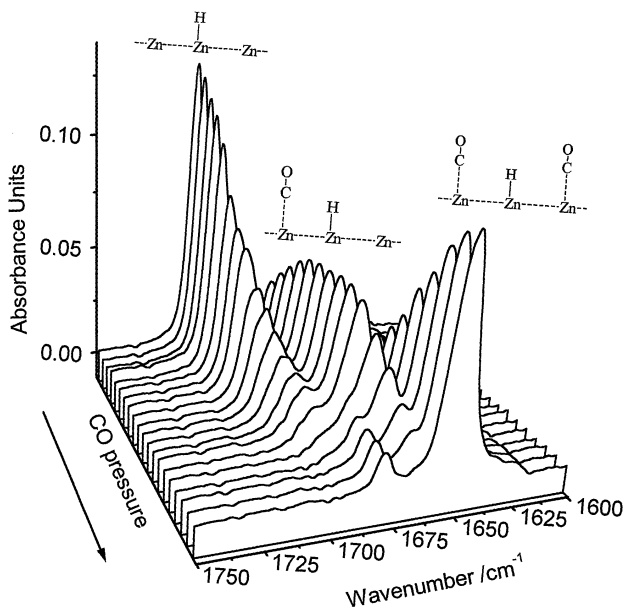
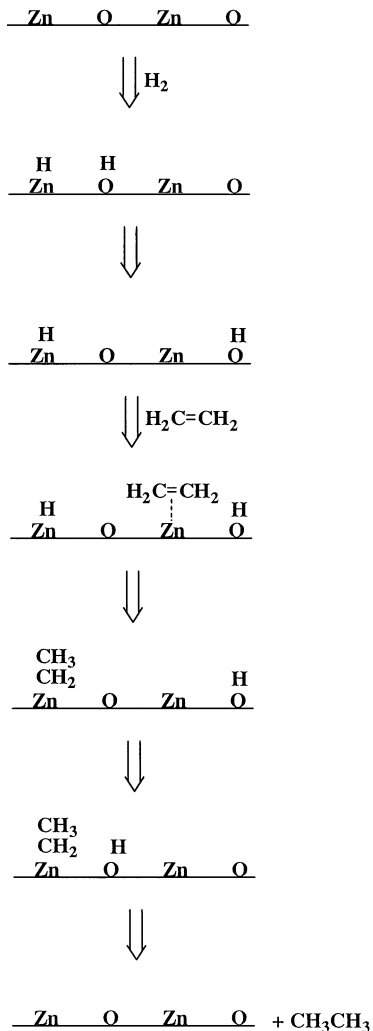


FIG. 17. IR spectra of CO adsorbed at 77 K on hydrogen-precovered ZnO samples; the effect of CO adsorption on the $\tilde{\nu}(\text{ZnH})$ modes is represented (unpublished data).

is inferred that the result must be related to the structure of the adsorbed hydrogen (resulting from heterolytic and not homolytic splitting). The mechanism shown in Scheme 12 has been proposed for this reaction. The ethylene molecules initially are adsorbed at empty Zn sites and then interact with hydride groups (obtained upon H_2 preadsorption) in adjacent positions, giving ethyl groups.



SCHEME 12

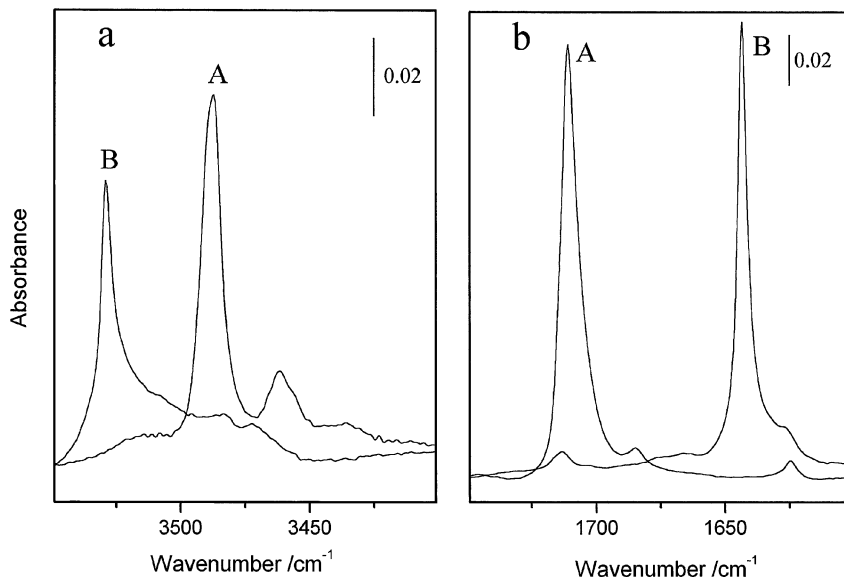


FIG. 18. Effect of the ethylene absorption on the $\tilde{\nu}(\text{OH})$ and $\tilde{\nu}(\text{ZnH})$ modes, parts (a) and (b), respectively. Spectra A and B report the regions before and after ethylene adsorption, respectively. (Unpublished results).

The IR results discussed previously clearly suggested the first step. However, the hydrogen migration illustrated in the second step is not demonstrated directly by the spectroscopic results. In particular, the $\text{H}_2\text{-CO}$ interaction experiments illustrated previously point to an opposite situation (the absence of hydrogen migration at room temperature). The closely correlated spectroscopic perturbations of hydride and hydroxyl groups induced by CO adsorption on the surrounding vacant Zn sites are much more readily explained in terms of static interactions induced by CO adsorption on hydride-OH pairs permanently located in adjacent position than on groups located at variable distances. Coadsorption of hydrogen and ethylene is illustrated in Fig. 18. The effects caused by ethylene adsorption on the $\tilde{\nu}(\text{ZnH})$ and $\tilde{\nu}(\text{OH})$ modes are similar to those caused by CO; this result clearly favors a similar interaction mechanism with formation of a π -complex between ethylene and vacant Zn sites adjacent to the ZnH-OH pairs on $(10\bar{1}0)$ faces and strongly suggests that oxygen sites are not directly involved in this interaction.

In summary, the formation of the Zn-ethyl intermediates is the result of the interaction of a ZnH (hydride) species with an ethene molecule adsorbed on an adjacent Zn center without direct intervention of an oxygen center and without hydrogen migration.

VI. Lanthanum Oxide

Lanthanum oxide is well-known as an active isomerization (406) and hydrogenation catalyst (407), and it has attracted much attention recently (along with other basic oxides, such as MgO and CaO) as a catalyst for the oxidative dehydrogenation and coupling of methane to C₂ hydrocarbons (408–410). Its activity for selective NO reduction of CH₄ in excess oxygen has also been demonstrated (411, 412).

These catalytic properties have been attributed either to the basicity of the coordinatively unsaturated surface oxygen ions located on steps, edges, corners, and other defects (413) or to the reactivity of oxygen vacancies present on the most commonly exposed (001) and (011) faces of the microcrystals (particularly when alkaline earth promoters are present) (411). Because both hypotheses are in agreement with the very low concentrations of active sites determined experimentally on lanthanum oxide, a clear discrimination between the two explanations is not straightforward. It is consequently useful to illustrate and analyze in detail the surface properties of pure lanthanum oxide as they emerge from using CO as a probe of the electric fields at the cationic sites (Lewis acid sites) and of the reactivity of strongly basic sites (if any). The procedure is that described previously for MgO. The IR spectra of CO adsorbed at 77 K on La₂O₃ outgassed at high temperature (Fig. 19) (414, 415) provide the following information: First, CO interacts with coordinatively unsaturated La³⁺ ions leading to the formation of La³⁺–CO adducts characterized by $\tilde{\nu}(\text{CO})$ in the range 2157 (for $\theta = 1$) to 2170 (for $\theta = 0$) cm⁻¹ (corresponding to $\Delta\tilde{\nu} = 14\text{--}27$ cm⁻¹). The band is complex, suggesting that at least two similar species are involved. From the high intensity of the $\tilde{\nu}(\text{CO})$ band, it is inferred that the positive centers are located on extended (001) and/or (011) faces (the structures of which are represented in Fig. 20).

Second, the observed species form a 2D array of oscillators (as expected for CO adsorbed on flat surfaces or terraces), as suggested by the gradual shift of the peak when the CO coverage changes from 0 to 1, because of the gradual modification of the adsorbate–adsorbate interactions. From the modest shift of the $\tilde{\nu}(\text{CO})$, it is also inferred that, notwithstanding the 3⁺ charge of the surface ion, the associated polarizing field is relatively low because of the neighboring oxygen ions and their relatively large radii. Calculations of the electric field associated with the La³⁺ centers are in progress to quantify these considerations. In summary, the La³⁺ ions located on low-index faces behave as very weak Lewis acid sites. This result is similar to that obtained for (100) faces of MgO and NaCl.

Third, CO interacts at 77 K with a small number of highly reactive O²⁻ centers (which have surface coverages less than 1%) (414, 415):



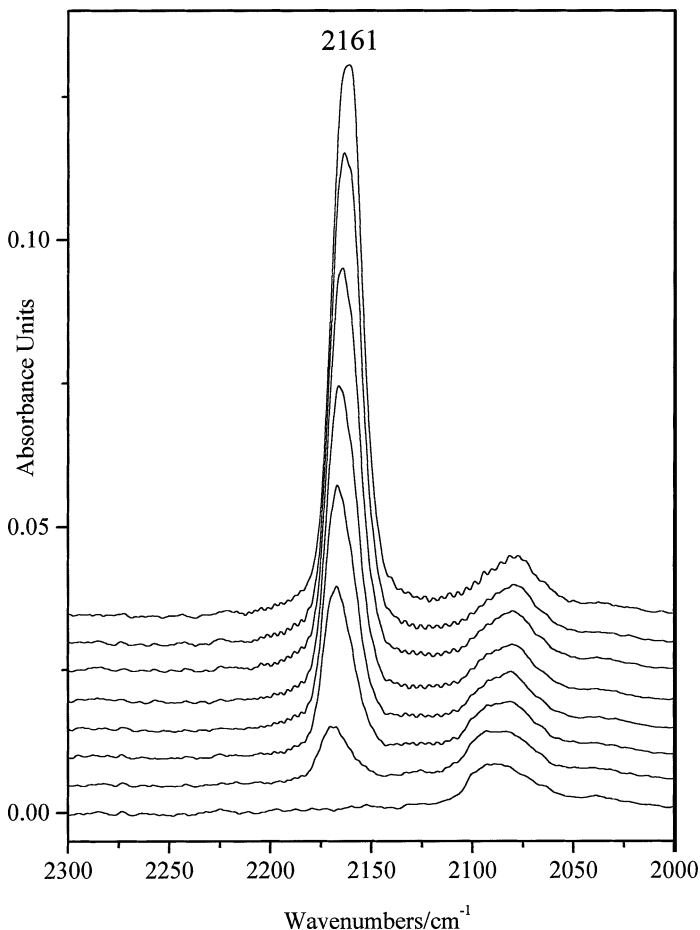


FIG. 19. IR spectra of ^{12}CO adsorbed at 77 K on La_2O_3 samples for coverages ranging from $\theta = 1$ (5.33 kPa) to $\theta \rightarrow 0$ [adapted from Bailes *et al.* (414) with permission of The Royal Society of Chemistry].

Note that the CO_2^{2-} (carbonite) ions are the only observed species when the reaction is carried out at 77 K and that their characteristic frequencies (1390 and 987 cm^{-1}) are very similar to those found for CO adsorbed on MgO at the same temperature (see Section IV.A.1). Moreover, similar species were observed on CaO and on SrO (see Section IV.B). Diffuse reflectance experiments carried out at 77 K showed that the formation of carbonite ions is accompanied by the appearance of a band at 30,000 cm^{-1} . It is concluded that a small number of highly basic centers are present on lanthanum oxides, the strength of which is comparable to that of the centers present on alkaline

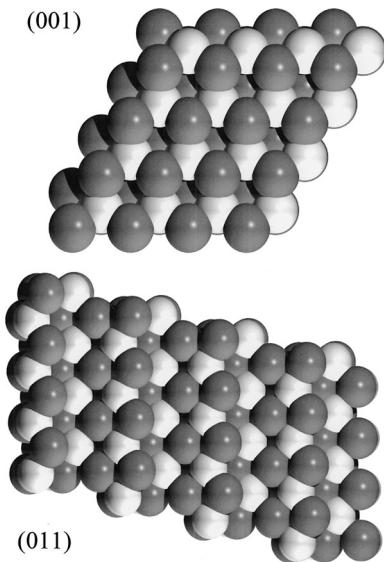
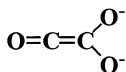


FIG. 20. Structure of the predominant (001) and (011) faces on La_2O_3 : in both cases La^{3+} is sixfold coordinated. La^{3+} are white; O^{2-} are gray.

earth oxides. By analogy with MgO , we conclude that these centers are coordinatively unsaturated O^{2-} ions located on corners and that their highly basic character is a consequence of the low Madelung potential associated with the low coordination.

Finally, when the microcrystalline sample is exposed to CO at room temperature, the carbonite bands appear, immediately followed by the gradual growth of at least 10 other bands in the range $1700\text{--}1000\text{ cm}^{-1}$. This behavior is similar to that reported earlier for MgO (Fig. 6). Some of these bands are oxygen sensitive (they are removed when the sample is exposed to oxygen), and so they are assigned to reduced species, whereas others are assigned to oxidized species (they grow upon exposure of the sample to oxygen). It has been shown that the CO_2^- species is the precursor of more complex species, such as $\text{C}_2\text{O}_3^{2-}$ (Scheme 13), which is formed first. Subsequently, CO disproportionation products [CO_3^{2-} and reduced oligomeric (CO_n^{2-}) species which are the oxidized and reduced species mentioned previously] are detected. The formation of oligomeric species is associated with the gradual



SCHEME 13

appearance of a broad band with a tail extending to the visible region (which is destroyed when the sample is exposed to oxygen).

In summary, the low-index faces of lanthanum oxide are quite unreactive, and the few very basic sites on which CO chemisorbs are located at defect positions (probably corners). The influence of oxygen vacancies on the chemistry of the CO/La₂O₃ system is not known, although oxygen vacancies have repeatedly been considered to be essential for promoting the catalytic activity (416, 417).

The similarities between the chemistry of the CO/La₂O₃ and CO/MgO systems have been emphasized previously. To test whether this analogy is confined to the CO probe, we compared the IR spectra of the NO/MgO (151–153) and NO/La₂O₃ systems (418). The IR spectra of the surface species generated in the two cases on NO adsorption are very similar, suggesting that the fundamental chemistry is also similar. Hence, the interaction of NO with strongly basic oxygen centers present in low concentrations occurs on both oxides.

VII. Cupric Oxide

Copper-based catalysts are known to be active for many industrial reactions, including methanol synthesis, the water–gas shift reaction, and catalytic oxidation of hydrocarbons (419–428). Copper is also being explored as a possible substitute for Pd and Pt for the reduction of nitrogen oxides in automobile exhaust conversion catalysts (429–433). Since CO is involved in several of these reactions, many IR investigations of adsorbed CO have been carried out to characterize copper-containing catalysts (434–449), including CuO/ZnO (435, 436), CuO/Al₂O₃ (438, 443), CuO/TiO₂ (447), and CuO/SiO₂ (439, 442, 445). As expected, because of the poorly defined morphological properties of these catalysts, no general agreement has been reached in the interpretation of the IR spectra. In particular, the strong and characteristic IR absorption at about 2120–2126 cm⁻¹ has been assigned either to Cu(II)···CO adducts (438, 439) or to Cu(I)···CO (442, 443, 445). To overcome the ambiguities, investigations of CO adsorption on model systems (single crystals or microcrystalline samples of Cu₂O with microparticles having a well-defined morphology) are quite useful.

A. POLYCRYSTALLINE SYSTEMS WITH WELL-DEFINED MORPHOLOGIES

TEM and SEM results show that Cu₂O powders sintered at high temperature (both before and after milling) and silica-supported Cu₂O microcrystals [obtained by impregnation of SiO₂ with aqueous Cu(NO₃)₂, followed by

thermolysis and activation *in vacuo* at high temperature] consist of microcrystals of well-defined morphology. The particles of $\text{Cu}_2\text{O}/\text{SiO}_2$ show a size distribution, typically in the range of 10 to about 50 nm (450).

Comparison of the particle projections in the plates shows that in all the samples many copper oxide particles exhibit hexagonal contours (clearly apparent in $\text{Cu}_2\text{O}/\text{SiO}_2$ samples). Because this is the shape obtained by projecting an octahedron onto the plane of one of its faces, it is inferred that (111) planes are predominantly exposed, in agreement with expectations based on previous discussions. The rounded shapes seen in the transmission electron micrographs can be accounted for by considering that although (111) planes can be assumed to be predominant, other faces are certainly also present in the copper oxide microcrystals, both pure and silica supported.

The low-index (111) face of Cu_2O is nonpolar and therefore expected to be stable; this explains why it is one of the most frequently exposed cleavage planes.

Computer simulations carried out by use of the MARVIN program (451) show that this face undergoes very little relaxation (the surface energy changes from 1.15 to 0.91 Jm^{-2}), with only little change of the Cu–O bond length and without significant modification of the surface structure, in agreement with the results of Schulz and Cox (448). On this face, the Cu^+ ions form alternating A and B rows. Rows A contain 2-coordinated Cu ions (as in the bulk structure), 3.02 \AA apart, and rows B contain alternating 2- and 1-coordinated Cu ions, with the distance between 1-coordinated Cu^+ ions being 6.04 \AA (Fig. 21).

B. CO ADSORPTION ON POLYCRYSTALLINE $\text{Cu}_2\text{O}/\text{SiO}_2$

CO adsorption on the systems discussed previously initially gives an IR peak at 2132 cm^{-1} , which then gradually develops into a doublet with bands at 2162–2150 and near 2120 cm^{-1} as the equilibrium pressure is increased (Fig. 22).

On the basis of the microcrystal morphology, the 2132-cm^{-1} band has been assigned to CO adsorbed on 1-coordinated Cu^+ sites on (111) faces. Because this frequency is lower than that of CO in the gas phase, it is inferred that in addition to the electrostatic interaction, σ and $d-\pi$ overlap forces stabilize the $\text{Cu}^+ \cdots \text{CO}$ bond. This conclusion is in agreement with the thermal stability of monocarbonyl species, the theoretical results obtained for CO on (111) surfaces of Cu_2O supported on SiO_2 , and the data obtained for the Cu^+ form of the zeolite ZSM-5 (22, 73, 265, 394, 449, 452–454). The width of the 2132 cm^{-1} band ($\text{FWHM} \cong 13$ or 14 cm^{-1}) indicates that the (111) faces are far from perfect. The lack of dependence on the coverage of the position of

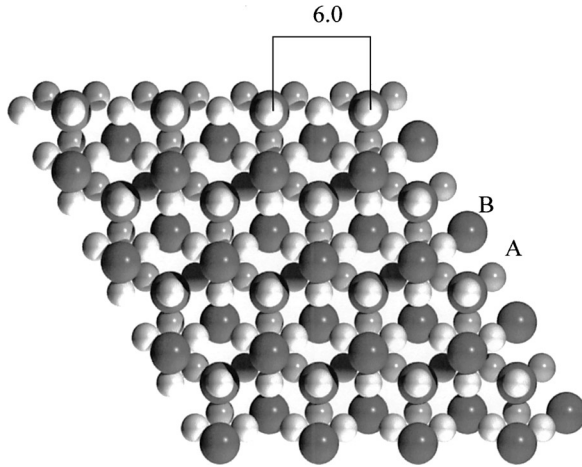


FIG. 21. Representation of the Cu_2O (111) neutral surface. On this surface Cu^+ ions (white) form alternating rows (A and B). Row A contains 2-coordinated Cu^+ ions, whereas in row B 2- and 1-coordinated copper ions are alternating. The distance between two 1-coordinated Cu^+ is reported in Å.

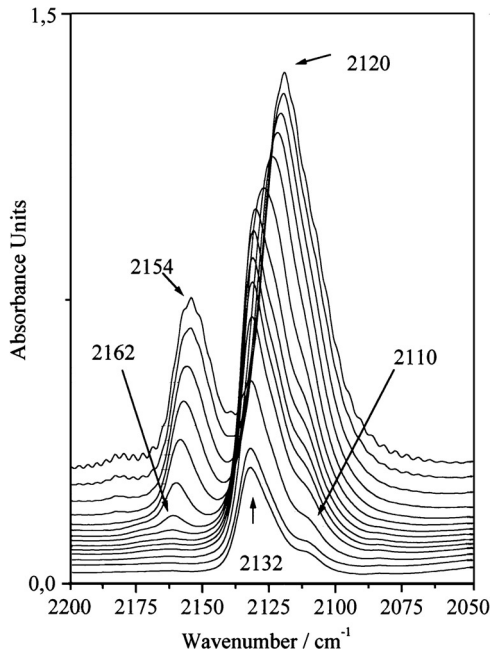


FIG. 22. IR spectra of ^{12}CO adsorbed at ~ 100 K on $\text{Cu}_2\text{O}/\text{SiO}_2$ at CO coverages ranging from $\theta = 1$ (2.66 kPa) to $\theta \rightarrow 0$ (0.133 Pa) [reproduced from Scarano *et al.* (450) with permission of Elsevier Science Publishers].

the 2132-cm^{-1} band of isolated $\text{Cu}^+ \cdots \text{CO}$ species on (111) faces (at $\theta \rightarrow 0$) is explained by the surface geometry of the (111) face. The minimum CO–CO distance in the adlayer corresponding to the 1-coordinated Cu^+ ions is about 6 Å. Lateral interactions (being proportional to $1/R^3$) are still negligible at this distance (as observed for other oxidic systems) (455, 456).

Once the full monolayer of $\text{Cu}^+ \cdots \text{CO}$ complexes has been completed, further CO adsorption leads to the gradual disappearance of the 2132-cm^{-1} band as two new components in the 2162- to 2154-cm^{-1} and 2132- to 2120-cm^{-1} ranges grow in for CO– $\text{Cu}_2\text{O}/\text{SiO}_2$. Two explanations can be given for this experimental observation. First, the initial $\text{Cu}^+(\text{CO})$ species (band at low frequency) start interacting with CO adsorbed on neighboring sites constituted by triplets of 2-coordinated Cu^+ ions (band at high frequency). Second, dicarbonyls may form on Cu(I) sites. Consistent with this scheme, the entire adsorption process is associated only with the highly reactive 1-coordinated Cu^+ ions via the pathway $\text{Cu}^+ \rightarrow \text{Cu}^+(\text{CO}) \rightarrow \text{Cu}^+(\text{CO})_2$, and the 2-coordinated Cu^+ ions are not involved. Therefore, the high- and low-frequency components observed at high coverage are attributed to the $\tilde{\nu}_{\text{sym}}$ and $\tilde{\nu}_{\text{asym}}$ modes of the dicarbonyl species. The surface density and geometry of the 2D layer corresponding to maximum coverage are similar for two models. The second model must be preferred because it explains the close similarity between the spectra of CO on $\text{Cu}_2\text{O}(111)$, $\text{Cu}^+(\text{CO})_2$ in the Cu^+ form of ZSM-5 (449), and in cuprous carbonyls (457).

There is little literature on the adsorption of other simple molecules on copper oxides. Propene is predominantly adsorbed in a molecular form on (111) faces. No information is available for H_2 adsorption on (111) faces.

C. CATALYTIC DEHYDROGENATION AND/OR OXIDATIVE DEHYDROGENATION OF METHANOL

Methanol oxydehydrogenation to give formaldehyde on copper catalysts is an efficient reaction that has attracted interest as a model for selective oxidations and because it is related to methanol synthesis (458, 459). The oxidation of alcohols on oxide surfaces is thought to occur in two steps (460, 461). First, the adsorbed alcohol or alkoxy species reacts with the oxide to give the corresponding aldehyde or ketone and a partially reduced catalyst surface. Then the reduced surface is reoxidized by gaseous oxygen and restored to its initial state. For the formation of alkoxy species and the following hydrogen abstraction, nucleophilic oxygen species are required, which are lattice oxygens (462). There is evidence for the segregation of bulk oxygen, O_{bulk} , onto the surface. This oxygen species can be converted into a nucleophilic subsurface oxygen, O_{sub} (acting as Brønsted base and catalyzing the dehydrogenation reaction path) or into a nucleophilic surface

oxygen species, O_{ads} (also acting as Brønsted base and catalyzing the oxidative dehydrogenation reaction path) (463).

Ion–molecule reaction mass spectrometry measurements gave evidence of an oscillatory reaction sequence for methanol oxidation, in which methoxy and formate species are formed simultaneously and the methanol–oxygen coadsorption plays a major role (464, 465). Of interest in the context of this review are the numerous investigations of the catalytic activities of single-crystal surfaces (460, 466, 467) and polycrystalline oxides (463, 465, 468) for the oxydehydrogenation of alcohols. In particular, the results of Cox and Schulz (467) show that single-crystal Cu_2O (111) surfaces catalyze the complete oxidation of methanol to CO , whereas the (100) surfaces developed the maximum selectivity for the partial dehydrogenation to CH_2O .

In situ techniques have allowed simultaneous measurement of catalytic and spectroscopic data (463, 468), establishing the morphology and electronic structure of the working catalyst under dynamic conditions. Copper suboxide was found to be the catalytically active phase, which represents a metastable state in UHV or under ambient conditions. This result suggests that the structure of the catalyst under reaction conditions can be significantly different from that determined after reaction or under *ex situ* conditions.

The preparation of well-defined single-crystal surfaces of copper oxides in UHV or of well-sintered powders, starting from polycrystalline materials, is difficult. Consequently, structure–catalytic property correlations remain to be established.

VIII. Oxides with the Corundum Structure

A. $\alpha\text{-Cr}_2\text{O}_3$

Chromium ions at the surfaces of inorganic oxides are characterized by a wide variability of the oxidation state, coordination number, and local structure. Consequently, Cr-based materials are especially attractive as catalysts. Much is known about the catalytic activity of pure Cr_2O_3 for various reactions (469), including polymerization of alkenes (470–472), hydrogenation–dehydrogenation of hydrocarbons (473–481), reduction of NO and decomposition of N_2O_4 (482), and oxidation of organic compounds (483, 484).

$\alpha\text{-Cr}_2\text{O}_3$ is an ideal model system because it can be obtained either in the form of microcrystalline powders (22, 23) with well-defined habits and exposing thermodynamically stable and extended faces or in the form of crystalline oxide films (4, 5, 485–487). In the following, the surface properties of $\alpha\text{-Cr}_2\text{O}_3$ polycrystalline samples at different degrees of sintering (and hence with the crystalline habits varied over a wide range) are summarized

on the basis of spectroscopic results, which are compared with those obtained for single crystals.

1. *Morphology and Surface Structures: Comparison of Dispersed Materials and Crystal Films*

α -Cr₂O₃ microcrystals can be prepared easily by combustion of ammonium dichromate, and their surface properties can be characterized by IR spectroscopy with CO and other small molecules (N₂, O₂, and H₂) as probes (488–493). The prepared α -Cr₂O₃ samples have high specific surface areas (about 40–70 m²g⁻¹), and the microparticles have dimensions in the range of 20–40 nm. The particles are irregularly shaped. However, as shown by the presence of interference fringes in the HRTEM images, they have crystalline character (77, 491, 492) (Fig. 23a).

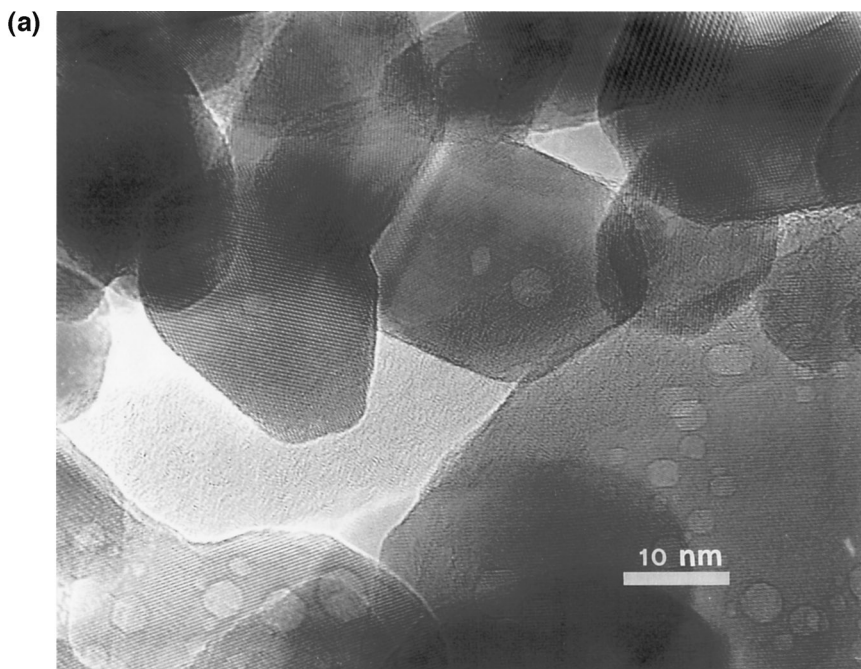


FIG. 23. HRTEM images of (a) high-surface-area, [reproduced from Scarano *et al.* (492) with permission of Elsevier Science Publishers] and (b) sintered α -Cr₂O₃ samples [adapted from Scarano *et al.* (491) with permission of Elsevier Science Publishers]; (c) SEM images of highly sintered α -Cr₂O₃ samples [reproduced from Scarano *et al.* (77) with permission of The Royal Society of Chemistry].

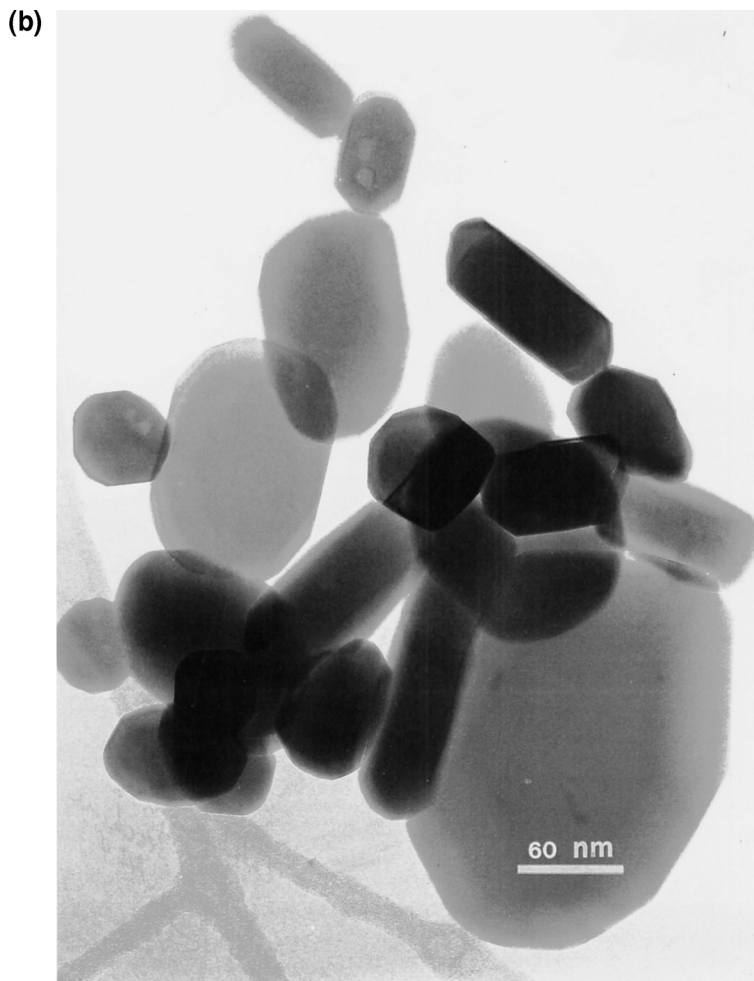
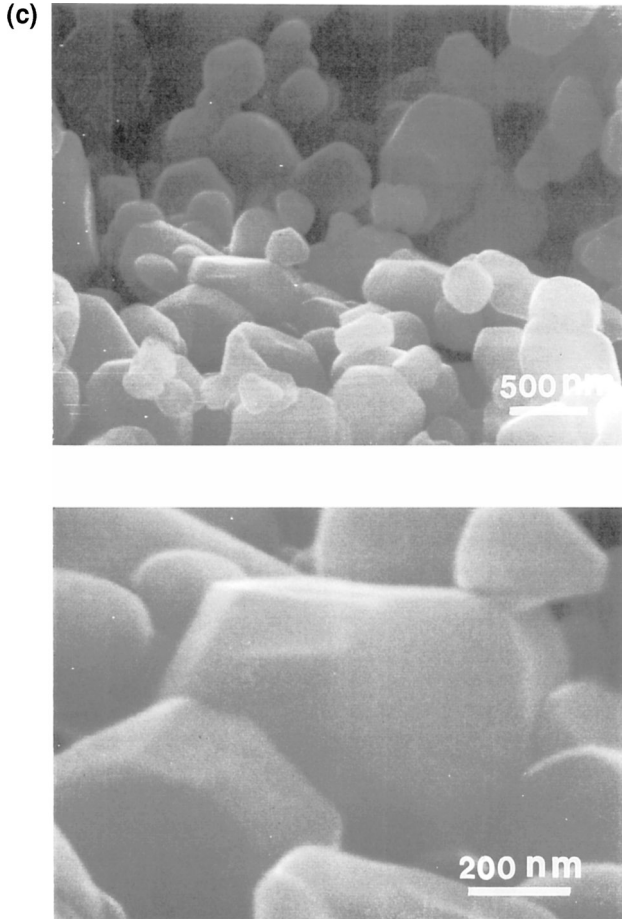


FIG. 23. (continued)

In sintered samples, the dimensions of the microcrystals are typically 50–100 nm, corresponding to specific surface areas of about $5 \text{ m}^2 \text{ g}^{-1}$. These assume the shapes of simple polyhedra, the edges of which are often straight without signs of imperfections, suggesting that the intersecting faces are regular. The particles are well-grown single microcrystals, as demonstrated by the interference fringes of the corresponding planes, which are observed when the particles are suitably oriented with respect to the electron beam (Fig. 23b).

FIG. 23. (*continued*)

The angles formed by the edge traces are statistically grouped into a few narrow intervals, suggesting that the morphologies of these well-grown crystals are represented by simple polyhedra that expose only a few planes. On the basis of the detailed analysis of the electron microscopy images, energy considerations, and computer simulations, it was concluded that the exposed planes are $(01\bar{1}2)$ and, to a lesser extent, $(\bar{2}116)$ and $(11\bar{2}0)$. These faces are all neutral, as expected for samples that have been treated at high temperatures and consequently assume the most thermodynamically stable morphology, as is generally observed for oxides.

Further sintering at high temperature increases the size of the microcrystals without significant modifications of the shape, as illustrated by SEM images (Fig. 23c). Such observations are indirect evidence suggesting that the distribution of faces is not seriously altered (77), but this interpretation appears to be inadequate because it does not take account of the accurate analysis of the crossing plane fringes and the simultaneous use of simulation methods.

Although the experimentally determined faces of sintered microcrystals are all neutral, there are many reports indicating that oriented Cr_2O_3 (0001) thin films are preferentially formed by epitaxial growth on metal single crystals (281, 494–496); well-ordered, nonpolar (10 $\bar{1}2$) surfaces have received far less attention.

The structures of the three families of faces, terminating the polyhedra of well-sintered samples, as obtained by simply cutting the crystal lattices along the (01 $\bar{1}2$), ($\bar{2}116$), and (11 $\bar{2}0$) planes taking into account surface relaxation have been discussed extensively (22) and are summarized only briefly here (Fig. 24).

First, the (01 $\bar{1}2$) face contains an array of equivalent Cr^{3+} ions in fivefold (square pyramidal) coordination separated by 0.365 nm (corresponding to 6.8 Cr ions/100 \AA^2). The plane defined by the the four oxygen ions surrounding each Cr^{3+} ion does not coincide with the surface plane, indicating that not only is the surface slightly ruffled but also the direction, where the electric field associated with positive charge is maximized, is not perpendicular to the surface plane. HRTEM images show that these faces are the predominant ones.

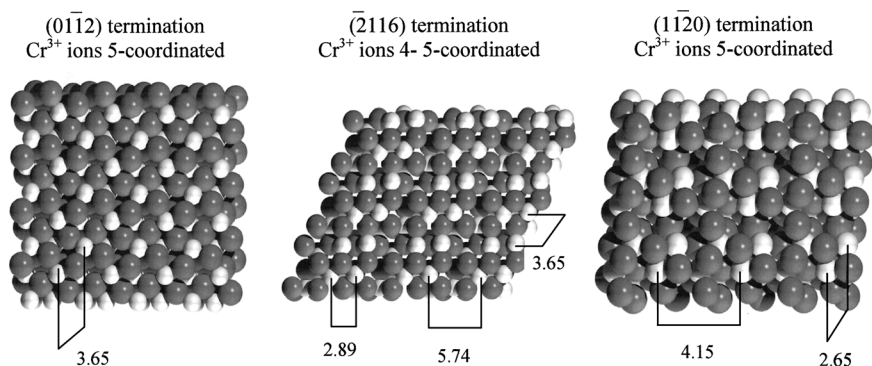


FIG. 24. Representation of the most commonly exposed $\alpha\text{-Cr}_2\text{O}_3$ faces. The distances (expressed in \AA) between the Cr^{3+} ions are reported. Cr^{3+} are white and O^{2-} are gray.

Second, the neutral face, belonging to the $(\bar{2}116)$ family, contains four- and fivefold coordinated ions, aligned along rows 0.365 nm apart. Within each row, the four- and fivefold coordinated sites are located in pairs only 0.289 nm apart, and the distance between the pairs is 0.574 nm. The density of sites is 7.65 Cr ions/100 \AA^2 . The presence of fourfold coordinated ions suggests that these faces should be more reactive and more prone to reconstruction phenomena than the $(01\bar{1}2)$ faces.

Finally, the $(11\bar{2}0)$ face is characterized by the highest density of sites (10.88 Cr ions/100 \AA^2). These Cr^{3+} sites are all fivefold coordinated and present in pairs 0.265 nm apart, and the distance between the pairs is 0.415 nm. Because the Cr^{3+} ions are greatly shielded by the surrounding oxygen ions (which are located at an upper level), this surface appears quite homopolar, and it is expected to be less reactive or even unreactive with probe molecules.

2. IR Spectra of Adsorbed CO

The typical sequence of spectra (in the 2200- to 2100- cm^{-1} range) observed at increasing coverages of CO on the three progressively sintered samples described previously (see Fig. 23) is shown in Fig. 25. As mentioned

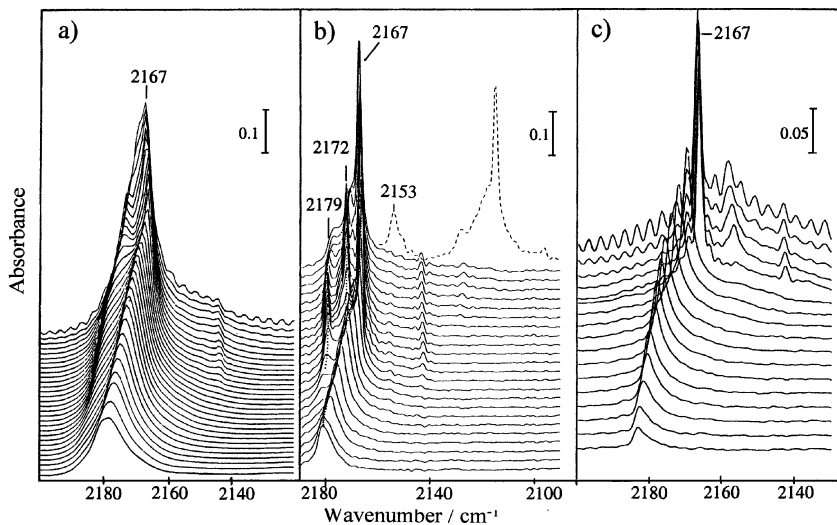


FIG. 25. IR spectra of ^{12}CO adsorbed at ~ 100 K on progressively sintered $\alpha\text{-Cr}_2\text{O}_3$ samples for CO coverages ranging from $\theta = 1$ (5.33 kPa) to $\theta \rightarrow 0$ on (a) high-surface-area samples, (b) sintered samples, and (c) highly sintered samples (dashed line in b): IR spectrum of $^{12}\text{CO}/^{13}\text{CO}$ (15 : 85) mixture at maximum coverage [reproduced from Zecchina *et al.* (22) with permission of Elsevier Science Publishers].

previously, these samples are characterized by crystallites of increasing size and morphological perfection (from ~ 20 – 40 to 50 – 100 nm up to 0.5 – 0.8 μm), with the sintering procedure having progressively eliminated or restructured the less stable faces (i.e., those containing the most coordinatively unsaturated ions). These morphological differences explain the following observations: (i) The intensity of the CO stretching bands gradually decreases with sintering, (ii) the IR spectrum undergoes a progressive simplification, and (iii) the FWHM of the single components gradually decreases (because inhomogeneous broadening effects associated with the surface irregularities are progressively eliminated). These observations further support the strategy of progressive sintering (*vide supra* Figs. 7, 10, and 12) for the characterization of sites located on surface planes of high structural perfection (comparable to that of single-crystal faces). On passing from the sequence of spectra represented in Fig. 25a to those shown in Fig. 25b, the carbonyl bands become more structured, and three intense narrow bands, at 2179 , 2172 , and 2167 cm^{-1} (measured at $\theta \cong 1$), are detected which are not clearly separated in Fig. 25a. These changes are associated with the increasing perfection of the exposed faces, and they are an indirect consequence of the formation of polyhedra with more defined structure. On the basis of the relative abundance of the faces defining the microcrystals shown in Fig. 1, the 2179 , 2172 - cm^{-1} doublet ($\theta \cong 1$) has been assigned to CO on five- and four-fold coordinated Cr^{3+} ions of the $(\bar{2}116)$ face, and the peak at 2167 cm^{-1} can be safely attributed to CO end-on adsorbed on Cr^{3+} ions of the $(01\bar{1}2)$ face.

Further sintering not only causes a drastic decrease in the overall intensity of the CO spectrum but also leads to the preferential disappearance of the peaks associated with the $(\bar{2}116)$ faces (Fig. 25c). Simultaneously, a new, broader peak appears at ~ 2157 cm^{-1} , which can be ascribed to CO adsorbed on highly shielded Cr ions exposed on the $(11\bar{2}0)$ faces. In agreement with this hypothesis, formation of this new band is highly reversible, and it quickly disappears upon outgassing of the sample at 110 – 120 K. This result indicates that after severe sintering treatments, the dominant faces are largely homopolar and characterized by Cr^{3+} ions in highly shielded positions.

A similar broad band (at ~ 2158 cm^{-1}) was found for CO on α - Al_2O_3 obtained by sintering of γ - and δ - Al_2O_3 at 1373 K (32, 497) and on sintered α - Fe_2O_3 (498). These observations suggest that the surfaces of all oxides treated at very high temperatures tend to acquire a homopolar character because the small positive ions occupy relaxed positions to minimize the surface energy.

To extract more structural information from the IR spectra of CO adsorbed on the different faces, the detailed behavior of the main peak, which

is associated with CO adsorbed through the carbon end on Cr^{3+} ions on the $(01\bar{1}2)$ faces (Fig. 25c), is discussed.

First, the peak is initially observed at 2181 cm^{-1} ($\theta \cong 0$, singleton) and then gradually moves to 2167 cm^{-1} ($\theta \rightarrow 1$) as a consequence of adsorbate–adsorbate interactions ($\Delta\tilde{\nu} = -14\text{ cm}^{-1}$). Simultaneously, the FWHM decreases from 4 to 1.5 cm^{-1} , thus indicating that the exposed $(01\bar{1}2)$ faces are extended and nearly defect free.

Second, isotopic substitution experiments using ^{12}CO – ^{13}CO mixtures show that the $\Delta\tilde{\nu} = -14\text{ cm}^{-1}$ shift is the result of two opposing effects, namely, dynamic ($\Delta\tilde{\nu}_{\text{dyn}} = 13\text{ cm}^{-1}$) and static ($\Delta\tilde{\nu}_{\text{st}} = -27\text{ cm}^{-1}$). By standard methods, the dynamic polarizability α_v was found from the $\Delta\tilde{\nu}_{\text{dyn}}$ value to be $\alpha_v = 0.1007\text{ \AA}$.

The stretching frequency of CO adsorbed on Cr^{3+} ions of $(01\bar{1}2)$ faces is blue shifted relative to the gas-phase CO frequency. Electrostatic forces and σ bonding play the most important roles in the adsorption. The Stark effect associated with the positive electric field centered at the Cr^{3+} sites increases the stretching frequency of adsorbed CO (268).

The observed shift with respect the gas phase is similar to that found for CO on other oxides, where no d electrons are involved. This result seems to suggest that d – π overlap does not occur. However, when the dynamic shifts and the dynamic polarizabilities are considered, the observed analogies with nontransition metal oxides are not so straightforward. It is a matter of fact that in the case of α - Cr_2O_3 the dynamic polarizability α_v , is definitely higher than expected for a surface complex, where only electrostatic forces and σ bonding are operating (ZnO/CO system). This observation has also been reported for other transition metal cations. In view of the great sensitivity of the α_v parameter to d – π contributions, the $\text{Cr}^{3+} \cdots \text{CO}$ bond is inferred to be characterized not only by σ donation but also by some d – π backdonation contributions (13, 92).

The adsorption of CO on a site is also accompanied by backrelaxation of the surrounding ions. This is a through-solid effect, which must be added to the through-space effects (static dipole–dipole interactions, etc.) to explain the larger $\Delta\tilde{\nu}_{\text{stat}}$ shift (53, 499, 500).

The CO adsorption on $(11\bar{2}0)$ faces (being predominant after severe sintering) is characterized by $\tilde{\nu}(\text{CO}) = 2157\text{ cm}^{-1}$. This frequency is in line with the structure of Cr^{3+} centers, which are more shielded by O^{2-} ions in the nearest positions; hence, they are associated with electric fields significantly lower than those characteristic of $(01\bar{1}2)$ faces. Consequently, the perturbation (and the related adsorption enthalpy) of the CO molecule adsorbed on these shielded Cr^{3+} sites is expected to be small and the corresponding stretching frequency to be only slightly blue shifted relative to that of gas-phase CO. Another consequence of the low interaction strength is a longer

equilibrium distance [$\sim 3.7 \text{ \AA}$ (77)] which will not permit any orbital overlap to occur (i.e., σ and $d-\pi$ effects are totally absent).

3. *Correlation of the Stretching Frequencies of Adsorbed CO with the Surface Electric Fields at Lewis Acid (Cr^{3+}) Sites*

Once the positions of surface cations and anions are determined, the electric fields at the center of mass of adsorbed CO can be calculated by the procedure outlined previously. After this preliminary step, the known electric field- $\tilde{\nu}(\text{CO})$ relationships (56) readily give the stretching frequencies of CO adsorbed at the Cr^{3+} centers located on both relaxed and unrelaxed faces. The computed frequencies are then compared with the experimental values. The following observations emerge (77):

1. For prismatic ($01\bar{1}2$) and ($11\bar{2}0$) faces of $\alpha\text{-Cr}_2\text{O}_3$, the $\nu(\text{CO})$ frequencies and the associated electric fields do not appreciably depend on relaxation.

2. For ($\bar{2}116$) faces, the frequencies and electric fields critically depend on the relaxation because the Cr^{3+} ions located in exposed positions undergo a remarkable inward relaxation.

3. The calculated frequencies are in satisfactory agreement with the experimental values for the ($01\bar{1}2$) and ($11\bar{2}0$) faces. This result again indicates that the $\text{Cr}^{3+} \cdots \text{CO}$ bond is mainly electrostatic in nature (even if a minor contribution of chemical overlap forces is present).

4. For species adsorbed on ($\bar{2}116$) faces, the experimental frequencies are closer to those calculated for relaxed structures than to those obtained for unrelaxed models. This result is expected because the backrelaxation induced by the reversibly adsorbed CO on this highly coordinatively unsaturated and strongly relaxed surface is quite modest.

In summary CO is a good probe of surface fields and, indirectly, of surface Lewis acidity, as has also been observed for other systems without d electrons. A close examination of other, more subtle effects (dipole-dipole interactions) shows that a small $d-\pi$ contribution is present which primarily affects the dynamic polarizability (i.e., the dynamic charge transfer from adsorbed CO to the surface centers and vice versa during the stretching motion).

4. *C_2H_4 Adsorption and $\text{C}_2\text{H}_4/\text{CO}$ Coadsorption*

In many chromium-containing oxides, such as Cr/SiO_2 and $\text{Cr}/\text{Al}_2\text{O}_3$ for ethene polymerization, the first step of ethene activation is the formation of $\text{C}_2\text{H}_4\text{-Cr}^{2+}$ (or $\text{C}_2\text{H}_4\text{-Cr}^{3+}$) molecular complexes. These molecular complexes are then transformed into more strongly adsorbed species of unknown

structure, which play a role in the initiation steps of the polymerization reaction (501–507). The understanding of the interaction of C_2H_4 with structurally well-defined Cr^{3+} centers, such as those located on low-index faces of $\alpha-Cr_2O_3$, is expected to assist the elucidation of the fundamental chemistry of the Cr^{3+}/C_2H_4 system (493). The main results obtained for polycrystalline samples (Fig. 26) can be briefly summarized as follows: (i) Ethene is molecularly adsorbed on a fivefold coordinated Cr^{3+} site of the predominant (01 $\bar{1}2$) face, giving a coordination complex with local C_{2v} symmetry in which ethene interacts with the electron-withdrawing Cr^{3+} centers through a π bond perpendicular to the plane of the alkene; (ii) the ethene molecule oligomerizes on only a few defective sites; and (iii) the polymerization activity of reduced samples is definitely greater than that of stoichiometric samples. It is inferred that the family of active sites is a small fraction of Cr^{2+} centers formed during the activation at high temperature in the presence of hydrocarbon impurities

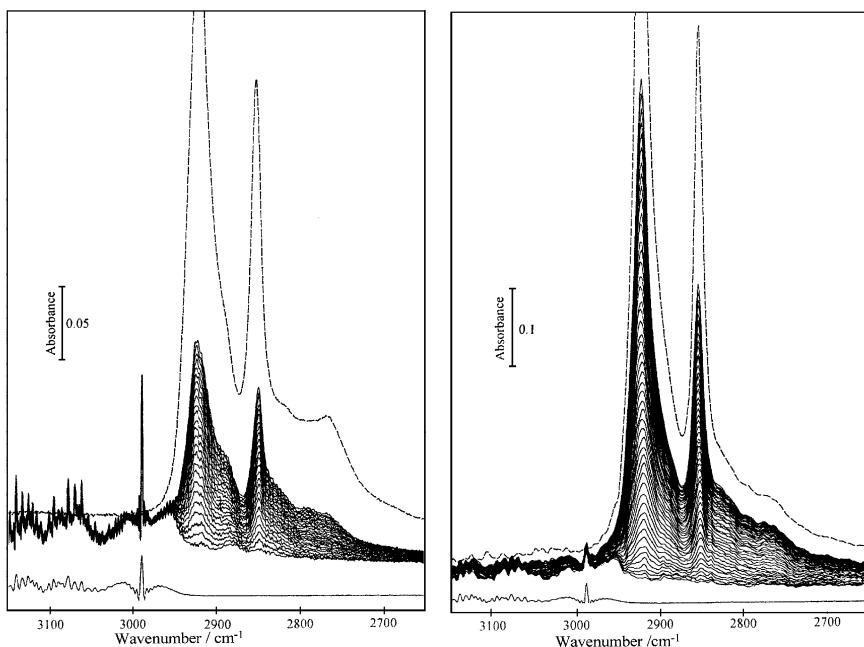


FIG. 26. IR time-resolved spectra of ethene polymerization reaction on (a) nearly stoichiometric and (b) reduced $\alpha-Cr_2O_3$ samples: CH_3 and CH_2 stretching mode regions. Continuous curves, IR spectra taken at 10-s intervals (a) and 7-s intervals (b) in the presence of $P = 5.32$ kPa of ethene; dashed curves after a total contact time of 30 (a) and 8 min (b) and ethene removal by outgassing at room temperature; curves on the bottom, ethene gas [reprinted with permission from Scarano *et al.* (493), Copyright 1994 American Chemical Society].

and presumably located on high-index faces, edges, and steps. Starting from these few reduced sites, the living polymer chains grow and spread out on the flat surfaces and tend to gradually cover the whole microcrystal (Fig. 27; see color insert). The IR spectra of these polymer chains demonstrate that the CH_2 groups of the chain interact with the Cr^{3+} centers of the flat surfaces. Anomalous low-frequency bands in both the (CH_2) stretching and bending regions demonstrate agostic-type interactions between $-\text{CH}$ and Cr^{3+} sites (Fig. 28). This weak agostic interaction is destroyed by CO because CO is

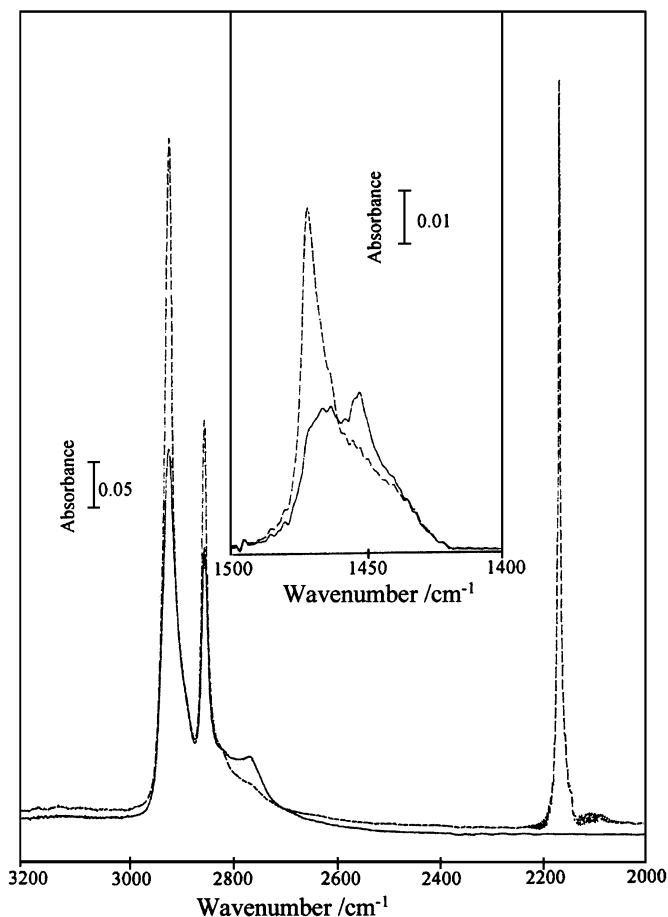


FIG. 28. Modifications of the IR spectrum of living polymer chains on stoichiometric $\alpha\text{-Cr}_2\text{O}_3$ induced by CO: solid curve, before ^{12}C adsorption; dashed curve, after ^{12}C adsorption ($p = 2.66$ kPa) (Inset) Expanded view of the $\delta(\text{CH}_2)$ mode region [reprinted with permission from Scarano *et al.* (493). Copyright 1994 American Chemical Society].

able to displace the $-\text{CH}$ groups from the Cr^{3+} centers (Figs. 27b and Fig. 28). The ability of Cr^{3+} surface ions to undergo agostic interactions with saturated $-\text{CH}$ groups has also been demonstrated by IR spectra of adsorbed *n*-heptane (493).

The main conclusions are that (i) Fivefold coordinated Cr^{3+} sites exposed on the $(01\bar{1}2)$ faces, although reactive in the formation of weak molecular Cr^{3+} -ethene complexes, are not active in catalytic polymerization, and (ii) polymerization (and oligomerization) activity is attributed only to Cr^{2+} centers, located at structural defects (such as edges, steps, and corners). This last conclusion strongly suggests that a highly coordinatively unsaturated state is a necessary prerequisite for the polymerization activity of Cr^{x+} centers.

5. H_2 Adsorption

Because of the similarity between the electronic structure of H-H and C-H bonds in hydrogen and hydrocarbon molecules, respectively, it is expected that Cr^{3+} sites of $\alpha\text{-Cr}_2\text{O}_3$ can be reactive in hydrogen adsorption. As shown in Fig. 29, H_2 adsorption on sintered $\alpha\text{-Cr}_2\text{O}_3$ samples leads to the development of a narrow band at about 3936 cm^{-1} . This band, never reported before, is clearly the $\tilde{\nu}(\text{HH})$ of hydrogen molecularly adsorbed on Cr^{3+} sites located on predominant $(01\bar{1}2)$ faces (unpublished results). We infer that the hydrogen molecule is adsorbed in end-on form and that the shift $\Delta\tilde{\nu} \cong -225\text{ cm}^{-1}$ is associated with the polarization induced by the electric field centered at the Cr^{3+} ions. This interaction is similar to that described for $\text{H}_3\text{C}-\text{H}$, and the spectroscopic consequences with regard to the stretching frequencies are also very similar (shift to lower $\tilde{\nu}$). That polarization effects can lower the $\tilde{\nu}(\text{HH})$ frequency has already been demonstrated for the titanosilicate ETS10/ H_2 system, in which H_2 interacts with Na^+ ions (508).

In addition to the bands for H_2 molecularly adsorbed on extended faces, very weak irreversible bands at 3600 and 1590 cm^{-1} are observed (results not reported here). These bands are the $\tilde{\nu}(\text{OH})$ and $\tilde{\nu}(\text{CrH})$ modes of hydrogen species dissociatively adsorbed on $\text{Cr}^{3+}\text{O}^{2-}$ pairs located at less abundant defects (e.g., edges and steps).

6. Interaction of $\alpha\text{-Cr}_2\text{O}_3$ with Other Simple Molecules

The adsorption of NO on morphologically well-defined samples has not been investigated in detail. On high-surface-area materials (509, 510), stable nitrosyl species are formed together with disproportionation products (N_2O and NO_2^-); this complex chemistry renders the interpretation of the resulting (complex) spectra difficult (unpublished results). However, the

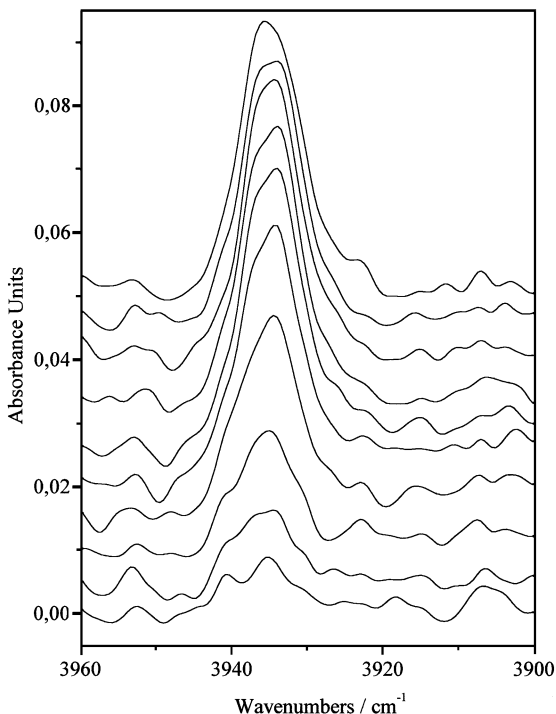


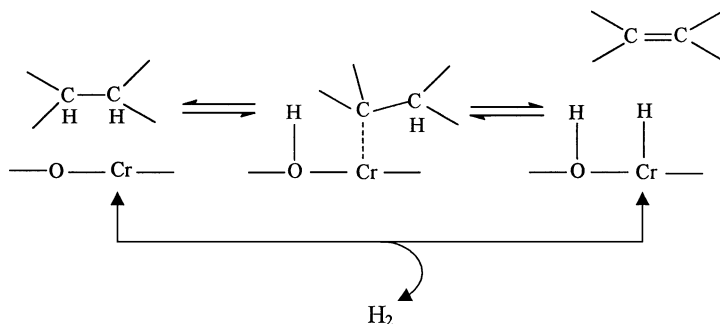
FIG. 29. IR spectra of H₂ adsorbed at 77 K on α -Cr₂O₃ samples in the $\bar{\nu}(\text{H-H})$ region for coverages ranging from $\theta = 1$ (5.33 kPa) to $\theta \rightarrow 0$ (unpublished).

higher stability of surface nitrosyls relative to the corresponding carbonyl species can be considered to be a general feature of transition metal oxide surface chemistry.

The catalytic activity of chromia for the NO + NH₃ reaction in the presence of oxygen and activity/morphology relations has been investigated (511, 512). The activities of amorphous and of crystalline α -chromia in various reaction mixtures (NH₃ + NO + O₂, NH₃ + O₂, and NH₃ + NO) have been compared. The specific activity and selectivity of each system were reviewed (476). Amorphous chromia was found to be more active than crystalline chromia in the typical temperature range (423–473 K) because of its higher density of labile oxygen sites.

7. Hydrogenation/Dehydrogenation Reactions

Because of the importance for industrial production of light alkenes such as propene (the precursor for high-purity polypropylene) and isobutylene



SCHEME 14

(used for the synthesis of MTBE and ETBE gasoline additives), the dehydrogenation of alkanes on supported chromium catalysts is briefly reviewed here. For more information, the reader is referred to exhaustive reviews (469, 475, 476, 479). A few results concerning the properties of the $\text{CrO}_x/\text{Al}_2\text{O}_3$ system with emphasis on the structures of the active sites, the influence of thermal treatments on the catalytic activity and selectivity, and the elucidation of the dehydrogenation mechanism are summarized here.

Although a consistent picture of the nature of the active species is not available (it has been almost impossible to discriminate between contributions of Cr^{3+} and Cr^{2+} ions as dehydrogenation centers), it was shown that both isolated and clustered Cr^{n+} can be the active sites. A plausible catalytic mechanism for alkane dehydrogenation on $\text{Cr}/\text{Al}_2\text{O}_3$ involves $\text{Cr}^{n+}/\text{O}^{2-}$ active pairs. The detailed mechanism can be described as follows (Scheme 14): (i) The adsorption of the alkane occurs on coordinatively unsaturated Cr^{n+} center, either isolated or clustered, with formation of the agostic-type complex $\text{H}_3\text{C}-\text{H} \cdots \text{Cr}^{3+}$ (precursor complex); (ii) the C-H bond of the alkane precursor complex interacts with an adjacent O^{2-} species having nucleophilic character to give OH and Cr-C bonds; and (iii) alkene is formed and released from the surface, and the catalytic surface is regenerated by formation of H_2 (469, 477, 479). When extensive C-H bond breaking and C=C formation occur, coke deposits form on the catalyst.

B. IRON OXIDE $\alpha\text{-Fe}_2\text{O}_3$

Iron-containing oxides (either pure or mixed) (513) are known to catalyze many reactions, including selective oxidations, dehydrogenations, oxydehydrogenations (514–516), and the water–gas shift (517).

In particular, the dehydrogenation of ethylbenzene to styrene, a large-scale process, is performed with iron oxide-containing catalysts in the

presence of steam (513). Kinetics experiments carried out with polycrystalline catalysts showed that the addition of promoters (e.g., potassium) increases the catalytic activity by one order of magnitude, probably because of the formation of an active KFeO_2 phase (518). It was also shown that different iron oxide phases can coexist and be interconnected depending on conditions such as temperature and oxygen partial pressure (519).

Another technologically important reaction is the Fischer–Tropsch synthesis, with iron oxide being one of the components of some catalysts. A detailed understanding of the complex mechanism of this reaction can be obtained by studying the chemisorption of simple molecules on well-characterized surfaces by means of advanced surface-sensitive spectroscopic techniques. A few investigations of the interaction of small molecules (such as CO , CO_2 , H_2O , O_2 , H_2 , and NO) (520–522) and organic molecules on iron oxide surfaces (523–527) have been carried out.

The comprehensive investigation of the interactions of simple alcohols (methanol, ethanol, propan-1-ol, and butan-1-ol) with Fe_2O_3 powders (514) by a combination of surface analytical techniques and conversion measurements under high vacuum and at atmospheric pressure is an example of the attempts to establish correlations between surface structure and catalytic activity. IR and XPS data showed that methanol is chemisorbed mainly dissociatively, giving formate species, whereas molecular chemisorption prevails for higher alcohols, which form hydrocarbons as the major products.

Because of the complexity of the catalytic reactions occurring on polycrystalline samples, many authors have attempted to explore well-defined model oxide surfaces (pure or alkali doped) (518) and to compare the results with those representing polycrystalline samples.

1. *Sintered Polycrystalline $\alpha\text{-Fe}_2\text{O}_3$: Morphology and Structure as Probed by CO*

$\alpha\text{-Fe}_2\text{O}_3$ microcrystals exposing a few predominant low-index faces with sufficiently well-defined morphology can be prepared by thermal decomposition of $\alpha\text{-FeO(OH)}$ (498). Needle-like crystallites, with 5000 Å average length, are formed, which preferentially expose ($1\bar{1}00$) prismatic faces (even if other prismatic faces are also present). This small proportion of faces with indices intersecting the c axis, such as ($\bar{4}401$) or ($\bar{1}2\bar{1}4$), are responsible for the irregular termination of the needle-like microcrystals. However, because of their small extension, they do not appreciably contribute to the great adsorption capacity (even though they can play a role in promoting catalytic reactions). As was also observed for $\alpha\text{-Cr}_2\text{O}_3$, there is no complete correspondence between the faces characterized by surface science methods and the faces of the sintered microcrystals.

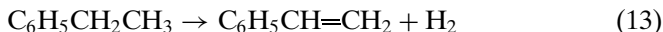
The (11 $\bar{2}$ 0) faces, dominant on polycrystalline samples, are characterized by highly shielded fivefold Fe³⁺ ions (5.43 Å apart) and partial homopolar character. The situation is similar to that encountered on prismatic (11 $\bar{2}$ 0) faces of α -Cr₂O₃ after sintering under severe conditions. When probed with CO, Fe³⁺ ions exposed on the (1 $\bar{1}$ 00) surfaces form weak Fe³⁺ ··· CO adducts, characterized by a very modest shift of the C–O stretching mode relative to the gas phase value ($\tilde{\nu} = 2164\text{--}2165.5\text{ cm}^{-1}$, $\Delta\tilde{\nu} = 20\text{--}22\text{ cm}^{-1}$). It is thus concluded that the local electric fields associated with Fe³⁺ ions at the surface of (1 $\bar{1}$ 00) faces are very weak and similar to those reported for Mg²⁺ on MgO (001) and Cr³⁺ on α -Cr₂O₃ (11 $\bar{2}$ 0) surfaces.

Dynamic and static shifts observed for CO adsorbed on α -Fe₂O₃, as determined in isotopic substitution experiments, are similar to those found for CO on MgO: $\Delta\tilde{\nu}_{\text{dyn}} = 1.5\text{ cm}^{-1}$ and $\Delta\tilde{\nu}_{\text{stat}} = -14\text{ cm}^{-1}$ (85, 93). This result is also in line with the weak polarization by the strongly shielded Fe³⁺ ions on (1 $\bar{1}$ 00) faces; α_{v} is smaller (0.027 Å³) than that of the CO gas (as was found for CO on MgO). The frequency of CO adsorbed on Fe³⁺ ions can be calculated on the basis of the $\Delta\tilde{\nu}/E$ relationships discussed previously (528).

In summary, it is inferred that the low-index (1 $\bar{1}$ 00) faces are almost unreactive and that the exposed Fe³⁺ ions have very weak Lewis acidity.

2. *Dehydrogenation of Ethylbenzene: A Case Study of Reaction Catalyzed by α -Fe₂O₃*

Ethylbenzene dehydrogenation:



has been reviewed by Kochloeff *et al.* (513). Only results that give some insight into the reaction mechanism and structure—activity correlations are addressed here. The adsorption of ethylbenzene, styrene, and water on crystalline films of different iron oxide phases and on potassium-promoted iron oxide (515, 517, 518) has been investigated by TDS, photoelectron spectroscopy (UPS and XPS), LEED, and STM. On purely oxygen-terminated FeO(111) films, only physisorption of ethylbenzene takes place. In contrast, molecular chemisorption of ethylbenzene and styrene is observed on the metal-terminated Fe₃O₄ (111), α -Fe₂O₃ (0001), and K_xFe_yO_z surfaces, and water is chemisorbed dissociatively. The dissociative and heterolytic chemisorption of water is made possible by the cooperative action of acidic iron and neighboring basic oxygen pairs so that OH[−] is formed on Fe³⁺ and H⁺ on the oxygen sites.

Hydrogen and water desorption measurements indicated that only the α -Fe₂O₃ (0001) face can dissociate hydrogen, which then reacts with lattice oxygen to form water, thereby reducing the oxide film. This result highlights the role of water in the catalytic dehydrogenation of ethylbenzene. Water not

only acts as a diluent, shifting the reaction equilibrium toward the product styrene and decreasing the formation of carbonaceous surface deposits, but also inhibits the reduction of Fe_2O_3 during the reaction.

Fe^{3+} ions on Fe-terminated (0001) faces of $\alpha\text{-Fe}_2\text{O}_3$ are threefold coordinated, which seems to suggest that the catalytic activity of this surface is associated with the low coordination numbers of Fe^{3+} . It is also inferred that the highly stable (1 $\bar{1}$ 00) face, which dominates the morphology of polycrystalline samples and which contains highly shielded Fe^{3+} ions, should not play a role in the catalytic reaction.

The dehydrogenation of ethylbenzene on iron oxide surfaces must occur by deprotonation of the ethyl group on basic oxygen sites and by a simultaneous or subsequent electron donation to Lewis acidic Fe^{3+} sites. The $\text{Fe}^{3+}\text{O}^{2-}$ pair is the catalytic center. Oxygen terminations of iron oxide containing Fe–O groups with double-bond character behave chemically like bare oxo anions and have a stronger basicity than regular lattice oxygen anions. Therefore, they are also potential sites for the abstraction of protons from the C–H bond of the ethyl group of ethylbenzene. Thus, the presence of oxygen in the reaction mixture may greatly affect the reaction path.

In contrast to the abundant literature of the catalytic properties of (0001) surfaces of $\alpha\text{-Fe}_2\text{O}_3$, studies of IR spectroscopy of the adsorbed species remain to be done.

C. $\alpha\text{-Al}_2\text{O}_3$

Because of its outstanding ceramic properties, $\alpha\text{-Al}_2\text{O}_3$ has been the subject of numerous experimental (529–533) and theoretical studies (534–541). This solid is also used extensively as a support for thin films and for the catalysts used in the industrially important ethylene epoxidation reaction (542).

Only a few attempts have been made to prepare $\alpha\text{-Al}_2\text{O}_3$ samples with well-defined morphology, for instance, by sintering transition aluminas ($\gamma\text{-Al}_2\text{O}_3$ and $\eta\text{-Al}_2\text{O}_3$). Unfortunately, the resulting low-surface-area samples, when studied by electron microscopy, did not reveal the desired simple, well-defined morphology that is a necessary prerequisite for the success of the characterization. When the particles obtained by sintering are irregularly shaped with only limited sizes of flat faces, the determination of the orientation of the most frequently exposed faces is difficult.

Nevertheless, the spectroscopic results obtained after CO adsorption at 77 K on these polycrystalline materials are informative. They can be summarized as follows (12, 530):

1. The stretching frequency of CO adsorbed on Al^{3+} ions is higher than that of gaseous CO, although the shift is very small ($\Delta\tilde{\nu} = 20 \text{ cm}^{-1}$).

2. The peak half-width is quite large ($\sim 20 \text{ cm}^{-1}$), as expected for a poorly morphologically defined sample for which inhomogeneous broadening effects occur.

3. The formation of the surface species is highly reversible, even at low temperatures.

The observed frequency and the low adsorption enthalpy are similar to those found for CO on the prismatic faces of chromia and ferric oxide. This comparison suggests that the electric fields at Al^{3+} centers sensed by CO are very weak. The reason for the predominance of faces characterized by highly shielded cations may be related to the high temperature of sintering needed to form the α phase, a parameter which favors the preferential formation of homopolar faces (500, 538, 543).

The frequency of CO adsorbed on $\alpha\text{-Al}_2\text{O}_3$ is less than that observed for CO adsorbed on γ and δ aluminas. This means that the low polarizing tendency of Al^{3+} on $\alpha\text{-Al}_2\text{O}_3$ is associated with the octahedral coordination of Al^{3+} in the corundum structure.

IX. Spinel

Notwithstanding the great variety in the family of spinels, surface investigations of well-crystallized systems with sufficiently defined morphology are surprisingly scarce. For this reason, we have initiated a systematic (and still largely unpublished) investigation of the surface properties of this class of compounds. In the following we illustrate for the first time the surface properties of the polycrystalline MgCr_2O_4 spinel (as probed with CO) for two main reasons: (i) The crystalline habit of the microcrystals is very well defined and (ii) the surface properties of this spinel, essentially dictated by the Cr^{3+} centers, can be naturally compared with those of $\alpha\text{-Cr}_2\text{O}_3$ (see Section VIII.A) and LaCrO_3 (Section X.A). Moreover, any reactivity related to Mg^{2+} centers can be compared with those of the same ionic species on MgO . These materials should permit an understanding of the effect of the framework on the adsorption properties of the Cr^{3+} and Mg^{2+} centers.

When sintered at 1073 K for several hours *in vacuo*, the microcrystals of MgCr_2O_4 assume a very regular habit, as demonstrated clearly by HRTEM (Fig. 30).

From Fig. 30, it is inferred that the spinel is highly crystalline, that each particle is a single microcrystal (see the clear and continuous plane interference fringes running along the entire crystal), and that most of the exposed faces are flat and without defects, as suggested by the straight edges formed by the intersections of the (111) faces. The predominantly exposed planes

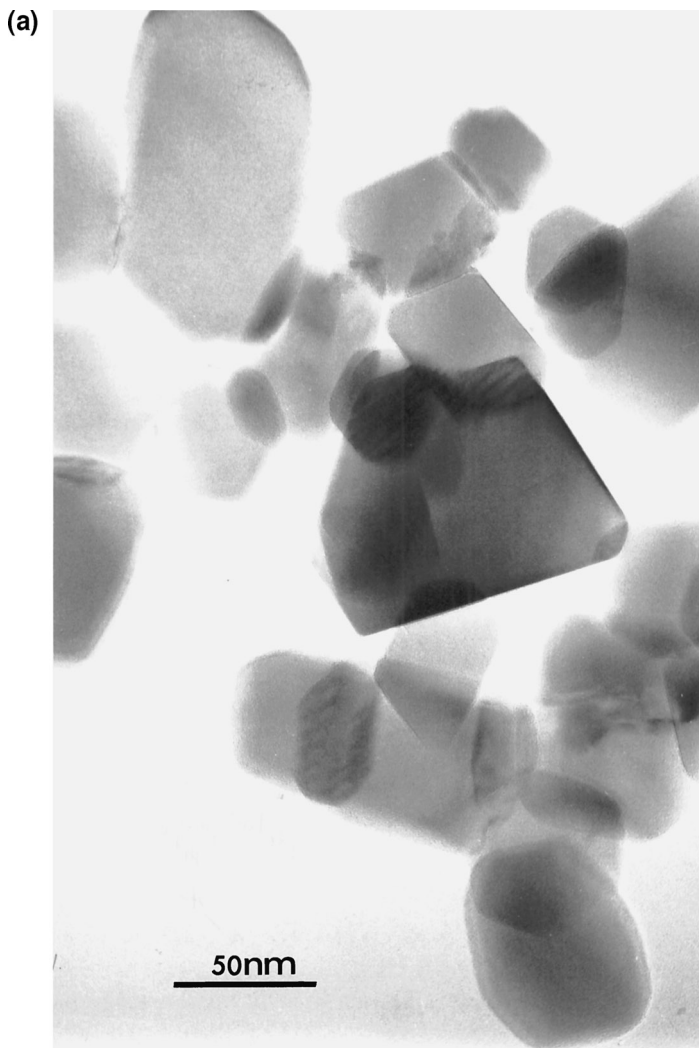


FIG. 30. (a) TEM image of MgCr_2O_4 crystallites. (b) HRTEM image of a MgCr_2O_4 single microcrystal with an exploded view of a selected region of the particle (unpublished results).

are the (111) and (311) faces, and the shape of the microcrystals can be approximated by the polyhedron shown in Fig. 1.

The IR spectrum of adsorbed CO should be dominated by the spectroscopic manifestations of CO adsorbed on the (111) face. Indeed, the IR spectrum of adsorbed CO (Fig. 31) is dominated by a major peak centered

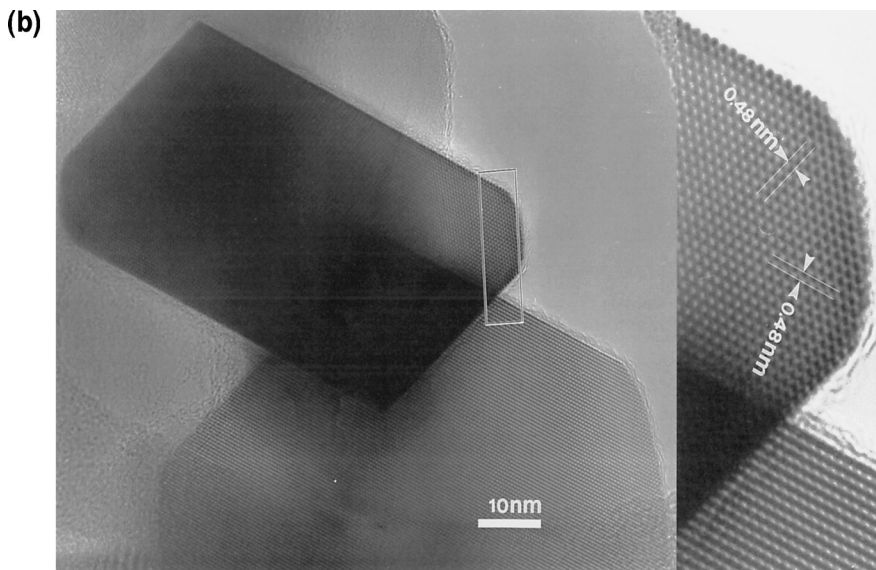
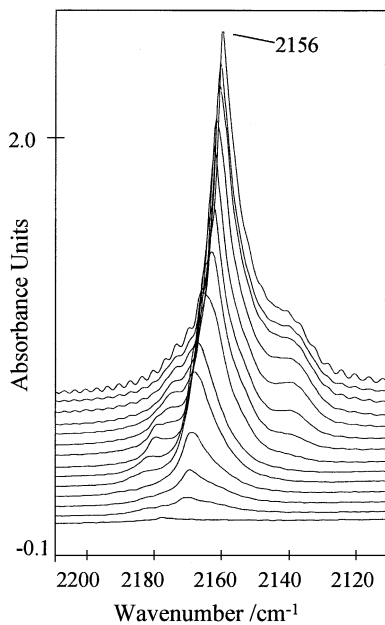


FIG. 30. (continued)

FIG. 31. IR spectra of ^{12}CO adsorbed at ~ 100 K on MgCr_2O_4 samples for CO coverages ranging from $\theta = 1$ (5.33 kPa) to $\theta \rightarrow 0$ (unpublished).

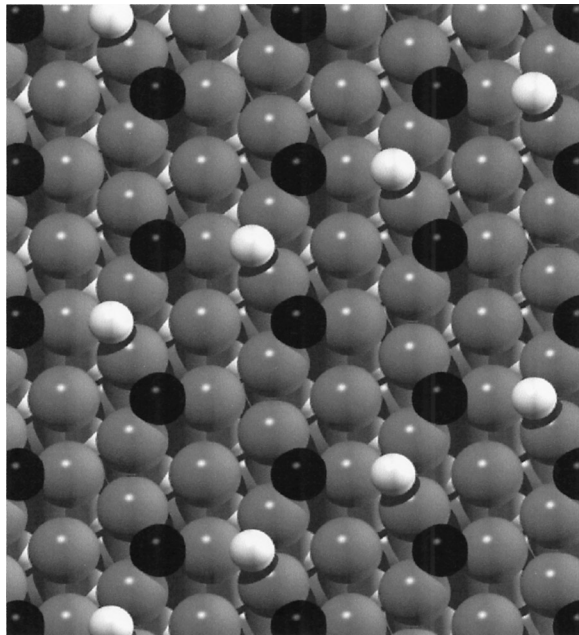


FIG. 32. Reconstructed (111) face of MgCr_2O_4 . The reconstruction was performed to obtain a neutral and nonpolar surface. On the topmost layer, 3-coordinated Cr^{3+} (white) and Mg^{2+} (black) species are present; O^{2-} ions gray.

at 2169 cm^{-1} at $\theta \cong 0$, which gradually shifts to 2156 cm^{-1} as the coverage is increased to $\theta \cong 1$ ($\Delta\bar{\nu} = -13\text{ cm}^{-1}$). Considering the previous discussion and taking into account that the frequency is similar to that observed for CO on $\alpha\text{-Cr}_2\text{O}_3$ and LaCrO_3 , it is inferred that the major peak is associated with CO interacting with Cr^{3+} centers located on (111) faces. A purely geometric model of this face (Fig. 32) shows the exposure of Cr^{3+} in threefold coordination which has a strong polarizing tendency.

Therefore, CO adsorbed on Cr^{3+} centers located on the (111) faces is expected to be characterized by somewhat higher frequencies. However, it has been shown for the (0001) face of $\alpha\text{-Cr}_2\text{O}_3$ (where Cr^{3+} is in a very similar environment) that Cr^{3+} moves inward to a more shielded position upon relaxation, which leads to a reduced electric field strength at the chromium centers. Because of the stability of the surface complexes even at room temperature, it is not excluded that π backdonation may also play a role in the bond between the CO and the Cr^{3+} centers (which usually shift the CO frequency downwards). As discussed previously (see Section IV.A.4) the shift $\Delta\bar{\nu}$ induced by increasing CO coverage is caused by lateral

adsorbate–adsorbate (static and dynamic: $\Delta\tilde{\nu} = \Delta\tilde{\nu}_{\text{stat}} + \Delta\tilde{\nu}_{\text{dyn}}$) interactions in a regular 2D array, as is usually found for CO on single-crystal faces.

This interpretation is supported by the spectra of adsorbed $^{12}\text{CO}/^{13}\text{CO}$ mixtures (15 : 85). At the maximum coverage, the ^{12}CO peak is located at 2147 cm^{-1} (compared with 2157 cm^{-1} for adsorption of isotopically pure ^{12}CO). Because the frequency of the ^{12}CO peak in the mixture is not influenced by dynamic effects, it is inferred that $\Delta\tilde{\nu}_{\text{stat}} = -22\text{ cm}^{-1}$ and $\Delta\tilde{\nu}_{\text{dyn}} = 10\text{ cm}^{-1}$. These values are compatible with the assignment given previously, and they also demonstrate that CO forms a regular 2D array, as expected.

In addition to the main peak in Fig. 31, two weak bands in the 2170- to 2185- cm^{-1} range are detected, and these also slightly shift with coverage. These bands are tentatively attributed to CO adsorbed on Cr^{3+} centers located on less extended faces or on edges or steps. No other bands are observed in the spectrum of adsorbed CO. Thus, Cr^{3+} -CO adducts are formed exclusively on the MgCr_2O_3 surface.

The following are the major conclusions: (i) The MgCr_2O_4 surface properties are dominated by the reactivity of Cr^{3+} centers, (ii) the Mg^{2+} ions do not play a detectable role in the CO/spinel chemistry within the investigated pressure range, and (iii) the surface oxygen ions do not have a basicity comparable to that of oxygen ions on MgO and La_2O_3 .

X. Perovskites

Perovskites (ABO_3) have been a focus of major research interest in the past few decades because of the broad variety of physical properties they exhibit, such as ferro-, piezo-, and pyroelectric, magnetic, and electrooptical properties. Perovskites are also important because (i) their crystalline structure can accommodate a wide range of cations (practically all stable elements can be incorporated); (ii) cations in the two crystallographic positions can be partially substituted; (iii) perovskites accommodate a wide range of defects or excess oxygen, thus stabilizing unusual oxidation states; and (iv) they are catalysts for many important reactions (544–551). The surface properties and, hence, the catalytic behavior of perovskites are related to the presence of cations with unusual coordinations and oxidation states and to the presence of nonstoichiometric oxygen. It is often difficult to establish precise relationship between surface structure and reactivity of these materials.

Because of the presence of defects which negatively influence the optical properties of perovskites and because of difficulties in controlling the stoichiometry, the application of vibrational spectroscopies to characterize the surface species on perovskites is only at a very early stage. Stoichiometric

perovskites are transparent to IR radiation. Therefore, LaCrO_3 has been chosen for a case study; the data reported here are presented for the first time. This solid has a model character, and it also finds many applications as an electrode material (552, 553), as heating elements in solid oxide fuel cells (554, 555), and as a catalyst (556). The reactions catalyzed by LaCrO_3 include a wide range of total and partial hydrocarbon oxidations (34, 557, 558), direct NO decomposition (559), and selective reduction of NO by CO to give N_2 (560). The catalytic performance of LaCrO_3 is inferior to that of other pure LaMO_3 perovskites ($M = \text{Fe, Co, Mn}$) or partially substituted systems such as $\text{La}_{1-x}\text{M}_x\text{CrO}_3$ or $\text{LaCr}_{1-x}\text{M}'_x\text{O}_3$ (559, 561, 562). LaCrO_3 has been chosen here because of its compositional simplicity and because the data obtained can be compared with those representing pure oxides (Cr_2O_3 and La_2O_3) (discussed in Sections VIII.A and VI, respectively).

HRTEM images (not shown) of LaCrO_3 sintered in air at 1100 K show large, well-shaped, and thick particles. Because of the large dimension of the microcrystals, interference fringe patterns are detected only for limited portions of thinner microcrystals. Although the images may confirm the high crystallinity of the material, they are not sufficient to describe unambiguously the microcrystalline morphology. Because no experimental results are available indicating the preferential crystal terminations of LaCrO_3 , we have shaped the polyhedron on the basis of Donnay–Harker rules (50–52, 77). The polyhedron that we consider is terminated by (010), (011), (111), (101), and (100) faces and is represented in Fig. 33.

Among all the terminations suggested by the Donnay–Harker rules only neutral and nonpolar surfaces are considered here because they are the most stable. In particular, to have a zero dipole moment perpendicular to the surface, only the terminations containing a plane symmetry have been chosen and, when necessary to guarantee the electroneutrality, surface reconstructions have been introduced. All the surfaces generated for LaCrO_3 following this procedure are complex, and we are not yet able to define their relative stabilities. Because of these difficulties, the real equilibrium morphology of microcrystals cannot be considered to be established without ambiguity. The following discussion is limited to the structure of the neutral and nonpolar low-index (100) and (101) faces. This selection does not imply that other terminations are not present. The structures of these faces are shown in Fig. 33. The (101) face exposes La^{3+} ions in the topmost layer (where their coordination number is half that in the bulk) and Cr^{3+} ions in fivefold coordination in a lower layer. On this face the surface reactivity should be dominated by La^{3+} species (the Cr^{3+} ions are shielded), and the reactivity should be similar to that found for La_2O_3 . This face can be considered as a La-terminated face. Both sixfold coordinated La^{3+} and fivefold coordinated Cr^{3+} are present on the (100) surface. However, in view of the high coordination of La^{3+} and the

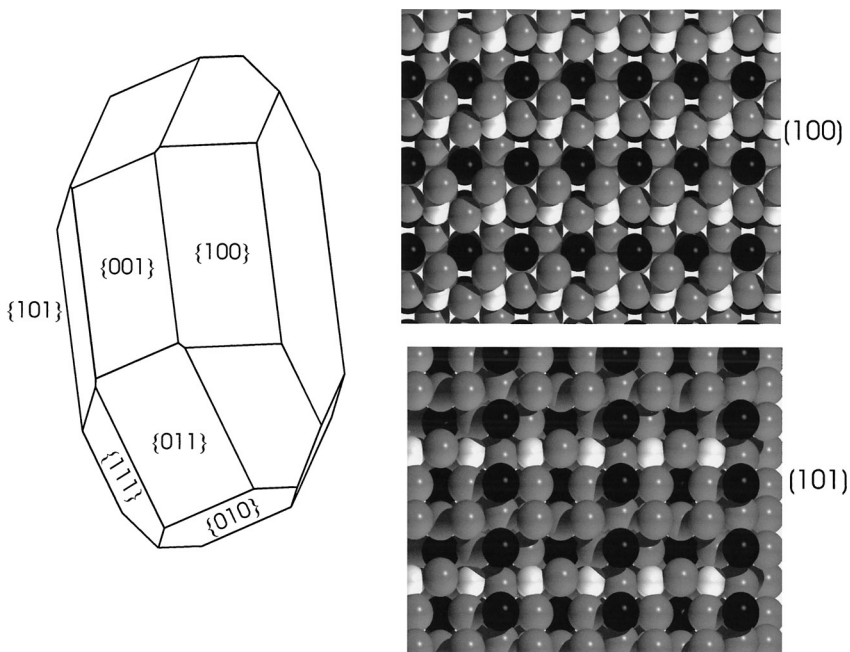


FIG. 33. Polyhedron with the indexed faces, mimicking the shape of LaCrO_3 particles (left). (Right) (100) and (101) faces exposing La^{3+} and Cr^{3+} species, La^{3+} are blacks, Cr^{3+} are white, and O^{2-} are gray.

small radius of Cr^{3+} , this face can be considered as a Cr^{3+} -terminated face. Therefore, its properties should be dominated by the surface chemistry of Cr^{3+} . It is emphasized that both hypotheses are only tentative.

The spectra of CO adsorbed at 77 K on LaCrO_3 activated at 1100 K include two main bands in the ranges 2180–2165 and 2162–2155 cm^{-1} (Fig. 34). Both absorptions are gradually red shifted at increasing coverages, as expected for CO adsorbed on flat surface. By comparison with the spectra of La_2O_3 (414) and Cr_2O_3 (491), it is tempting to assign the peak at 2162–2155 cm^{-1} (the formation of the species is highly reversible) to CO adsorbed on La^{3+} -terminated surfaces and to assign the peak at 2180–2165 cm^{-1} (the species is more stable toward outgassing) to CO on Cr^{3+} -terminated surfaces. There is a third, weak band characterized by a frequency very close to that of CO gas (a similar weak band was observed for CO on $\alpha\text{-Cr}_2\text{O}_3$). This band is tentatively attributed to multicenter interactions.

Data obtained with diluted isotopic mixtures show that the coverage-induced total shift is the result of dynamic and static effects: $\Delta\tilde{\nu}_{\text{dyn}} = 13 \text{ cm}^{-1}$

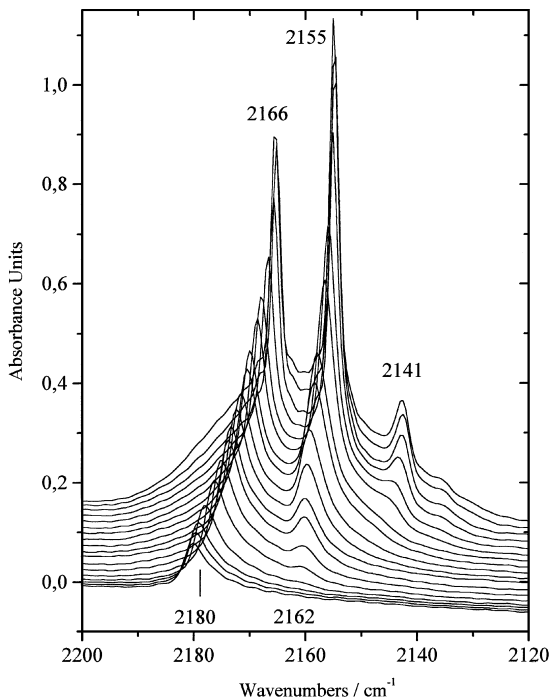


FIG. 34. IR spectra of ^{12}CO adsorbed at ~ 77 K on LaCrO_3 samples outgassed at 1100 K, for coverages ranging from $\theta = 1$ (5.33 kPa) to $\theta \rightarrow 0$ (unpublished).

and $\Delta \tilde{\nu}_{\text{stat}} = -27 \text{ cm}^{-1}$ for the peak in the range $2180\text{--}2165 \text{ cm}^{-1}$, and $\Delta \tilde{\nu}_{\text{dym}} = 7 \text{ cm}^{-1}$ and $\Delta \tilde{\nu}_{\text{stat}} = -13 \text{ cm}^{-1}$ for the peak in the range $2162\text{--}2155 \text{ cm}^{-1}$ (spectra not shown). This behavior supports the view that sites of different nature, likely Cr^{3+} and La^{3+} ions, are involved.

To gain information about the structure of the Cr^{3+} -terminated faces (according to the hypothesis that the Cr^{3+} centers are associated with the band at higher frequency), the following experiment was designed. The surface of LaCrO_3 was covered by CO *first*. Then the amount of adsorbed CO was gradually reduced by lowering the pressure of CO until only a small fraction of the Cr^{3+} sites were occupied by CO (bottom spectrum on the right side of Fig. 35). On this sample, N_2 was then gradually adsorbed up to full monolayer coverage (successive spectra, from bottom to top, on the right side of Fig. 35). The $\nu(\text{CO})$ peak undergoes a shift $\Delta \tilde{\nu}_{\text{stat}} = -28 \text{ cm}^{-1}$, which is entirely static in character (the surrounding molecules are N_2 so that dynamic effects are absent). The shift is nearly identical to that caused by CO, suggesting that it is a through-space effect. The shift is not continuous but occurs

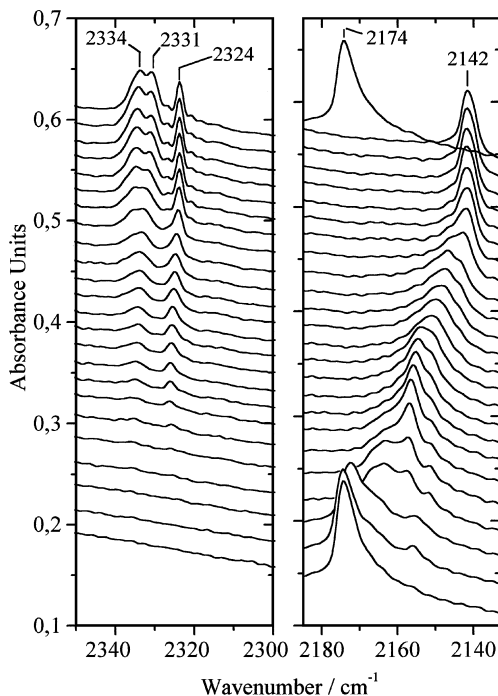


FIG. 35. Effect of N_2 adsorption at 77 K on CO-precovered (low- θ) $LaCrO_3$ samples out-gassed at 1100 K for coverages ranging from $\theta = 1$ (5.33 kPa) to $\theta \rightarrow 0$. (left) nitrogen absorption region and (right) CO absorption region (unpublished data).

in four steps, corresponding to the filling of four vacant sites surrounding each isolated Cr^{3+} -CO species. This observation seems to be inconsistent with the structure of the (100) face, on which the Cr^{3+} ions are aligned in rows and, hence, have only two nearest neighbors. To interpret the spectra, a 2D arrangement of Cr^{3+} centers, with a Cr-Cr distance of 4 Å, would be required. It is therefore inferred that the (100) face may not be appropriate to explain the spectra. It is evident that the problem of the Cr^{3+} -terminated face cannot be considered to be solved, and this experiment is reported here to show the new difficulties which are encountered when two ions are simultaneously exposed on surfaces (as on perovskites). It is evident that much more work is needed to clarify this point.

The spectrum of nitrogen is also quite informative (Fig. 35, left). The spectrum includes two main absorptions shifted to frequencies higher than that of N_2 gas. On the basis of the considerations stated previously, the low-frequency peak at 2124 cm^{-1} is assigned to La^{3+} -terminated surfaces and the complex absorption at higher $\tilde{\nu}$ to N_2 adsorbed on Cr^{3+} centers. The

same bands are observed for N₂ on LaCrO₃ (spectra not shown). The high-frequency absorption peak is in a frequency range similar to that found for the N₂ on α -Cr₂O₃.

In summary, we conclude the following:

1. Cr³⁺ and La³⁺ ions behaves as medium/strong acid centers such as those on Cr₂O₃ and La₂O₃; their different acid strengths are shown by both CO and N₂ probes.
2. CO does not probe the presence of the strong basicity observed on La₂O₃.
3. Investigations of CO/N₂ mixtures provides information about the structures of the Cr³⁺-terminated faces.
4. It is confirmed that the N₂ molecule can be used as a sensitive probe of the local electric fields.

A natural continuation of this work would be an investigation of the effect of cation substitution on the adsorption properties of LaCoO₃.

XI. Oxides with AB₂ Structure (TiO₂ and ZrO₂): Surface Structure, Reactivity, and Catalytic Activity

A. TiO₂

The coordinative and/or dissociative adsorption of various probe molecules has been used to characterize the surface properties of TiO₂, which finds applications as a catalyst, photocatalyst, and sensor. Among the molecules used as probes, we mention CO (37, 38, 563–576), CO₂ (563, 565, 577), NO (578, 579), water (580, 581), pyridine (582, 583), ammonia (584, 585), alcohols (586, 587), ethers (including perfluoroethers) (588), ozone (589), nitrogen oxide (590), dioxygen (591), formic acid (592–594), benzene (584), benzoic acid (595), and chromyl chloride (596).

In an investigation of the rutile form of TiO₂ powder, two CO desorption processes were observed (567) (at 175 and 475 K) and tentatively attributed to the C-end interaction of CO with surface oxygen ions and to the O-end interaction with surface defect sites, respectively. The existence of two different adsorbed species was also shown by IR spectroscopy by Tanaka and White (565), who observed bands at 2185 and 2115 cm⁻¹ (the lower-frequency band corresponding to a more strongly bonded species). Only the high-frequency component was observed by Morterra *et al.* (571) for CO on Na-doped rutile. An attempt to correlate the IR spectra of CO adsorbed at 77 K with the structural and morphological transformations (characterized by HRTEM) accompanying the anatase–rutile phase transition was made by Cerrato *et al.* (597). On passing from the nearly pure anatase phase

(Titanoxid P25, Degussa) to the pure rutile modification (obtained by firing at 1073 K), a progressive sintering of the TiO_2 microcrystals was observed, leading to a decrease of the surface area from about 50 to $8 \text{ m}^2 \text{ g}^{-1}$. Simultaneously, the morphology changed from well-defined microcrystals predominantly exposing the (010) planes to highly irregular and stepped particles, possibly exposing an appreciable amount of other high-index faces (of unknown nature). These changes were reflected in a significant modification of the IR spectrum, changing from an intense, narrow band at 2179 cm^{-1} [assigned to Ti^{4+} -CO adducts formed on the (010) faces], typical of the anatase phase to a spectrum including two much broader absorptions, at 2175 and 2156 cm^{-1} (the second band being more intense). The reduced CO stretching frequency found for CO on rutile is a clear indication of the reduction of the polarizing tendency of the Ti centers, which in turn is suggestive of a tendency of rutile to expose surfaces with increasing homopolar character upon treatment under vacuum at high temperature (22).

The CO/anatase system was investigated at room temperature, when only about 10–15% of the total surface Lewis acid sites were covered by CO (38, 41). The IR spectra depend strongly on the degree of hydration of the surface and the presence of contaminants. Two different families of surface Lewis acid sites were identified, one deriving from the removal of molecularly adsorbed water and the second (stronger) originating from removal of surface OH groups (41). The two families of sites give rise to reversibly formed adducts with CO bands at about 2187 and 2206 cm^{-1} , respectively. The first family (2187 cm^{-1}) is by far the predominant one and is plausibly associated with Ti^{4+} ions on extended faces. The CO extinction coefficients of the two species were found to be $2.6 \pm 0.3 \times 10^6 \text{ mol}^{-1} \text{ cm}$ for the band at 2187 cm^{-1} and $3.8 \pm 0.2 \times 10^6 \text{ mol}^{-1} \text{ cm}$ for the band at 2206 cm^{-1} (571). Removal of OH groups at high temperature also yields a third (weak) family of weaker cationic sites revealed by pyridine but not by CO.

Experiments performed at room temperature suffer from the limitation that only a small fraction of the surface sites are detected by adsorption of CO. Therefore, measurements at lower temperature (e.g., 77 K) are necessary to permit probing of all the surface sites. Spectra recorded at 77 K for CO on Titanoxide P25 anatase are summarized in Fig. 36. As discussed previously, this material consists of morphologically well-defined microcrystals that preferentially expose the (010) face. The spectrum of CO adsorbed at maximum coverage is dominated by a band at 2179.5 cm^{-1} (37). The extremely narrow band ($\text{FWHM} < 1.5 \text{ cm}^{-1}$) of this component suggests that the respective Ti-CO complexes are formed on regular surface planes and that the observed band at $\theta = 1$ is the collective in-phase stretching mode of an ordered 2D layer of parallel CO molecules polarized by fivefold coordinated ions exposed on the predominant (010) planes. The Ti^{4+} - Ti^{4+} distance on this plane is approximately 0.3 nm, and strong repulsive interactions

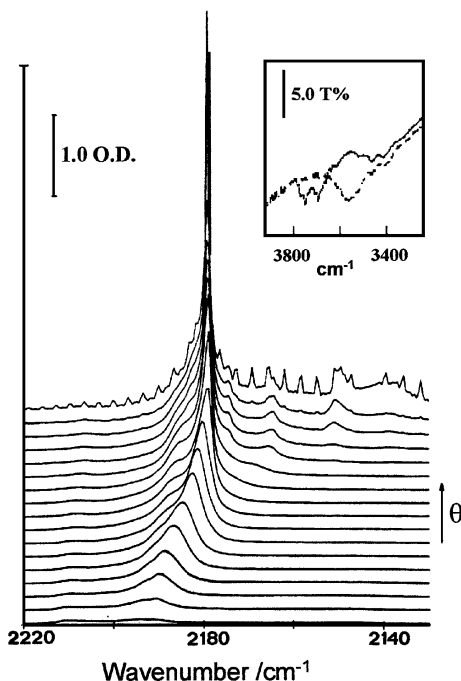


FIG. 36. IR spectra of ^{12}CO adsorbed at ~ 77 K on TiO_2 samples outgassed at 873 K at coverages ranging from $\theta = 1$ (5.33 kPa) to $\theta \rightarrow 0$. (Inset) Spectra in the OH region before (—) and after (\cdots) contact with CO [reproduced from Spoto *et al.* (37) with permission from Pergamon Press].

between CO molecules adsorbed on the first nearest neighbors are therefore expected. Consequently, the maximum occupation of the surface sites is only 50% (corresponding to ~ 2.8 CO/nm 2).

Decreasing CO coverage leads to a blue shift of the main peak from 2179.5 to 2192.5 cm^{-1} (singleton frequency) ($\Delta\tilde{\nu} = 13$ cm^{-1}), accompanied by a change of the band half-width from ~ 1.5 to ~ 13 cm^{-1} . These effects indicate the gradual disappearance of the ordered phase of adsorbed CO with formation of a more diluted phase with reduced adsorbate–adsorbate interactions. On the basis of $^{12}\text{CO}/^{13}\text{CO}$ isotopic substitution experiments, the contributions of dynamic ($\Delta\tilde{\nu}_{\text{dyn}}$) and static ($\Delta\tilde{\nu}_{\text{stat}}$) effects to the total shift ($\Delta\tilde{\nu}_{\text{tot}} = 13$ cm^{-1}) were estimated to be 3.5 and -16.5 cm^{-1} , respectively. These values and the value of the dynamic polarizability, $\alpha_{\text{v}} = 0.025$ \AA^3 , suggest that the surface Ti^{4+} –CO bonds are dominated by electrostatic (polarization) forces.

Much less intense features were observed at 2211.5 (shifted to 2207 cm^{-1} at low coverage)—approximately 2175, 2166, 2153, and 2138 cm^{-1} . The first

band clearly corresponds to the band observed at 300 K and assigned to Ti^{4+} -CO complexes on the stronger Lewis acid sites (fourfold coordinated α sites located on different high-index planes and on defects). The bands at ~ 2175 and 2166 cm^{-1} were assigned to more weakly bonded species formed during the subsequent occupation of the sites on the (010) face; a tilted configuration of these species was suggested. The 2153- and 2138-cm^{-1} absorptions are attributed to hydrogen-bonded species (formed between CO and the residual surface OH groups responsible for the absorptions in the range $3800\text{--}3600\text{ cm}^{-1}$; Fig. 36, inset) and physically adsorbed CO, respectively.

Similar spectra were reported separately (39) and interpreted analogously, except for the band at 2166 cm^{-1} , which was assigned to CO adsorbed on 5-coordinated Ti^{4+} ions in acid-base pairs and, hence, having very low electrophilicity.

The major conclusions are summarized as follows:

1. The extended faces behave as a 2D array of weak Lewis acid centers (Ti_{5c}^{4+}). These faces appear to be stable and unreactive.
2. Stronger Lewis acid sites associated with Ti_{4c}^{4+} centers exist only on higher-index faces or on defects such as edges and steps.
3. CO probes did not detect any strongly basic sites.
4. Activation *in vacuo* at high temperature (needed to eliminate most of the hydroxyl groups) is usually accompanied by a loss of oxygen and of stoichiometry (with the accompanying optical effects preventing spectroscopic observations).

The properties of TiO_2 surfaces can be selectively modified by incorporation of, for example, sulfates, phosphates, peroxides, and vanadium pentoxide. The resulting tailored products may have catalytic properties superior to those of TiO_2 . This is a broad and important subject, which does not fit within the limited scope of this review.

B. ZrO_2

1. *Pure ZrO_2*

Several groups (598–602) investigated the surface properties of a highly sintered monoclinic (ZrO_2) by IR spectroscopy of CO adsorbed at 77 K. Morterra *et al.* reported a stepwise formation of five different bands (labeled A–E in Ref. 600) upon increasing the CO equilibrium pressure. This behavior is similar to that observed for CO on ZnO (Section V.A.1) and can be attributed to the development of lateral interactions between CO oscillators with increasing coverage. The different bands correspond to different local geometries around a given $\text{Zr}^{4+} \cdots \text{CO}$ adduct. The main differences between CO/ZrO_2 and CO/ZnO are two narrow bands, at 2172 and

2167 cm^{-1} , at $\theta = \theta_{\max}$ (HWHM $\cong 3\text{--}3.5\text{ cm}^{-1}$) on ZrO_2 , in contrast to a single band for CO on ZnO. The spectrum probably reflects the presence of two well-developed and defect-free faces on the microcrystals of monoclinic ZrO_2 . As was observed for CO on ZnO as the coverage decreased, new bands appear and disappear, indicating a complex behavior corresponding to different CO environments on the two faces. The peak at 2167 cm^{-1} has been tentatively ascribed to CO adsorbed on (111) faces, where the Zr^{4+} ions are separated by 0.35 nm and form a rhombohedral array. With diluted isotopic mixtures, the dynamic and static shifts have been evaluated: $\Delta\tilde{\nu}_{\text{dyn}} = 3\text{ cm}^{-1}$ and $\Delta\tilde{\nu}_{\text{stat}} = -25\text{ cm}^{-1}$, respectively. From the $\Delta\tilde{\nu}$ value, α_v was calculated to be 0.024 \AA , which suggests that electrostatic polarization forces are mainly involved. The static shift is close to that observed for CO on ZnO.

The structural and morphological properties of monoclinic ZrO_2 samples calcined at increasing temperatures were investigated by XRD, HRTEM, and IR techniques (603, 604). The data show that the (111) face is predominant, and the (001) and (011) faces were observed only for samples sintered at low temperatures. Two types of surface OH groups and undissociated, strongly coordinated H_2O molecules were detected by IR spectroscopy. Computer simulations of the (111), (001), and (011) faces were used to explain the experimental results.

A detailed investigation of the surface properties of the tetragonal phase of ZrO_2 by HRTEM and IR techniques has also been reported (605). The tetragonal phase of zirconia is metastable at low temperatures. Therefore, yttria-stabilized samples were prepared and characterized (606–608). The structural, morphological, and surface hydration features of tetragonal ZrO_2 were investigated by XRD, HRTEM, and IR techniques (606), and the interactions of the surfaces with CO (607) and CO_2 (608) were reported.

2. Surface-Modified ZrO_2

The surface properties of ZrO_2 can be selectively modified with additives such as these mentioned for TiO_2 . Sulfates markedly improve the catalytic properties (609–613); this broad and important subject deserves a separate review and is beyond the scope of this article.

XII. Transition Metal Ions Supported on Amorphous Silica: $\text{Cr}^{x+}/\text{SiO}_2$

As stated previously, amorphous silica consists of a disordered array of SiO_4 tetrahedra connected by Si–O–Si bridges. Unlike the other oxides

reviewed previously, SiO₂ is considered to be fully covalent, and this is the principal reason why we consider it here, even though it is amorphous.

The Si–O–Si angle of the group bridging the corner-sharing tetrahedra can vary over a broad interval (120–160°) without a substantial energy change, and this result explains the high thermal stability of the amorphous phase (46).

The surface of virgin silica is fully covered by hydroxyl groups, which can be only partially eliminated by outgassing *in vacuo* at high temperatures. The IR spectroscopy of silanols in the absence and presence of adsorbates has been investigated intensively (46, 614–616) and is not reviewed here. Briefly, the surface silanols are weakly acidic and can react with supported transition metal oxides, thus acting as anchoring sites for low-valent transition metal ions. The structure, reactivity, and catalytic properties of these grafted ions (and, generally, of oxides supported in low concentrations on silica) represent the main subject of this case study. This system was chosen not only because of the outstanding catalytic properties of some of these material, but also because of the need for deeper understanding of the factors influencing the coordination states of surface ions. Silica appears to be a good candidate because of its covalent bonding and tetrahedral structure. A detailed comparison is given of the properties of low-valent transition metal ions supported on SiO₂, MgO, and ZnO.

The structure and reactivity of Fe²⁺, Mn²⁺, Co²⁺, Ni²⁺, and Cr²⁺ anchored to silica surfaces (or, alternatively, of FeO, MnO, CoO, NiO, and CrO supported on silica surfaces) have been investigated extensively with CO and NO as probe molecules (617–619). The most important results can be summarized as follows:

1. In the presence of low equilibrium pressures of CO, M^{x+}–CO (M = Fe, Co, Ni, Mn, and Cr) complexes are formed that are characterized by $\nu(\text{CO})$ stretching frequencies higher than that of CO gas. This means that we are dealing with nonclassical metal carbonyls and that the M^{x+}–CO bond has predominantly σ donor character.

2. At the highest CO pressures (and the lowest temperatures), the formation of multicarbonyl structures M^{x+}–(CO)_n is sometimes observed (Ni²⁺ and Cr²⁺) (506, 618–621). Ni²⁺/SiO₂ and Cr²⁺/SiO₂ are the only silica-supported catalysts active for alkene oligomerization at ambient temperature.

Although the first result is in line with those obtained for MgO–NiO, MgO–CoO, and ZnO–CoO solid solution, the second suggests that the chemistry of silica-supported ions has some unique characteristics that merit further consideration. The ability to form multicarbonyl species suggests a state of coordinative unsaturation higher than that observed for the same or similar ions in solid solutions and represents a strong indication that high

degrees of coordinative unsaturation and catalytic activity are related to each other.

Here, we focus on $\text{Cr}^{2+}/\text{SiO}_2$, a catalyst that has been extensively investigated because of its applications in ethene polymerization (Phillips and Union Carbide processes) (469, 501, 503, 622, 623). The Phillips catalyst is prepared by reacting chromic acid with silanols to give surface chromates, which are then reduced by CO, leading to the formation of a surface silicate with divalent chromium. In the practical catalyst, the reduction of the surface chromate is carried out with ethene. The reaction between chromic acid and surface hydroxyl groups is likely not the only one occurring on the surface. For example, in the presence of water vapor, which is an oxidant for Cr^{2+} , interaction with hydroxyl clusters may lead to triply anchored species and ultimately to anchored Cr^{3+} . The Union Carbide catalyst is prepared by the reaction of chromocene with surface silanols, leading to the formation of cyclopentadiene (624). The activity of each catalyst is attributed primarily to divalent, low-coordinated species (506, 624, 625).

On the surface of amorphous silica supports, there are numerous conceivable locations of the Cr^{2+} ions. These differ from each other in the number of ligands [two oxygen atoms of the $\equiv\text{SiO}^-$ groups and a variable number of oxygen atoms of the $(\equiv\text{SiO}^\delta-\text{Si}\equiv)$ bridges in adjacent positions, as illustrated schematically in Fig. 37]. This structural variability is favored by the amorphous nature of the support and can be influenced by the thermal treatments (high-temperature treatments favor a penetration of Cr^{2+} into the flexible silica framework) (620). The ligands surrounding the Cr^{2+} center are not equivalent; two of them are negatively charged (SiO^-) and hence strongly interacting, whereas the others are nearly neutral and consequently classified as weakly interacting.

A way to ascertain the coordination state of the anchored ions and, hence, their accessibility to adsorbing molecules is represented by the quantification of their capacity to adsorb molecular probes such as CO (and NO) and by the measurement of the IR spectrum of the resulting surface carbonyls (and nitrosyls). Thus, we obtain information about the propensity of the surface ions to insert ligands in their incomplete coordination spheres and, hence, indirect information about the location and structure of sites existing prior to adsorption. Of course, as mentioned previously, the probing with complexing molecules is always associated with a perturbation of the surface structures (this phenomenon is equivalent to surface relaxation). This unavoidable effect must be considered when structures of sites prior to adsorption are proposed.

The IR spectra recorded for CO on a $\text{Cr}^{2+}/\text{SiO}_2$ as the coverage increased (506) are illustrated in Fig. 38. The IR spectra can be grouped into two series. The first, corresponding to low coverage ($n_{\text{CO}}/n_{\text{Cr}^{2+}} \leq 2$), is associated

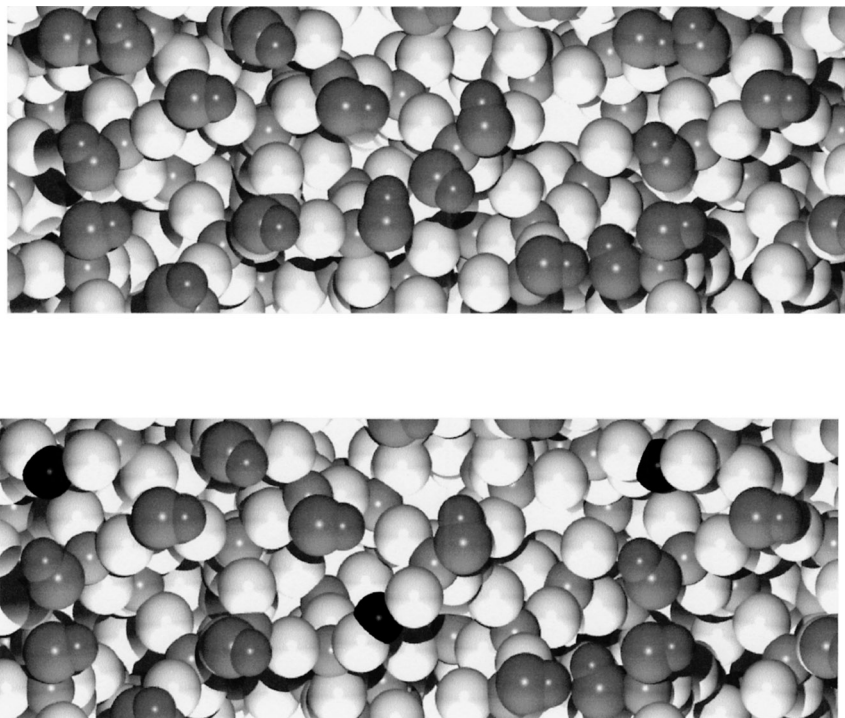


FIG. 37. (Top) Representation of silica surface obtained by cutting amorphous SiO_2 . O^{2-} species exposed at the surface are saturated by hydrogen (hydroxyl groups). (Bottom) Representation of Cr-silica surface obtained by eliminating two hydroxyl groups for each anchored chromium species (Cr^{n+} , black; surface hydroxyls, gray; bulk oxygens; white; Si^{4+} , light gray).

with the progressive intensification of the stretching bands of adsorbed CO characterized by values of $\tilde{\nu}(\text{CO})$ exceeding that of CO gas. The second series (corresponding to high coverages) is characterized by the progressive erosion of the bands formed in the first phase and by the formation of new species with $\tilde{\nu}(\text{CO})$ bands with values less than that of CO gas.

The four IR bands (~ 2200 , 2191, 2184, and 2178 cm^{-1}) characterizing the first phase are the $\tilde{\nu}(\text{CO})$ bands of CO ligands filling the coordination vacancies of anchored Cr^{2+} and Cr^{3+} . An analysis of their evolution with the CO equilibrium pressure led to the following conclusions: (i) The bands at 2184 and 2178 cm^{-1} indicate dicarbonyl species formed at Cr^{2+} sites with the lowest coordination; (ii) the band at 2191 cm^{-1} belongs to Cr^{2+} species bonded to only one CO molecule at room temperature (which are thus apparently less coordinatively unsaturated); and (iii) the band at about 2200 cm^{-1}

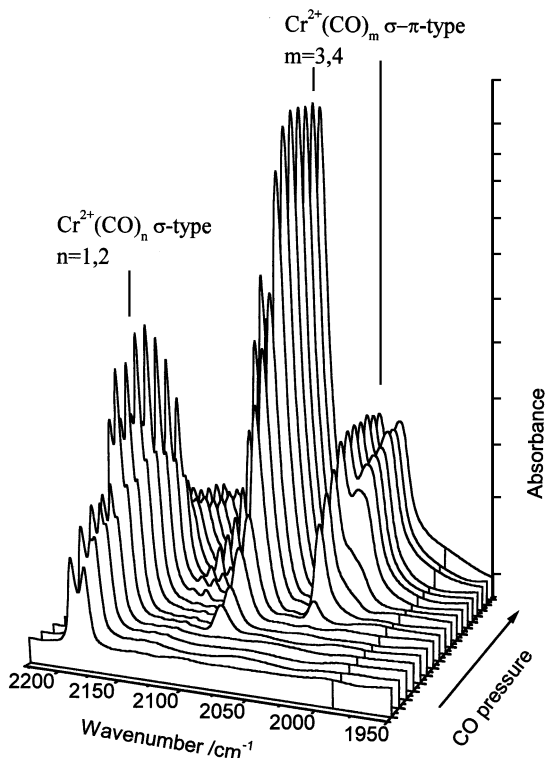


FIG. 38. IR spectra of ^{12}CO adsorbed at 77 K on Cr/silica at coverages ranging from $\theta = 1$ (5.33 kPa) to $\theta \rightarrow 0$. The spectra were collected for this review following the procedure described by Zecchina *et al.* (507).

is likely associated with CO interacting with Cr^{3+} (debate continues about this assignment) (506, 621).

These results mean that the surface ions are located on the silica surface in at least three different local environments (in approximate agreement with the picture illustrated in Fig. 37). The frequencies of the $\tilde{\nu}(\text{CO})$ stretching modes (all higher than that of the CO gas) are similar to those observed for CO on ZnO; thus, electrostatic and σ -type overlap forces are mainly involved. Most likely, the electrostatic interaction prevails in the complexes absorbing at 2200 cm^{-1} (as expected for an ion carrying a charge of +3).

In summary, as was found for other oxides, in the first phase of the adsorption process CO behaves as a probe of the Lewis acidity associated with the coordination vacancies. Moreover, the most coordinatively unsaturated Cr^{2+} sites are able to bond to a second CO ligand, even at the lowest equilibrium

pressures, according to a two-step process [the structure of the dicarbonyl species has been discussed (506, 621)].

When the CO equilibrium pressure is gradually raised, the IR peaks at 2191, 2184, and 2198 cm^{-1} , attributed to the σ -bonded complexes formed in the first stage, are gradually eroded with formation of new, intense bands in the range 2120–2000 cm^{-1} ; the band at 2200 cm^{-1} is unaffected. These observations can be interpreted as follows: With the exception of the species represented by the band at 2200 cm^{-1} , all other species are able to bind additional CO ligands, leading to the formation of new, labile $\text{Cr}^{2+}(\text{CO})_n$ ($2 \leq n \leq 4$) complexes. This behavior suggests that the Cr^{2+} species involved are highly coordinatively unsaturated.

Here, the evolution of the spectra is described in detail. The crucial question is the following: Why does the addition of further CO ligands cause such a dramatic shift toward lower frequency and an equally dramatic increase of the integrated intensity? The only possible answer is that both frequency shift and intensity enhancement are associated with an abrupt increase of the d - π interaction. Metal carbonyls of the type $\text{M}(\text{CO})_n\text{X}_2$ ($\text{X} = \text{Br}, \text{Cl}, \text{etc.}$) indeed have bands in the same frequency range with similar intensity patterns (453, 626). However, the high lability of the tri- and tetracarbonyl complexes (they decompose as a result of outgassing at 77 K) poses a problem. The reduced frequency of the CO groups, which is supposed to indicate an increase of d - π overlap contributions and hence a strengthening of the Cr^{2+} -CO bonds, should be accompanied by a stability enhancement (whereas the opposite is observed). This apparent contradiction can be explained if we assume that the addition of the third and fourth CO ligands is not simply a ligand insertion into preexisting coordinative vacancies but rather a ligand displacement reaction whereby the bonding of the CO ligands is accompanied by the simultaneous displacement of one or two weakly bonded surface ligands (presumably the bridging oxygen of the $\equiv\text{SiO}^{\delta-}\text{Si}\equiv$ groups). The total enthalpy change involved in the process may be small (and hence the removal of CO can be facile) because the energy required for the creation of a vacancy at the Cr^{2+} centers is counterbalanced by the energy release associated with the coordination of a surface ligand. In other words, the Cr^{2+} centers on silica show some mobility and under appropriate conditions, can change their positions on the surface under the influence of complexing agents (strong relaxation) and optimize their interactions with CO via d - π interaction. It is therefore concluded that some of the coordination vacancies measured by CO cannot be considered as truly existing *in vacuo* and that different probe molecules can give different answers. This conclusion is well documented by the results of experiments concerning the adsorption of NO (more strongly bonded than CO) and N_2 (more weakly bonded than CO) (506, 623, 627). In particular, it has been observed that the weakly bonded

N_2 ligand is not able to induce appreciable surface mobility or relaxation. The tendency toward strong relaxation in the presence of adsorbates differentiates the chemistry of transition metal ions on silica from the chemistry of the same ions on crystalline oxides (on which relaxation and mobility are definitely smaller). This property is likely to play a fundamental role in determining the properties of Cr^{2+} (Ni^{2+}) on silica in catalytic processes (e.g., ethene polymerization) for which a large number of coordination vacancies are needed.

$\text{Cr}^{2+}/\text{SiO}_2$ is an efficient catalyst for ethene polymerization, even at room temperature (in the industrial process the temperature is about 380 K). For this reason, it is an ideal system for *in situ* spectroscopic investigations of a working catalyst.

Many questions remain about the initiation, propagation, and termination steps of the ethene polymerization mechanism. The most important models proposed to date are the Cossee model, which requires a vacant coordination site on the metal center in the position adjacent to the growing alkyl chain, where ethene is coordinated before insertion into the chain (628), and the Green–Rooney model, which requires the presence of a metal–carbene species and a vacant site where ethene is coordinated prior to insertion (629).

A common feature of the two models is that the metal centers should have at least two coordination vacancies prior to the interaction with ethene—one for the alkyl or the carbene species and one for the coordination of ethylene. On the basis of the results discussed so far (which have demonstrated that a significant fraction of Cr^{2+} centers is highly coordinatively unsaturated), it can be understood why $\text{Cr}^{2+}/\text{silica}$ is such a good catalyst, whereas Cr^{3+} ions on chromia/silica or exposed on extended faces of $\alpha\text{-Cr}_2\text{O}_3$ are not.

One of the most debated problems of both mechanisms concerns the initiation step, i.e., how the alkyl or the carbene species are created at the naked Cr^{2+} centers by interaction with ethene. IR spectroscopy has been used in attempts to solve this problem. Time-resolved spectra taken at room temperature immediately after contacting of ethene (Fig. 39) with a model $\text{Cr}^{2+}/\text{SiO}_2$ catalyst reduced in CO (506, 630) led to the following conclusions: (i) The pair of bands at 2920 and 2851 cm^{-1} , which grow with time in a parallel way at a nearly constant rate, are assigned to the stretching modes of the CH_2 groups of the living polymer chains; (ii) no absorptions of vibrations of CH_3 groups can be observed in the early stages of the polymerization, although the corresponding modes have extinction coefficient larger than that of CH_2 ; and (iii) no absorptions associated with carbene species can be observed in the series of spectra shown in Fig. 39.

From these results, it is inferred that the initiation mechanism involves a metallacyclic intermediate. The observation by Ruddick and Baydal (625) that 1-hexene formed from a metallacyclic precursor is produced at the early

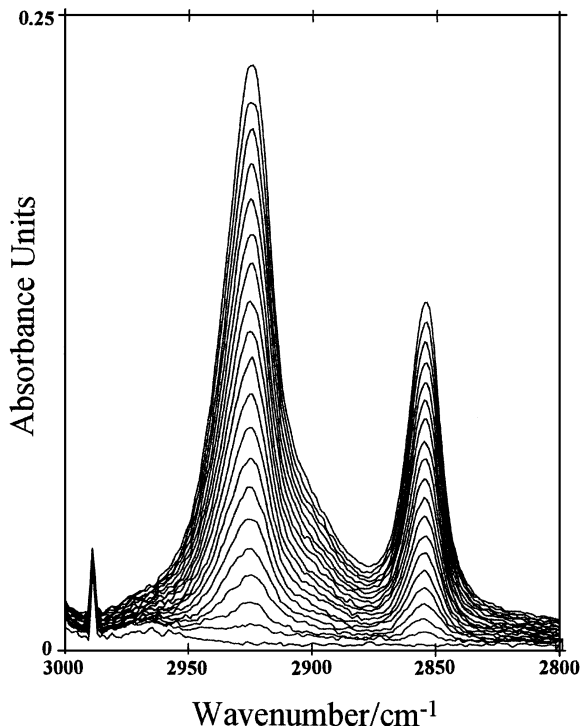


FIG. 39. IR time-resolved spectra of ethene polymerization reaction on Cr/silica. Last spectrum after 15 s [adapted from Zecchina *et al.* (506) with permission from Elsevier Science Publishers].

stages of polymerization confirms this mechanism. An implication of this conclusion is that the Cr^{2+} centers that are active at room temperature must have at least three “available” coordination vacancies, a result in agreement with the conclusions obtained from CO adsorption. Another conclusion is that only extremely accessible (and mobile) centers can be active in ethene polymerization, which explains the uniqueness of silica as a support. Substitutional transition metal ions exposed on low-index faces of ionic oxides do not meet these requirements and thus are not active. Only ions in rare defect sites (such as those found on partially reduced chromia) are sufficiently coordinatively unsaturated to act as catalytic centers. Of course, all these considerations for the Cr^{2+} /silica system are valid only for those sites that are active even at room temperature and cannot be extended to sites that work at higher temperatures or to sites obtained from the precursor by reduction by ethene. It is not excluded that on these sites a different mechanism may operate.

XIII. Electric Field and Acidity at Cationic Sites

As we have shown, there is a clear correlation between the frequency shift of the stretching frequency of CO adsorbed at positively charged centers at the surfaces of non-transition metal oxides and halides and the electric field sensed by the molecule (Stark effect). This is the reason why CO is considered a specific and sensitive probe of the surface fields of ionic solids.

A similar frequency-field correlation is likely to exist for molecularly adsorbed N₂, although the stretching frequency of this molecule is less sensitive to Stark effect perturbations (and far fewer data are available).

Even potentially more important is the observation that the stretching frequency of molecular hydrogen adsorbed at cationic sites is also strongly affected by positive polarizing fields. From the few low-temperature experiments reported (and those documented in this review), it is emerging clearly that $\tilde{\nu}(\text{H-H})$ is red shifted upon adsorption of H₂ at positive centers and that the $\Delta\tilde{\nu}/\tilde{\nu}$ ratio is much larger than that found for CO and, *a fortiori*, for N₂. This result suggests that H₂ may be used much more as an efficient probe of surface fields.

In this context, the most data are available for the molecular CO probe (15, 22, 29, 631). For a given surface cation without *d* electrons of suitable energy, the strength of the electric field *E* detected by CO is dependent on the coordination state and the charge/radius ratio of the cation on which adsorption occurs. Taken together, these two facts form the basis of the idea that the blue-shift $\Delta\tilde{\nu}$ of the CO frequency can be used to determine the Lewis acid strength of positive surface centers. The electric field-frequency correlation is the basis of the *spectroscopic method for the determination of the strengths of Lewis acid sites*. It has been shown that the method has general validity (at least for cationic sites without *d* electrons) and that it can be extended to evaluate the strengths of Brønsted sites (where the positive center is H⁺). The validity of the method for the determination of the Brønsted acid strength has been illustrated for zeolites (632). Nevertheless, in this review the Brønsted acidity of hydroxyl groups on oxidic surfaces is not discussed because most of the reported experiments have been performed with highly dehydroxylated surfaces.

The $\Delta\tilde{\nu}$ -*E* correlation cannot be extended straightforwardly to the interactions of CO with transition metal ions because, in addition to *d*- π overlap, backdonation can complicate the situation.

As discussed previously, the interaction of CO with positive centers with Lewis acidic character not only alters the frequency of CO but also modifies the static dipole and dynamic polarizability (α_v) of the CO. This is clearly demonstrated in Fig. 40, in which the dynamic polarizability of CO

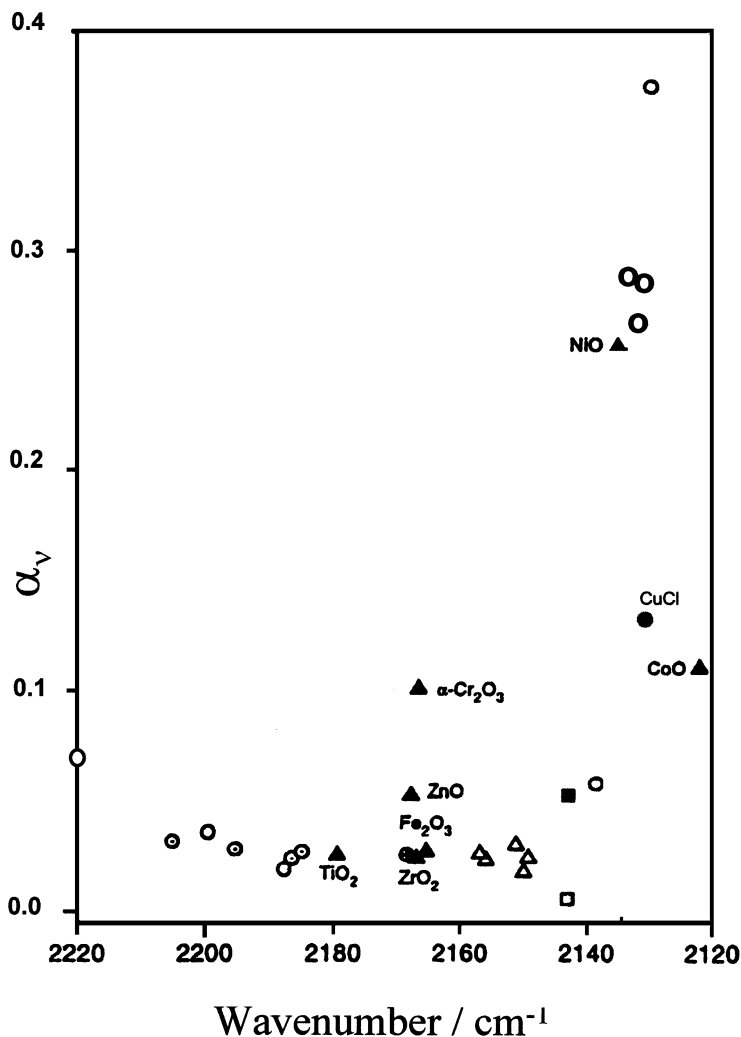


FIG. 40. Dynamic polarizability α_v as a function of $\tilde{\nu}(\text{CO})$ frequency of CO adsorbed on oxidic systems (transition metal oxides are included) [adapted from Zecchina *et al.* (22) with permission of Elsevier Science Publishers].

adsorbed on various oxides is reported as a function of the $\tilde{\nu}(\text{CO})$ frequency (498, 571). The results summarized in Fig. 40 demonstrate the following:

1. When the surface cation–CO interaction is mainly electrostatic, the dynamic polarizability increases slightly, in a linear fashion, with increasing

frequency (the change of α_v can be used to estimate the strength of the electric field and indirectly the Lewis acid strength as shown for the shift of the CO stretch).

2. When low-valent transition metal ions are involved (Ni^{2+} , Co^{2+} , and Cu^+), d - π overlap forces become important, and the dynamic polarizability is greatly enhanced. In this case, the CO cannot be considered as a good probe of Lewis acid strength (the stretching frequency is close to or even less than that of CO gas).

The explanation for the abrupt increase of α_v illustrated in Fig. 40 can be understood if we consider that the dynamic polarizability is proportional to the charge oscillation from the surface to the molecule (and vice versa) that occurs during the vibrational motion and that this charge oscillation is greatly favored by d - π overlap forces (via the so-called donation-backdonation mechanism). The position of the value for CO- Cr^{3+} in the diagram is most striking; it confirms that electrostatic forces dominate, and it also suggests that a small d - π contribution is present as well. Furthermore, the α_v of CO adsorbed on ZnO seems to be slightly higher than expected on the basis of a purely electrostatic model.

Molar extinction coefficients of adsorbed CO (ϵ_{CO}) have been carefully determined for $\text{M}^{n+} \cdots \text{CO}$ adducts on several oxides. A moderate monotonic increase of ϵ_{CO} with increasing $\tilde{\nu}(\text{CO})$ was found in the 2250- to 2150- cm^{-1} interval. Only for high $\tilde{\nu}(\text{CO})$ values (greater than about 2240 cm^{-1}) was a more significant increase of ϵ_{CO} reported (633). The moderate and monotonic increase in the 2250- to 2150- cm^{-1} range is similar to that found independently for α_v . This is expected, since α_v and ϵ are related through the equation

$$\epsilon_{\text{CO}} = 4\pi^3 \alpha_v \tilde{\nu}^2 \quad (14)$$

The linear relationships between $\Delta\tilde{\nu}$ and E and between $\Delta\alpha_v$ and E illustrated so far represent useful and fast, but nevertheless indirect, methods for establishing a scale of the Lewis acid strengths of oxide and halide surfaces. These correlations need to be substantiated by a direct estimation of the cation-CO interaction energy. This has been done by Bolis *et al.* (17, 69) by studying the relationship between the adsorption enthalpy of CO on metal oxides and oxidic systems and the CO stretching frequency shifts (Table II). The data reported in Table II and Fig. 41 show a good linear correlation, with the corresponding best fit giving the following relationship (where $\Delta\tilde{\nu}(\text{CO})$ is in cm^{-1} and $\Delta H_{\text{ads}}^\circ$ is in kJ mol^{-1}):

$$\Delta\tilde{\nu}(\text{CO}) = -1.015 \Delta H_{\text{ads}}^\circ - 3.7 \quad (15)$$

The good linearity of the data plotted in Fig. 41 ($R = 0.977$) and the fact that the intercept, at $-\Delta H_{\text{ads}}^\circ = 0 \text{ kJ mol}^{-1}$, is nearly 0 cm^{-1} is remarkable.

TABLE II
*Molar Standard Enthalpies of Adsorption ($\Delta H_{\text{ads}}^{\circ}$) and Stretching Frequency Shifts [$\Delta\bar{\nu}(\text{CO})$]
of CO Adsorbed on Various d , d^0 , and d^{10} Metal Ions*

Sample	$-\Delta H_{\text{ads}}^{\circ}$ (kJ mol ⁻¹)	$\Delta\bar{\nu}(\text{CO})$ (cm ⁻¹)	Reference
CO gas	0	0	Ewing (634)
NaCl	20	16	Bolis <i>et al.</i> (635)
KZSM-5 zeolite	28	23	Bolis <i>et al.</i> (636)
NaY zeolite	24	26	Egerton and Stone (637, 638)
NaY zeolite	30	26	Bolis <i>et al.</i> (635)
BaY zeolite	35	24	Egerton and Stone (637, 638)
NaZSM-5 zeolite	38	35	Bolis <i>et al.</i> (636)
CaY zeolite	45	42	Egerton and Stone (637, 638)
Ce ²⁺ -doped Al ₂ O ₃	43	41	Bolis <i>et al.</i> (17)
Ca ²⁺ -doped Al ₂ O ₃	45	42	Bolis <i>et al.</i> (69)
ZnO	46	39	Bolis <i>et al.</i> (635)
CaY zeolite	51	51	Bolis <i>et al.</i> (635)
TiO ₂ (site \diamond) ^a	53	44	Bolis <i>et al.</i> (635)
Al ₂ O ₃ (site A) ^a	58	62	Bolis <i>et al.</i> (69)
ZnY zeolite	59	64	Bolis <i>et al.</i> (635)
TiO ₂ (site \diamond) ^a	61	52	Bolis <i>et al.</i> (635)
ZnY zeolite	71	64	Egerton and Stone (637, 638)
TiO ₂ (site \diamond)	71	65	Bolis <i>et al.</i> (635)
Al ₂ O ₃ (site B) ^a	73	72	Bolis <i>et al.</i> (69)
Al ₂ O ₃ (site C) ^a	83	87	Bolis <i>et al.</i> (69)

^aFor the definition of the surface site, see the corresponding reference.

It must be considered that (i) the IR spectra reported in the cited references have typical resolutions of about 2 cm⁻¹; (ii) calorimetric measurements are made at a well-defined temperature (typically, 303 K), whereas IR spectra are only nominally collected at room temperature since the heating effect of the IR beam on the sample is not precisely known; and (iii) in the presence of different adspecies, the estimated heat values are not likely to correspond to the $\theta = 0$ limit. These results clearly demonstrate that the spectroscopic method for the establishment of reasonable Lewis acid strengths of oxides is based on solid ground. We emphasize here that the electric field sensed by the probe molecule at a given site is always the result of the sum of contributions from the cation and from the surrounding anions; consequently, what is probed is never a property of a single ion. The same consideration holds for calorimetric measurements.

The situation regarding a base strength scale (Lewis and Brønsted) is far more complex and less well developed than that regarding Lewis acid strengths. A spectroscopically simple, versatile, and universal probe has not yet been found (although many probe molecules, including CO and methane,

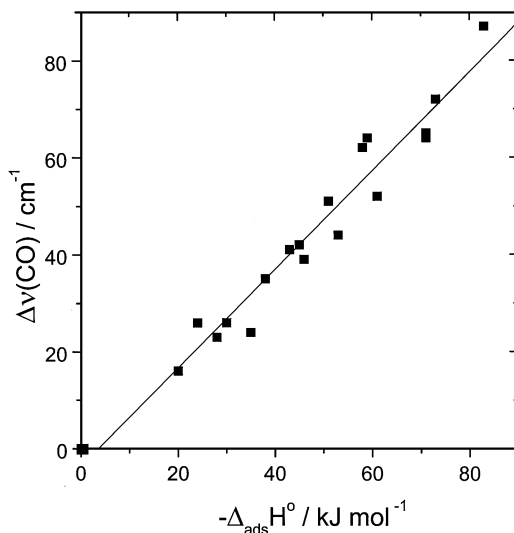


FIG. 41. CO stretching frequency shift vs molar standard enthalpies of adsorption for CO adsorbed on various d , d^0 , and d^{10} metal ions (from data reported in refs. 17, 68, 635, 636, and 638).

have been found to respond selectively in some cases to the perturbation caused by negatively charged centers).

XIV. Conclusions

One of the aims of this review was to illustrate the links between the growing field of the surface science of oxides and halides and the field of the surface properties of dispersed materials consisting of crystallites with dimensions of nanometers. We hope to have shown that the connection between the two domains is stronger than has been expected and that it is developing strongly with the evolution in understanding of surface properties (obtained by means of vibrational spectroscopy of suitably chosen molecular probes such as CO, N₂, and H₂) of crystallites of increasing dimension and perfection. For this purpose the evolution upon sintering of the samples of the spectra of molecular probes adsorbed on MgO, NiO, NaCl, α -chromia, Cu₂O, ZnO, TiO₂, and ZrO₂ among others, has been examined in detail. CO has been used preferentially as a probe of the surface properties (as indicated by the modifications of the vibrational properties induced by the adsorption process. Other simple molecules, such as NO, N₂, H₂, CO₂, O₂, and ethene, have been used less frequently to probe surface reactivity, but they also offer

excellent prospects. A common conclusion is emerging: Oxides and halides sintered at high temperature all expose the thermodynamically stable low-index faces characterized by the highest stability.

When probed with the weak base CO, the surface chemistry of these stable faces appears to be dominated by the weak Lewis acid properties of the surface cations. The weak bond between CO and a surface cation is essentially electrostatic. The same holds true for N₂ and H₂ used as probes of the surface fields. These faces are quite unreactive and not very promising as catalysts. Stronger interactions are observed for cations located at structural defects (such as steps and corners) or artificially introduced defects (foreign ions on or in solid solutions, electron-rich centers etc.). These centers are natural candidates catalysts. There are a few exceptions to the preceding rules: For example, Cu⁺ on Cu₂O or CuCl, Cr²⁺ on silica, and Zn²⁺ on ZnO (all characterized by low coordination) bind CO by chemical forces (of the σ or σ - π type). Transition metal ions exposed at the surfaces of oxides are more reactive than their non-*d* counterparts. Defect sites (including those generated by introduction of surface impurities such as sulfate groups) play an important role in determining the surface reactivity (although this review is far from exhaustive on this point).

We believe that detailed knowledge of the structures of frequently exposed surfaces that is emerging from comparisons of the spectra of the same molecules adsorbed on both dispersed materials and single crystals is the starting point and the basis for further understanding of the catalytic events occurring at the surface of oxides and halides.

ACKNOWLEDGMENTS

This work is part of projects coordinated by A. Zecchina and G. Gzorozi cofinanced by Italian MURST (Cofin 1998 and 2000, Area 03). We are indebted to V. Bolis, R. Dovesi, E. Giamello, C. Morterra, and P. Ugliengo for helpful discussions. We thank S. Bertarione, R. Gimondo, and A. Damin for performing some of the unpublished experiments and computer modeling.

REFERENCES

1. Henrich, V. E., and Cox, P. A., "The Surface Science of Metal Oxides." Cambridge Univ. Press, Cambridge, UK, 1994.
2. Noguera, C., "Physics and Chemistry at Oxide Surface" Cambridge Univ. Press, Cambridge, UK, 1996.
3. Freund, H.-J., *Angew. Chem., Int. Edit. Engl.* **36**, 452 (1997).
4. Winkelmann, F., Wolrab, S., Libuda, J., Baumer, M., Cappus, D., Menges, M., Al-Shamery, K., Kühlenbeck, H., and Freund, H. J., *Surf. Sci.* **307-309**, 1148 (1994).
5. Freund, H. J., Dillman, B., Seiferth, O., Klivenyi, G., Bender, M., Ehrlich, D., Hemmerich, I., and Cappus, D., *Catal. Today* **32**, 1 (1996).
6. Barteau, M. A., *Chem. Rev.* **96**, 1413 (1996).

7. Xu, C., and Goodman, D. W., in "Handbook of Heterogeneous Catalysis" (G. Ertl, H. Knözinger, and J. Weitkamp, Eds.), Vol. 2, p. 826. Wiley-VCH, Weinheim, 1997.
8. Sauer, J., Ugliengo, P., Garrone, E., and Saunders, V. R., *Chem. Rev.* **94**, 2095 (1994).
9. Van Santen, R. A., and Kramer, G. J., *Chem. Rev.* **95**, 637 (1995).
10. Zecchina, A., S. C., and Morterra, C., *Appl. Spectrosc. Rev.* **21**, 259 (1985).
11. Zecchina, A., Garrone, E., and Guglielminotti, E., in "Catalysis" (G. C. Bond, and G. Webb, Eds.), Vol. 6, p. 90. Royal Society of Chemistry, London, 1983.
12. Morterra, C., and Magnacca, G., *Catal. Today* **27**, 497 (1996).
13. Zaki, M. I., and Knözinger, H., *J. Catal.* **119**, 311 (1989).
14. Mestl, G., and Knözinger, H., in "Handbook of Heterogeneous Catalysis" (G. H. Ertl, H. Knözinger, and J. Weitkamp, Eds.), Vol. 2, p. 539. Wiley-VCH, Weinheim, 1997.
15. Knözinger, H., in "Handbook of Heterogeneous Catalysis" (G. Ertl, H. Knözinger, and J. Weitkamp, Eds.), Vol. 2, p. 707. Wiley-VCH, Weinheim, 1997.
16. Lavallay, J. C., *Catal. Today* **27**, 377 (1996).
17. Bolis, V., Cerrato, G., Magnacca, G., and Morterra, C., *Thermochim. Acta* **312**, 63 (1998).
18. Cardona-Martinez, M., and Dumesic, J. A., *Adv. Catal.* **38**, 149 (1992).
19. Roquerol, J., *Pure Appl. Chem.* **47**, 315 (1976).
20. Corma, A., *Chem. Rev.* **95**, 559 (1995).
21. Busca, G., *Phys. Chem. Chem. Phys.* **1**, 723 (1999).
22. Zecchina, A., Scarano, D., Bordiga, S., Ricchiardi, G., Spoto, G., and Geobaldo, F., *Catal. Today* **27**, 403 (1996).
23. Zecchina, A., Scarano, D., and Bordiga, S., in "Handbook of Heterogeneous Catalysis" (G. Ertl, H. Knözinger, and J. Weitkamp, Eds.), Vol. 2, p. 728. Wiley-VCH, Weinheim, 1997.
24. West, A. R., "Basic Solid State Chemistry," Wiley, New York, 1997.
25. Cimino, A., and Stone, F. S., in "Handbook of Heterogeneous Catalysis" (G. Ertl, H. Knözinger, and J. Weitkamp, Eds.), Vol. 2, p. 845. Wiley-VCH, Weinheim, 1997.
26. Boccuzzi, F., Morterra, C., Scala, R., and Zecchina, A., *J. Chem. Soc. Faraday Trans. II* **2059**, (1981).
27. Goodenough, J. B., in "Progress in Solid State Chemistry" (H. Reiss, Ed.), Vol. 5, p. 145. Pergamon, Oxford, 1971.
28. Zhou, W., Jefferson, D. A., and Liang, W. Y., *Surf. Sci.* **209**, 444 (1989).
29. Islam, M. S., Ilett, D. J., and Parker, S. C., *J. Phys. Chem.* **98**, 9637 (1994).
30. Thomas, J. M., and Thomas, W. J., "Principles and Practice of Heterogeneous Catalysis." VCH, Weinheim, 1997.
31. Rao, C. N. R., and Gopalakrishnan, J., in "Cambridge Solid State Series" (R. W. Cahn, E. A. Davis, and I. M. Ward, Eds.), p. 32. Cambridge Univ. Press, Cambridge, UK, 1986.
32. Marchese, L., Bordiga, S., Coluccia, S., Martra, G., and Zecchina, A., *J. Chem. Soc. Faraday Trans.* **89**, 3483 (1993).
33. Singh, K. K., and Edwards, P. P., *Adv. Solid State Chem.* **3**, 99 (1993).
34. Tejuca, L. G., Fierro, J. L. G., and Tascón, J. M. D., *Adv. Catal.* **36**, 237 (1989).
35. Linsebigler, A. L., Guangquan, L., and Yates, J. T., Jr., *Chem. Rev.* **95**, 735 (1995).
36. Anpo, M., and Che, M., *Adv. Catal.* **44**, 119 (1999).
37. Spoto, G., Morterra, C., Marchese, L., Orio, L., and Zecchina, A., *Vacuum* **41**, 37 (1990).
38. Hadjiivanov, K. I., Davydov, A. A., and Klissurski, D. G., *Kinet. Catal.* **29**, 140 (1988).
39. Hadjiivanov, K. I., and Klissurski, D. G., *Chem. Soc. Rev.*, **25**, 61 (1996).
40. Yin, X., Miura, R., Endou, A., Gunji, I., Yamaguchi, R., Kubo, M., Stirling, A., Fahmi, A., and Miyamoto, A., *Appl. Surf. Sci.* **119**, 199 (1997).
41. Morterra, C., *J. Chem. Soc. Faraday Trans. I* **84**, 1617 (1988).
42. Luke, B. T., *J. Phys. Chem.* **97**, 7505 (1993).

43. Bär, M. R., and Sauer, J., *J. Chem. Phys. Lett.* **226**, 405 (1994).
44. Leonardelli, S., Facchini, L., Fretigny, C., Tougne, P., and Legrand, A. P., *J. Am. Chem. Soc.* **114**, 6412 (1992).
45. McDaniel, P. M., in "Handbook of Heterogeneous Catalysis" (G. Ertl, H. Knözinger, and J. Weitkamp, Eds.), Vol. 5, p. 2400. Wiley-VHC, Weinheim, 1997.
46. Knözinger, H., in "The Hydrogen Bond. Recent Developments in Theory and Experiments" (P. Schuster, G. Zundel, and C. Sandorfy, Eds.), Vol. 3, p. 1263. North-Holland, Amsterdam, 1976.
47. Datye, A. K., in "Handbook of Heterogeneous Catalysis" (G. Ertl, H. Knözinger, and J. Weitkamp, Eds.), Vol. 2, p. 493. Wiley-VCH, Weinheim, 1997.
48. Heidberg, J., Kampshoff, E., Kühnemund, R., Suhren, M., and Weiss, H., *Surf. Sci.* **269/270**, 128 (1992).
49. Richardson, H. H., and Ewing, G. E., *J. Phys. Chem.* **91**, 5833 (1987).
50. Donnay, J. D. H., and Harker, D., *J. Mineral Soc. Am.* **22**, 446 (1937).
51. Donnay, J. D. H., *Compt. Rend. Acad. Sci.* **252**, 908 (1961).
52. Hartman, P., *Acta Cryst.* **11**, 459 (1958).
53. Gay, D. H., and Rohl, A., *J. Chem. Soc. Faraday Trans.* **91**, 925 (1995).
54. Dovesi, R., Saunders, VV. R., Roetti, C., Causà, M., Harrison, N. M., Orlando, R., Zicovich-Wilson, C. M., CRYSTAL98 user's manual, University of Torino, Torino, 1998.
55. Hush, N. S., and Williams, M. L., *J. Mol. Spectrosc.* **50**, 349 (1974).
56. Pacchioni, G., Cogliandro, G., and Bagus, P. S., *Int. J. Quant. Chem.* **42**, 1115 (1992).
57. Gravelle, P. C., *Adv. Catal.* **22**, 191 (1972).
58. Fubini, B., *Thermochim. Acta* **135**, 19 (1988).
59. Ge, Q., Kose, R., and King, D. A., *Adv. Catal.* **45**, 207 (2000).
60. Bolis, V., Fubini, B., Garrone, E., and Morterra, C., *J. Chem. Soc. Faraday Trans.* **185**, 1383 (1989).
61. Bolis, V., Morterra, C., Volante, M., Orio, L., and Fubini, B., *Langmuir* **6**, 695 (1990).
62. Morterra, C., Bolis, V., and Magnacca, G., *J. Chem. Soc. Faraday Trans.* **92**, 1991 (1996).
63. Wintterlin, J., *Adv. Catal.* **42**, 131 (2000).
64. Bolis, V., Fubini, B., Giamello, E., and Reller, A., *J. Chem. Soc. Faraday Trans. I* **85**, 855 (1989).
65. Bolis, V., Fubini, B., and Giamello, E., *Mater. Chem. Phys.* **29**, 153 (1991).
66. Morterra, C., Cerrato, G., Bolis, V., and Fubini, B., *Spectrochim. Acta A* **49**, 1269 (1993).
67. Morterra, C., Bolis, V., and Magnacca, G., *Langmuir* **10**, 1812 (1994).
68. Morterra, C., Magnacca, G., Bolis, V., Cerrato, G., Baricco, M., Gianchello, A., and Fucale, M., *Stud. Surf. Sci. Catal.* **96**, 361 (1995).
69. Bolis, V., Magnacca, G., and Morterra, C., *Res. Chem. Intermed.* **25**, 25 (1999).
70. Tanabe, K., and Hölderich, W. F., *Appl. Catal. A* **181**, 359 (1999).
71. Hall, P., in "Handbook of Heterogeneous Catalysis" (G. Ertl, H. Knözinger, and J. Weitkamp, Eds.), Vol. 2, p. 689. Wiley-VCH, Weinheim, 1997.
72. Zecchina, A., Lamberti, C., and Bordiga, S., *Catal. Today* **41**, 169 (1998).
73. Escalona Platero, E., Scarano, D., Spoto, G., and Zecchina, A., *Faraday Discuss. Chem. Soc.* **80**, 183 (1985).
74. Zecchina, A., Garrone, E., and Guglielminotti, E., in "Catalysis," Vol. 6, p. 90. Royal Society of Chemistry, London, 1983.
75. Zecchina, A., and Otero Areán, C., *Catal. Rev.-Sci. Eng.* **35**, 261 (1993).
76. Colbourn, E. A., *Surf. Sci. Rep.* **15**, 281 (1992).
77. Scarano, D., Ricchiardi, G., Bordiga, S., Galletto, P., Lamberti, C., Spoto, G., and Zecchina, A., *Faraday Discuss. Chem. Soc.* **105**, 119 (1996).
78. Parker, S. C., Kelsey, T. E., Oliver, P. M., and Titiloye, J. O., *Faraday Discuss. Chem. Soc.* **95**, 75 (1993).

79. Zecchina, A., Scarano, D. P. G., and Lamberti, C., *Nuovo Cimento D* **19**, 1773 (1997).
80. Ertl, G., *Science* **254**, 1750 (1991).
81. Freund, H. J., Bäumer, M., and Kuhlenbeck, H., *Adv. Catal.* **42**, 334 (2000).
82. Idriss, H., and Barteau, M. A., *Adv. Catal.* **45**, 262 (2000).
83. Iwasawa, Y., in "Handbook of Heterogeneous Catalysis" (G. Ertl, H. Knözinger, and J. Weitkamp, Eds.), Vol. 2, p. 853. Wiley-VCH, Weinheim, 1997.
84. Modie, A. F., and Warble, C. E., *J. Cryst. Growth* **10**, 26 (1974).
85. Coluccia, S., Baricco, M., Marchese, L. G. M., and Zecchina, A., *Spectrochim. Acta A* **49**, 1289 (1993).
86. Marchese, L., Coluccia, S. G. M., and Zecchina, A., *Surf. Sci.* **269/270**, 135 (1992).
87. Scarano, D., Spoto, G., Bordiga, S., Coluccia, S., and Zecchina, A., *J. Chem. Soc. Faraday Trans.* **88**, 291 (1992).
88. Coluccia, S., and Marchese, L., *Catal. Today* **41**, 229 (1998).
89. Kölbl, H., Ralek, M., and Jiru, P., *Z. Naturforsch. A* **25**, 670 (1970).
90. Smart, R. S. C., Slager, T., Little, L. H., and Greenler, R. G., *J. Phys. Chem.* **77**, 1019 (1973).
91. Guglielminotti, E., Coluccia, S., Garrone, E., Cerruti, L., and Zecchina, A., *J. Chem. Soc. Faraday Trans.* **1** **75**, 96 (1979).
92. Zaki, M. I., and Knözinger, H., *Spectrochim. Acta A* **43**, 1455 (1987).
93. Zecchina, A., Coluccia, S., Spoto, G., Scarano, D., and Marchese, L., *J. Chem. Soc. Faraday Trans.* **86**, 703 (1990).
94. Babaeva, M. A., Bystrov, D. S., Kovaligia, A. Y., and Tsyganenko, A. A., *J. Catal.* **123**, 396 (1990).
95. Yoshinobu, J., Ballinger, T. H., Xu, Z., Jänsch, H. J., Zaki, M. I., Xu, J., and Yates, J. T., *Surf. Sci.* **255**, 295 (1991).
96. Ito, T., Kobayashi, H., and Tashiro, T., *Nuovo Cimento D* **19**, 1695 (1997).
97. Lunsford, J. H., and Jayne, J. P., *J. Chem. Phys.* **44**, 1492 (1966).
98. Morris, R. M., Kaba, R. A., Groshens, T. G., Klabunde, K. J., Blatisberger, R. T., Woolsey, N. F., and Stenberg, V. I., *J. Am. Chem. Soc.* **102**, 3419 (1980).
99. Morris, R. M., and Klabunde, K. J., *J. Am. Chem. Soc.* **105**, 2633 (1983).
100. Zecchina, A., and Stone, F. S., *J. Chem. Soc. Chem. Comm.*, 582 (1974).
101. Zecchina, A., and Stone, F. S., *J. Chem. Soc. Faraday Trans. I* **74**, 2278 (1978).
102. Bailes, M., and Stone, F. S., *Mater. Chem. Phys.* **29**, 489 (1991).
103. Huzimura, R., Yianigisawa, Y., Matsumura, K., and Yamabe, S., *Phys. Rev. B* **41**, 3786 (1990).
104. Larson, R., Lykvist, R., and Rebenstorf, B., *Z. Phys. Chem. N. F.* **263**, 6 (1982).
105. Dixon, D. A., Gole, J. L., and Komornicki, A., *J. Phys. Chem.* **92**, 1378 (1988).
106. Hauge, R. H., Gronsdén, S. E., and Margrave, J. L., *J. Chem. Soc. Dalton Trans.*, 745 (1979).
107. Paukshits, E. A., Soltanov, R. I., and Yurchenko, N. E., *Reaction Kinet. Catal. Lett.* **16**, 93 (1981).
108. Paukshits, E. A., and Yurchenko, N. E., *Usp. Khim.* **52**, 426 (1983).
109. Paukshits, E. A., and Yurchenko, N. E., *Russian Chem. Rev.* **52**, 426 (1983).
110. Furuyama, S., Fujii, H., Kawamura, M., and Morimoto, T., *J. Phys. Chem.* **82**, 1028 (1978).
111. Henry, R., Chapon, C., and Duriez, C., *J. Chem. Phys.* **95**, 700 (1991).
112. He, J. W., Estrada, C. A., Corneille, J. S., Wu, M. C., and Goodman, D. W., *Surf. Sci.* **261**, 164 (1992).
113. He, J. W., Corneille, J. S., Estrada, C. A., Wu, M. C., and Goodman, D. W., *J. Vac. Sci. Technol. A* **10**, 2248 (1992).
114. Wichtendahl, R., Rodríguez-Rodrigo, M., Härtel, U., Kuhlenbeck, H., and Freund, H. J., *Phys. Stat. Sol. A* **173**, 93 (1999).
115. Wichtendahl, R., Rodríguez-Rodrigo, M., Härtel, U., Kuhlenbeck, H., and Freund, H. J., *Surf. Sci.* **423**, 90 (1999).

116. Redhead, P. A., *Vacuum* **12**, 203 (1962).
117. Audibert, P., Sidoumou, M., and Suzanne, J., *Surf. Sci. Lett.* **273**, L467 (1992).
118. Gerlach, R., Glebov, A., Lange, G., Toennies, J. P., and Weiss, H., *Surf. Sci.* **331–333**, 1490 (1995).
119. Heidberg, J., Kandel, M., Meine, D., and Wildt, U., *Surf. Sci.* **331–333**, 1467 (1995).
120. Dovesi, R., Orlando, R., Ricca, F., and Roetti, C., *Surf. Sci.* **186**, 267 (1987).
121. Pacchioni, G., Neyman, K. M., and Rösch, N., *J. Electron Spectrosc. Related Phenom.* **69**, 13 (1994).
122. Nygren, M. A., Pettersson, L. G. M., Barandiarán, Z., and Seijo, L., *J. Chem. Phys.* **100**, 2010 (1994).
123. Nygren, M. A., and Pettersson, L. G. M., *J. Chem. Phys.* **105**, 9339 (1996).
124. Mejias, J. A., Márquez, A. M., Fernández Sanz, J., Fernández-García, M., Ricart, J. M., Sousa, C., and Illas, F., *Surf. Sci.* **327**, 59 (1995).
125. Neyman, K. M., Ruzankin, S. P., and Rösch, N., *Chem. Phys. Lett.* **246**, 546 (1995).
126. Pelmenchikov, A. G., Morosi, G., Gamba, A., and Coluccia, S., *J. Phys. Chem. B* **102**, 2226 (1998).
127. Yudanov, I. V., Ruzankin, S. P., Neyman, K. M., and Rösch, N., *Int. J. Quantum Chem.* **65**, 975 (1997).
128. Illas, F., Pacchioni, G., Pelmenchikov, A. G., Pettersson, L. G. M., Dovesi, R., Pisani, C., Neyman, K. M., and Rösch, N., *Chem. Phys. Lett.* **306**, 202 (1999).
129. Heidberg, J., Kandel, M., Meine, D., Redlich, B., and Wetter, D., Paper presented at the International Workshop on Oxide Surfaces, Schloss Elmau, 1999.
130. Noda, C., Richardson, H. H., and Ewing, G. E., *J. Chem. Phys.* **92**, 2099 (1990).
131. Noda, C., and Ewing, G. E., *Surf. Sci.* **240**, 181 (1990).
132. Disselkamp, R., Chang, H.-C., and Ewing, G. E., *Surf. Sci.* **240**, 193 (1990).
133. Joshi, A. B., and Norton, M. G., *Appl. Surf. Sci.* **115**, 307 (1997).
134. Sangwal, K., Sanz, F., Servat, J., and Gorostiza, P., *Surf. Sci.* **383**, 78 (1997).
135. Perry, S. S., and Merrill, P. B., *Surf. Sci.* **383**, 268 (1997).
136. Hammaker, R. A., Francis, S. A., and Eischens, R. P., *Spectrochim. Acta* **21**, 1295 (1965).
137. Crosseley, A., and King, D. A., *Surf. Sci.* **68**, 528 (1977).
138. Mahan, G. D., and Lucas, A. A., *J. Chem. Phys.* **68**, 1344 (1978).
139. Persson, B. N. J., and Ryberg, R., *Phys. Rev. B* **24**, 6954 (1981).
140. Griffin, G. L., and Yates, J. T., *J. Chem. Phys.* **77**, 3751 (1982).
141. Seanor, D. A., and Amberg, C. H., *J. Chem. Phys.* **42**, 2967 (1965).
142. Coluccia, S., Boccuzzi, F., Ghiotti, G., and Morterra, C., *J. Chem. Soc. Faraday Trans. 1* **78**, 2111 (1982).
143. Coluccia, S., *Z. Phys. Chem. Neue Folge* **121**, 141 (1980).
144. Knözinger, E., Jacob, K. H., and Hofmann, P., *J. Chem. Soc. Faraday Trans.* **89**, 1101 (1993).
145. Garrone, E., and Stone, F. S., *J. Chem. Soc. Faraday Trans. 1* **83**, 1237 (1987).
146. Paganini, M. C., Chiesa, M., Giamello, E., Coluccia, S., Martra, G., Murphy, D., and Pacchioni, G., *Surf. Sci.* **421**, 246 (1999).
147. Garrone, E., Zecchina, A., and Stone, F. S., *J. Chem. Soc. Faraday Trans. 1* **80**, 2723 (1984).
148. Che, M., Coluccia, S., and Zecchina, A., *J. Chem. Soc. Faraday Trans. 1* **73**, 1324 (1977).
149. Trablesi, M., Coulomb, J. P., Degenhardt, D., and Lauter, H., *Surf. Sci.* **377–379**, 38 (1997).
150. Angot, T., and Suzanne, J., in "The Structure of Surfaces III," Vol. 24, p. 671. Springer-Verlag, Heidelberg, 1991.
151. Cerruti, L., Modone, E., Guglielminotti, E., and Borello, E., *J. Chem. Soc. Faraday Trans. 1* **70**, 729 (1974).
152. Kortüm, G., and Quabeck, H., *Berlin Bunsenges. Phys. Chem.* **73**, 1020 (1969).
153. Escalona Platero, E., Spoto, G., and Zecchina, A., *J. Chem. Soc. Faraday Trans. 1* **81**, 1283 (1985).

154. Lunsford, J. H., *J. Chem. Phys.* **46**, 4437 (1967).
155. Zecchina, A., Lofthouse, M. G., and Stone, F. S., *J. Chem. Soc. Faraday Trans. I* **71**, 1476 (1975).
156. Garrone, E., Guglielminotti, E., Zecchina, A., and Giamello, E., *J. Chem. Soc. Faraday Trans. I* **80**, 2723 (1984).
157. Garrone, E., and Stone, F. S., *Stud. Surf. Sci. Catal.* **21**, 97 (1985).
158. Ugliengo, P., Garrone, E., and Giamello, E., *Z. Phys. Chem. Neue Folge* **152**, 284 (1987).
159. Garrone, E., Zecchina, A., and Stone, F. S., *J. Chem. Soc. Faraday Trans. I* **84**, 2843 (1988).
160. Ramis, G., Busca, G., and Lorenzelli, V., *Mater. Chem. Phys.* **29**, 425 (1991).
161. Tench, A. J., and Giles, D., *J. Chem. Soc. Faraday Trans. I* **68**, 103 (1972).
162. Coluccia, S., Garrone, E., and Borello, E., *J. Chem. Soc. Faraday Trans. I* **79**, 607 (1983).
163. Coluccia, S., Lavagnino, S., and Marchese, L., *J. Chem. Soc. Faraday Trans. I* **83**, 477 (1987).
164. Borello, E., Coluccia, S., and Zecchina, A., *J. Catal.* **93**, 331 (1985).
165. Garrone, E., Marchese, L., and Giamello, E., *Spectrochim. Acta A* **43**, 1567 (1987).
166. Martra, G., Borello, E., Giamello, E., and Coluccia, S., *Stud. Surf. Sci. Catal.* **90**, 169 (1994).
167. Thiel, A., and Madey, T. E., *Surf. Sci. Rep.* **7**, 211 (1987).
168. Brown, G. E., Jr., Henrich, V. E., Casey, W. H., Clark, D. L., Eggleston, C., Felmy, A., Goodman, D. W., Grätzel, M., Maciel, G., McCarthy, M. I., Nealsen, K. H., Sverjensky, D. A., Toney, M. F., and Zachara, J. M., *Chem. Rev.* **99**, 77 (1999).
169. Anderson, P. J., Horlock, R. F., and Oliver, J. F., *J. Chem. Soc. Faraday Trans. I* **61**, 2754 (1965).
170. Coluccia, S., Marchese, L., Lavagnino, S., and Ampo, M., *Spectrochim. Acta A* **43**, 1573 (1987).
171. Coluccia, S., Lavagnino, S., and Marchese, L., *Mater. Chem. Phys.* **18**, 455 (1988).
172. Echterhoff, R., and Knözinger, E., *J. Mol. Struct. TEOCHEM* **174**, 343 (1988).
173. Knözinger, E., Jacob, K.-H., Singh, S., and Hofmann, P., *Surf. Sci.* **290**, 288 (1993).
174. Goniakowski, J., Russo, S., and Noughera, C., *Surf. Sci.* **284**, 315 (1993).
175. Thiel, A., and Madey, T. E., *Chem. Phys. Lett.* **209**, 340 (1993).
176. Scamehorn, C. A., Hess, A. C., and McCarthy, M. I., *J. Chem. Phys.* **99**, 2786 (1993).
177. Scamehorn, C. A., Hess, A. C., and McCarthy, M. I., *J. Chem. Phys.* **103**, 1547 (1994).
178. Langel, W., and Parinello, M., *J. Chem. Phys.* **103**, 3240 (1994).
179. Anchell, J. L., and Hess, A. C., *J. Phys. Chem.* **100**, 18317 (1996).
180. Russo, S., and Noughera, C., *Surf. Sci.* **262**, 245 (1992).
181. Refson, K., Wogelius, R. A., Fraser, D. G., Payne, M. C., Lee, M. H., and Milman, V., *Phys. Rev. B* **52**, 10823 (1995).
182. Ferry, D., Glebov, A., Senz, V., Suzanne, J., Toennies, J. P., and Weiss, H., *Surf. Sci.* **377-379**, 377 (1997).
183. Ferry, D., Glebov, A., Senz, V., Suzanne, J., Toennies, J. P., and Weiss, H., *J. Chem. Phys.* **105**, 1697 (1995).
184. Heidberg, J., Redlich, B., and Wetter, D., *Berlin Bunsenges. Phys. Chem.* **99**, 1333 (1995).
185. Coustet, V., and Jupille, J., *Surf. Interface Anal.* **22**, 280 (1994).
186. Coustet, V., and Jupille, J., *Nuovo Cimento D* **19**, 1657 (1997).
187. Xu, C., Estrada, C. A., and Goodman, D. W., *Phys. Rev. Lett.* **67**, 2910 (1991).
188. Abriou, D., and Jupille, J., *Surf. Sci. Lett.* **430**, L527 (1999).
189. Xu, C., and Goodman, D. W., *Chem. Phys. Lett.* **265**, 341 (1997).
190. Ito, T., and Lunsford, J. H., *Nature* **314**, 721 (1985).
191. Driscoll, D. J., Martir, W., Wang, X.-J., and Lunsford, J. H., *J. Am. Chem. Soc.* **107**, 58 (1985).
192. Ito, T., Wang, X.-J., Lin, C.-H., and Lunsford, J. H., *J. Am. Chem. Soc.* **107**, 5062 (1985).

193. Ito, T., Tashiro, T., Kawasaki, M., Watanabe, T., Toi, K., and Kobayashi, H., *J. Phys. Chem.* **95**, 4476 (1991).
194. Li, C., Li, G., and Xin, Q., *J. Phys. Chem.* **98**, 1933 (1994).
195. Ferrari, A. M., Huber, S., Knözinger, H., Neyman, K. M., and Rösch, N., *J. Phys. Chem.* **102**, 4548 (1998).
196. Pelmenshikov, A. G., Morosi, G., Gamba, A., Coluccia, S., Martra, G., and Paukshitis, E. A., *J. Phys. Chem.* **100**, 5011 (1996).
197. Scarano, D., Zecchina, A., Bordiga, S., Lamberti, C., and Spoto, G., Paper presented at the International Workshop on Oxide Surfaces, Schloss Elmau, 1999.
198. Ferry, D., and Suzanne, J., *Surf. Sci. Lett.* **293**, L19 (1996).
199. Ferry, D., Suzanne, J., Hoang, P. N. M., and Girardet, C., *Surf. Sci.* **375**, 315 (1997).
200. Ferry, D., Hoang, P. N. M., Suzanne, J., Bibérian, J.-P., and Van Hove, M. A., *Phys. Rev. Lett.* **78**, 4237 (1997).
201. Lemberston, J. L., Perot, G., and Guisnet, M., *J. Catal.* **89**, 69 (1984).
202. Spoto, G., Bordiga, S., and Zecchina, A., *J. Mol. Catal.* **94**, 187 (1988).
203. Foyt, D. C., and White, J. M., *J. Catal.* **47**, 260 (1977).
204. Takezawa, N., Hanamaki, C., and Kobayashi, J., *J. Catal.* **38**, 101 (1975).
205. Liang, S. H. C., and Gay, I. D., *J. Catal.* **101**, 293 (1986).
206. Anpo, M., Yamada, Y., Doi, T., Matsuura, S., Coluccia, S., and Zecchina, A., *Stud. Surf. Sci. Catal.* **48**, 1 (1989).
207. Keller, G. E., and Bhasin, M. M., *J. Catal.* **73**, 9 (1982).
208. Ruckenstein, E., and Khan, A. Z., *J. Catal.* **141**, 628 (1993).
209. Amorebieta, V. T., and Colussi, A. J., *J. Phys. Chem.* **92**, 4576 (1988).
210. Børve, K. J., and Pettersson, L. G. M., *J. Phys. Chem.* **95**, 7401 (1991).
211. Børve, K. J., *J. Chem. Phys.* **95**, 4626 (1991).
212. Johnson, M. A., Stefanovich, E. V., and Truong, T. N., *J. Phys. Chem. B* **101**, 3196 (1997).
213. Wu, M.-C., Truong, C. M., Coulter, D., and Goodman, D. W., *J. Am. Chem. Soc.* **114**, 7565 (1992).
214. Wu, M.-C., Truong, C. M., and Goodman, D. W., *Phys. Rev. B* **46**, 12688 (1992).
215. Wu, M.-C., Truong, C. M., Coulter, D., and Goodman, D. W., *J. Vac. Sci. Technol. A* **11**, 2174 (1993).
216. Iwamatu, E., and Aika, K., *J. Catal.* **117**, 416 (1989).
217. Di Cosimo, J. I., Díez, V. K., and Apesteguía, C. R., *Appl. Catal. A* **137**, 149 (1994).
218. Thomasson, P., Tyagi, O. S., and Knözinger, H., *Appl. Catal. A* **181**, 181 (1999).
219. Lunsford, J. H., Yang, X., Haller, K., Laane, J., Mestl, G., and Knözinger, H., *J. Phys. Chem.* **97**, 13810 (1993).
220. Zhang, G., Hattori, K., and Tanabe, K., *Appl. Catal.* **36**, 189 (1988).
221. Vinek, H., Noller, H., Ebel, M., and Schwarz, K., *J. Chem. Soc. Faraday Trans. I* **73**, 734 (1977).
222. Hofmann, P., and Knözinger, E., *Nuovo Cimento D* **19**, 1687 (1997).
223. Lichanot, A., Larrieu, C., Zicovich-Wilson, C., Roetti, C., Orlando, R., and Dovesi, R., *J. Phys. Chem. Solids* **59**, 1119 (1998).
224. Murphy, D., Giamello, E., and Zecchina, A., *J. Phys. Chem.* **97**, 1739 (1993).
225. Nelson, R. L., and Tench, A. J., *Trans. Faraday Soc.* **63**, 3039 (1967).
226. Nelson, R. L., and Hale, J. W., *Discuss. Faraday Soc.* **52**, 77 (1971).
227. Tench, A. J., and Pitt, G. T., *Chem. Phys. Lett.* **26**, 590 (1974).
228. Coluccia, S., Deane, A. M., and Tench, A. J., *J. Chem. Soc. Faraday Trans.* **174**, 2913 (1978).
229. Giamello, E., Paganini, M. C., Murphy, D., Ferrari, A. M., and Pacchioni, G., *J. Phys. Chem. B* **101**, 971 (1997).
230. Giamello, E., Ferrero, A., Coluccia, S., and Zecchina, A., *J. Phys. Chem.* **95**, 9385 (1991).

231. Giamello, E., Murphy, D., Coluccia, S., and Zecchina, A., *J. Chem. Soc. Faraday Trans.* **90**, 3167 (1994).
232. Giamello, E., and Murphy, D., *J. Phys. Chem.* **99**, 15172 (1995).
233. Pacchioni, G., and Pescarmona, P., *Surf. Sci.* **412/413**, 675 (1998).
234. Pacchioni, G., Ferrari, A. M., and Ieranò, G., *Faraday Discuss.* **106**, 155 (1997).
235. Scorza, E., Birkenheuer, U., and Pisani, C., *J. Chem. Phys.* **107**, 9645 (1997).
236. Ojamäe, L., and Pisani, C., *J. Chem. Phys.* **109**, 10984 (1998).
237. Giamello, E., Murphy, D., Marchese, L., Martra, G., and Zecchina, A., *J. Chem. Soc. Faraday Trans.* **89**, 3715 (1993).
238. Giamello, E., Murphy, D., Garrone, E., and Zecchina, A., *Spectrochim. Acta A* **49**, 1323 (1993).
239. Zecchina, A., Scarano, D., Marchese, L., Coluccia, S., and Giamello, E., *Surf. Sci.* **194**, 531 (1988).
240. Marchese, L., Coluccia, S., Martra, G., Giamello, E., and Zecchina, A., *Mater. Chem. Phys.* **29**, 437 (1991).
241. Pacchioni, G., Ferrari, A. M., and Giamello, E., *Chem. Phys. Lett.* **255**, 58 (1996).
242. Giamello, E., Ugliengo, P., and Garrone, E., *J. Chem. Soc. Faraday Trans.* **185**, 1373 (1989).
243. Giamello, E., Garrone, E., Ugliengo, P., Che, M., and Tench, A. J., *J. Chem. Soc. Faraday Trans.* **185**, 3987 (1989).
244. Tench, A. J., and Che, M., *Adv. Catal.* **31**, 77 (1982).
245. Haber, J., in "Proceedings of the 8th International Conference on Catalysis" Vol. 1, p. 85, Dechema/VCH, Frankfurt/Weinheim, 1984.
246. Che, M., and Tench, A. J., *Adv. Catal.* **32**, 1 (1983).
247. Che, M., Giamello, E., and Tench, A. J., *Colloids Surf.* **13**, 231 (1985).
248. Anpo, M., Che, M., Fubini, B., Garrone, E., Giamello, E., and Paganini, M. C., *Topics Catal.* **8**, 189 (1999).
249. Coluccia, S., Garrone, E., Guglielminotti, E., and Zecchina, A., *J. Chem. Soc. Faraday Trans.* **177**, 1064 (1981).
250. Che, M., Tench, A. J., Coluccia, S., and Zecchina, A., *J. Chem. Soc. Faraday Trans.* **172**, 1553 (1976).
251. Chiesa, M., Paganini, M. C., Giamello, E., and Murphy, D. M., *Langmuir* **13**, 5306 (1997).
252. Nakamura, M., Mitsuhashi, H., and Takezawa, N., *J. Catal.* **138**, 686 (1992).
253. Winter, E. R. S., *J. Catal.* **19**, 32 (1970).
254. Snis, A., and Miettingen, H., *J. Phys. Chem. B* **102**, 2555 (1998).
255. Pacchioni, G., Ricart, J. M., and Illas, I., *J. Am. Chem. Soc.* **116**, 10152 (1994).
256. Garrone, E., and Stone, F. S., in "Proceedings of the 8th International Congress on Catalysis," Vol. 3, p. 441. Dechema/VCH, Frankfurt/Weinheim, 1984.
257. Garrone, E., Zecchina, A., and Stone, F. S., *J. Catal.* **62**, 396 (1980).
258. Coluccia, S., personal communication.
259. Zecchina, A., and Stone, F. S., *J. Catal.* **101**, (1986).
260. Escalona Platero, E., and Zecchina, A., *J. Catal.* **104**, 299 (1987).
261. Tanabe, K., and Nishizaki, T., in "Proceedings of the 6th International Congress on Catalysis" (C. G. Bond, P. B. Hells, and F. C. Thompkins, Eds.), p. 863. Chemical Society, London, 1977.
262. Armor, J. N., *Appl. Catal.* **78**, 141 (1991).
263. Zecchina, A., *Mater. Chem. Phys.* **13**, 379 (1985).
264. Ahdjoudj, J., Morkovits, A., and Minota, C., *Catal. Today* **50**, 541 (1999).
265. Escalona Platero, E., Scarano, D., Zecchina, A., Meneghini, G., and De Franceschi, R., *Surf. Sci.* **350**, 113 (1996).
266. Escalona Platero, E., Coluccia, S., and Zecchina, A., *Surf. Sci.* **171**, 465 (1986).

267. Escalona Platero, E., Coluccia, S., and Zecchina, A., *Langmuir* **1**, 407 (1985).
268. Pacchioni, G., Cogliandro, G., and Bagus, P. S., *Surf. Sci.* **255**, 344 (1991).
269. Neyman, K. M., and Rösch, N., *Chem. Phys.* **177**, 561 (1993).
270. Klier, K., *Collect. Czech. Chem. Commun.* **28**, 2996 (1963).
271. Cappus, D., Klinkmann, J., Kuhlénbeck, H., and Freund, H.-J., *Surf. Sci. Lett.* **325**, L421 (1995).
272. Veaecky, S. M., Xu, X., and Goodman, J. Vac. Sci. Technol. A **12**, 2114 (1994).
273. Pacchioni, G., and Bagus, P. S., in "Springer Series on Surface Science" (H.-J. Freund and E. Umbach, Eds.), Vol. 33, p. 180. Springer-Verlag, Heidelberg, 1993.
274. Escalona Platero, E., Spoto, G., Coluccia, S., and Zecchina, A., *Langmuir* **3**, 291 (1987).
275. Kuhlénbeck, H., Odörfer, G., Jäger, R., Xu, C., Mull, T., Baumeister, B., Illing, G., Menges, M., Freund, H.-J., Weide, D., Andresen, P., Watson, G., and Plummer, E. W., *Vacuum* **41**, 34 (1990).
276. Kuhlénbeck, H., Odörfer, G., Illing, G., Menges, M., Mull, T., Freund, H.-J., Pöhlchen, M., Staemmler, V., Witzel, S., Scharfschwerdt, C., Wennemann, K., Liedtke, T., and Neumann, M., *Phys. Rev. B* **43**, 1969 (1991).
277. Freitag, A., Staemmler, V., Cappus, D., Ventrice, J., Al-Shamery, C. A., Kuhlénbeck, H., and Freund, H.-J., *Chem. Phys. Lett.* **210**, 10 (1993).
278. Gorschlüter, A., and Mertz, H., *Phys. Rev. B* **49**, 17293 (1994).
279. Haßel, M., Kuhlénbeck, H., Freund, H.-J., Shi, S., Freitag, A., Staemmler, V., Lütkehoff, S., and Neumann, M., *Chem. Phys. Lett.* **240**, 205 (1995).
280. Shi, S., and Staemmler, V., *Phys. Rev. B* **52**, 12345 (1995).
281. Bender, M., Ehrlich, D., Yakovkin, I. N., Rohr, F., Bäumer, M., Kuhlénbeck, H., Freund, H.-J., and Staemmler, V., *J. Phys. C* **7**, 5289 (1995).
282. Fromme, B., Möller, M., Anschütz, T., Bethke, C., and Kisker, E., *Phys. Rev. Lett.* **77**, 1548 (1996).
283. Bäumer, M., Cappus, D., Illing, G., Kuhlénbeck, H., and Freund, H.-J., *J. Vac. Sci. Technol. A* **10**, 2407 (1992).
284. Garrone, E., Fubini, B., Escalona Platero, E., and Zecchina, A., *Langmuir* **5**, 240 (1989).
285. Escalona Platero, E., Fubini, B., and Zecchina, A., *Surf. Sci.* **179**, 404 (1987).
286. Bandara, A., Dobashi, S., Kubota, J., Onada, K., Wada, A., Domen, K., Hirose, C., and Kano, S. S., *Surf. Sci.* **387**, 312 (1997).
287. Cappus, D., Xu, C., Ehrlich, D., Dillmann, B., Ventrice, J. C. A., Al-Shamery, K., Kuhlénbeck, H., and Freund, H.-J., *Chem. Phys.* **177**, 533 (1993).
288. Polcik, M., Lindsley, R., Baumgärtel, P., Terborg, R., Schoff, O., Kulkarni, S., Bradshaw, A. M., Toomes, R., and Woodrouff, D. P., *Faraday Discuss.* **114**, 141 (1999).
289. Schönnenbeck, M., Cappus, D., Klinkmann, J., Freund, H.-J., Petterson, L. G. M., and Bagus, P. S., *Surf. Sci.* **347**, 337 (1996).
290. Gevirczman, R., and Kozirovski, Y., *Trans. Faraday Soc.* **67**, 2686 (1971).
291. Gevirczman, R., Kozirovski, Y., and Folman, M., *Trans. Faraday Soc.* **65**, 2206 (1969).
292. Smart, R. S. C., *Trans. Faraday Soc.* **67**, 1183 (1971).
293. Zecchina, A., Scarano, D., and Garrone, E., *Surf. Sci.* **160**, 492 (1985).
294. Heidberg, J., Stein, H., and Weiss, H., *Surf. Sci. Lett.* **184**, L431 (1987).
295. Scarano, D., and Zecchina, A., *J. Chem. Soc. Faraday Trans. I* **82**, 3611 (1986).
296. Zecchina, A., and Scarano, D., *Surf. Sci.* **166**, 347 (1986).
297. Dai, D. J., and Ewing, G. E., *J. Electron. Spectrosc. Related Phenomena* **64/65**, 101 (1993).
298. Chang, H.-C., Richardson, H. H., and Ewing, G. E., *J. Chem. Phys.* **89**, 7561 (1988).
299. Richardson, H. H., Chang, H.-C., Noda, C., and Ewing, G. E., *Surf. Sci.* **216**, 93 (1989).
300. Heidberg, J., Grunwald, M., Hustedt, M., and Traeger, F., *Surf. Sci.* **368**, 126 (1996).
301. Heidberg, J., Kampshoff, E., and Suhren, M., *J. Chem. Phys.* **95**, 9408 (1991).
302. Carré, M.-N., Lemoine, D., Picaud, S., and Girardet, C., *Surf. Sci.* **347**, 128 (1996).

303. Schmicker, D., Toennies, P., Vollmer, R., and Weiss, H., *J. Chem. Phys.* **95**, 9412 (1991).
304. Ewing, G. E., *Int. Rev. Phys. Chem.* **10**, 391 (1991).
305. Richardson, H. H., Baumann, C., and Ewing, G. E., *Surf. Sci.* **185**, 15 (1987).
306. Hardy, J. P., Ewing, G. E., and Stables, R., *Surf. Sci. Lett.* **159**, L474 (1985).
307. Heidberg, J., Hustedt, M., Oppermann, J., and Paszkiewicz, P., *Surf. Sci.* **352/354**, 447 (1996).
308. Heidberg, J., Grunwald, M., Hustedt, M., and Traeger, F., *Surf. Sci.* **368**, 133 (1996).
309. Heidberg, J., Gushanskaya, N., Schönekäs, O., and Schwarte, R., *Surf. Sci.* **331–333**, 1473 (1995).
310. Berg, O., and Ewing, G. E., *Surf. Sci.* **220**, 198 (1989).
311. Berg, O., and Ewing, G. E., *J. Chem. Phys.* **98**, 5050 (1993).
312. Quatrocci, L. M., and Ewing, G. E., *J. Chem. Phys.* **96**, 4205 (1992).
313. Peters, S. J., and Ewing, G. E., *Langmuir* **13**, 6345 (1997).
314. Weiss, H., *Surf. Sci.* **331–333**, 1453 (1995).
315. Leggett, K., Polyani, J. C., and Young, P. A., *J. Chem. Phys.* **93**, 3654 (1990).
316. Berg, O., and Ewing, G. E., *J. Phys. Chem.* **95**, 2908 (1991).
317. Dunn, S. K., and Ewing, G. E., *J. Phys. Chem.* **96**, 5284 (1992).
318. Dunn, S. K., and Ewing, G. E., *J. Phys. Chem.* **97**, 7993 (1993).
319. Dunn, S. K., and Ewing, G. E., *Chem. Phys.* **177**, 571 (1993).
320. Dunn, S. K., and Ewing, G. E., *Faraday Discuss. Chem. Soc.* **96**, 95 (1993).
321. Bourdon, E. B. D., Cho, C.-C., Das, P., Polyani, J. C., Stanners, C. D., and Xu, G.-Q., *J. Chem. Phys.* **95**, 1361 (1991).
322. Willian, K., Berg, O., and Ewing, G. E., *J. Chem. Soc. Faraday Trans.* **92**, 4853 (1996).
323. Hauffe, K. C., *Adv. Catal.* **7**, 213 (1955).
324. Vrieland, E. G., and Selwood, P. W., *J. Catal.* **3**, 539 (1964).
325. Cimino, A., Schiavello, M., and Stone, F. S., *Discuss. Faraday Soc.* **41**, 350 (1966).
326. Garcia-Moliner, F., *Catal. Rev.* **2**, 1 (1968).
327. Dowden, D. A., *Catal. Rev.* **5**, 1 (1971).
328. Madey, T. E., Yates, J. T., Jr., Sandstrom, D. R., and Voorhoeve, R. J. H., in "Treatise on Solid State Chemistry," Vol. 6b. Plenum, New York, 1976.
329. Morrison, S. R., "The Chemical Physics of Surfaces." Plenum, New York, 1977.
330. Angeletti, C., Cimino, A., Indovina, V., Pepe, F., and Schiavello, M., *J. Chem. Soc. Faraday Trans. 1* **77**, 641 (1981).
331. Somorjai, G. A., "Introduction to Surface Science and Catalysis." Wiley, New York, 1994.
332. Behringer, R. E., *J. Chem. Phys.* **29**, 537 (1958).
333. Cimino, A., De Angelis, P. A., Minelli, G., Persini, T., and Scarpino, P., *Solid State Chem.* **33**, 403 (1980).
334. Cimino, A., De Angelis, P. A., and Minelli, G., *Surf. Interf. Anal.* **5**, 150 (1983).
335. Cimino, A., Lo Jacono, M., Porta, P., and Valigi, M., *Z. Phys. Chem. Neue Folge* **51**, 301 (1966).
336. Borowiecki, T., *Appl. Catal.* **10**, 273 (1984).
337. Courty, P., and Marcilly, C., *Stud. Surf. Sci. Catal.* **15**, 485 (1983).
338. Cimino, A., *Mater. Chem. Phys.* **13**, 221 (1985).
339. Cimino, A., De Angelis, B. A., and Minelli, G., *J. Electron. Spectrosc.* **13**, 291 (1978).
340. Hagan, A., Lofthouse, M. G., and Stone, F. S., *Stud. Surf. Sci. Catal.* **3**, 417 (1979).
341. Cimino, A., Gazzoli, D., Indovina, V., Inversi, M., Moretti, G., and Occhiuzzi, M., *Stud. Surf. Sci. Catal.* **48**, 279 (1989).
342. Cimino, A., Gazzoli, D., Indovina, V., Moretti, G., Occhiuzzi, M., and Pepe, F., *Top. Catal.* **8**, 171 (1999).
343. Wynblatt, P., and McCune, R. C., in "Surface and Near-Surface Chemistry of Oxide Materials," p. 247. Elsevier, Amsterdam, 1994.
344. Bond, G. C., and Sarsam, S. P., *Appl. Catal.* **38**, 365 (1988).

345. Zecchina, A., Spoto, G., Coluccia, S., and Guglielminotti, E., *J. Chem. Soc. Faraday Trans. I* **80**, 1875 (1984).
346. Zecchina, A., Spoto, G., Coluccia, S., and Guglielminotti, E., *J. Chem. Soc. Faraday Trans. I* **80**, 1891 (1984).
347. Stone, F. S., and Vickerman, J. C., *Trans. Faraday Soc.* **67**, 316 (1971).
348. Stone, F. S., and Vickerman, J. C., *Trans. Faraday Soc.* **67**, 665 (1971).
349. Leofanti, G., Padovan, M., Garilli, M., Carmello, D., Zecchina, A., Spoto, G., Bordiga, S., Turnes Palomino, G., and Lamberti, C., *J. Catal.* **189**, 91 (2000).
350. Pomonis, P., and Vickerman, J. C., *J. Catal.* **55**, 88 (1978).
351. Yoshida, T., Tanaka, T., Yoshida, H., Funabiki, T., and Yoshida, S., *J. Phys. Chem.* **100**, 2302 (1996).
352. Cimino, A., Bosco, R., Indovina, V., and Schiavello, M., *J. Catal.* **5**, 271 (1966).
353. Cimino, A., Indovina, V., Pepe, F., and Schiavello, M., *J. Catal.* **14**, 49 (1969).
354. Cimino, A., Indovina, V., Pepe, F., and Schiavello, M., in "Proceedings of the 4th International Congress on Catalysis," Paper No. 12. Moscow, 1968.
355. Cimino, A., and Indovina, V., *J. Catal.* **17**, 54 (1970).
356. Cimino, A., and Pepe, F., *J. Catal.* **25**, 362 (1972).
357. Cimino, A., *Chim. Ind. (Milan)* **56**, 27 (1974).
358. Takezawa, N., Terunuma, H., Shimokawabe, M., and Kobayashi, H., *Appl. Catal.* **23**, 291 (1986).
359. Takahama, T., Oshima, H., Ueno, A., and Kotera, Y., *Appl. Catal.* **5**, 59 (1983).
360. Rostrup-Nielsen, J. R., *Stud. Surf. Sci. Catal.* **36**, 73 (1988).
361. Ashcroft, A. T., Cheetham, A. K., Green, M. L. H., and Veron, P. D. F., *Nature* **352**, 225 (1991).
362. Yamazaki, O., Nozaki, T., Omata, K., and Fujimoto, K., *Chem. Lett.*, 1153 (1992).
363. Ruckenstein, E., and Hu, Y. H., *Appl. Catal. A* **133**, 149 (1995).
364. Hu, Y. H., and Ruckenstein, E., *Catal. Lett.* **36**, 145 (1996).
365. Yamazaki, O., Tomishige, K., and Fujimoto, K., *Appl. Catal. A* **13**, 649 (1996).
366. Cheng, Y.-G., Yamazaki, O., Tomishige, K., and Fujimoto, K., *Catal. Lett.* **39**, 91 (1996).
367. Cheng, Y.-G., Tomishige, K., Yokoyama, K., and Fujimoto, K., *Appl. Catal. A* **165**, 35 (1999).
368. Cheng, Y.-G., Tomishige, K., Yokoyama, K., and Fujimoto, K., *J. Catal.* **184**, 479 (1997).
369. Hu, Y. H., and Ruckenstein, E., *J. Catal.* **163**, 306 (1996).
370. Hu, Y. H., and Ruckenstein, E., *Langmuir* **13**, 2055 (1997).
371. Zecchina, A., Spoto, G., Coluccia, S., and Garrone, E., *J. Chem. Phys.* **80**, 467 (1984).
372. Zecchina, A., Spoto, G., and Coluccia, S., *J. Mol. Catal.* **11**, 351 (1982).
373. Sojka, Z., Giamello, E., Che, M., Zecchina, A., and Dyrek, K., *J. Phys. Chem.* **92**, 1541 (1988).
374. Giamello, E., Sojka, Z., Che, M., and Zecchina, A., *J. Phys. Chem.* **90**, 6084 (1986).
375. Zecchina, A., Spoto, G., Coluccia, S., and Guglielminotti, E., *J. Phys. Chem.* **88**, 2576 (1984).
376. Zecchina, A., Spoto, G., Borello, E., and Giamello, E., *J. Phys. Chem.* **88**, 2582 (1984).
377. Zecchina, A., Spoto, G., Garrone, E., and Bossi, A., *J. Phys. Chem.* **88**, 2588 (1984).
378. Cordischi, D., Indovina, V., and Occhiuzzi, M., *J. Chem. Soc. Faraday Trans. I* **76**, 1147 (1980).
379. Giamello, E., Garrone, E., Guglielminotti, E., and Zecchina, A., *J. Mol. Catal.* **24**, 59 (1984).
380. Zecchina, A., and Spoto, G., *Z. Phys. Chem. Neue Folge* **137**, 173 (1983).
381. Zecchina, A., and Spoto, G., *J. Catal.* **96**, 586 (1985).
382. Escalona Platero, E., Coluccia, S., and Zecchina, A., *J. Catal.* **103**, 270 (1987).

383. Garrone, E., Giamello, E., Ferraris, M., and Spoto, G., *J. Chem. Soc. Faraday Trans.* **88**, 333 (1992).
384. Garrone, E., Giamello, E., Coluccia, S., Spoto, G., and Zecchina, A., in "Proceedings of the 9th International Congress on Catalysis" (J. Phillips, and M. Ternan, Eds.), Vol. 4, p. 1577. Chemical Institute of Canada, Ottawa, 1988.
385. Giamello, E., Garrone, E., Coluccia, S., Spoto, G., and Zecchina, A., *Stud. Surf. Sci. Catal.* **56**, 817 (1990).
386. Indovina, V., Cimino, A., Inversi, M., and Pepe, F., *J. Catal.* **58**, 396 (1979).
387. Ghiotti, G., and Boccuzzi, F., *J. Chem. Soc. Faraday Trans. II* **79**, 1843 (1983).
388. Scarano, D., Zecchina, A., Spoto, G., and Geobaldo, F., *J. Chem. Soc. Faraday Trans.* **91**, 4445 (1995).
389. Zecchina, A., Scarano, D., and Spoto, G., *J. Mol. Catal.* **38**, 287 (1986).
390. Hirschwald, W., *Curr. Topics Mater. Sci.* **7**, 448 (1981).
391. Ernst, L., *Curr. Topics Mater. Sci.* **7**, 364 (1981).
392. Bonasewicz, P., and Littbarski, X., *Curr. Topics Mater. Sci.* **7**, 371 (1981).
393. Hoffman, D., *Curr. Topics Mater. Sci.* **7**, 304 (1981).
394. Scarano, D., Spoto, G., Bordiga, S., Zecchina, A., and Lamberti, C., *Surf. Sci.* **276**, 281 (1992).
395. Denisenko, L. A., Tsyganenko, A. A., and Filimonov, L. A., *React. Kinet. Catal. Lett.* **25**, 23 (1984).
396. Gay, R. R., Nodine, M. H., Henrich, V. E., Zeiger, H. J., and Solomon, E. L., *J. Am. Chem. Soc.* **102**, 6752 (1980).
397. D'Amico, K. L., McFeely, F. R., and Solomon, E. L., *J. Am. Chem. Soc.* **105**, 6380 (1983).
398. Eischens, R. P., Pliskin, W. A., and Low, M. J. D., *J. Catal.* **1**, 180 (1962).
399. Dent, A. L., and Kokes, R. J., *J. Phys. Chem.* **73**, 3772 (1969).
400. Boccuzzi, F., Borello, E., Zecchina, A., Bossi, A., and Camia, M., *J. Catal.* **51**, 150 (1978).
401. Boccuzzi, F., Garrone, E., Zecchina, A., Bossi, A., and Camia, M., *J. Catal.* **51**, 160 (1978).
402. Denisenko, L. A., Tsyganenko, A. A., and Filimonov, V. N., *React. Kinet. Catal. Lett.* **22**, 265 (1983).
403. Anderson, A. B., and Ray, N. K., *J. Am. Chem. Soc.* **107**, 253 (1985).
404. Dent, A. L., and Kokes, R. J., *J. Phys. Chem.* **73**, 3781 (1969).
405. Gates, B. C., "Catalytic Chemistry." Wiley, New York, 1992.
406. Rosynek, M. P., Fox, J. S., and Jensen, J. L., *J. Catal.* **76**, 64 (1981).
407. Imizu, Y., Sato, K., and Hattori, H., *J. Catal.* **77**, 65 (1982).
408. Choudhary, V. R., and Rane, V. H., *J. Chem. Soc. Faraday Trans.* **90**, 3357 (1994).
409. Lacombe, S. C. G., and Miridatos, C., *J. Catal.* **151**, 439 (1994).
410. Lacombe, S., Zanthoff, H., and Mirodatos, C., *J. Catal.* **155**, 106 (1995).
411. Zhang, X., Walters, A. B., and Vannice, M. A., *Catal. Today* **27**, 41 (1996).
412. Huang, S. J., Walters, A. B., and Vannice, M. A., *J. Catal.* **173**, 229 (1998).
413. Maitra, A. M., *Appl. Catal.* **104**, 1 (1993).
414. Bailes, M., Bordiga, S., Stone, F. S., and Zecchina, A., *J. Chem. Soc. Faraday Trans.* **92**, 4675 (1996).
415. Tsyganenko, A. A., Lamotte, J., Gallas, J. P., and Lavalley, J. C., *J. Phys. Chem.* **93**, 4179 (1989).
416. Kalenik, Z., and Wolf, E. E., *Catal. Lett.* **9**, 441 (1991).
417. Ilett, D. J., and Islam, M. S., *J. Chem. Soc. Faraday Trans.* **89**, 3833 (1993).
418. Klingenberg, B., and Vannice, M. A., *Appl. Catal. B* **21**, 19 (1999).
419. Thomas, C. L., "Catalytic Processes and Proven Catalysts." Academic Press, New York, 1970.

420. Campbell, J. M., "Catalysts and Surfaces." Chapman and Hall, London, 1988.
421. Bowker, M., Houghton, H., and Waugh, K. C., *Faraday Trans.* **77**, 3023 (1981).
422. Prasad, R., Kennedy, L. A., and Ruckenstein, E., *Catal. Rev.-Sci. Eng.* **26**, 1 (1984).
423. Matsuda, S., and Kato, A., *Appl. Catal.* **8**, 149 (1983).
424. Campbell, C. T., and Daube, K. A., *J. Catal.* **104**, 109 (1987).
425. Chinchén, G. C., Denny, P. J., Parker, D. G., Spencer, M. S., Waugh, K. C., and Whan, D. A., *Appl. Catal.* **30**, 333 (1987).
426. Dines, T. J., Rochester, C. H., and Ward, D. A., *J. Chem. Soc. Faraday Trans.* **87**, 653 (1991).
427. Bettahar, M. M., Costantin, G., Savary, L., and Lavalley, J. C., *Appl. Catal. A* **145**, 1 (1996).
428. Chen, H. Y., Chen, L., Lin, J., Tan, K. L., and Li, J., *Inorg. Chem.* **36**, 1417 (1997).
429. Ertl, G., Hierl, R., Knözinger, H., Thiele, N., and Urbach, H. P., *Appl. Surf. Sci.* **5**, 49 (1980).
430. Iwamoto, M., Yokoo, S., Sakai, K., and Kagawa, S., *J. Chem. Soc. Faraday Trans.* **77**, 1629 (1981).
431. Iwamoto, M., Furukawa, H., and Kagawa, S., in "New Development in Zeolites Science and Technology" (Y. Murukama, A. Ichijima, and J. W. Ward, Eds.), Vol. 28, p. 943. Elsevier, Amsterdam, 1986.
432. Iwamoto, M., and Hamada, H., *Catal. Today* **10**, 57 (1991).
433. Valyon, J., and Hall, W. K., *J. Phys. Chem.* **97**, 1204 (1993).
434. De Jong, K. P., Geus, J. W., and Joziassé, J., *J. Catal.* **65**, 437 (1991).
435. Bocuzzi, F., Ghiotti, G., and Chiorino, A., *Surf. Sci.* **156**, 933 (1985).
436. Ghiotti, G., Bocuzzi, F., and Chiorino, A., *J. Chem. Soc. Chem. Commun.*, 1012 (1985).
437. Fu, Y., Tian, Y., and Lin, P., *J. Catal.* **132**, 85 (1991).
438. Marion, M. C., Garbowski, E., and Primet, M., *J. Chem. Soc. Faraday Trans.* **86**, 3027 (1990).
439. Millar, G. J., Rochester, C. H., and Waugh, K. C., *J. Chem. Soc. Faraday Trans.* **87**, 1467 (1991).
440. Kantcheva, M., Hadjiivanov, K., Davydov, A., and Budneva, A., *Appl. Surf. Sci.* **55**, 49 (1992).
441. Itho, Y., Nishiyama, S., Tsuruya, S., and Massai, M., *J. Phys. Chem.* **98**, 960 (1994).
442. Padley, M. B., Rochester, C. H., Hutchings, G. J., and King, F., *J. Chem. Soc. Faraday Trans.* **90**, 203 (1994).
443. Waqif, M., Lakhar, M., Saur, O., and Lavalley, J. C., *J. Chem. Soc. Faraday Trans.* **90**, 2815 (1994).
444. Borgard, G. D., Molvik, S., Balaraman, P., Root, T. W., and Dumesic, J. A., *Langmuir* **11**, 2065 (1995).
445. Hadjiivanov, K. I., Kantcheva, M. M., and Klissurski, D. G., *J. Chem. Soc. Faraday Trans.* **92**, 4595 (1996).
446. Iwamoto, M., and Hoshiro, Y., *Inorg. Chem.* **35**, 6918 (1996).
447. Bocuzzi, F., Chiorino, A., Martra, G., Gargano, M., Ravasio, N., and Carrozzini, B., *J. Catal.* **165**, 129 (1997).
448. (a) Schulz, K. H., and Cox, D. F., *Surf. Sci.* **278**, 9 (1992); (b) Schulz, K. H., and Cox, D. F., *Surf. Sci.* **262**, 318 (1992).
449. (a) Lamberti, C., Bordiga, S., Salvalaggio, M., Spoto, G., Zecchina, A., Geobaldo, F., Vlaic, G., and Bellatreccia, M., *J. Phys. Chem.* **101**, 344 (1997); (b) Zecchina, A., Bordiga, S., Turnes Palomino, G., Scarano, D., Lamberti, C., and Salvalaggio, M., *J. Phys. Chem. B* **103**, 3833 (1999); (c) Lamberti, C., Turnes Palomino, G., Bordiga, S., Berlier, G., D'Acapito, F., and Zecchina, A., *Angew. Chem. Int. Ed. Engl.*, **39**, 2138 (2000).
450. Scarano, D., Bordiga, S., Lamberti, C., Spoto, G., Ricchiardi, G., Zecchina, A., and Otero Areán, C., *Surf. Sci.* **411**, 272 (1998).
451. Gadalla, A. M. M., and White, J., *Trans. Br. Ceram. Soc.* **63**, 39 (1964).

452. Little, L. H., Kiselev, A. V., and Lygin, V. I., in "Infrared Spectra of Adsorbed Species," p. 47. Academic Press, London, 1966.
453. Braterman, P. S., "Metal Carbonyl Spectra." Academic Press, London, 1975.
454. Kettle, S. F. A., *Curr. Topics Chem.* **71**, 111 (1977).
455. Restori, R., and Schwarzenback, D., *Acta Crystallogr. B* **42**, 201 (1986).
456. "Catalysis, Materials Modelling User's Guide." Molecular Simulations, San Diego, 1996.
457. Pasquali, M., Marchetti, F., and Floriani, C., *Inorg. Chem.* **17**, 1684 (1978).
458. Schulz, K. H., and Cox, D. F., *J. Catal.* **143**, 464 (1993).
459. Askgaard, T. S., Nørskov, J. K., Ovesen, C. V., and Stoltze, P., *J. Catal.* **156**, 229 (1995).
460. Muhler, M., in "Handbook of Heterogeneous Catalysis" (G. Ertl, H. Knözinger, and J. Weitkamp, Eds.), Vol. 5, p. 2274. Wiley-VCH, Weinheim, 1997.
461. Mars, P., and van Krevelen, D. W., *Chem. Eng. Sci.* **3**, 41 (1954).
462. Bielanski, A., and Haber, J., "Oxygen in Catalysis." Dekker, New York, 1991.
463. Neisus, T., Böttger, I., Kitzelmann, E., Weinberg, G., Demuth, D., Schedel-Niedrig, T., and Schlögl, R., personal communication.
464. Amariglio, A., Benali, O., and Amariglio, H., *J. Catal.* **118**, 164 (1989).
465. Werner, H., Herein, D., Schulz, G., Wild, U., and Schlögl, R., *Catal. Lett.* **49**, 109 (1997).
466. Fu, S. S., and Somorjai, G. A., *Appl. Surf. Sci.* **48/49**, 93 (1991).
467. Cox, D. F., and Schulz, K. H., *J. Vac. Sci. Technol. A* **8**, 2599 (1990).
468. Knop-Gericke, A., Hävecker, M., Schedel-Niedrig, T., and Schlögl, R., Paper presented at the 4th European Congress on Catalysis, EUROPACAT-4, Rimini, Italy, 1999.
469. Weckhuysen, B. M., Wachs, I. E., and Schonheydt, R. A., *Chem. Rev.* **96**, 3327 (1996).
470. Yermakov, Y., and Zakharov, V., *Adv. Catal.* **24**, 173 (1975).
471. McDaniel, M. P., *J. Catal.* **76**, 17, 29 (1982).
472. Merryfield, R., McDaniel, M., and Parks, G., *J. Catal.* **77**, 348 (1982).
473. Connor, W. C., and Kokes, R. J., *J. Phys. Chem.* **73**, 2436 (1969).
474. Sanfilippo, D., Buonomo, F., Fusco, G., Lupieri, M., and Miracca, I., *Chem. Eng. Sci.* **47**, 2313 (1992).
475. Buonomo, F., Sanfilippo, D., and Trifirò, F., in "Handbook of Heterogeneous Catalysis" (G. Ertl, H. Knözinger, and J. Weitkamp, Eds.), Vol. 5, p. 2145. Wiley-VCH, Weinheim, 1997.
476. Janssen, F. J., in "Handbook of Heterogeneous Catalysis" (G. Ertl, H. Knözinger, and J. Weitkamp, Eds.), Vol. 4, p. 1646. Wiley-VCH, Weinheim, 1997.
477. Cavani, F., Koutyrev, M., Trifirò, F., Bartolini, A., Ghisletti, D., Iezzi, R., Santucci, A., and Del Piero, G., *J. Catal.* **158**, 236 (1996).
478. Takahara, I., Chang, W.-C., Mimura, N., and Saito, M., *Catal. Today* **45**, 55 (1998).
479. Weckhuysen, B. M., and Schoonheydt, R. A., *Catal. Today* **51**, 223 (1999).
480. Hakuli, A., Harlin, M. E., Backman, L. B., and Krause, A. O. I., *J. Catal.* **184**, 349 (1999).
481. Gorriz, O. F., and Cadús, L. E., *Appl. Catal. A Gen.* **180**, 247 (1999).
482. Kung, H. H., "Transition Metal Oxides: Surface Chemistry and Catalysis." Elsevier, Amsterdam, 1989.
483. Kim, D. S., and Wachs, I. E., *J. Catal.* **142**, 166 (1993).
484. Kittaka, S., Umezu, T., Ogawa, H., Maegawa, H., and Takenaka, T., *Langmuir* **14**, 832 (1998).
485. Kühlenbeck, H., Xu, C., Dillmann, B., Haßel, M., Adam, B., Ehrlich, D., Wohlrab, S., Freund, H.-J., Ditzinger, U. A., Neddermeyer, H., Neuber, M., and Neumann, M., *Berlin Bunsen. Phys. Chem.* **96**, 15 (1992).
486. Cappus, D., Menges, M., Xu, C., Ehrlich, D., Dillmann, B., Ventrice, C. A., Jr., Bäumer, M., Wohlrab, S., Winkelmann, F., Kühlenbeck, H., and Freund, H.-J., *J. Electron. Spectrosc.* **68**, 347 (1994).

487. Seiferth, O., Wolter, K., Dillmann, B., Klivenyi, G., Freund, H.-J., Scarano, D., and Zecchina, A., *Surf. Sci.* **421**, 176 (1999).
488. Scarano, D., and Zecchina, A., *Spectrochim. Acta A* **43**, 1441 (1987).
489. Scarano, D., Zecchina, A., and Reller, A., *Surf. Sci.* **198**, 11 (1998).
490. Escalona Platero, E., Otero Areán, C., Scarano, D., Spoto, G., and Zecchina, A., *Mater. Chem. Phys.* **29**, 347 (1991).
491. Scarano, D., Zecchina, A., Bordiga, S., Ricchiardi, G., and Spoto, G., *Chem. Phys.* **177**, 547 (1993).
492. Scarano, D., Spoto, G., Bordiga, S., Ricchiardi, G., and Zecchina, A., *J. Electron. Spectrosc.* **64/65**, 307 (1993).
493. Scarano, D., Spoto, G., Bordiga, S., Carnelli, L., Ricchiardi, G., and Zecchina, A., *Langmuir* **10**, 3094 (1994).
494. Rohr, F., Bäumer, M., Freund, H.-J., Mejias, J. A., Staemmler, V., Müller, S., Hammer, L., and Heinz, K., *Surf. Sci.* **372**, L291 (1997).
495. Foord, J. S., and Lambert, R. M., *Surf. Sci.* **161**, 513 (1985).
496. Foord, J. S., and Lambert, R. M., *Surf. Sci.* **169**, 327 (1986).
497. Zecchina, A., Escalona Platero, E., and Otero Areán, C., *J. Catal.* **107**, 244 (1987).
498. Zecchina, A., Scarano, D., and Reller, A., *J. Chem. Soc. Faraday Trans. I* **84**, 2327 (1988).
499. Blonski, S., and Garofalini, S. H., *Surf. Sci.* **295**, 263 (1993).
500. Hartmån, P., *J. Cryst. Growth* **96**, 667 (1989).
501. McDaniel, M. P., *Adv. Catal.* **33**, 47 (1985).
502. Ghiotti, G., Garrone, E., and Zecchina, A., *J. Mol. Catal.* **46**, 61 (1988).
503. Karol, F. J., Brown, G. L., and Davidson, J. M., *J. Polym. Sci. Part A1* **11**, 413 (1973).
504. Ghiotti, G., Garrone, E., and Zecchina, A., *J. Mol. Catal.* **65**, 73 (1991).
505. Spoto, G., Bordiga, S., Garrone, E., Ghiotti, G., and Zecchina, A., *J. Mol. Catal.* **74**, 175 (1992).
506. Zecchina, A., Spoto, G., Ghiotti, G., and Garrone, E., *J. Mol. Catal.* **86**, 423 (1994).
507. Zecchina, A., Spoto, G., and Bordiga, S., *Faraday Discuss. Chem. Soc.* **87**, 1 (1989).
508. Zecchina, A., Otero Areán, C., Turnes Palomino, G., Geobaldo, F., Lamberti, C., Spoto, G., and Bordiga, S., *Phys. Chem. Chem. Phys.* **1**, 1649 (1999).
509. Curry-Hyde, H. E., Munsch, H., Baiker, A., Schraml-Marth, M., and Wokaun, A., *J. Catal.* **133**, 397 (1992).
510. Schraml-Marth, M., Wokaun, A., and Baiker, A., *J. Catal.* **138**, 306 (1992).
511. Curry-Hyde, M. E., and Baiker, A., *Appl. Catal.* **90**, 183 (1992).
512. Schraml-Marth, M., Wokaun, A., Curry-Hyde, H. E., and Baiker, A., *J. Catal.* **133**, 415 (1992).
513. Kochloeff, K., in "Handbook of Heterogeneous Catalysis" (G. Ertl, H. Knözinger, and J. Weitkamp, Eds.), Vol. 5, p. 2151. Wiley-VHC, Weinheim, 1997.
514. Glisenti, A., Favero, G., and Granozzi, G., *J. Chem. Soc. Faraday Trans.* **94**, 173 (1998).
515. Kuhrs, C., Joseph, Y., Ranke, W., Shaikhutdinov, S., and Weiss, W., Paper presented at the 4th European Congress on Catalysis EUROPA CAT IV, Rimini, Italy, 1999.
516. Zscherpel, D., Weiss, W., and Schlögh, R., *Surf. Sci.* **382**, 326 (1997).
517. Geus, J. W., *Appl. Catal.* **25**, 313 (1986).
518. Shaikhutdinov, S. R. K., Joseph, Y., Kuhrs, C., Ranke, W., and Weiss, W., *Faraday Discuss. Chem. Soc.* **114**, 363 (1999).
519. Muan, A., *Am. J. Sci.* **256**, 171 (1958).
520. Busca, G., and Cotena, N., *Mater. Chem. Phys.* **3**, 49 (1978).
521. Busca, G., and Lorenzelli, V., *Mater. Chem. Phys.* **5**, 213 (1980).
522. Busca, G., and Lorenzelli, V., *J. Catal.* **72**, 303 (1981).
523. Cox, P. A., "The Transition Metal Oxides." Oxford Univ. Press, Oxford, 1992.

524. Busca, G., and Lorenzelli, V., *J. Catal.* **66**, 155 (1980).
525. Busca, G., and Lorenzelli, V., *J. Chem. Soc. Faraday Trans. I* **78**, 2911 (1982).
526. Ishikawa, T., Cai, W. Y., and Kandori, K., *Langmuir* **9**, 1125 (1993).
527. Iizuka, T., Ikeda, H., Terao, T., and Tanabe, K., *Aust. J. Chem.* **35**, 927 (1982).
528. Larsson, R., Lykvist, R., and Rebenstorf, Z., *Z. Phys. Chem. (Leipzig)* **263**, 1089 (1982).
529. Morterra, C., Ghiotti, G., Garrone, E., and Boccuzzi, F., *J. Chem. Soc. Faraday Trans. I* **72**, 2722 (1976).
530. Morterra, C., Magnacca, G., and Del Favero, N., *Langmuir* **9**, 642 (1993).
531. Gautier, M., Renaud, G., Van, L. P., Villette, B., Pollak, M., Thromat, N., Jollet, F., and Duarud, J.-P., *J. Am. Ceram. Soc.* **77**, 323 (1994).
532. Stará, I., Zeze, D., Matolín, V., Pavluch, J., and Gruzza, B., *Appl. Surf. Sci.* **115**, 46 (1997).
533. Ahn, J., and Rabalais, J. W., *Surf. Sci.* **388**, 121 (1997).
534. Tasker, P. W., *Adv. Ceram.* **10**, 176 (1988).
535. Mackrodt, W. C., *J. Chem. Soc. Faraday Trans. II* **2 85**, 541 (1989).
536. Guo, J., Ellis, D. E., and Lam, D. J., *Phys. Rev. B* **45**, 13647 (1992).
537. Pisani, C., Causà, M., Dovesi, R., and Roetti, C., *Prog. Surf. Sci.* **25**, 119 (1987).
538. Causà, M., Dovesi, R., Pisani, C., and Roetti, C., *Surf. Sci.* **215**, 259 (1989).
539. Salasco, L., Dovesi, R., Orlando, R., Causà, M., and Saunders, V. R., *Mol. Phys.* **72**, 267 (1991).
540. Manassidis, I., and Gilaan, M. J., *J. Am. Ceram. Soc.* **77**, 335 (1994).
541. Nygren, M. A., Gay, D. H., and Catlow, C. R. A., *Surf. Sci.* **380**, 113 (1997).
542. Verykios, X. E., Stein, F. P., and Coughlin, R. W., *Catal. Rev.-Sci. Eng.* **22**, 197 (1980).
543. Streitz, F. H., and Mintmine, J. W., *Phys. Rev. B* **50**, 11996 (1994).
544. Libby, W. F., *Science* **171**, 361 (1967).
545. Viswanathan, B., *Catal. Rev.-Sci. Eng.* **34**, 337 (1992).
546. Belessi, V. C., Trikalitis, P. N., Ladavos, A. K., Bakas, T. V., and Pomonis, P. J., *Appl. Catal. A* **177**, 53 (1999).
547. Vannice, M. A., *Catal. Rev.-Sci. Eng.* **176**, 1355 (1976).
548. Fierro, J. L. G., *Catal. Rev.-Sci. Eng.* **34**, 321 (1992).
549. Fierro, J. L. G., and Seijama, T., *Catal. Rev.-Sci. Eng.* **34**, 281 (1992).
550. Shimizu, T., *Catal. Rev.-Sci. Eng.* **34**, 355 (1992).
551. Wagner, F. T., and Somorjai, G. A., *Nature* **285**, 599 (1980).
552. Kendall, K., *Ceram. Bull.* **70**, 1159 (1991).
553. Groupp, L., and Anderson, H. U., *J. Am. Chem. Soc.* **59**, 449 (1976).
554. Meadowcroft, D. B., and Wimmer, J., *Am. Ceram. Soc. Bull.* **58**, 610 (1979).
555. Anderson, H. U., *Solid State Ionics* **52**, 33 (1992).
556. Viswanathan, B., in "Properties Applications of Perovskite-Type Oxides" (L. G. Tejuca and J. L. G. Fierro, Eds.), p. 271. Dekker, New York, 1993.
557. Zwinkels, M. F. M., Järås, S. G., Menon, G., and Griffin, T. A., *Catal. Rev.-Sci. Eng.* **35**, 319 (1993).
558. Alcock, C. B., Carberry, J., R., D., and Gunasekaran, N., *J. Catal.* **143**, 533 (1993).
559. Yokoi, Y., and Uchida, H., *Catal. Today* **42**, 167 (1998).
560. Mizuno, N., Yamato, M., Tanaka, M., and Misono, M., *Chem. Mater.* **1**, 232 (1989).
561. Saracco, G., Scibilia, G., Iannibello, A., and Baldi, G., *Appl. Catal. B* **218**, 229 (1996).
562. Viswanathan, B., *Catal. Rev.-Sci. Eng.* **34**, 337 (1992).
563. Göpel, W., Rucker, G., and Feirabend, R., *Phys. Rev. B* **28**, 3427 (1983).
564. Lu, G., Linsebigler, A., and Yates, J. T., Jr., *J. Phys. Chem.* **102**, 3005 (1995).
565. Tanaka, K., and White, J. M., *J. Phys. Chem.* **86**, 4708 (1982).
566. Kobayashi, H., and Yamaguchi, M., *Surf. Sci.* **214**, 466 (1989).
567. Beck, D. D., White, J. M., and Ratcliffe, C. T., *J. Phys. Chem.* **90**, 3132 (1986).

568. Busca, G., Saussey, H., Saur, O., Lavalley, J. C., and Lorenzelli, V., *Appl. Catal.* **14**, 245 (1985).
569. Olivieri, G., Ramis, G., Busca, G., and Escribano, V. S., *J. Mater. Chem.* **3**, 1239 (1993).
570. Raupp, G. B., and Dumesic, J. A., *J. Phys. Chem.* **89**, 5240 (1985).
571. Morterra, C., Garrone, E., Bolis, V., and Fubini, B., *Spectrochim. Acta A* **43**, 1577 (1987).
572. Pacchioni, G., Ferrari, A. M., and Bagus, P. S., *Surf. Sci.* **350**, 159 (1996).
573. Sorescu, D. C., and Yates, J. T., Jr., *J. Phys. Chem. B* **102**, 4556 (1998).
574. Tsyganenko, A. A., Denisenko, L. A., Zverev, S. M., and Filimonov, V. N., *J. Catal.* **94**, 10 (1985).
575. Hadjiivanov, K., Lamotte, J., and Lavalley, J.-C., *Langmuir* **13**, 3374 (1997).
576. Dutta, P. K., Ginwalla, A., Hogg, B., Patton, B. R., Chwierot, B., Liang, Z., Gouma, P., Mills, M., and Akbar, S., *J. Phys. Chem.* **103**, 4412 (1999).
577. Yates, D. J. C., *J. Phys. Chem.* **65**, 746 (1961).
578. Boccuzzi, F., Guglielminotti, E., and Chiorino, A., *Sensors Actuators B* **7**, 645 (1992).
579. Henderson, M. A., *Surf. Sci.* **355**, 151 (1996).
580. Bredow, T., and Jug, K., *Surf. Sci.* **327**, 398 (1995).
581. Henderson, M. A., *Langmuir* **12**, 5093 (1996).
582. Morterra, C., Cerrato, G., Visca, M., and Lenti, D. M., *Chem. Mater.* **3**, 132 (1991).
583. Suzuki, S., Yamaguchi, Y., Onishi, H., Sasaki, T., Fukui, K., and Iwasawa, Y., *J. Chem. Soc. Faraday Trans.* **94**, 161 (1998).
584. Hadjiivanov, K., Klissurski, D., Busca, G., and Lorenzelli, V., *J. Chem. Soc. Faraday Trans.* **87**, 175 (1991).
585. Markovits, A., Ahdjoudj, J., and Minot, C., *Surf. Sci.* **365**, 649 (1996).
586. Ramis, G., Busca, G., and Lorenzelli, V., *J. Chem. Soc. Faraday Trans. I* **83**, 1591 (1987).
587. Bates, S. P., Gillan, M. J., and Kresse, G., *J. Phys. Chem. B* **102**, 2017 (1998).
588. Munro, D. A., and Ng, L. M., *Langmuir* **12**, 739 (1996).
589. Bulanin, K. M., Lavalley, J. C., and Tsyganenko, A. A., *J. Phys. Chem.* **99**, 10294 (1995).
590. Shultz, A. N., Hetherington, W. M., Baer, D. R., Wang, L.-Q., and Engelhard, M. H., *Surf. Sci.* **392**, 1 (1997).
591. Hadjiivanov, K., Bushev, V., Kantcheva, M., and Klissurski, D., *Langmuir* **10**, 464 (1994).
592. Idriss, H., Lusvardi, V. S., and Barteau, M. A., *Surf. Sci.* **348**, 39 (1996).
593. Chambers, S. A., Thevuthasan, S., Kim, Y. J., Herman, G. S., Wang, Z., Tober, E., Ynzunza, R., Morais, J., Peden, C. H. F., Ferris, K., and Fadley, C. S., *Chem. Phys. Lett.* **267**, 51 (1997).
594. Fukui, K., Onishi, H., and Iwasawa, Y., *Chem. Phys. Lett.* **280**, 296 (1997).
595. Guo, Q., Cocks, I., and Williams, E. M., *Surf. Sci.* **393**, 1 (1997).
596. Alam, M., Henderson, M. A., Kaviratna, P. D., Herman, G. S., and Peden, C. H. F., *J. Phys. Chem.* **102**, 111 (1998).
597. Cerrato, G., Marchese, L., and Morterra, C., *Appl. Surf. Sci.* **70/71**, 200 (1993).
598. Bensitel, M., Saur, O., Lavalley, J. C., and Mabilon, G., *Mater. Chem. Phys.* **17**, 249 (1987).
599. Kondo, J., Abe, H., Sakata, Y., Maruya, K., Domen, K., and Onishi, T., *J. Chem. Soc. Faraday Trans.* **84**, 511 (1988).
600. Morterra, C., Orio, L., and Emanuel, C., *J. Chem. Soc. Faraday Trans* **86**, 3003 (1990).
601. Morterra, C., Orio, L., V. B., and Ugliengo, P., *Mater. Chem. Phys.* **29**, 457 (1991).
602. Morterra, C., Bolis, V., Fubini, B., Orio, L., and Williams, T. B., *Surf. Sci.* **251/252**, 540 (1991).
603. Cerrato, G., Bordiga, S., Barbera, S., and Morterra, C., *Appl. Surf. Sci.* **115**, 53 (1997).
604. Cerrato, G., Bordiga, S., Barbera, S., and Morterra, C., *Surf. Sci.* **377-379**, 50 (1997).
605. Morterra, C., Cerrato, G., Ferroni, L., Negro, A., and Montanaro, L., *Appl. Surf. Sci.* **65/66**, 257 (1993).
606. Morterra, C., Cerrato, G., Ferroni, L., and Montanaro, L., *Mater. Chem. Phys.* **37**, 243 (1994).

607. Morterra, C., Cerrato, G., Bolis, V., Lamberti, C., Ferroni, L., and Montanaro, L., *J. Chem. Soc. Faraday Trans.* **91**, 113 (1995).
608. Morterra, C., Cerrato, G., and Ferroni, L., *J. Chem. Soc. Faraday Trans.* **91**, 125 (1995).
609. Hino, H., and Arata, K., *J. Chem. Soc. Chem. Commun.*, 851 (1980).
610. Kayo, A., Yamaguchi, T., and Tanabe, K., *J. Catal.* **83**, 99 (1983).
611. Arata, K., *Adv. Catal.* **37**, 165 (1990).
612. Pinna, F., Signoretto, M., Strukul, G., Cerrato, G., and Morterra, C., *Catal. Lett.* **26**, 339 (1994).
613. Morterra, C., Cerrato, G., Pinna, F., Signoretto, M., and Strukul, G., *J. Catal.* **149**, 181 (1994).
614. Kustov, L. M., Borovkov, Y. V., and Kazansky, V. B., *J. Catal.* **72**, 149 (1981).
615. Bocuzzi, F., Coluccia, S., Ghiotti, G., Morterra, C., and Zecchina, A., *J. Phys. Chem.* **82**, 1298 (1978).
616. Boehm, H. P., and Knözinger, H., in "Catalysis-Science and Technology," Vol. 4, p. 39. Springer, New York, 1983.
617. Rebenstorf, B., *Acta Chem. Scand. A* **31**, 877 (1977).
618. Rebenstorf, B., and Larsson, R., *Z. Anorg. Allg. Chem.* **478**, 119 (1981).
619. Zecchina, A., Garrone, E., Ghiotti, G., Morterra, C., and Borello, E., *J. Phys. Chem.* **79**, 966 (1975).
620. Ghiotti, G., Garrone, E., and Zecchina, A., *J. Mol. Catal.* **46**, 2621 (1988).
621. Garrone, E., Ghiotti, G., Morterra, C., and Zecchina, A., *Z. Naturforsch. B* **42**, 728 (1987).
622. Karol, F. J., Karapiska, G. L., Wu, C., Dow, A. W., Johnson, R. N., and Carrick, W. L., *J. Polym. Sci. Part A1* **10**, 2621 (1972).
623. Karol, F. J., and Wu, L., *J. Polym. Sci. Part A1* **13**, 1607 (1975).
624. Zecchina, A., Spoto, G., and Bordiga, S., *Faraday Discuss. Chem. Soc.* **87**, 162 (1989).
625. Ruddick, V. J., and Baydal, J. P. S., *J. Phys. Chem. B* **102**, 2991 (1998).
626. Kettle, S. F. A., and Paul, I., *Adv. Organomet. Chem.* **10**, 199 (1972).
627. Spoto, G., and Zecchina, A., unpublished results.
628. Cossee, P., *J. Catal.* **3**, 80 (1964).
629. Irvin, K. J., Rooney, J. J., Stewart, C. D., Green, M. L. H., and Mahtab, R., *J. Chem. Soc. Chem. Comm.*, 604 (1978).
630. Vikulov, K., Spoto, G., Coluccia, S., and Zecchina, A., *Catal. Lett.* **16**, 117 (1992).
631. Lamberti, C., Bordiga, S., Geobaldo, F., Zecchina, A., and Otero Areán, C., *J. Chem. Phys.* **103**, 3158 (1995).
632. Zecchina, A., and Otero Arean, C., *Chem. Soc. Rev.* **25**, 187 (1996).
633. Smirnov, K. S., and Tsyganenko, A. A., *Opt. Spectrosc.* **60**, 667 (1986).
634. Ewing, G. E., *J. Chem. Phys.* **37**, 2250 (1962).
635. Bolis, V., Fubini, B., Garrone, E., and Morterra, C., *Stud. Surf. Sci. Catal.* **48**, 159 (1989).
636. Bolis, V., Zecchina, A., Bordiga, S., Turnes Palomino, T., and Lamberti, C., manuscript in preparation.
637. Egerton, T. A., and Stone, F. S., *J. Chem. Soc. Faraday Trans. I* **66**, 2364 (1970).
638. Egerton, T. A., and Stone, F. S., *J. Chem. Soc. Faraday Trans. I* **69**, 22 (1973).

Catalytic Hydrodenitrogenation

R. PRINS

*Laboratory for Technical Chemistry
Federal Institute of Technology
8092 Zurich, Switzerland*

The literature of the catalytic hydrodenitrogenation of nitrogen-containing compounds present in oil fractions is reviewed. Hydrodesulfurization is also discussed, but only insofar as it is relevant to hydrodenitrogenation. The emphasis is on the mechanisms of hydrodenitrogenation and how nitrogen can be removed from specific molecules. Two types of catalysts are discussed extensively, the classic metal sulfides (Co–Mo, Ni–Mo, Co–W, and Ni–W) and the recently introduced metal carbides and nitrides. Information about catalyst synthesis and structure is reviewed with the aim of improving the understanding of the catalytic mechanisms. Methods for improving the activity of metal sulfide catalysts by the addition of phosphate and fluorine additives, by supports other than alumina, and by means of metal sulfides other than the classic bimetallic ones are discussed as well. © 2001 Academic Press.

I. Introduction

In an oil refinery, oil is distilled into several fractions, including naphtha and gas oil. These fractions must be purified to diminish the contents of sulfur, nitrogen, and metals so that fewer air-polluting emissions of sulfur

Abbreviations: CHE, cyclohexene; DFT, density functional theory; DHQ, decahydroquinoline; EXAFS, extended X-ray absorption fine structure spectroscopy; HDN, hydrodenitrogenation; HDS, hydrodesulfurization; IEP, isoelectric point; k , reaction rate constant; K , adsorption equilibrium constant; K_{DHQ} , equilibrium constant for the adsorption of DHQ on the site for the reaction of PCHA; K_{NH_3} , equilibrium constant for the adsorption of NH_3 on the site for the hydrogenation of OPA; K_{OPA} , equilibrium constant for the adsorption of OPA on the site for the hydrogenation of OPA; K_{PCHA} , equilibrium constant for the adsorption of PCHA on the site for the elimination of NH_3 ; K_{PCHE} , equilibrium constant for the adsorption of PCHE on the site for the hydrogenation of PCHE; K'_{DHQ} , equilibrium constant for the adsorption of DHQ on the site for the hydrogenation of PCHE; K'_{NH_3} , equilibrium constant for the adsorption of NH_3 on the site for the hydrogenation of PCHE; K'_{OPA} , equilibrium constant for the adsorption of OPA on the site for the hydrogenation of PCHE; MCH, methylcyclohexane; MCHA, methylcyclohexylamine; MCHE, methylcyclohexene; OEA, O-ethylaniline; OHI, octahydroindole; OPA, O-propylaniline; PB, propylbenzene; PCH, propylcyclohexane; PCHA, propylcyclohexylamine; PCHE, propylcyclohexene; Q, quinoline; QEXAFS, quick extended X-ray absorption fine structure spectroscopy; TEM, transmission electron microscopy; THQ-1, 1,2,3,4-tetrahydroquinoline; THQ-5, 5,6,7,8-tetrahydroquinoline.

and nitrogen oxides are formed when these oil fractions are burned in cars and trucks. Furthermore, most catalysts used in a refinery for the processing of oil fractions cannot tolerate sulfur and metals. The removal of N, S, and metals is performed in so-called hydrotreating processes in which the feedstock reacts with hydrogen in the presence of a catalyst. This treatment is referred to as hydrotreating only when it is not accompanied by cracking of the hydrocarbons, and thus the boiling point of the oil fraction is hardly reduced. Hydrocracking, on the other hand, not only removes N, S, and metals but also leads to cracking of hydrocarbons to give lighter products. Thus, (heavy) gas oil is cracked to give middle distillates. Hydrocracking is carried out under much more severe conditions than hydrotreating (1, 2). For instance, hydrocracking can be performed at 10 MPa and 673 K, whereas hydrodesulfurization is performed at 3 MPa and 623 K. Mild hydrocracking is a process variant which has recently become popular because the moderate conditions under which it is performed enable the use of existing hydrotreater reactors but still result in some conversion to lighter products.

Most oil streams in a refinery must be hydrotreated; consequently, hydrotreating is the largest application in industrial catalysis based on the amount of material processed per year. On the basis of the amount of catalyst sold per year, hydrotreating catalysts rank third after exhaust gas catalysts and fluid cracking catalysts.

Industrial hydrotreating catalysts contain molybdenum and cobalt or nickel, supported on γ - Al_2O_3 (3–6). Since oil fractions always contain S, a metal or metal oxide that would be introduced as catalyst would quickly become sulfided by the H_2S that is produced during hydrotreating. In practice, one therefore sulfides supported metal oxides under controlled conditions before starting the hydrotreating process. When supported alone on alumina, molybdenum sulfide has a much higher activity for the removal of S, N, and O atoms than cobalt or nickel sulfide. Therefore, molybdenum sulfide is traditionally considered to be the actual catalyst. Sulfided $\text{Co-Mo/Al}_2\text{O}_3$ and $\text{Ni-Mo/Al}_2\text{O}_3$, on the other hand, have substantially higher catalytic activities than $\text{Mo/Al}_2\text{O}_3$. Consequently, cobalt and nickel are referred to as promoters (3–6). Cobalt is used mainly as a promoter for sulfided $\text{Mo/Al}_2\text{O}_3$ in hydrodesulfurization (HDS), whereas nickel is the choice for hydrodenitrogenation (HDN). In addition to molybdenum and cobalt or nickel, hydrotreating catalysts often contain additives incorporating elements such as phosphorus, boron, fluorine, or chlorine, which may influence the catalytic as well as the mechanical properties.

Hydrotreating catalysts originated in the 1920s when German researchers developed unsupported metal sulfide catalysts to liquefy coal. However, it was not until the 1970s that the structures of these catalysts and the mechanisms of their catalytic action began to be understood. It was established that under catalytic reaction conditions, most of the molybdenum in industrial

hydrotreating catalysts is present as small MoS₂ particles in the pores of the γ -Al₂O₃ support. It was not until the 1980s that the location of the cobalt and the nickel promoter ions in the hydrotreating catalysts was more or less determined. The role of phosphate and fluorine additives is still under investigation.

The chemical properties of tungsten are similar to those of molybdenum; tungsten is more expensive, however, and its industrial use is therefore limited. Especially when hydrogenation is carried out under severe conditions, such as in hydrocracking, sulfided Ni–W/Al₂O₃ catalysts have advantages over sulfided Ni–Mo/Al₂O₃.

This article is focused on HDN, the removal of nitrogen from compounds in oil fractions. Hydrodemetallization, the removal of nickel and vanadium, is not discussed, and HDS is discussed only as it is relevant to HDN. Section II is a discussion of HDN on sulfidic catalysts; the emphasis is on the mechanisms of HDN and how nitrogen can be removed from specific molecules with the aid of sulfidic catalysts. Before the discussion of these mechanisms, Section II.A provides a brief description of the synthesis of the catalyst from the oxidic to the sulfidic form, followed by current ideas about the structure of the final, sulfidic catalyst and the catalytic sites. All this information is presented with the aim of improving our understanding of the catalytic mechanisms. Section II.B includes a discussion of HDN mechanisms on sulfidic catalysts to explain the reactions that take place in today's industrial HDN processes. Section II.C is a review of the role of phosphate and fluorine additives and current thinking about how they improve catalytic activity. Section II.D presents other possibilities for increasing the activity of the catalyst, such as by means of other transition-metal sulfides and the use of supports other than alumina.

Section III is a discussion of HDN by catalysts different from metal sulfides, such as metals, metal carbides, and metal nitrides. The latter two classes of compounds have drawn much attention in the preceding decade in several fields of catalysis. Their possible role in hydrotreating is analyzed critically.

II. HDN on Sulfidic Catalysts

A. STRUCTURE OF THE CATALYST

1. *Structure of the Oxidic Catalyst Precursor*

Hydrotreating catalysts can be prepared by a two-step pore volume impregnation procedure or by coimpregnation (3–6). In the former method, γ -Al₂O₃ is impregnated with an aqueous solution of (NH₄)₆Mo₇O₂₄, followed by drying and calcination (heating in air). In a second step, the

resulting material is impregnated with an aqueous solution of $\text{Co}(\text{NO}_3)_2$ or $\text{Ni}(\text{NO}_3)_2$ and dried and calcined. Alternatively (and preferentially in the industry), all inorganic materials are coimpregnated, and the resulting catalyst precursor is dried and calcined. Results of several investigations indicate interactions between molybdenum and nickel or cobalt in the catalyst in the oxidic state. Thus, the order of impregnation and calcination—first molybdenum and then cobalt or nickel or vice versa—plays an important role in the activity of the final sulfided catalyst. Catalysts in which the support is impregnated first with a solution containing molybdenum invariably have a higher activity. It has been suggested that the cobalt and nickel cations interact with the polymolybdate phase by forming a metal heteropolymolybdate (7, 8). Several publications deal with this subject: For instance, the infrared absorption bands of NO adsorbed on Co–Mo/ Al_2O_3 are shifted from those of NO on Co/ Al_2O_3 (9), and Raman bands indicating polymeric molybdenum oxide species decrease in intensity with increasing cobalt loading in an oxidic Co–Mo catalyst (10). The results suggest that cobalt cations interact especially with the most polymerized molybdenum oxide species to form species in which cobalt and molybdenum interact. In this way the promoter cations stay at the surface and close to the molybdenum cations and are positioned to form the active Ni–Mo–S structure during sulfidation. Furthermore, the promoter ions interact to a lesser extent with the support and thus can be used more efficiently after sulfidation. The reason for the interaction of cobalt or nickel cations with the molybdenum oxyanions or polymeric molybdenum-containing species is that the isoelectric point (IEP) of the molybdenum-containing compounds is much lower than that of the alumina surface. The IEP is the pH value at which the surface is not charged when in contact with an electrolyte solution; surfaces are positively charged by proton uptake at a pH value less than the IEP and negatively charged at pH values greater than the IEP. Under the usual impregnation conditions (pH about 5), the oxidic molybdenum-containing species are negatively charged, and the alumina surface is positively charged. As a result, the cobalt and nickel cations adsorb on the oxidic molybdenum-containing species.

2. Structure of the Sulfidic Catalyst

The oxidic catalyst precursors, which are formed during the impregnation, drying, and calcination steps, are transformed into the actual hydrotreating catalysts by sulfidation in a mixture of H_2 and one or more compounds containing sulfur. H_2S , thiophene, CS_2 , dimethyl disulfide, or the oil fraction to be hydrotreated can be used for the sulfidation. The properties of the final sulfidic catalyst depend to a great extent on the calcination and sulfidation steps. Calcination at high temperature induces a strong interaction between molybdenum and cobalt or nickel cations and the Al_2O_3 support.

Consequently, it is difficult to transform the oxidic species into sulfides. Mössbauer spectroscopy of Co–Mo/Al₂O₃ catalysts showed that at increasingly high calcination temperatures, increasingly more Co²⁺ ions are incorporated into the bulk of the alumina (11). The higher the calcination temperature, the higher the sulfidation temperature needed to bring these cations back to the surface to provide a high catalytic activity for hydrotreating. At temperatures that are too high, however, the metal sulfides sinter or do not form the catalytically active Co–Mo–S structure. Optimum calcination and sulfidation temperatures are in the range 673–773 K for Al₂O₃-supported catalysts (12).

The sulfidation mechanism was investigated by temperature-programmed sulfidation, as the oxidic catalyst was heated in a flow of H₂S and H₂, and the consumption of H₂S and H₂ and the evolution of H₂O were measured continuously (13). It was found that H₂S is taken up and H₂O given off, even at room temperature, indicating a sulfur–oxygen exchange reaction. This conclusion was confirmed by quick extended X-ray absorption fine structure (QEXAFS) studies (Fig. 1, phase 2), which also demonstrated

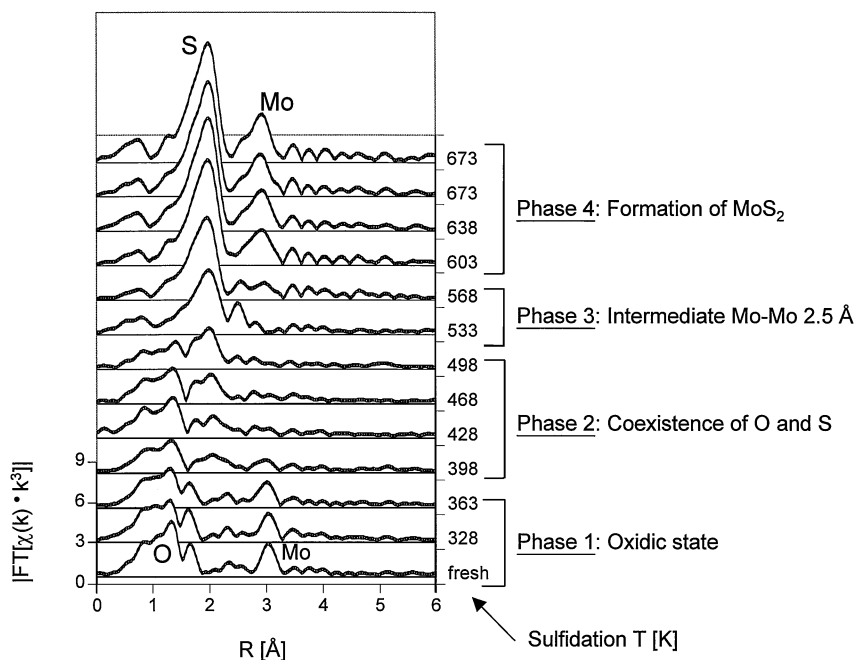


FIG. 1. Quick EXAFS spectra of the sulfidation of a Mo/Al₂O₃ catalyst, measured during continuous heating of the catalyst in 5% H₂S in H₂ from room temperature to 673 K at 5 K/min and holding at 673 K for 30 min.

that the Mo(VI) species containing both oxygen and sulfur transform into intermediate MoS_3 -type species at temperatures between 520 and 570 K (Fig. 1, phase 3) (14). At higher temperature, the MoS_3 is reduced to MoS_2 (Fig. 1, phase 4) with concomitant H_2 consumption and H_2S evolution (13).

During sulfidation and during hydrotreating catalysis, the conditions are highly reducing, and H_2S is always present; it follows from thermodynamics that molybdenum should be in the form of MoS_2 . Nevertheless, results obtained by X-ray photoelectron spectroscopy have shown that complete sulfidation of molybdenum, and especially of tungsten, is difficult. Apparently, some of the Mo(VI) ions interact so strongly with the Al_2O_3 support that they can be sulfided only at temperatures higher than 773 K. Molybdenum and tungsten can be sulfided more easily, however, in the presence of cobalt or nickel cations. EXAFS molybdenum K-edge absorption spectra demonstrated that, in well-sulfided Mo/ Al_2O_3 catalysts, the Mo–S and Mo–Mo distances are the same as in MoS_2 (15, 16); the only difference is that in the catalyst each molybdenum atom is surrounded, on average, by fewer than six molybdenum atoms, as for pure MoS_2 . EXAFS is a bulk technique by means of which the environment of surface molybdenum atoms as well as that of molybdenum atoms in the interior of the MoS_2 particles is determined. Consequently, a coordination number lower than 6 indicates that the proportion of surface molybdenum atoms is substantial and that the MoS_2 particles on the support surface typically contain about 60 molybdenum atoms each (16, 17).

MoS_2 has a layer lattice, and the sulfur–sulfur interaction between successive MoS_2 layers is weak. Crystals grow as platelets with relatively large dimensions parallel to the basal sulfur planes and small dimensions perpendicular to the basal plane. High-resolution transmission electron microscopy of model HDS catalysts consisting of MoS_2 crystallites on planar Al_2O_3 showed that the MoS_2 crystallites occurred as platelets with a height-to-width ratio between 0.4 and 0.7 (Fig. 2). Investigations of model catalysts consisting of MoS_2 grown on $\gamma\text{-Al}_2\text{O}_3$ films on the surfaces of MgAl_2O_4 supports have shown that MoS_2 grows with its basal plane parallel to the (111) surface of $\gamma\text{-Al}_2\text{O}_3$ and perpendicular to the (100) $\gamma\text{-Al}_2\text{O}_3$ surface (18). This observation suggests that the edges of the MoS_2 platelets are bonded to the (100) surface of $\gamma\text{-Al}_2\text{O}_3$ by Mo–O–Al bonds.

Nickel may be present in three forms after sulfidation: as Ni_3S_2 crystallites on the support, as nickel atoms adsorbed on the edges of MoS_2 crystallites (the so-called Ni–Mo–S phase), and as nickel cations at octahedral or tetrahedral sites in the $\gamma\text{-Al}_2\text{O}_3$ lattice (Fig. 3). Analogously, cobalt can be present as segregated Co_9S_8 , as Co–Mo–S, and as cobalt cations in the support. Depending on the relative concentrations of nickel (or cobalt) and molybdenum and on the pretreatment conditions, a sulfided catalyst may



FIG. 2. TEM image of a sulfided Ni-Mo/Al₂O₃ catalyst.

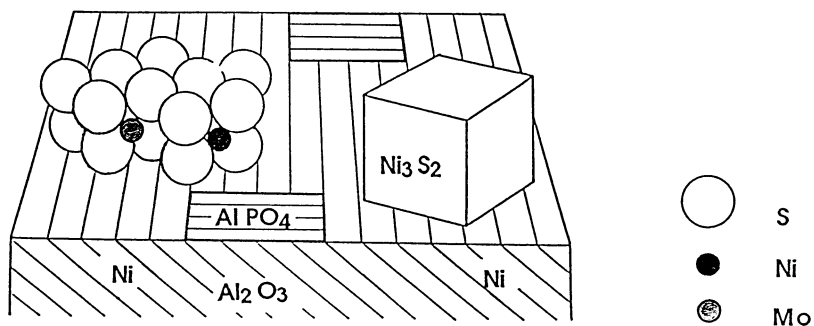


FIG. 3. Three forms of nickel present in a sulfided Ni-Mo/Al₂O₃ catalyst: as active sites on the MoS₂ edges (the so-called Ni-Mo-S phase), as segregated Ni₃S₂, and as Ni²⁺ ions in the support lattice.

contain a relatively large amount of either Ni_3S_2 (or Co_9S_8) or the Ni–Mo–S (or Co–Mo–S) phase.

Mössbauer (11), infrared, and EXAFS results confirmed the Ni–Mo–S (or Co–Mo–S) edge decoration model. The occurrence of nickel or cobalt adsorbed on MoS_2 is unexpected from the stand-point of thermodynamics, the most stable phases of nickel and cobalt under sulfiding conditions being Ni_3S_2 and Co_9S_8 , respectively. Nevertheless, the infrared spectra of NO molecules adsorbed on sulfided Co–Mo/ Al_2O_3 catalysts indicated that as the cobalt content increased at a fixed molybdenum content, the number of NO molecules adsorbed on cobalt sites increased and the number of NO molecules adsorbed on molybdenum sites decreased (19). Cobalt atoms at edge-decoration sites cover molybdenum atoms and block adsorption of NO on these molybdenum atoms. (Because we do not know whether MoS_2 should be considered as an ionic or a covalent solid, we use the word “atom” rather than “ion” for molybdenum, cobalt, nickel, and sulfur). The observed behavior is therefore in accord with the edge-decoration location.

EXAFS studies showed that a nickel atom in a sulfided Ni–Mo catalyst supported on $\gamma\text{-Al}_2\text{O}_3$ or on carbon is surrounded by four or five sulfur atoms at a distance of 2.2 Å, by one or two molybdenum atoms at a distance of 2.8 Å, and by one nickel atom at a distance of 3.2 Å (20). These data are consistent with a model in which the nickel atoms are located at the MoS_2 edges in the molybdenum plane in a square pyramidal coordination. The nickel atoms are connected to the MoS_2 by four sulfur atoms, and depending on the H_2S partial pressure a fifth sulfur atom may be present in the apical position in front of the nickel atom (Fig. 4). Recent density functional

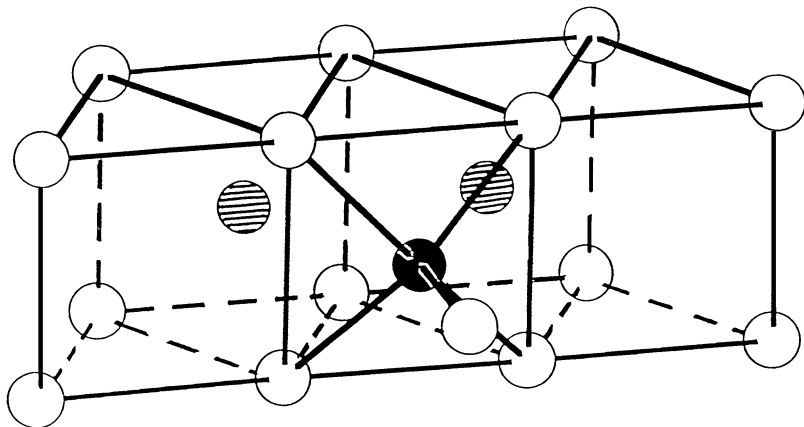


FIG. 4. Structure involving the nickel atoms in the Ni–Mo–S phase as determined by EXAFS spectroscopy(20); solid circle, nickel; open circles, sulfur; and shaded circles, molybdenum atoms.

theory (DFT) calculations suggested a different edge-decoration model (21). Instead of substituting molybdenum atoms at the $(10\bar{1}0)$ molybdenum edge, cobalt atoms were claimed to prefer to substitute molybdenum atoms at the $(\bar{1}010)$ sulfur edge. Other DFT calculations, however, indicated that these particular edge positions are an artifact of the too small MoS_2 clusters used to model MoS_2 in the calculations (22). DFT calculations with larger MoS_2 clusters showed that the most favorable location of the promoter atoms is the substitutional position at the molybdenum edge. The cobalt and nickel atoms extend, as it were, the MoS_2 lattice by taking up molybdenum positions (22). This conclusion is in good agreement with the EXAFS results (Fig. 4).

Mössbauer data of Crajé *et al.* (23) showed that the cobalt quadrupole splitting in $\text{Co-Mo/Al}_2\text{O}_3$ varies continuously with the cobalt loading and sulfiding temperature, which was suggested to be a consequence of the increasing size and ordering of the cobalt sulfide particles at the MoS_2 edges (23). At very low cobalt loadings and after sulfiding at relatively low temperatures, all the cobalt atoms can be positioned around the MoS_2 edges and the catalytic activity initially increases with increasing Co/Mo ratio. If all the edge positions are occupied, then additional cobalt atoms must be located on top of the cobalt atoms that are already present or must be present separately in Co_9S_8 crystallites. High sulfiding temperatures also lead to growth of the cobalt sulfide species as a result of growth of the MoS_2 crystallites and, as a consequence, a decrease in the MoS_2 edge area. Ultimately, relatively large Co_9S_8 particles form and are in contact with the MoS_2 particles. Since the Co_9S_8 particles have a low catalytic activity and cover the MoS_2 particles, the HDS activity of Co-Mo catalysts decreases at increasingly high Co/Mo ratios. Maximum activity is usually observed at a Co/Mo ratio of 0.3–0.5. This result implies that the MoS_2 particles present on the Al_2O_3 support must be so small that the ratio of the number of molybdenum edge atoms to the total number of molybdenum atoms is the same (i.e., 0.3–0.5) (24). Commercial catalysts usually have Co/Mo or Ni/Mo ratios slightly greater than 0.5, with molybdenum loadings of about 10–15 wt%.

3. Active Sites

As will be shown in Section II.B, HDN proceeds via several reactions. Which of the metal atoms described in Section II.A.2 are responsible for these reactions? Are molybdenum sites the catalytically active sites and, if so, how are they promoted by cobalt and nickel, or do the cobalt and nickel atoms constitute new sites which are supported on and influenced by MoS_2 ?

It was commonly assumed that the catalytically active sites in a hydrotreating catalyst are the molybdenum atoms at the surfaces of the MoS_2 crystallites, with at least one sulfur vacancy at a site to allow the reacting

molecule to bond chemically to the molybdenum atom (3–6). Since sulfur atoms in the basal planes of MoS_2 are much more difficult to remove than sulfur atoms at edges and corners, exposed molybdenum atoms are predominantly present at edges and corners. Catalysis therefore occurs at MoS_2 edges and corners rather than on the basal plane, as verified by results of a surface-science study in which a MoS_2 single crystal, with a high basal plane to edge surface area ratio, was found to have a low HDS activity. Its activity increased after the sulfur atoms were sputtered away from the basal plane and exposed to the molybdenum atoms (25). Scanning tunneling microscopy was used recently to image MoS_2 nanoparticles on a gold surface (26). Most MoS_2 nanoparticles had triangular shapes rather than the hexagonal shapes observed by electron microscopy for MoS_2 crystallites on Al_2O_3 . Exposure of the MoS_2 nanoparticles to hydrogen led to the creation of sulfur vacancies. Such vacancies at the MoS_2 edge are supposed to be the catalytically active sites for HDS.

The HDS and HDN activities of a $\text{MoS}_2/\text{Al}_2\text{O}_3$ catalyst both increase substantially on addition of cobalt or nickel. Several explanations for the promoter function of cobalt and nickel have been proposed (3–6). One model is based on the assumption that the promoter atoms induce a surface reconstruction of the edges of the MoS_2 layers, leading to a greater number of exposed molybdenum atoms and, thus, to enhanced activity (24). On the other hand, infrared (19) and EXAFS (16, 20) investigations demonstrated that the molybdenum atoms are covered by the sulfur and the promoter atoms. Thus, if only the molybdenum atoms were active, the activity should decrease upon addition of cobalt or nickel atoms.

Another model is based on the proposal that segregated cobalt sulfide is the promoter and that it supplies MoS_2 with hydrogen atoms. These “spilled-over” hydrogen atoms are inferred to create reduced centers on the MoS_2 surface, which are the catalytically active sites (27, 28); the Co_9S_8 would then have “remote control” over the MoS_2 surface. Combined Mössbauer and HDS activity studies demonstrated, however, that the promoter effect of cobalt is related to the cobalt atoms in the Co–Mo–S phase and not to separate Co_9S_8 (29). Small amounts of cobalt strongly increased the thiophene HDS activity and led preferentially to Co–Mo–S. Co_9S_8 formed only at higher cobalt loadings at which the activity had already leveled off. The catalytic activity actually decreased when Co_9S_8 became the dominant phase at high cobalt loadings.

A third model therefore attributed the promotion effect to cobalt present in the Co–Mo–S phase, with cobalt atoms located at the MoS_2 surface; a significant contribution of separate Co_9S_8 was excluded (29). This so-called Co–Mo–S model (or Ni–Mo–S model for Ni–Mo catalysts) is currently the one most widely accepted.

The Co–Mo–S model does not indicate whether the catalytic activity arises from molybdenum promoted by the presence of cobalt or from the cobalt sites. Both cobalt and nickel sulfide, supported on carbon, have higher HDS activities than MoS₂/C (30). Therefore, it has been suggested that the cobalt in the Co–Mo–S phase and the nickel in the Ni–Mo–S phase might be the catalysts and not the promoters. In the past, the idea that cobalt and nickel might be the catalysts in sulfided Co–Mo and Ni–Mo systems was rejected because sulfided Co/Al₂O₃ and Ni/Al₂O₃ catalysts have very low HDS activities. However, during the usual pretreatment of Co/Al₂O₃ or Ni/Al₂O₃ catalysts (that lack molybdenum), cobalt and nickel cations interact strongly with Al₂O₃. Therefore, during subsequent sulfidation, the metal cations are not sulfided at all and do not contribute to the HDS activity. Alternatively, severe sulfidation brings the metal cations back to the surface but lowers their dispersion and activity.

Carbon-supported cobalt and nickel sulfide catalysts, when carefully prepared, are indeed highly active. The activity of a sulfided Co–Mo/C catalyst, per cobalt atom, correlated much better with the estimated number of surface cobalt atoms in a sulfided Co/C catalyst than with the estimated number of edge molybdenum atoms in a MoS₂/C catalyst (31). The observation that the hydrogenation activity of Co–Mo (or Ni–Mo) catalysts resembles that of sulfided cobalt (or nickel) catalysts and is different from that of supported MoS₂ is further evidence that cobalt and nickel are the catalytic sites rather than Mo. As previously mentioned, infrared (19) and Mo-edge EXAFS data (16, 20) showed that molybdenum in Co–Mo and Ni–Mo catalysts is fully coordinated and not accessible to reactant molecules. The molybdenum therefore cannot be catalytically active. An EXAFS study (32) of the adsorption of selenophene (the selenium analog of thiophene) on a sulfided Ni–Mo/Al₂O₃ catalyst seemed to confirm this conclusion. Startsev *et al.* claimed that selenophene adsorption changed the nickel but not the molybdenum EXAFS spectrum, indicating that selenophene coordinated to nickel and not to molybdenum; molybdenum was evidently not accessible to selenophene. However, Medici *et al.* (33) observed that the Ni-edge EXAFS measured by Startsev *et al.* cannot be simulated by selenophene adsorbed on nickel. Leliveld *et al.* (34) repeated the selenophene EXAFS experiments of Startsev *et al.* (32) and showed that after reaction of selenophene and hydrogen with a Co–Mo catalyst at 473 K, selenium was exclusively coordinated to the cobalt atoms. At 673 K, on the other hand, the selenium atoms were found in bridge positions between cobalt and molybdenum. The authors interpreted this as evidence of two different vacancy sites in which the selenium atom can adsorb. One site has a sulfur vacancy associated with cobalt, and the other has a vacancy between cobalt and molybdenum. In subsequent work, the authors admitted, however, that an alternative explanation

is possible (35). It may be that at higher temperatures a redistribution takes place involving the selenium atoms originally bonded to cobalt in a terminal position and sulfur atoms in bridging positions between cobalt and molybdenum. Because of the stronger M–Se bonds, this seems a very likely possibility. Nevertheless, it seems clear that the first reaction takes place on cobalt and not on molybdenum.

Recent discussions of the catalytic sites have concentrated on a combined action of nickel (or cobalt) and molybdenum (21, 22, 36–38). In HDS, a sulfur-containing molecule is supposed to adsorb on a site with a sulfur vacancy and react to give a hydrocarbon molecule and a sulfur atom. This sulfur atom occupies the vacancy and must be removed by hydrogenation before the catalytic cycle can start again. It has been pointed out that a sulfur atom between a nickel (or cobalt) and a molybdenum atom is less strongly bonded than a sulfur atom between two molybdenum atoms; therefore, it can be more easily removed. This would explain the promoter action of nickel and cobalt on molybdenum in HDS. If HDN were to occur analogously to HDS, a nitrogen atom should be taken up by the metal sulfide catalyst particles and later removed by hydrogenation. This seems less likely than the equivalent sulfur uptake and removal in HDS, and it is suggested that the sites used in HDN are different from those used in HDS. As shown in the following section, C–S bond breaking is kinetically important in HDS, whereas the hydrogenation of N-containing aromatic rings is kinetically the most important step in HDN.

After this discussion of which metal atoms play a role in the catalytic site, the next question is how they are situated at the catalyst surface and what is the structure of the catalytic sites. Therefore, we first consider the edges of pure and promoted MoS₂. Raybaud *et al.* reported DFT calculations representing the edge surface of unpromoted (22) and promoted MoS₂ (38). Stoichiometric, hexagonal MoS₂ particles contain two types of edges (Fig. 5). The (10 $\bar{1}$ 0) edge is terminated by molybdenum atoms, and it is therefore called the molybdenum edge; in contrast, sulfur atoms terminate the ($\bar{1}$ 010) edge (sulfur edge). The local density functional calculations showed that addition of sulfur atoms to the molybdenum edge is an exothermic process for sulfur coverages up to 50% (22). Sulfur removal from the sulfur edge is endothermic. At low H₂S pressures in the gas phase, and thus at low H₂S/H₂ partial pressure ratios, the molybdenum atoms at the Mo edge have four nearest sulfur neighbors (Fig. 5). At a high H₂S/H₂ ratio (≥ 0.01), the molybdenum atoms have six nearest sulfur neighbors (Fig. 6), where the extra sulfur atoms are in bridging positions between molybdenum edge atoms.

The most stable position for the cobalt promoter atoms was calculated to be at the edge, substituting as it were for the molybdenum atoms (38). The promoter decreased the equilibrium sulfur coverage of the edge from 50 to 0–17% for Co/Mo(edge) = 1, and it weakened the sulfur–metal bond

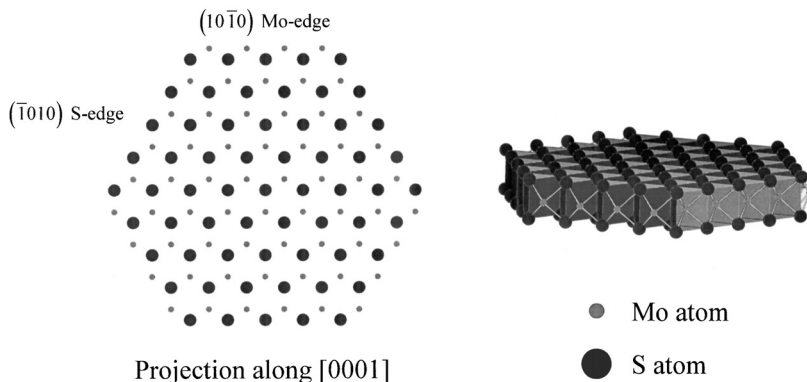


FIG. 5. Stoichiometric, hexagonally shaped MoS_2 particle with 25 Å diameter and 40% molybdenum edge atoms. The $(10\bar{1}0)$ edges are terminated by molybdenum atoms and the $(\bar{1}010)$ edges by sulfur atoms.

energy. In a (naive) ionic model of the bonding in metal sulfides, this result makes sense because the charge on Co^{2+} is lower than that on Mo^{4+} . The coordination of cobalt at the edge is almost identical to that of the molybdenum edge atoms in Figs. 5 and 6, apart from shorter Co–S than Mo–S distances.

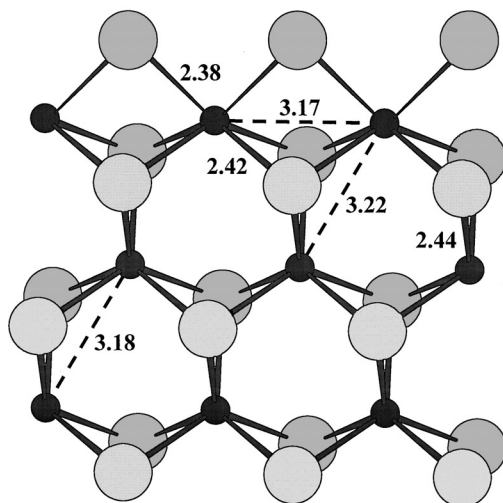


FIG. 6. Energy-optimized structure representing the molybdenum atoms at the Mo-terminated edge of MoS_2 particles at 50% sulfur coverage (22). The molybdenum atoms are represented in black, and the large sulfur atoms are shown in gray; the distances are in Angstroms.

The DFT calculations showed that the edge structure of MoS₂ and promoted MoS₂ can be substantially different from that of ideally cleaved MoS₂ slabs. The surface can relax and can take up sulfur atoms, as was predicted years ago by Farragher (39). The molybdenum (or cobalt or nickel) structures presented in Figs. 5 and 6 may represent the actual sites during catalysis. It is more likely, however, that some reorganization occurs before catalysis takes place. For instance, one could envisage that the bridging edge sulfur atoms in Fig. 6 shift to nonbridging on-top positions, thus creating a vacancy at the cobalt, nickel, or molybdenum atoms at the edge. A reacting molecule can then adsorb with its sulfur atom (in HDS) or nitrogen atom (in HDN) in this vacancy. Such a reorganized site may be the site where elimination of NH₃ from a nitrogen-containing molecule takes place. Probably the more open sites, with two vacancies (as in Fig. 5), are the sites where aromatic molecules are hydrogenated. At such sites, the aromatic ring can be π bonded (η^6) to the exposed molybdenum, cobalt, or nickel atoms at the molybdenum edge, as in Fig. 5.

In most publications concerned with these catalysts, no distinction is made between the structures of nickel and cobalt; it is commonly assumed that both are situated at identical positions at the MoS₂ edge, in the Ni–Mo–S and Co–Mo–S structures. The DFT calculations of Raybaud *et al.* (38) suggest that the sulfur coverage of these sites is lower in the nickel case than in the cobalt case. Future theoretical studies may indicate whether this difference is sufficient to explain why Ni–Mo is the better hydrogenation catalyst and Co–Mo the better HDS catalyst.

B. REACTION MECHANISMS

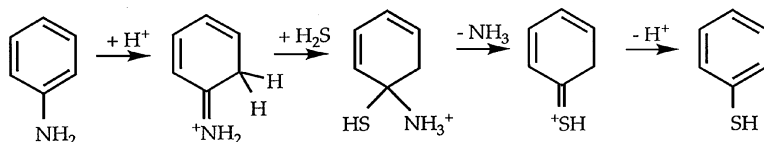
1. C–N Bond Breaking

a. *Aromatic C–N Bond Breaking.* C–N bonds in aromatic rings are much stronger than those in aliphatic rings. Consequently, C–N bonds in rings, as in pyridine and pyrrole, can be broken only after hydrogenation of the ring to give piperidine and pyrrolidine, respectively. Direct cleavage of a C–X bond external to an aromatic ring, as in C₆H₅–X, to give benzene and HX is the rule for X = Cl and SH. For X = OH and NH₂, direct cleavage occurs only to a limited extent and only at high H₂/H₂S ratios and high temperatures (above 673 K). The strength of the C–O bond in phenol and that of the C–N bond in aniline are increased through conjugation with the aromatic ring. Under normal hydrotreating conditions, the C–N bond can therefore be broken only when it is aliphatic. Hydrogenation of the N-containing heterocycle or of the aromatic ring to which the amine group is attached is necessary in order to obtain a substantial degree of nitrogen removal. Consequently, the products of HDN (and also

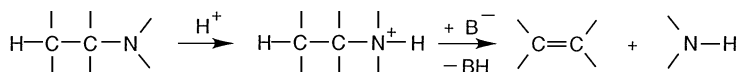
of hydrodeoxygenation) are aliphatic, whereas those of HDS (and hydrodechlorination) are aromatic; correspondingly, HDN consumes more hydrogen. This difference is a consequence of the lower energies of the C_6H_5-Cl and C_6H_5-SH bonds relative to the C_6H_5-OH and $C_6H_5-NH_2$ bonds.

How aniline reacts to benzene is not clear. This reaction is often referred to as hydrogenolysis because it behaves as a concerted reaction in which the C-N bond is split and the fragments are simultaneously hydrogenated. Such hydrogenolysis reactions are well-known for hydrocarbons on metal catalysts and are believed to occur on ensembles of metal atoms. The hydrocarbon molecule adsorbs on the metal surface, and neighboring carbon atoms bind to neighboring metal atoms. In this way, the C-C bond is weakened and broken, and hydrogen atoms on nearby metal atoms are used to hydrogenate the fragments. It is difficult to believe that such a hydrogenolysis reaction can occur on the surface of a metal sulfide. First, the distance between the metal atoms in a metal sulfide is much longer than in a metal, thus making it unlikely that there is a geometrical fit for the four-center $M-(C)-M-(N)$ reaction intermediate. Second, if hydrogenolysis of C-N bonds occurs, then hydrogenolysis of C-C bonds should also occur because these bonds are not much stronger than the aliphatic C-N bonds. On sulfided catalysts, in the presence of H_2S , however, only very little C-C bond breaking occurs.

Thus, how is benzene formed directly from aniline? Although a definite answer has not yet been given, it should be kept in mind that hydrogen favors the direct reaction of aniline to give benzene, whereas H_2S disfavors it (40). This means that an acid-catalyzed mechanism similar to that of the Bucherer reaction, in which naphthol is transformed into naphthylamine (41), seems unlikely. In that case, aniline might have reacted to give thiophenol via enol-keto tautomerism and NH_2-SH exchange by addition of H_2S and elimination of NH_3 [by analogy to reactions described in Refs. (42-44)]. The resulting thiophenol could then have reacted to give benzene (45) (Scheme 1). Another possibility for the direct conversion of aniline to benzene could involve partial hydrogenation of aniline to give dihydroaniline, followed by elimination of ammonia. The disadvantage of this mechanism is that the ammonia elimination has to take place by syn elimination rather than via the much



SCHEME 1



SCHEME 2

more common antielimination. Still another possibility is hydrogenolysis on a single molybdenum or nickel (or cobalt) atom on the metal sulfide surface. An argument against single-atom hydrogenolysis is that hydrogenolysis on metal surfaces is supposed to occur on ensembles of several metal atoms.

b. *Aliphatic C–N Bond Breaking.* As explained previously, the removal of nitrogen from nitrogen-containing aliphatic heterocycles is easier than that from aromatic heterocycles. Therefore, the principal mechanism for HDN starts with hydrogenation of the nitrogen-containing aromatic heterocycles. Thereafter, the nitrogen atom can be removed from the resulting aliphatic C–N fragment by classic organic chemistry such as elimination or by NH_2 -SH substitution, followed by C–S hydrogenolysis on oxidic or sulfidic cobalt- or nickel-promoted molybdenum or tungsten catalysts (46–48). In the Hofmann elimination, an acid helps to quaternize the nitrogen atom, thereby creating a better leaving group, whereas a base promotes elimination by removal of a β -hydrogen atom (Scheme 2).

There is evidence of the existence of Brønsted acid sites in sulfided molybdenum, Co–Mo, and Ni–Mo catalysts (49). It has also been shown that it is easy to remove NH_3 from aliphatic amines having hydrogen atoms on the carbon atoms in the β position and that the rate is higher for molecules with more β -hydrogen atoms (50). Thus, the rate of HDN of *t*-pentylamine is higher than that of pentylamine at 523 K, and the rate of HDN of 2,6-dimethylpiperidine is higher than that of piperidine at 548 K. The rate of HDN of neopentylamine (2,2-dimethylpropylamine, which has no β -hydrogen atoms) is negligible under these conditions. These experiments were done with a sulfided Ni–Mo/ Al_2O_3 catalyst at a total pressure of 2 MPa and a partial pressure ratio $\text{H}_2\text{S}/\text{H}_2 = 1.7 \times 10^{-3}$.

A remaining question about the elimination process on a solid surface is the geometric structure of the adsorbed molecule during reaction. If the elimination is a concerted reaction, the acidic function of the catalyst surface (which binds the amine part of the reactant) and the basic function (which abstracts the β -hydrogen atom) should act simultaneously. In that case, it seems as if the reacting amine can assume only a configuration close to the syn configuration shown in Fig. 7. However, syn eliminations are less common than trans eliminations, and we have shown that the elimination of ammonia from amines occurs primarily via trans elimination [F. Rota, V. Ranade, and R. Prins, *J. Catal.* **200** (2001), to be published]. This problem was realized even

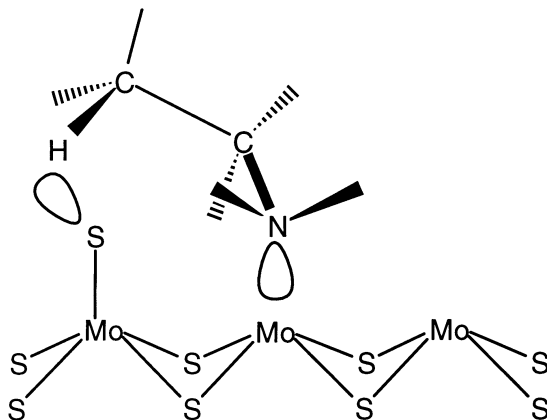


FIG. 7. Syn configuration of the reacting amine during E_2 elimination at a MoS₂ surface.

in the 1960s when the analogous elimination of water from an alcohol catalyzed by Al₂O₃ was studied. To solve this problem, Pines and Manassen (51) suggested that the trans elimination of water occurs by bonding of the OH group of the alcohol on one wall of a crevice in the Al₂O₃ surface, with bonding of the β -hydrogen part of the molecule on the opposite wall. Knözinger *et al.* (52) attempted to explain the trans elimination by assuming adsorption on neighboring acid and basic sites on the same surface and by taking rocking vibrations into account. A careful look at the geometric constraints shows, however, that trans β -hydrogen abstraction is actually very possible if a sulfur atom protrudes from the surface, as in Fig. 8. In that case, the N-C-C-H plane of the amine can be inclined to the edge surface but parallel to the sulfur rows instead of being almost perpendicular to the sulfur rows (Fig. 7). Similarly, trans elimination can be explained by the combination of a basic sulfur

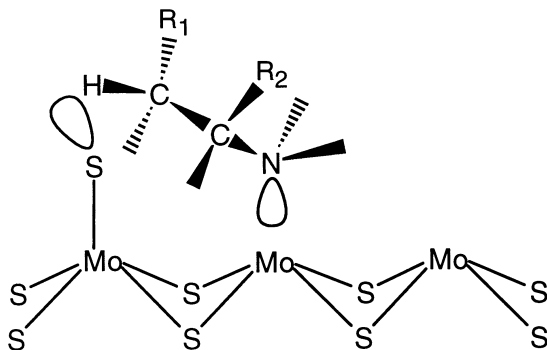
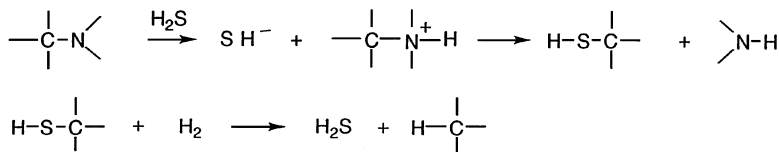


FIG. 8. Anticonfiguration of the reacting amine during E_2 elimination at a MoS₂ surface.



SCHEME 3

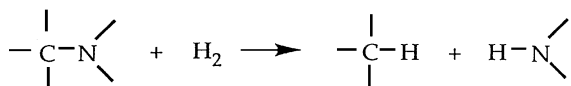
atom and an acidic SH group. In that case, the SH group may protrude from the surface, as does the sulfur atom in Fig. 8, while the sulfur atom is in the edge (one of the four sulfur atoms around each molybdenum atom in Fig. 8).

In the transition state structure represented by Fig. 8, alkyl groups R_1 and R_2 on the neighboring α and β carbon atoms must be oriented away from the catalyst surface because of steric hindrance, although the molecule has to adopt the less stable *gauche* conformation. This explains why *cis*-alkenes are formed preferentially (52).

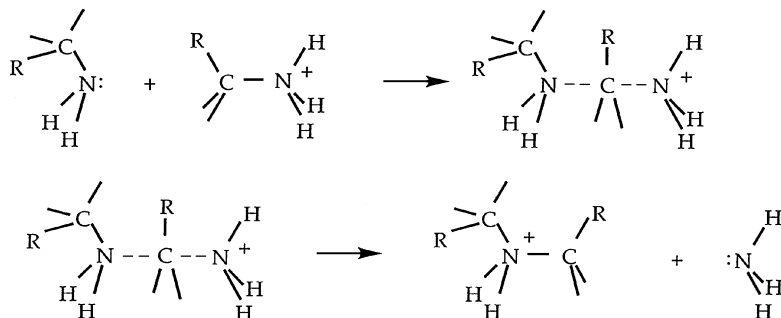
Amines which have no β -hydrogen atoms can still be denitrogenated, although at higher temperatures. Thus, benzylamine ($\text{C}_6\text{H}_5\text{---CH}_2\text{---NH}_2$) was completely denitrogenated to give toluene at 623 K (53). This result can be explained by nucleophilic substitution of the amine group by an SH group, followed by hydrogenolysis of the C-S bond, which is known to be very easy (54, 55). The removal of nitrogen then occurs as shown in Scheme 3.

An alternative explanation of C-N bond breaking in molecules that lack β -hydrogen atoms would be direct hydrogenolysis of the alkylamine to give a hydrocarbon and NH_3 (Scheme 4). This reaction does not seem to be important, however, because of the observed positive effect of H_2S on C-N bond breaking. Apparently, the route via nucleophilic substitution of the amino group by an SH group, followed by C-S hydrogenolysis, is faster than direct $\text{C}(\text{sp}^3)\text{---N}$ hydrogenolysis. Evidence of direct hydrogenolysis of an aliphatic C-N bond (i.e., a concerted reaction in which a C-N bond is broken and C-H and N-H bonds are formed) has not yet been presented for metal sulfide catalysts. Therefore, the term hydrogenolysis should not be used to describe C-N bond breaking until hydrogenolysis has been demonstrated mechanistically.

The acid-catalyzed amine disproportionation, $\text{R}_1\text{NH}_2 + \text{R}_2\text{NH}_2 \rightarrow \text{R}_1\text{R}_2\text{NH} + \text{NH}_3$, always occurs in parallel with HDN. Mechanistically, it is another example of $\text{S}_{\text{N}}2$ nucleophilic substitution, namely, of the NH_2 group



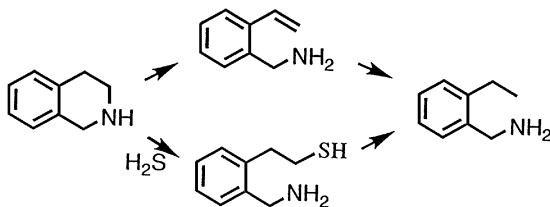
SCHEME 4



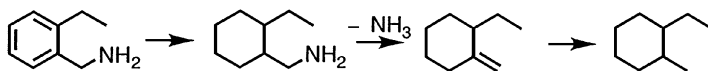
SCHEME 5

of one amine molecule by the amine group of another amine molecule (56) (Scheme 5). If the resulting dialkylamine contains β -hydrogen atoms, it can undergo elimination as well ($\text{R}_1\text{-NH}_2^+\text{-CH}_2\text{-CH}_2\text{-R}_2 \rightarrow \text{R}_1\text{-NH}_2 + \text{CH}_2 = \text{CH-R}_2 + \text{H}^+$). Therefore, and also because of the formation of the dialkylamine via nucleophilic substitution, it is not always possible to disentangle the roles of nucleophilic substitution and elimination in the HDN of aliphatic amines. Since branching at the α and β carbon atoms lowers the rate of elimination to a lesser extent than the rate of nucleophilic substitution, branching favors elimination (57). This explains why although a substantial amount of dialkylamine is observed in the HDN of pentylamine (56) and of piperidine (58), only a small amount is observed in the HDN of decahydroquinoline (59).

The foregoing discussion has shown that the main routes for the removal of a nitrogen atom are by elimination and by nucleophilic substitution followed by hydrogenolysis. This explains why the predominant C_9 hydrocarbon that results from the HDN of isoquinoline is the aromatic 2-methylethylbenzene (45, 53), whereas the main HDN product of quinoline is the aliphatic propylcyclohexane (45, 60). Hydrogenation of isoquinoline gives 1,2,3,4-tetrahydroisoquinoline. One of the C-N bonds of this molecule can be broken by elimination followed by hydrogenation or by substitution by H_2S followed by hydrogenolysis (Scheme 6). The resulting 2-methylamino



SCHEME 6

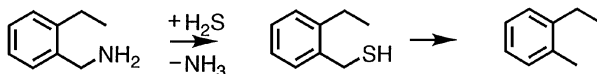


SCHEME 7

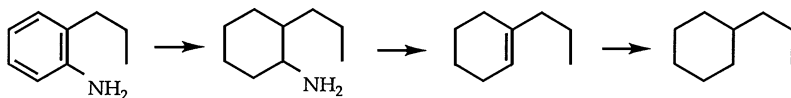
ethylbenzene has no hydrogen atoms in the β position in relation to the nitrogen atom; breaking of the last C–N bond by elimination is therefore not possible. Hydrogenation of the benzene ring would create a β -hydrogen atom, after which NH_3 elimination could take place, leading to 2-methylethylcyclohexane (Scheme 7). In reality, 2-methylethylbenzene, not 2-methylethylcyclohexane, is formed. This result demonstrates that substitution and hydrogenolysis are faster than hydrogenation of the benzene ring (53) (Scheme 8). In a control experiment, Vivier *et al.* (53) showed that under the same conditions, benzylamine ($\text{C}_6\text{H}_5\text{-CH}_2\text{-NH}_2$) reacted completely to give toluene and ammonia. In the same way, *N*-methylaniline quickly reacted to give aniline and methane with only a small amount of ammonia being formed (61, 62). These results clearly show that aliphatic C–N bonds can be broken much more easily than C–N bonds, in which the C atom is part of an aromatic ring.

In the HDN of quinoline, on the other hand, the different position of the nitrogen atom does not allow substitution in the final C–N bond breaking. After hydrogenation of quinoline to give 1,2,3,4-tetrahydroquinoline and breaking of the first C–N bond (either by elimination or by substitution and C–S hydrogenolysis), the nitrogen atom in 2-propylaniline is attached to a C(sp^2) atom rather than to a C(sp^3) atom. Consequently, substitution of the amine group by a SH group is highly unlikely. The only route left for nitrogen removal is further hydrogenation of the benzene ring. This hydrogenation introduces β -hydrogen atoms which can be used in the elimination reaction. Initially, propylcyclohexene is formed, which at the relatively high H_2 pressure applied in HDN reacts mainly to propylcyclohexane (Scheme 9).

When both elimination and substitution followed by C–S hydrogenolysis are possible, elimination usually dominates, especially when there is branching at the α and/or β carbon atoms. Thus, 80% methylcyclohexene and 20% methylcyclohexane were formed as initial products in the HDN of 2-methylcyclohexylamine (40), demonstrating that elimination is the main route of nitrogen removal.



SCHEME 8

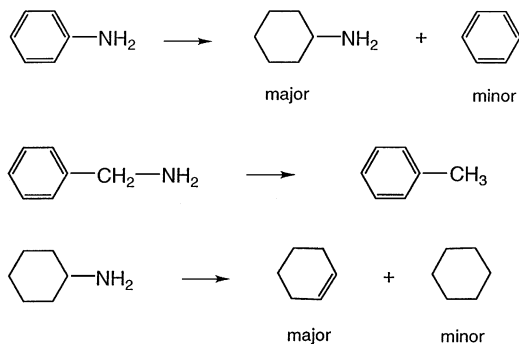


SCHEME 9

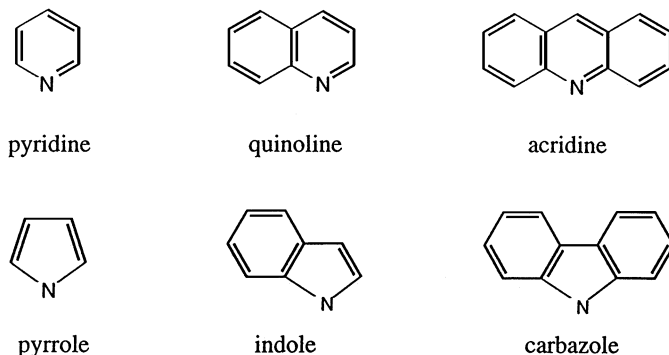
In conclusion, the results presented in this and the previous sections show that the HDN of polycyclic aromatic nitrogen compounds starts by hydrogenation of the nitrogen-containing aromatic ring followed by ring opening/elimination to give an aliphatic amine or an arylamine or cyclohexylamine. These exocyclic amines react further according to one of the three reactions indicated in Scheme 10. The first of these reactions is a hydrogenation to give the major cyclohexylamine product and (possibly) a hydrogenolysis to give the minor product benzene. A high H_2 pressure and low H_2S pressure accelerate these reactions. The second and third reactions are accelerated by H_2S . In the reaction of benzylamine to give toluene and in the reaction of cyclohexylamine to give cyclohexene, the acceleration results because H_2S is the reactant in the S_N2 reaction. In the elimination of NH_3 from cyclohexylamine, adsorbed H_2S increases the acidity of the catalyst.

2. HDN of Specific Molecules

Polycyclic aromatic nitrogen compounds, such as quinoline, indole, acridine, and carbazole, are the main nitrogen-containing compounds in oil fractions, and monocyclic pyridine and pyrrole as well as anilines are present in coal tar (Scheme 11). Saturated cyclic amines are found as products of ring hydrogenation of the compounds shown in Scheme 11 after HDN. Aliphatic amines are rarely found in fuels and only in low concentrations after HDN since their nitrogen atoms are easily removed.



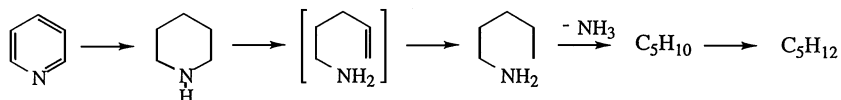
SCHEME 10



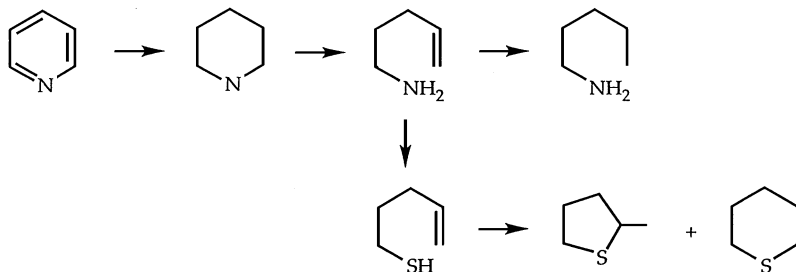
SCHEME 11

Much higher H_2 pressures are required for substantial conversions in HDN than in HDS. This difference is explained by the greater aromaticity of a ring containing nitrogen than a ring containing sulfur. Consequently, HDS can take place by hydrogenolysis, even of C–S bonds next to an aromatic ring, as in thiophenol. In hydrodenitrogenation, on the other hand, the nitrogen-containing ring must be hydrogenated before the subsequent ring opening and hydrogenation can occur.

a. *Pyridine and Piperidine.* Nitrogen is removed from pyridine as shown in Scheme 12 (45, 58, 63, 64). The first hydrogenation reaction is inferred to be catalyzed by sulfur-poor sites on the metal sulfide surface since H_2S has a negative influence on this step. The second, ring-opening reaction and the fourth, nitrogen-removal reaction probably occur by elimination and lead to alkene intermediates. Pentene, the product of the elimination of pentyamine, was found, but 5-aminopentene-1 (1-pent-4-enylamine), the product of elimination of piperidine, has never been observed in HDN, probably because there is a fast consecutive hydrogenation to give pentyamine before desorption from the catalyst surface takes place. HDN experiments carried out at high H_2S pressure ($P_{H_2} = 4$ MPa and $P_{H_2S} = 1.8$ MPa) clearly indicated that this amino-alkene was present during the reaction. At high H_2S partial pressure, 2-methyl-thiacyclopentane and thiacyclohexane were found as products (65, 66). The high H_2S concentration induced a nucleophilic



SCHEME 12



SCHEME 13

substitution of the amino group of 5-aminopentene-1 by the SH group, and the resulting 5-thiopentene-1 (1-pent-4-enethiol) reacted intramolecularly to give a five- or six-membered thiacycloalkane. The fact that these two molecules were observed in the HDN of pyridine, piperidine, and 5-aminopentene-1, but not in that of 1-pentylamine, strongly supports the mechanism shown in Scheme 13. Ring opening and removal of nitrogen are promoted by H_2S , which makes it very likely that these are elimination reactions that take place on relatively sulfur-rich sites on the surface of the metal sulfide catalyst.

The rate of hydrogenation of pyridine is about as low as that of the ring-opening elimination of piperidine on Ni-Mo, Co-Mo, and Ni-W catalysts at a temperature of about 573 K and pressure of 3 MPa. This observation means that H_2S may have a promoting as well as a poisoning effect on the HDN of pyridine under these conditions. At a low $\text{H}_2\text{S}/\text{H}_2$ ratio, pyridine hydrogenation to piperidine runs smoothly, but ring opening of piperidine by β -hydrogen elimination is slow, thus leading to a low overall HDN conversion to C_5 hydrocarbons (Table I). Under such conditions, the effect of adding nickel to molybdenum is not very important for total HDN to give C_5 products (Table I). This observation has led some (67, 68) to conclude that nickel does not promote molybdenum for HDN as it does for HDS.

At a higher $\text{H}_2\text{S}/\text{H}_2$ ratio, hydrogenation of pyridine to piperidine is slower, but ring opening is accelerated. Thus, even at a lower pyridine conversion, the yield of hydrocarbons increases (69) (Table I). At an even higher $\text{H}_2\text{S}/\text{H}_2$ ratio, the negative effect of H_2S on pyridine hydrogenation is responsible for low conversions to pyridine and low HDN conversions. At lower H_2 pressures and higher temperatures, pyridine hydrogenation becomes rate determining, and H_2S becomes increasingly toxic. At high H_2 pressures and low temperatures, H_2S acts as a promoter because the ring-opening reaction becomes rate determining. Under such conditions, nickel clearly promotes the HDN of pyridine (Table I).

TABLE I
Influence of H₂S on the Conversion and Product Yields (%) in the HDN of Pyridine and Piperidine (PIP) at 593 K and 3 MPa Catalyzed by Sulfided Mo/Al₂O₃ and Ni-Mo/Al₂O₃^a

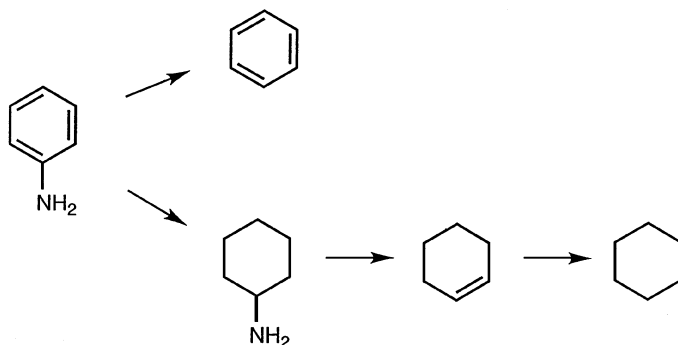
Catalyst	Reactant	H ₂ S/H ₂ = 0			H ₂ S/H ₂ = 3.10 ⁻³		
		Conversion	PIP	C ₅	Conversion	PIP	C ₅
Mo	Pyridine	40	34	4	26	16	7
NiMo	Pyridine	57	49	4	48	18	24
Mo	Piperidine	13		5	23		14
NiMo	Piperidine	16		6	60		48

^aFrom Mou Jian *et al.* (69).

At relatively high concentrations of amine intermediates, *N*-pentylpiperidine forms as a by-product by the disproportionation of piperidine and pentylamine (45, 59). This by-product is denitrogenated at high conversions of the reactant.

Several investigations of the HDN of pyridine or piperidine were carried out at atmospheric pressure (67, 70, 71). As expected from thermodynamics, the conversion of pyridine at atmospheric pressure is low. HDN of piperidine was carried out on alumina (70) and amorphous silica-alumina (71) at atmospheric pressure. Under such conditions and in the absence of a (de)hydrogenation component in the catalyst, piperidine is converted mainly to pyridine. At the same time, the reaction of highly reactive intermediates is not suppressed by hydrogenation, and a substantial number of C₁₀ hydrocarbons were formed. Acid-catalyzed reactions of the pentadienes, formed by elimination of ammonia from piperidine, account for the formation of these higher hydrocarbons. Hydrogen-transfer reactions between the resulting unsaturated higher hydrocarbons and piperidine explain the occurrence of saturated hydrocarbons as well as pyridine.

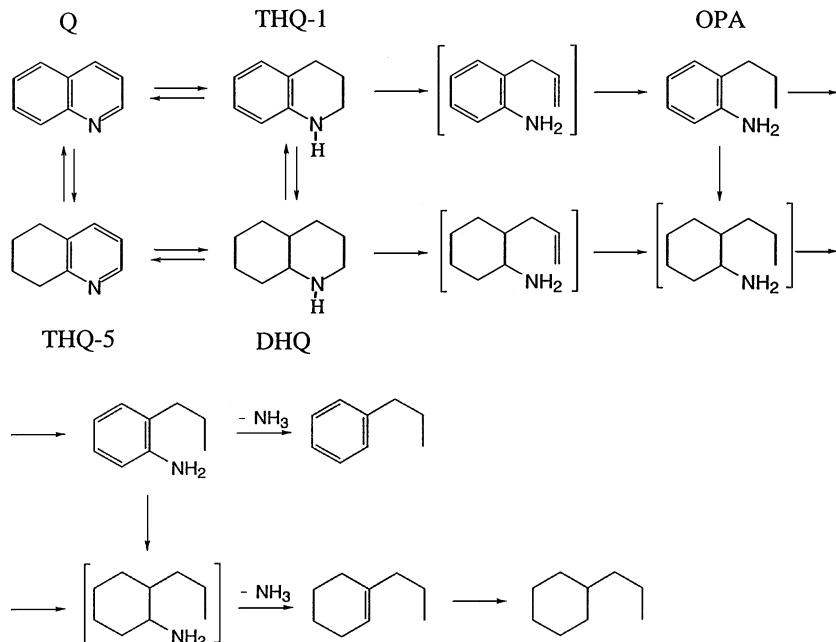
b. *Aniline*. Hydrogenation of the aromatic ring is not only a prerequisite for the removal of the nitrogen atom from pyridine, it is also important for the removal of the nitrogen atom from aniline. As shown previously, the HDN of aniline occurs mainly via hydrogenation to give cyclohexylamine, which very quickly undergoes elimination of NH₃ to give cyclohexene (45, 72). Cyclohexene is then hydrogenated to cyclohexane. A small part of the aniline, however, is directly transformed to benzene and ammonia, as observed for aniline and alkylanilines (72–75). Because aniline adsorbs much more strongly than benzene on (de)hydrogenation sites of the catalyst and expels benzene from these sites (by competitive adsorption), hardly any



SCHEME 14

cyclohexene is formed by hydrogenation of benzene as long as aniline is present (76). For the same reason, dehydrogenation of cyclohexene to benzene is important only at high conversions. Apart from very high conversions, the reaction network of the HDN of aniline can therefore be described simply by two parallel reactions. On the one hand, aniline gives benzene, and on the other hand, via a consecutive reaction, it gives cyclohexylamine and then cyclohexene and finally cyclohexane (Scheme 14). Later, it is shown that cyclohexylamine can even react directly to cyclohexane by nucleophilic substitution of the NH_2 group by a SH group, followed by C-S hydrolysis.

c. *Quinoline*. Because of the bicyclic nature of quinoline, with a carbocyclic as well as a heterocyclic six-membered ring, there are two ways in which the nitrogen atom can be removed (Scheme 15). One path is via *o*-propylaniline (OPA), and the second is via decahydroquinoline (DHQ). Since the C-N bond in the aromatic heterocycle is too strong to break (as in pyridine), hydrogenation of the heterocycle is necessary in both pathways. In the first, the heterocycle in quinoline (Q) is hydrogenated to 1,2,3,4-tetrahydroquinoline (THQ-1). This is a very fast reaction and, under most conditions, equilibrium is reached between Q and THQ-1 (60). Thereafter, ring opening of the heterocycle to OPA takes place via the highly reactive *o*-propenylaniline intermediate. In principle, propylaniline should be able to undergo denitrogenation just as aniline does. It might therefore be expected that the HDN of quinoline would take place predominantly via OPA. This is not necessarily the case, however, since competitive HDN studies of aniline and DHQ showed that DHQ adsorbs much more strongly than aniline (or even OPA) (77). In the presence of DHQ, Q, or THQ-1, the rate of HDN of OPA is therefore suppressed (60, 78). At 643 K and 3 MPa, and in the



SCHEME 15

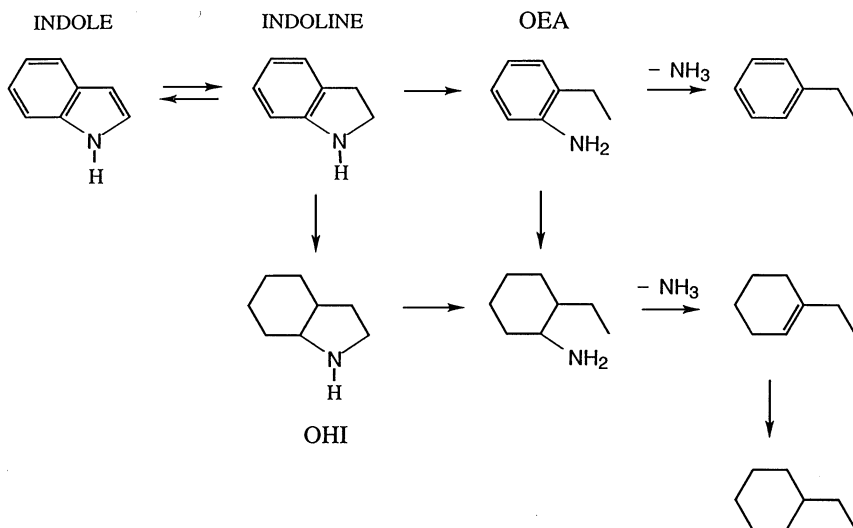
presence of H₂S, only about 40% of the HDN of quinoline takes place via the THQ1–OPA pathway (79).

In the second HDN pathway of quinoline, quinoline is first fully hydrogenated to DHQ via the sequence THQ-1, DHQ or 5,6,7,8-tetrahydroquinoline (THQ-5), and then DHQ. The hydrogenations of the carbocycles of Q and THQ-1 are slow at temperatures below 623 K. A high conversion of Q to DHQ is promoted by a high H₂ pressure and a low H₂S/H₂ ratio. Furthermore, a sufficiently high temperature aids the conversion of Q to DHQ (this is a matter of kinetics); however, the temperature should not be too high because thermodynamics would then favor aromatics. DHQ undergoes removal of the nitrogen atom via ring-opening elimination to *o*-propenylcyclohexylamine, which is expected to have a high adsorption constant and a high rate of hydrogenation (it has therefore not been observed). HDN experiments carried out at high H₂ as well as high H₂S pressures provided evidence of the formation of *o*-propenyl-cyclohexylamine. As in the HDN of pyridine and of piperidine, it was shown that a high H₂S pressure in the HDN of THQ-1 leads to the formation of five- and six-membered thiacycloalkane rings, in this case octahydro-2H-1-benzothiopyrane and

octahydro-2-methylbenzothiophene (66). In normal HDN, however, *o*-propylcyclohexylamine is quickly hydrogenated. The resulting *o*-propylcyclohexylamine is also highly reactive and has been observed only in low concentrations (76). It quickly reacts via NH_3 elimination to give *o*-propylcyclohexene, which mainly undergoes hydrogenation to propylcyclohexane, as long as a substantial amount of amine is present to block its dehydrogenation to propylbenzene. For the same reason, the reaction of propylbenzene to propylcyclohexane can be ignored.

Since the DHQ pathway is usually more important for the removal of nitrogen from quinoline than the OPA pathway, the HDN of quinoline is similar to that of pyridine. Initially, total hydrogenation of the reactant takes place, followed by two consecutive C–N bond breakings and, eventually, hydrogenation to give aliphatic products. H_2S promotes the HDN of quinoline at 623–643 K and 3–7 MPa (80, 81). This result demonstrates that hydrogenation is not rate determining. As in the case of pyridine, the kinetic situation is not simple. Both hydrogenation and C–N bond breaking are slow, and the kinetics cannot be described by a model including a rate determining step. The effect of the H_2S partial pressure on the two pathways for the HDN of quinoline is different (81, 82). In the route from THQ-1 via OPA to *o*-propylcyclohexylamine, the C–N bond-breaking elimination is promoted by H_2S , whereas the hydrogenation of OPA is inhibited by H_2S . As a result, there is an accumulation of OPA with increasing H_2S pressure. In the route from Q via DHQ to *o*-propylcyclohexylamine, the hydrogenation of Q to give DHQ is suppressed by H_2S , and the C–N bond-breaking elimination of DHQ is promoted by H_2S . Therefore, at increasing H_2S pressures, less DHQ is observed in the reaction mixture because it is produced at a lower rate and reacts at a higher rate.

d. *Indole*. Indole is comparable to quinoline in incorporating a carbocyclic as well as a heterocyclic ring. The heterocycle, however, is five-membered and less aromatic than the six-membered pyridine ring of quinoline. Therefore, the exclusive initial reaction in HDN is the hydrogenation of the heterocyclic ring to form indoline (2,3-dihydroindole). On the basis of a presumed analogy to the two reaction paths of THQ-1 to DHQ and OPA for quinoline HDN, one would expect that in the case of indole two paths are important as well—one proceeding via hydrogenation of indoline to octahydroindole (OHI) and the other via ring opening of indoline to *o*-ethylaniline (OEA). In contrast to quinoline HDN, however, it is generally assumed that the path via OEA is the main one for indole (45, 73, 83). Analogous to the conversion of aniline and OPA, the conversion of OEA takes place mainly via hydrogenation to *o*-ethylcyclohexylamine and subsequently to ethylcyclohexene and ethylcyclohexane (45, 83–85). On the other hand, it



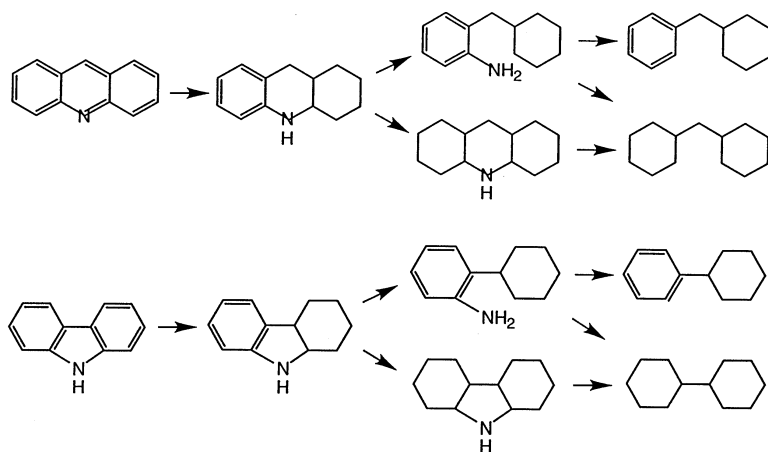
SCHEME 16

has been observed that indole and indoline strongly inhibit the conversion of aniline (and thus ethylaniline) (84), just as quinoline and tetrahydroquinoline inhibit the conversion of propylaniline. This result suggests that, as in the HDN network of quinoline, the totally hydrogenated OHI intermediate may be as important as *o*-ethyl-aniline. Indications of such a contribution were observed by Zhang and Ozkan (86). In a recent study of six methyl-substituted indoles, Kim and Massoth (87) also considered the OHI route. The resulting analysis showed that this route is more important than the ethylaniline route for Ni–Mo catalysts, whereas the reverse is true for Co–Mo catalysts (87). Apparently, the OHI route is more important on a Ni–Mo catalyst than on a Co–Mo catalyst because of the higher hydrogenation activity of the former (Scheme 16).

The reactions described in the foregoing—hydrogenation and C–N bond breaking via elimination or nucleophilic substitution followed by C–S hydrolysis—explain the main products and intermediates observed in the HDN of pyridine, aniline, quinoline, and indole on sulfided (nickel- or cobalt-promoted) molybdenum or tungsten catalysts. Investigations of the minor components showed that acid-catalyzed cracking and isomerization reactions also play a role. These reactions explain the formation of some indane, methylindole, and methylpropylcyclopentane in the HDN of quinoline (88). Acid-catalyzed disproportionation is responsible, for example, for the increase in *o*-toluidine (2-methylaniline) and mesidine (2,4,6-trimethylaniline) in the HDN of 2,6-dimethylaniline at increasing H_2S pressure (74).

e. *Nitrogen-Containing Polycyclic Molecules.* The HDN of large aromatic molecules that contain nitrogen occurs in principle as described previously for smaller molecules. First, the ring containing nitrogen and the neighboring ring are hydrogenated; then C–N bond breaking occurs via elimination. For example, two adjacent rings of acridine are first hydrogenated to give octahydroacridine, which reacts further, as does 1,2,3,4-tetrahydroquinoline (see Section II.B.2.c) (45, 89). Thus, the aliphatic C–N bond breaks through elimination, and the resulting cyclohexyl-2-aminophenylmethane reacts as propylaniline does. Another possibility is further hydrogenation to perhydroacridine with loss of the nitrogen atom by double elimination (Scheme 17). Carbazole, the five-ring equivalent of acridine, is hydrogenated to give hexahydrocarbazole, which reacts as indoline does (see Section II.B.2.d). Hexahydrocarbazole can form 2-cyclohexylaniline by breaking of the aliphatic C–N bond, and it can react further as does propylaniline. Hexahydrocarbazole can also be hydrogenated further to perhydrocarbazole, which then forms bicyclohexyl by losing nitrogen through two eliminations and hydrogenations (45, 90) (Scheme 17).

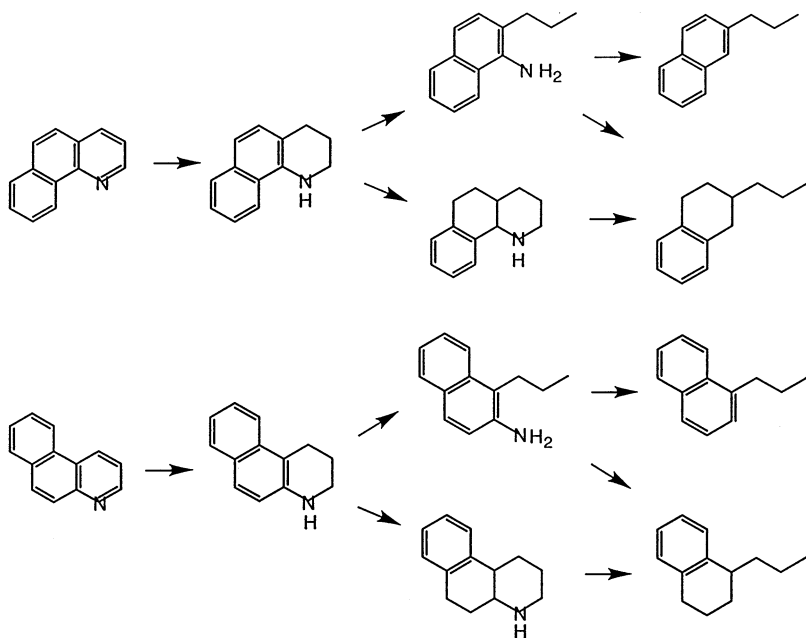
The HDN of benzoquinolines has been investigated as well. In the HDN of 5,6-benzoquinoline (91, 92) and of 7,8-benzoquinoline (91, 93), the nitrogen-containing ring is hydrogenated first. Regarding 1,2,3,4-tetrahydroquinoline, these 1,2,3,4-tetrahydrobenzoquinolines undergo opening of the hydrogenated ring by elimination followed by hydrogenation, giving 1-propyl-2-naphthylamine or 2-propyl-1-naphthylamine, respectively (Scheme 18). These naphthylamines react in principle as 2-propylaniline does. Thus, 1- or 2-propylnaphthalene is formed by direct C–N bond breaking, and aminopropyltetrahydronaphthalene is formed by hydrogenation;



SCHEME 17

the latter reacts further to propyltetrahydronaphthalene. The only difference between these reaction networks and that of propylaniline is that direct C–N bond breaking in naphthylamine is more important (40% instead of 10% at 613 K and 7 MPa). This difference can be explained by hydrogenolysis since the $C(sp^2)$ –N bond in naphthylamine is weaker than that in aniline (91). Hydrogenation followed by elimination would also explain this result because the aromaticity of naphthalene is less than that of benzene, and the double bonds are more localized. The 1,2,3,4-tetrahydrobenzoquinolines can also react further by hydrogenation to octahydrobenzoquinolines, which are denitrogenated as decahydroquinoline, leading to propyltetrahydronaphthalene (Scheme 18).

Regarding the compounds discussed in the preceding sections, increased hydrogen pressure favors hydrogenation, whereas higher H_2S pressure favors C–N bond breaking. Multiring compounds usually react faster than smaller aromatic nitrogen-containing compounds because, on the one hand, their adsorption constants are larger and, on the other hand, the aromatic character of the heteroring is weaker. Thus, quinoline is hydrogenated much faster to 1,2,3,4-tetrahydroquinoline than pyridine is to piperidine, and naphthylamine reacts several times faster than aniline (94). Compounds such as



SCHEME 18

5,6- and 7,8-benzoquinoline, which are angular like phenanthrene, are hydrogenated more slowly than quinoline, however (91).

3. Hydrotreating of Mixtures

The occurrence of competitive adsorption may complicate matters, and the conclusions stated previously may no longer pertain. A compound that is intrinsically more reactive than another may react more slowly than the other when both are present in a mixture because of stronger adsorption of the other compound. Such inhibition effects may be caused not only by the reacting molecules but also by the hydrotreating products, such as intermediates and end products including H_2S and NH_3 .

A Langmuir–Hinshelwood type of rate expression is often used to describe the effect of the competitive adsorption of components m in the reaction mixture on the rate of hydrotreating of compound i :

$$r_i = k_i K_i c_i / \left(1 + \sum K_m c_m \right) \quad (1)$$

All components are supposed to adsorb on the same site, and the influence of H_2 adsorption is neglected or, at constant H_2 pressure, lumped together with k . Comparing the hydrotreating rate r_i of only compound i with the rate r'_i of compound i in the presence of another compound j (with compound i always present at the same concentration c_i), one obtains

$$r'_i / r_i = \left(1 + \sum K_m c_m \right) / \left(1 + \sum K_n c_n \right) \quad (2)$$

where m refers to all the components present during the hydrotreating of compound i alone, and n refers to all the components in the mixture of i and j . If, in both cases, adsorption is dominated by one component, then this equation simplifies to

$$r'_i / r_i = K_a c_a / K_b c_b \quad (3)$$

The adsorption equilibrium constant K was shown to increase quite strongly in the order aromatic hydrocarbons < sulfur compounds < oxygen compounds < nitrogen compounds (45, 95). Consequently, reactions of compounds of one of these classes will generally be inhibited by compounds of another class—to their right in this order of adsorption constants. Thus, under most conditions, HDS is strongly inhibited by the presence of nitrogen compounds, and HDN is only slightly influenced by the presence of sulfur compounds (45, 63). For example, thiophene HDS is slowed by the presence of pyridine in the reaction mixture.

The effect of thiophene on the HDN of pyridine is more complex. At low temperatures, thiophene causes a slight decrease in the HDN of pyridine

because of competitive adsorption. At high temperatures, however, thiophene accelerates the HDN of pyridine because it reacts to give H₂S, and H₂S has a positive influence on the ring opening of piperidine and the removal of nitrogen from pentylamine.

The negative influence of nitrogen compounds on the HDS of thiophene was quantified at 7 MPa and 633 K. The adsorption constants of most nitrogen compounds, determined with the aid of a Langmuir–Hinshelwood model, follow the same trend as their proton affinities in the gas phase (Table II) (77).

A remarkable promoting effect of nitrogen compounds was observed in the HDS of dibenzothiophene (89, 96, 97). The sulfur atom of dibenzothiophene can be removed via two routes (98). Since the C–S bond is relatively weak, the two C–S bonds in dibenzothiophene can be broken by hydrogenolysis to give biphenyl as the product. Alternatively, one of the six-rings of dibenzothiophene can be hydrogenated and the first C–S bond can then be broken by elimination or by hydrogenolysis. The sulfur atom of the resulting 2-cyclohexylthiophenol is removed by hydrogenolysis, leading to cyclohexylbenzene. Biphenyl is the main product when a Co–Mo catalyst is used at a moderate hydrogen partial pressure (98), whereas when Ni–Mo (the better hydrogenation catalyst) is used and the pressure is 10 MPa, both products are formed in about equal amounts (96). Nagai *et al.* (89, 96) observed that at temperatures above 573 K, addition of acridine and other nitrogen-containing molecules (as well as tetralin) during the HDS of dibenzothiophene led to a lower HDS conversion, as expected from the foregoing discussion. However, the formation of biphenyl was enhanced while that of cyclohexylbenzene was (more strongly) inhibited. Nitrogen compounds

TABLE II
Adsorption Equilibrium Constants K and Proton Affinities (PA) for Some Nitrogen-Containing Compounds in the HDS of Thiophene (T) (77) at 633 K and 7 MPa and in the HDS of Dibenzothiophene (DBT) at 533 K and 10.1 MPa (96)

Reactant compound	K (kPa ⁻¹)		PA (kJ/mol)
	T	DBT	
NH ₃	0.05		866
Aniline	0.09	0.2	891
Pyridine	0.43	1.1	929
1,2,3,4-Tetrahydroquinoline	0.46		941
Piperidine	0.58		962
Quinoline	0.98	1.3	954
Decahydroquinoline	2.0		
Acridine		2.0	970

thus acted as strong poisons for the hydrogenation of dibenzothiophene but promoted its hydrogenolysis. The inhibitory effect of nitrogen compounds on the formation of hexahydro-dibenzothiophene from dibenzothiophene was fitted with a Langmuir–Hinshelwood equation. The resulting adsorption constants of the nitrogen compounds are presented in Table II. At the low reaction temperature of 533 K, the promotion of biphenyl formation was stronger than the inhibition of cyclohexylbenzene formation. Consequently, the total conversion of dibenzothiophene in the presence of acridine was even enhanced, as confirmed by LaVopa and Satterfield for the addition of quinoline (97). The reason for the enhancement of the formation of biphenyl from dibenzothiophene in the presence of nitrogen compounds is unclear.

Hydrotreating of mixtures of sulfur-, oxygen-, and nitrogen-containing compounds along with aromatic hydrocarbons has shown that the order of reactivity is thiophene > phenol > aniline \gg benzene (45). Increasing the pressure of aniline in such a mixture led to a decrease in the conversion of all constituents, demonstrating that aniline is the most strongly adsorbed component in the mixture. Accordingly, an increase in the pressure of phenol induced a decrease in the conversion of phenol but had no influence on the conversion of aniline. This result shows that although phenol cannot displace aniline from the catalyst surface, it is relatively strongly adsorbed and therefore has a negative influence on its own hydrodeoxygenation rate. Although thiophene is known to have the lowest adsorption equilibrium constant of all the constituents, an increase in the thiophene pressure had a negative influence on the conversion of all components. This result is explained by the presence of product H_2S , which can adsorb on the catalyst and transform sulfur-poor sites into sulfur-rich sites. Consequently, the hydrogenation activity of the catalyst is diminished. Because hydrogenation is rate-determining under the prevailing conditions (523–723 K, $P_{H_2} = 9.7$ MPa, $P_{thiophene} = P_{phenol} = P_{aniline} = 67$ kPa, $P_{benzene} = 130$ kPa, and $P_{H_2S} = 10$ kPa) in the hydrotreating of thiophene, phenol, and aniline (45), the hydrotreating rates of these compounds are decreased.

Compounds of the same class can also mutually influence their hydrotreating rates. Competitive reactions of pyrrole, pyrrolidine (tetrahydropyrrole), pyridine, and piperidine on Ni–Mo/ Al_2O_3 and on Ni–W/ Al_2O_3 catalysts showed that pyridine and pyrrolidine strongly inhibit the pyrrole HDN (99). Although the reaction order in pure pyrrole was less than 1, indicating that pyrrole adsorbed strongly, pyridine and pyrrolidine apparently adsorbed even more strongly. As expected, the more strongly basic pyrrolidine had the stronger influence. In the same way, the HDN of indole was substantially inhibited, whereas the HDN of quinoline was only slightly decreased when both reactants were present (95). This can be explained as follows: The main reaction path in the HDN of indole is via indoline (dihydroindole) and

o-ethylaniline, whereas that of quinoline is via decahydroquinoline. Since decahydroquinoline is a secondary amine and indoline an *N*-alkylaniline, decahydroquinoline is a much stronger base (Table II) and thus the strongest inhibitor of all the compounds in the reaction mixture. Therefore, the influence of quinoline on the HDN of indole is greater than that of indole on the HDN of quinoline. Similarly, since the adsorption equilibrium constant of aniline is one of the smallest of all the nitrogen-containing compounds, the HDN of aniline is strongly inhibited by indole and pyrrole and even slightly by naphthalene (84). Other examples of the effects of competitive adsorption are given by Girgis and Gates (95).

4. Kinetics of HDN

The increasing importance of hydrotreating in oil refining is contrasted to the limited body of knowledge of its kinetics, especially of hydrodenitrogenation (4, 95). Knowledge of the kinetics of a reaction is important for process operations. It may also yield information about the nature and density of catalytic sites, facilitating the interpretation of the influence of reaction conditions, the reaction mechanism, the properties of the catalyst, and its preparation.

As shown in Section II.B.2, HDN reaction networks are usually quite complex. Several intermediates are involved, and the reactions may take place on different catalytic sites. Furthermore, since the reactants and intermediates strongly adsorb on the catalytic sites, kinetic modeling of a HDN network is difficult, and many authors have simplified the analysis of their kinetic data. Hydrogenation and C–N bond cleavage reactions in the HDN network take place on different catalytic sites. Nevertheless, it has often been assumed that all the reaction steps in a kinetic analysis take place on the same catalytic sites. Furthermore, several authors assumed that a pseudo-zero or first-order reaction can be used in the calculation of the model parameters (95). All these assumptions greatly reduce the applicability of the modeling results, however, even without considering the approximations made in the modeling methods.

Langmuir–Hinshelwood rate expressions of all the reactions of the network were used in the kinetic modeling of the HDN of quinoline by Satterfield *et al.* (80, 81, 88). Their assumption that there is a single catalytic site for all reactions is too simple. Nevertheless, they collected an impressive body of kinetic data and pinpointed the reactions that were close to equilibrium and those which were kinetically significant. Gioia and Lee (100) extended these studies to higher pressures (up to 15 MPa H₂). Only one model survived their regression analysis of the kinetic data. In this model, it was necessary to assume that 1,2,3,4-THQ reacted directly not only to *o*-propylaniline but also to propylbenzene (PB) and propylcyclohexene (PCHE). Their analysis does not appear to be very reliable, however. First,

30% of the HDN products were not identified. Second, it is chemically impossible that PB and PCHE form in one reaction from 1,2,3,4-THQ. A possible explanation is that diffusion influenced the concentrations of the intermediates. The hydrogenation of *o*-propylaniline to *o*-propylcyclohexylamine may be fast at high H₂ pressures. Then, there would not be enough time for these intermediates to diffuse out of the pores and be detected. Thus, it would appear as if there were a direct reaction from 2-propylaniline to PB and PCHE. The use of a batch reactor and hexadecane as a solvent may have intensified the diffusion problems.

Langmuir–Hinshelwood kinetics and a one-site model were also used by Hanlon (64) to represent the HDN of pyridine. In accord with Satterfield and Cocchetto (60), Hanlon found that aliphatic amines are more strongly adsorbed than aromatic amines: $K = 1000, 600, 300,$ and 50 kPa^{-1} at 583 K for pentylamine, piperidine, pyridine, and ammonia, respectively. Because a single-site model was assumed, the results should be considered qualitative rather than quantitative. Two intriguing results revealed the necessity for further investigation. On the one hand, Hanlon (64) observed that the rate constant of the conversion of piperidine was about one-third smaller when calculated from the results representing the HDN of piperidine than when calculated from the results representing the HDN of pyridine. This difference suggests that the concentration of alkene intermediates was higher in the former case and led to catalyst coking and loss of activity. On the other hand, Hanlon (64) observed that the rate of the piperidine conversion is proportional to the H₂S/H₂ ratio. As discussed in Section II.B.2.a, piperidine reacts to give 5-aminopentene-1 by elimination or to give 5-mercaptopentylamine by nucleophilic substitution at one of the carbon atoms next to the nitrogen atom. The positive influence of H₂S observed by Hanlon (64) is explained by the fact that both elimination and nucleophilic substitution are acid catalyzed. No hydrogen is involved in these reactions, however.

A two-site model and Langmuir–Hinshelwood kinetics for the hydrogenation and C–N bond cleavage were used by Pille and Froment (101) to represent the HDN of pyridine. Unfortunately, they assumed that piperidine reacted to pentylamine via hydrogenolysis and, therefore, that the rate of the C–N bond cleavage of piperidine was first order in the hydrogen pressure. Their conclusion that a Freundlich isotherm had to be used to describe the adsorption of piperidine must therefore be reinvestigated. The data in their plot of experimental against calculated conversions were close to the 45° line, showing very good agreement between the model and the experiment. Nevertheless, their assumption concerning the rate-determining step of the piperidine conversion is wrong. The results show that it is very risky to use kinetic modeling to derive information about the mechanisms of complex catalytic reactions. Only through a combined effort of chemists and chemical engineers can kinetic data be interpreted meaningfully.

A two-site model was used as well by Shih *et al.* (102) for the HDN of quinoline. They assumed not only pseudo-first-order kinetics but also that all nitrogen-containing species, including ammonia, have the same adsorption equilibrium constant; this is clearly not the case (77).

The HDN network of quinoline is too complex to yield reliable model parameters. Of course, reaction intermediates might be modeled separately, and once a substantial number of the kinetic parameters are known, an effective modeling of the entire quinoline HDN network can be attempted. OPA is a major intermediate in the HDN network of quinoline and one of the representative nitrogen-containing compounds in oil distillates. A kinetic study of the HDN of OPA on Mo/Al₂O₃ and NiMo/Al₂O₃ catalysts, with and without phosphate, was performed to determine how the various reactions depend on the composition of the catalyst (75, 103). Several kinetic parameters in the network of OPA (Section II.B.2.b) can be ignored. The concentration of the propylcyclohexylamine (PCHA) intermediate is always very low so that PCHA can be omitted from the kinetic analysis and PCHE can be treated mathematically as a primary HDN product. The reactions converting PB to PCHE and PCHE to PB are kinetically insignificant as long as OPA is present because of competitive adsorption of OPA. The network can therefore be simplified to that shown in the bottom of Fig. 9. Furthermore, the adsorption constants of PCHE, PB, and propylcyclohexane (PCH) are negligible compared to those of OPA and NH₃. On the other hand, reactions which are chemically different may take place on different catalytic sites. The small degree of C(sp²)-N bond cleavage of OPA to give PB (less than 10%) did not allow a decision as to whether this reaction takes place on catalytic sites different from those responsible for OPA hydrogenation. However, different adsorption equilibrium constants were assumed for the hydrogenation of OPA and PCHE. The analysis leads to the following

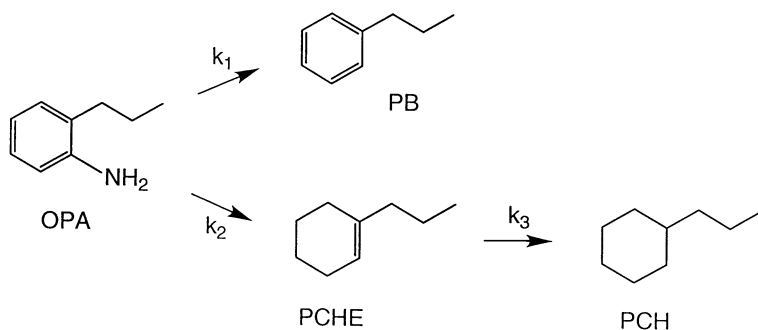


FIG. 9. Simplified kinetic network of the HDN of *o*-propylaniline.

Langmuir–Hinshelwood rate equations:

$$\frac{dP_{OPA}}{d\tau} = - \frac{(k_1 + k_2)K_{OPA}P_{OPA}}{1 + K_{OPA}P_{OPA} + K_{NH_3}P_{NH_3}} \quad (4)$$

$$\frac{dP_{PCHE}}{d\tau} = \frac{k_2K_{OPA}P_{OPA}}{1 + K_{OPA}P_{OPA} + K_{NH_3}P_{NH_3}} - \frac{k_3K_{PCHE}P_{PCHE}}{1 + K'_{OPA}P_{OPA} + K'_{NH_3}P_{NH_3}} \quad (5)$$

$$\frac{dP_{PB}}{d\tau} = \frac{k_1K_{OPA}P_{OPA}}{1 + K_{OPA}P_{OPA} + K_{NH_3}P_{NH_3}} \quad (6)$$

$$\frac{dP_{PCH}}{d\tau} = \frac{k_3K_{PCHE}P_{PCHE}}{1 + K'_{OPA}P_{OPA} + K'_{NH_3}P_{NH_3}} \quad (7)$$

$$P_{NH_3} = P_{OPA}^0 - P_{OPA} \quad (8)$$

where the adsorption equilibrium constants K_{OPA} and K_{NH_3} refer to the site for hydrogenation of OPA, and the constants K'_{OPA} and K'_{NH_3} refer to the site for PCHE hydrogenation (Fig. 9).

Fitting the partial pressure against space time results of a single HDN experiment of OPA (Fig. 10) did not give unique parameter values for the

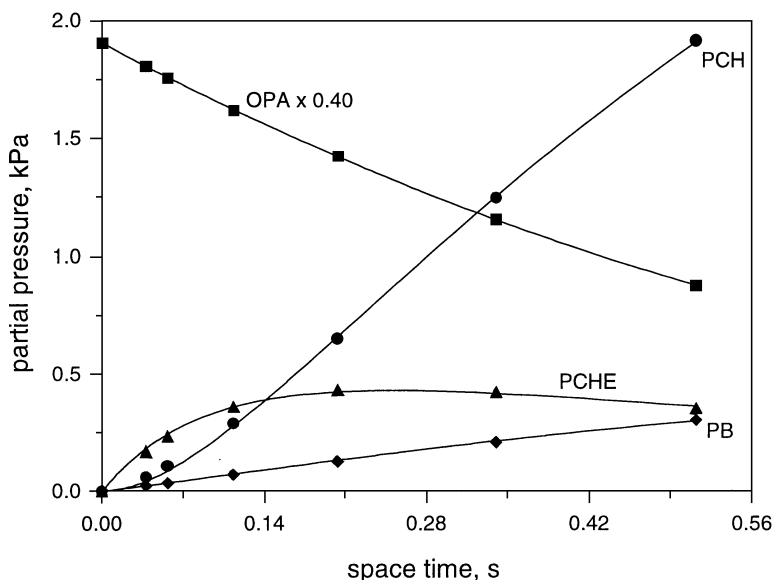


FIG. 10. Product composition as a function of space time in the HDN of *o*-propylaniline catalyzed by Ni–Mo/Al₂O₃ at 623 K and 3 MPa.

rate and adsorption constants. The data obtained by varying the space time starting with one initial partial pressure showed too strong a correlation to enable the determination of a unique set of kinetic parameters. Only the combined results of a set of experiments, obtained by varying the space time at several initial partial pressures of OPA, enabled the determination of kinetic parameters with narrow confidence ranges and high confidence levels. Furthermore, the kinetic parameters representing the olefin hydrogenation reaction (PCHE to PCH) in the HDN of OPA were determined by letting cyclohexene (CHE) react together with NH_3 or OPA under HDN reaction conditions. The adsorption (inhibition) constants representing NH_3 or OPA in this hydrogenation reaction were obtained with the equation

$$-1n(1 - x_{\text{CHE}}) = \frac{k_{\text{CHE}} K_{\text{CHE}}}{1 + K'_i P_i} \cdot \tau \quad (9)$$

where K'_i is the adsorption equilibrium constant of the inhibitor on the olefin hydrogenation site, and P_i is the partial pressure of the inhibitor in the reactant stream.

The results of the fitting for Ni-Mo-P/Al₂O₃ are given in Fig. 10. The values of the rate and adsorption constants characterizing the Mo/Al₂O₃, Mo-P/Al₂O₃, Ni-Mo/Al₂O₃, and Ni-Mo-P/Al₂O₃ catalysts at 623 K and 3 MPa are given in Table III. The Ni-Mo/Al₂O₃ and Ni-Mo-P/Al₂O₃ catalysts have a low PB selectivity ($100 k_1/(k_1 + k_2) = 7-12\%$), whereas the Mo/Al₂O₃ and Mo-P/Al₂O₃ catalysts gave about 30% PB (although at a much lower activity). The results also clearly demonstrate that OPA adsorbs with a different strength on the catalytic site in the HDN of OPA (K_{OPA}) than on the site for the hydrogenation of CHE (K'_{OPA}), although in both cases a hydrogenation reaction is rate limiting. This result indicates that the

TABLE III
Rate Constants k (in Units of kPa s^{-1}) and Adsorption Constants K (in Units of kPa^{-1})
of the HDN Network of OPA at 623 K, 3.0 MPa, and $P_{\text{H}_2\text{S}} = 6.5 \text{ kPa}$ for Various Catalysts

Parameter	Catalysts			
	Mo/Al ₂ O ₃	MoP/Al ₂ O ₃	Ni-Mo/Al ₂ O ₃	Ni-MoP/Al ₂ O ₃
k_1	0.2	0.3	0.4	0.8
k_2	0.8	0.8	5.8	6.4
$k_3 K_{\text{PCHE}}$	7.6	6.2	38	48
K_{OPA}	0.3	0.5	0.7	1.2
K_{NH_3}	0.4	0.4	0.5	1.0
K'_{OPA}	0.2	0.3	0.4	0.9
K'_{NH_3}	0.4	0.6	0.5	1.0

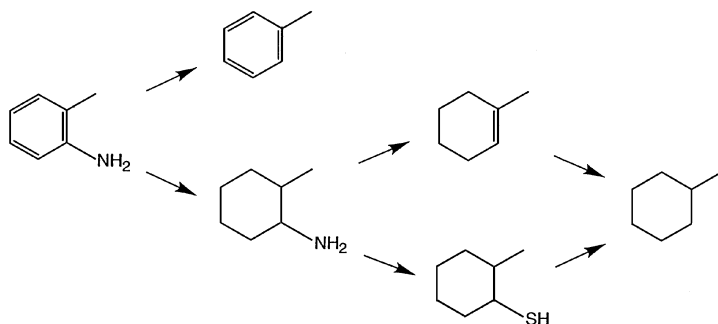
catalytic site for the hydrogenation of the phenyl group in aniline is different from that for the hydrogenation of an olefin. Although the HDN of OPA and the hydrogenation of CHE take place on different catalytic sites, OPA adsorbs on the catalytic site for the hydrogenation of CHE and hinders this hydrogenation reaction. The same effect was observed in the hydrogenation of ethylbenzene (75, 103).

o-PCHA does not play a role in the kinetic description of the HDN of OPA because its rate of formation by hydrogenation of *o*-toluidine is much lower than that of its further reaction. To estimate the rate of the HDN of PCHA and the strength of its adsorption, an investigation was made of the corresponding *o*-methylcyclohexylamine (MCHA), because PCHA is not commercially available (40, 76). The results of the HDN of MCHA at low space times suggested not only that methylcyclohexene (MCHE) is a primary product but also that methylcyclohexane (MCH) is a primary product.

This apparent direct C–N bond breaking may result from hydrogenolysis or from NH_2 –SH exchange, followed by hydrogenolysis of the resulting *o*-methylcyclohexylthiol. It may also be a consequence of diffusion limitations. Once the MCHE intermediate is formed at the catalytically active surface inside the catalyst pores, it reacts to give the final MCH product. If this hydrogenation of MCHE is much faster than the diffusion of MCHE out of the pores, less MCHE will be able to diffuse out of the pores. In that case, the experimentally observed MCHE concentration outside the pores underestimates the concentration of MCHE and overestimates that of the MCH product in the pores. Mathematically, this is equivalent to a direct path of the reactant MCHA to the product MCH. A considerable contribution of diffusion to the low MCHE and high MCH concentrations was indeed observed. Furthermore, the conversion of cyclohexene in the presence of MCHA demonstrated diffusion limitations (76).

Nevertheless, even under conditions for which diffusion limitations could be excluded, MCHA was still converted directly to MCH. By adding substantial partial pressures of H_2S , it was shown that the formation of MCH resulted from the nucleophilic substitution of MCHA to give 2-methylcyclohexylthiol and subsequent fast hydrogenolysis to give MCH. These results mean that the network of the HDN of anilines is quite complex; the network of *o*-methylaniline (*o*-toluidine) is shown in Scheme 19.

Data characterizing the HDN of DHQ also suggested that diffusion plays a role since the PCH selectivity did not go to zero when extrapolated to low space times (Fig. 11) (59). In this case, the nitrogen atom in DHQ is part of a ring, and even “double hydrogenolysis” would have been necessary to explain the direct formation of PCH from DHQ. However, this makes no sense chemically. Again, diffusion can explain these results. The PCHA and PCHE intermediates, which are formed from DHQ at the catalytically active surface



SCHEME 19

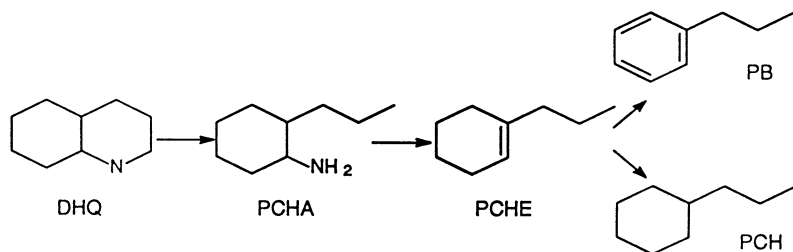
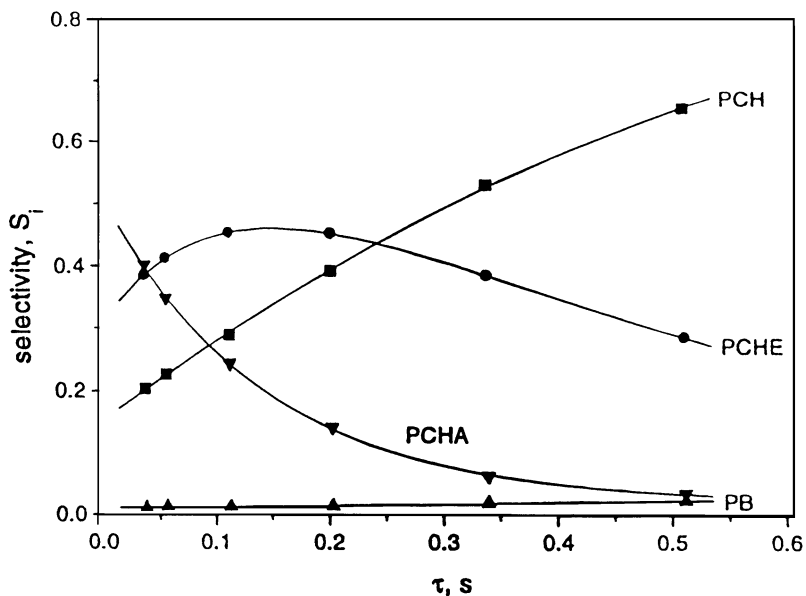


FIG. 11. Product selectivities as a function of space time in the HDN of decahydroquinoline catalyzed by Ni-Mo/Al₂O₃ at 623 K and 3 MPa.

TABLE IV
Rate Constants k (in Units of $kPa s^{-1}$) and Adsorption Equilibrium Constants K (in Units of kPa^{-1}) in the HDN of DHQ at 623 K, 3.0 MPa, and $P_{H_2S} = 6.5 kPa$ for Various Catalysts

Parameter	Catalysts			
	Mo/Al ₂ O ₃	MoP/Al ₂ O ₃	Ni-Mo/Al ₂ O ₃	Ni-MoP/Al ₂ O ₃
k_1	1.9	1.5	5.1	4.6
$k_2 K_{PCHA}$	50	51	48	47
$k_3 K_{PCHA}$	10	4	4	4
$k_4 K_{PCHE}$	5	6	27	41
K_{DHQ}	0.2	0.4	0.4	0.4
K'_{DHQ}	0.8	0.9	1.6	3.5

inside the catalyst pores, react to give the final PCH product. If this occurs intrinsically at a much higher rate than diffusion out of the pores, then an apparent direct path of reactant DHQ to product PCH is needed to fit the data. In that case, the selectivity to PCH does not extrapolate to zero at decreasing conversion.

The kinetic parameters in the HDN network of DHQ were determined as described in the previous section for the parameters in the HDN network of OPA (59, 103). The results obtained at 623 K and 3.0 MPa are presented in Table IV. Addition of nickel to the catalyst increased the rate constant k_1 of the first elimination reaction by a factor of 2 or 3 and the effective rate constant $k_4 K_{PCHE}$ of the olefin hydrogenation by a factor of 5–7. Nickel enhances the rate-determining hydrogenation of the phenyl group in the HDN of OPA by a factor of 6 or 7 (Table III). Nickel clearly increases the rates of all the reactions, but the rates of hydrogenation are increased to a greater extent than the rates of elimination. The explanation of the weaker effect of nickel on the elimination reaction might be that not only is a Lewis acid metal site (Mo⁴⁺ or Ni²⁺) required for elimination but also a basic S²⁻ or SH⁻ site is required. The properties of this basic site should be only slightly dependent on the metal present. The adsorption equilibrium constant K_{DHQ} of DHQ on the site of its ring-opening elimination is similar for all four catalysts (Table IV). This result also suggests that the elimination is primarily determined by the presence of S²⁻ or SH⁻ and to a lesser extent by the presence of molybdenum or nickel. The adsorption equilibrium constant of DHQ on the site of the reaction of DHQ to PCHA is much smaller than that describing its inhibition effect in the hydrogenation of CHE (59, 103). This result confirms the conclusion that different catalytic sites are involved in these chemically different reactions. The site on which the elimination of DHQ takes place contains basic sulfur and thus adsorbs the amine DHQ

relatively weakly. The hydrogenation site most likely contains less sulfur, and DHQ can then adsorb relatively strongly with its nitrogen atom on the more acidic molybdenum or nickel atom (Figs. 5 and 6).

C. STRUCTURE AND FUNCTION OF PHOSPHORUS AND FLUORINE PROMOTERS

1. *Phosphorus as a Promoter*

Industrial hydrotreating catalysts contain sulfided nickel and molybdenum or cobalt and molybdenum on an alumina support. γ - Al_2O_3 is the preferred support because of its good textural and mechanical properties. Hydrotreating catalysts often contain additives such as phosphate or fluoride as well. Phosphate is added as phosphoric acid or ammonium phosphate to the impregnating solution in the catalyst preparation to enhance the solubility of molybdate by the formation of phosphomolybdate complexes (104). It was claimed as early as 1953 that phosphorus increases not only the molybdenum loading that can be obtained in a single impregnation step but also the HDS activity (105). Recent experience in industry as well as studies with model compounds demonstrated a substantial promotional effect of phosphorus in HDN (106–111) but only a weak effect in HDS (107, 109, 112). Therefore, phosphorus is especially incorporated into Ni–Mo/ Al_2O_3 HDN catalysts. A promotional effect of phosphorus was also observed in the HDS and HDN of gas oil, enriched with pyridine, catalyzed by W/ Al_2O_3 (113).

Many explanations have been offered for the influence of phosphorus: improved dispersion of molybdenum (or tungsten), improved dispersion of nickel (or cobalt), different MoS_2 morphology, changes in the acidity of the support, chemical modification of the active molybdenum and nickel (or cobalt) sites, better resistance to coke formation during hydrotreating because of decreased acidity of the γ - Al_2O_3 support surface (107), and increased C–N bond cleavage due to an increase in the surface acidity of the support (109). Currently, two explanations seem most likely. One explanation is the increased stacking of the MoS_2 layers, leading to more accessible hydrogenation sites at the top MoS_2 layer. The other explanation is the formation of nickel and/or molybdenum phosphide at the edges of the MoS_2 . What are the arguments in favor of these two explanations?

During impregnation and calcination, phosphate interacts strongly with the γ - Al_2O_3 support and forms AlPO_4 . As a result, micropores are closed, the surface area and pore volume of the catalyst decrease with increasing phosphorus contents (107, 109, 114), and the mechanical and thermal stability of the resulting catalyst increases (115). Sulfidation does not influence the AlPO_4 structure, and therefore the composition and texture of the support of a hydrotreating catalyst are different from those of the initial γ - Al_2O_3 material. The support consists of both γ - Al_2O_3 and AlPO_4 and has a pore size distribution substantially different from that of the original γ - Al_2O_3 .

The interaction between oxidic nickel or cobalt and the phosphated support becomes weaker (114, 115). Less nickel or cobalt is lost to the support, and more is available for the formation of the active Ni–Mo–S phase on the catalyst surface.

Furthermore, the interaction between molybdenum and tungsten and the support is weaker, leading to less mononuclear molybdate and tungstate and more polymolybdate and polytungstate. After sulfidation, these polynuclear oxyanions give larger MoS₂ or WS₂ particles, often with a higher stacking of the MoS₂ or WS₂ slabs. Thus, NO chemisorption showed a decreased dispersion of MoS₂ (116). Electron microscopy confirmed that the MoS₂ slabs are somewhat larger in a phosphate-containing catalyst than in a phosphate-free catalyst and that they have a higher degree of stacking (117). The same was observed for WS₂ catalysts (113, 118). Although the MoS₂ slabs at the MoS₂–Al₂O₃ interface may have Mo–O–Al bonds with the support, the other MoS₂ slabs on top do not have such bonds and will therefore be fully sulfided. X-ray photoelectron spectra demonstrated that phosphate improves the sulfidability of Mo/Al₂O₃ catalysts (116). Because of this difference in chemical composition, single slabs and slabs at the bottom of a stack (near the support) might have chemical properties different from those of the MoS₂ slabs at the top of a stack. This idea was suggested as a possible explanation for the difference in the hydrotreating activity of phosphate-modified and phosphate-free Ni–Mo catalysts (109).

Such a difference in stacking might also explain the increase in intrinsic activity obtained as a result of sulfiding Ni–Mo/Al₂O₃ or Co–Mo/Al₂O₃ at high temperatures. A comparison of the activity for thiophene HDS with the number of cobalt atoms in the Co–Mo–S structure obtained from ⁵⁷Co Mössbauer emission data showed that Co–Mo/Al₂O₃ catalysts that were sulfided at temperatures above 873 K are intrinsically more active per cobalt atom in the Co–Mo–S phase than those sulfided at 673 K. The intrinsically more active phase was referred to as Co–Mo–S II and the less active phase as Co–Mo–S I (119). The type I structure was assumed to be bonded to the support through Mo–O–Al linkages, whereas the type II structure might have few if any such linkages. Since the Mössbauer and EXAFS signals of the type I and type II structures are the same, the local cobalt and nickel environments must be the same in both cases. This result suggests that for steric reasons, the type I structure is less active than the type II structure. Catalyst-support linkages in type I probably hinder reactant molecules from approaching the catalytic sites. The high activities of carbon-supported CoMo catalysts have also been attributed to the presence of Co–Mo–S type II structures because of a weak catalyst–carbon interaction (120). Similarly, high-temperature sulfidation might lead to enhanced stacking and, therefore, to an intrinsically more active Co–Mo–S type II phase. Transmission electron microscopy (TEM)

studies of W/Al_2O_3 catalysts showed that the average number of stacked WS_2 layers (N) was greater after sulfidation at 873 K ($N = 4.5$) than after sulfidation at 673 K ($N = 2$). The addition of phosphate had the same effect of increased stacking as did an increase in sulfidation temperature (118).

Daage and Chianelli (121) claimed that the top and bottom layers of unsupported stacks of MoS_2 have a much higher activity for hydrogenation of dibenzothiophene than the intermediate MoS_2 layers, whereas the direct hydrogenolysis of the C–S bonds in dibenzothiophene to biphenyl occurs equally well on all MoS_2 layers. Steric factors have been invoked to explain this situation. Vertical adsorption, which should be possible on the molybdenum sites of all layer edges, was assumed to be necessary for hydrogenolysis. On the other hand, π adsorption, flat on molybdenum site, results in hydrogenation, and this geometry is unlikely on the molybdenum sites at the edges of the intermediate MoS_2 layers.

The elucidation of the phosphate effect has been complicated by the fact that industrial feeds contain many different components. Furthermore, in the HDN of the usual test molecules, such as quinoline, pyridine, and indole, several different reactions and intermediates are involved. Thus, at least four different reactions play a role in the HDN of quinoline (109): hydrogenation of aromatic rings (Q to THQ and DHQ and OPA to *o*-propylcyclohexylamine), C–N bond breaking (DHQ to *o*-propylcyclohexylamine and on to PCHE as well as THQ-1 to OPA), hydrogenation of alkenes (PCHE to PCHA), and hydrogenolysis (OPA to PB). Jian and Prins (122) showed that the effect of phosphate depends on the type of reaction. Phosphate strongly increases the rates of hydrogenation reactions such as the hydrogenation of aniline, benzene, and cyclohexene (see Section II.B.4 Tables III and IV). A negative effect was observed, however, in the HDN of piperidine and DHQ, in which the ring-opening C–N bond elimination is rate-determining (122).

To determine whether a change in dispersion or in the type of catalytic sites is responsible for these different effects of phosphate, Jian and Prins (59, 75) investigated the kinetics of these hydrogenation and elimination reactions. Unfortunately, no simple chemisorption method has proved capable of determining the dispersion of supported metal sulfides (6). Therefore, an indirect method, involving the determination of rate and adsorption equilibrium constants (the first proportional to the number of sites and the second dependent only on the type of site) had to be used.

As shown in Table IV, addition of phosphate to a $Ni-Mo/Al_2O_3$ catalyst decreased the rate constant k_1 for the cleavage of the C–N bond in DHQ but left the adsorption equilibrium constant K_{DHQ} of the reactant unchanged (59). This result suggests that phosphate does not change the elimination sites but decreases their number. The reason for this effect might be that

phosphate decreases the surface area of the alumina and thus leaves less surface area for the same amount of MoS_2 , resulting in larger MoS_2 crystallites and a lower edge dispersion.

Introducing phosphorus into a $\text{Ni-Mo/Al}_2\text{O}_3$ catalyst increased the rate constant k_2 of the hydrogenation of propylaniline (OPA) as well as the corresponding adsorption equilibrium constant of OPA (Table III). The latter result indicates that different sites are present in a $\text{Ni-Mo-P/Al}_2\text{O}_3$ catalyst than in $\text{Ni-Mo/Al}_2\text{O}_3$ for the hydrogenation of the aromatic ring. Judging from the higher rate constant for hydrogenation of PCHE, the same seems to be true for the sites on which alkenes are hydrogenated.

How phosphate can improve the hydrogenation capacity of a $\text{Ni-Mo/Al}_2\text{O}_3$ catalyst is not clear. The decreased dispersion of Ni-MoS_2 resulting from the addition of phosphate makes the positive effect of phosphate on hydrogenation reactions even more puzzling. A kinetic study showed that phosphate increases the rate constant of the hydrogenation of OPA as well as its adsorption equilibrium constant (75). This result indicates that phosphate changes the nature of the sites. One possibility is that phosphate in the neighborhood of the Ni-MoS_2 particles is reduced to PH_3 by spilled-over hydrogen atoms (109, 123). This PH_3 might then induce a P-S exchange at the edges of the Ni-MoS_2 , leading to a catalyst phase with (a partially) phosphide-like character (75, 124, 125). To test this possibility, pure unsupported MoP was prepared according to a recently published method (126) and tested in the HDN of OPA. The intrinsic activity of this MoP was compared to that of a sulfided $\text{Mo/Al}_2\text{O}_3$ catalyst by measuring the surface area of the unsupported MoP and estimating the edge surface area of the MoS_2 . The molybdenum atoms at the MoP surface were seven times more active than those at the edge of the MoS_2 surface (127). The activity of Ni_2P and Co_2P was investigated in the HDN of quinoline (123). Ni_2P had an even higher activity than a commercial $\text{Ni-Mo/Al}_2\text{O}_3$ catalyst.

In conclusion, phosphate clearly has a positive effect on HDN. Currently, there are two explanations for this: (i) the increased stacking of the MoS_2 layers, leading to more accessible hydrogenation sites at the top MoS_2 layer, and (ii) the formation of nickel and/or molybdenum phosphide at the edges of the MoS_2 .

2. Fluorine as a Promoter

Fluorine is also used commercially as an additive in hydrotreating catalysts. Fluorine is added especially to hydrocracking catalysts because it increases the acidity of the catalyst and thus promotes acid-catalyzed cracking of hydrocarbons. Test reactions, such as the cracking of cumene to give benzene and propene, have demonstrated clearly that fluorine rather than

molybdenum or nickel (or cobalt) accounts for the cracking (128). Positive effects of fluorine have also been observed in HDS, HDN, and hydroisomerization. The effect of fluorine has been attributed to changes in the dispersion and distribution of the active phase(s), an increase in acidity, an improvement in the sulfidability, and to the change from the Ni–Mo–S type I to the Ni–Mo–S type II structure.

Like phosphate, fluoride ions are able to interact strongly with the γ -Al₂O₃ support. They replace OH⁻ ions on the support surface and lower the IEP from 7.6 for pure Al₂O₃ to 5.5 for 5 wt% fluorine on Al₂O₃ (129). The smaller number of OH⁻ ions leads to a decrease in the number of MoO₄²⁻ ions that can react with the support during adsorption (130). The lower IEP leads to a more negatively charged surface during pore volume impregnation. Consequently, the interaction between molybdenum or tungsten and the support in fluoride-containing catalysts becomes weaker, and more polymolybdate or polytungstate is formed during pore volume impregnation. As in the case of phosphate, electron microscopy showed that these polynuclear oxyanions are sulfided to give larger MoS₂ slabs with a smaller relative surface edge area. This result explains why adding fluorine to a Mo/ γ -Al₂O₃ catalyst causes a continuous decrease in the NO chemisorption and the activity for HDS of thiophene; addition of 1.5 wt% fluorine led to a decrease in the HDS activity of about 30% (131). The MoS₂ slabs also have a higher degree of stacking.

Although the interaction between oxidic nickel or cobalt and the γ -Al₂O₃ support also becomes weaker upon the addition of fluorine, this is not necessarily a disadvantage. Less nickel or cobalt is lost to the support and more is available for the formation of the active Ni–Mo–S phase on the catalyst surface. Adding small amounts of fluorine and chlorine (0.5 wt%) to a Co–Mo/Al₂O₃ catalyst resulted in a moderate (20%) increase in the catalytic activity for HDS of thiophene. At high loadings (5 wt%), on the other hand, a strong decrease in activity was found (132). Other authors confirmed these results for Ni–Mo/Al₂O₃ (133) as well as for Co–Mo/Al₂O₃ catalysts (134), but the reported activity per unit surface area must be recalculated to activity per unit mass of catalyst. The decrease in activity at high loading must be attributed to a decrease in dispersion, as for the Mo/Al₂O₃ catalyst (131). The increase in activity at low fluorine-loading is probably the result of an improved dispersion of cobalt and nickel. The role of fluorine in the HDS of gas oil conversion catalyzed by fluorine-modified Ni–Mo/Al₂O₃ was even more complex (135). A minimum activity was observed for 0.5 wt% fluorine and a maximum activity for 2.5 wt% fluorine. On the other hand, the activity for the HDN of pyridine, which was added to the gas oil, showed only a maximum as a function of the fluorine-loading. Several counteracting effects of fluorine were suggested to explain these observations: Fluorine may change

not only the dispersion and sulfidability of molybdenum and nickel (133), but also their distribution over the surface of the support. In particular, the latter effect may modify the ratio of the unpromoted MoS_2 phase to the promoted Ni–Mo–S phase on the support and thus catalysis. It is clear that several properties are affected by the addition of fluorine, and it is difficult to attribute the changes in these factors unequivocally to a catalytic effect of fluorine.

Sodium and calcium cations decreased the catalytic activity for HDS of thiophene catalyzed by Co–Mo/ Al_2O_3 and, at 5 wt% loading, caused complete elimination of the HDS activity (132). This extremely strong poisoning effect of sodium and calcium was ascribed to the formation of Na_2MoO_4 and CaMoO_4 , both of which are unaffected by sulfidation. That sodium is not a poison per se was shown by the normal thiophene HDS activity of a Co–Mo on amorphous silica-alumina doped with sodium (136) and of a Ni–Mo/ Al_2O_3 catalyst made by impregnation of Al_2O_3 with solutions of $\text{Na}_2\text{Mo}_3\text{S}_{13}$ and $\text{Ni}(\text{NO}_3)_2$ (137). The HDN activity of such sodium-containing catalysts has not been investigated, however.

The effect of fluorine on HDS and HDN has also been investigated for W/ Al_2O_3 and Ni–W/ Al_2O_3 catalysts. Fluorine led to a moderate increase in the HDS activity and a significant increase in the HDN activity of W/ Al_2O_3 for the processing of a gas oil (1.3 wt% S) enriched with 0.08 wt% nitrogen as pyridine (138). Addition of fluorine to a Ni–W/ Al_2O_3 catalyst had little or no effect on thiophene HDS, a negative effect on butene hydrogenation, and a positive effect on the HDN of pyridine (139).

These effects of fluorine on tungsten-containing catalysts have been explained in the same way as those observed for molybdenum-containing catalysts. However, W/ γ - Al_2O_3 catalysts are known to be difficult to sulfide. Therefore, the effect of fluorine on sulfidability should be more important for catalysts containing tungsten than for catalysts containing molybdenum. At high calcination temperatures and moderate sulfidation temperatures, the degree of sulfidation is often not more than 50% for W/ Al_2O_3 catalysts. The presence of nickel improves sulfidability; however, the degree of sulfidation is usually not higher than 70% for NiW/ Al_2O_3 when sulfidation is performed at temperatures below 723 K. For the equivalent NiMo/ γ - Al_2O_3 catalysts, on the other hand, it may be higher than 95%. Some authors have therefore ascribed the promoting effect of fluorine mainly to the better sulfidability of the tungsten catalyst. Indeed, in many cases, TEM has shown that more of the typical WS_2 structures are observed as the fluorine content is increased. Furthermore, the WS_2 crystallites are longer and the stacks of these WS_2 crystallites higher (138), suggesting that fluorine increases the sulfidability of tungsten catalysts. X-ray photoelectron spectra have shown, however, that the ratio of the sulfidic W(IV) and oxidic W(VI) 4f peaks hardly changes upon addition of fluorine. In some cases, a slight decrease in this ratio was

observed (139). The changes in the structure of WS_2 , observed with TEM, were apparently not representative of the average state of the tungsten.

Sun and Prins (140) attempted to separate the effects of sulfidation from other effects on the tungsten catalysts. First, they conducted temperature-programmed sulfidation experiments and demonstrated that fluorine hardly improves the sulfidability of tungsten catalysts that had been prepared in the usual way from ammonium metatungstate. Then, they prepared tungsten and nickel-tungsten catalyst precursors supported on $\gamma\text{-Al}_2\text{O}_3$ and on $\text{F}/\gamma\text{-Al}_2\text{O}_3$ by impregnating the supports with a $(\text{NH}_4)_2\text{WS}_4$ solution [and subsequently with a $\text{Ni}(\text{NO}_3)_2$ solution] in an air-free environment. After direct sulfidation of the catalyst precursors in H_2S and H_2 , without intermediate calcination, all the catalysts showed a high degree of sulfidation. QEXAFS measurements of the catalysts prepared from $(\text{NH}_4)_2\text{WS}_4$ and sulfided at 673 K showed a strong peak of sulfur atoms in contact with tungsten (Fig. 12, right), whereas

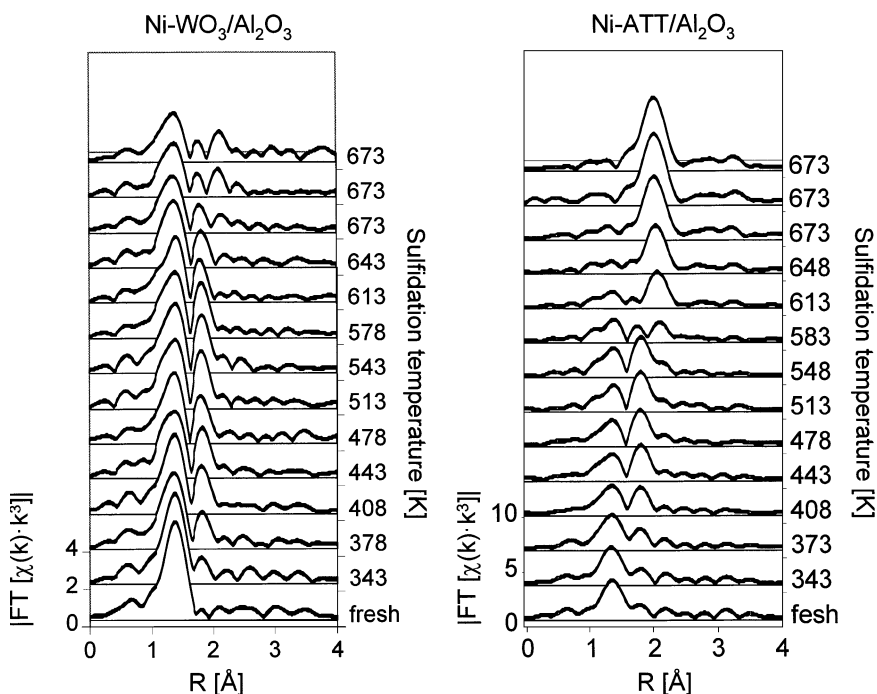


FIG. 12. Quick EXAFS spectra measured during the sulfidation of Ni-W/Al₂O₃ catalysts, during continuous heating of the catalyst in 5% H_2S in H_2 from room temperature to 673 K at 5 K/min and holding at 673 K for 30 min. The Ni-WO₃ catalyst was prepared from ammonium metatungstate, and the Ni-ATT catalyst was prepared from $(\text{NH}_4)_2\text{WS}_4$.

the Ni–W catalyst prepared from metatungstate barely showed this peak (Fig. 12, left). Although the Ni–W catalyst prepared from $(\text{NH}_4)_2\text{WS}_4$ was fully sulfided, fluorine addition to this catalyst improved its activity for the HDN of toluidine. This result demonstrates that sulfidation is not the main cause of the better activity of tungsten and molybdenum catalysts that contain fluorine.

What is responsible for the improved HDN activity of these catalysts? This question has yet to be answered. Analysis of the separate reactions in the toluidine HDN network demonstrated that the rate-determining hydrogenation of the phenyl ring in toluidine was accelerated. This observation is in agreement with results of a study of the effect of fluorine on the hydroisomerization and hydrocracking of heptane (141). That study showed that fluorine changes the balance between the (de)hydrogenation function and the acid function of a sulfided NiW/ γ - Al_2O_3 catalyst in favor of the former. A possible explanation for the higher hydrogenation activity is that fluorine induces the MoS_2 and WS_2 crystallites to grow perpendicular to the support surface. Such a stacking may lead to a better accessibility of sites at the MoS_2 and WS_2 edges, especially those required for the hydrogenation of aromatics. Increased stacking would explain why phosphate and fluorine exhibit similar effects, although they behave differently with regard to the chemistry. Van Veen *et al.* suggested that the effect of phosphorus (142) as well as fluorine (106) is a consequence of the formation of the Ni–Mo–S type II structure instead of the Ni–Mo–S type I structure.

D. OTHER METAL SULFIDES AND SUPPORTS

Although Ni–Mo and Co–Mo catalysts have been used for a long time, the search for more active catalysts continues. As a result of new legislation for low-sulfur diesel fuel, this search has intensified. Pecoraro and Chianelli (143) were the first to investigate systematically first-, second-, and third-row transition metal sulfides as catalysts. They showed that the unsupported sulfides of ruthenium, osmium, rhodium, and iridium have much higher activities than those of molybdenum and tungsten for the HDS of dibenzothiophene. A similar study of transition metal sulfides in HDN was performed by Eijssbouts *et al.* (144–146), who demonstrated that molybdenum and tungsten are not the most active metal sulfides in HDN. In the HDN of quinoline, for which hydrogenation is rate-determining, the order of activity for equal molar amounts of transition metal sulfides supported on active carbon was as follows: Ir > Os > Pt > Re > Rh > Pd, Ru > Mo > W (146). In the HDN of 2-propylaniline, for which hydrogenation is rate-determining as well, the order of activity was found to be Ir > Re > Os > Ru > Rh > Pt > Mo, W, Pd (146). In the HDN of DHQ, for which C–N bond breaking

through Hofmann elimination is rate-determining, the order was found to be Ir > Os, Rh > Ru > Mo, Pt > Re > W (145).

Ledoux and Djellouli (147) reported that of the second-row transition metal sulfides on activated carbon, ruthenium was better than palladium, rhodium, and molybdenum for HDN of pyridine. Per mole of molybdenum, Mo/C was even better than a commercial Ni–Mo/Al₂O₃ catalyst. In the combined HDN of pyridine and HDS of thiophene, the order of activity was Ir > Pt > Rh > Ru > Pd. All these carbon-supported metal sulfides had higher activity per mole of metal than conventional Ni–Mo/Al₂O₃ and Co–Mo/Al₂O₃ catalysts (148). As shown later, some of the high activity of transition metal sulfides supported on active carbon is caused by the carbon support. Nevertheless, there is no doubt that the best transition metal sulfides are at least as good as Ni–Mo or Co–Mo catalysts. Thus, an Ir/Al₂O₃ catalyst is more active than an Ni–Mo/Al₂O₃ catalyst per mole of metal (iridium or molybdenum) for HDN and has a higher HDN/HDS selectivity (149). Of course, it is important that the molar activity is higher. If, however, a high loading cannot be attained, or if the intrinsic activity decreases with loading (because of decreased dispersion), it will still be difficult to find a better HDN catalyst than Ni–Mo.

Higher activity can probably be achieved not only by using metal sulfides other than the conventional Ni–Mo or Co–Mo catalysts (or the equivalent tungsten-containing catalysts) or by adding phosphorus or fluorine to a conventional catalyst but also by changing the support. Many groups have therefore investigated supports other than Al₂O₃. An extensive review of Ni–Mo and Co–Mo catalysts supported on silica, silica-alumina, zeolites, activated carbon, and titania was presented by Luck (150).

Commercial silica often contains hundreds of parts per million (ppm) of calcium, sodium, iron, and aluminum impurities. Although the latter two may be beneficial for hydrotreating, it has been reported that calcium and sodium have negative effects, made worse by the weak interactions of calcium and sodium with the support so that these impurities come into contact with the molybdenum-containing phase. Even on pure silica, however, the activity of Co–Mo and Ni–Mo catalysts for HDS and HDN is low when these catalysts are prepared according to the usual procedures. The reason for the low activities is that the IEP of SiO₂ is low and, as a result, the dispersion of the oxidic phase, and thus of the eventual sulfidic phase, is also low. Active catalysts can be obtained by reversing the sequence of impregnation (nickel before molybdenum) and by omitting the calcination step so that sulfidation occurs immediately after drying (151, 152).

Silica-alumina and zeolites are used commercially in hydrocracking catalysts. Ni–Mo on silica-alumina is a better HDN catalyst than Ni–Mo/Al₂O₃ and is used in the first reactor of a two-stage hydrocracking process (1).

Correspondingly, a Ni–Mo/SiO₂–Al₂O₃ catalyst was found to be about 50% more active than a Ni–Mo/Al₂O₃ catalyst for the HDN of model compounds such as quinoline and propylaniline (153). Ni–Mo or Ni–W on a zeolite such as USY result in a good bifunctional hydrocracking catalyst that can be used in the second hydrocracking reactor (154). A physical mixture of NiMo/Al₂O₃ with ruthenium sulfide on zeolite Y had a higher HDN activity (155), which was ascribed to the better hydrogenation of the nitrogen-containing aromatic reactants by RuS₂ and the better breaking of the aliphatic C–N bond by Ni–MoS₂ (156).

Carbon and titania-supported catalysts are more active than alumina-supported catalysts per mole of metal present in the catalyst, but only carbon-supported catalysts have higher activity per gram of catalyst. The explanation for the difference is that titania has at most a surface area of 50 m²/g, about five times less than that of Al₂O₃. Therefore, less metal sulfide can be put on to the support, and this deficit is not sufficiently compensated by the higher intrinsic activity. Several groups have therefore tried to obtain a TiO₂ with high surface area by combining the high surface area of Al₂O₃ with the chemical properties of TiO₂. For example, a layer of TiO₂ was deposited on Al₂O₃ by chemical vapor deposition of TiCl₄ and subsequent hydrolysis (157). Furthermore, a mixed TiO₂–Al₂O₃ was produced by coprecipitation of aluminium and titanium alkoxides. In this way, not only was a high intrinsic activity per mole of molybdenum achieved but also a higher activity per gram of Mo/TiO₂–Al₂O₃ than per gram of Mo/Al₂O₃ was achieved (158–160). Unfortunately, the same result has not been obtained for cobalt- and nickel-promoted catalysts.

In contrast, Co–Mo/TiO₂–Al₂O₃ and Ni–Mo/TiO₂–Al₂O₃ catalysts were found to have lower activities than the corresponding alumina-supported catalysts for the HDS of thiophene and of dibenzothiophene. In accord with this result, the promoter effect of cobalt and nickel is about three times less on TiO₂ than on Al₂O₃. It is not known whether this difference is caused by poor contact between the promoter and MoS₂. Testing the same catalysts for the HDS of gas oil spiked with pyridine surprisingly showed that Co–Mo and Ni–Mo had higher HDS activity on TiO₂–Al₂O₃ than on Al₂O₃ per gram of catalyst. On the other hand, the activity for the HDN of pyridine was about the same for both supports (160). Results with catalysts prepared by coprecipitation from aqueous solution by urea hydrolysis showed a higher thiophene HDS activity for Co–Mo and Ni–Mo on TiO₂–Al₂O₃ than on Al₂O₃ (161). Nevertheless, these improvements were not better than those achieved with SiO₂–Al₂O₃-supported catalysts. Much work remains to be done before TiO₂–Al₂O₃ may become a useful industrial catalyst support for hydroprocessing (e.g., long-term chemical and mechanical stability must be investigated). Therefore, it is unlikely that TiO₂–Al₂O₃-supported catalysts

will be put on the market in the near future. A similar conclusion can be reached about catalysts on other supports such as ZrO_2 and $\text{Zr}_3(\text{PO}_4)_4$ (162). Although catalysts including these supports are intrinsically more active than alumina-based catalysts, substantial improvement in activity per unit mass of catalyst has not been achieved.

In contrast to TiO_2 -supported catalysts, carbon-supported catalysts have high intrinsic activities as well as large surface areas of the support (120, 152, 163). As a result, even the activity per unit mass of catalyst may be higher than that of alumina-supported catalysts. Carbon also has the advantage that less coke is deposited on it (164). Basic nitrogen compounds have an affinity for acidic support sites and undergo coking, thereby deactivating nearby metal sulfide centers. Carbon-supported Ni–Mo catalysts therefore showed less coke formation in the HDN of quinoline and a higher activity (165). It has also been reported that carbon-supported Ni–Mo catalysts are less likely to be poisoned by nitrogen-containing compounds during HDS than their alumina-supported counterparts (166).

The type of carbon used as a support clearly plays a role. Activated carbon with a high surface area and a substantial number of polar groups for anchoring molybdenum, which keeps the dispersion of the active material high, gives catalysts with much better activities than other carbons. Unfortunately, activated carbon has a low density; therefore, the activity per unit volume of catalyst is only slightly higher than that of alumina-supported catalysts. Since it is (reactor) volume that counts, carbon supports have not been used in industrial processes. Other drawbacks of carbon are its microporosity and its low mechanical strength. Possibilities for circumventing these drawbacks are the application of carbon black composite materials (167) or covering the surface of alumina with a thin layer of carbon by pyrolysis of cyclohexene and ethene (168).

The reason for the higher intrinsic activity of titania- and carbon-supported catalysts may be a weaker interaction between the active phase and the support (120). The weaker interaction with the support would lead to a higher degree of sulfidation and stacking. The formation of the Ni–Mo–S type II structure has also been suggested as an explanation, but this may actually be the same explanation. Furthermore, Laine *et al.* (169) suggested that the micropores of active carbon take up the excess sulfur from the edges of the metal sulfide crystallites and thus regenerate the active sites. This can be the case only if the regeneration of the sulfur vacancy is the rate-determining step. Experiments at different pressures showed that carbon with narrow micropores gives catalysts that are more active for thiophene HDS at 0.1 MPa than carbon with wider micropores; the reverse was found to be true at 3 MPa (170). This result demonstrates that the regeneration model does not function at higher pressures.

III. HDN on Metals, Metal Carbides, and Metal Nitrides

Section II.B showed that because of the strong $C(sp^2)-N$ bond, hydrogenation of aromatic rings in aromatic nitrogen-containing heterocycles is a necessary first step. Thereafter, the removal of the nitrogen atom via elimination or nucleophilic $SH-NH_2$ substitution followed by $C-S$ bond breaking can take place. Similar reactions (i.e., the hydrogenation of aromatic heterocycles containing nitrogen and the removal of nitrogen), can also take place on other types of catalysts. It has been known for decades that metals can be involved in such reactions. Metals can hydrogenate aromatic rings even at low temperatures. Furthermore, they can break $C-N$ bonds and thus remove nitrogen from aliphatic compounds containing nitrogen (171). However, they can break both $C-N$ bonds and $C-C$ bonds. This so-called hydrogenolysis property of metals leads in many instances to substantial cracking of the product molecules to smaller (gaseous) molecules. In the petroleum industry, this would result in a lower yield of liquid product, and consequently metal catalysts are not used in HDN. A second reason for not using metal catalysts is that HDN in isolation, without HDS, is not possible because oil fractions always contain sulfur as well as nitrogen. The relatively high concentrations of H_2S that are produced during normal hydrotreating would directly lead to sulfidation of any metal catalyst.

Recently, however, schemes for a hydrotreating process in which metals may play a role have come under consideration. New legislation will require very low levels of sulfur in gasoline and diesel fuel (<50 ppm) by the Year 2005. This goal might be attained by means of a two-stage hydrotreating process (2). In this process configuration, the majority of the original sulfur is removed with a classic metal sulfide catalyst in a first-stage reactor. The product is sent to a second-stage hydrotreating reactor in which the final sulfur specification of 50 ppm is reached. The relatively small amount of sulfur present in the product of the first reactor (e.g., 200 ppm) is very difficult to remove because this sulfur is present in highly unreactive molecules such as 4,6-dimethyl dibenzothiophene. This calls for highly active HDS catalysts, which are difficult to find among the metal sulfides. Because the concentration of H_2S in the second reactor is low, metal catalysts that are not overly sensitive to sulfur can be used, such as Pt-Pd catalysts on acidic supports (172). Other metals, or metal carbides or metal nitrides, may also play a role in future two-stage hydrotreating processes.

Catalysis on metal carbides and nitrides is a new branch of catalysis that started in the 1980s. Volpe and Boudart (173) discovered that it is easy to prepare Mo_2N and W_2N samples with high surface areas by nitriding MoO_3 and WO_3 , respectively, with ammonia. Lee *et al.* (174) synthesized high-surface-area Mo_2C by carburizing MoO_3 with methane. Subsequently, it was

discovered that the same methods also lead to supported carbides and nitrides. The resulting materials were tested for several catalytic reactions, such as hydrocarbon transformations (isomerization and hydrogenolysis), HDS, and HDN. Since the early 1990s, the number of investigations carried out in this field has increased dramatically, and many papers deal not only with their preparation and characterization but also with their catalytic properties. This section is focused on investigations that describe these carbides and nitrides as potential HDN catalysts. Results of related studies (for HDS and hydrogenolysis) are mentioned only when necessary to aid understanding.

A. STRUCTURE OF THE CATALYST

Metal carbides and metal nitrides are basically metals with carbon and nitrogen atoms, respectively, that are incorporated at interstitial positions. Several structures are possible (175). Complete filling of all octahedral sites in an fcc metal lattice gives an NaCl-type structure common to transition metal monocarbides such as VC and NbC. Random filling of half the octahedral sites results in a subcarbide structure such as Mo₂C and W₂C. Orderly filling of half of the trigonal-prismatic sites in the hexagonal metal lattice gives the WC structure. Bimetallic carbides have more complex structures.

Oxycarbides have also been described (176). They are of interest for catalysis because oxophilic metals may not form carbides easily; in preparations from metal oxides by treatment with methane, oxycarbides rather than carbides may form. Furthermore, carbides and nitrides are usually passivated after preparation; they are slowly exposed to oxygen or air to form a thin protective oxide layer on the metal carbide surface. In this passivated form, these materials are not pyrophoric and can be transported through the air. After insertion into a catalytic reactor, they must be reactivated either by methane or ammonia treatment, as used in their preparation, or by reduction with hydrogen. In these cases, pure carbide or nitride is not always reformed at the surface; an oxycarbide or oxynitride is often formed instead.

B. MECHANISMS

Pure metal carbides and nitrides have metallic properties. The interstitial C or N atoms increase the distance between the metal atoms somewhat, leading to a decrease in the width of the metal d band and a weaker metal character. Thus, metal carbides formed from metals in the middle of the periodic table, such as molybdenum and tungsten, behave more like metals on the right side of the table, such as platinum. Consequently, the hydrogenation and hydrogenolysis properties of these metal carbides, although still present, are not as strong. Like many pure metals, carbides and nitrides of molybdenum and tungsten are still active for hydrogenolysis (177), which will prevent

applications in classic HDN because of the loss of the liquid product to gaseous molecules.

Product loss through hydrogenolysis is a well-known problem. In catalytic reforming, hydrocarbons must be transformed into other hydrocarbons with higher octane numbers. Metals can do this, but even a metal with an almost filled d band, such as platinum, still catalyzes unwanted hydrogenolysis. The solution to this problem in catalytic reforming was to temper the hydrogenolysis properties of platinum by adsorbing sulfur atoms on the metal or by alloying platinum with an inactive metal such as tin (178). The remaining uncovered platinum atoms in the surface are isolated, and no clusters of neighboring platinum atoms are available to break the C–C bonds. At the same time, the hydrocarbon isomerization capability of platinum is suppressed, however, and another catalytic function has to be added to bring back isomerization capability. This was realized by using an acidic support that can isomerize hydrocarbons but is not acidic enough to catalyze cracking. In industry, Al_2O_3 acidified with chlorine or fluorine is often used (179).

The problem related to the hydrogenolysis of metal carbides and nitrides in hydrotreating can be solved in a similar way by isolating the metal atoms by sulfur adsorption on the surface or by alloying with inactive metals. Oil fractions contain substantial amounts of sulfur, and the problem is to prevent bulk sulfidation. Therefore, a feed that contains only a relatively small amount of sulfur, such as the product from a first-stage hydrotreating reactor, will be more appropriate for the application of metal carbides or nitrides in hydrotreating. Sulfur adsorption or alloying will suppress not only C–C bond breaking but also C–N bond breaking. Therefore, as in catalytic reforming, a new catalytic function must be built in to enable breaking of the C–N bond and removal of nitrogen. Acidity of the support or acidity on the metal carbide or nitride may be the solution. Oxycarbides and oxynitrides contain oxygen atoms in the lattice which may form hydroxyl groups at the surface. These hydroxyl groups may have Brønsted acid properties, or a metal atom at the surface next to an oxygen atom may have Lewis acid properties. Consequently, oxycarbides and oxynitrides have metallic as well as acidic properties, and they are bifunctional (180, 181). In this respect, they are like metal oxides with metals in low oxidation states and metal sulfides and can catalyze the removal of nitrogen from aromatic heterocycles.

C. HDN OF SPECIFIC COMPOUNDS

Interest in the use of metal carbides and nitrides in hydrotreating was aroused by a publication by Schlatter *et al.* (182) in 1988. They reported that Mo_2C and Mo_2N (unsupported as well as supported on Al_2O_3) were highly active for HDN of quinoline in autoclaves under industrially realistic

conditions (e.g., 6.9 MPa and 673 K) (182). The activities that were attained in this exploratory study were similar to the activity of a commercial sulfided Ni–Mo/Al₂O₃ catalyst. When tested in the absence of sulfur, Mo₂C in particular showed a much higher selectivity for aromatic hydrocarbons than sulfided Ni–Mo/Al₂O₃. This result shows that Mo₂C and Mo₂N can remove nitrogen from propylaniline directly by hydrogenolysis of the C–N bond, without having to hydrogenate the phenyl ring. When sulfur was added to the feed (as CS₂), however, the PB to PCH ratio was much lower and more representative of a sulfided Mo/Al₂O₃ catalyst. It was suggested that a surface layer of MoS₂ forms on the Mo₂C under such conditions since the metal sulfide is thermodynamically preferred. In that case, the HDN mechanism is similar to that discussed in Section II.B for metal sulfide catalysts. This inference means that hydrogenolysis of the aniline C–N bond is relatively insignificant and that HDN occurs mainly via hydrogenation of the phenyl ring of the aniline. As a result, the aromatic content of the product is lower than when the molybdenums carbide or nitride are used in the absence of sulfur.

Subsequent work by Lee *et al.* (183) and Abe *et al.* (184) with Mo₂N confirmed the results of Schlatter *et al.* They obtained much higher selectivities to aromatic products in the absence of sulfur because their lower pressure (0.1 MPa) and higher temperature (723 K) favored the formation of aromatics. Under these conditions, they observed substantial hydrogenolysis. Thus, benzene and toluene rather than PB were the main products of the HDN of quinoline. Stanczyk *et al.* (185) observed a high selectivity for aromatic products and substantial hydrogenolysis as well. They studied the HDN of 1,2,3,4-THQ on molybdenum and niobium oxynitrides at 673 K and 4.5 MPa. The ratio PB to PCH was close to 1, indicating that the reaction of propylaniline to PB was much more important on MoN_xO_y than on sulfided Ni–Mo/Al₂O₃ (Section II.B.2.c). The relatively large amounts of ethylaniline, methylaniline, and aniline (as well as ethylbenzene and toluene) demonstrated that hydrogenolysis of the propylaniline, or rather of the propylbenzene product, was substantial.

Several unsupported metal carbides and nitrides (of titanium, vanadium, niobium, molybdenum and tungsten) were investigated as catalysts for HDS, HDN, and hydrodeoxygenation by Ramanathan and Oyama (186). A model feed containing 3000 ppm sulfur (as dibenzothiophene), 2000 ppm nitrogen (as quinoline), 500 ppm oxygen (as benzofuran), and 20% aromatic hydrocarbon (as tetralin) was tested at 643 K and 3.1 MPa in a microflow reactor. Mo₂C, Mo₂N, and WC showed HDN activities to hydrocarbons comparable to that of a commercial sulfided Ni–Mo/Al₂O₃ catalyst. Only Mo₂C showed a good HDS activity, and VN showed a high hydrodeoxygenation activity

under these conditions with a high nitrogen content in the feed. The VN catalyst produced mainly ethylbenzene in the conversion of benzofuran, whereas the Ni–Mo/Al₂O₃ catalyst yielded mostly ethylcyclohexane. Hydrogenolysis of the C–O bond in phenol (which is weaker than the C–N bond in aniline) is probably substantial, even on surface-sulfided VN. The PCH to PB ratio resulting from the HDN was greater than 1 for all these catalysts, as it was for the sulfided Ni–Mo/Al₂O₃. This result suggests that the large amount of sulfur in the feed transformed the metal carbides and nitrides into sulfides, at least at the surface. No traces of sulfide phases were revealed by X-ray diffraction, however, and only small amounts of sulfur were found by X-ray photoelectron spectroscopy. Therefore, the authors concluded that the materials are sulfur tolerant.

Similar experiments, again with a mixed feed of dibenzothiophene, quinoline, benzofuran, and tetralin, were conducted with a series of bimetallic oxynitride compounds, such as V–Mo–O–N, Mo–W–O–N, Co–Mo–O–N, and Co–W–O–N (187). Several of these materials had higher HDN activities than their monometallic equivalents and were comparable to a Ni–Mo/Al₂O₃ catalyst, but their HDS and hydrodeoxygenation activities were lower. Whereas molybdenum and tungsten, alloyed with early transition metals such as vanadium, chromium, and niobium, were found to be sulfur resistant, according to X-ray diffraction data, manganese and cobalt oxynitride alloys showed bulk sulfidation to give MnS and Co₄S₃, respectively. Oyama *et al.* (188) also studied bimetallic oxycarbides such as Nb–Mo–O–C, Ni–Mo–O–C, Mo–W–O–C, and Ni–W–O–C, which were found to have moderate activities similar to those of the monometallic carbides. Only Nb–Mo–O–C had a higher activity than NbC or Mo₂C. X-ray diffraction patterns measured before and after the reaction showed that whereas Mo–W–O–C and Nb–Mo–O–C were sulfur resistant during the reaction, Ni–Mo–O–C and Ni–W–O–C were transformed into sulfides.

Sajkowski and Oyama (189) reported high activities of unsupported Mo₂N and Mo₂C catalysts supported on Al₂O₃ in a hydrotreating study of a coal-derived gas oil and a coal-derived residuum feed at 633 K and 13.7 MPa. These feeds contained about 4000 ppm nitrogen, 120 or 800 ppm sulfur, and 3500 or 18,600 ppm oxygen, respectively. The authors compared the activities based on sites titrated by CO on the nitride and carbide and titrated by O₂ on sulfided Mo/Al₂O₃ and Ni–Mo/Al₂O₃ catalysts. They reached the conclusion that the carbide and nitride were intrinsically five times more active than the classic catalysts. Although this result points to a high intrinsic activity of these new materials, it does not demonstrate that they are indeed intrinsically more active because currently there is no reliable method for counting the number of active sites at the surfaces of metal sulfides. Under

certain conditions, oxygen chemisorption does indeed give results that correlate with activity, but it has been shown that O_2 chemisorption on sulfides is corrosive and therefore dependent on the measurement conditions. O_2 chemisorption probably overestimates the number of sites. Thus, the quoted fivefold higher intrinsic activity of Mo_2N and Mo_2C has to be taken as an upper limit. In any case, industry is interested in actual activities rather than intrinsic catalytic activities, based on volume rather than on weight, because existing reactors have to be filled with these catalysts. In both cases, the Mo_2N and Mo_2C catalysts were less active per unit of reactor volume than the classic $Ni-Mo/Al_2O_3$ catalyst.

In the same study (189), Sajkowski and Oyama reported that X-ray diffraction did not show any crystalline MoS_2 , but that X-ray photoelectron spectroscopy showed a sulfur-to-molybdenum ratio of 0.26 at the surface. They concluded that the formation of MoS_2 at the surface of the nitride and carbide crystallites could not be ruled out. The question of surface sulfidation was addressed by van Veen *et al.* (190) and Aegerter *et al.* (191). The TEM results of van Veen *et al.* showed that the surface of an unsupported Mo_2N sample was transformed into molybdenum sulfide (Fig. 13), whereas the X-ray data showed that the bulk structure of molybdenum carbide (or nitride) was retained. The same X-ray result was obtained by Aegerter *et al.* (191). Their infrared spectra of adsorbed CO, however, indicated that the surfaces of the Mo_2C and Mo_2N catalysts had become sulfided. Furthermore, the HDS product selectivities did not differ from those of a sulfided Mo/Al_2O_3 catalyst. The Mo_2C and Mo_2N particles apparently act as rigid supports on which a thin layer of sulfided molybdenum forms under HDS conditions.

Indole conversion was investigated at atmospheric pressure by Li *et al.* (192) and at 9 MPa in the presence of 70 ppm of H_2S by Miga *et al.* (181). In the latter study, more of the fully hydrogenated ethylcyclohexane than ethylbenzene was produced in the presence of bulk molybdenum oxynitride, suggesting that MoS_2 was the active component. The HDN of pyridine was investigated at atmospheric pressure with a Mo_2C catalyst (193) and with several metal nitrides (194): The results show substantial hydrogenolysis of the pentane product. At 3 MPa and 573 K, pyridine was almost totally denitrogenated on nitrated $Ni-Mo/Al_2O_3$ catalysts in the absence of sulfur (195). As expected for a metal or metal nitride catalyst, some hydrogenolysis was observed. The $Ni-MoN/Al_2O_3$ catalysts not only gave higher conversions of pyridine than a sulfided $Ni-Mo/Al_2O_3$ catalyst but also were much more active for denitrogenation. Metallic nickel, but not Ni_3N , was observed by X-ray diffraction, in line with thermodynamics. A Ni_3Mo_3N phase was probably responsible for the high activity and the promotion effect of nickel.

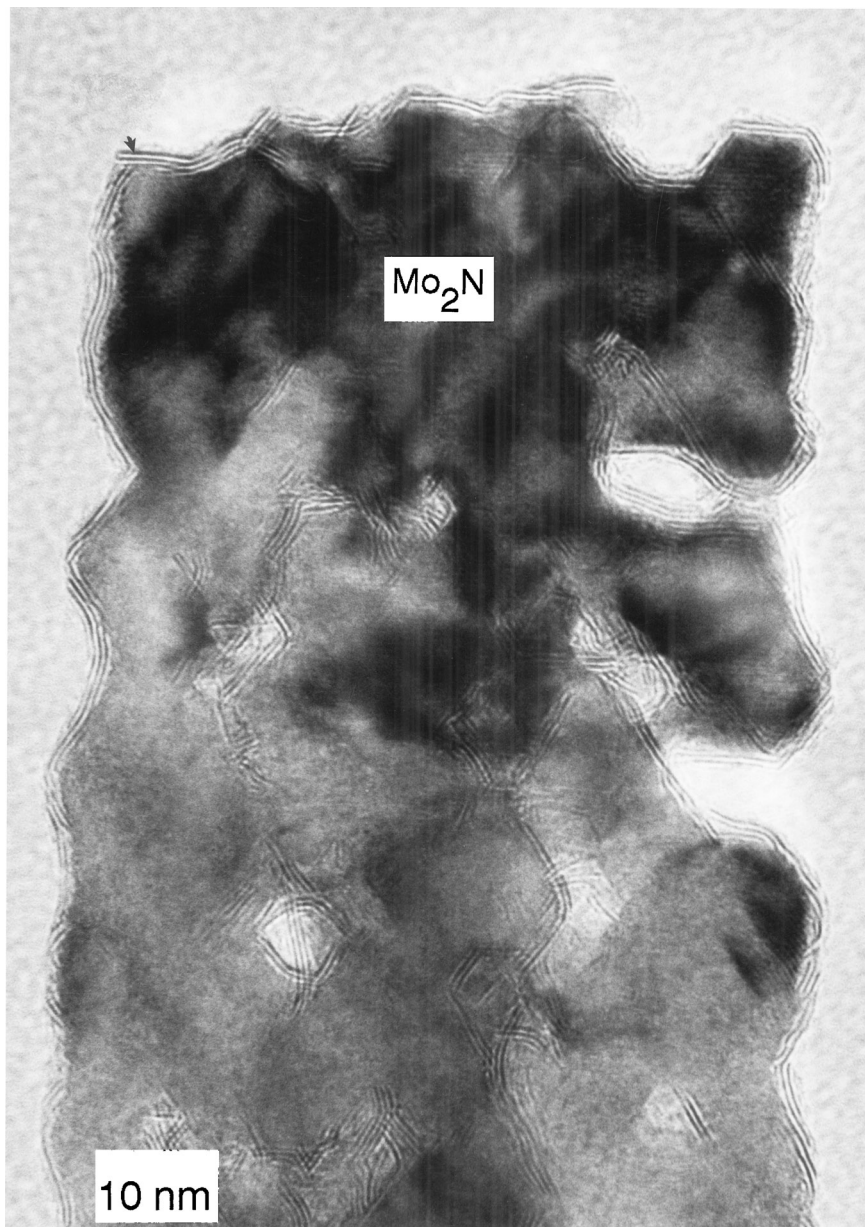


FIG. 13. Micrograph of a spent Mo_2N catalyst with a surface layer of MoS_2 (190).

IV. Conclusions

Progress in the understanding and implementation of this understanding in hydroprocessing have been impressive in the past few decades. Nevertheless, major challenges remain, as is all too clear from the sulfur and nitrogen targets set by the 2005 legislation for automotive fuels. These targets, and the even more stringent ones that undoubtedly will follow, will be met only if an active exploratory as well as fundamental research effort is pursued. Newly emerged materials such as carbides and nitrides have shown promise, but the discussion in Section III has shown that these materials have metallic properties which may constitute problems. The dilemma in hydroprocessing is that in principle metals have the highest catalytic activity, but they also have the highest affinity for sulfur. Consequently, the metal surface becomes covered with sulfur, and the initially high activity decreases to a level that might be even lower than those of pure metal sulfides. As indicated previously, the solution to this problem might be to use a multireactor approach. The majority of the sulfur in a feed is removed with a sulfur-tolerant catalyst, such as the classic Co–Mo or Ni–Mo catalysts. The remaining sulfur and the majority of the nitrogen can then be removed in a second-step reactor filled with a much more active, but also much more sulfur-sensitive, catalyst. In this application, the new materials will have to compete with supported alloys such as Pt–Pd that have already been introduced in commercial operation by some oil companies. Notwithstanding their industrial use, it is not understood why such alloys supported on zeolites are so sulfur insensitive, and much research needs to be done in this respect.

Regarding HDN, future work will undoubtedly pay more attention to synergetic effects between HDS and HDN. HDS and HDN in isolation are well understood, and general patterns of the mutual influences of HDS and HDN have been uncovered (Section II.B.3). However, experience gained in experiments with relatively high sulfur concentrations might need reconsideration when products with very low sulfur contents are to be processed in the second-step reactors alluded to previously. HDN reactions of nitrogen-containing compounds are quite complex. Reactions of mixtures, especially of nitrogen- and sulfur-containing mixtures, will be even more difficult to understand at the molecular level. Only through a combined effort of chemists and chemical engineers will satisfactory progress be made.

ACKNOWLEDGMENTS

I thank Dr. P. J. Kooijman of the National Centre for High Resolution Electron Microscopy, Delft University of Technology, Delft, The Netherlands, for measuring the electron microscopy graph.

REFERENCES

1. Satterfield, C. N., "Heterogeneous Catalysis in Industrial Practice," pp. 339–417, McGraw-Hill, New York, 1991.
2. Stork, W. H. J., *Stud. Surf. Sci. Catal.* **106**, 41 (1997).
3. Topsøe, H., Clausen, B. S., and Massoth, F. E., "Hydrotreating Catalysis, Science and Technology." Springer, Berlin, 1996.
4. Ho, T. C., *Catal. Rev. -Sci. Eng.* **30**, 117 (1988).
5. Prins, R., de Beer, V. H. J., and Somorjai, G. A., *Catal. Rev.-Sci. Eng.* **31**, 1 (1989).
6. Prins, R., in "Handbook of Heterogeneous Catalysis" (G. Ertl, H. Knözinger, and J. Weitkamp, Eds.), Vol. 4. Wiley-VCH, Weinheim, 1997.
7. Adachi, M., Contescu, C., and Schwarz, J. A., *J. Catal.* **162**, 66 (1996).
8. Kasztelan, S., Grimblot, J., and Bonnelle, J. P., *J. Phys. Chem.* **91**, 1503 (1987).
9. Topsøe, N., and Topsøe, H., *J. Catal.* **75**, 354 (1982).
10. Gao, X., and Xin, Q., *Catal. Lett.* **18**, 409 (1993).
11. Wivel, C., Clausen, B. S., Candia, R., Mørup, S., and Topsøe, H., *J. Catal.* **87**, 497 (1984).
12. Prada Silvy, R., Grange, P., and Delmon, B., *Stud. Surf. Sci. Catal.* **52**, 233 (1990).
13. Arnoldy, P., van den Heijkant, J. A. M., de Bok, G. D., and Moulijn, J. A., *J. Catal.* **92**, 35 (1985).
14. Cattaneo, R., Weber, T., Shido, T., and Prins, R., *J. Catal.* **191**, 225 (2000).
15. Clausen, B. S., Topsøe, H., Candia, R., Villadsen, J., Lengeler, B., Als-Nielsen, J., and Christensen, F., *J. Phys. Chem.* **85**, 3868 (1981).
16. Bouwens, S. M. A. M., Prins, R., de Beer, V. H. J., and Koningsberger, D. C., *J. Phys. Chem.* **94**, 3711 (1990).
17. Shido, T., and Prins, R., *J. Phys. Chem. B* **102**, 8426 (1998).
18. Sakashita, Y., and Yoneda, T., *J. Catal.* **185**, 487 (1999).
19. Topsøe, N., and Topsøe, H., *J. Catal.* **84**, 386 (1983).
20. Louwers, S. P. A., and Prins, R., *J. Catal.* **133**, 94 (1992).
21. Byskov, L. S., Nørskov, J. K., Clausen, B. S., and Topsøe, H., *J. Catal.* **187**, 109 (1999).
22. Raybaud, P., Hafner, J., Kresse, G., Kasztelan, S., and Toulhoat, H., *J. Catal.* **189**, 129 (2000).
23. Crajé, M. W. J., Louwers, S. P. A., de Beer, V. H. J., Prins, R., and van der Kraan, A. M., *J. Phys. Chem.* **96**, 5445 (1992).
24. Farragher, A. L., and Cossee, P., in "Proceedings of the 5th International Congress on Catalysis" (J. W. Hightower, Ed.), Vol. 2, p. 1301. North-Holland, Amsterdam, 1973.
25. Farias, M. H., Gellman, A. J., Somorjai, G. A., Chianelli, R. R., and Liang, K. S., *Surf. Sci.* **140**, 181 (1984).
26. Helveg, S., Lauritsen, J. V., Laegsgaard, E., Stensgaard, I., Nørskov, J. K., Clausen, B. S., Topsøe, H., and Besenbacher, F., *Phys. Rev. Lett.* **84**, 951 (2000).
27. Delmon, B., *Bull. Soc. Chim. Belgium* **88**, 979 (1979).
28. Grange, P., and Vanhaeren, X., *Catal. Today* **36**, 375 (1997).
29. Wivel, C., Candia, R., Clausen, B. S., Mørup, S., and Topsøe, H., *J. Catal.* **68**, 453 (1981).
30. Duchet, J. C., van Oers, E. M., de Beer, V. H. J., and Prins, R., *J. Catal.* **80**, 386 (1983).
31. Vissers, J. P. R., de Beer, V. H. J., and Prins, R., *J. Chem. Soc. Faraday Trans. I* **83**, 2145 (1987).
32. Startsev, A. N., Shkuropat, S. A., Kriventsov, V. V., Kochubey, D. I., and Zamaraev, K. I., *Mendeleev Commun.*, 6 (1991).
33. Medici, L., Harada, M., and Prins, R., *Mendeleev Commun.*, 121 (1996).
34. Leliveld, R. G., van Dillen, A. J., Geus, J. W., and Koningsberger, D. C., *J. Phys. Chem.* **101**, 11160 (1998).
35. Leliveld, R. G., van Dillen, A. J., Geus, J. W., and Koningsberger, D. C., *J. Catal.* **175**, 108 (1998).

36. Nørskov, J. K., Clausen, B. S., and Topsøe, H., *Catal. Lett.* **13**, 1 (1992).
37. Toulhoat, H., Raybaud, P., Kasztelan, S., Kresse, G., and Hafner, J., *Catal. Today* **50**, 629 (1999).
38. Raybaud, P., Hafner, J., Kresse, G., Kasztelan, S., and Toulhoat, H., *J. Catal.* **190**, 128 (2000).
39. Farragher, A. L., *Adv. Coll. Interface Sci.* **11**, 3 (1979).
40. Rota, F., and Prins, R., *Topics Catal.* **11/12**, 327 (2000).
41. March, J., "Advanced Organic Chemistry," 3rd. ed., p. 590. Wiley, New York, 1985.
42. Chang, C. D., and Lang, W. H., US Patent No. 4380669 to Mobil Company 1980; Chang, C. D., and Perkins, P. D., Europe Patent No. 0082613 to Mobil Company (1983).
43. Stamm, Th., Kouwenhoven, H. W., Seebach, D., and Prins, R., *J. Catal.* **155**, 268 (1995).
44. Tschumper, A., and Prins, R., *Appl. Catal.* **172**, 285 (1998); **174**, 129 (1998).
45. Schulz, H., Schon, M., and Rahman, N. M., *Stud. Surf. Sci. Catal.* **27**, 201 (1986).
46. Nelson, N., and Levy, R. B., *J. Catal.* **58**, 485 (1979).
47. Zdrzil, M., *J. Catal.* **141**, 316 (1993).
48. Rajagopal, S., and Miranda, R., *J. Catal.* **141**, 318 (1993).
49. Topsøe, N. Y., Topsøe, H., and Massoth, F. E., *J. Catal.* **119**, 252 (1989).
50. Portefaix, J. L., Cattenot, M., Guerriche, M., Thivolle-Cazat, J., and Breysse, M., *Catal. Today* **10**, 473 (1991).
51. Pines, H., and Manassen, J., *Adv. Catal.* **16**, 49 (1966).
52. Knözinger, H., Bühl, H., and Kochloefl, K., *J. Catal.* **22**, 57 (1972).
53. Vivier, L., Dominguez, V., Perot, G., and Kasztelan, S., *J. Mol. Catal.* **67**, 267 (1991).
54. Wilson, R. L., and Kembal, C., *J. Catal.* **3**, 426 (1964).
55. Kieran, P., and Kembal, C., *J. Catal.* **4**, 380 (1965).
56. Cattenot, M., Portefaix, J. L., Afonso, J., Breysse, M., Lacroix, M., and Perot, G., *J. Catal.* **173**, 366 (1998).
57. March, J., "Advanced Organic Chemistry," 3rd. ed., p. 255 and 873. Wiley, New York, 1985.
58. Hadjiloizou, G. C., Butt, J. B., and Dranoff, J. S., *Ind. Eng. Chem. Res.* **31**, 2503 (1992).
59. Mou, Jian, and Prins, R., *Ind. Eng. Chem. Res.* **37**, 834 (1998).
60. Satterfield, C. N., and Cocchetto, J. F., *Ind. Eng. Chem. Proc. Des. Dev.* **20**, 53 (1981).
61. Finiels, A., Geneste, P., Moulinas, C., and Olivé, J. L., *Appl. Catal.* **22**, 257 (1986).
62. Shanthi, K., Pillai, C. N., and Kuriacose, J. C., *Appl. Catal.* **46**, 241 (1989).
63. Satterfield, C. N., Modell, M., and Wilkens, J. A., *Ind. Eng. Chem. Proc. Des. Dev.* **19**, 154 (1980).
64. Hanlon, R. T., *Energy Fuels* **1**, 424 (1987).
65. Cerny, M., *Coll. Czech. Chem. Commun.* **47**, 928 (1982).
66. Cerny, M., and Trka, A., *Coll. Czech. Chem. Commun.* **48**, 1749 (1983).
67. Ledoux, M. J., Agostini, G., Benazouz, R., and Michaux, O., *Bull. Soc. Chim. Belgium* **93**, 635 (1984).
68. Sobczak, J., Vit, Z., and Zdrzil, M., *Appl. Catal.* **45**, L23 (1988).
69. Mou, Jian, Rico Cerda, J. L., and Prins, R., *Bull. Soc. Chim. Belgium* **104**, 225 (1995).
70. Ledoux, M. J., and Sedrati, M., *J. Catal.* **83**, 229 (1983).
71. Rajagopal, S., Grimm, T. L., Collins, D. J., and Miranda, R., *J. Catal.* **137**, 453 (1992).
72. Geneste, P., Moulinas, C., and Olivé, J. L., *J. Catal.* **105**, 254 (1987).
73. Moreau, C., Aubert, C., Durand, R., Zmimita, N., and Geneste, P., *Catal. Today* **4**, 117 (1988).
74. van Gestel, J., Leglise, J., and Duchet, J. C., *Appl. Catal.* **92**, 143 (1992).
75. Mou, Jian, Kapteijn, F., and Prins, R., *J. Catal.* **168**, 491 (1997).
76. Rota, F., and Prins, R., *Stud. Surf. Sci. Catal.* **127**, 319 (1999).
77. LaVopa, V., and Satterfield, C. N., *J. Catal.* **110**, 375 (1988).

76. Perot, G., Brunet, S., Canaff, C., and Toulhoat, H., *Bull. Soc. Chim. Belgium* **96**, 865 (1987).
79. Mou, Jian, and Prins, R., *J. Catal.* **179**, 18 (1998).
80. Satterfield, C. N., and Gültekin, S., *Ind. Eng. Chem. Proc. Des. Dev.* **20**, 62 (1981).
81. Yang, S. H., and Satterfield, C. N., *Ind. Eng. Chem. Proc. Des. Dev.* **23**, 20 (1984).
82. Olalde, A., and Perot, G., *Appl. Catal.* **13**, 373 (1985).
83. Massoth, F. E., Balusami, K., and Shabtai, J., *J. Catal.* **122**, 256 (1990).
84. Callant, M., Grange, P., Holder, K. A., and Delmon, B., *Bull. Soc. Chim. Belgium* **100**, 823 (1991).
85. Bunch, A., Zhang, L., Karakas, G., and Ozkan, U. S., *Appl. Catal. A* **190**, 51 (2000).
86. Zhang, L., and Ozkan, U. S., *Stud. Surf. Sci. Catal.* **101**, 1223 (1996).
87. Kim, S. C., and Massoth, F. E., *J. Catal.* **189**, 70 (2000).
88. Satterfield, C. N., and Yang, S. H., *Ind. Eng. Chem. Proc. Des. Dev.* **23**, 11 (1984).
89. Nagai, M., Masunaga, T., and Hana-oka, N., *J. Catal.* **101**, 284 (1986).
90. Nagai, M., Masunaga, T., and Hana-oka, N., *Energy Fuels* **2**, 645 (1988).
91. Moreau, C., Durand, R., Zmimita, N., and Geneste, P., *J. Catal.* **112**, 411 (1988).
92. Shabtai, J., Yeh, G. J. C., Russell, C., and Oblad, A. G., *Ind. Eng. Chem. Res.* **28**, 139 (1989).
93. Malakani, K., Magnoux, P., and Perot, G., *Appl. Catal.* **30**, 371 (1987).
94. Moreau, C., Bekakra, L., Olive, J. L., and Geneste, P., in "Proceedings of the 9th International Congress on Catalysis" (M. J. Philips and M. Ternan, Eds.), p. 58. Chemical Institute of Canada, Ottawa, 1988.
95. Girgis, M. J., and Gates, B. C., *Ind. Eng. Chem. Res.* **30**, 2021 (1991).
96. Nagai, M., Sato, T., and Aiba, A., *J. Catal.* **97**, 52 (1986).
97. LaVopa, V., and Satterfield, C. N., *Chem. Eng. Commun.* **70**, 171 (1988).
98. Houalla, M., Nag, N. K., Sapre, A. V., Broderick, D. H., and Gates, B. C., *Am. Inst. Chem. Eng. J.* **24**, 1015 (1978).
99. Morávek, V., Duchet, J. C., and Cornet, D., *Appl. Catal.* **66**, 257 (1990).
100. Gioia, F., and Lee, V., *Ind. Eng. Chem. Proc. Des. Dev.* **25**, 918 (1986).
101. Pille, R., and Froment, G., *Stud. Surf. Sci. Catal.* **106**, 403 (1997).
102. Shih, S. S., Mathur, K. N., Katzer, J. R., Kwart, H., and Stiles, A. B., *Prep. Am. Chem. Soc. Div. Pet. Chem.* **22**, 919 (1977).
103. Prins, R., Mou, Jian, and Flechsenhar, M., *Polyhedron* **16**, 3235 (1996).
104. Mickelson, G. A., US Patent Nos. 3 749 633, 3 749 664, 3 755 148, 3 755 150, and 3 755 196, (1973).
105. Heresnape, J. N., and Morris, J. E., British Patent No. 701 217 (1953).
106. van Veen, J. A. R., Colijn, H. A., Hendriks, P. A. J. M., and van Welsenes, A. J., *Fuel Proc. Technol.* **35**, 137 (1993).
107. Fitz, C. W., and Rase, H. F., *Ind. Eng. Chem. Prod. Res. Dev.* **22**, 40 (1983).
108. Tischer, R. E., Narain, N. K., Stiegel, G. J., and Cillo, D. L., *Ind. Eng. Chem. Prod. Res. Dev.* **26**, 422 (1987).
109. Eijsbouts, S., van Gestel, J. N. M., van Veen, J. A. R., de Beer, V. H. J., and Prins, R., *J. Catal.* **131**, 412 (1991).
110. Ramirez de Agudelo, M. M., and Morales, A., in "Proceedings of the 9th International Congress on Catalysis" (M. J. Philips and M. Ternan, Eds.), p. 42. Chemical Institute of Canada, Ottawa, 1988.
111. Lewis, J. M., Kydd, R. A., Boorman, P. M., and Van Rhyn, P. H., *Appl. Catal.* **84**, 103 (1992).
112. Bouwens, S. M. A. M., van der Kraan, A. M., de Beer, V. H. J., and Prins, R., *J. Catal.* **128**, 559 (1991).
113. Cruz Reyes, J., Avalos Borja, M., López Cordero, R., and López Agudo, A., *Appl. Catal.* **120**, 147 (1994).

114. DeCanio, E. C., Edwards, J. C., Scalzo, T. R., Storm, D. A., and Bruno, J. W., *J. Catal.* **132**, 498 (1991).
115. López Cordero, R., Esquivel, N., Lazaro, J., Fierro, J. L. G., and López Agudo, A., *Appl. Catal.* **48**, 341 (1989).
116. Fierro, J. L. G., López Agudo, A., Esquivel, N., and López Cordero, R., *Appl. Catal.* **48**, 353 (1989).
117. Ryan, R. C., Kemp, R. A., Smegal, J. A., Denley, D. R., and Spinnler, G. A., *Stud. Surf. Sci. Catal.* **50**, 21 (1989).
118. Cruz Reyes, J., López Agudo, A., López Cordero, R., Avalos Borja, M., Fuentes, S., and Farias, M. H., *Catal. Lett.* **42**, 119 (1996).
119. Candia, R., Sørensen, O., Villadsen, J., Topsøe, N. Y., Clausen, B. S., and Topsøe, H., *Bull. Soc. Chim. Belgium* **93**, 763 (1984).
120. Vissers, J. P. R., Scheffer, B., de Beer, V. H. J., Moulijn, J. A., and Prins, R., *J. Catal.* **105**, 277 (1987).
121. Daage, M., and Chianelli, R. R., *J. Catal.* **149**, 414 (1994).
122. Mou, Jian, and Prins, R., *Catal. Lett.* **35**, 193 (1995).
123. Robinson, W. R. A. M., van Gestel, J. N. M., Korányi, T. I., Eijsbouts, S., van der Kraan, A. M., van Veen, J. A. R., and de Beer, V. H. J., *J. Catal.* **161**, 539 (1996).
124. Mou, Jian, and Prins, R., *Catal. Today* **30**, 127 (1996).
125. Mangnus, P. J., van Langeveld, A. D., de Beer, V. H. J., and Moulijn, J. A., *Appl. Catal.* **68**, 161 (1991).
126. Li, W., Dhandapani, B., and Oyama, S. T., *Chem. Lett.* **3**, 207 (1998).
127. Stinner, C., Prins, R., and Weber, T., *J. Catal.* **191**, 438 (2000).
128. Lewis, J. M., Kydd, R. A., and Boorman, P. M., *J. Catal.* **120**, 413 (1989).
129. Mulcahy, F. M., Houalla, M., and Hercules, D. M., *J. Catal.* **106**, 210 (1987).
130. Yamagata, N., Owada, Y., Okazaki, S., and Tanabe, K., *J. Catal.* **47**, 358 (1977).
131. Miciukiewicz, J., Qader, Q., and Massoth, F. E., *Appl. Catal.* **49**, 247 (1989).
132. Muralidhar, G., Massoth, F. E., and Shabtai, J., *J. Catal.* **85**, 44 (1984).
133. Papadopoulou, Ch., Lycourghiotis, A., Grange, P., and Delmon, B., *Appl. Catal.* **38**, 255 (1988).
134. Matralis, H. K., Lycourghiotis, A., Grange, P., and Delmon, B., *Appl. Catal.* **38**, 273 (1988).
135. Fierro, J. L. G., Cuevas, R., Ramírez, J., and López Agudo, A., *Bull. Soc. Chim. Belgium* **100**, 945 (1991).
136. Venezia, A. M., Raimondi, F., La Parola, V., and Deganello, G., *J. Catal.*, **194**, 393–400 (2000).
137. Fedin, V., Czyzniewska, J., Prins, R., and Weber, T., *Appl. Catal.*, **213**, 123 (2001).
138. Benítez, A., Ramírez, J., Vazquez, A., Acosta, D., and López Agudo, A., *Appl. Catal.* **133**, 103 (1995).
139. Benítez, A., Ramírez, J., Fierro, J. L. G., and López Agudo, A., *Appl. Catal.* **144**, 343 (1996).
140. Sun, M., and Prins, R., *Stud. Surf. Sci. Catal.* **127**, 113 1999; *J. Catal.* **201** (2001) to be published.
141. Benítez, A., Ramírez, J., Cruz-Reyes, J., and López Agudo, A., *J. Catal.* **172**, 137 (1997).
142. van Veen, J. A. R., Gerkema, E., van der Kraan, A. M., Hendriks, P. A. J. M., and Beens, H., *J. Catal.* **133**, 112 (1992).
143. Pecoraro, T. A., and Chianelli, R. R., *J. Catal.* **67**, 430 (1981).
144. Eijsbouts, S., de Beer, V. H. J., and Prins, R., *J. Catal.* **109**, 217 (1988).
145. Eijsbouts, S., Sudhakar, C., de Beer, V. H. J., and Prins, R., *J. Catal.* **127**, 605 (1991).
146. Eijsbouts, S., de Beer, V. H. J., and Prins, R., *J. Catal.* **127**, 619 (1991).
147. Ledoux, M. J., and Djellouli, B., *J. Catal.* **115**, 580 (1989).

148. Vit, Z., and Zdrzil, M., *J. Catal.* **119**, 1 (1989).
149. Cinibulk, J., and Vit, Z., *Appl. Catal. A* **180**, 15 (1999).
150. Luck, F., *Bull. Soc. Chim. Belgium* **100**, 781 (1991).
151. de Beer, V. H. J., van der Aalst, M. J. M., Machiels, C. J., and Schuit, G. C. A., *J. Catal.* **43**, 78 (1976).
152. Duchet, J. C., van Oers, E. M., de Beer, V. H. J., and Prins, R., *J. Catal.* **80**, 386 (1983).
153. Qu, L., Flechsenhar, M., and Prins, R., to be published.
154. Maxwell, I. E., Minderhoud, J. K., Stork, W. H. J., and van Veen, J. A. R., in "Handbook of Heterogeneous Catalysis" (G. Ertl, H. Knözinger, and J. Weitkamp, Eds.), Vol. 4, p. 2017. Wiley-VCH, Weinheim, 1997.
155. Harvey, T., and Matheson, T. W., *J. Catal.* **101**, 253 (1986).
156. Zotin, J. L., Cattenot, M., Portefaix, J. L., and Breyse, M., *Bull. Soc. Chim. Belgium* **104**, 213 (1995).
157. Segawa, K., and Satoh, S., *Stud. Surf. Sci. Catal.* **127**, 129 (1999).
158. Ramírez, J., Ruiz-Ramírez, L., Cedeño, L., Harle, V., Vrinat, M., and Breyse, M., *Appl. Catal. A* **93**, 163 (1993).
159. Olguín, E., Vrinat, M., Cedeño, L., Ramírez, J., Borque, M., and López-Agudo, A., *Appl. Catal. A* **165**, 1 (1997).
160. Borque, M. P., López-Agudo, A., Olguín, E., Vrinat, M., Cedeño, L., and Ramírez, J., *Appl. Catal. A* **180**, 53 (1999).
161. Rana, M. S., Srinivas, B. N., Maity, S. K., Murali-Dhar, G., and Prasada Rao, T. S. R., *Stud. Surf. Sci. Catal.* **127**, 397 (1999).
162. Ziyad, M., Rouimi, M., and Portefaix, J. L., *Appl. Catal. A* **183**, 93 (1999).
163. Vissers, J. P. R., Bachelier, J., ten Doeschate, H. J. M., Duchet, J. C., de Beer, V. H. J., and Prins, R., in "Proceedings of the 8th International Congress on Catalysis" Vol. 2, p. 387. VCH, Weinheim, 1984.
164. de Beer, V. H. J., Derbyshire, F. J., Groot, C. K., Prins, R., Scaroni, A. W., and Solar, J. M., *Fuel* **63**, 1095 (1984).
165. Boorman, P. M., and Chong, K., *Energy Fuels* **6**, 300 (1992).
166. Hillerova, E., Vit, Z., Zdrzil, M., Shkuropat, S. A., Bogdanets, E. N., and Startsev, A. N., *Appl. Catal.* **67**, 231 (1991).
167. Vissers, J. P. R., Lensing, T. J., de Beer, V. H. J., and Prins, R., *Appl. Catal.* **30**, 21 (1987).
168. Vissers, J. P. R., Mercx, F. P. M., Bouwens, S. M. A. M., de Beer, V. H. J., and Prins, R., *J. Catal.* **114**, 291 (1988).
169. Laine, J., Labady, M., Severino, F., and Yunes, S., *J. Catal.* **166**, 384 (1997).
170. Severino, F., Laine, J., and López-Agudo, A., *J. Catal.* **189**, 244 (2000).
171. Meitzner, G., Mykytka, W. J., and Sinfelt, J. H., *J. Catal.* **98**, 513 (1986).
172. Reinhoudt, H. R., Troost, R., van Langeveld, A. D., van Veen, J. A. R., Sie, S. T., and Moulijn, J. A., *Stud. Surf. Sci. Catal.* **127**, 251 (1999).
173. Volpe, L., and Boudart, M., *J. Solid State Chem.* **59**, 332 (1985).
174. Lee, J. S., Oyama, S. T., and Boudart, M., *J. Catal.* **106**, 125 (1987).
175. Oyama, S. T., in "The Chemistry of Transition Metal Carbides and Nitrides" (S. T. Oyama, Ed.), p. 1. Blackie Academic, London, 1996.
176. Leary, K. J., Michaels, J. N., and Steacy, A. M., *J. Catal.* **107**, 393 (1987).
177. Neylon, M. K., Choi, S., Kwon, H., Curry, K. E., and Thompson, L. T., *Appl. Catal.* **183**, 253 (1999).
178. Dautzenberg, F. M., Helle, J. N., Biloen, P., and Sachtler, W. M. H., *J. Catal.* **63**, 119 (1980).
179. Prins, R., in "Chemistry and Chemical Engineering of Catalytic Processes" (R. Prins and G. C. A. Schuit, Eds.), p. 389. Sijthoff & Noordhoff, Rockville, MD, 1980.

180. Sellem, S., Potvin, C., Manoli, J. M., Contant, R., and Djéga-Mariadassou, G., *J. Chem. Soc. Chem. Commun.*, 359 (1995).
181. Miga, K., Stanczyk, K., Sayag, C., Brodzki, D., and Djéga-Mariadassou, G., *J. Catal.* **182**, 63 (1999).
182. Schlatter, J. C., Oyama, S. T., Metcalfe, J. E., and Lambert, J. M., *Ind. Eng. Chem. Res.* **27**, 1648 (1988).
183. Lee, K. S., Abe, H., Reimer, J. E., and Bell, A. T., *J. Catal.* **139**, 34 (1993).
184. Abe, H., Cheung, T., and Bell, A. T., *Catal. Lett.* **21**, 11 (1993).
185. Stanczyk, K., Kim, H. S., Sayag, C., Brodzki, D., and Djéga-Mariadassou, G., *Catal. Lett.* **53**, 59 (1998).
186. Ramanathan, S., and Oyama, S. T., *J. Phys. Chem.* **99**, 16365 (1995).
187. Ramanathan, S., Yu, C. C., and Oyama, S. T., *J. Catal.* **173**, 10 (1998).
188. Oyama, S. T., Yu, C. C., and Ramanathan, S., *J. Catal.* **184**, 535 (1999).
189. Sajkowski, D. J., and Oyama, S. T., *Appl. Catal.* **134**, 339 (1996).
190. van Veen, J. A. R., Minderhoud, J. K., Buglass, J. G., Lednor, P. W., and Thompson, L. T., *Mater. Res. Soc. Symp. Proc.* **368**, 51 (1995).
191. Aegerter, P. A., Quigley, W. W. C., Simpson, G. J., Ziegler, D. D., Logan, J. W., McCrea, K. R., Glazier, S., and Bussell, M. E., *J. Catal.* **164**, 109 (1996).
192. Li, S., Lee, J. S., Hyeon, T., and Suslick, K. S., *Appl. Catal.* **184**, 1 (1999).
193. Choi, J. G., Brenner, J. R., and Thompson, L. T., *J. Catal.* **154**, 33 (1995).
194. Milad, I. K., Smith, K. J., Wong, P. C., and Mitchell, K. A. R., *Catal. Lett.* **52**, 113 (1998).
195. Chu, Y., Wei, Z., Yang, S., Li, C., Xin, Q., and Min, E., *Appl. Catal.* **176**, 17 (1999).

Index

A

Ab initio method, prediction of microcrystal morphology, 280

Acetic acid
dissociative adsorption, 229–230
reactions on Cu/SiO₂, 219–231

Acetoxylation, with supported Pd catalysts, 60

Acetylene, interaction with MgO, 298

Acidic properties
and electric field, at cationic sites, 375–379
oxide and halide surfaces, 282–283

Adsorbate–adsorbate interactions, on MgO(001) faces, 293–294

Alcohol oxidation
Cr-catalyzed, 10–13
Ru catalysts incorporating Ru³⁺, 53–54
with supported Pd catalysts, 60–61
V-catalyzed, 10

Aldehyde, sacrificial, in metal-assisted oxidations, 38–39

Alkaline earth oxides
cubic structure, 300–301
surface reactivity, 301–302

Alkane
autoxidation with chelated Co polymers, 34
V hydroxylation, 7–9

Alkyl exchange, during olefin polymerization, 100–101

Alkyl hydroperoxides, as oxidants, supported Mo catalysts with, 41–49

Allylic alcohols, Ti epoxidation, 5–7

Aluminophosphates, Co-substituted, 32–34

Aluminum oxide, spectroscopic results after CO adsorption, 353–354

Amines, denitrogenation, 416–417

Ammonia, interaction with MgO, 296

Anchoring

covalent, to inorganic supports, 19–21

metallocene catalysts to supports, 136–142

Mo polymers, 46

oxidation catalyst, promotion of, 75

Aniline
benzene formed from, 413–414
HDN, 422–423

Aromatic compounds
Cu-catalyzed oxidation, 35–36
Fe- and Mn-catalyzed oxidation, 26–27
V-catalyzed hydroxylation, 9–10

Atactic polypropylenes, 119

B

Basic properties, oxide and halide surfaces, 282–283

Batch reactor, 174

Benzene
aniline reaction to, 413–414
product of quinoline HDN, 454

Benzene ring, hydrogenation, 418

Benzoquinolines, HDN, 427–428

Bis(cyclopentadienyl)titanium catalysts, 98–99

Bis(idenyl)zirconocene catalysts, 121
substituted, 127, 129

Bond energy, CO on NiO(001), 308

Borane monomers, in copolymerization of olefins, 148–149

n-Butane, isobutane conversion to, 233

C

Calcium oxide, CO adsorbed on, 300–301

Calorimetric methods, applied to adsorption sites, 282

Campbell's degree of rate control, 187–189

Carbon dioxide, interaction with MgO, 295

- Carbon molecular sieves, Mo-impregnated, 47–48
- Carbon monoxide
adsorbed on
 α -Al₂O₃, 353–354
CaO and SrO, 300–301
 α -Cr₂O₃, 342–345
LaCrO₃, 360–362
Mg sites, 290–292
polycrystalline Cu₂O/SiO₂, 334–336
ZnO, 321–327
CO/anatase system, 364–366
CO/MgO system, IR spectroscopy, 286–290
CO/NiO system, IR spectroscopy, 305–308
interaction with NaCl, 311–312
- Carbon monoxide probes
lanthanum oxide, 330
MgCr₂O₄, 354–358
NiO–MgO solid solutions, 315
polycrystalline α -Fe₂O₃, 351–352
- Carbon supports
hydrotreating catalysts, 450
porous, Mo, 47–48
- Carbonyl bands, adducts, 292–293
- Catalytic reactors, descriptions, 174–176
- C–C bonds, activation on Pt(111) and Pt(211), 213–215
- Cerium oxidation catalysts, 62
- C–H bonds
aliphatic, Co oxidation, 32–34
Cr oxidation, 10–13
- Chiral active centers, olefins, 130–131
- Chiral ligands, introduced into polymers, 45
- Chloride surfaces, vibrational spectroscopies, 276–279
- Chlorine, remaining in polymer from catalyst, 94
- meta*-Chloroperbenzoic acid, plus *N*-methyl-morpholine-*N*-oxide, 19
- α -Chromic oxide
C₂H₄ adsorption and C₂H₄/CO coadsorption, 345–348
CO adsorbed on, IR spectroscopy, 342–345
dispersed materials and crystal films, comparison, 338–342
H₂ adsorption, 348
hydrogenation/dehydrogenation reactions, 349–350
interaction with NO, 348–349
polycrystalline surface properties, 337–338
- Chromium
Cr^{x+}/SiO₂, 367–374
epoxidations catalyzed by, 13
MgCr₂O₄ surface properties, 354–358
- Chromium oxidation catalysts, alcohol, 10–13
- CH_xO species, interactions with Cu surfaces, 223, 226–227
- C₂H_x species, adsorbed on Pt, 206–208, 215–219
- C–N bond breaking
aliphatic, 414–419
aromatic, 412–414
- Cobalt
Co–Mo–S model, 408–409
promoter action in HDS, 410
- Cobalt catalysts
CoMo, carbon interaction, 441
Co–Mo/Al₂O₃, 403–407
- Cobalt oxidation catalysts
aliphatic C–H bonds with O₂ or peroxides, 32–34
phenolic reactants, 31–32
thiol, 30–31
- Cobalt oxide
CoO–MgO solid solutions, 318–319
sintered, CO on, 309–311
- Cocatalysts
functions, 106–109
olefin polymerization, 103–109
- Collision theory, 172
- Compensation effects, unintentional, 217
- Condensation, MAO cocatalyst, 106–108
- Conservation, sensitivity, 184–187
- Continuous-flow stirred tank reactor, 174–176
- Copolymerization
metallocenes for, 112–116
olefins, with borane monomers, 148–149
- Copolymers
cycloolefin, 144–145
films made from, 112
- Copper oxidation catalysts
aromatic compounds, 35–36
supported Cu perhalophthalocyanines, 37–38
wet oxidation with liquid-phase reactants, 36–37

- Copper/SiO₂, reactions of ethanol, ethyl acetate, and acetic acid on, 219–231
- Corundum structure, oxides, 270–271, 337–354
- Cubic structure
alkaline earth oxides, 300–301
halides, 311–312
- Cubic systems, solid solutions, 312–319
- Cupric oxide
polycrystalline Cu₂O/SiO₂, CO adsorption on, 334–336
polycrystalline systems, 333–334
- Cuprite structure, 270
- Cuprous oxide, single crystals, 270
- Cyclohexane autoxidation, Co-AlPO-5 in, 33
- Cyclohexene autoxidation, Cr-catalyzed, 11
- Cycloolefins
copolymers, 144–145
homopolymerization, 142–143
- Cyclopolymerization, dienes, 147–149
- D**
- Decahydroquinoline
HDN network, 439–440
in HDN of quinoline, 423–425
- Decavanadate pillars, 8–9
- De Donder relations, kinetic parameters identified from, 179–181
- Deep oxidation, with liquid-phase reactants, 36–37
- Dehydrogenation
alkanes on supported Cr catalysts, 349–350
catalytic or oxidative, methanol, 336–337
ethylbenzene, catalyzed by α -Fe₂O₃, 352–353
isobutane on supported Pt/Sn, 191–204
- Density functional theory, 406–407, 412
- Depollution, anchored Fenton catalysts in, 29
- Deuterium
incorporated into isobutane, 196–197
tracing, reaction kinetics analysis, 198–199
- Diatomic molecules, vibrational spectra, 276–278
- Dibenzothiophene, HDS, 430–431
- Dienes, metallocene-catalyzed polymerization, 147–149
- Dihydroxylation, olefins, Os-catalyzed, 68–69
- Dimensionless sensitivity, 182–183
- 2,4-Dimethyl-1-heptene, formed by 1,2 insertions, 132–134
- Diol spacer, between tartrates, 6
- Dioxiranes, ketones converted to, 71–73
- Diphenylmethane, Cr-catalyzed autoxidation, 11
- Dispersed materials, surface definition, 274–276
- E**
- Edge decoration model, Ni–Mo–S, 406–407
- Elastomers, produced by metallocene catalysts, 103
- Electric fields
and acidity at cationic sites, 375–379
at Lewis acid (Ca³⁺) sites, 345
- Electron donors, propylene polymerization, 93
- Electrostatic fields, at surfaces of oxides and halides, 280–282
- Elimination
ring-opening, piperidine, 421
syn and trans, 414–416
- Enthalpy changes
adsorption of acetic acid, 229
differential, hydrogen and isobutylene adsorption, 194–195
and results of reaction kinetics analysis, 218–219
- Entrapment, Mn(BPY)₂²⁺ in zeolite cages, 15–16
- Entropy
fitted, 203, 218
local, 239–240
rotational and vibrational, 169–171
standard changes for adsorption of acetic acid, 229
- Environmental applications
catalysts, 162
Cu₂O, 333
hydrotreating, 400
- Epoxidation
enantioselective, Mn catalysts for, 17–21
by metal-centered peracid, 38
Mn and Fe porphyrin catalysts, 24–25
- Equilibrium constant, isobutane dehydrogenation, 200–201

- Ethane hydrogenolysis, on silica-supported Pt, 204–219
- Ethanol, reactions on Cu/SiO₂, 219–231
- Ethene, adsorbed on Cr³⁺, 346
- Ethyl acetate
dissociative adsorption, 229–230
reactions on Cu/SiO₂, 219–231
- o*-Ethylaniline, indoline ring opening to, 425
- Ethylbenzene, dehydrogenation, catalyzed by α -Fe₂O₃, 352–353
- Ethylene
adsorption on Pt(111) and Pt(211), 210–213
C₂H₄/CO coadsorption on α -Cr₂O₃, 345–348
homopolymerization,
metallocene-catalyzed, 109–112
polymerization, heat removal, 92
and propylene, copolymerization, 113, 116
ZnO-catalyzed hydrogenation, 327–329
- Ethylene oxide, MgO-catalyzed oligomerization, 303
- Experimental results
ethane hydrogenolysis on Pt, 205–206
isobutane dehydrogenation on supported Pt/Sn, 193–197
reactions of ethanol, ethyl acetate, and acetic acid on Cu/SiO₂, 220–223
- F**
- Faces
 α -Cr₂O₃ sintered microcrystals, 341–348
LaCrO₃, neutral and nonpolar, 359–363
MgO(001), adsorbate–adsorbate interactions on, 293–294
- Fenton reactions, with immobilized Fe catalysts, 28–29
- Ferric oxide
dehydrogenation of ethylbenzene, 352–353
sintered polycrystalline α -Fe₂O₃, 351–352
- Films
 α -Cr₂O₃, 338–342
made from copolymers, 112
surface definition, 274–276
- Flexibility, ligand, increased, 126–127
- Fluorine, as promoter of hydrotreating catalysts, 443–447
- Fluorine centers, role in reactivity of electron-rich MgO surfaces, 299–300
- Force field method, prediction of microcrystal morphology, 280
- Full width at half maximum, adducts, 292–293
- G**
- Gas-phase reactions, transition state theory, 168–169
- Geometric methods, prediction of microcrystal morphology, 279
- Giant clusters, Pd, ligand-stabilized, 61
- H**
- Halides
cubic structure, 311–312
HRTEM and SEM, 274–276
redox properties, 283–284
rock salt structure, 268–270
catalytic activity, 284–319
surfaces
acidic and basic properties, 282–283
electrostatic fields at, 280–282
Wurtzite structure, 270
catalytic activity, 319–329
- HDN, *see* Hydrodenitrogenation
- HDS, *see* Hydrodesulfurization
- Heat of adsorption, CO adsorbed on Mg sites, 290–292
- Hexagonal structure, oxides: La₂O₃, 271
- High-resolution transmission electron microscopy, *see* HRTEM
- High-surface-area solids, surface morphology, 278–279
- Homopolymerization
cycloolefin, 142–143
ethylene, metallocene-catalyzed, 109–112
- Horiuti–Polanyi reaction scheme, 192, 197–199
- HRTEM, oxides and halides, 274–276
- Hydride transfer, rate constant, 242
- Hydrocracking, heavy gas oil, 400
- Hydrocracking catalysts
F added to, 443–444
silica-alumina in, 448–449
- Hydrodenitrogenation
catalyst structure
active sites, 407–412

oxidic catalyst precursor, 401–402
sulfidic catalyst, 402–407
fluorine as promoter, 443–447
kinetics, 432–440
on metals, metal carbides, and metal nitrides, 451–457
metal sulfides and supports, 447–450
phosphorus as promoter, 440–443
reaction mechanisms
 C–N bond breaking, 412–419
 hydrotreating mixtures, 429–432
 specific molecules, 419–429
Hydrodesulfurization
 dibenzothiophene, 430–431
 fluorine effect, 445
 Ni and Co promoter action, 410
 phosphorus effect, 440
Hydrogen
 adsorption
 on α -Cr₂O₃, 348
 differential enthalpy changes, 194–195
 on Pt(111) and Pt(211), 208–210
 adsorption sites on ZnO, model, 325–327
 effect on polyethylene molecular weight, 111–112
 interaction with MgO, 294–295
 probe of ZnO surface sites, 325
Hydrogenation
 alkanes on supported Cr catalysts, 349–350
 ethylene, ZnO-catalyzed, 327–329
 propylcyclohexene, 434–436
Hydrogenolysis
 ethane, on silica-supported Pt, 204–219
 metal carbides and nitrides, 453
Hydrogen peroxide, oxidant for Mo
 oxidation catalyst, 49–52
Hydrogen transfer, during olefin polymerization, 100–101
Hydrotreating
 of mixtures, 429–432
 role of metals, metal carbides, and metal nitrides, 451–456
Hydrotreating catalysts
 active sites, 407–412
 C–N bond breaking, 412–419
 history of, 400–401
 oxidic catalyst precursor structure, 401–402
 P and F as promoters, 440–447
 sulfidic catalyst structure, 402–407

I

Immobilization
 noncovalent, methods, 21
 Os compound as diolate complex, 69
Impregnation, inorganic materials by Mo, 41–42
Indole
 conversion, 456
 HDN, 425–426
Infrared spectroscopy
 CO adsorbed on α -Cr₂O₃, 342–345
 combined with microcalorimetry, 282
 CO/MgO system, 286–290
 CO/NiO system, 305–308
 NO/NiO system, 308–309
Initiation step, metallacyclic intermediate role, 373–374
Inorganic compounds, Fe-catalyzed and Mn-catalyzed oxidation, 27–28
Inorganic supports
 covalent anchoring to, 19–21
 V epoxidation and alkane hydroxylation catalysts, 8–9
Insertion
 in copolymerization, mechanism, 113–114
 olefins, 125–127
 propene into metal-carbon bond, 151
Iron catalysts
 immobilized, Fenton and related reactions with, 28–29
 olefin polymerization, 95
 porphyrin and phthalocyanine, 21–28
Isobutane
 dehydrogenation on supported Pt/Sn, 191–204
 on solid acid catalysts
 kinetic model parameterization, 238–243
 reaction kinetics analysis results, 243–244
 reaction scheme, 231–238
 sensitivity of kinetic model, 244, 257
Isobutylene
 adsorption, differential enthalpy changes, 194–195
 deuterium incorporation, 196–197
Isoquinoline, hydrogenation, 417–418
Isotactic polypropylenes, 119–122

K

Ketones, conversion to dioxiranes, 71–73

Kinetic model

- choice of reaction scheme, 165–166
- parameterization, 229–230, 238–243
- in terms of transition states, 177–179
- rate constant estimation, 167–176
- sensitivity analysis of, 199–200

Kinetic parameters, reaction scheme, 176–189

Kinetics

- HDN, 432–440
- metallocenes, 97–99

L

Langmuir–Hinshelwood kinetics, 432–433

Lanthanum, hexagonal structure, 271

Lanthanum oxide

- carbonite bands, 332–333
- CO as probe, 330
- highly basic centers, 331–332

Layered double hydroxides

- CuMgAl-LDH-CO₃, 36
- decavanadate pillared, 8–9
- intercalated with polymeric W anions, 64–65
- Mo-exchanged, 49–50
- RuCoAl-LDH-CO₃, 53–54
- with sulfonated phthalocyanines, 31

Leaching

- Cr into solution, 11
- metal from solid catalyst, 39
- W, 66

Liquid-phase catalysts, supported, Pd, 61–62

Liquid-phase reactants, deep oxidation with, 36–37

M

Magnesium

- adducts, carbonyl band widths, 292–293

MgCr₂O₄ surface properties, 354–358

Magnesium oxide

- catalysis of
 - (CH₂)₂O oligomerization, 303
 - phenol alkylation and amidation, 304

CO/MgO system, IR spectroscopy, 286–290

CoO–MgO solid solutions, 318–319

electron-rich surfaces, reactivity of, 299–300

interaction with other simple molecules, 294–298

metal-doped, 298–299

MgO(001) faces, adsorbate–adsorbate interactions on, 293–294

NiO–MgO solid solutions, 315–317

NiO–MgO system as catalyst, 317–318

Manganese catalysts

- for enantioselective epoxidation, 17–21
- nonheme-type, in two-electron achiral redox processes, 15–17
- porphyrin and phthalocyanine, 21–28
- solid, one-electron redox reactions, 13–15

MAO, *see* Methylalumoxane

Material balances, for reactants and products of reaction, 174–176

MCM-41

- catalyst retention in, 5
- Cr(salen)⁺ complex in, 13
- Cu-exchanged, 35
- immobilization of dioxoMo(VI) complexes, 48
- Mn-exchanged, 20–21
- Mo entities on, 41–42
- Ti silsesquioxane in, 4

Metal

assisted oxidations with sacrificial aldehyde, 38–39

catalytic species, extraction from supports, 2

MgO doped with, 298–299

Metal carbides, HDN on, 451–456

Metal-free oxidation catalysts

- dioxiranes, 71–73
- nitroxyl radicals, 73–74
- peracids, 70–71

Metallocene catalysts

advantages of, 102–103

α -olefin polymerization

- polypropylene microstructures, 118–125
- regio- and stereospecificity, 116–117
- anchoring to supports, 136–142
- ethylene homopolymerization, 109–112
- olefin polymerization, 95

- Metallocenes
 cycloolefin homopolymerization, 142–143
 kinetics, 97–99
 stabilities of, 127–129
 Metal nitrides, HDN on, 451–456
 Metal oxide, solid solutions, 312–314
 Metal sulfides, HDN, 447–450
 Methane, interaction with MgO, 297–298
 Methanol, oxidative dehydrogenation, 336–337
 Methylalumoxane
 adsorption on supports, 136
 cocatalyst for olefin polymerization, 102, 106–109
 as scavenger, 139–140
 structure, 104
 Methylcyclohexene, hydrogenation, 437
 Methyl methacrylate, polymerization, 150–151
N-Methyl-morpholine-*N*-oxide, plus *meta*-chloroperbenzoic acid, 19
 Methyltrioxorhenium, 67–68
 Microcrystals
 CoO, 309–311
 α -Cr₂O₃, morphology and surface structures, 338–342
 lanthanum oxide, 332–333
 morphology prediction
 force field and ab initio methods, 280
 geometric methods, 279
 ZnO, 320
 Microkinetic analyses, catalytic reaction, 162–163
 Microstructure, polypropylenes, 118–125
 Model equations, CSTR, 198
 Molecular weight
 polyethylenes produced by metallocene catalysts, 111–112
 polymers, controlling, 125
 Molybdenum blue–charcoal catalyst, 51
 Molybdenum catalysts
 alkyl hydroperoxides as oxidants, 41–49
 Co–Mo/Al₂O₃, 403–407
 H₂O₂ as oxidant, 49–52
 molecular O₂ as oxidant, 52
 Ni–Mo/Al₂O₃, 444–445
 Ni–Mo–P/Al₂O₃, 436
 Molybdenum disulfide, Ni atoms adsorbed on, 404–407
 Mustard, conversion to nontoxic sulfoxide, polyMo in, 48
- N**
- Nickel
 Ni–Mo/Al₂O₃ catalysts, 444–445
 Ni–Mo–P/Al₂O₃ catalysts, 436
 Ni–Mo–S edge decoration model, 406–407
 Nickel complexes, in olefin polymerization, 95, 97
 Nickel oxide
 CO/NiO system, IR spectroscopy, 305–308
 NiO–MgO solid solutions, 315–317
 NiO–MgO system as catalyst, 317–318
 NO/NiO system, IR spectroscopy, 308–309
 Nickel sulfide catalysts, C-supported, 409
 Nitric oxide
 disproportionation into N₂O, 318
 interaction with
 α -Cr₂O₃, 348–349
 MgO, 295
 NO/NiO system, IR spectroscopy, 308–309
 probe for NiO–MgO solid solutions, 315–317
 Nitrogen
 on LaCrO₃, spectrum, 362–363
 polycyclic molecules containing, HDN of, 427–429
 Nitroxyl radicals, as oxidation catalysts, 73–74
 Norbornene, metallocene-catalyzed polymerization, 143
- O**
- Octahedral molecular sieves, Mn redox solids as, 13–14
 Octahydroindole, indoline hydrogenation to, 425–426
 Olefins
 cis dihydroxylation products, 16–17
 copolymerization, metallocene role, 112–116
 dihydroxylation, 55
 Os catalysts, 68–69
 epoxidation with alkyl hydroperoxides, 41–42
 insertion of, 125–127
 oligomerization, 129–135

- Olefins (*continued*)
 polymerization, mechanism, 99–102
 primary, observed in reactor effluent, 234–235
 α -Olefins, metallocene-catalyzed polymerization, 116–125
- Oligomerization
 adsorbed olefin species, 235–236
 (CH₂)₂O, MgO-catalyzed, 303
 olefins, 129–135
- Organometallic sources, Ti, 4–5
- Osmium dihydroxylation catalysts, olefins, 68–69
- Oxides
 corundum structure, 270–271, 337–354
 electric field and acidity at cationic sites, 375–379
 hexagonal structure, La₂O₃, 271
 HRTEM and SEM, 274–276
 perovskite structure, 272
 redox properties, 283–284
 rock salt structure, 268–270
 catalytic activity, 284–319
 surfaces
 acidic and basic properties, 282–283
 electrostatic fields at, 280–282
 vibrational spectroscopies, 276–279
 TiO₂, 272–273, 363–366
 Wurtzite structure, 270
 catalytic activity, 319–329
 ZrO₂, 366–367
- Oxidic catalyst precursor, HDN, 401–402
- Oxycarbides, hydrotreating catalysts, 452
- Oxygen
 molecular
 interaction with MgO, 295
 as oxidant for supported Mo catalysts, 52
 singlet, generators, 50
- Oxygen-rebound mechanism, 25
- P**
- Palladium catalysts
 supported
 acetoxylation with, 60
 alcohol oxidation with, 60–61
 liquid-phase, 61–62
 Wacker-type, 56–59
- Paper industry, Fe and Mn oxidation of aromatic compounds, 26–27
- Paraffin
 hydroxylation
 Fe and Mn in, 25–26
 and ketonization, 55
 oxidation, Cu perhalophthalocyanine catalysts, 37–38
- Penicillin G, conversion to sulfoxide, 51
- Peracid
 metal-centered epoxidations, 38
 regeneration, 70–71
- Perfluorophenylborane, cocatalyst for olefin peroxidation, 105–106
- Perfluorophenylborate, as promoter, 108–109
- Perovskites
 LaCrO₃, structure of neutral and nonpolar faces, 359–363
 stoichiometry, 358–359
 structure, 272
- Perruthenate, derived catalyst, 54
- Phenol, alkylation and amination, MgO-catalyzed, 304
- Phenolic reactants, Co oxidation, 31–32
- Phillips catalyst, polyolefin manufacture, 93–94
- Phosphate, effect on hydrogenation reactions, 442–443
- Phosphorus, as promoter of hydrotreating catalysts, 440–443
- Phthalocyanine
 Co, 30–32
 Mn and Fe, 21–28
- Pillared clay
 Cr, 12
 Cu²⁺ associated with, 36
 Ti, 5–6
 V, 8–9
- Piperidine, HDN, 420–422
- Plastics
 advantage of metallocene catalysts, 102–103
 polyolefins, 90–91
- Platinum
 Pt(111)
 C–C bond activation on, 213–215
 ethylene adsorption on, 210–211
 hydrogen adsorption on, 208–210
 Pt(211)
 C–C bond activation on, 213–215
 ethylene adsorption on, 211–213
 hydrogen adsorption on, 208–210

- silica-supported, ethane hydrogenolysis on, 204–219
 - Platinum/tin catalysts, supported, isobutane dehydrogenation on, 191–204
 - Plug flow reactor, 174–175
 - Polybenzimidazole, affinity for Mo complexes, 46–47
 - Polycyclic molecules, N-containing, HDN of, 427–429
 - Polyethylene
 - molecular weight, hydrogen effect on, 111–112
 - produced by metallocene catalysts, 103
 - Polymerization
 - olefins, mechanism, 99–102
 - propylene, 138
 - electron donors, 93
 - Polymers
 - Mo, anchoring, 46
 - molecular weight, controlling, 125
 - polyoxyethylene, base-catalyzed synthesis, 304
 - three-dimensional structures, 151–152
 - Polymer supports
 - chiral Schiff base covalent linking, 18–19
 - colloidal, Mo-exchanged, 50–51
 - Mo complexes, 42–47
 - V epoxidation and alkane hydroxylation catalysts, 7–8
 - Polyolefins
 - manufacturing processes, 91–92
 - technological importance, 90–91
 - Polyoxyethylene, base-catalyzed synthesis, 304
 - Polypropylene
 - metallocene polymerization catalysts, 95
 - microstructures, 118–125
 - Polytartrates, Ti, branched, 6–7
 - Porous carbon supports, Mo, 47–48
 - Porphyrins
 - Co, 30–32
 - Mn and Fe, 21–28
 - Potassium, effect on reactivity of silica-supported Pt/Sn, 201–204
 - Powders, ZnO microcrystalline, 320
 - Probes
 - adsorbed, vibrational spectra, 278–279
 - CO, *see* Carbon monoxide probes
 - o*-Propylaniline, in HDN of quinoline, 423–425, 434–439
 - Propylcyclohexene, hydrogenation, 434–436, 443
 - Propylene
 - and ethylene, copolymerization, 113, 116
 - polymerization, 138
 - electron donors, 93
 - stereoblock, 124–125
 - P–W catalysts, 63–64
 - Pyridine, HDN, 420–422, 433, 456
 - thiophene effect, 429–431
- Q**
- Quinoline
 - HDN, 418, 423–425, 447, 454
 - HDN network, 434
- R**
- Rate constant
 - adsorption and desorption, 240
 - estimation for kinetic model, 167–176
 - forward and reverse, 186–187
 - hydride transfer, 242
 - individual, net rate sensitivity to, 181–184
 - Rate control
 - degree of: Campbell's, 187–189
 - temperature effect, 257
 - Rate-determining step, confusion regarding, 188–189
 - Reaction kinetics
 - ethane hydrogenolysis on Pt, 205–206
 - isobutane dehydrogenation on Pt/Sn, 197–200
 - Reaction kinetics analysis
 - based on simplified rate expression, 200–204
 - C₂H_x species adsorbed on Pt, 215–219
 - ethanol, ethyl acetate, and acetic acid on Cu/SiO₂, 228–231
 - isobutane on solid acid catalysts, 243–244
 - Reaction scheme
 - choice, for kinetic model, 165–166
 - ethane hydrogenolysis, 215–217
 - ethanol, ethyl acetate, and acetic acid on Cu/SiO₂, 228
 - formulation, case studies for, 189–257
 - isobutane
 - dehydrogenation on Pt/Sn, 197–198
 - on solid acid catalysts, 231–238
 - kinetic parameters, 176–189

- Redox couples, supported, in Wacker catalysis, 59
- Redox properties, oxides and halides, 283–284
- Redox reactions
 one-electron, solid Mn catalysts, 13–15
 two-electron, nonheme-type Mn catalysts, 15–17
- Regiospecificity, metallocene-catalyzed polymerization of α -olefins, 116–117
- Resins, cross-linked polystyrene, Mo support, 42, 45
- Retention mechanism, in copolymerization, 114–115
- Reversibility
 microscopic, 173
 reaction steps, 180
- Rhenium oxidation catalysts, 67–68
- Rock salt structure, oxides and halides, 268–270, 284–319
- Ruthenium catalysts, paraffin hydroxylation and ketonization, 55
- Ruthenium oxidation catalysts
 in epoxidation, 55
 incorporating Ru³⁺, for alcohols, 53–54
 water, 56
- S**
- Salen ligands
 Cr, 13
 immobilization methods, 21
- Scanning electron microscopy, oxides and halides, 274–276
- Schiff bases
 chiral, covalent linking to polymeric supports, 18–19
 immobilization, 17
- β -Scission process, 233–234, 241
- SEM, *see* Scanning electron microscopy
- Sensitivity
 conservation, 184–187
 net rate, to individual rate constants, 181–184
- Sensitivity analysis, of kinetic model, 199–200, 244, 257
- Ship-in-a-bottle synthesis
 Mn(BPY)₂²⁺, 15–16
 porphyrins in zeolites, 22
 zeolite entrapment of salen ligands by, 21
- Silicas
 amorphous, transition metal ions supported on, 367–374
 impurities in, effects on hydrotreating, 448
 mesoporous
 Mo complexation onto, 48–49
 Mo-substituted, 52
 Zr-containing, 40
- Silicon dioxide
 amorphous, with and without transition metal ions, 273–274
 Cr^{x+}/SiO₂, 367–374
 Cu/SiO₂, reactions of ethanol, ethyl acetate, and acetic acid on, 219–231
 polycrystalline Cu₂O/SiO₂, CO adsorption on, 334–336
- Simplified rate expression, reaction kinetics analysis based on, 200–204
- Single crystals, oxides, surface definition, 274–276
- Singlet oxygen, generators, 50
- Sintered materials
 dimensions of α -Cr₂O₃ microcrystals, 339–342
 polycrystalline α -Fe₂O₃, 351–352
 surface morphologies, 276–278
- Slabs
 MoS₂, Mo–O–Al bonds, 441
 Pt, adsorption on, 206–213
- Sodium chloride, CO interaction with, 311–312
- Solid acid catalysts, isobutane on
 kinetic model parameterization, 238–243
 reaction kinetics analysis results, 243–244
 reaction scheme, 231–238
 sensitivity of kinetic model, 244, 257
- Solid solutions, cubic systems, 312–319
- Spinels
 MgCr₂O₄ surface properties, 354–358
 normal and inverse structures, 271–272
- Stereoblock propylenes, 124–125
- Stereospecificity
 mechanism
 insertion of olefins, 125–127
 oligomerization of olefins, 129–135
 stabilities of metallocenes, 127–129
 metallocene-catalyzed polymerization of α -olefins, 116–117
- Sticking coefficients, isobutane on Pt, 203
- Stretching frequency, CO adsorbed on

Al³⁺ ions, 353–354
Cr³⁺ ions, 344–345
Strontium oxide, CO adsorbed on, 300–301
Styrene polymerization catalysts, 146–147
Sulfidic catalyst, HDN, 402–407
Sulfoxidation, Cu-catalyzed, 37
Sulfur, Ni–Mo–S edge decoration model, 406–407
Supported liquid-phase catalysts, Pd, 61–62
Surface reactivity, alkaline earth oxides, 301–302
Syndiotactic polypropylene, 122–124

T

Tartrate, modified solid Ti catalyst, 5–6
Temperature
catalyst performance dependent on, 140
effect on
olefin yield, 111
rate control, 257
glass transition, 143–144
heat removal from ethylene polymerization, 92
oligomerization, 135
polymerization, 149
Tetraethoxysilane, partly replaced by Ti(OiPr)₄, 5
Tetragonal phase, ZrO₂, 367
1,2,3,4-Tetrahydroquinoline, HDN, 423–425
2,2,6,6-Tetramethyl-1-piperidinyloxy, as oxidation catalyst, 73–74
Thermodynamic consistency, 172–173
Thiophene
effect on pyridine HDN, 429–431
HDS, 441
Tin, Pt/Sn catalysts, isobutane dehydrogenation on, 191–204
Titanium, zeolites, 3
Titanium dioxide
hydrotreating catalysts, 449–450
rutile and anatase, 272–273
surface structure and reactivity, 363–366
Titanium epoxidation catalysts
solid achiral, 4–5
supported Sharpless, 5–7
Titanium(IV) alkyls, reduction during olefin evolution, 100

Titanium trichloride, Ziegler–Natta catalysts incorporating, 93
Todorokite structure, Mn, 14
Toluene, product of quinoline HDN, 454
Transition metal ions
amorphous TiO₂ with and without, 273–274
supported on amorphous silica, 367–374
Transition states, parameterization of kinetic model in terms of, 177–179
Transition state theory, 167–171
Translational entropies, 171
Triazacyclononane, complex with Mn, 17
Triisobutylaluminum, as scavenger, 139
2,4,6-Trimethyl-1-heptene, formed by 1,2-insertions, 134
Tungsten catalysts, fluorine effects, 445–447
Tungsten oxidation catalysts
heteronuclear peroxoW associations, 63–64
H₂O₂ as oxygen donor, 62–63
use of LDHs, 65

V

Vanadium epoxidation catalysts
inorganic supports, 8–9
polymer supports, 7–8
Vanadium hydroxylation catalysts
alkane, 7–9
aromatic compounds, 9–10
Vanadium oxidation catalysts, alcohol, 10
Vibrational spectra, oxide and chloride surfaces, 276–279
Vinylidene species, di-σ/π, 213

W

Wacker-type catalysts, Pd, 56–59
Water
interaction with MgO, 296–297
oxidation, Ru catalysts, 56
Wurtzite structure, oxides and halides, 270
catalytic activity, 319–329

Z

Zeolite A, Mnⁿ⁺ immobilized on, 14–15
Zeolites
calcined, MoCl₅-impregnated, 41

- Zeolites (*continued*)
 calcined, MoCl₅-impregnated (*continued*)
 in hydrocracking catalysts,
 448–449
 Pd/Cu ion-exchanged, 58
 Pt/Sn/KLTL, 192–193, 203–204
 as solid solutions, 314
Zeolite USY, support of chiral Mo
 complexes, 48–49
Zeolite Y
 encapsulated Fe-phthalocyanine, 26
 Mn(BPY)₂²⁺ in, 15–16
Zeolite ZSM-5, Fe-exchanged, 28–29
Ziegler–Natta catalysts, polyolefin
 manufacture, 92–93
- Zinc oxide
 activation temperatures, 320
 band model of catalysis, 319–320
 CO adsorbed on, 321–325
 H₂ adsorbed on, 325
 reactions catalyzed by, 327–329
Zirconium dioxide
 pure, 366–367
 surface-modified, 367
Zirconium oxidation catalysts, 40
Zirconocenes
 catalytic activities, 120–122
 combined with MAO, 102–103
 structure, condensation rate dependent
 on, 107–108

Preface

This volume of *Advances in Catalysis* builds foundations of fundamental understanding at the atomic and molecular scales in support of technologically important catalytic processes. The first two chapters forge links between molecular (homogeneous) catalysis and catalysis occurring analogously—and sometimes more successfully—on surfaces. The following three chapters are concerned with advances in classical surface catalysis building on concepts of reaction kinetics and surface characterization.

De Vos, Sels, and Jacobs illustrate strategies of immobilizing molecular oxidation catalysts on supports. The catalysts include complexes of numerous metals (e.g., V, Cr, Mn, Fe, Co, and Mo), and the supports include oxides, zeolites, organic polymers, and activated carbons. Retention of the catalytically active metal species on the support requires stable bonding of the metal to the support at every step in the catalytic cycle, even as the metal assumes different oxidation states. Examples show that catalysts that are stably anchored and do not leach sometimes outperform their soluble analogs in terms of lifetimes, activities, and selectivities.

Kaminsky assesses metallocene-catalyzed polymerization of olefins and diolefins, briefly placing the subject in the historical context of Ziegler–Natta and Phillips polymerization and summarizing recent advances that illustrate how design of catalytic sites on solid supports leads to control over the stereochemical and physical properties of polymeric products. Single-site catalysts consisting, for example, of zirconium complexes combined with methylalumoxane permit control over the polymer tacticity and molecular weight distribution and make possible the synthesis of new copolymers and elastomers in addition to the conventional homopolymers of ethylene and propylene. This is a subject that knits together molecular catalysis, surface catalysis, and polymer science. The lively research in olefin polymerization today is motivated substantially by the growing industrial applications of new metallocene catalysts.

Cortright and Dumesic present an update of progress in reaction kinetics, showing how it is providing a broader and sturdier foundation for heterogeneous catalysis. The chapter illustrates how the power of computers and modern theoretical methods, exemplified by density functional theory, allow the incorporation of numerous elementary steps and realistic models of

catalytic sites into reaction kinetics models. Examples with comparisons of experimental and theoretical results show the success of the methods.

Zecchina *et al.* consider the characterization of structure, morphology, and surface reactivity of microcrystals of a wide range of oxides and halides. They address the morphology of microcrystals by high-resolution transmission electron microscopy, which allows the determination of the most abundant crystal faces. The structural information is used to analyze and interpret the vibrational spectra of adsorbed probe molecules and reaction intermediates, calorimetric data are related to the information from vibrational spectroscopy. The chapter includes examples illustrating the relationships between surface structures of oxides and halides and their catalytic properties. The approach and the data characterizing samples with controlled morphologies tie together dispersed catalytic materials, on the one hand, and single crystals and epitaxial films, on the other hand.

Prins summarizes advances in understanding of the reactions in catalytic hydrodenitrogenation (HDN), which is important in hydroprocessing of fossil fuels. Hydroprocessing is the largest application in industrial catalysis based on the amount of material processed. The chapter addresses the structures of the oxide precursors and the active sulfided forms of catalysts such as Ni-promoted Mo or W on alumina as well as the catalytically active sites. Reaction networks, kinetics, and mechanisms (particularly of C–N bond rupture) in HDN of aliphatic, aromatic, and polycyclic compounds are considered, with an evaluation of the effects of competitive adsorption in mixtures. Phosphate and fluorine promotion enhance the HDN activity of catalysts; explanations for the effect of phosphate are summarized, but the function of fluorine remains to be understood. An account of HDN on various metal sulfides and on metals, metal carbides, and metal nitrides concludes this chapter.

H. KNÖZINGER
B. C. GATES

Contributors

Numbers in parentheses indicate the pages on which the authors' contributions begin.

- S. BORDIGA, *Department of Inorganic, Physical and Material Chemistry, University of Turin, I-10125 Turin, Italy* (265)
- R. D. CORTRIGHT, *Department of Chemical Engineering, University of Wisconsin, Madison, Wisconsin 53706* (161)
- DIRK E. DE VOS, *Centre for Surface Chemistry and Catalysis, Katholieke Universiteit Leuven, 3001 Leuven, Belgium* (1)
- J. A. DUMESIC, *Department of Chemical Engineering, University of Wisconsin, Madison, Wisconsin 53706* (161)
- PIERRE A. JACOBS, *Centre for Surface Chemistry and Catalysis, Katholieke Universiteit Leuven, 3001 Leuven, Belgium* (1)
- WALTER KAMINSKY, *Institute for Technical and Macromolecular Chemistry, University of Hamburg, 20146 Hamburg, Germany* (89)
- C. LAMBERTI, *Department of Inorganic, Physical and Material Chemistry, University of Turin, I-10125 Turin, Italy; and INFN U.d.R. di Torino Università* (265)
- R. PRINS, *Laboratory for Technical Chemistry, Federal Institute of Technology, 8092 Zurich, Switzerland* (399)
- D. SCARANO, *Department of Inorganic, Physical and Material Chemistry, University of Turin, I-10125 Turin, Italy* (265)
- BERT F. SELS, *Centre for Surface Chemistry and Catalysis, Katholieke Universiteit Leuven, 3001 Leuven, Belgium* (1)
- G. SPOTO, *Department of Inorganic, Physical and Material Chemistry, University of Turin, I-10125 Turin, Italy* (265)
- A. ZECCHINA, *Department of Inorganic, Physical and Material Chemistry, University of Turin, I-10125 Turin, Italy* (265)